STABILITY ANALYSIS OF TUNNELS AND UNDERGROUND OPENINGS

A Thesis submitted by

Fadhil Kurdi Mohammed Al-Asadi

For the award of

Doctor of Philosophy

Year 2020

ABSTRACT

This thesis investigates both undrained and drained stability of three various configurations of underground openings related to tunnelling (i.e. tunnel heading, single circular tunnel and twin circular tunnels) in both two-dimensional (2D) and three-dimensional (3D) spaces. Finite element limit analysis (*FELA*) is used to determine lower and upper bound stability limits for a range of various geometrical and material scenarios. The thesis is divided into two parts.

Part A focuses on the undrained stability analysis using Broms and Bennermarks' original stability number (*N*). For the 2D undrained analysis, the factor of safety values was calculated using the shear strength reduction method (*SSRM*) in *FELA*, while for the 3D undrained analysis, the critical supporting pressure values were calculated using the load multiplier method (*LMM*) in *FELA*. The relationships between the factor of safety and the stability number (*N*), which includes design soil and geometry parameters, were investigated for active (collapse) and passive (blowout) failures. Several design charts, tables and equations were produced to better assist in understanding these relationships.

Part B focuses on drained analysis using tunnel stability factors (F_c, F_s and F_γ). This approach is convenient for stability analysis of underground openings with a wide range of angle of internal friction (ϕ = 0 - 40˚) and depth ratios (*C/D* = 1 - 10). The critical support pressure required to maintain stability can then be determined by substituting the corresponding factors in a conventional equation that is analogous to Terzaghi's bearing capacity equation.

Although the *FELA* technique can define the actual failure load from below (lower bound solution) and from above (upper bound solution), the obtained results were compared with available solutions (theoretical, experimental and numerical) in the published literature. Also, the finite difference method (*FDM*), via the software *FLAC* 2D has been used over the same parametric range to validate the 2D (*FELA*) results for tunnel heading, single circular tunnel and twin circular tunnels under undrained condition.

This thesis contributes significantly to practising engineers as comprehensive design tables, figures and equations have been produced for the design of tunnel stability using the rigorous upper and lower bound solutions in both 2D and 3D spaces.

CANDIDATE'S CERTIFICATION

This Thesis is entirely the work of Fadhil Kurdi Mohammed Al-Asadi except where otherwise acknowledged. The work is original and has not previously been submitted for any other award, except where acknowledged.

Principal Supervisor: Dr Jim Shiau

Associate Supervisor: Dr Ali Mirzaghorbanali

Student and supervisors' signatures of endorsement are held at the University.

ACKNOWLEDGEMENTS

"In the name of Allah, the beneficent, the merciful."
I want to initiate the acknowledgment with Allah (God) who has provided me with the strength and wisdom to finish my thesis.

Special thanks are given to the Iraqi Ministry of Higher Education and Scientific Research for providing me with the scholarship to achieve this research. The financial support from the ministry is much appreciated.

I am thankful for the people who made this journey possible.
First and foremost, I would like to thank my supervisor, Dr Jim Shaiu, for his continuous technical expertise, availability, enthusiasm, encouragement and support. The tremendous time and effort spent with the published five Q1 journals during the study period as well as the final polishing of this thesis are much appreciated.

Secondly, I would like to thank all my colleagues at Dr Shiau's Underground Tunnelling Research Group at USQ. I am thankful to Mathew Sams, Mohammad Mirza Hassan, Ji-Sung Lee, Shanika Kiriella, Brian Lamb, Jay Lobwein and Alexander Bell, for their friendship during this journey. I am also thankful to my co-supervisor Dr Ali Mirzaghorbanali, for his support whenever needed.

Last but not least, I would like to thank my family for their much-needed encouragement and moral support. To my wife and my son and daughter, thank you for providing me with the confidence to do so with my head held high. I could never have stayed the course were it not for the love and support of my wife "Iman", you never failed me when I needed the support. It is to my wife and Taha and Abrar that I dedicate this thesis.

This thesis would not have been possible without all the above support.

TABLE OF CONTENTS

LIST OF FIGURES

LIST OF TABLES

LIST OF ABBREVIATIONS

2D	Two-dimensional
3D	Three-dimensional
C	Cover depth above the tunnel crown
D	Tunnel diameter or height
C/D	Tunnel cover-to-diameter ratio
c´	Drained soil cohesion
E	Surface failure extent
E/D	Surface failure ratio
FD	Finite difference
FDM	Finite difference method
FELA	Finite element limit analysis
FLAC	Fast Lagrangian analysis of continua
FoS	Factor of safety
F_c	Stability factor for cohesion
F_s	Stability factor for surcharge
F_γ	Stability factor for unit weight
H	Tunnel axis depth from the ground surface
LB	Lower bound
LMM	Load multiplier method
N	Stability number
N_c	Critical stability number
OPR	Overburden pressure ratio

OptumG2	2D finite element limit analysis software
OptumG3	3D finite element limit analysis software
P	Unlined length behind the tunnel face
P/*D*	Unlined heading ratio
PRM	Pressure relaxation method
S	The centre-to-centre distance between the tunnels
S/D	Spacing ratio
$(S/D)_{min}$	Minimum spacing ratios
S_c	Critical shear strength at collapse
SPR	Supporting pressure ratio
SSRM	Shear strength reduction method
S_u	Undrained shear strength of the soil
UB	Upper bound
$\gamma D/S_u$	Shear strength ratio
σ_s	Ground surface pressure
σ_t	Tunnel internal pressure
ϕ	Soil internal friction angle
ϕ'	Drained soil internal friction angle
γ	Soil self-weight

CHAPTER 1: INTRODUCTION

1.1 Background

The steady increase in population growth in the world's cities led to increasing demand for traffic systems (roads, railroads, metros) and community services (sewers, water pipelines). Due to the scarcity of available areas and surface congestion, tunnels and ground structures are used to accommodate the required infrastructures.

Construction of tunnels or underground openings in soft ground inevitably induces ground movement and may affect the nearby surface and subsurface facilities. Ensuring stability is directly related to the safety of the adjacent structures and successful construction of the tunnel or the underground opening. Therefore, stability analysis for tunnels has been carried out using various methods, and many publications have been produced (Davis et al. 1980; Atkinson & Mair 1981; Leca & Dormieux 1990; Assadi & Sloan 1991; Anagnostou & Kovári 1996; Lyamin & Sloan 2000; Vermeer et al. 2002; Wilson et al. 2011; Mollon et al. 2013; Sloan 2013; Yamamoto et al. 2013; Krabbenhoft & Lyamin 2015; Yang et al. 2015; Zhang et al. 2015; Ukritchon, Yingchaloenkitkhajorn, et al. 2017; Shiau & Al-Asadi 2018)

The rapid development of computers and simulation software coupled with advances of tunnelling techniques and machinery means that tunnels are now safer, cheaper, and more time-efficient than ever concerning operation and construction. Some infrastructure, such as the crossing of a subway line under the historical buildings, can only be implemented by using tunnelling machines for their unique controls in minimising disturbances caused by excavation (Guglielmetti et al. 2008). As stated by Pelizza (1996) "going underground is not only to free the ground surface but also to improve the quality of life".

As no universally recognised tunnel analysis method is available for the stability problems, it still is a subject where some improvement could be made to aid tunnel designers. Thus, the goal of this study is to equip design engineers with simple design tools to determine the stability of underground openings.

1.2 Research Objectives and Scope of Work

The primary objective of this thesis is to develop numerical models that accurately simulate the internal pressure of a boring machine during tunnel construction. The research problems being studied are the undrained and drained stability of three various configurations of underground openings related to tunnelling (i.e. tunnel heading, single circular tunnel and twin circular tunnels) in two- and three-dimensional spaces. Both two- and three- dimensional finite element limit analyses are conducted using the shear strength reduction method (for 2D analysis) and the limit analysis (for 3D analysis) with homogenous undrained and drained soil models. Parametric investigations are implemented using dimensionless ratios for tunnel geometry and soil parameters and stability.

For the stability problem in a cohesive soil, the solution is defined using the Broms and Bennermark approach. This approach has been adopted in this research with the aim of producing systematic solutions which can be used to estimate the collapse and blowout conditions based on respective stability number. This method is particularly useful to relate factors of safety to a wide range of loading scenarios, tunnels configurations and soil parameters. Also, the associated failure extent of the ground surface has been determined in the event of the tunnel collapse, which is useful for the analytical upper bound that requires a priori assumption in relation to the general form of the failure mechanism.

The empirical method remains as the most widely used for drained tunnel stability analysis in cohesive-frictional soil. It is the aim of this study to develop novel tunnel stability factors (F_c, F_s and F_γ) for calculating the critical internal pressure required to maintain stability at collapse for various soil and geometry parameters in 2D and 3D spaces. This approach is not unfamiliar to engineers, as these comprehensive tunnel stability factors are analogous to the bearing capacity factors (N_c, N_s and N_γ) used in Terzaghi's bearing capacity equation. The produced solutions would contribute significantly to the tunnel engineers in their daily practices.

1.3 Organisation of the Thesis

Chapter 2 - Literature Review

This chapter presents the literature review related to the stability of tunnels and underground openings in a wide range of soils (cohesive, cohesive-frictional and cohesionless) under undrained and drained conditions. Also, the methods for tunnel and underground openings stability analysis in 2D and 3D are reviewed. These include analytical, experimental and numerical.

Chapter 3: Numerical Modelling Review

This chapter presents the two types of computer modelling techniques that are used in this study. Review the development of the finite element limit analysis and the modelling techniques in both of the finite element limit analysis and the finite difference method (*FLAC*). This followed by a discussion of the methods implemented in these programs, the shear strength reduction method and the pressure relaxation method.

Part A: Undrained Analysis

This part of the thesis presents the stability of three various configurations of underground opening related to tunnelling (tunnel heading, single circular tunnel and twin circular tunnels) in a homogeneous cohesive soil under undrained conditions. In such soil where no volume loss during plastic shearing, stability results are independent of loading directions, and the combination of surcharge, self-weight and internal supporting pressures can produce failure either in collapse or blowout. Therefore, the stability of tunnels and underground openings (in collapse or blowout) can be described by Broms and Bennermark's stability number (N), which combine soil and geometry parameters with all stresses into a single dimensionless number

Chapter 4: Undrained Analysis of 2D Tunnel Heading

This chapter investigates the two-dimensional stability of an idealised plane strain tunnel heading in a cohesive soil under undrained conditions. The shear strength reduction method in *FELA* is used to obtain rigorous upper bound and lower bound factors of safety for the models under different combinations of pressures. The factor of safety results, which are functions of the stability number and depth ratio, are

compared and validated by using the finite difference method as well as other existing solutions available in the literature. The dimensionless ratios employed in this study make the design charts suitable to cover a broad range of tunnel geometries and soil parameters. The charts can also be used to provide an estimation of internal tunnelling pressures, making them useful for designers and practising engineers.

Chapter 5: Undrained Analysis of 2D Single Circular Tunnel

This chapter investigates the two-dimensional stability of an idealised plane strain single circular tunnel in a cohesive soil under undrained conditions by using the two-dimensional finite element limit analysis (*FELA*) program and the shear strength reduction method (*SSRM*). The variations of the factor of safety and the critical stability number are presented for a series of tunnel cover-to-diameter ratios (*C/D*) in both collapse and blowout scenarios. The obtained results are compared and validated by using the finite difference method as well as other existing solutions available in the literature. The dimensionless ratios employed in this study make the design charts suitable to cover a broad range of tunnel geometries and soil parameters.

Chapter 6: Undrained Analysis of 3D Analysis of Single Circular Tunnel

This chapter investigates the three-dimensional stability of a single circular tunnel in a cohesive soil under undrained conditions using three-dimensional upper and lower bound finite element limit analysis. Dimensionless ratios are used in this study to cover practical soil parameters and tunnel depths for collapse and blowout analyses. Numerical results of critical stability numbers are compared with two-dimensional and three-dimensional solutions available in the literature. Stability design charts and tables produced in this paper can be used to estimate safety factors for various design parameters.

Chapter 7: Undrained Analysis of 2D Analysis of Twin Circular Tunnel

This chapter investigates the stability of twin circular tunnels horizontally aligned in cohesive undrained soil under plane strain conditions. The shear strength reduction method (*SSRM*) in the two-dimensional finite element limit analysis (*FELA*) program is used to obtain rigorous upper and lower bounds of the factor of safety for various depth ratios (*C*/*D*) and centre to centre spacing ratios (*S*/*D*) between the tunnels. The variations of the factor of safety have been presented for different combinations of

stability numbers (N) and geometries (C/D and S/D). The factor of safety and the stability number results are compared and validated by using the finite difference method as well as other existing solutions available in the literature.

Chapter 8: Undrained Analysis of 3D Analysis of Twin Circular Tunnel

This chapter investigates the three-dimensional (3D) heading stability of twin circular tunnels horizontally aligned in cohesive undrained clayey soil. A recently developed 3D finite element limit analysis technique is used to obtain rigorous upper bound and lower bound critical stability numbers at collapse and blowout. The interaction effects of the distance between the tunnels on the stability are determined for a series of tunnel cover-to-diameter ratios. As an additional verification of the rigorous bounding solutions, the obtained stability results are compared with other published solutions available in the literature.

Part B: Drained Analysis

This part focuses on the use of tunnel stability factors to estimate critical supporting pressures. The primary method adopted is a conventional equation based on the soil property and tunnel stability factors, analogous to the bearing capacity factors (N_c, N_s and N_γ) of strip footings. The chapters in this part investigate the 2D and the 3D stability of tunnels and underground openings in a general soil ($\phi = 0^\circ - 40^\circ$) under drained conditions, based on tunnel stability factors (F_c, F_s and F_γ).

Chapter 9: Drained Analysis of 2D Analysis of Tunnel Heading

This chapter investigates the two-dimensional stability of an idealised plane strain tunnel heading in a general soil ($\phi = 0^\circ - 40^\circ$) under drained conditions. The finite element limit analysis (*FELA*) is employed to determine rigorous upper bound (*UB*) and lower bound (*LB*) solutions of stability factors (F_c, F_s and F_γ), which are functions of the depth ratio (C/D) and soil internal friction angle (ϕ). The obtained results are compared and validated by using the finite-difference method as well as other available published results in the literature.

Chapter 10: Drained Analysis of 2D Analysis of Single Circular Tunnel

This chapter investigates the two-dimensional stability of an idealised plane strain single circular tunnel in a general soil ($\phi = 0^\circ - 40^\circ$) under drained conditions. The

finite element limit analysis (*FELA*) is employed to determine rigorous upper bound (*UB*) and lower bound (*LB*) solutions of stability factors (F_c, F_s and F_γ), which are functions of the depth ratio (*C/D*) and soil internal friction angle (ϕ). These factors can be used to determine the radial pressure acting on the exposed periphery of the tunnel to maintain stability at collapse. The obtained results are compared and validated by using the finite-difference method as well as other available published results in the literature.

Chapter 11: Drained Analysis of 3D Analysis of Single Circular Tunnel

This chapter investigates the three-dimensional stability of a single circular tunnel in a general soil (ϕ = 0˚ – 40˚) under drained conditions. Numerical simulations are performed to study the face stability of a circular tunnel for various soil properties and tunnel cover-to-diameter ratios. Three-dimensional finite element limit analysis (*FELA*) is employed to determine rigorous upper and lower bounds solutions of tunnel stability factors (F_c, F_s and F_γ), which are functions of the depth ratio and soil internal friction angle. These stability factors are used to estimate the critical heading pressures at collapse. The obtained results are compared with existing published solutions in the literature.

Chapter 12: Drained Analysis of 2D Analysis of Twin Circular Tunnel

This chapter investigates the two-dimensional stability of an idealised plane strain twin circular tunnels in a general soil (ϕ = 0˚ – 40˚) under drained conditions. The finite element limit analysis (*FELA*) is employed to determine rigorous upper bound (*UB*) and lower bound (*LB*) solutions of stability factors (F_c, F_s and F_γ), which are functions of the depth ratio (*C/D*), soil internal friction angle (ϕ) and centre to centre spacing ratios (*S*/*D*) between the tunnels. These factors can be used to determine the radial pressure acting on the exposed periphery of the tunnel to maintain stability at collapse. The obtained results are compared and validated by using the available published results in the literature.

Chapter 13: Drained Analysis of 3D Analysis of Twin Circular Tunnel

This chapter investigates the three-dimensional stability of twin circular tunnels in a general soil (ϕ = 0˚ – 40˚) under drained conditions. Numerical simulations are performed to study the face stability of circular tunnels in various soil properties and

tunnel diameter-to-depth ratios. Three-Dimensional finite element limit analysis (*FELA*) is employed to determine rigorous upper and lower bounds solutions of tunnel stability factors (F_c, F_s and F_γ), which are functions of the depth ratio, soil internal friction angle and centre to centre spacing ratios between the tunnels. These stability factors are used to estimate the critical radial pressure acting on the exposed periphery of the tunnel at collapse. The obtained results are compared with existing published solutions in the literature.

Chapter 14: Conclusion

This chapter concludes the thesis by summarising the work and highlighting the major findings. Recommendations are also made regarding future research related to the topic of stability problems based on the findings of this thesis. Figure 1.1 outlines the thesis structure and the relationship between the chapters.

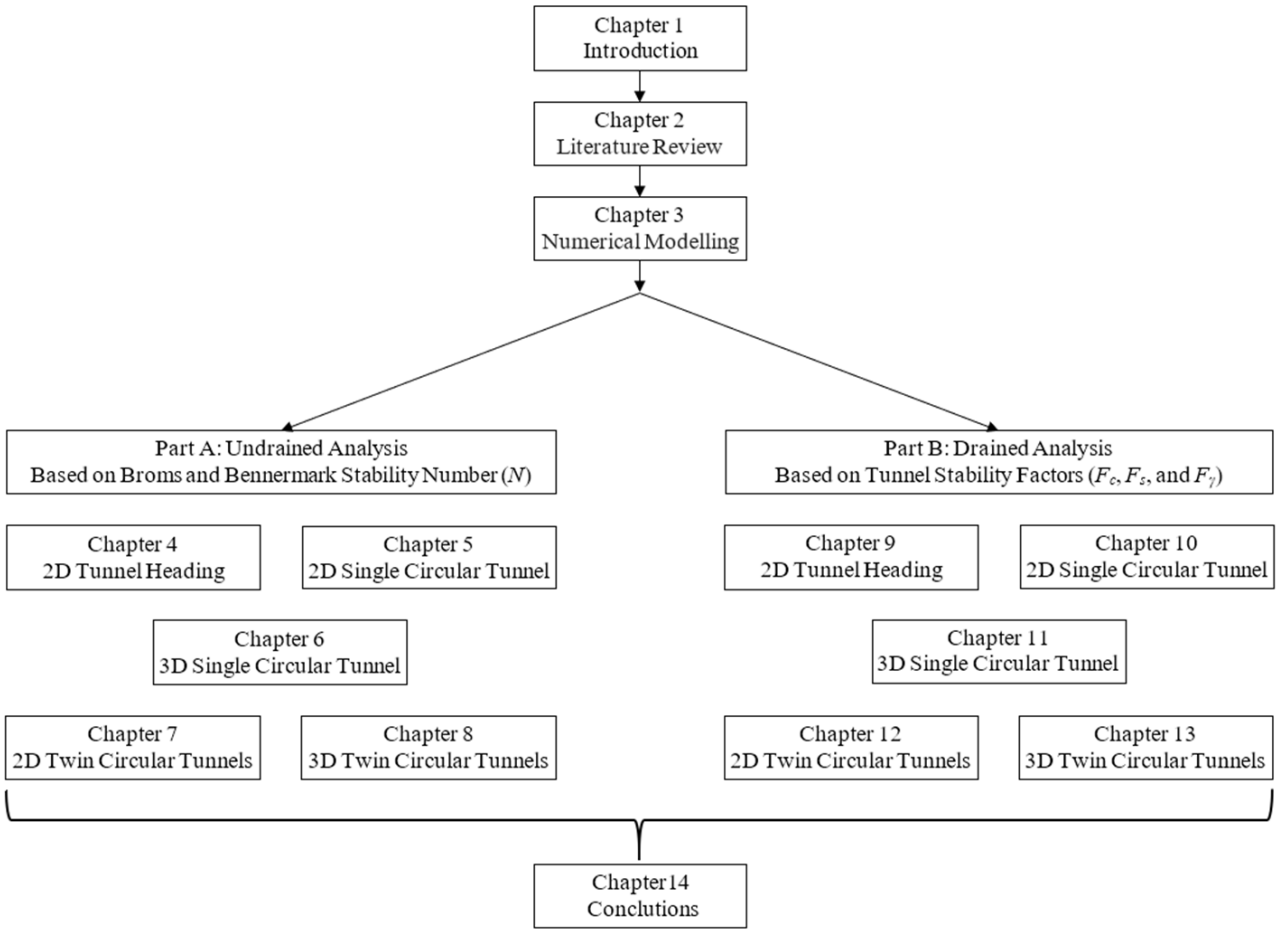

Figure 1.1. Outlines of the thesis structure and the relationship between the chapters.

1.4 Publications

The following Q1 journal papers have been published during the period of PhD study.

- Shiau, J & Al-Asadi, F 2018, 'Revisiting Broms and Bennermarks' original stability number for tunnel headings', *Géotechnique Letters*, vol. 8, no. 4, pp. 310-315. https://doi.org/10.1680/jgele.18.00145
- Shiau, J & Al-Asadi, F 2020, 'Determination of critical tunnel heading pressures using stability factors', *Computers and Geotechnics*, vol. 119, p. 103345. https://doi.org/10.1016/j.compgeo.2019.103345
- Shiau, J & Al-Asadi, F 2020, 'Two-dimensional tunnel heading stability factors F_c, F_s and F_γ', *Tunnelling and Underground Space Technology*, vol. 97, p. 103293. https://doi.org/10.1016/j.tust.2020.103293
- Shiau, J & Al-Asadi, F 2020, 'Three-Dimensional Analysis of Circular Tunnel Headings using Broms and Bennermarks' Original Stability Number', *International Journal of Geomechanics*. https://doi.org/10.1061/(ASCE)GM.1943-5622.0001734
- Shiau, J & Al-Asadi, F 2020, 'Three-Dimensional Heading Stability of Twin Circular Tunnels', *Geotechnical and Geological Engineering*. https://doi.org/10.1007/s10706-020-01201-z
- Shiau, J & Al-Asadi, F 2020, 'Stability Analysis of Twin Circular Tunnels Using Shear Strength Reduction Method', *Géotechnique Letters*, vol. 10, no. 2, pp. 1-9. https://doi.org/10.1680/jgele.19.00003

The following Q1 journal papers are currently under review.

- Shiau, J & Al-Asadi, F 2020, 'Twin Tunnels Stability Factors F_c, F_s and F_γ', *Geotechnical and Geological Engineering* (Under review; submitted on 25 February 2020).
- Shiau, J & Al-Asadi, F 2020, 'Revisiting Circular Tunnel Stability using Broms and Bennermarks' Original Stability Number', International Journal of Geomechanics (Submitted on 27 February 2020).

CHAPTER 2: LITERATURE REVIEW

2.1 Introduction

In most of the world's congested cities, and due to the depletion of surface areas, tunnels are built to accommodate highways (Streets, subways, railroad) and public services (water duct and sewer lines).

Peck (1969) proposed three design criteria to be considered in tunnel design and construction that are stability analysis, structural design of the lining and settlement in the short and long term. This thesis focuses on the first criterion (stability analysis) because the second criterion is mostly a structural problem, while the third criterion is the consequences of the instability. The investigation of the stability of the tunnels and the underground openings are conducted either under undrained condition or under drained condition depending on the permeability and the type of soil. The permeability of the soil can be used as a measure to determine the conditions of the stability analysis. Anagnostou and Kovári (1996) proposed that the drained conditions tend to apply when the ground permeability is higher than 10-7 to 10-6 m/s such as in sandy soil. In the other hand, because the collapse of the tunnel is usually a sudden incident, hence for a clayey, low-permeability soil, it is convenient to use the undrained shear strength for the stability analysis (Davis et al. 1980).

The following literature reviews are directly linked to the stability problems of tunnels and underground openings in both cohesive undrained soil and cohesive and/or frictional soils.

2.2 Stability Analysis in Cohesive Soils

The stability of tunnels and underground openings is most often described by the stability number (*N*) in Broms and Bennermark (1967). The stability number (*N*) is defined in equation (2.1).

$$N = \frac{\sigma_s + \gamma H - \sigma_t}{S_u} \tag{2.1}$$

Where σ_s is the surcharge on the ground surface and σ_t is the internal tunnel pressure. H is the depth of the opening axis that is equal to $(C + D/2)$, C is the tunnel cover and D is the diameter of the opening. S_u and γ represent the undrained shear strength and the unit weight of the soil, respectively (Figure 2.1).

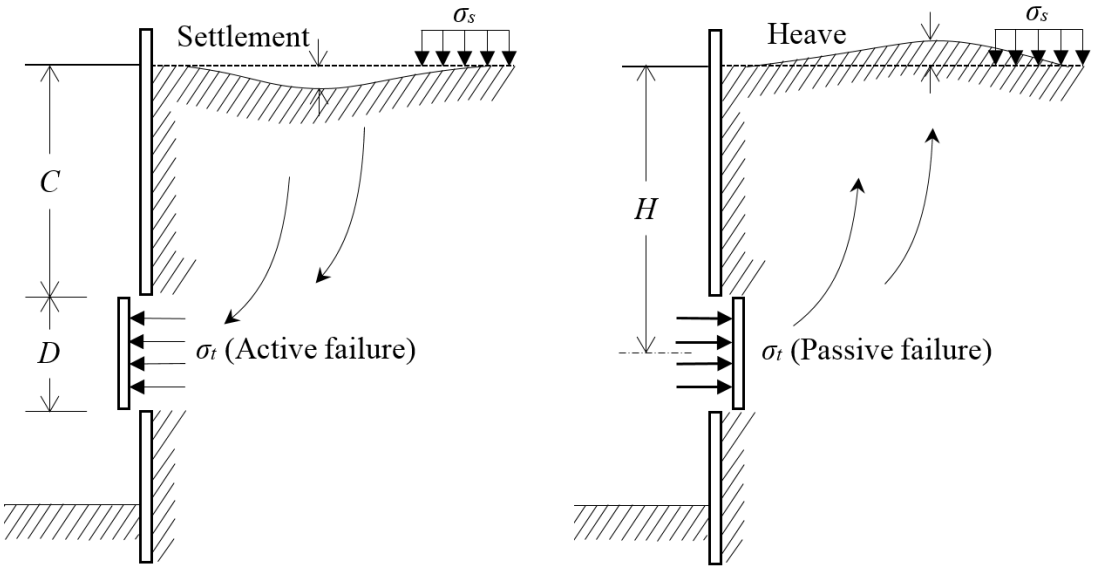

Figure 2.1. Vertical wall stability model of Broms and Bennermark (1967).

Following the bottom heave study of strutted excavations by Bjerrum and Eide (1956), it was concluded that failure occurs when the difference between the overburden pressure and the supporting pressure $(\sigma_s + \gamma H - \sigma_t)$ exceeds the undrained shear strength (S_u) by six to eight times. The value of "six to eight" is Broms and Bennermark's critical stability number (N_c) and it is dependent on the shape of the opening and the roughness of the vertical retaining wall. There was no mention of the depth ratio (C/D) effect on the critical stability number (N_c) in their study. Also, they stated that a general failure occurs when the centre of the opening is located at a depth

less than four diameters of the openings; otherwise, the failure will be local and extends one diameter above the opening (Figure 2.2).

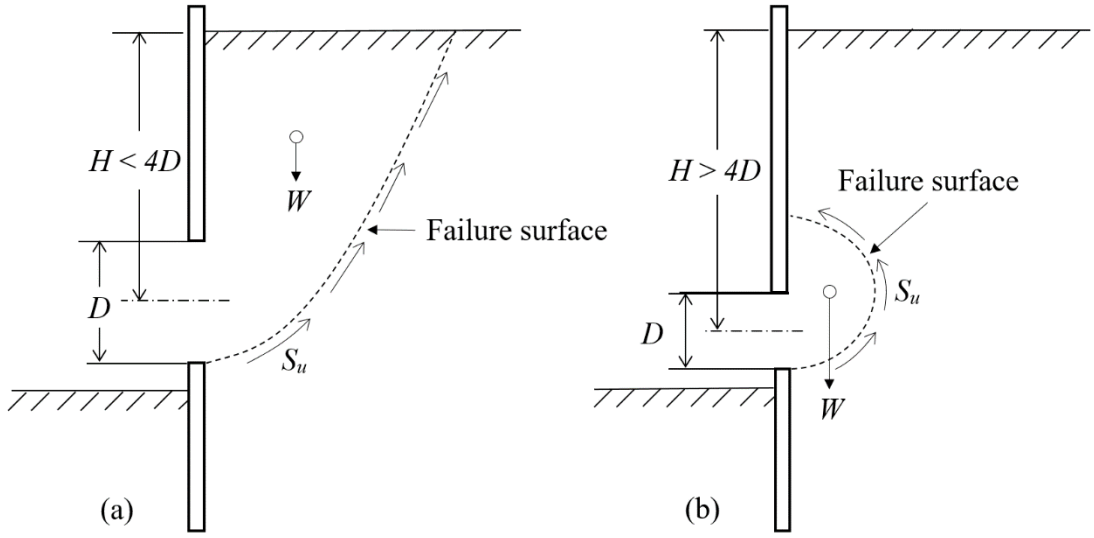

Figure 2.2. (a) General shear failure, (b) Local shear failure (Broms and Bennermark, 1967).

Following this important research, many laboratory experiments and centrifuge model tests were carried out. During the 1970s at Cambridge University, numerous studies were completed on centrifuge models by Atkinson and Cairncross (1973), they investigated the stability of unlined circular tunnels in overconsolidated kaolin clay and proposed a limit equilibrium mechanism which appears to give good predictions of the drained collapse load, at least for small values of *C/D*.

Mair (1979) investigated the experimental and theoretical undrained collapse of two-dimensional circular tunnel sections and three-dimensional cylindrical tunnel headings in normally consolidated kaolin clay under different geometry and gravity regimes.

Using centrifuge tests for shallow tunnels (*C/D* = 1 – 3.5), Kimura and Mair (1981) investigated the effect of the heading ratio *P/D* on the stability of an unsupported three-dimensional cylindrical heading. They concluded that the critical stability number (*N*) value depends on the geometry of the unlined tunnel heading ratio (*P/D*) and depth ratio (*C/D*), as shown in Figure 2.3.

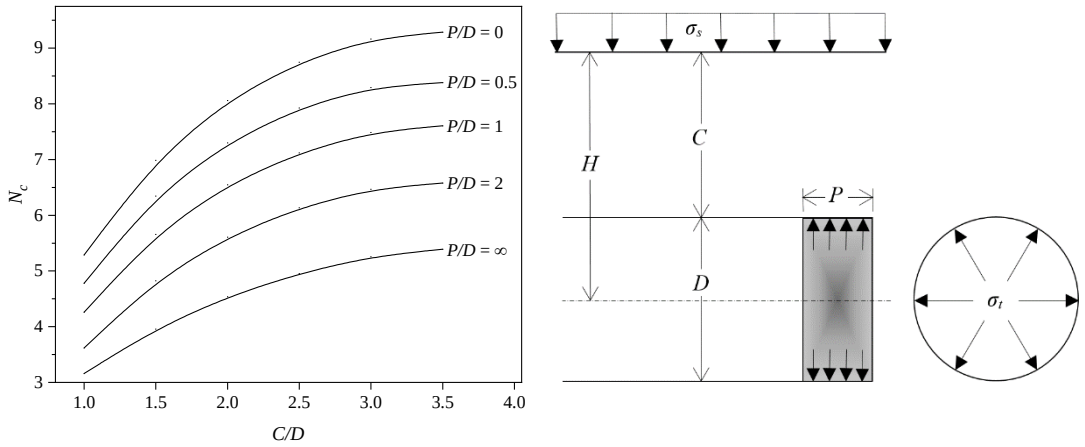

Figure 2.3. N_c vs C/D for various heading ratio (P/D) by Kimura and Mair (1981).

Their experiments showed that a significant drop in the stability occurred as P/D increased from 0 to 1, with the collapse mechanism becoming essentially two-dimensional once this ratio exceeded 3. Davis et al. (1980) followed Broms and Bennermarks' stability number (N) and derived analytical upper and lower bound undrained stability solutions for shallow underground openings. The problem was defined as to calculate the critical values of pressure ratio ($(\sigma_s - \sigma_t)/S_u$) that is a function of independent parameters such as the depth ratio (C/D) and the strength ratio ($\gamma D/S_u$), as indicated in Equation 2.2.

$$\frac{\sigma_s - \sigma_t}{S_u} = f\left(\frac{C}{D}, \frac{\gamma D}{S_u}\right) \tag{2.2}$$

It is well known that the undrained stability solution is independent of loading directions in the homogeneous soils owing to $\phi_u = 0$, Davis's pressure ratio approach did not appear to reduce the complexity of presenting the results. Indeed, the strength ratio ($\gamma D/S_u$) has been considered in Broms and Bennermarks' stability number equation, which is more effective and efficient in this aspect (Shiau & Al-Asadi 2018).

Interestingly, ($\gamma D/S_u$) has little effect on the final critical stability number (N_c) solutions unless it is very large, meaning that either the tunnel diameter D is very large (C/D very small) or S_u is very small, it was a noticeable effect on the stability results. In this case, the soil pressure distribution is highly nonlinear. Numerically speaking, it is an unstable case, and one may not get a solution for such an extreme case. If we do get a solution, it may become inaccurate due to numerical non-convergence. This is also self-evidenced from the linear relationship between the pressure ratio ($(\sigma_s - \sigma_t)/S_u$) and

the strength ratio ($\gamma D/S_u$) in the published literature (Augarde et al. 2003; Wilson et al. 2011; Ukritchon & Keawsawasvong 2017; Zhang et al. 2018).

Since the introduction of the rigid block mechanism by Davis et al. (1980) to the stability analysis in cohesive soils, many kinematic approaches have been proposed. Osman et al. (2006) have developed upper bounds solutions for obtaining the stability of a circular tunnel in clay, based on an assumed collapse mechanism, that is, within the boundary of the deformation mechanism, the soil was assumed to deform compatibly following a Gaussian distribution, and outside this mechanism, the soil was assumed to be rigid. Klar et al. (2007) suggested a new kinematic approach in limit analysis theory for two-dimensional (2D) and three-dimensional (3D) stability analyses of circular tunnels in a purely cohesive soil based on an admissible continuous velocity field. Osman (2010) investigated the undrained stability number of twin tunnels using upper-bound calculations. A new methodology for calculating an upper bound for twin tunnels based on the superposition of the plastic deformation mechanisms of each tunnel was proposed.

(Mollon et al. 2009, 2010; Mollon et al. 2011) improved the rigid block failure mechanisms, to produce appropriate solutions in a good agreement with the results of centrifuge tests in cohesive and frictional soils. They argue that the analytical approach based on rigid blocks failure mechanisms yields misleading results for purely cohesive soils when compared with centrifuge tests results. The reason for that, in a cohesive soil, the collapse of the tunnel does not appear to be rigid blocks motion as in frictional soil, but a smooth movement of the soil particles "flowing" towards the tunnel (Schofield 1980).

Therfore, Mollon et al. (2013) developed two continuous velocity fields for the collapse and blowout of a pressurised tunnel face in purely cohesive soil. Those continuous velocity fields were based on the normality condition, which states that any plastic deformation in a purely cohesive soil develops without any volume change. The continuous velocity field results have shown significant improvements compared with the other approaches.

Zhang et al. (2018) presented a kinematic approach of limit analysis to the face stability of circular tunnels in undrained clay, adopting a continuous velocity field to determine the critical collapse and blow-out pressures. They show that the strength

ratio ($\gamma D/S_u$) has little influence on the Broms and Bennermarks' original stability number (N). Huang et al. (2019) developed a new failure mechanism based on a velocity field for the stability of a plane strain circular tunnel in undrained soil. They compared the obtained mechanism with some analytical and numerical failure mechanisms.

However, the application of the limit analysis, with an assumption of the collapse mechanism, becomes limited to solve only simple problems. Moreover, the accuracy of the results depends on the assumptions involved in defining the failure mechanism. To overcome these limitations, more robust numerical formulations were developed by using finite elements and mathematical programming while implementing the limit analysis. For various underground openings and tunnels geometries, the rigorous upper and lower bounds solutions were obtained by many researchers.

Applying the early versions of *FELA* methods (finite element and linear programming), Assadi and Sloan (1991) investigate the stability of shallow square tunnel in undrained condition, followed by Sloan and Assadi (1991) published on a similar topic but with the soil cohesion increasing with depth. This approach was then extended to account for 2D circular tunnels in Sloan and Assadi (1992) and plane strain headings in Sloan and Assadi (1994). The two-dimensional heading problem was revisited by Augarde et al. (2003) using an improved version of non-linear programming (Lyamin & Sloan 2002b, 2002a).

The most recent papers are based on this nonlinear programming approach, and further developments have been produced on the stability of circular tunnels in non-homogeneous clayey soil (Wilson et al. 2011). Square and rectangular tunnels have also been considered in Wilson et al. (2013) and Abbo et al. (2013), respectively. As well as this, twin tunnel configurations of both circular and square tunnels stability in undrained condition have also analysed in (Wilson et al. 2014, 2015), respectively.

The upper and lower bounds of the finite element limit analysis are used in several studies to validate the results and improve the proposed failure mechanisms. (Bottero et al. 1980; Sloan 1989; Sloan & Kleeman 1995; Ukritchon et al. 2003). The advantage of using a numerical formulation for the bound theorems is that it can handle complex loading, complicated geometries and a variety of material failure conditions. Further, there is no need to assume any collapse mechanism in such a numerical technique.

More recently, Ukritchon and Keawsawasvong (2017) studied the collapse of an opening in an underground wall in anisotropic and non-homogeneous clayey soils. Unlike these researchers, Shiau & Al-Asadi 2018 and Shiau & Al-Asadi (2020d) revisited the problem by adopting Broms and Bennermarks' original stability number *N* using a shear strength reduction technique and 2D and 3D finite element method.

Comprehensive design tables and charts were produced with examples illustrated (Shiau et al. 2017; Shiau et al. 2018). Using finite element software (Plaxis), Ukritchon, Yingchaloenkitkhajorn, et al. (2017) investigated the three-dimensional (3D) undrained stability of tunnel face in heterogeneous clayey soil (the cohesion of the soil increases with depth).

The numerical simulations are important methods for investigating the stability of twin tunnels. Xie et al. (2004) investigated the undrained stability of parallel circular tunnels with differing diameters. The tunnels were modelled under plane strain conditions using displacement finite element software and analytical limit analysis. In an attempt to understand the results provided by their finite element software, the concept of a 'stability analysis line' was introduced where the stability at various stages of construction was considered. The effect of the depth ratio and the spacing between the two tunnels were investigated, and it was found that, for a very narrow spacing between the tunnels, the stability may increase as the spacing is decreased further.

Using 3D numerical analysis, Ng et al. (2004) have investigated the load-transfer mechanism and the influence of the lagging distance between the tunnels excavated faces for large parallel hypothetical twin tunnels constructed in stiff clay by employing three-dimensional coupled finite element analysis. Chehade and Shahrour (2008) used Plaxis software to simulate the construction procedure of twin tunnels with various distances between their centres, and then considered its influence on tunnels stability.

By using three-dimensional numerical techniques *(FLAC3D*), Chakeri et al. (2011) studied the changes in stress distribution, deformations and surface settlements resulting from the construction of twin tunnels in Tehran, Iran. Mirhabibi and Soroush (2012) used ABAQUS to estimate the influence of construction load on the movement of soil surrounding two tunnels.

The laboratory experiments and centrifuge model tests have proved invaluable for suggesting likely modes of collapse in theoretical studies. By conducting small scale

model tests for closely spaced tunnels in clay, Kim et al. (1998) examined the effect of shield tunnel construction on the structural liners of existing nearby tunnels.

Wu and Lee (2003) carried out a series of centrifuge model tests for single and parallel plane strain tunnels in clays to study ground movements and the associated collapse mechanisms. The centrifuge tests were compared with the stability results from a weightless, rigid block upper bound plasticity analysis and to a series of field measurements from actual tunnels. The velocity fields from the two methods were found to give similar results. Their findings show that the stability is not always the most critical when the spacing between the tunnels is the narrowest.

Lee et al. (2006) expanded upon the findings of Wu and Lee (2003) using similar centrifuge tests with a numerical finite-difference program (*FLAC*) to investigate the surface settlement, excess pore water pressure generation, tunnel stability and arching effects that develop around single and dual circular tunnels in soft clayey soil. Their focus was on arching effects, and they used the concept of an arching ratio to describe the evolution of arching effects in the soil surrounding the tunnels. The centrifuge tests were complemented by displacement finite element analyses, which gave results consistent with those from the centrifuge.

Because the soil is not only in cohesive undrained condition but mostly in drained cohesive-frictional condition, the next section reviews the published literature on the stability of tunnels and underground openings in cohesive and/or frictional drained soil.

2.3 Stability Analysis in Cohesive and/or Frictional Soils

In cohesive-frictional soils, analytical approaches are mainly based on limit equilibrium methods or limit analysis methods. Horn (1961) was one of the first to introduce a model for assessing the limit support pressure of the tunnel face under drained conditions. He considered the limit equilibrium of a 3D sliding wedge at the tunnel face loaded by a soil silo. Anagnostou and Kovári (1996) applied the wedge model to calculate the limit support pressure in the homogeneous stratum. Broere (2001) extended the wedge model to a layered stratum. He subdivided the failure wedge in front of the tunnel face into smaller blocks based on the thickness of the soil layers. For the limit analysis methods, Atkinson and Potts (1977) investigated

theoretically and experimentally the 2D stability of unlined cross-section of shallow circular tunnels in cohesionless soil. Based on the lower bound theorem of plasticity, Mühlhaus (1985) produced analytical stability solutions for circular tunnels in two and three dimensions under drained and undrained conditions. Several kinematic approaches based on continuous velocity fields in limit analysis theory have been proposed. The rigid block mechanism was first introduced by Leca and Dormieux (1990) who obtained upper bound solutions for the limit support pressure based on the movement of rigid blocks with conical shapes in frictional material. Following this research, many enhancements were provided. (Soubra 2000, 2002; Subrin & Wong 2002) derived the upper-bound limits for the limit support pressure in a dry Mohr-Coulomb material. Mollon et al. (2009) introduced new multi-block translational failure mechanisms (five truncated rigid conical blocks) to improve the existing lower-bound solutions by Leca and Dormieux for the collapse pressure of a shallow shield circular tunnel, as shown in Figure 2.4.

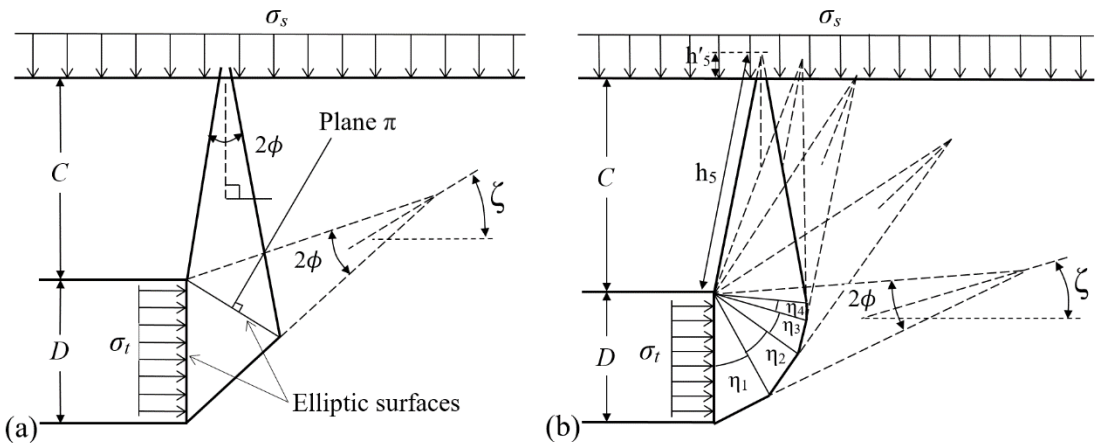

Figure 2.4. (a) Leca-Dormieux (1990) mechanism, (b) Mollon et al. (2009) multiblock mechanism.

For frictional soil and by using a spatial discretisation technique, Mollon et al. (2010) developed a new failure mechanism to cover the whole circular face of the tunnel instead of an inscribed vertical ellipse as in the mechanisms of Leca and Dormieux. Based on the rotational rigid-block movement observed in the experimental tests for a circular tunnel in frictional soil, Mollon et al. (2011) generated three-dimensional failure surface point by point to study the stability in collapse and blowout. They showed that the rotational mechanisms provide a significant improvement in contrast with the translational mechanisms. The improvements of (Mollon et al. 2009, 2010;

Mollon et al. 2011) led to relevant solutions consistent with the results of real projects in the case of frictional soils. However, for purely cohesive soils, likely, a failure mechanism by the motion of one or multi-rigid blocks is not convenient. Therefore, the numerical methods are probably optimal for tunnels stability analysis.

Most of the previous studies of tunnel stability have been based on upper bound techniques involving various failure mechanisms. However, for deeper tunnels, the rigid block method obtains less accurate solutions, while this could be improved further with more complex mechanisms, upper bound solutions inherently give unsafe estimates on the true collapse loads. Furthermore, it is more difficult to propose an efficient rigid-block mechanism for purely cohesive soils than for cohesive-frictional materials (Mollon et al. 2013).

In practice, upper bounds are more valuable when they are accompanied by lower bounds so that the exact solution can be bracketed from above and below. The application of computational limit analysis to the stability of shallow tunnels in cohesive-frictional soils, Lyamin and Sloan (2000) and Lyamin et al. (2001) considered the stability of plane-strain circular and square tunnels in cohesive-frictional soils. The drained stability of the tunnel was described by the load parameters σ_t/c, where σ_t is the internal tunnel pressure and c is the cohesion under drained loading conditions. But it appears that no generally accepted solutions to be available in the literature for tunnels made in high frictional soils where c equal to zero.

Using two methods of upper bound solutions (rigid blocks failure mechanism and finite-element upper bound solution with linear programing), Yang and Yang (2010) investigated the required support pressure for shallow rectangular tunnel stability in cohesive-frictional soil.

Experimental tests can be used to study tunnel face stability problems and the failure modes of the surrounding soil. Chambon and Corte (1994) conducted a series of centrifuge model tests to determine the tunnel face stability in dry sandy soil. Their results indicated that the relative depths of the tunnels and the density of sand had little influence on the limit support pressure. Also, their results indicated that the failure zone in front of the tunnel face was bulb-shaped, and the relationship between the limiting support pressure and the tunnel diameter was found to be linear, as shown in Figure 2.5.

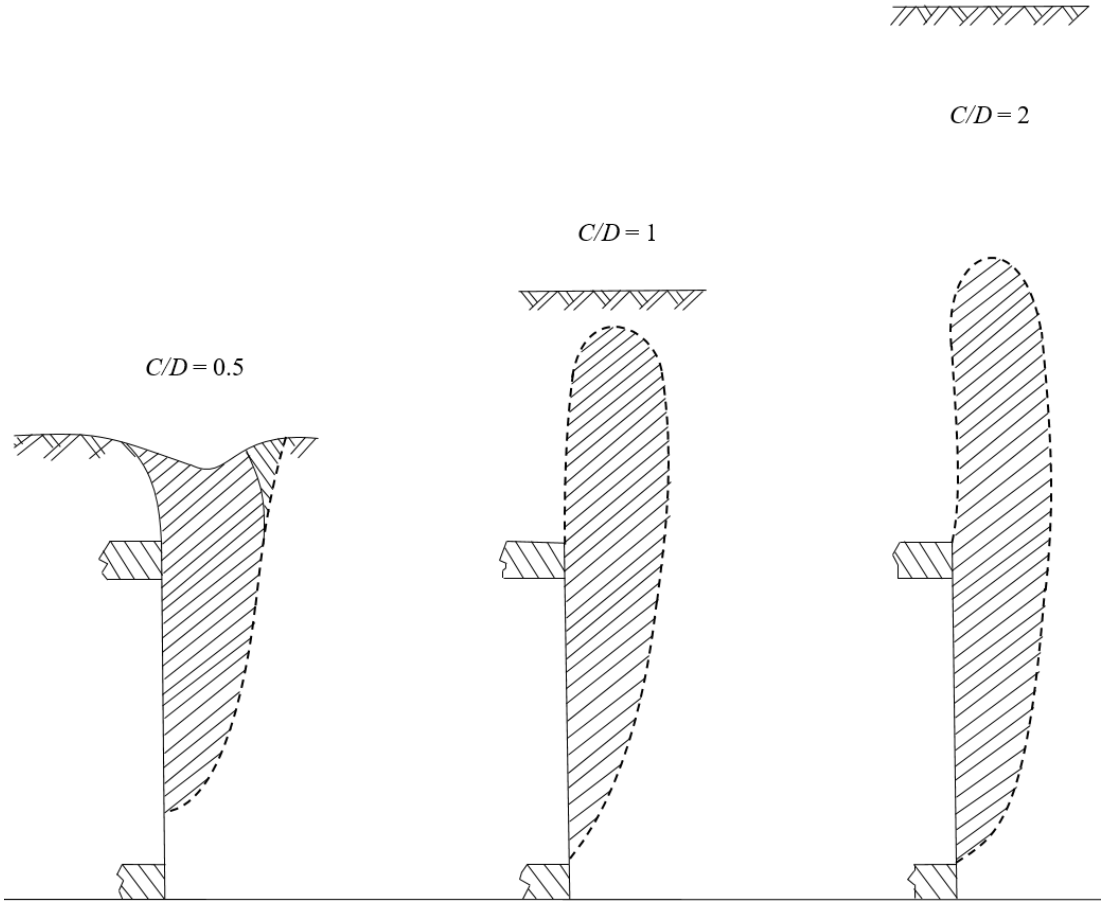

Figure 2.5. The failure mechanism of a shallow tunnel in experimental tests for dry sandy soil (Chambon and Corte, 1994).

Takano et al. (2006) performed 1g experimental tests in which an X-ray computed tomography scanner was used to visualise the 3D shape of the failure mechanism. Kirsch (2010) achieved small-scale model tests under normal gravity (1g) to investigate the face stability of shallow tunnels and to show that the necessary support pressure is independent of the overburden and the initial soil density. By using 3D large-scale model tests, Chen et al. (2013) investigated the stability and the ground settlement of shallow tunnel (C/D = 0.5 - 2, where D = 1m) in cohesionless soil. They suggested that the face support pressure is independent of the depth of the tunnel once the depth ratio is larger than or equal to one.

All the studies mentioned previously only considered the stability of single tunnels. For the stability of a pair of circular tunnels, a number of investigations have been reported by several researchers.

The earliest numerical study of twin tunnels was performed by Ghaboussi and Ranken (1977). They investigated the effects of the interaction on the construction of parallel tunnels using two-dimensional (2D) finite element analyses with linearly elastic models. They found that as the spacing between the two tunnels decreased, there was a gradual increase in the vertical stresses between the tunnels and a corresponding increase in the horizontal stresses. Their results indicated that for a distance width of about twice the tunnel diameter or greater, the displacements of each of the two parallel tunnels were essentially identical to those of corresponding single tunnel construction.

(Yamamoto et al. 2013, 2014) used *FELA* to consider the undrained stability of dual square and circular tunnels and found the tunnel stability reaches a minimum value when the tunnels are one to two tunnel widths apart.; they concentrated on the bearing capacity problem over the tunnels.

The idea of considering drained stability based on a single equation was first suggested by Atkinson and Mair (1981). They proposed a formula for shield tunnels in dry cohesionless soil to calculate the minimum support pressure (σ_t) at collapse; this is shown in Equation (2.3).

$$\sigma_t = \sigma_s F_s + \gamma D F_\gamma \tag{2.3}$$

Where σ_s is the possible surcharge loading on the ground surface, F_s is the surcharge stability factor, γ is the soil unit weight, D is the diameter of the tunnel and F_γ is the soil weight stability factor. Equation (2.2) was extended by Anagnostou and Kovári (1996) to cover cohesive-frictional soils, as shown in equation (2.4).

$$\sigma_t = -cF_c + \sigma_s F_s + \gamma D F_\gamma \tag{2.4}$$

Where c is the effective cohesion and F_c is the cohesion stability factor.

The first comprehensive numerical study on the face stability of shield tunnels using a conventional equation and the tunnel stability factors was carried out by Vermeer et al. (2002) who performed 3D finite element analyses for tunnel face stability analyses in the sand. They concluded that the stability factor F_γ is independent of the depth of the tunnel for friction angles larger than twenty degrees, and the limit support pressure decreases as the friction angle of the soil increases.

For practical calculation of the critical support pressure, Mollon et al. (2010) produce the critical stability factors (N_γ, N_c and N_s) for a shallow tunnel (C/D = 0.4, 0.6, 0.8, 1,

1.3, 1.6 and 2) in frictional soil ($\phi \geq 15^{\circ}$) and then, the critical pressure can be computed using the superposition method.

Using the Kinematical Element Method (q), Qarmout et al. (2019) proposed a new failure mechanism consists of two blocks to produce tunnel stability factors (similar to bearing capacity factors) for shallow circular tunnels (C/D = 0.5, 1, 1.5, 2 and 2.5) in frictional soil ($\phi \geq 15^{\circ}$). These factors can be used in a traditional equation to calculate the upper bound support pressure at the collapse. Their approach underestimates the required internal pressure, in comparison with other studies. This is probably due to the limited number of rigid blocks used in this analysis, and the upper bound kinematic approach results are inherently unsafe.

As no generally accepted design or analysis methods are available for the stability problems in cohesive-frictional soil, this thesis proposes to study the problem using a so-called stability factor approach, aiming to produce comprehensive tunnel stability factors (F_c, F_s and F_γ) to estimate the critical internal pressure required to maintain stability at collapse. Three various configurations of underground tunnelling (i.e. tunnel heading, single circular tunnel and twin circular tunnels) in two- and three-dimensional spaces are studied using rigorous upper and lower bound finite element limit analysis techniques. It is expected that the solutions produced would contribute significantly to the current tunnel practices.

CHAPTER 3: NUMERICAL MODELLING REVIEW

3.1 Introduction

Stability analysis is used to predict the collapsing load a structure can support without inducing failure. There are four main methods used to determine stability analysis; limit equilibrium, limit analysis, slip-line methods and the displacement finite element method. OptumCE packages (*OptumG2* and *OptumG3*) are finite element software for analysing strength and deformation of geotechnical problems. The programs have common features to many other finite element geotechnical programs, however, differs on a few points. Rigorous calculations on upper and lower bounds to determine an exact solution can be computed directly, rather than the traditional step by step elastoplastic process. Maximum loads and bearing capacities can be computed with a set of fixed soil and structural parameters. Conversely, a set of load values can be fixed, and commutation of the upper and lower bounds can be determined (OptumCE 2017, 2018).

3.2 Finite Element Limit Analysis (*FELA*)

In this study, the numerical stability solutions are based on the finite element formulation of the plastic limit theorems (i.e. lower and upper bounds). The lower bound theorem employs the notion of a statically admissible stress field, which is simply a stress field that satisfies equilibrium, the stress boundary conditions and the yield criterion. For a perfectly plastic material model with an associated flow rule, it can be shown that the load carried by any statically admissible stress field is a lower bound on the true limit load.

The upper bound theorem employs the notion of a kinematically admissible velocity field, which is simply a velocity field that satisfies the velocity boundary conditions and the plastic flow rule. For such a field, it can be shown that an upper bound on the

collapse load is obtained by equating the power expended by the external loads to the power dissipated internally by plastic deformation.

The following discussions are based on the work of (Sloan 1988b, 1989; Sloan & Kleeman 1995; Lyamin & Sloan 2002a, 2002b; Krabbenhøft et al. 2005; Krabbenhøft et al. 2007; Krabbenhøft et al. 2008; Sloan 2013)

3.2.1 Development of finite element lower bound

Lysmer (1970) was an early pioneer in applying finite elements and optimisation theory to compute rigorous lower bounds for plane-strain geotechnical problems. He linearised the yield surface using an internal polyhedral approximation that replaced each non-linear yield inequality constraint by a series of linear inequalities. Although Lysmer's finite-element approach for computing lower bounds was a pivotal conceptual advance, it has significant limitations that prevented it from being used widely in practice.

Following Lysmer's seminal work, Anderheggen and Knöpfel (1972), Pastor (1978) and Bottero et al. (1980) proposed various discrete methods for two-dimensional lower-bound limit analysis that were all based on linear triangles and linear programming. Soon after, Pastor and Turgeman (1982) proposed a lower-bound technique for modelling the important case of axisymmetric loading. Although potentially powerful, these early methods were limited by the computational performance of the linear programming codes at the time and could solve only relatively small problems.

In an effort to address this issue, (Sloan 1988a, 1988b) proposed a fast linear programming formulation that can solve small to medium scale two-dimensional problems on a standard desktop machine. This procedure is based on a novel active set algorithm, which employs a steepest-edge search in the optimisation iterations, and fully exploits the highly sparse nature of the lower-bound constraint matrix.

Although lower-bound methods based on linear programming are capable of providing useful solutions for two- dimensional problems of moderate size, they are poorly suited to three-dimensional analysis, as huge numbers of inequalities arise when the yield criterion is linearised. Moreover, it is not always clear how to linearise a three-dimensional yield surface optimally. Both of these issues can be avoided by leaving the yield constraints in their native form and adopting non-linear programming

algorithms to solve the resulting optimisation problem. Indeed, with this approach, three-dimensional formulations present no special difficulties, other than adding geometrical complexity and increasing the number of unknowns.

An early discrete lower-bound formulation based on non-linear programming was described in Belytschko and Hodge (1970). This procedure used piecewise-quadratic equilibrium stress fields, and maximised the collapse load, subject to the non- linear yield constraints, using a sequential unconstrained minimisation technique. Although it furnishes rigorous lower bounds, the method proved to be slow for large- scale problems.

In a subsequent modification of Lysmer's formulation, Basudhar et al. (1979) incorporated the nonlinear yield constraints directly, converted the constrained optimisation problem to an unconstrained one using the extended penalty method of Kavlie and Moe (1971).

Following this work, Arai and Tagyo (1985) used constant-stress elements, and the sequential unconstrained minimisation technique with the conjugate gradient algorithm of Fletcher and Reeves (1964), to obtain a statically admissible stress field for geotechnical problems.

Lyamin (1999) and Lyamin and Sloan (2002b) dramatically improved the practical utility of the discrete lower-bound method by employing linear stress elements, imposing the non-linear yield conditions in their native form, and solving the resulting non-linear optimisation problem using a variant of an algorithm developed for mixed limit analysis formulations (Zouain et al. 1993).

The solution method used by Lyamin and Sloan (2002b) is an interior point, two-stage, quasi-Newton scheme that exploits the underlying structure of the lower-bound optimisation problem. Since its iteration count is largely independent of the grid refinement for a given problem, the method can handle large-scale two-dimensional meshes with several thousand elements in a few seconds and is many times faster than traditional linear programming formulations. Further advantages include the ability to model three-dimensional problems, where the number of unknowns can be huge, as well as any convex yield criterion.

Following the work of Lyamin and Sloan (2002b), Krabbenhoft and Damkilde (2003) proposed another efficient lower-bound method, aimed primarily at solving structural engineering problems, based on non-linear programming.

Owing to the presence of singularities in their yield surfaces, where the gradients with respect to the stresses become undefined, the Tresca and Mohr-Coulomb criteria pose special difficulties in the finite-element limit analysis. Lyamin and Sloan (2002b) overcame this difficulty by local smoothing of the yield surface vertices, with an accompanying modification to the search direction to preserve feasibility during the optimisation iterations. An attractive alternative method for solving lower-bound limit analysis problems, which does not require differentiability of the yield surface in the optimisation process, is to use second-order cone programming (Ciria 2004; Makrodimopoulos & Martin 2006). This solution method can be applied to a variety of yield criteria in two dimensions, including the Tresca and Mohr-Coulomb models, and has proved to be robust and efficient for large-scale geotechnical problems (Krabbenhøft et al. 2007). In three-dimensional cases, second-order cone programming can be used for Von Mises and Drucker–Prager yields criteria, but not for Tresca or Mohr-Coulomb models. For the latter, which are of particular interest in geotechnical applications, it is possible to use a different cone-based solution algorithm that is known as semi-definite programming (Krabbenhøft et al. 2008). Like the second-order cone programming method, this approach does not require smoothing of any yield surface vertices, and it has proved to be both robust and efficient for large- scale applications Krabbenhøft et al. (2007).

In summary, the second-order cone programming and semi-definite programming methods are, respectively, the solution methods of choice for the Tresca/Mohr-Coulomb models under two- and three- dimensional conditions. For yield criteria that are curved in the meridional plane, however, such as the Hoek-Brown model for rock, these procedures are inapplicable, and the more general interior point solution algorithm proposed by Lyamin and Sloan (2002b) is appropriate. The following section outlines the finite element lower bound formulation proposed in Lyamin and Sloan (2002b).

3.2.2 Finite element lower bound formulation

The finite element lower bound formulation proposed by (Lyamin & Sloan 2002b) has proved very successful in large-scale practical applications. The linear elements used to compute the statically admissible stress field are shown in Figure 3.1.

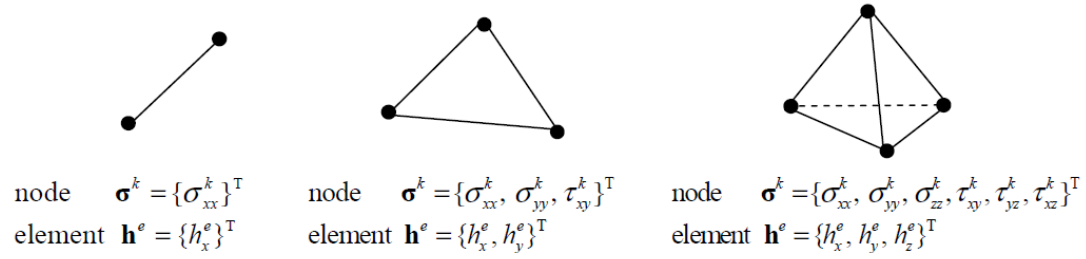

Figure 3.1. Linear elements for lower bound limit analysis.

The lower bound procedure is formulated as a nonlinear optimisation problem, where the nodal stresses and/or element body forces are the unknowns and the objective function to be maximised corresponds to the collapse load. The unknowns are subject to equilibrium equality constraints for each continuum element, equilibrium equality constraints for each discontinuity, stress boundary conditions, and a yield condition inequality constraint for each node. Each of these aspects is now briefly described for the two-dimensional case (similar relations can be developed for three dimensions).

Objective Function

The objective function corresponds to a force (the collapse load) which is to be maximised. The common case of optimising the normal and shear load along a boundary segment in two-dimensions is shown in Figure 3.2.

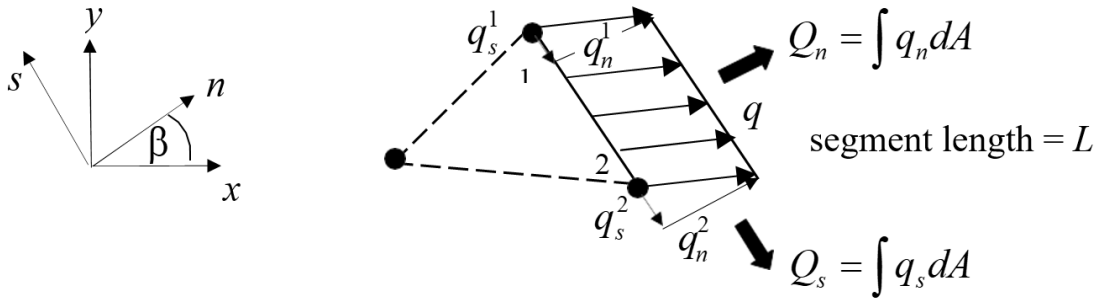

Figure 3.2. Optimising the load along a boundary.

Since the stresses vary linearly, the normal and shear loads on an element edge of length L are given by

$$\begin{Bmatrix} Q_n \\ Q_s \end{Bmatrix} = \frac{L}{2}\left(\begin{Bmatrix} q_n^1 \\ q_s^1 \end{Bmatrix} + \begin{Bmatrix} q_n^2 \\ q_s^2 \end{Bmatrix} \right)$$

where the local surface stresses q_n and q_s can be expressed in terms of the Cartesian stresses at node k using the standard transformation equations

$$\begin{Bmatrix} q_n^k \\ q_s^k \end{Bmatrix} = \begin{bmatrix} \cos^2\beta & \sin^2\beta & \sin 2\beta \\ -\frac{1}{2}\sin 2\beta & \frac{1}{2}\sin 2\beta & \cos 2\beta \end{bmatrix} \begin{Bmatrix} \sigma_{xx}^k \\ \sigma_{yy}^k \\ \tau_{xy}^k \end{Bmatrix} \tag{3.1}$$

When summed over each loaded boundary edge, the contributions Q_n and Q_s give the total force which is to be maximised for the whole structure. In the case of body force loading, which is most often due to unit weight, the objective function contribution for each element is merely the body force component times the element volume.

Continuum Equilibrium

Over each two-dimensional element, the stresses vary according to the relations

$$\sigma = \sum_{k=1}^{3} N^k \sigma^k \tag{3.2}$$

where N^k is the shape functions at some node k. After substituting these into the standard equilibrium equations for a solid

$$\begin{aligned} \frac{\partial \sigma_{xx}}{\partial x} + \frac{\partial \tau_{xy}}{\partial y} + h_x + g_x = 0 \\ \frac{\partial \sigma_{yy}}{\partial y} + \frac{\partial \tau_{xy}}{\partial x} + h_y + g_y = 0 \end{aligned} \tag{3.3}$$

we obtain two equality constraints for each element. When summed over all elements in the mesh, these define the global equilibrium constraints for the mesh.

Discontinuity Equilibrium

To improve the accuracy of the computed collapse load, stress discontinuities are permitted at all edges that are shared by adjacent elements. Figure 3.3 illustrates such a stress discontinuity positioned between the edges of two adjacent triangles. To satisfy equilibrium, and therefore be statically admissible, the normal and shear stresses must be the same on both sides of the discontinuity according to the relations

$$\left\{\begin{matrix}\sigma_{nn}^1\\ \tau_{ns}^1\end{matrix}\right\}=\left\{\begin{matrix}\sigma_{nn}^2\\ \tau_{ns}^2\end{matrix}\right\},\left\{\begin{matrix}\sigma_{nn}^3\\ \tau_{ns}^3\end{matrix}\right\}=\left\{\begin{matrix}\sigma_{nn}^4\\ \tau_{ns}^4\end{matrix}\right\} \tag{3.4}$$

where for some node *k*

$$\left\{\begin{matrix}\sigma_{nn}^k\\ \tau_{ns}^k\end{matrix}\right\}=\begin{bmatrix}\cos^2\beta & \sin^2\beta & \sin 2\beta\\ -\frac{1}{2}\sin 2\beta & \frac{1}{2}\sin 2\beta & \cos 2\beta\end{bmatrix}\left\{\begin{matrix}\sigma_{xx}^k\\ \sigma_{yy}^k\\ \tau_{xy}^k\end{matrix}\right\} \tag{3.5}$$

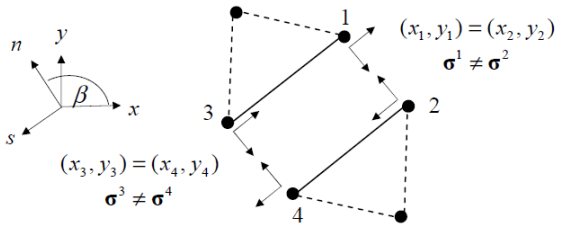

Figure 3.3. Statically admissible stress discontinuity.

Thus each pair of nodes on a stress discontinuity imposes two equilibrium equality constraints on the associated nodal stresses. Summing over all nodal pairs on the discontinuities gives the global set of discontinuity equilibrium constraints. Recently, Krabbenhøft et al. (2005) proposed a simple and elegant technique for modelling discontinuities in the upper bound method which is also applicable to the lower bound method (Lyamin et al. 2005). The basic idea, illustrated for the two-dimensional case in Figure 3.4, is to model each stress discontinuity by a patch of standard continuum elements and collapse certain nodal pairs to the same coordinates.

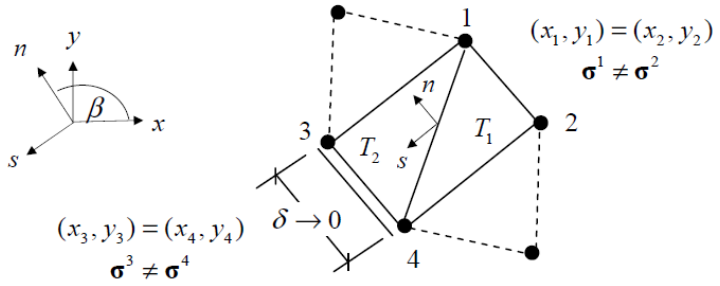

Figure 3.4. Patch-based stress discontinuity.

(Lyamin et al. 2005) show that using Equations (3.2) and (3.3) to impose the standard equilibrium conditions over triangles T_1 and T_2, and setting $(x_1, y_1) = (x_2, y_2)$ and $(x_3, y_3) = (x_4, y_4)$, leads to the equilibrium relations (6). Thus, the normal and shear stresses are continuous across the discontinuity, but the tangential stress σ_{ss} can jump. This type of formulation permits discontinuities to be modelled using standard continuum elements and is very simple to implement.

Stress Boundary Conditions

To satisfy equilibrium, the transformed stresses for any boundary node must match the prescribed surface stresses ***t***.

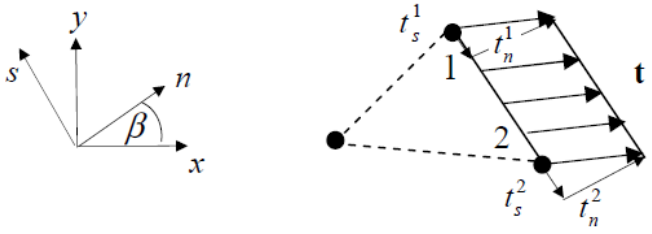

Figure 3.5. Stress boundary conditions.

With reference to Figure 3.5, this requirement may be expressed by the equations

$$\begin{Bmatrix} \sigma_{nn}^1 \\ \tau_{ns}^1 \end{Bmatrix} = \begin{Bmatrix} t_n^1 \\ t_s^1 \end{Bmatrix}, \begin{Bmatrix} \sigma_{nn}^3 \\ \tau_{ns}^2 \end{Bmatrix} = \begin{Bmatrix} t_n^2 \\ t_s^2 \end{Bmatrix}$$

Where $\{\sigma_{nn}^k, \tau_{ns}^k\}$ for node k are again given by Equation (3.5). These constraints are applied to all edges where surface stresses are prescribed.

Yield Conditions

Provided the stresses vary linearly over an element and the yield function $f(\boldsymbol{\sigma})$ is convex, the yield condition is satisfied at every point in the domain if the inequality constraint $f(\boldsymbol{\sigma}^k) \le 0$ is imposed at each node k. In the twodimensional case, this implies that the nodal stresses for each triangle are subject to three non-linear inequality constraints, as shown in Figure 3.6.

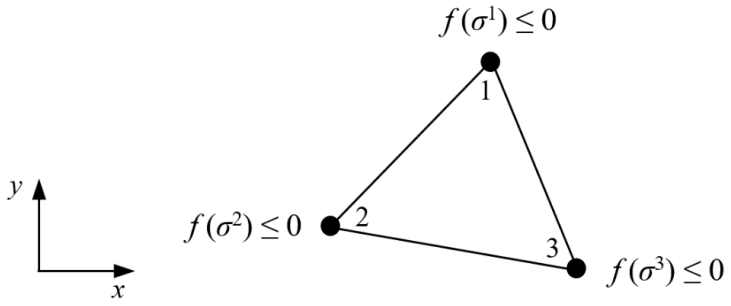

Figure 3.6. Yield conditions.

Lower Bound Nonlinear Optimisation Problem

Summing the objective function coefficients and constraints for a given mesh leads to a nonlinear optimisation problem where the unknowns are stresses and body loads. Let $\mathbf{c_1}$ and $\mathbf{c_2}$ denote global vectors of objective function coefficients, $\boldsymbol{\sigma}$ denote a global vector of unknown nodal stresses, $\mathbf{h}$ denotes a global vector or element body forces (unit weights), $\boldsymbol{c_1^T\sigma + c_2^T h}$ denote the collapse load, $\mathbf{A}$ denote matrices of equality constraint coefficients, $\mathbf{b}$ denote vectors of coefficients, and f_k ($\boldsymbol{\sigma}$) denotes the yield function at node *k*. The optimisation problem for the finite element lower bound then takes the form

Objective function

Maximum collapse load	$\max\left(c_1^T\sigma + c_2^T h\right)$	

Subject to

Continuum equilibrium	$A_{11}\sigma + A_{12}h = b_1$	(3.6)
Discontinuity equilibrium	$A_2\sigma = b_2$	
Stress boundary conditions	$A_3\sigma = b_3$	
Yield condition for each nod k	$f_k\left(\sigma^k\right) \le 0$	

The solution to the nonlinear programming problem (8), which constitutes a statically admissible stress field, can be found efficiently by solving the system of nonlinear equations that define its Kuhn Tucker optimality conditions. The two-stage quasi-Newton solver designed by Lyamin (1999) and Lyamin and Sloan (2002b) for this purpose usually requires less than about 50 iterations, regardless of the problem size. Because it does not require the yield surface to be linearised, this type of lower bound formulation can be extended to three dimensions and used with a wide range of yield criteria.

3.2.3 Development of finite element upper bound

Early discrete formulations of the upper-bound theorem, based on finite elements and linear programming, were proposed by Anderheggen and Knöpfel (1972) and Maier et al. (1972). Although quite general, these methods were concerned primarily with structural applications. The subsequent plane-strain procedures of Pastor and Turgeman (1976) and Bottero et al. (1980), which focused on geotechnical

applications with Tresca and Mohr-Coulomb yield criteria, permit a limited number of velocity discontinuities to occur between elements, but require the direction of shearing to be specified a priori.

Following these early procedures that focused on plane problems, Pastor and Turgeman (1982) extended the upper- bound formulation of Bottero et al. (1980) to handle axisymmetric geometries, but only for Von Mises and Tresca materials.

While the above upper-bound methods inherit all the key advantages of the finite-element technique and hence can model complex problems in two dimensions, they were not widely applied in practice because of the CPU time required to solve their associated linear programming problems. In an effort to rectify this handicap, (Sloan 1989) proposed an upper-bound method based on the steepest-edge active set solution scheme (Sloan 1988b), which had proved successful for lower-bound limit analysis,

Owing to the nature of the algorithm used to solve the associated linear optimisation problem, however, the procedure proved to be inefficient for large-scale examples involving thousands of elements. The need to specify both the location and the direction of shearing for each discontinuity in an upper-bound analysis is a significant drawback since it requires a good guess of the likely collapse mechanism in advance. This shortcoming was addressed by Sloan and Kleeman (1995), who generalised the upper-bound formulation of Sloan (1989) to include velocity discontinuities at all edges shared by adjacent triangles.

The plate formulation described by Hodge and Belytschko (1968) was one of the first attempts to develop a finite- element upper-bound method based on non-linear programming. Their analysis used classical theory to specify the deformation field solely by the velocity normal to the original middle surface of the plate.

Following this initial work, various other non-linear programming formulations were proposed for computing upper bounds on the load capacity of plates, shells and structures (Biron & Charleux 1972; Nguyen et al. 1978). Huh and Yang (1991) developed a general upper-bound procedure for plane stress problems using triangular elements with a linear velocity field.

In a further development, Capsoni and Corradi (1997) proposed another discrete upper-bound approach where the straining modes are modelled independently of rigid-body motions.

In a different non-linear approach, Jiang (1994) proposed an upper-bound formulation, based on a regularised model of limit analysis (Friaaˆ, 1979), which assumes the material is visco-plastic and uses two parameters to characterise its creep behaviour.

To solve the resulting non-linear optimisation problem, Jiang (1994) employed the augmented Lagrangian method in conjunction with the algorithm of Uzawa (Fortin & Glowinski 1983). In a later paper, Jiang (1995) established that the same non- linear programming scheme could be applied to perform upper-bound limit analysis directly. Jiang's formulations perform well for a variety of two-dimensional examples but have not been extended to deal with discontinuities in the velocity field or three-dimensional geometries. Parallel to this development, Liu et al. (1995) proposed a direct iterative method for performing three-dimensional upper-bound limit analysis. This scheme treats the rigid zones separately from the plastic zones during each iteration and neatly avoids the numerical difficulties that stem from a non- differentiable objective function in the former.

Following in the footsteps of their successful lower-bound formulation, Lyamin and Sloan (2002a) developed an upper-bound finite-element method that was also based on non-linear programming. This procedure assumes that the velocities vary linearly over each element and that each element is associated with a constant-stress field and a single plastic multiplier rate. Using the approach developed in Sloan and Kleeman (1995), the formulation of Lyamin and Sloan (2002a) allows velocity discontinuities along shared element edges, with the velocity jumps across each discontinuity being defined by additional non-negative unknowns (plastic multipliers). Krabbenhøft et al. (2005) modified the upper-bound formulation of Lyamin and Sloan (2002a) by proposing a new stress-based method that uses patches of continuum elements to incorporate velocity discontinuities in two and three dimensions.

The following section outlines the finite element upper bound formulation proposed by Lyamin and Sloan (2002a), with a new patch-based method for modelling velocity discontinuities (Krabbenhøft et al. 2005; Krabbenhøft et al. 2007).

3.2.4 Finite element upper bound formulation

The procedure of Lyamin and Sloan (2002a) and Krabbenhøft et al. (2005), which is the first to incorporate velocity discontinuities in three dimensions with general types of yield criteria, is applicable to largescale problems and is also being commercialised.

The elements used to compute the kinematically admissible velocity field, shown in Figure 3.7, use a linear variation of the velocities and constant stresses.

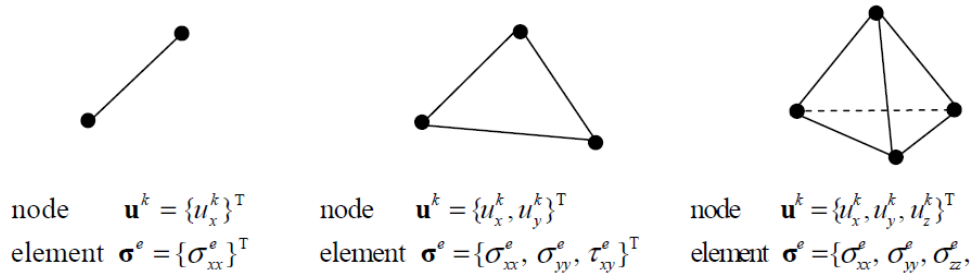

Figure 3.7. Linear elements for upper bound limit analysis.

The upper bound procedure is formulated as a nonlinear optimisation problem, where nodal velocities and element stresses are the unknowns and the objective function to be minimised is the internal power dissipation. To satisfy the requirements of the upper bound theorem, the unknowns are subject to constraints arising from the flow rule, the velocity boundary conditions, and the yield condition. Each of these aspects is now briefly described for the twodimensional case (similar relations can be developed for three dimensions).

Objective Function

In the finite element upper bound formulation, the objective function corresponds to the internal dissipated power. This quantity is minimised and equated to the work expended by the external loads to give the limit load. Noting that the stresses and plastic strain rates are constant over each element, and summing over all the elements, the internal power dissipation may be written as

$$P^{int} = \int \boldsymbol{\sigma}^T \dot{\boldsymbol{\varepsilon}}^p \mathrm{d}V = \sum_e (\boldsymbol{\sigma}^T \dot{\boldsymbol{\varepsilon}}^p V)^e \tag{3.7}$$

For each element, there exists a matrix $\mathbf{B^e}$ that relates the (constant) plastic strain rates to the nodal velocities according to

$$\dot{\varepsilon}^p = \frac{1}{V^e} B^e u^e \tag{3.8}$$

$\mathbf{B}^e$ is the strain-displacement matrix from conventional finite element analysis, multiplied by the element volume. Inserting Equation 3.8 into Equation (3.7) gives the total internal dissipated power for the mesh, in terms of the unknowns stresses and velocities, as

$$P^{\text{int}} = \sigma^T B u$$

where **σ** is a global vector of element stresses, **u** is a global vector of nodal velocities and $B = \sum_e B^e$

$$\dot{\varepsilon}^p_{xx} = \dot{\lambda}\partial f / \partial \sigma_{xx}$$
$$\dot{\varepsilon}^p_{yy} = \dot{\lambda}\partial f / \partial \sigma_{yy}, \quad \dot{\lambda} \geq 0, \quad \dot{\lambda} f(\boldsymbol{\sigma}^e) = 0$$
$$\dot{\gamma}^p_{xy} = \dot{\lambda}\partial f / \partial \tau_{xy}$$

$$\dot{\boldsymbol{\varepsilon}}^p = \dot{\lambda}\nabla f(\boldsymbol{\sigma}^e), \quad \dot{\lambda} \geq 0, \quad \dot{\lambda} f(\boldsymbol{\sigma}^e) = 0 \tag{3.9}$$

Where $\dot{\lambda}$ is the plastic multiplier Combining Equations (3.8) and (3.9), the flow rule constraints for each element may be expressed as

$$\mathbf{B}^e \mathbf{u}^e = \dot{\alpha}\nabla f(\boldsymbol{\sigma}^e), \quad \dot{\alpha} \geq 0, \quad \dot{\alpha} f(\boldsymbol{\sigma}^e) = 0 \tag{3.10}$$

Where $\dot{\alpha} = V^e \dot{\lambda}$. Thus, for the two-dimensional case, the flow rule generates four equality constraints and one inequality constraint on the velocity field per element. Since the yield function is not linearised, all the equality constraints are generally nonlinear.

Discontinuity Flow Rule

Velocity discontinuities can be incorporated using the patch-based formulation of Krabbenhøft et al. (2005). The concept behind this procedure is identical to that discussed previously for the lower bound method, with each discontinuity being modelled by a collapsed patch of standard continuum elements. For the two-dimensional case, shown in Figure 3.8, each discontinuity comprises two triangles and has six unknown stresses.

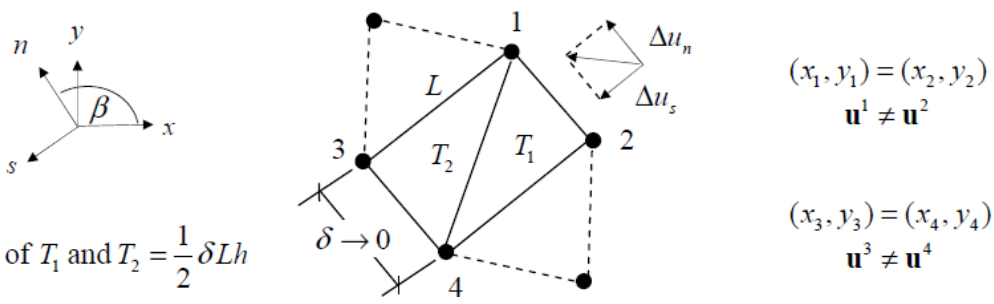

Figure 3.8. Patch-based velocity discontinuity.

If we let the discontinuity width $\delta \to 0$, it may be shown Krabbenhøft et al. (2005) that the local strains in each triangle approach the following values

$$\begin{aligned} \dot{\varepsilon}_{ss}^{p} &\to 0 \\ \dot{\varepsilon}_{nn}^{p} &\to \Delta u_n / \delta \\ \dot{\gamma}_{ns}^{p} &\to \Delta u_s / \delta \end{aligned} \tag{3.11}$$

Where $(\Delta u_n\ \Delta u_s)$ are finite velocity jumps in the normal and tangential directions which are related to the Cartesian velocity jumps by

$$\begin{Bmatrix} \Delta u_n \\ \Delta u_s \end{Bmatrix} = \begin{bmatrix} \cos\beta & \sin\beta \\ -\sin\beta & \cos\beta \end{bmatrix} \begin{Bmatrix} \Delta u_x \\ \Delta u_y \end{Bmatrix}$$

From Equation (3.11) we see that the strains become infinite as $\delta \to 0$, but the strains time the element volume remain finite according to

$$\begin{aligned} \dot{\varepsilon}_{ss}^{p} \times V^{e} &= 0 \\ \dot{\varepsilon}_{nn}^{p} \times V^{e} &= \frac{\Delta u_n}{\delta} \times \frac{1}{2} \delta L h = \Delta u_n L h / 2 \\ \dot{\gamma}_{ns}^{p} \times V^{e} &= \frac{\Delta u_s}{\delta} \times \frac{1}{2} \delta L h = \Delta u_s L h / 2 \end{aligned} \tag{3.12}$$

where h is the out-of-plane element thickness. The above relations confirm that discontinuous velocity jumps can be modelled by merely imposing the flow rule constraints (12) over each triangle and setting $(x_1, y_1) = (x_2, y_2)$ and $(x_3, y_3) = (x_4, y_4)$. This allows discontinuity elements to be treated in the same way as continuum elements and is simple to implement. Moreover, it is extendable to three dimensions and permits general types of yield criteria to be modelled.

Velocity Boundary Conditions

As shown in Figure 3.9, the transformed velocities must match the prescribed velocities for any boundary node.

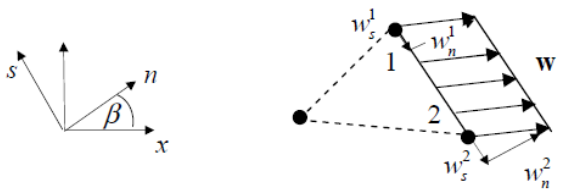

Figure 3.9. Velocity boundary conditions.

In two dimensions, this requirement may be expressed by four equality constraints

$$\begin{Bmatrix} u_n^1 \\ u_s^1 \end{Bmatrix} = \begin{Bmatrix} w_n^1 \\ w_s^1 \end{Bmatrix}, \begin{Bmatrix} u_n^2 \\ u_s^2 \end{Bmatrix} = \begin{Bmatrix} w_n^2 \\ w_s^2 \end{Bmatrix}$$

where, for some node k, the transformed nodal velocities are given by standard relations

$$\begin{Bmatrix} u_n^k \\ u_s^k \end{Bmatrix} = \begin{bmatrix} \cos\beta & \sin\beta \\ -\sin\beta & \cos\beta \end{bmatrix} \begin{Bmatrix} u_x^k \\ u_y^k \end{Bmatrix}$$

These constraints must be applied to all boundary nodes that have prescribed velocities.

Yield Conditions

The yield condition $f(\boldsymbol{\sigma})$ can be satisfied at every point in the mesh if we impose the inequality constraint $f(\boldsymbol{\sigma}^e) \leq 0$ for each element *e*. In two-dimensions, this implies that the stresses for each triangular element are subject to one nonlinear inequality constraint.

Upper Bound Nonlinear Optimisation Problem

After assembling the objective function coefficients and constraints for a mesh, the upper bound nonlinear optimisation problem can be expressed as

Objective function

Minimum dissipated power $\min\left(\sigma^T B u\right)$

Subject to

Flowrule $$Bu = \sum_e \dot{\alpha}^e \nabla f\left(\sigma^e\right) \qquad (3.13)$$

$$\dot{\alpha}^e \geq 0$$

$$\dot{\alpha}^e f\left(\sigma^e\right) = 0$$

Velocity boundary condition $Au = b$

Yield condition for each element *e* $f\left(\sigma^e\right) \leq 0$

where σ is a global vector of unknown element stresses, u is a global vector of unknown nodal velocities, B is a global compatibility matrix, $\sigma^T B u$ is the dissipated power, A is a matrix of equality constraint coefficients, b is a known vector of coefficients, $\dot{\alpha}^e$ is the plastic multiplier times the volume for element *e*, and $f(\sigma^e)$ is

the yield function for element *e*. The solution to Equation (3.13) constitutes a kinematically admissible velocity field and can be found efficiently by treating the system of nonlinear equations that define the Kuhn Tucker optimality conditions. Interestingly, these optimality conditions do not involve $\dot{\alpha}^e$, so these quantities do not need to be included as unknowns. The two-stage quasi-Newton solver proposed by Lyamin (1999) and Lyamin and Sloan (2002a) usually requires less than about 50 iterations, regardless of the problem size, and results in a very efficient formulation.

3.3 Numerical Modelling in *OptumG2* and *OptumG3*

OptumG2 and *OptumG3* are finite element software packages designed to solve boundary geotechnical problems. There are many basic features used to detail the tunnelling analysis, with each problem following a similar procedure. The outlines for both of the software background are presented in Figures 3.10 and 3.11. The design grid is centred in the overview, and the Stage Manager to the right, while the four tabs; Geometry, Materials, Features and Results are presented above the grid.

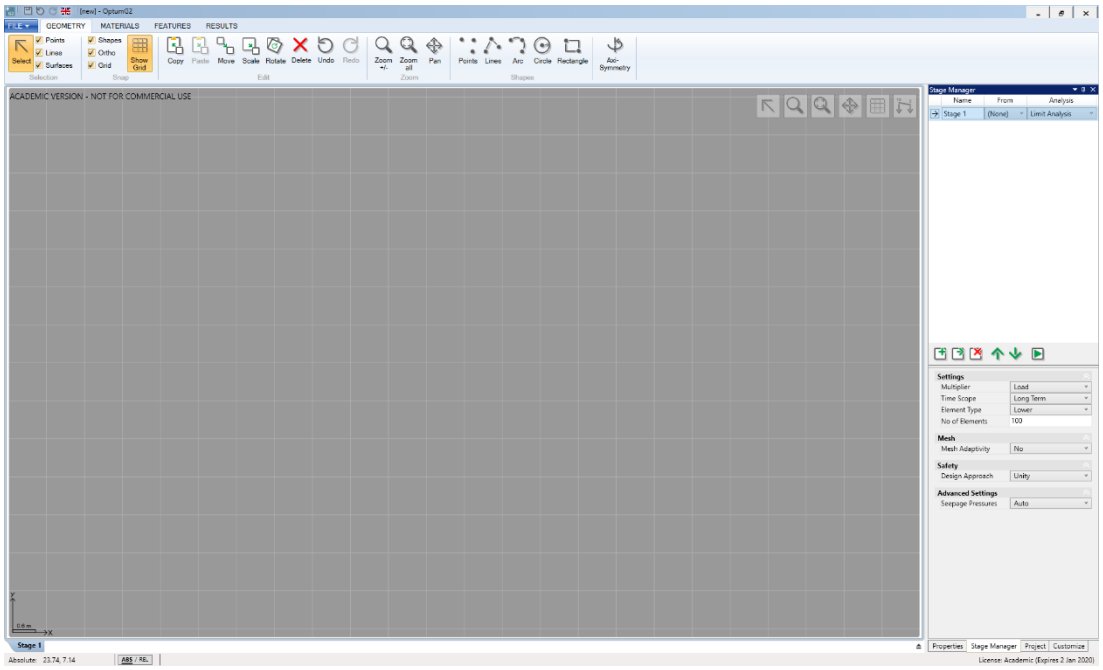

Figure 3.10. *OptumG2*, software background view (OptumCE, 2017).

Firstly, the geometry of the problem is outlined by using functions such as Point, Line, Arc, Circle and Rectangle on the 2D grid and Box, Sphere, Cone, Prism and N-Prism on the 3D grid. These functions are also shown in Figures 3.10 and 3.11.

The outline of the problem is completed by utilising the generic editing tools; copy, paste, move, scale, rotate, delete, undo and redo.

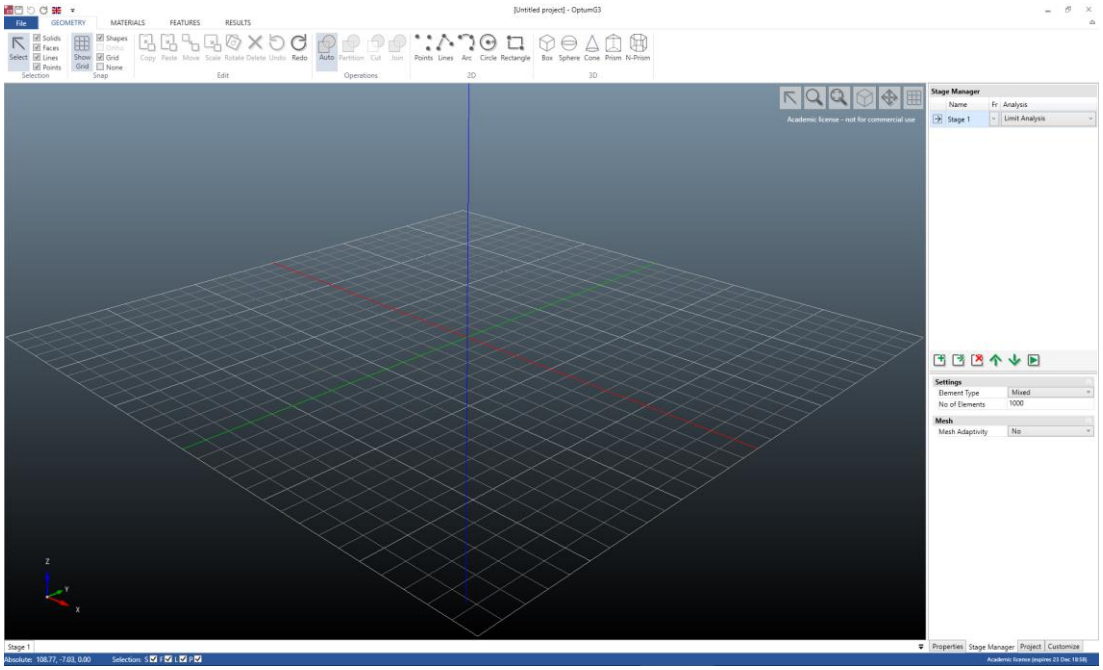

Figure 3.11. *OptumG3*, software background view (OptumCE, 2018).

Each line, point and surface are allocated an identification number and coordinate. Similar to any software package, zooming in and out, zoom to scale, and pan are tools to help the user build the model. Once the geometry of the model is complete, the materials are chosen. A material library is internally built in the software for the user. There are different material categories available in *OptumG2* and *OptumG3* (Figures 3.12 and 3.13).

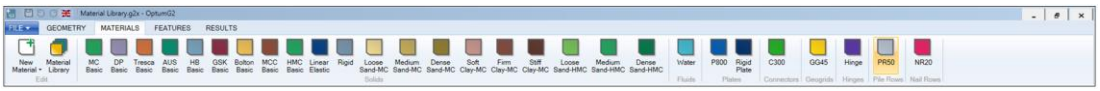

Figure 3.12. *OptumG2*, material library (OptumCE, 2017).

Figure 3.13. *OptumG3*, material library (OptumCE, 2018).

Shown in Figures 3.14 and 3.15 are examples of the Mohr-Coulomb soil properties which may be altered to suit. The detailed common properties include; General,

Material, Stiffness, Strength, Flow Rule, Tension Cut-Off, Unit weights and Initial Conditions.

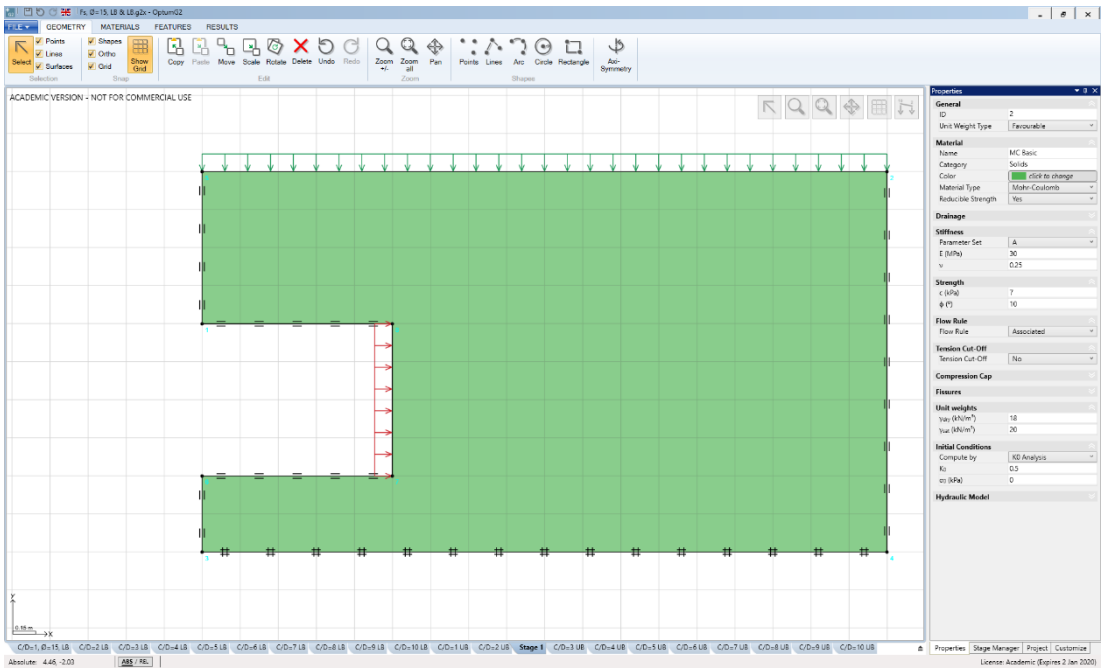

Figure 3.14. *OptumG2*, simple basic geometry functions and material properties for Mohr-Coulomb soil (OptumCE, 2017).

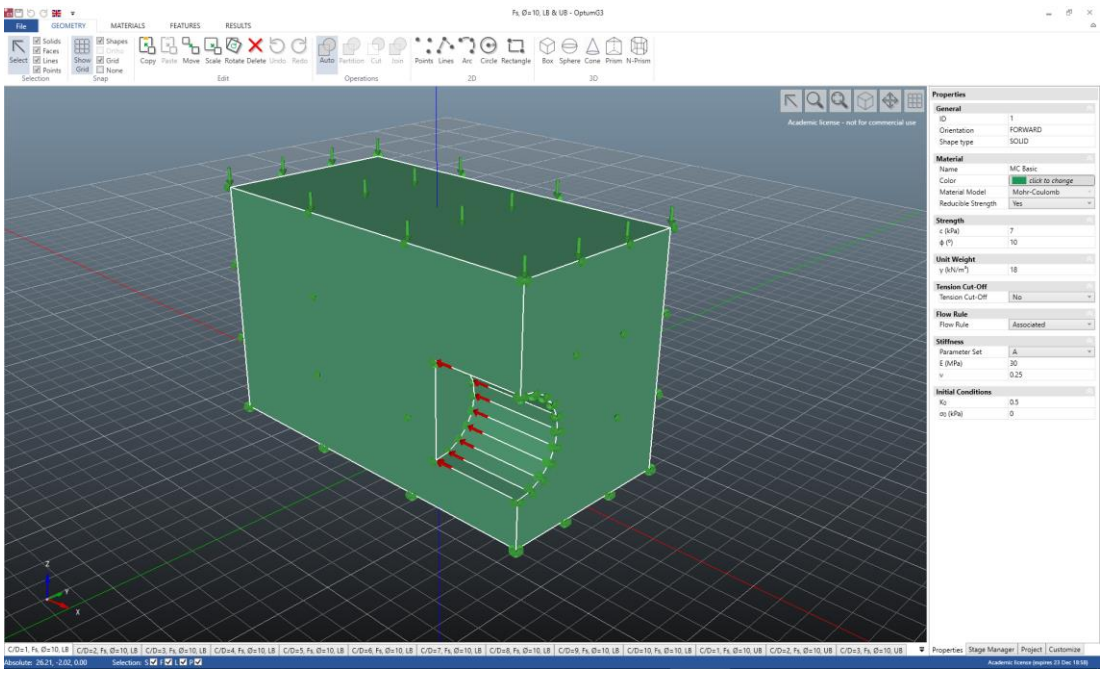

Figure 3.15. *OptumG3*, simple basic geometry functions and material properties for Mohr-Coulomb soil (OptumCE, 2018).

For the model boundary constraint, various supports may be required. The three main support features in *OptumG2 and OptumG3* are the Full, Normal and Tangential supports. Application is achieved to lines and surfaces by selecting and assigning the support mechanism. Full support prevents displacements in all directions, while the Normal and Tangential supports restrain movement in the perpendicular and parallel directions of the lines or surfaces, respectively (Figure 3.16).

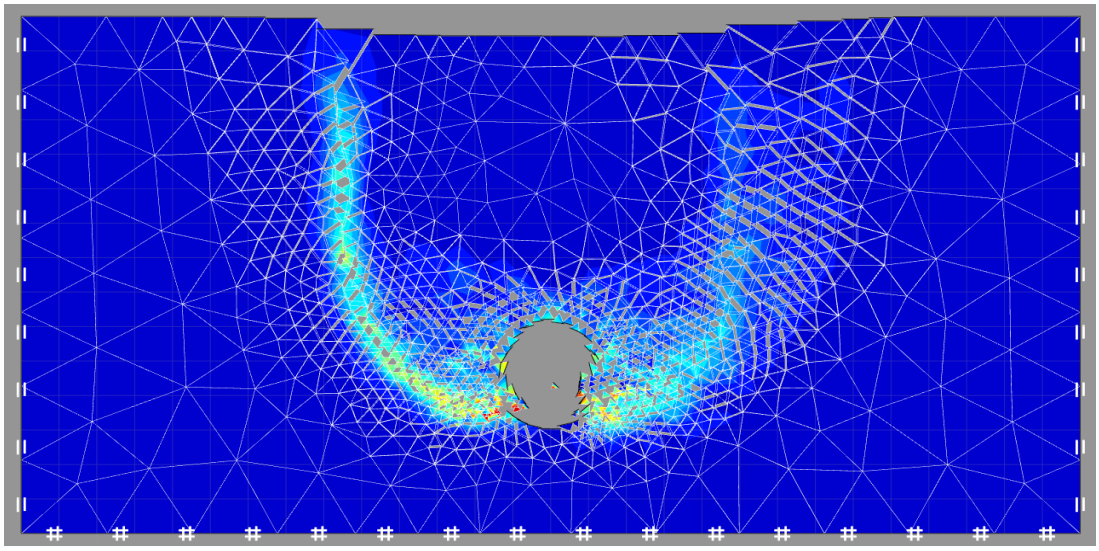

Figure 3.16. *OptumG2*, standard fixities for the domain boundary (OptumCE, 2017).

There are a number of other features within *OptumG2* that may be used for a wide range of problems. The features include; Connector, Fixed End Anchor, Plate, Geogrid, Shear Joint, Mesh Size and Mesh Fan. In *OptumG3* the available features are the shell and shear joint. These features are mostly used for specialised analyses of geotechnical and structural problems.

Different loading conditions may be chosen for the modelling of problems. The load features can be divided into two groups; Fixed Loads and Multiplier Loads, denoted by green and red, respectively. The Multiplier Loads have initially placed a value of 1 kN/m^2. The loads can be either Concentrated, Distributed or Body Loaded which apply to nodes, lines, surfaces and solids, as shown in Figures 3.17 and 3.18.

Figure 3.17. *OptumG2*, load features (OptumCE 2017).

Figure 3.18. *OptumG3*, load features (OptumCE 2018).

The choice of fixed or multiplier loading will be generally controlled by the type of analysis required. For example, if the minimum support pressure required to maintain the stability at the collapse for a tunnel heading, the uniform distributed Multiplier Load should be applied on the face of the tunnel as illustrated in Figures 3.14 and 3.15. The Stage Manager is the tab to the bottom right-hand corner used to select the type of analysis. The initial conditions and respective analysis type are both tabbed for each model structure. The Analysis tab in *OptmG2* consists of Mesh, Seepage, Initial Stress, Elastic, Limit Analysis, Strength Reduction, Elastoplastic, Multiplier Elastoplastic and Consolidation, while in *OptumG3* the Analysis tab comprises of Mesh, Initial Stress, Elastic, Limit Analysis, Elastoplastic and Feasibility.

The analysis chosen will depend on the settings selected. For example, if the Strength Reduction Analysis (*OptumG2*) is elected, the reduced in strength properties of the soil until a failing limit. For Tresca material, the strength reduction factor can be viewed as a factor of safety (*FoS*) value shown in Equation 3.14.

$$FoS = S_u / S_c \tag{3.14}$$

Where S_u is the available undrained shear strength of the soil and S_c is the critical strength necessary to maintain limiting equilibrium. In Limit Analysis, the fixed loads are kept constant while the multiplier loads are amplified until a state of incipient collapse is attained. The factor by which the multiplier loads need to be amplified to cause collapse is also referred to as the collapse multiplier. In addition to determining the collapse multiplier for a set of external loads, it is also possible to compute the factor by which gravity should be amplified in order to achieve a state of collapse. This feature is useful, for example, in connection with slope stability.

In *OptumG2*, The Element Type can be either Lower, Upper, 6-node Gauss, 15-node Gauss or Others. In *OputmG3*, there are three types of elements; Lower, Mixed and Upper. Mixed is a new type of element that combines the features of lower and upper elements, which result in an accurate solution. This study selected the upper and lower bounds for load multiplier and strength reduction techniques in both analyses 3D and 2D. The No. of Elements tab includes the total number of elements used across the model geometry and consequently affects the accuracy. The Mesh Adaptivity is used

to refine the failure mechanism. The Start Elements includes the number of elements in the initial mesh, while the Adaptivity Control tab is the control variable adopted. For both analyses (2D and 3D), it was recommended to adopt three or four iterations. The full outlines of the Stage Manager are presented in Figures 3.19.

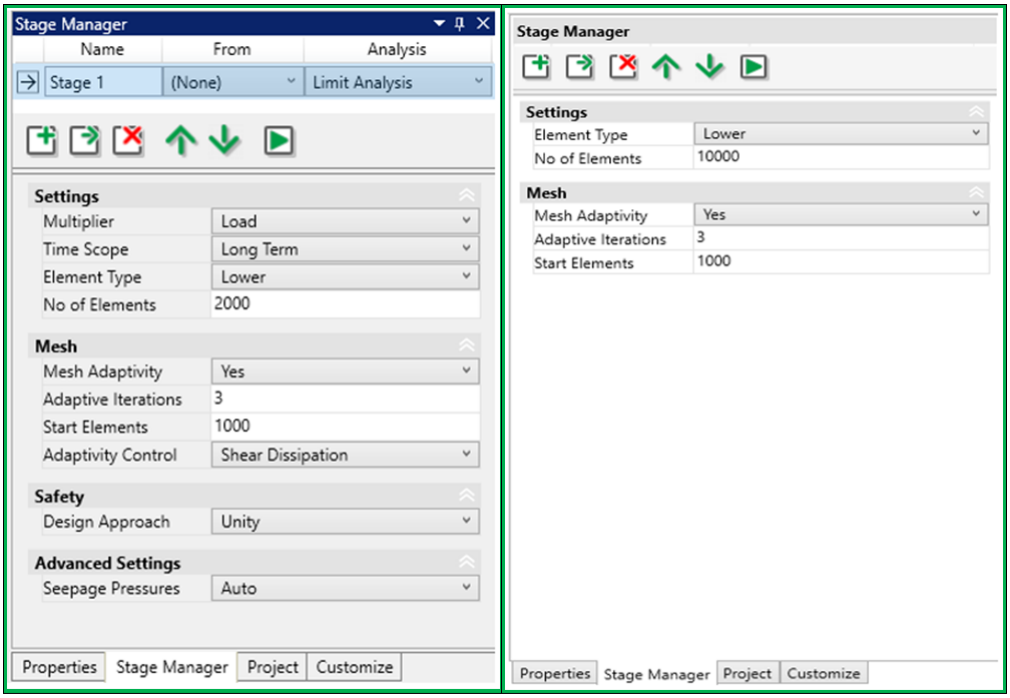

(a) (b)

Figure 3.19. Stage manager overview for limit analysis, (a) *OptumG2*, (b) *OptumG3*.

Figures 3.20 and 3. 21 show the 2D and 3D tunnel head stability problem, respectively. The models are analysed using Limit Analysis with the load Multiplier and presented with an animation of shear dissipation contour with Mesh Overlay.

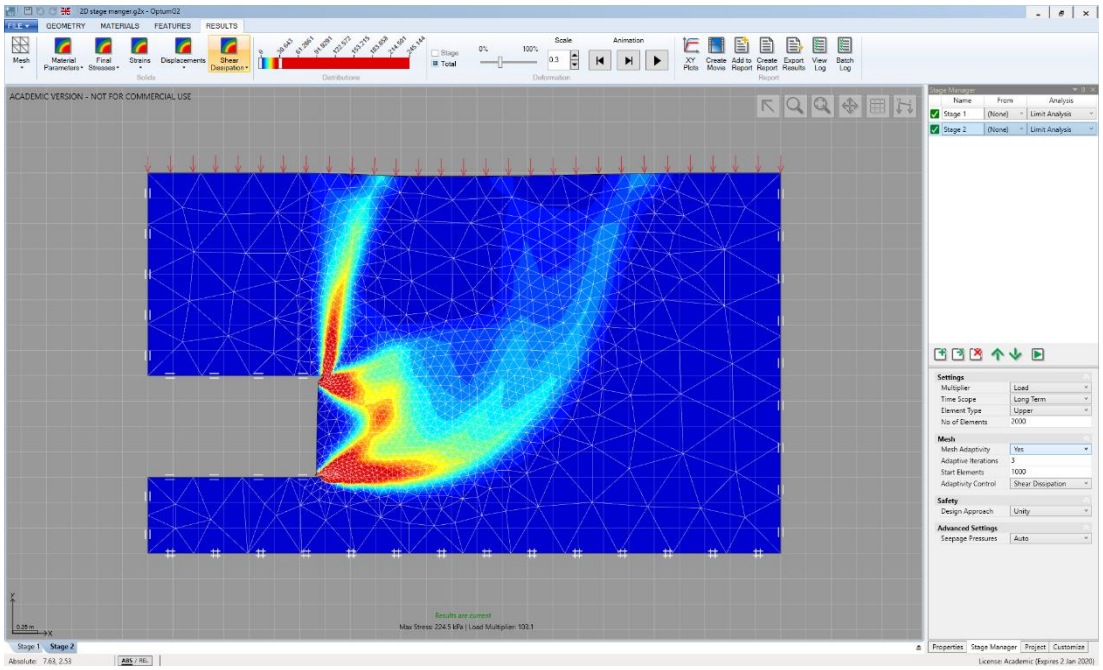

Figure 3.20. *OptumG2*, shear dissipation with a mesh overlay (OptumCE 2017).

The shear dissipation is the key quantity to indicate the plasticity, and it is equal to the shear stress times the shear strain at failure. Therefore, the contour animations clearly show the failure mechanism of the tunnel head and specify the usefulness.

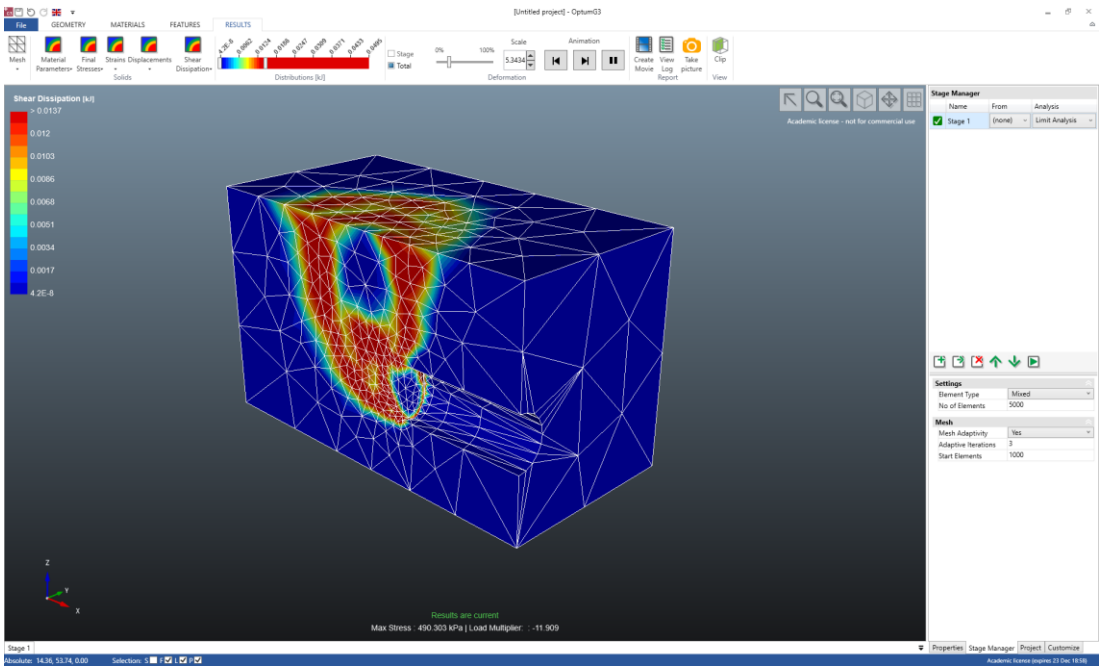

Figure 3.21. *OptumG3*, shear dissipation with a mesh overlay (OptumCE 2018).

3.4 Finite Difference Method (*FDM*)

This method discretises the domain similar to the *FEM*; elements and nodes are used. The main difference is the approach used to solve the unknown parameters. This method uses an explicit approach that works on the principle that a disturbance in the mesh will only be felt at adjacent nodes if a small enough time step is used. This approach is mainly used for dynamic problems but can be used as a quasi-static method if dampening is applied to the dynamic problem. This approach allows the analysis of the solution procedure with time, which allows observation of movement after each step, a significant advantage over *FEM*. No matrices are generated, which means that much less computer memory is required, and also that required computer power isn't linked with the size of displacements. This method is also associated and can be used to simulate stability and settlement problems together. Details of method description may be found in Narasimhan and Witherspoon (1976).

3.4.1 Fast lagrangian analysis of continua (*FLAC*)

FLAC is a two-and three-dimensional explicit finite difference program associated with geotechnical and geomechanical engineering. *FLAC* utilises Lagrangian analysis, dynamic equation of motion and numbers of built-in constitutive models to solve the problem.

In *FLAC*, due to small-time steps in the problem-solving process, the information would not physically transfer from one element to the other. Each element acts as a base on the linear or nonlinear stress/strain regulation to respond to the exerted force and boundary condition (Wang et al. 2011).

3.4.2 Numerical modelling in *FLAC*

FLAC recommends the following steps to be undertaken to execute a successful two and three-dimensional numerical analysis:

a) Defining the objective of the work: Defining the objective of the work will reduce the complication of the work that may impact on the accuracy of the results.

b) Creating a conventional vision of the model: This will allow the user to approximate the model and results. The conceptual model also helps decide on the best tool and model structure.

c) Build and run an idealised model: Running the simple idealised model will help detect issues that might not be possible when dealing with complicated models. It also helps to understand the system and the structure of the physical model.

d) Determine problem-specific data: The accuracy of the numerical model depends on the reliability of the input. Therefore, the geometric details, initial condition, external loads and material property need to be defined before analysing.

e) Prepare a series of detailed model runs: There are important elements, such as running time, which need to be considered for an effective and efficient parametric study. The computational processing time is particularly important when it comes to three-dimensional models. Applying monitoring stages in a model would help in checking with the physical data, which is beneficial in terms of a better interpretation of the results.

f) Perform the model calculation: It is recommended to conduct a few individual detailed runs, and once the results are confirmed, a series of the runs can be performed.

g) Present results for interpretation: The final phase of successful modelling is to interpret the results. The results can best be presented graphically in the form of contours and vector plots.

In general, having a set of boundaries and an initial value, *FDM* is capable of solving the problem by using differential equations. *FLAC* uses this technique and reproduces the finite difference equation in each step of the analysis, and then the software is capable of storing the solutions in the form of the matrix (FLAC 2D 2003). Every set of the pilot equation that has been used will be substituted by the algebraic term written in relation to field variables, such as displacement, stress etc.

The explicit *FDM* reproduces those stored equations in every step on analysis. In addition to the explicit method, *FLAC* uses the Lagrangian method to coordinate the grid at each step. Displacement of the material will be added to coordinates to illustrate the material deformation. Figure 3.22 shows the steps required to create a successful two-dimension model in *FLAC*.

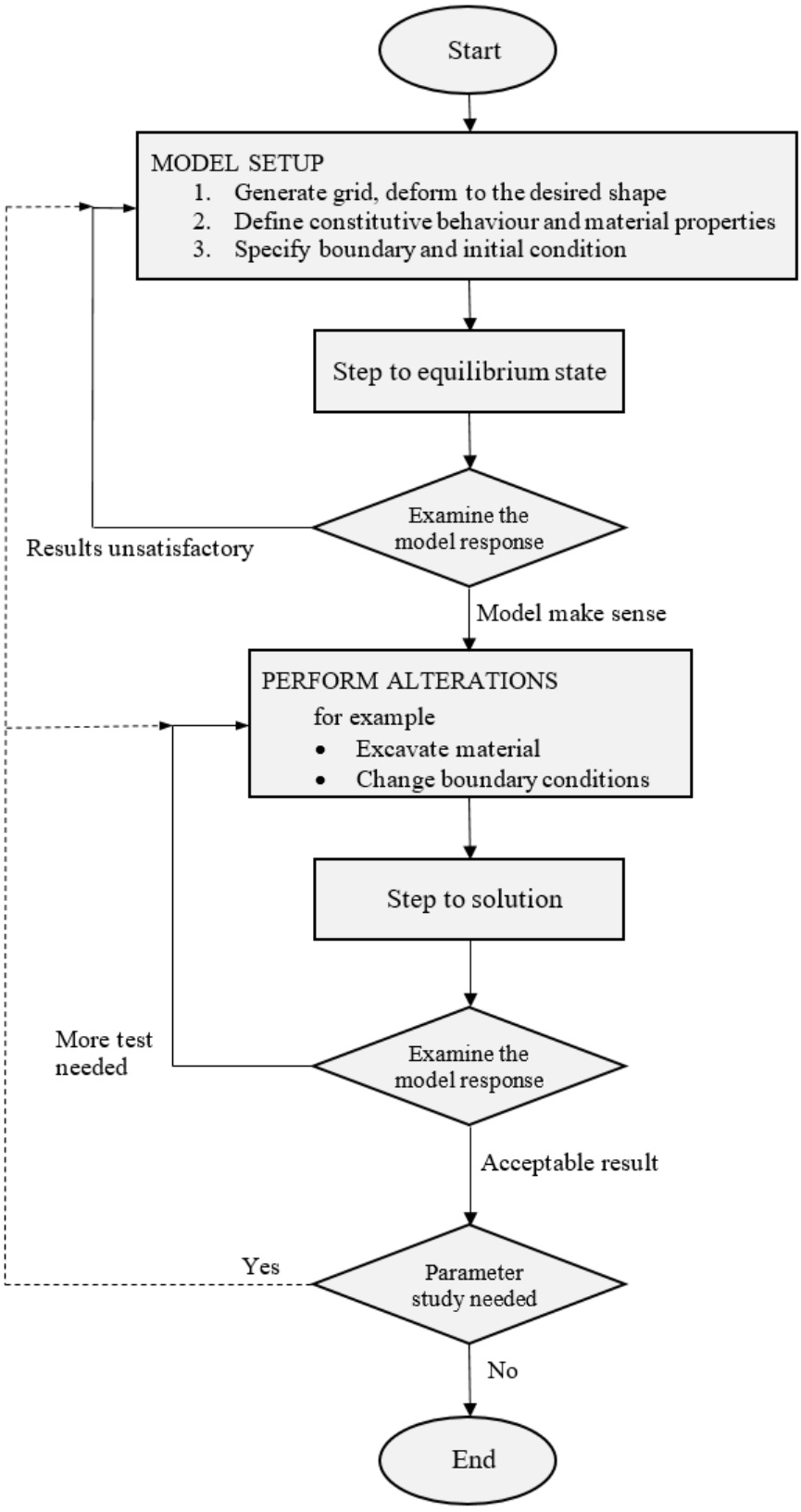

Figure 3.22. Numerical modelling setup in *FLAC* (FLAC 2D 2003).

The *FLAC* solution considers the dynamic equation of motion in its process of finding the static solution. This ability will ensure that the numerical system remains stable when the physical system is in an unstable condition. This is particularly important in nonlinear materials where there is always the possibility of high instability. In reality, some of the strain energy in the system will dissipate by converting into kinetic energy.

To encounter such a situation, *FLAC* models this process directly, because the inertial parameters combine in kinetic energy and are dissipated. Figure 3.23 illustrates the general progress of the explicit method, which has been implemented in *FLAC*.

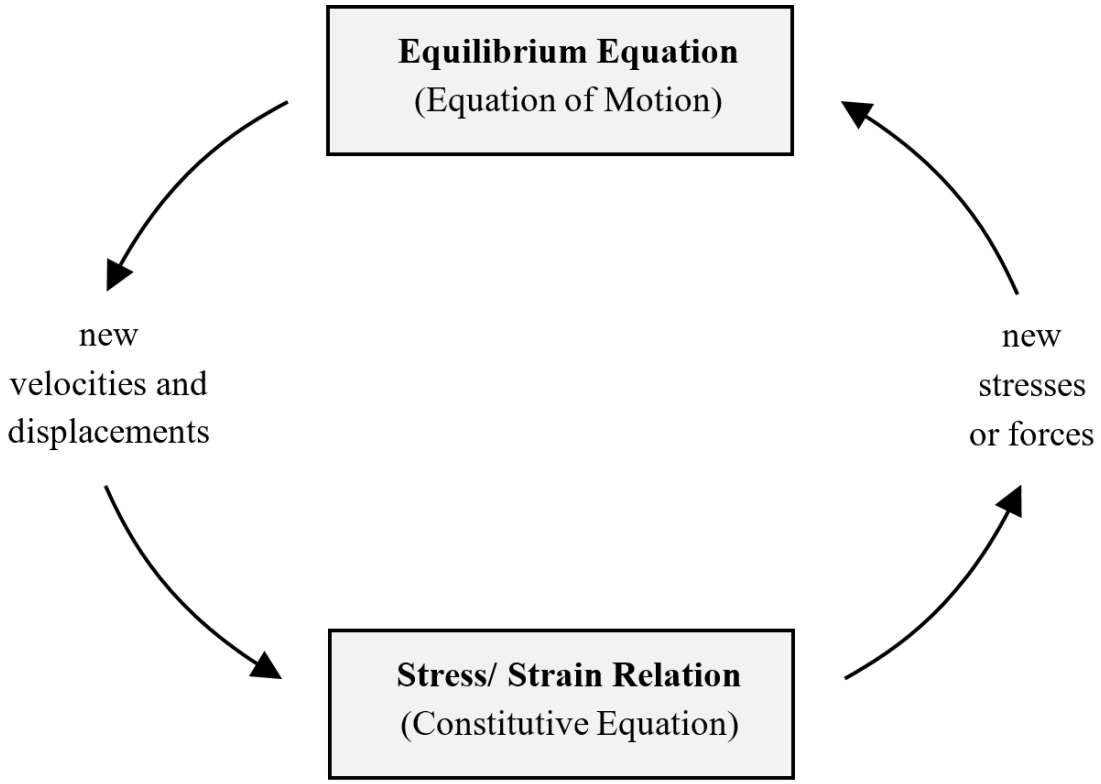

Figure 3.23. General explicit calculation loop (FLAC 2D 2003).

The process starts with the equation of motion, which drives new displacement and velocity from stresses. The strain rate would be driven from velocity to form new stress. The entire loop explained above would take place in one timestep. It should be noted that each box in the above figure will update the grid parameters from the known constant variables. For example, the "stress/strain relation" box would consider the new velocity, which has already been calculated to compute the new stress rates.

The explicit method has several advantages in comparison with the implicit technique mainly associated with the finite element method. Table 3.1 shows the comparison of the explicit and implicit method.

Table 3.1. Comparison of explicit and implicit methods.

Explicit	Implicit
Timestep must be smaller than a critical value for stability.	Timestep can be arbitrarily large, with unconditionally stable schemes.
A small amount of computational effort per timestep.	A large amount of computational effort per timestep.
No significant numerical damping introduced for a dynamic solution.	Numerical damping dependent on timestep present with unconditionally stable schemes.
No iterations are necessary to follow nonlinear constitutive law.	The iterative procedure is necessary to follow a nonlinear constitutive law.
Provided that the timestep criterion is always satisfied, nonlinear laws are always followed in a valid physical way.	Always necessary to demonstrate that the abovementioned procedure is (a) stable and (b) follows the physically correct path (for path-sensitive problems).
Matrices are never formed. Memory requirements are always at a minimum. No bandwidth limitations.	Stiffness matrices must be stored. Must find ways to overcome associated problems, such as bandwidth. Memory requirements tend to be large.
Since matrices are never formed, large displacements and strains are accommodated without additional computing effort.	Additional computing effort is needed to follow large displacements and strains.

In summary, the explicit method fits best for nonlinear, large strain and physically unstable systems.

3.4.3 Lagrangian analysis

The Lagrangian strategy uses a similar principle to the finite difference method by dividing the continuum material into a number of connected elements. Since *FLAC* does not need to form a global stiffness matrix, amending the coordinate's change at

every time step became unimportant. Unlike the Eulerian method, the Lagrangian equation, incremental displacement will be added to coordinates, and the grid will distort to suit the material.

Grid generation

The model will subdivide to a finite difference meshed by the user to compose quadrilateral elements. Using the triangular element would eliminate problems that may occur in constant strain finite elements. *FLAC* separates these mesh elements into two overlaid constant-strain triangular elements. The triangles are illustrated as a, b, c and d in Figure 3.24.

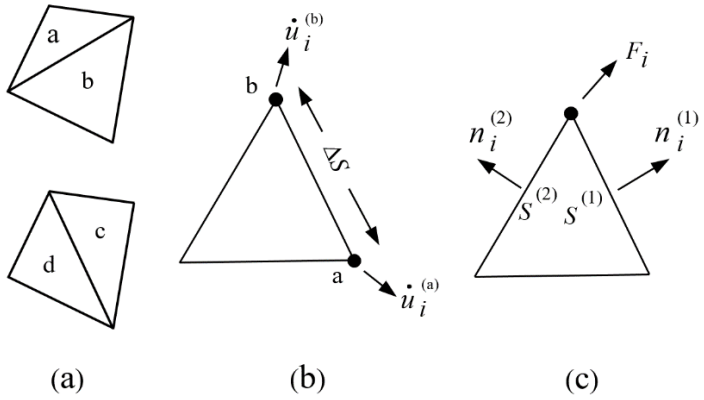

Figure 3.24. (a) Overlaid quadrilateral elements used in *FLAC*, (b) Typical triangular element with velocity vectors, (c) Nodal force vector (FLAC 2D 2003).

FLAC uses the mixed discretisation method suggesting different discretisation for isotropic and deviatoric sections of materials stress and strain. The detail process was described by Marti and Cundall (1982). It should be noted that while deviatoric is fixed, the volumetric strain would be an average of each pair of triangles. So, for triangle a and b in Figure 3.24a, the strain rate would be the mean of both triangles as presented in equation 3.15.

$$e_m = \frac{e_{11}^a + e_{22}^a + e_{11}^b + e_{22}^b}{2} \tag{3.15}$$

The similar approach would be considered for triangle c and d. However, it is important to note that this process is for a plane strain condition and an axisymmetric condition, all three direct strains need to be considered to obtain the average stress.

The numerical simulation programs will face difficulties when applying the constitutive models to characterise the geomechanical material of the soil. Those are physical instability, the path dependency of nonlinear materials and non-linearity of stress-strain behaviour of the material. The *FLAC* uses its explicit and dynamic problem-solving ability with the aid of the constitutive models ranging from linear elastic models to highly nonlinear plastic models to address this issue. Currently, *FLAC* has fourteen constative models used to model represent the geomechanical material behaviour:

- Null model: to represent the excavated/removed material.
- Elastic, isotropic model: This model represents the homogeneous, continuous materials where stress-strain behaviour presents as a linear relationship.
- Elastic, transversely isotropic mode: The elastic, transversely isotropic model allows the software to simulate layered elastic materials.
- Drucker Prager model: This model is used for materials with a low frictional angle, such as soft clay.
- Mohr-Coulomb model: This is a common plastic model, which represents the shear failure of the soil and rocks.
- Ubiquitous joint model: This model represents the anisotropic plastic models, which includes weak planes enclosed in the Moher coulomb model.
- Strain softening/hardening model: This criterion will represent the nonlinear softening and hardening behaviour of the material base on the Moher Coulomb properties.
- Bilinear strain softening/hardening ubiquitous joint model: This model will represent the softening or hardening material behaviour of the weak plane based material.
- Double yielded model: The double yielded failure criterion characterises the material that undergoes irreversible compaction.
- Modified cam clay model: This criterion will be used to represent the cases where the volume change, bulk property and shear resistivity requires consideration.
- Hoek Brown model: Hoek Brown characterises stress conditions, resulting in a failure in rocks.
- The modified Hoek Brown model: This model represents the post-failure plastic behaviour in term of the dilation angle.

- Cysoil model: The cap-yield soil used to represent the nonlinear behaviour of the soil.
- Simplified cysoil model: Simplified cysoil uses hyperbolic model parameters, which are input by the user. It also uses the Moher coulomb failure envelope.

The software uses the above criteria to simulate the behaviour of the structures constructed of various materials, which reach the plasticity deformation when it reaches the yielding limit.

3.4.4 Shear strength reduction method (*SSRM*)

With the development of computer technology over the past decades, numerical modelling has become an essential tool in geotechnical engineering. Stability analysis can be performed by the calculation of factors of safety in *FLAC* using the shear strength reduction method (*SSRM*). The *SSRM* is commonly applied through the factor of safety calculation by gradually reducing the shear strength of the testing material to estimate the point where the system reaches a state of limiting equilibrium. This method is popular in the stability analysis of slopes, retaining walls and tunnels; however, it has rarely been used in stability analysis of sinkholes.

This study uses the shear strength reduction method (*SSRM*) with the aid of the built-in program language, *FISH*, to analyse the stability problem.

This method was utilised as early as 1975 by Zeinkiewicz et al. (1975), followed by Naylor (1982), Matsui and San (1992), Ugai and Leshchinsky (1995), Griffiths and Lane (1999), Michalowski (2002), Zheng et al. (2005) and numerous other researchers. The *SSRM* is coded in the finite difference software *FLAC* as well as many other computational tools, such as Plaxis (2011) and *OptumG2* (OptumCE 2017). In the method of shear strength reduction, a factor of safety is defined as the ratio of the actual undrained shear strength and the critical undrained shear strength, as shown in equation (3.16).

$$FoS = \frac{S_u}{S_c} \tag{3.16}$$

Where (S_u) is the actual undrained shear strength of the soil and (S_c) is a critical shear strength at collapse. In practice, the factor of safety above one demonstrates a stable condition. In this study, the soil body is defined as a homogeneous, undrained clay, following the Tresca material. The shear strength reduction method (*SSRM*) is usually

applied to the conventional model of Mohr-Columb material. The safety factor is defined as follows:

$$c^{trial} = \frac{1}{F^{trial}} c \tag{3.17}$$

$$\phi^{trial} = \arctan\left(\frac{1}{F^{trial}} \tan\phi \right) \tag{3.18}$$

With this method, *FLAC* first brackets down the results to "stable" and "unstable". Both the cohesion c and friction angle ϕ values are gradually reduced until the model reaches the failure state. In the second stage, the solution gradually reduces between "stable" and "unstable" until the solution falls below the tolerance (FLAC 2D 2003). To determine the boundary between a stable and unstable model, a series of individual runs with different strength reduction factors will be performed to determine if the model is at equilibrium, or if the continuing plastic flow has already reached. The final failure point, with the aid of successive bracketing of strength reduction factor, would identify the failure point (FLAC 2D 2003).

3.4.5 Pressure relaxation method (*PRM*)

With the development of powerful computers over the last three decades, numerical modelling has proceeded to become a dominant technique for problem resolution. The pressure relaxation method developed with the built-in program language of *FLAC* (*FLACish* or *FISH*). An approach such as this was first developed by Panet and Guenot (1983). In this method, the internal tunnel pressure (σ_t) is gradually reduced to zero from a starting amount equalling the equivalent in situ soil pressure. This approach can simulate reductions in the internal tunnel pressure (σ_t) as well as the soil's response.

The internal pressure σ_t is reduced by multiplying the at-rest pressure, where no movement occurs, by a reduction factor, which is based on the number and range of relaxation steps. At each subsequent relaxation step, the internal pressure is less than the at-rest pressure, and consequently, the soil moves into the tunnel void until the internal forces in the soil reach equilibrium, balanced or otherwise. In the elastic state, internal forces have reached a balanced state (total unbalanced force in *FLAC* approaches zero), no more movement takes place, and the circular tunnel is considered stable. Once the internal pressure is reduced to the extent where the internal forces are no longer sufficient to retain the earth pressures, total unbalanced forces will never approach zero, and the tunnel is considered unstable.

A screenshot of the inputs section of the *FLAC* script is shown in Figure 3.25. The developed script is quite user-friendly, and given *FLAC*'s ability to queue jobs, it is very efficient and time effective to set up and run parametric studies.

```
; -----Pressure Relaxation Method
; -----For solving 2D tunnel heading problems (Settlement and Stability)
; -----Developed by Jim Shiau, PhD (Newcastle)
; -----@ University of Southern Queensalnd, Toowoomba, QLD, 4350, Australia
; -----@ 20 July 2014
        new
        set echo on
        set plot emf
        config extra=20;
        set overwrite on
        set log Pulling_Sigma_t_output.txt
def para_meter
; -----------This is the place you can change problem geometry
; ----------- and material property
; -----------change the following parameters to suit your need
        pathname = 'C:\CASE4'   ; Files will be saved here!!
        Save_or_not = 'NO'      ; "YES" - save all files (*.sav and *.emf)

        Start_from_p = 0        ; Start from zero relax %
        end_at_p = 100          ; A complete relaxation (no internal support)
        No_relax = 10           ; No of steps for relaxation

        Pulling = 'YES'         ; "YES" - pulling sigma t (for blow out analysis)
        No_pulling = 10         ;  np steps

        C = 48.0                ;  Soil cover (m)
        D = 6.0                 ;  Diameter of the tunnel (m)

        SOIL_DEN = 1834.86      ; Soil density (kG/m3)
        SOIL_COH = 18000        ; Soil cohsion (N/m2, Pa)
        SOIL_FRI = 20           ; zero for clay (degree)
        SOIL_DIL = 10           ; ** watch this dilation angle very carefully**
        SOIL_TENS = 1e10        ; high soil tension to prevent tension failure (N/m2, Pa)
        SOIL_Young = 16E6       ; Youngs Modulus (N/m2, Pa)
        SOIL_poisson = 0.33     ; Poisson's ratio

        Set_grav = 1*9.81       ; centrifuge modelling - put more g
; -----------Surface pressure set to zero in most cases (in pascal, N/m2)------
; --------------For strong cases, non-zero sigma_s is reuqired to fail the soil.
; --------------For soft cases, better set sigma_s=0.
        Sigma_s = 0             ; For soft cases, better set sigma_s=0
; --------------For strong cases, non-zero sigma_s is reuqired to fail the soil.
        No_step= 7000           ; no of steppings for each relaxation
        XElementSize = 0.5      ; element size;divide equally with B & H
        YElementSize = 0.5      ; element size;divide equally with B & H
;;;;;;;;CHANGE the above parameters to suit your need;;;;;;;;;;
end
```

Figure 3.25. Inputs section of the pressure relaxation script for *FLAC*.

PART A:

UNDRAINED ANALYSIS

(Chapters 4 - 8)

CHAPTER 4: UNDRAINED ANALYSIS OF 2D TUNNEL HEADING

4.1 Introduction

The development of modern society and the increase of population introduce the need for greater utilisation of underground spaces in urban areas. Furthermore, the mining industry is continually looking to refine the depth excavation stability issue. One of the main problems when constructing a tunnel is to ensure the stability of the tunnel heading. Ensuring tunnel face stability is directly related to the safe and successful construction of the underground structure. This chapter will discuss the stability of an idealised tunnel heading in undrained soil conditions. The heading is rigidly supported along its length, while the face is subjected to internal pressure, and free to move. The problem approximates a longwall in an underground excavation. Failure of the heading in collapse and blowout is studied by different combinations of internal pressure and surface surcharge. Shear strength reduction technique and finite element limit analysis are utilised to study two-dimensional heading stability. Both the upper and lower bound factor of safety values are determined for a wide range of heading configurations and stability scenarios. The obtained results of the factor of safety (*FoS*) for various depths are presented in the form of dimensionless stability charts and verified by the finite difference method (*FDM*) as well as other existing solutions available in the literature. Some practical examples are provided to demonstrate the usefulness of the design charts and tables. These charts give a good approximation of *FoS* and can be used by engineers in preliminary designs.

4.2 Problem Definition and Modelling Technique

Figure 4.1 shows the problem definition of an idealised tunnel heading. The soil medium is considered as undrained and is modelled as a uniform Tresca material. The undrained shear strength (S_u) and the unit weight (γ) describe soil properties used, while the tunnel has a height (D), cover depth (C) above its crown and axis depth (H) below the ground surface. The face of the heading is free to move and is subjected to

a normal internal pressure σ_t, while the ground surface is subjected to a vertical surcharge σ_s. These pressures, together with soil self-weight, are varied to test the collapse and blowout stability of the models.

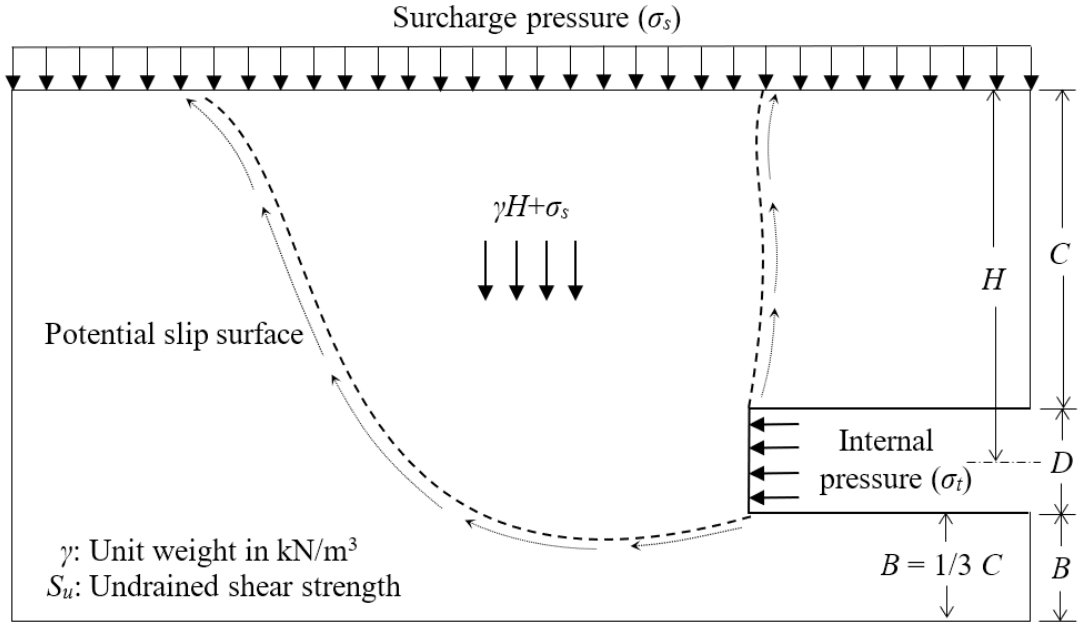

Figure 4.1. Problem definition.

In undrained soil $(\phi_u = 0)$, the shear strength is independent of the loading direction, and the tunnel heading stability can be well-expressed by using Broms and Benermark's stability number (N), as shown in Equation 4.1.

$$N = \frac{\sigma_s + \gamma H - \sigma_t}{S_u} \tag{4.1}$$

Numerical results based on shear strength reduction method (OptumCE 2017) are represented by a factor of safety (FoS) that is a function of the depth ratio (C/D) and the stability number (N), as shown in Equation 4.2.

$$FoS = f\left(\frac{C}{D}, N = \frac{\sigma_s + \gamma H - \sigma_t}{S_u}\right) \tag{4.2}$$

The stability number N can be either positive, zero or negative, depending on the actual input design parameters (σ_s, σ_t, γ, C, D, H and S_u). Thus, to cover all possible scenarios of failure, the present study investigates the stability of tunnel headings by relating FoS to a broad range of stability numbers (N = -15 to 15) and depth ratios (C/D = 1 to 10). For example, to generate a value of N = +5 for C/D = 3, the chosen parameters are $\sigma_s = 0$, $\sigma_t = 153$ kPa, $\gamma = 18$ kN/m^3, $C = 18$m, $D = 6$m, $H = 21$m, and $S_u = 45$ kPa.

The rigorous upper bound and lower bound factors of safety for the cases being studied are computed by using the shear strength reduction method (Krabbenhoft and Lyamin (2015). The adaptive mesh used in this study is shown in Figure 4.2. The numerical procedures used are based on the limit theorems of classical plasticity (Lyamin & Sloan 2002a, 2002b).

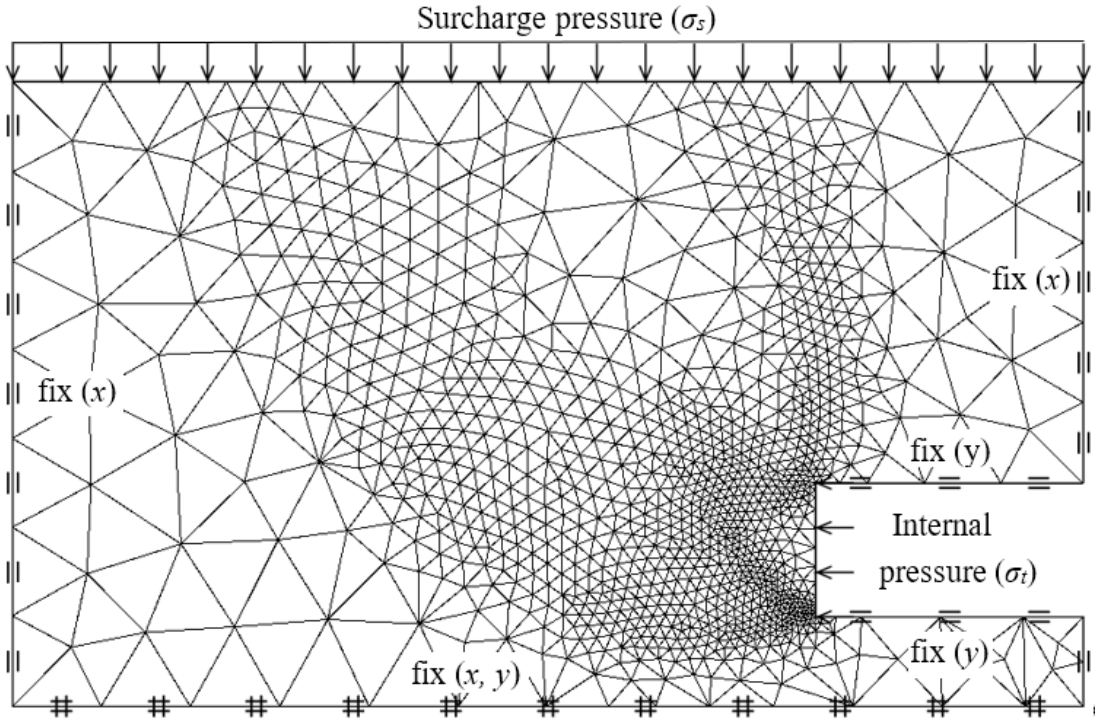

Figure 4.2. A typical adaptive mesh used for the problem.

Result verification is normally required in computational research. For this purpose, the finite difference (*FD*) method, via the software *FLAC* with built-in implementation of the strength reduction technique, has also been used over the same parametric range.

4.3 Results and Discussion

A wide range of stability numbers (N = -15 to +15) and depth ratios (C/D =1 to 10) are investigated to cover all possible situations associated with a tunnel heading stability. Figure 4.3 shows the full range of the results (*LB*, *UB* and *FD*) related to the collapse and blowout of a tunnel heading model with a depth ratio of three (C/D = 3). It can be seen that the curves are hyperbolic, and a pair of asymptote lines exist. The general equation for this graph was found to be $FoS = N_c / N$. Any combination of N and FoS on this curve yields a unique N_c value, which is constant for a specific depth ratio.

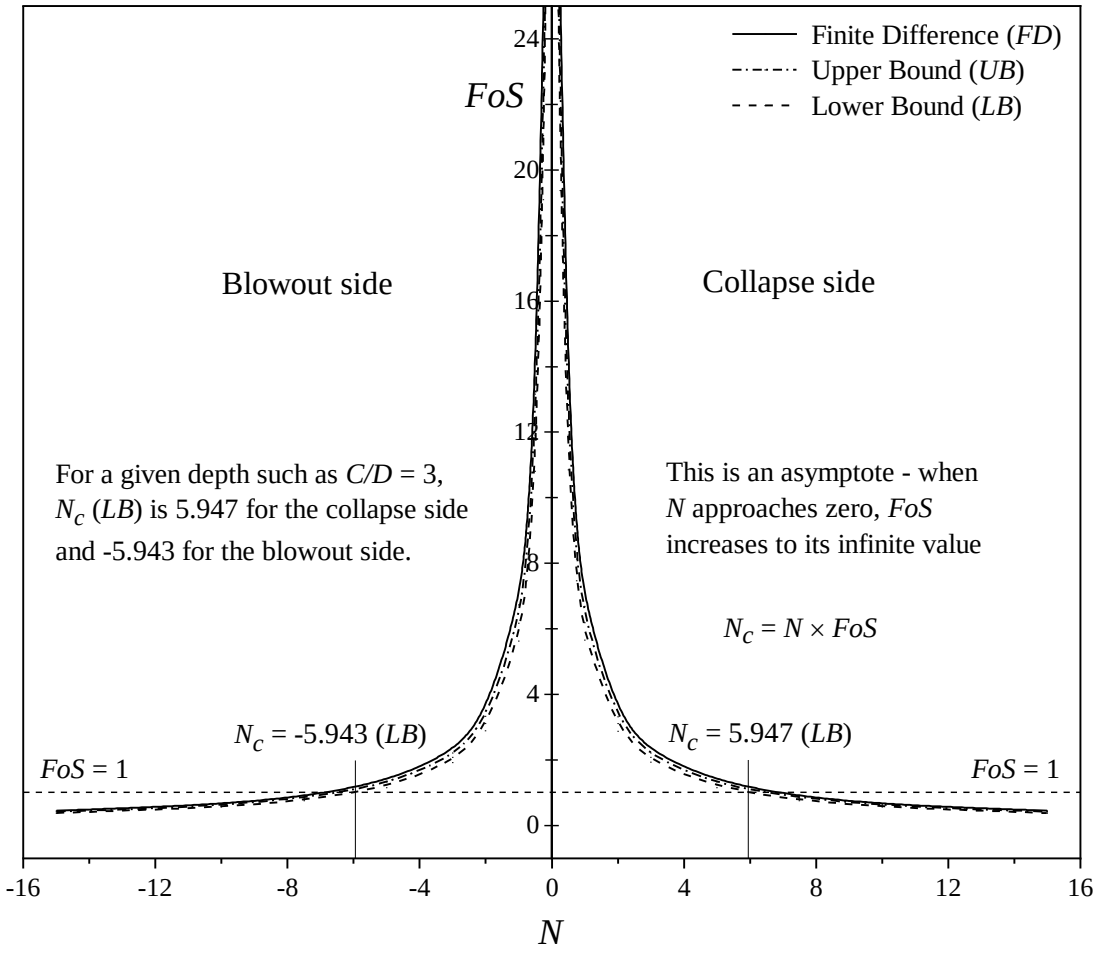

Figure 4.3. *FoS* vs. *N* for *C/D* = 3.

This N_c value is Broms and Bennermarks' original critical stability number. For the depth ratio *C/D* = 3, *LB* solutions give N_c = +5.947 on the collapse side and N_c = -5.943 on the blowout side. Graphically, the two values can be read from the intersection points by drawing a *FoS* = 1 horizontal line, as can be seen in Figure 4.3. Complete *FoS* results are presented in Tables 4.1- 4.3.

Broms and Bennermark's stability number (*N*) consists of two parts: overburden pressure ratio ($OPR = (\sigma_s + \gamma H)/S_u$) and supporting pressure ratio ($SPR = \sigma_t/S_u$). When the *OPR* is equal to the *SPR*, *N* is equal to zero, and *FoS* is at a maximum (infinite). It is noted that a 'weightless scenario' exists on the asymptote line where the stability number is approaching zero, and the factor of safety is at an infinite value. When the *OPR* is larger than the *SPR*, *N* is greater than zero. The factor of safety (*FoS*) gradually decreases as *N* increases and the soil moves in the "collapse" direction. As *N* further increases, an incipient collapse is reached where *FoS* = 1 and the corresponding *N* is the critical N_c.

Table 4.1. *FoS* results for various values of *C/D* and *N* (*LB*, Collapse and Blowout).

	C/D									
N	1	2	3	4	5	6	7	8	9	10
-15	0.277	0.351	0.396	0.433	0.461	0.484	0.503	0.517	0.535	0.545
-12	0.333	0.419	0.475	0.520	0.553	0.578	0.604	0.621	0.642	0.654
-10	0.416	0.521	0.594	0.650	0.693	0.727	0.756	0.776	0.802	0.823
-7.5	0.557	0.700	0.794	0.865	0.920	0.970	1.007	1.035	1.065	1.093
-5	0.830	1.049	1.192	1.297	1.379	1.453	1.512	1.556	1.602	1.650
-4	1.041	1.310	1.486	1.624	1.729	1.815	1.888	1.940	2.004	2.049
-3	1.388	1.743	1.978	2.147	2.308	2.414	2.524	2.589	2.671	2.737
-2.5	1.666	2.096	2.377	2.598	2.766	2.903	3.021	3.104	3.206	3.278
-2.	2.080	2.615	2.969	3.215	3.443	3.600	3.752	3.888	3.988	4.065
-1.5	2.776	3.494	3.962	4.331	4.609	4.839	5.035	5.173	5.343	5.463
-1	4.147	5.183	5.872	6.391	6.781	7.097	7.402	7.605	7.820	8.009
-0.75	5.488	6.856	7.759	8.380	8.912	9.388	9.709	10.012	10.272	10.433
-0.5	8.053	10.014	11.291	12.231	12.898	13.507	14.013	14.339	14.858	15.136
-0.25	14.499	17.716	19.936	21.172	21.644	21.637	21.776	21.762	21.621	21.899
0	Infinity	Infinity	Infinity	Infinity	Infinity	Infinity	Infinity	Infinity	Infinity	Infinity
0.25	14.753	18.116	20.253	21.520	21.923	21.852	21.776	21.840	21.830	21.886
0.5	8.018	10.065	11.309	12.268	13.038	13.671	14.136	14.674	14.926	15.334
0.75	5.439	6.867	7.759	8.408	8.989	9.406	9.739	10.061	10.390	10.602
1	4.113	5.199	5.888	6.423	6.790	7.106	7.465	7.678	7.852	8.037
1.5	2.777	3.501	3.965	4.327	4.604	4.825	5.037	5.211	5.361	5.481
2	2.080	2.615	2.963	3.235	3.431	3.616	3.764	3.878	3.992	4.084
2.5	1.666	2.101	2.379	2.596	2.762	2.895	3.022	3.126	3.216	3.288
3.	1.388	1.746	1.993	2.155	2.300	2.417	2.514	2.603	2.672	2.744
4.	1.041	1.313	1.487	1.623	1.727	1.810	1.889	1.954	2.010	2.055
5	0.834	1.050	1.193	1.300	1.379	1.449	1.512	1.564	1.610	1.646
7.5	0.553	0.700	0.794	0.865	0.920	0.964	1.007	1.043	1.073	1.100
10.	0.418	0.526	0.594	0.648	0.691	0.724	0.756	0.782	0.805	0.819
12.5	0.333	0.421	0.475	0.520	0.553	0.580	0.605	0.627	0.641	0.658
15	0.278	0.349	0.397	0.433	0.460	0.482	0.503	0.519	0.537	0.548

Table 4.2. *FoS* results for various values of *C*/*D* and *N* (*UB*, Collapse and Blowout).

	C/D									
N	1	2	3	4	5	6	7	8	9	10
-15	0.289	0.367	0.418	0.456	0.487	0.512	0.540	0.554	0.569	0.582
-12	0.347	0.440	0.502	0.548	0.584	0.614	0.647	0.665	0.685	0.701
-10	0.433	0.551	0.627	0.684	0.731	0.769	0.809	0.827	0.853	0.874
-7.5	0.578	0.733	0.838	0.913	0.974	1.023	1.079	1.108	1.144	1.167
-5	0.866	1.099	1.254	1.370	1.462	1.539	1.618	1.654	1.707	1.753
-4	1.083	1.376	1.568	1.713	1.826	1.920	2.023	2.075	2.135	2.186
-3	1.446	1.833	2.088	2.281	2.437	2.565	2.698	2.753	2.842	2.918
-2.5	1.733	2.201	2.508	2.741	2.922	3.072	3.236	3.320	3.416	3.498
-2.	2.167	2.747	3.132	3.428	3.649	3.834	4.040	4.131	4.256	4.365
-1.5	2.889	3.669	4.181	4.569	4.870	5.119	5.393	5.534	5.693	5.829
-1	4.325	5.504	6.264	6.833	7.297	7.662	8.080	8.256	8.517	8.729
-0.75	5.772	7.320	8.348	9.113	9.723	10.205	10.765	11.079	11.369	11.636
-0.5	8.638	10.985	12.488	13.634	14.556	15.323	16.122	16.507	16.990	17.442
-0.25	17.123	21.738	24.677	26.891	28.695	30.211	31.804	32.445	33.346	34.160
0	Infinity	Infinity	Infinity	Infinity	Infinity	Infinity	Infinity	Infinity	Infinity	Infinity
0.25	17.123	21.738	24.677	26.891	28.695	30.211	31.751	32.445	33.346	34.160
0.5	8.638	10.985	12.488	13.634	14.556	15.323	16.122	16.507	16.990	17.442
0.75	5.772	7.320	8.348	9.113	9.723	10.205	10.765	11.079	11.369	11.636
1	4.325	5.504	6.264	6.833	7.297	7.662	8.080	8.256	8.517	8.729
1.5	2.889	3.669	4.181	4.562	4.870	5.119	5.395	5.541	5.693	5.832
2.	2.167	2.747	3.132	3.428	3.649	3.834	4.040	4.131	4.256	4.365
2.5	1.734	2.201	2.508	2.737	2.922	3.072	3.237	3.324	3.416	3.499
3.	1.446	1.833	2.088	2.281	2.437	2.565	2.698	2.753	2.842	2.918
4.	1.084	1.376	1.568	1.711	1.826	1.920	2.023	2.078	2.135	2.187
5	0.866	1.099	1.254	1.370	1.462	1.539	1.618	1.654	1.707	1.753
7.5	0.578	0.733	0.838	0.913	0.974	1.023	1.079	1.108	1.144	1.167
10	0.433	0.551	0.627	0.684	0.731	0.769	0.809	0.827	0.853	0.874
12.5	0.347	0.440	0.502	0.548	0.584	0.614	0.647	0.665	0.685	0.701
15	0.289	0.367	0.418	0.456	0.487	0.512	0.540	0.554	0.569	0.582

Table 4.3. *FoS* results for various values of *C/D* and *N* (*FD*, Collapse and Blowout).

	C/D									
N	1	2	3	4	5	6	7	8	9	10
-15	0.310	0.390	0.440	0.470	0.500	0.530	0.550	0.560	0.580	0.600
-12	0.370	0.470	0.530	0.570	0.600	0.630	0.660	0.680	0.700	0.720
-10	0.470	0.580	0.650	0.710	0.750	0.790	0.820	0.850	0.870	0.900
-7.5	0.620	0.780	0.870	0.950	1.010	1.050	1.100	1.130	1.170	1.200
-5.	0.940	1.160	1.310	1.420	1.510	1.580	1.650	1.700	1.750	1.790
-4	1.164	1.461	1.641	1.775	1.880	1.975	2.060	2.117	2.183	2.250
-3.	1.560	1.940	2.180	2.370	2.520	2.640	2.740	2.840	2.910	2.990
-2.5	1.862	2.338	2.625	2.840	3.008	3.160	3.295	3.388	3.492	3.600
-2.	2.340	2.900	3.270	3.550	3.770	3.950	4.110	4.240	4.360	4.470
-1.5	3.104	3.896	4.375	4.733	5.013	5.267	5.492	5.646	5.821	6.000
-1	4.660	5.770	6.500	7.040	7.470	7.830	8.140	8.410	8.640	8.860
-0.75	6.180	7.650	8.590	9.300	9.870	10.340	10.750	11.090	11.410	11.700
-0.5	9.150	11.260	12.630	13.640	14.460	15.140	15.710	16.240	16.690	17.090
-0.25	16.990	20.610	22.950	24.670	26.030	27.160	28.080	28.860	29.520	30.140
0	Infinity	Infinity	Infinity	Infinity	Infinity	Infinity	Infinity	Infinity	Infinity	Infinity
0.25	16.970	20.880	23.320	25.170	26.620	27.770	28.760	29.570	30.110	30.550
0.5	9.070	11.230	12.620	13.650	14.480	15.180	15.760	16.290	16.750	17.180
0.75	6.140	7.620	8.590	9.300	9.860	10.340	10.750	11.090	11.420	11.700
1	4.630	5.740	6.480	7.030	7.460	7.820	8.130	8.400	8.640	8.860
1.5	3.104	3.875	4.375	4.733	5.013	5.267	5.492	5.646	5.809	5.987
2.	2.330	2.900	3.260	3.530	3.750	3.930	4.090	4.240	4.360	4.470
2.5	1.862	2.325	2.625	2.840	3.008	3.160	3.295	3.388	3.485	3.592
3.	1.560	1.940	2.180	2.360	2.500	2.620	2.720	2.820	2.900	2.980
4.	1.164	1.453	1.641	1.775	1.880	1.975	2.060	2.117	2.178	2.245
5	0.940	1.160	1.310	1.420	1.510	1.580	1.640	1.690	1.740	1.780
7.5	0.620	0.780	0.870	0.950	1.010	1.050	1.100	1.130	1.160	1.190
10.	0.470	0.580	0.650	0.710	0.750	0.790	0.820	0.850	0.870	0.900
12.5	0.370	0.460	0.530	0.570	0.600	0.630	0.660	0.680	0.700	0.720
15	0.310	0.390	0.440	0.470	0.500	0.530	0.550	0.560	0.580	0.600

When the *OPR* is less than the *SPR*, *N* is less than zero. In this case, the soil moves in the "blowout" direction. The factor of safety (*FoS*) gradually decreases as -*N* increases until an incipient blowout is reached where *FoS* = 1. The corresponding -*N* is the critical -N_c for blowout failure.

Broms and Bennermark's original Equation 4.1 can be re-arranged into a form that is more amenable to analysis, as shown in Equation 4.3.

$$\sigma_t = \sigma_s + \gamma H - N_c \times S_u \tag{4.3}$$

Using Equation 4.3, a critical supporting pressure σ_t can be determined as long as N_c (where *FoS* = 1) is known. Note that N_c is a function of the depth ratio *C/D* regardless of the undrained shear strength of the soil.

It is important to study the effect of *C/D* on the critical stability number N_c. Figure 4.4 shows such a relationship between N_c and *C/D*. The data used to prepare this figure is shown in Table 4.4.

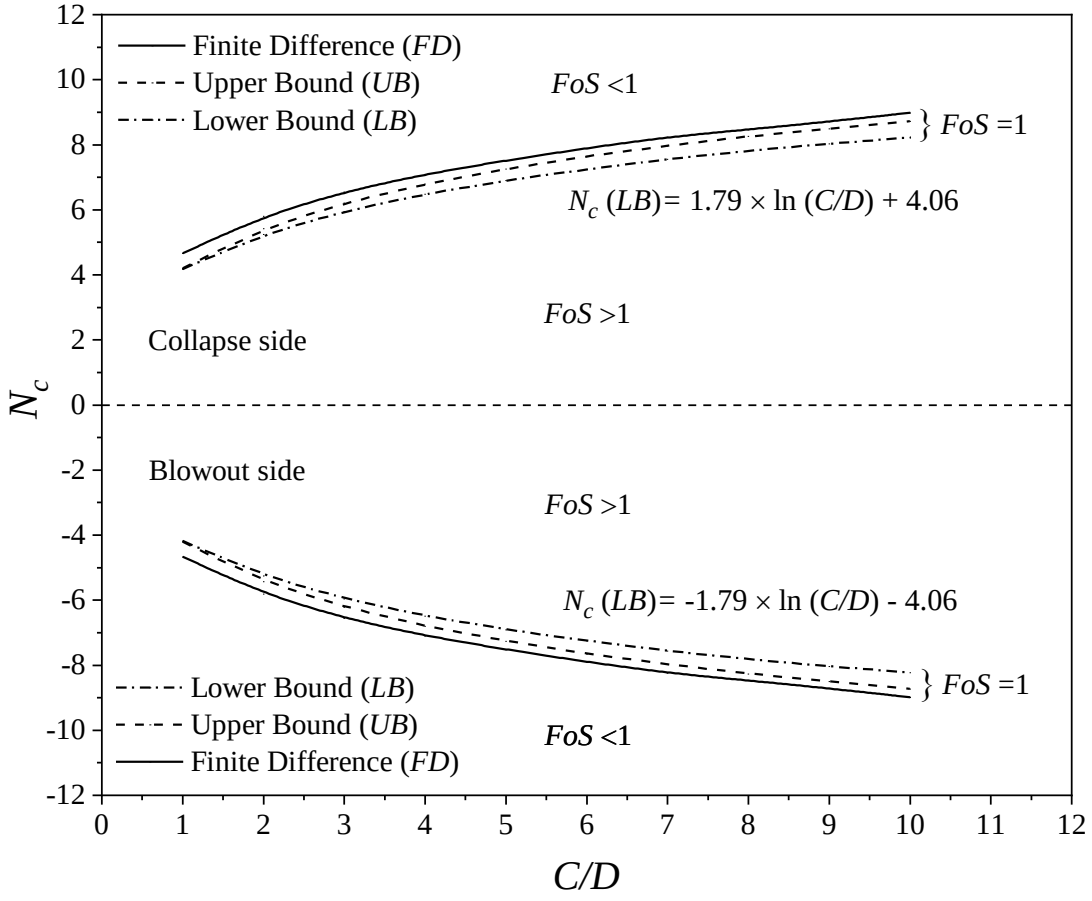

Figure 4.4. Comparison of N_c results (*FoS* = 1) in collapse and blowout.

Table 4.4. Comparison of N_c results (FoS = 1) in collapse and blowout.

C/D	Collapse			Blowout		
	LB	*UB*	*FD*	*LB*	*UB*	*FD*
1	4.165	4.334	4.656	-4.164	-4.333	-4.656
2	5.252	5.503	5.813	-5.241	-5.503	-5.844
3	5.947	6.271	6.563	-5.943	-6.271	-6.563
4	6.491	6.843	7.100	-6.496	-6.853	-7.100
5	6.906	7.305	7.519	-6.914	-7.305	-7.519
6	7.238	7.679	7.900	-7.258	-7.679	-7.900
7	7.555	8.093	8.238	-7.552	-8.090	-8.238
8	7.816	8.311	8.469	-7.760	-8.301	-8.469
9	8.041	8.539	8.713	-8.014	-8.539	-8.731
10	8.221	8.748	8.981	-8.194	-8.744	-9.000

In Figure 4.4, the critical stability number (N_c) increases nonlinearly as C/D increases, and the gradient of the curve decreases for large values of N_c. The area bounded by the collapse and the blowout curves represents the safe zone where $FoS > 1$. As the stability number (N) approaches zero ($OPR = SPR$), the factor of safety becomes infinite.

In general, the finite difference results for the critical stability number N_c are always larger than the upper bound and lower bound results. It appears that the finite difference approach for this problem is not conservative, and the exact solution is somewhere-between the limits of the *LB* and the *UB*. Since the lower bound theorem offers a safe assessment of the limit pressure for a stability problem, the computed lower bound solutions were chosen for the regression analysis.

Equation 4.4 is an accurate curve-fitting for the relationship between N_c and C/D with a correlation coefficient (R^2) = 0.998.

$$N_c = 1.79 \times \ln(C/D) + 4.06 \tag{4.4}$$

Substituting Equation 4.4 into Equation 4.3, a critical supporting pressure σ_t can be computed using Equation 4.5 with known design parameters (σ_s, γ, H, S_u and C/D).

$$\sigma_t = \sigma_s + \gamma H - (1.79 \times \ln(C/D) + 4.06) \times S_u \tag{4.5}$$

Noting that $N_c = N \times FoS$ (Figure 4.3), a factor of safety can always be computed using Equation 4.6.

$$FoS = N_c / N \tag{4.6}$$

Where N is the "designed" stability number which consists of the following design parameters: σ_s, σ_t, γ, H, and S_u. Equation 4.6 is further arranged into the form shown in Equation 4.7 by substituting N_c from Equation 4.4.

$$FoS = \frac{1.79 \times \ln(C / D) + 4.06}{N} \tag{4.7}$$

Equation 4.7 can be further expanded to Equation 4.8 for collapse analysis, noting that $N = (\sigma_s + \gamma H - \sigma_t) / S_u$

$$FoS = \frac{(1.79 \times \ln(C / D) + 4.06) \times S_u}{\sigma_s + \gamma H - \sigma_t} \tag{4.8}$$

And Equation 4.9 is used for blowout analysis by substituting the negative value of N_c.

$$FoS = \frac{(-1.79 \times \ln(C / D) - 4.06) \times S_u}{\sigma_s + \gamma H - \sigma_t} \tag{4.9}$$

Figure 4.5 shows a comparison of N_c results of this study with the existing solutions. The data used to prepare this figure is shown in Table 4.5.

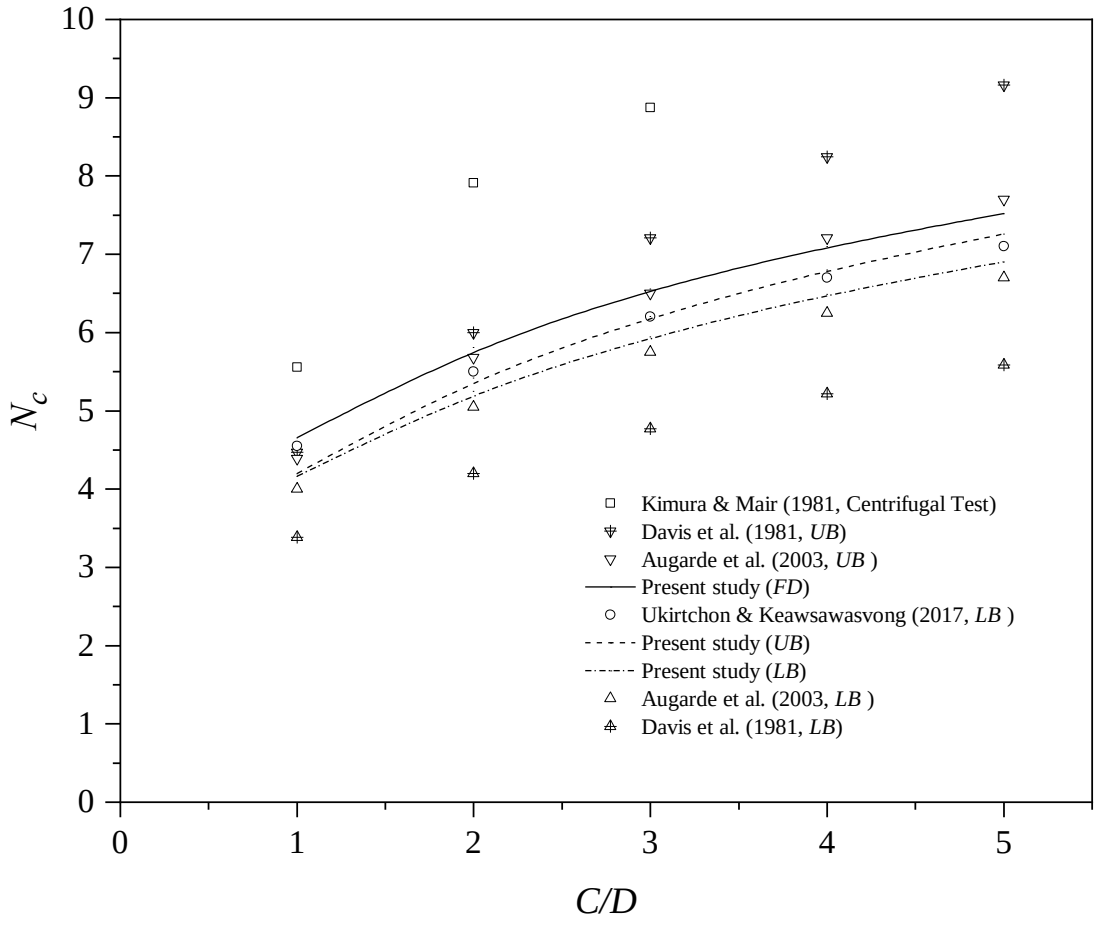

Figure 4.5. Comparison of N_c between the present study and published solutions.

Table 4.5. Comparison of N_c between the present study and published solutions.

C/D	Davis et al. (1980, *UB*) Tunnel heading	Augarde et al. (2003, *UB*) Tunnel heading	Present study (*FD*) Tunnel heading	Ukritchon et al. (2017, *LB*) Opening in underground wall	Present study (*UB*) Tunnel heading	Present study (*LB*) Tunnel heading	Augarde et al. (2003, *LB*) Tunnel heading	Davis et al. (1980, *LB*) Tunnel heading
1	4.47	4.39	4.66	4.55	4.2	4.17	4.00	3.39
2	6.00	5.68	5.81	5.50	5.42	5.25	5.05	4.20
3	7.21	6.50	6.56	6.20	6.21	5.95	5.75	4.77
4	8.25	7.21	7.10	6.70	6.80	6.49	6.25	5.22
5	9.17	7.7	7.52	7.10	7.26	6.91	6.7	5.58

Good agreement was found between this study and the published solutions by (Augarde et al. (2003). The current *UB* and *LB* solutions have been significantly improved owing to the use of adaptive mesh in this paper. It is not surprising to see that the analytical *LB* yields conservative results while the analytical *UB* provides an unsafe solution for the stability of plane strain tunnel headings (Davis et al. (1980), and hence should not be used in practice. The three-dimensional centrifugal test results in Kimura and Mair (1980) are consistently higher than those from the current study of plane strain tunnel headings.

4.4 The Extent of Surface Failure

Figures 4.6 to 4.8 (right-hand side) show the absolute displacement $\left(|u| = \sqrt{u_x^2 + u_y^2}\right)$ contour plots for *C/D* = 3, 6 and 9 respectively. These plots indicate the potential failure mechanism and the ground surface failure extent, although the actual contour values of the plots are not important (not real displacement) in limit analysis with the perfect plasticity theorem. Please note that these plots are not based on the same scale.

On the left-hand side of the Figures 4.6 to 4.8, vector plots of the velocity field are presented, showing the magnitude and direction of particle movement. The shorter vectors along the slip surface indicate a smaller movement of soil due to soil friction; whereas; in the centre of failure zone above the tunnel, the motion is nearly towards the tunnel face, having a greater displacement. All of the effected overburdening soil is being funnelled towards the opening of the tunnel, as seen by the density of the vectors around the tunnel face. There are obvious differences in both shape and the number of absolute displacement contours as the tunnel cover-to-diameter ratio increases. Having these plots does increase the confidence level with regards to finding possible slip planes within the overburden in front and above the tunnel face.

For all *C/D*, the failure zone extent (*E*) increases with the increasing of depth ratios. The potential slip surface extends below the base of the tunnel face for deep cases but reduces for shallow cases. It can be observed that the cohesive soil mass moves toward the tunnel like a flow.

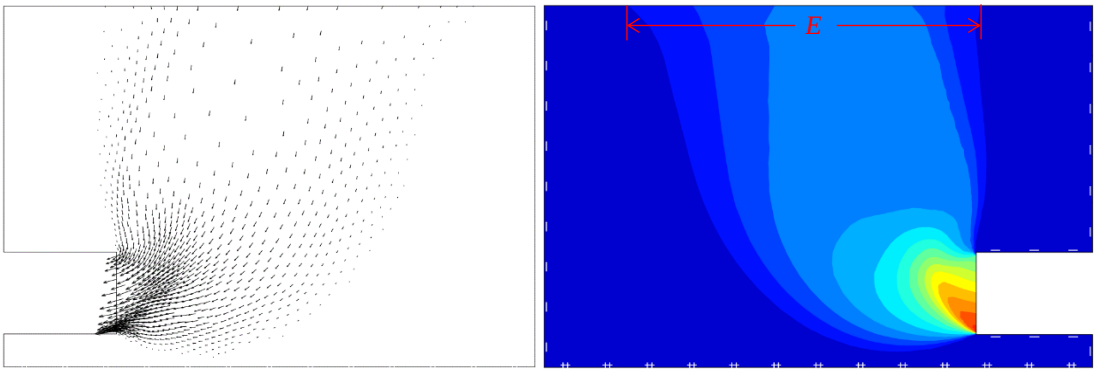

Note that the actual contour values of the plots are not important in limit analysis with the perfect plasticity theorem.

Figure 4.6. Absolute displacement contour |*u*| (right hand side) and velocity vector plots (left hand side) for *C/D* = 3.

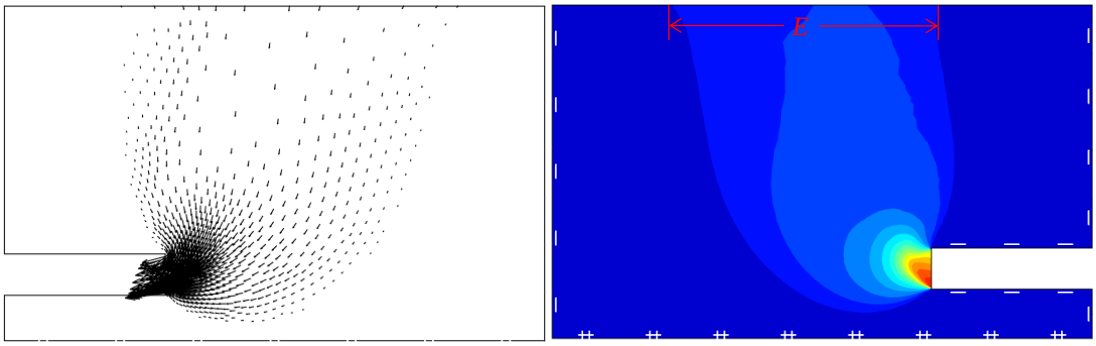

Note that the actual contour values of the plots are not important in limit analysis with the perfect plasticity theorem.

Figure 4.7. Absolute displacement contour |*u*| (right hand side) and velocity vector plots (left hand side) for *C/D* = 6.

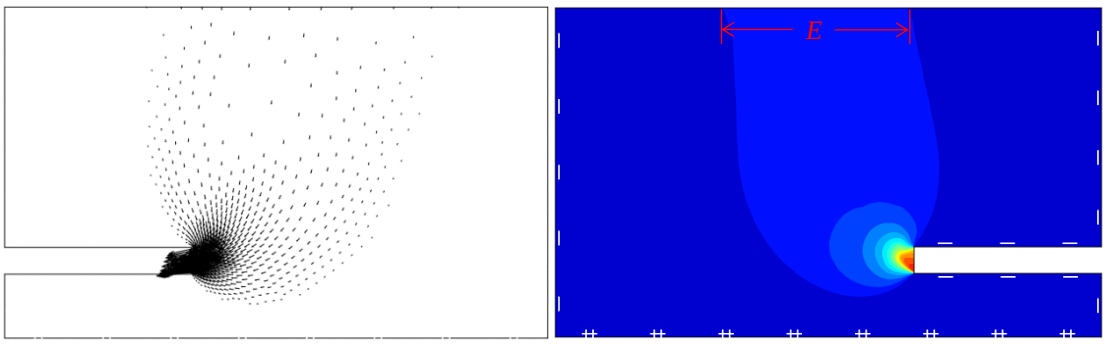

Note that the actual contour values of the plots are not important in limit analysis with the perfect plasticity theorem.

Figure 4.8. Absolute displacement contour |*u*| (right hand side) and velocity vector plots (left hand side) for *C/D* = 9.

No rigid block of particles movement can be recognised as in cohesionless soil, and that is the reason why the kinematic approaches are difficult to apply in cohesive soil (Mollon et al. 2013).

Noting that the surface failure extent ratio (*E/D*) increases as the depth ratio (*C/D*) increases. *E* is the measured horizontal surface distance from the output plots, as shown in the figures. This can be justified by the conical shape of the failure mechanism. The extent of the surface failure and the corresponding depth ratio are recorded in Table 4.6.

The data in Table 4.6 has been graphically presented in Figure 4.9, which shows a nonlinear relationship between (*E/D*) and (*C/D*). Given *C/D* = 1 and *D* = 1 metre, the cover depth (*C*) above the crown of the tunnel is 1 metre, and the resulting extent of the surface failure (*E*) is about 2 metre. When the depth ratio *C/D* is increased to 10, the extent of the surface failure (*E*) increases to 8.90 metres. Table 4.6 and Figure 4.9 are useful to practical engineers during the stage of tunnel construction.

Table 4.6. Surface failure ratios (*E/D*).

Depth Ratio (C/D^*)	The ratio of failure extent to tunnel diameter (E/D^*)
1	2.04
2	3.37
3	4.56
4	5.61
5	6.52
6	7.28
7	7.90
8	8.37
9	8.70
10	8.89

∗Tunnel Heading height *D* = 1m

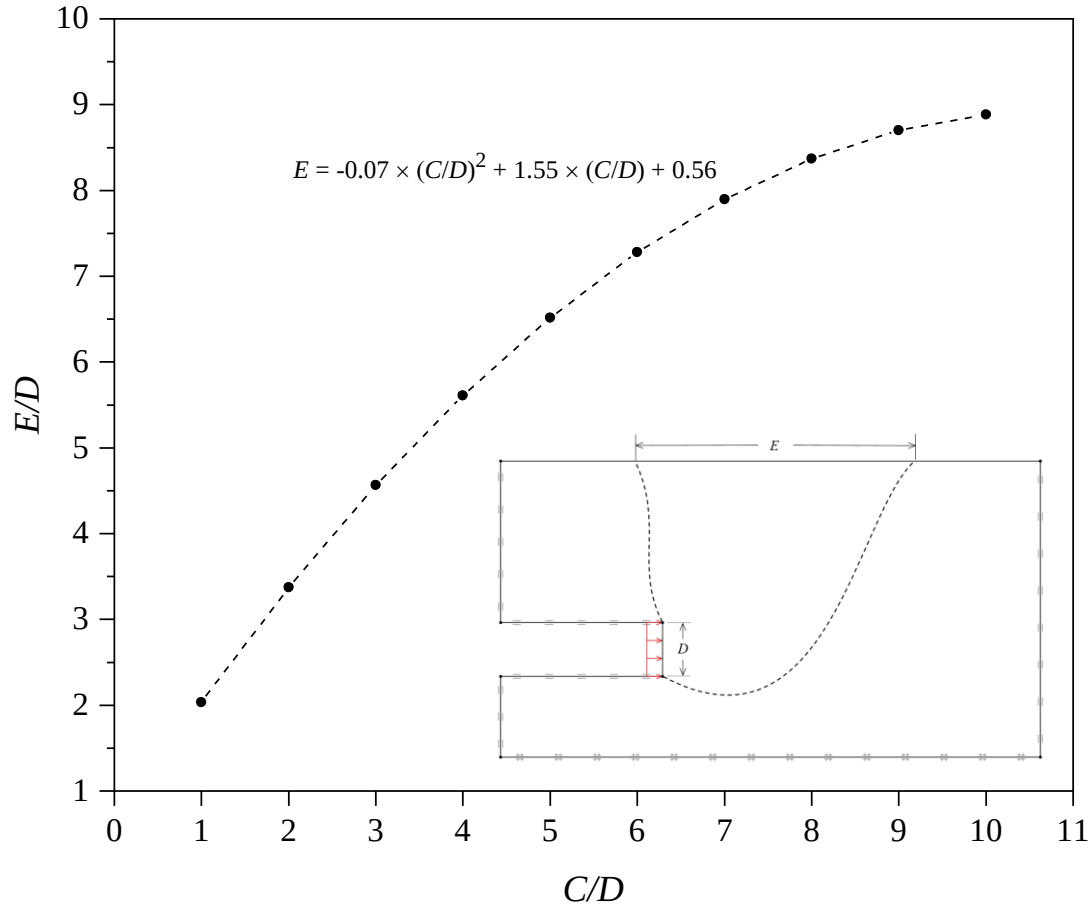

Figure 4.9. Surface failure ratio (*E/D*) vs (*C/D*).

4.5 Stability Chart and Practical Examples

The design chart is best demonstrated through some examples which can be broadly categorised into either analysis or design problems. Since the lower bound theorem offers a safe assessment of the critical stability number, a design contour chart for factors of safety (*FoS*) has been constructed in Figure 4.10 based on *LB* results.

4.5.1 Face support for TBM excavation.

It is proposed to use a *TBM* to excavate a deep tunnel below the central business district through undrained clay. The designer needs to determine the safe operating range for tunnel face support pressure (σ_t) provided by the *TBM*. The given parameters are; σ_s = 216 kPa, S_u = 72 kPa, γ = 18 kN/m^3, C = 36 m, and D = 6 m.

1. Given C/D = 6, $N_c \simeq 7.26$ for *LB* collapse and $N_c \simeq -7.26$ for *LB* blowout (Table 4.4 or Figure 4.4 or Equation 4.4).
2. Using Equation 4.8, σ_t = 395.28 kPa (*FoS* = 1, for collapse, *LB*).

3. Using Equation 4.9, σ_t = 1440.72 kPa (*FoS* =1, for blowout, *LB*).
4. The safe operating range (*FoS* ≥ 1) for tunnel face support pressure is:

   395.28 kPa (collapse limit) ≤ σ_t ≤ 1440.72 kPa (blowout limit).
5. Depending on the *FoS* used in design considerations, this operating range can be further reduced.
6. Using Equation 4.8 with *FoS* =2.5, σ_t = 708.90 kPa for collapse side.
7. Using Equation 4.9 with *FoS* =2.5, σ_t = 1127.10 kPa for blowout side.
8. The safe operating range for *FoS* ≥ 2.5 is:

   708.90 kPa (collapse side) ≤ σ_t ≤ 1127.10 kPa (blowout side)

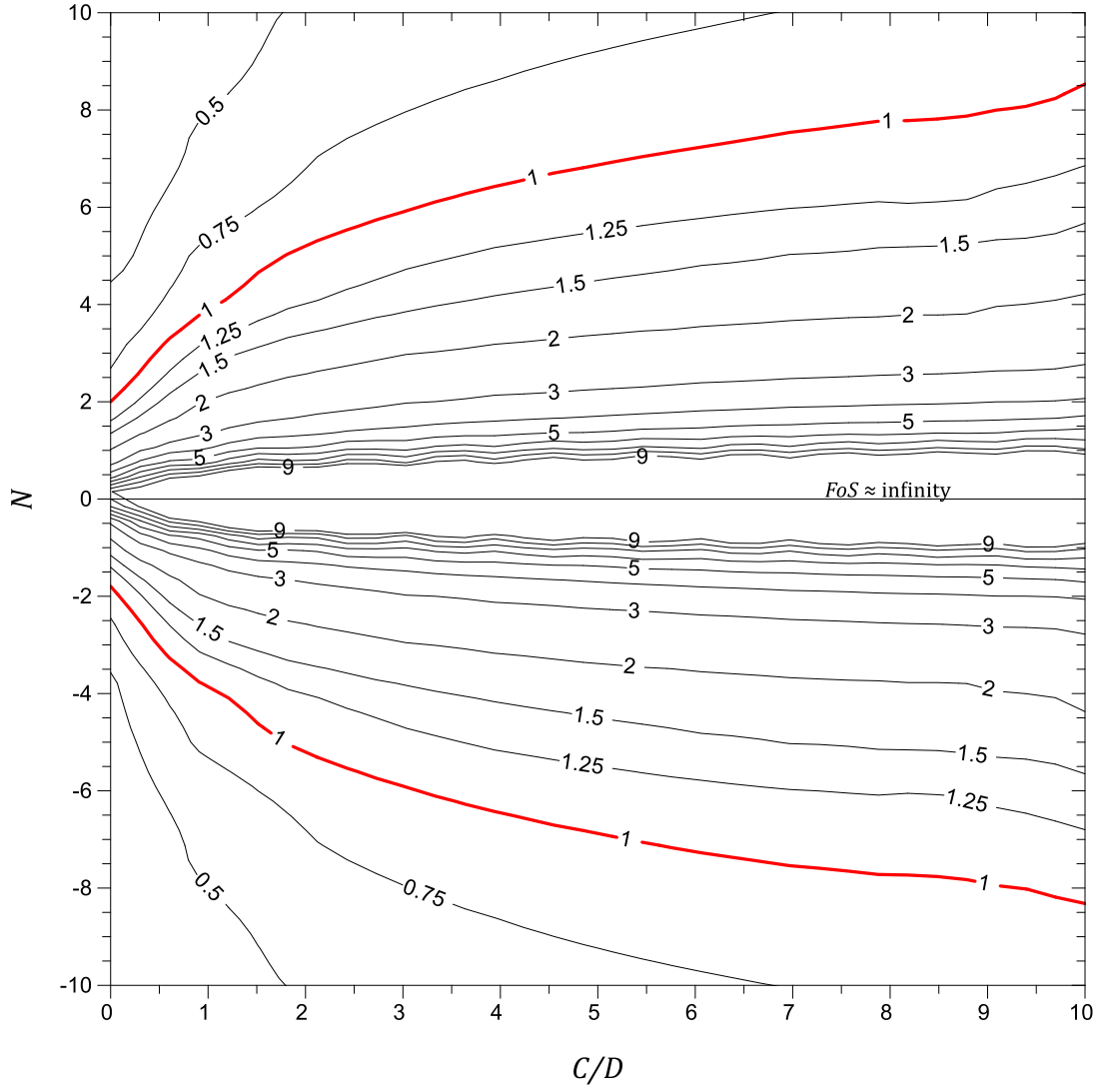

Figure 4.10. *FoS* (*LB*) design chart for heading stability.

4.6 Conclusion

Broms and Bennermarks' original stability number combines overburden pressures (surcharge and self-weight) with internal supporting pressures and is applicable to undrained clay. This critical stability number was studied for 2D tunnel heading problems. Numerical results for factors of safety were obtained for a wide range of stability numbers for collapse and blowout by using rigorous upper and lower bound limit analyses and the finite difference method. Design charts, tables, and equations were produced using dimensionless ratios. Examples have been given to illustrate the practicality of the charts.

Broms and Bennermarks' original stability number approach is applied to study the stability of 2D single circular tunnels in Chapter 5.

CHAPTER 5: UNDRAINED ANALYSIS OF 2D SINGLE CIRCULAR TUNNEL

5.1 Introduction

The evaluation of the stability of tunnels is important in determining the safe working pressures, the structural design of the lining segments and to prevent damage to surface or subsurface structures.

In the previous chapter, the stability of plane strain tunnel heading was addressed. This chapter will discuss another stability problem of an idealised circular tunnel in undrained soil conditions. The problem approximates the stability of a very long unlined circular tunnel. This case is equivalent to a long cylindrical cavity, aiming to determine the radial pressure a cylindrical tunnel shield must resist.

Failure of the tunnel in collapse and blowout is initiated by different combinations of overburden pressure and internal radial pressure. Shear strength reduction technique is utilised to study two-dimensional tunnel stability by using finite element limit analysis, to compute the upper and lower bound factor of safety values, for a wide range of depth ratios and stability scenarios. The obtained results of the factor of safety (*FoS*) for various depths are presented in the form of dimensionless stability charts and verified by the finite difference method as well as other existing solutions available in the literature. Some practical examples are provided to demonstrate the usefulness of the design charts and tables. These charts give a good approximation of *FoS* and can be used by engineers in preliminary designs.

5.2 Modelling Technique and Problem Statement

Figure 5.1 shows the problem definition of the idealized unlined circular tunnel. The soil medium is considered as undrained and is modelled as a uniform Tresca material, which is the same as a Mohr-Coulomb material with zero internal friction angle. The undrained shear strength (S_u) and the unit weight (γ) describe soil properties used, while the tunnel has a diameter (D), cover depth (C) above its crown and axis depth (H) below the ground surface.

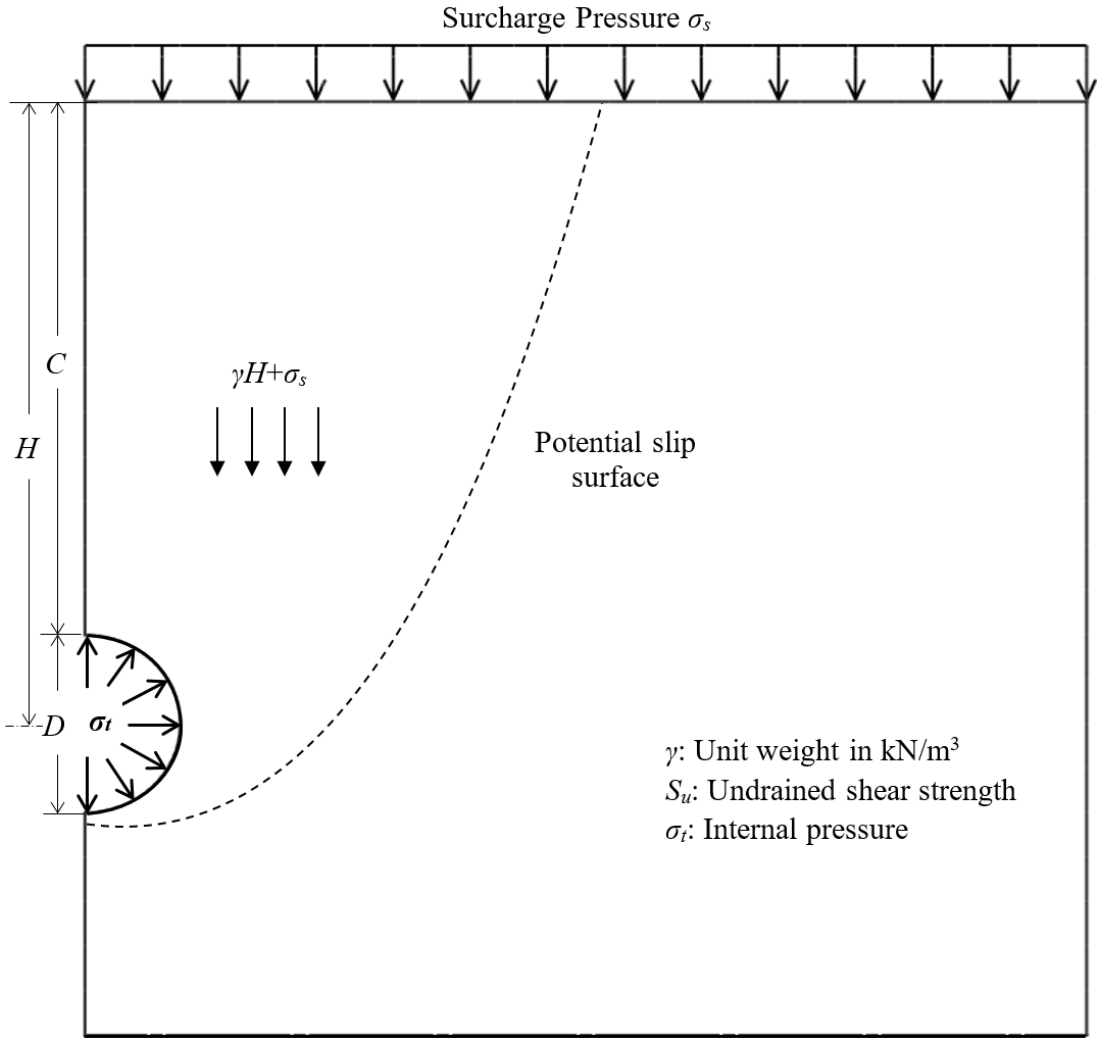

Figure 5.1. Problem definition.

The tunnel is subjected to a radial internal pressure σ_t, while the ground surface is subjected to a vertical surcharge σ_s. These pressures, together with soil self-weight (γH), are varied to test the collapse and blowout stability of the models for various depth ratios (C/D). It is important to note that the active (collapse) failure is driven by the action of gravity and the surcharge pressure, with the resistance being provided by the internal tunnel pressure and the shear strength of the soil. The passive (blowout) failure is driven by the tunnel pressure and resisted by the action of the surcharge, gravity and shear strength of the soil.

For tunnelling in undrained soil, the effects of the soil weight and the difference between the pressures (σ_s and σ_t) on stability can be investigated by using Broms and Bennermarks' stability number (N), as shown in Equation 5.1.

$$N = \frac{\sigma_s + \gamma H - \sigma_t}{S_u} \tag{5.1}$$

The circular tunnel is symmetrical about the vertical plane (Figure 5.1); therefore, the critical stability calculations are based on one half of the total domain. A typical plane strain *FELA* adaptive mesh used in this study is shown in Figure 5.2. The boundary conditions are as follows: the ground surface is free to displace, the sides have roller boundaries, and the base is fixed in *x* and *y* directions.

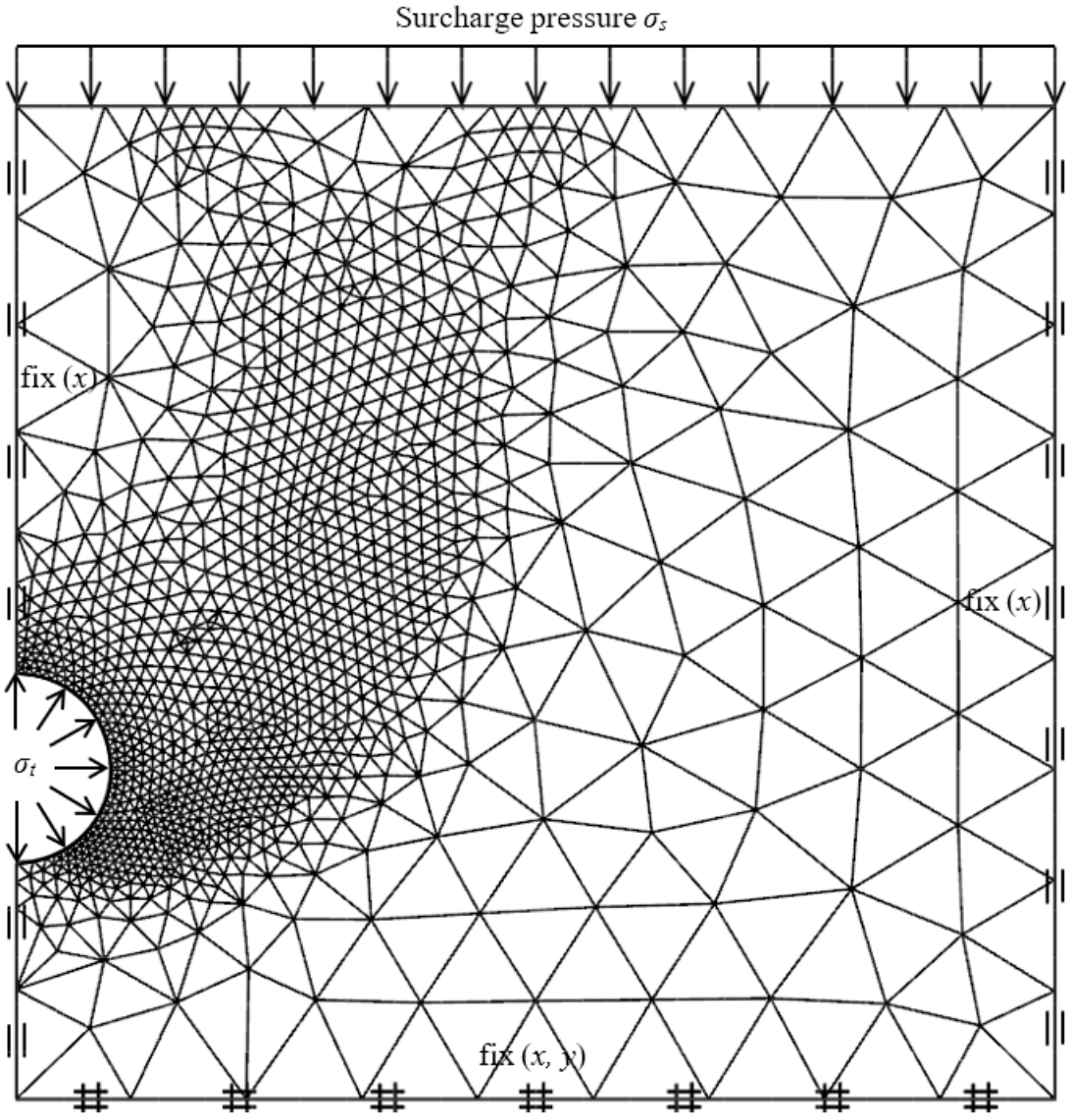

Figure 5.2. A typical adaptive mesh used for the problem.

In case of using half of the domain, the vertical plane of the symmetry is fixed in the *x*-direction only. An automatically adaptive mesh refinement was employed in both the *UB* and *LB* simulations to enable accurate limit loads to be obtained through the

use of the bounds gap error estimator (OptumCE 2017). Three iterations of adaptive meshing with the number of elements increasing from 1000 to 2000 were used for all analyses. The large size of the model is essential as it ensures that the entire soil mass is modelled accurately, and the failure mechanism does not intersect the boundaries of the model.

The numerical results of the shear strength reduction method (*SSRM*) are represented by a factor of safety (*FoS*) that is a function of the depth ratio (*C*/*D*) and the "designed" stability number (*N*), as shown in Equation (5.2).

$$FoS = f\left(\frac{C}{D}, N = \frac{\sigma_s + \gamma H - \sigma_t}{S_u}\right) \tag{5.2}$$

In practice, the "designed" stability number *N* can be either positive, zero or negative. Furthermore, failure may occur either in collapse or blowout, depending on different combinations of pressures, soil parameters, and geometries. Thus, to cover all possible situations of failure, the present study investigates the stability of circular tunnel by relating *FoS* to a broad range of stability numbers (*N* = -15 to 15) and depth ratios (*C/D* = 1 - 10). The dimensionless ratios used in the paper allow the results of this study to be used in practice.

The method of shear strength reduction is widely known in finite element analyses and has been frequently used for slope stability analyses. Although this is so, it has rarely been used for tunnel stability analyses. As this method yields a factor of safety (*FoS*), it is believed that it may provide some practical benefit for designers. One such method involving factors of safety has been described by Bishop (1955) for slope stability.

It is defined as $FoS = S_u / S_c$, where S_u is the available undrained shear strength of the soil and S_c is the critical strength necessary to maintain limiting equilibrium. The shear strength of the material is reduced until the limiting condition is found. If the material triggers the failure condition initially, then the undrained shear strength is increased until the limiting equilibrium or failure state is reached.

The rigorous upper bound and lower bound factors of safety for the cases being studied are computed by using the shear strength reduction method (Krabbenhoft and Lyamin (2015). The numerical procedures used are based on the limit theorems of classical plasticity. A full detailed description of the theory and development of this

method can be found in Sloan (2013). Details of the numerical *FELA* formulation can be found in Lyamin and Sloan (2002a, 2002b).

Relying on one single numerical model or method is usually not convincing. Result verification is normally required in computational geomechanics research. For this purpose, the finite difference method (*FDM*), via the software *FLAC* with built-in implementation of the strength reduction technique, has been used over the same parametric range. *FISH* programming language was also developed to generate the mesh in the *FLAC* environment and solve the issue automatically. By using the *FISH* script, parametric studies can be conducted efficiently and effectively with a quick change of material input (Shiau & Sams 2019).

5.3 Results and Discussion

5.3.1 Discussing N, FoS, N_c, and σ_t

A wide range of stability numbers (N = -15 to +15) and depth ratios (C/D = 1 to 10) are investigated to cover all possible situations associated with a plane strain circular tunnel stability. Tables 5.1 - 5.3 present three complete sets of *FoS* results for (*LB*, *UB*, and *FD*), respectively.

Table 5.1. *FoS* results for various values of *C/D* and *N* (*LB*, Collapse and Blowout).

	C/D (*LB*)									
N	1	2	3	4	5	6	7	8	9	10
-15	0.159	0.224	0.269	0.302	0.328	0.344	0.367	0.386	0.398	0.411
-12.5	0.191	0.268	0.323	0.363	0.393	0.413	0.443	0.462	0.478	0.491
-10	0.236	0.335	0.402	0.453	0.492	0.517	0.553	0.574	0.598	0.616
-7.5	0.317	0.448	0.536	0.600	0.652	0.686	0.731	0.766	0.795	0.821
-5	0.471	0.663	0.799	0.899	0.975	1.026	1.101	1.149	1.181	1.232
-4	0.603	0.853	1.020	1.139	1.233	1.320	1.390	1.450	1.507	1.553
-3	0.771	1.101	1.307	1.483	1.616	1.693	1.821	1.889	1.972	2.031
-2.5	0.965	1.364	1.632	1.822	1.972	2.112	2.224	2.320	2.411	2.484
-2	1.132	1.602	1.930	2.197	2.393	2.510	2.687	2.804	2.935	3.030
-1.5	1.608	2.274	2.719	3.037	3.287	3.521	3.706	3.866	4.019	4.141
-1	2.134	3.091	3.720	4.187	4.597	4.869	5.189	5.431	5.643	5.822
-0.75	2.738	3.976	4.805	5.422	5.946	6.283	6.724	7.046	7.297	7.534
-0.5	3.809	5.573	6.765	7.693	8.392	8.883	9.480	9.929	10.309	10.630
-0.25	6.245	9.235	11.205	12.806	13.943	14.755	15.778	16.430	17.077	17.725
0	Infinity	Infinity	Infinity	Infinity	Infinity	Infinity	Infinity	Infinity	Infinity	Infinity
0.25	12.908	14.741	16.058	16.992	17.828	18.211	19.119	19.626	20.153	20.567
0.5	6.059	7.651	8.637	9.369	9.895	10.259	10.843	1.824	11.588	11.897
0.75	3.749	5.008	5.749	6.340	6.774	6.981	7.458	7.697	7.934	8.203
1	2.734	3.691	4.278	4.714	5.065	5.284	5.637	5.866	6.013	6.229
1.5	1.608	2.274	2.719	3.037	3.287	3.521	3.706	3.866	4.019	4.141
2	1.283	1.783	2.094	2.322	2.514	2.635	2.811	2.936	3.042	3.112
2.5	0.965	1.364	1.632	1.822	1.972	2.112	2.224	2.320	2.411	2.484
3	0.839	1.167	1.373	1.539	1.673	1.754	1.858	1.946	2.020	2.083
4	0.603	0.853	1.020	1.139	1.233	1.320	1.390	1.450	1.507	1.553
5	0.494	0.688	0.823	0.919	0.994	1.045	1.118	1.163	1.209	1.247
7.5	0.328	0.459	0.547	0.610	0.662	0.695	0.743	0.772	0.806	0.827
10	0.244	0.342	0.405	0.458	0.497	0.518	0.555	0.578	0.600	0.620
12.5	0.195	0.272	0.327	0.367	0.397	0.416	0.443	0.464	0.482	0.495
15	0.162	0.229	0.272	0.304	0.330	0.344	0.371	0.388	0.402	0.412

Table 5.2. *FoS* results for various values of *C*/*D* and *N* (*UB*, Collapse and Blowout).

	C/D (*UB*)									
N	1	2	3	4	5	6	7	8	9	10
-15	0.162	0.230	0.275	0.309	0.336	0.359	0.378	0.395	0.410	0.422
-12.5	0.194	0.275	0.330	0.370	0.403	0.431	0.453	0.473	0.492	0.507
-10	0.242	0.344	0.411	0.462	0.502	0.538	0.565	0.591	0.614	0.634
-7.5	0.320	0.457	0.547	0.615	0.670	0.717	0.752	0.786	0.816	0.845
-5	0.477	0.681	0.816	0.918	0.999	1.071	1.124	1.176	1.219	1.261
-4	0.611	0.867	1.036	1.163	1.263	1.347	1.419	1.481	1.537	1.587
-3	0.781	1.120	1.345	1.514	1.649	1.769	1.859	1.947	2.018	2.087
-2.5	0.977	1.388	1.658	1.860	2.021	2.156	2.270	2.370	2.459	2.540
-2	1.148	1.655	1.989	2.244	2.445	2.622	2.757	2.888	2.998	3.104
-1.5	1.629	2.313	2.763	3.100	3.368	3.593	3.783	3.950	4.099	4.233
-1	2.163	3.141	3.802	4.298	4.690	5.048	5.313	5.563	5.791	5.980
-0.75	2.773	4.046	4.905	5.553	6.079	6.530	6.879	7.211	7.488	7.752
-0.5	3.858	5.674	6.912	7.823	8.561	9.215	9.705	10.165	10.580	10.970
-0.25	6.323	9.406	11.474	13.035	14.275	15.372	16.197	16.939	17.636	18.232
0	Infinity	Infinity	Infinity	Infinity	Infinity	Infinity	Infinity	Infinity	Infinity	Infinity
0.25	13.192	15.088	16.394	17.426	18.249	19.055	19.635	20.182	20.679	21.149
0.5	6.193	7.827	8.840	9.604	10.200	10.739	11.159	11.553	11.910	12.204
0.75	3.853	5.115	5.895	6.471	6.934	7.334	7.655	7.929	8.200	8.423
1	2.774	3.765	4.388	4.856	5.207	5.531	5.772	5.997	6.203	6.383
1.5	1.629	2.313	2.763	3.100	3.368	3.593	3.783	3.950	4.099	4.233
2	1.302	1.814	2.145	2.390	2.589	2.753	2.886	3.008	3.112	3.215
2.5	0.977	1.388	1.658	1.860	2.021	2.156	2.270	2.370	2.459	2.540
3	0.851	1.192	1.415	1.580	1.712	1.829	1.917	1.997	2.071	2.136
4	0.611	0.867	1.036	1.163	1.263	1.347	1.419	1.481	1.537	1.587
5	0.502	0.707	0.844	0.942	1.022	1.092	1.145	1.195	1.239	1.279
7.5	0.331	0.469	0.558	0.625	0.679	0.725	0.762	0.795	0.824	0.851
10	0.248	0.350	0.418	0.468	0.509	0.543	0.570	0.595	0.617	0.639
12.5	0.198	0.280	0.334	0.374	0.407	0.435	0.456	0.476	0.494	0.510
15	0.164	0.233	0.278	0.312	0.339	0.362	0.380	0.397	0.411	0.425

Table 5.3. *FoS* results for various values of *C/D* and *N* (*FD*, Collapse and Blowout).

	C/D (*FD*)									
N	1	2	3	4	5	6	7	8	9	10
-15	0.170	0.240	0.280	0.310	0.340	0.360	0.380	0.400	0.410	0.430
-12.5	0.200	0.280	0.330	0.370	0.400	0.430	0.460	0.470	0.490	0.510
-10	0.250	0.350	0.420	0.470	0.510	0.540	0.570	0.600	0.620	0.640
-7.5	0.330	0.470	0.550	0.620	0.670	0.720	0.760	0.790	0.820	0.850
-5	0.490	0.690	0.830	0.930	1.010	1.080	1.130	1.190	1.230	1.280
-4	0.628	0.883	1.040	1.165	1.265	1.348	1.428	1.488	1.540	1.600
-3	0.810	1.140	1.370	1.530	1.670	1.780	1.880	1.970	2.040	2.110
-2.5	1.004	1.412	1.664	1.864	2.024	2.156	2.284	2.380	2.464	2.560
-2	1.190	1.690	2.020	2.270	2.480	2.650	2.790	2.920	3.030	3.130
-1.5	1.673	2.353	2.773	3.107	3.373	3.593	3.807	3.967	4.107	4.267
-1	2.240	3.220	3.870	4.360	4.760	5.090	5.380	5.630	5.850	6.050
-0.75	2.880	4.150	5.000	5.650	6.170	6.600	6.970	7.300	7.600	7.660
-0.5	4.020	5.820	7.050	7.970	8.720	9.330	9.870	10.340	10.760	11.130
-0.25	6.610	9.690	11.760	13.320	14.560	15.610	16.500	17.290	17.990	18.610
0	Infinity	Infinity	Infinity	Infinity	Infinity	Infinity	Infinity	Infinity	Infinity	Infinity
0.25	13.120	15.380	16.740	17.800	18.670	19.420	20.140	20.760	21.350	21.910
0.5	6.330	7.970	8.990	9.750	10.370	10.890	11.350	11.750	12.100	12.430
0.75	3.950	5.200	5.990	6.560	7.020	7.410	7.750	8.050	8.310	8.550
1	2.850	3.830	4.450	4.910	5.270	5.580	5.830	6.060	6.290	6.480
1.5	1.720	2.387	2.833	3.167	3.420	3.660	3.840	4.000	4.160	4.280
2	1.340	1.850	2.170	2.410	2.610	2.770	2.920	3.040	3.150	3.240
2.5	1.032	1.432	1.700	1.900	2.052	2.196	2.304	2.400	2.496	2.568
3	0.880	1.210	1.430	1.600	1.720	1.830	1.930	2.010	2.090	2.160
4	0.645	0.895	1.063	1.188	1.283	1.373	1.440	1.500	1.560	1.605
5	0.520	0.720	0.850	0.950	1.030	1.100	1.150	1.200	1.240	1.280
7.5	0.340	0.480	0.560	0.630	0.690	0.730	0.770	0.800	0.830	0.860
10	0.260	0.360	0.420	0.470	0.510	0.540	0.580	0.600	0.620	0.640
12.5	0.210	0.280	0.340	0.380	0.410	0.440	0.460	0.480	0.500	0.510
15	0.170	0.240	0.280	0.310	0.340	0.360	0.380	0.400	0.420	0.430

Figure 5.3 shows the full range of the results (*LB*, *UB* and *FD*) relating to collapse and blowout of unlined circular tunnels with a depth ratio of three (*C/D* = 3). It is to be noted that the curves are hyperbolic. A pair of asymptote lines are displayed. The equation to describe this graph is $N_c = N \times FoS$. Noting that a unique N_c value for a specific depth ratio can be obtained by using any combination of *N* and *FoS*. This unique N_c value is Broms and Bennermarks' critical stability number. For the depth ratio *C/D* = 3, *LB* solutions give N_c = +4.08 on the collapse side and N_c = -4.08 on the blowout side. By drawing an *FoS* = 1 horizontal line, the two values can be read from the intersection points graphically.

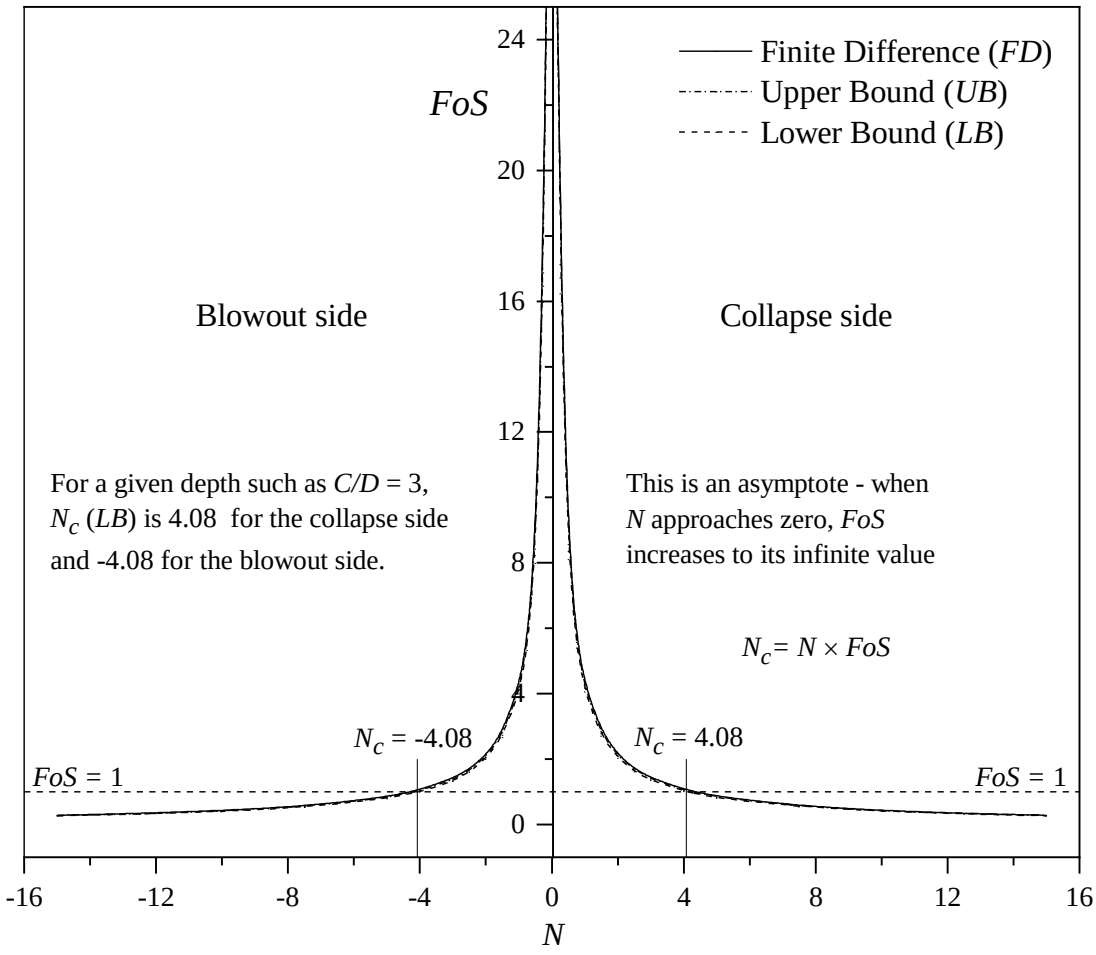

Figure 5.3. *FoS* vs. *N* for *C/D* = 3.

Two ratios can be defined in Broms and Bennermarks' stability number (*N*) equation: namely the overburden pressure ratio $OPR = (\sigma_s + \gamma H) / S_u$ and the supporting pressure ratio $SPR = \sigma_t / S_u$ By adding these two pressure ratios together, it can

produce three various failure mechanisms (e.g. collapse, weightless scenario, or blowout).

- $N > 0$ (*OPR > SPR;* soil movement in collapse direction)
- $N = 0$ (*OPR = SPR;* weightless scenario)
- $N < 0$ (*OPR < SPR;* soil movement in blowout direction)

Broms and Bennermarks' N_c Equation 5.1 can be re-arranged into a form that is more amenable to analysis, as shown in Equation 5.3.

$$\sigma_t = \sigma_s + \gamma H - N_c \times S_u \tag{5.3}$$

By using Equation 5.3, a critical supporting pressure σ_t can be determined as long as N_c (where *FoS* = 1) is known. Note that N_c is a function of the depth ratio *C/D* regardless of the undrained shear strength of the soil.

It is important to study the effect of *C/D* on the critical stability number N_c. Figure 5.4 shows such a relationship between N_c and *C/D*. The data used to prepare this figure is shown in Table 5.4.

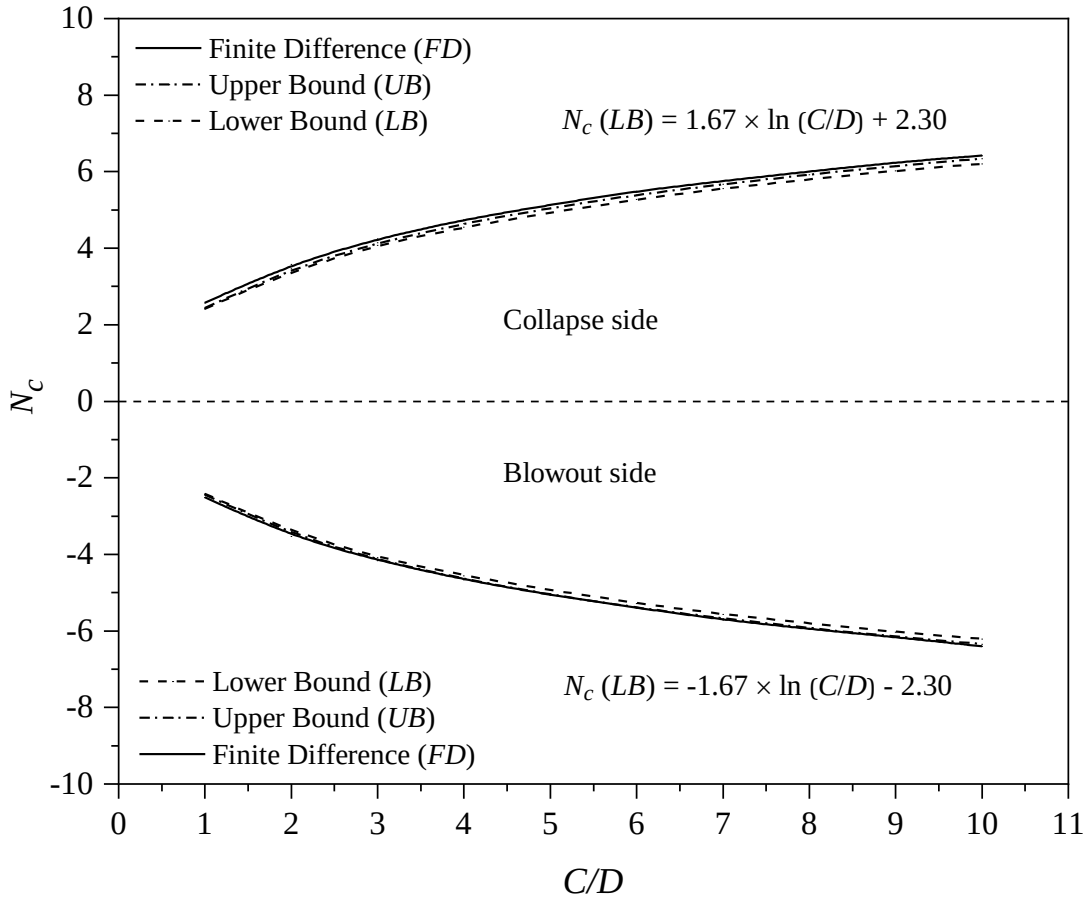

Figure 5.4. Comparison of N_c results (*FoS* = 1) in collapse and blowout.

Table 5.4 Comparison of N_c results (FoS = 1) in collapse and blowout.

C/D	Collapse			Blowout		
	LB	*UB*	*FD*	*LB*	*UB*	*FD*
1	2.412	2.443	2.580	-2.412	-2.443	-2.510
2	3.411	3.469	3.580	-3.411	-3.469	-3.530
3	4.079	4.144	4.250	-4.079	-4.144	-4.160
4	4.555	4.65	4.750	-4.555	-4.65	-4.660
5	4.931	5.052	5.130	-4.931	-5.052	-5.060
6	5.281	5.389	5.490	-5.281	-5.389	-5.390
7	5.559	5.675	5.760	-5.559	-5.675	-5.710
8	5.799	5.925	6.000	-5.799	-5.925	-5.950
9	6.028	6.148	6.240	-6.028	-6.148	-6.160
10	6.211	6.349	6.420	-6.211	-6.349	-6.400

In Figure 5.4, the critical stability number (N_c) increases nonlinearly as C/D increases, and the gradient of the curve decreases for large values of N_c. The area bounded by the collapse and the blowout curves represents the safe zone where $FoS > 1$. Note that, the numerical upper and lower bounds are generally within about 2% of one another, with the true solution lying between the two bounds. In general, the finite difference results for the critical stability number N_c are slightly greater than the upper bound and lower bound results. Equation 5.4 is an accurate curve-fitting for the relationship between N_c (LB) and C/D with a correlation coefficient (R^2) = 0.997.

$$N_c = 1.67 \times \ln(C/D) + 2.30 \tag{5.4}$$

Once the value of (N_c) is known, an appropriate factor of safety may be applied to it to deduce a safe working load range for tunnelling operations. Substituting Equation 5.4 into Equation 5.3, a critical supporting pressure σ_t can be computed using Equation 5.5 with known design parameters such as σ_s, γ, H, S_u and C/D.

$$\sigma_t = \sigma_s + \gamma H - (1.67 \times \ln(C/D) + 2.30) \times S_u \tag{5.5}$$

Noting that $N_c = N \times FoS$ (Figure 5.3), a factor of safety can always be computed using Equation 5.6.

$$FoS = N_c / N \tag{5.6}$$

Where N is the "designed" stability number, which consists of the following design parameters: σ_s, σ_t, γ, H, and S_u. Equation 5.6 is further arranged into the form shown in Equation 5.7 by substituting N_c from Equation 5.4.

$$FoS = \frac{1.67 \times \ln(C / D) + 2.30}{N} \tag{5.7}$$

Equation 5.7 can be further expanded to Equation 5.8 for collapse analysis, given that:

$$N = (\sigma_s + \gamma H - \sigma_t) / S_u$$

$$FoS = \frac{(1.67 \times \ln(C / D) + 2.30) \times S_u}{\sigma_s + \gamma H - \sigma_t} \tag{5.8}$$

Equation 5.9 is used for blowout analysis by substituting the negative value of N_c.

$$FoS = \frac{(-1.67 \times \ln(C / D) - 2.30) \times S_u}{\sigma_s + \gamma H - \sigma_t} \tag{5.9}$$

5.3.2 Comparison of results

It is essential to compare and validate N_c results obtained by the present study with those in published literature. Figure 5.5 shows a comparison between N_c results of this study and those for tunnel heading by Shiau and Al-Asadi (2018).

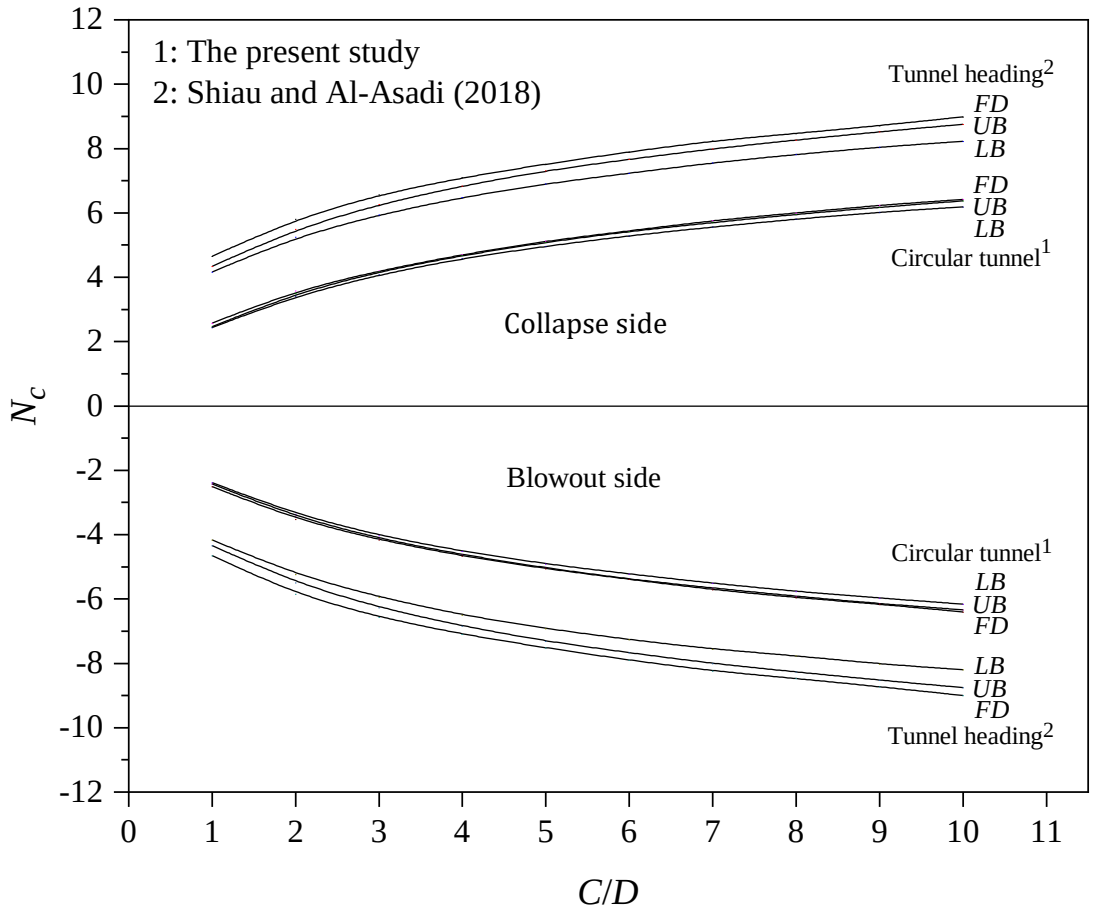

Figure 5.5. Comparison of N_c between the present study and tunnel heading.

It should be noted that the stability of a plane strain circular tunnel is more critical than that of a tunnel heading, and this is due to the difference in the geometry of the problems. Having said that, this is mostly due to the difference in the problem geometry. Strictly speaking, they should not be compared directly.

Figure 5.6 compares N_c results of this study with those of Davis et al. (1980), Sloan and Assadi (1992) and Wilson et al. (2011). The results of Davis et al. (1980) and Sloan and Assadi (1992) are based on analytical limit analysis and are for depth ratio equal to or less than 5 ($C/D \leq 5$).

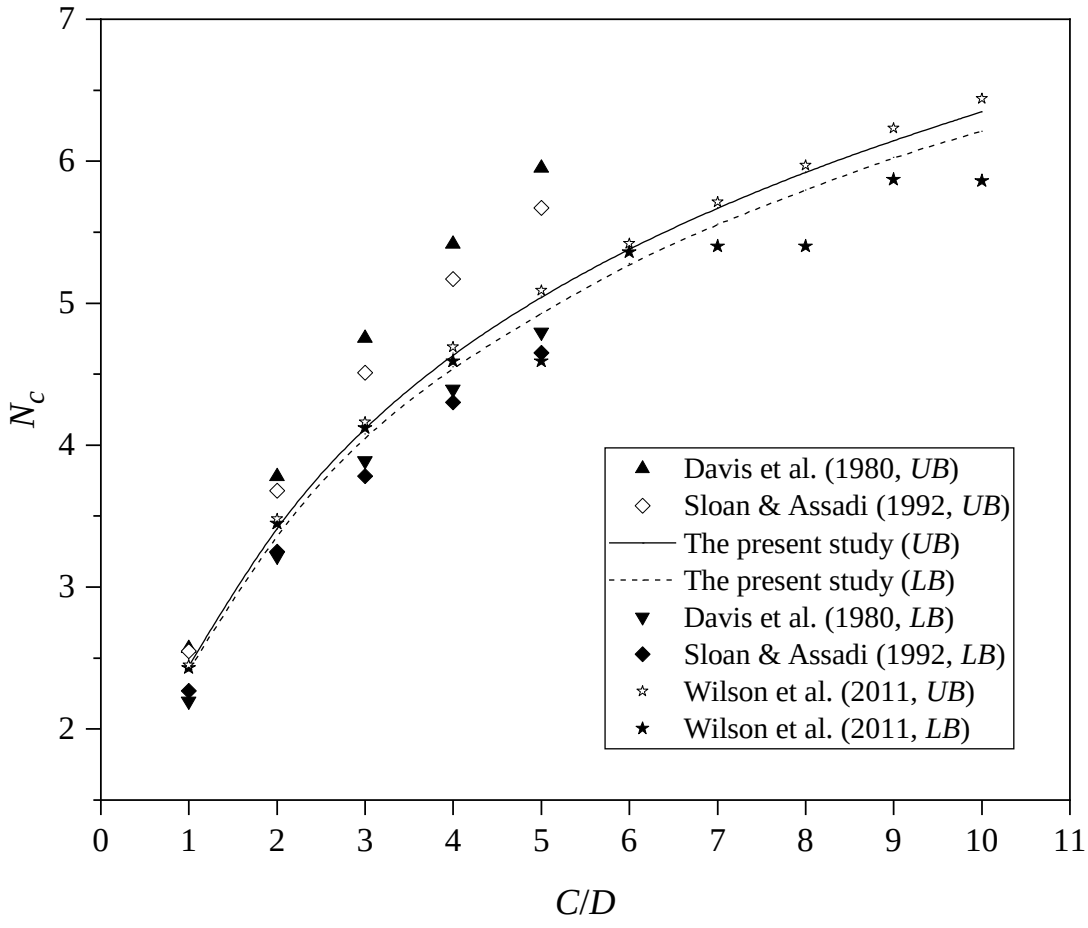

Figure 5.6. Comparison of N_c between the present study and existing solutions.

It was noted that the gap error between the bounds (*LB* and *UB*) is not small in their study. On the other hand, good agreement is observed between the *FELA* results of this study and those of Wilson et al. (2011) for *UB* results. However, there is a fluctuation in the *LB* results of Wilson et al. (2011) when the depth ratio is greater than 4. This could be attributed to the difficulty in mesh arrangement for deep cases.

Figure 5.7 compares the N_c results of this study with those of centrifuge experiments by Kimura and Mair (1981). The stability bounds predicted by this study are in good agreement with the experimental results.

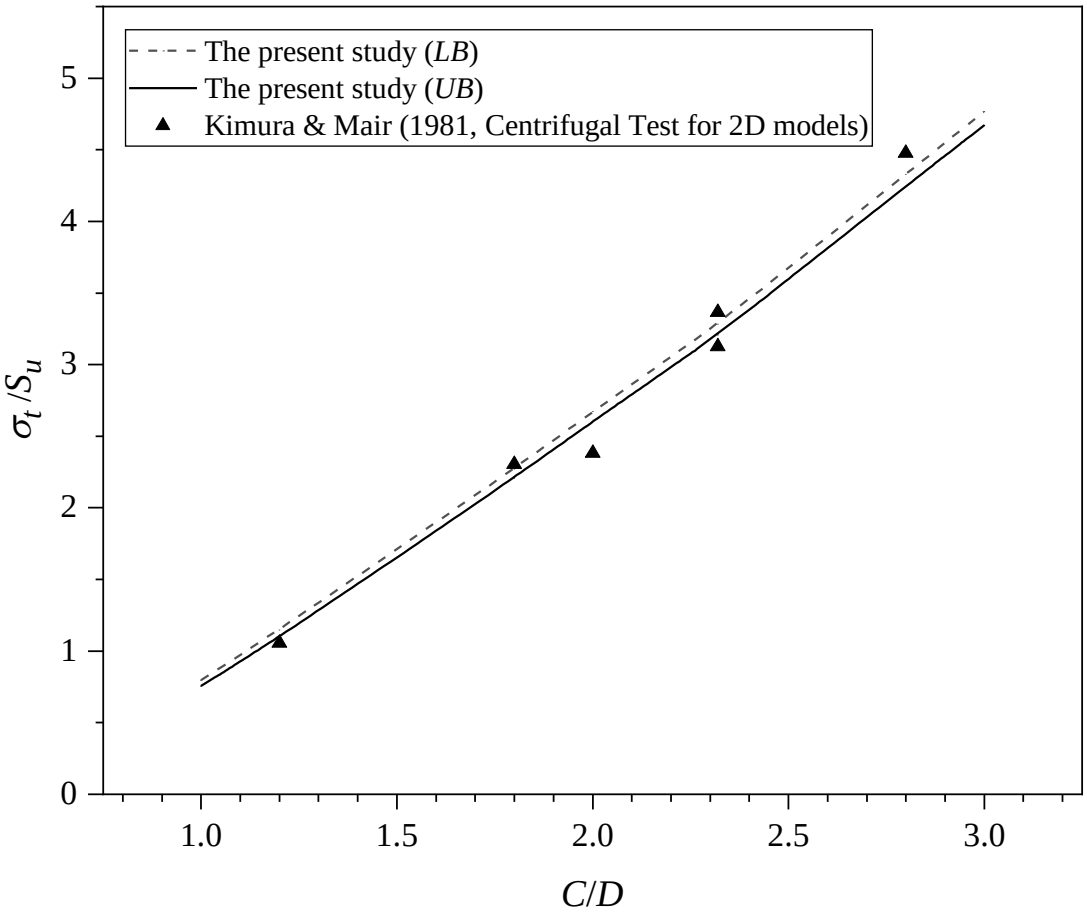

Figure 5.7. Comparison with experimental study ($\gamma D/S_u$ = 2.6, Kimura & Mair 1981).

5.4 The Extent of Surface Failure

Absolute displacement $|u| = \sqrt{(u_x^2 + u_y^2)}$ plots can be used to give an indication of failure mechanism and the ground surface failure extent. Figures 5-8 to 5-10 (left-hand side) show |u| contour plots for *C/D* = 3, 6 and 9, respectively.

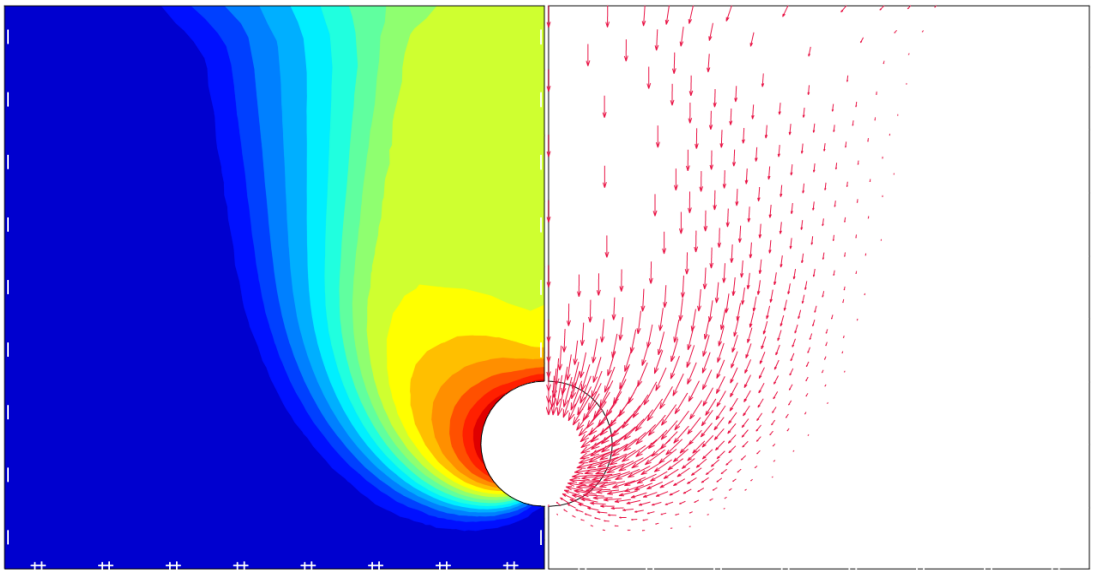

Note that the actual contour values of the plots are not important in limit analysis with the perfect plasticity theorem.

Figure 5.8. Absolute displacement ($|u|$) contour and displacement vector (*C/D* = 3).

For all *C/D*, the failure zone gets wider for increasing depth ratio. Floor heaving is most severe for deep cases but reduces for shallow cases. A similar observation is presented in the power dissipation charts by Wilson et al. (2011).

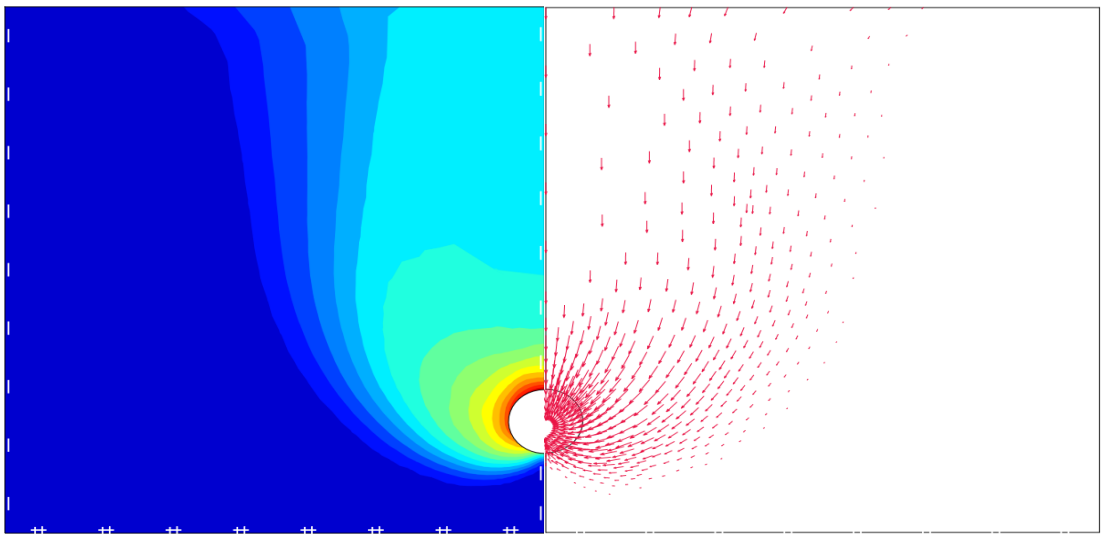

Note that the actual contour values of the plots are not important in limit analysis with the perfect plasticity theorem.

Figure 5.9. Absolute displacement ($|u|$) contour and displacement vector (*C/D* = 6).

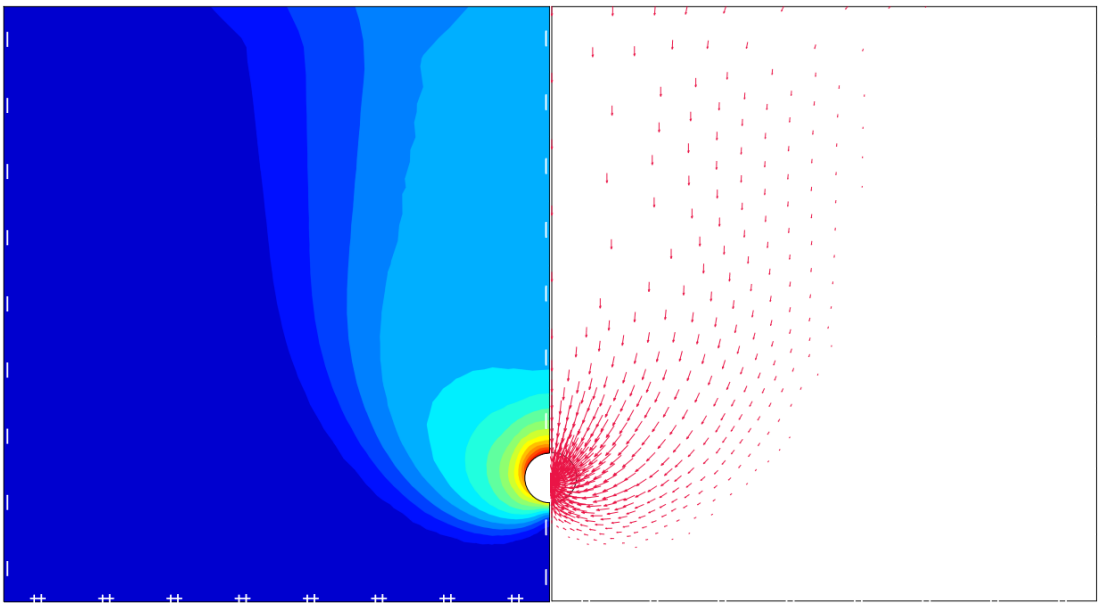

Note that the actual contour values of the plots are not important in limit analysis with the perfect plasticity theorem.

Figure 5.10. Absolute displacement ($|u|$) contour and displacement vector (C/D = 9).

It is to be noted that the actual displacement contour values of the plots are not important in limit analysis with perfect plasticity theorem (Sloan 2013; Shiau & Sams 2019; Shiau & Al-Asadi 2020a, 2020b, 2020c). It can be observed that the cohesive soil mass moves toward the tunnel like a flow. No rigid block of particles movement can be recognised as in cohesionless soil, and that is the reason why the kinematic approaches are difficult to apply in cohesive soil (Mollon et al. 2011, 2013). Also, shown on the right-hand side of Figures 5.8 to 5.10 is the displacement vector plots. The shorter vectors along the slip surface indicate a smaller movement of soil due to soil friction; whereas; in the centre of mass above the tunnel, the motion is nearly vertical, having a greater displacement. All of the effected overburdening soil is being funnelled towards the opening of the cavity, as seen by the density of the vectors around the area. There are obvious differences in both shape and the number of absolute displacement contours as the tunnel cover-to-diameter ratio increases.

Having these plots does increase the confidence level with regards to finding possible slip planes and ground surface failure extent. The extent of the surface failure and the corresponding depth ratio have been recorded in Table 5.5 and graphically presented in Figure 5.11, which shows a simple linear relationship between (E/D) and (C/D). Noting that the failure extent ratio (E/D) increases as the depth ratio (C/D) increases, the greater surface failure (compared to the tunnel diameter) could be the justification of a conical shape failure mechanism.

Table 5.5. Surface failure ratios.

Depth Ratio (C/D^*)	Measured, half surface failure extent, $E/2$ (m)	The ratio of failure extent to tunnel diameter (E/D^*)
1	2.3	4.6
2	3.9	7.8
3	5.4	10.8
4	6.8	13.6
5	8.2	16.4
6	9.4	18.8
7	10.7	21.4
8	11.9	23.8
9	13.0	26.0
10	14.2	28.4

∗ Tunnel diameter D = 1 (m)

Given C/D = 1 and D = 1 metre, the cover depth (C) above the crown of the tunnel is 1 metre, and the resulting extent of the surface failure (E) is 4.6 metres. When the depth ratio C/D is increased to 10, the extent of the surface failure (E) increases to 28.4 metres. The extent of the surface failure has increased by a factor greater 6, as shown in Equation 5.10.

$$E / D = 2.63 \times (C / D) + 2.68 \tag{5.10}$$

There is a strong relationship between the surface failure ratio and the depth ratio in cohesive soil. Table 5.5 and Figure 5.11 are useful to practical engineers during the stage of tunnel construction.

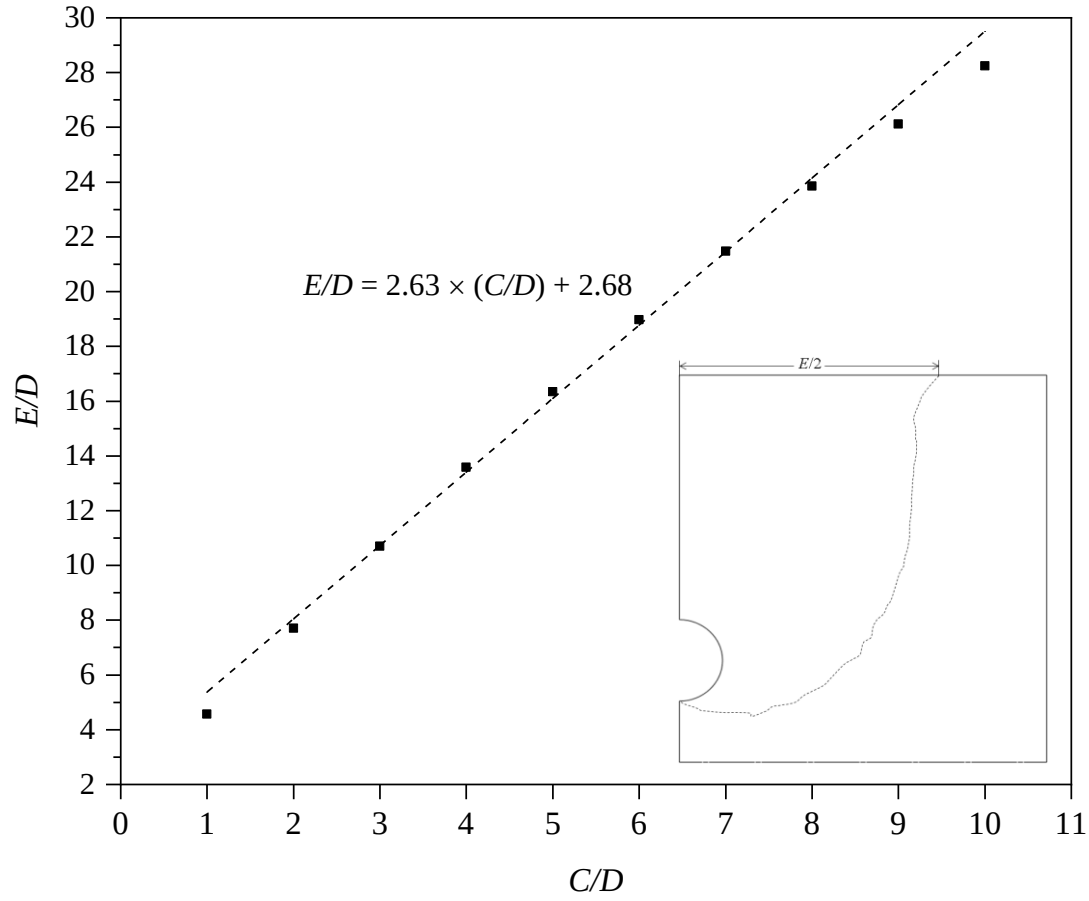

Figure 5.11. Surface failure ratio (*E/D*) vs (*C/D*).

5.5 Example and Practical Uses

Since the lower bound theorem offers a safe assessment of the critical stability number, a design contour chart for factors of safety (*FoS*) is presented in Figure 5.12 based on *LB* results. For practical design purposes, this stability chart can be used by the engineer to relate the depth ratio (*C*/*D*), stability number (*N*), and a factor of safety (*FoS*). This is a convenient approach, as all relevant parameters can be observed clearly in one plot.

5.5.1 Example:

During the construction of a tunnel in clayey soil, the cylindrical tunnel shield is unable to resist the uniform radial pressure of the soil for a short period. A decision needs to be made as to whether the tunnel would be stable during this period.

Given C = 20 m, D = 4 m, σ_t = 300 kPa, σ_s = 30 kPa, S_u = 28 kPa and γ = 18 kN/m^3, determine whether this circular tunnel problem would result in collapse or blowout, and what is the *FoS* for the problem?

1. Using Equation 5.1, the "designed" stability number N = 4.5.
2. Since N greater than zero, the velocity field would be in collapse direction.
3. For $N > 0$ (active movement), Equation 5.8 gives a *FoS* (*LB*) of 1.11.
4. With C/D = 5 and N = 4.5, Figure 5.12 gives an approximate value of *FoS* (*LB*) = 1.10.

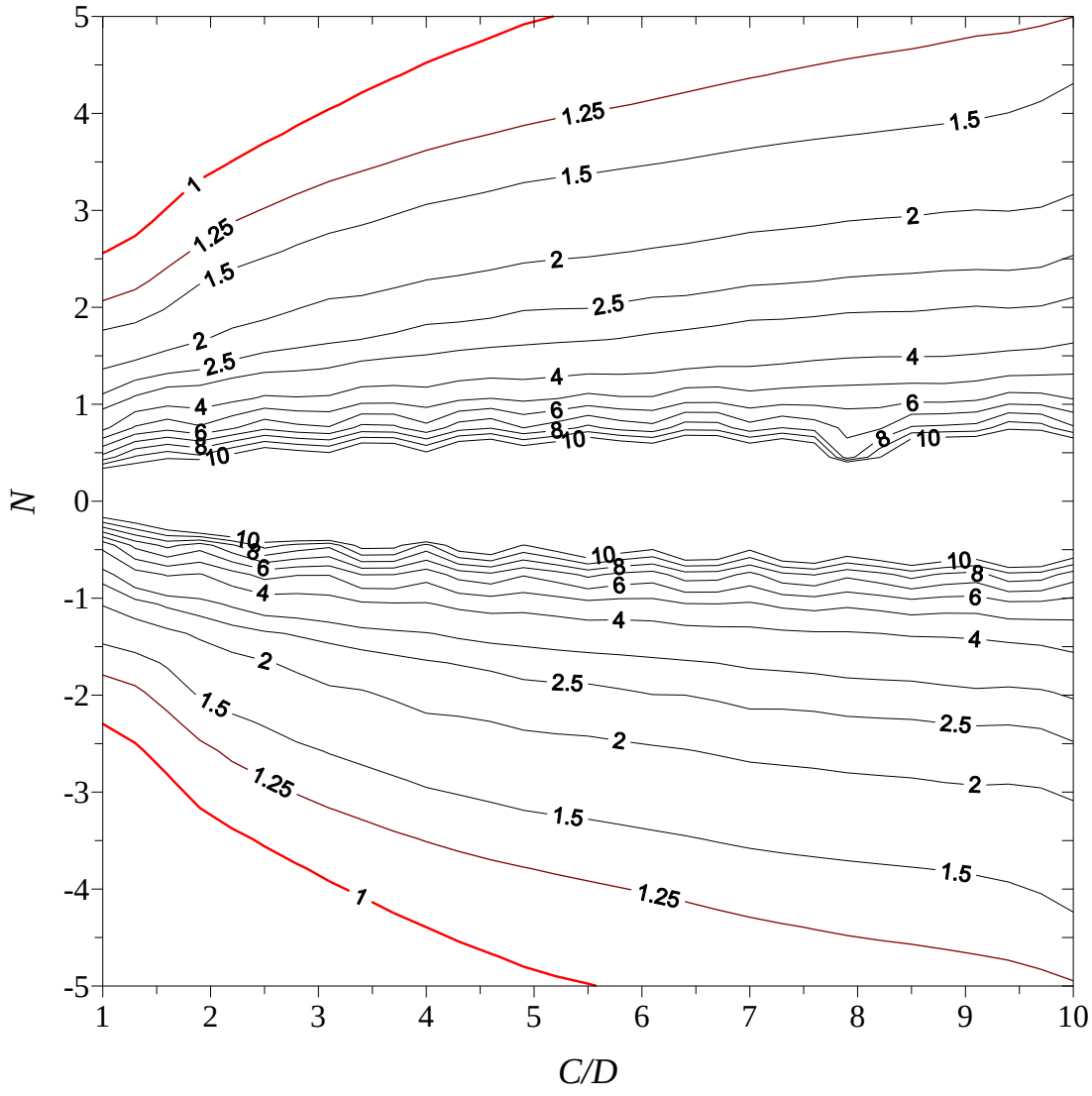

Figure 5.12. *FoS* (*LB*) design chart for circular tunnel stability.

5.6 Conclusion

Broms and Bennermarks' original stability number combines overburden pressures (surcharge and self-weight) with internal supporting pressures and is applicable to undrained clay. This original stability number has been successfully studied in this chapter for circular tunnel problems using the shear strength reduction method and the finite element limit analysis.

Numerical results for factors of safety were obtained for a wide range of stability numbers for collapse and blowout scenarios. A unique critical stability number (N_c) was then obtained by multiplying the "designed" stability number and the corresponding *FoS* for each depth ratio (*C/D*). The extent of surface failure was also investigated in this study.

The rigorous *UB* and *LB* results of *FoS* and N_c produced in this paper can be used with confidence in the design for tunnel stability. This undrained approach is to be continued in Chapter 6 for a full 3D tunnel heading analysis.

CHAPTER 6: UNDRAINED ANALYSIS OF 3D SINGLE CIRCULAR TUNNEL

6.1 Introduction

The assessment of the face stability of tunnels is an important criterion of the shield-tunnelling in soft ground. Shield machines (earth, slurry and air) provide support pressure on the advancing tunnel face. If the applied pressure is insufficient, the tunnel heading will collapse (active failure). On the other hand, for shallow tunnels, if the pressure is excessively high, the soil mass in front of the heading will result in blow-out (passive failure).

In the previous chapters, the stability of plane strain underground openings and tunnels in undrained soil conditions are investigated by using two-dimensional programs, which are finite element limit analysis and finite difference method. 2D results for the stability are more conservative when compared to 3D; this is because the two-dimensional cavity width is a cross-section of a cavity with unconstrained length when compared to the three-dimensional cavity opening which is constrained in size.

This chapter investigates the stability of three-dimensional circular tunnel heading in undrained soil conditions. The heading is rigidly supported along its length, while the face is subjected to internal pressure, and free to move. Failure of the heading in collapse and blowout is studied by different combinations of internal pressure and overburden pressure at the axis of the tunnel.

Finite element limit analysis and load multiplier method are utilised to compute the three-dimensional upper and lower bound critical supporting pressure values for a wide range of heading configurations and stability scenarios in collapse and blowout. The obtained results of the stability (N_c) and factor of safety (FoS) for various depths are presented in the form of dimensionless stability charts and verified by the existing solutions available in the literature. Some practical examples are provided to demonstrate the usefulness of the design charts and tables. These charts give a real approximation of stability and can be used by engineers in preliminary designs and construction for tunnels.

6.2 Problem Statement and Modelling Methodology

Figure 6.1 shows the problem statement of a three-dimensional half-circular tunnel. The soil medium is considered as a perfectly plastic Mohr-Coulomb material with an angle of internal friction equal to zero. The tunnel has a diameter (D), cover depth (C) and axis depth (H) from the ground surface. σ_t is a normal uniform pressure on the face of the tunnel, and σ_s is a vertical surcharge pressure on the ground surface.

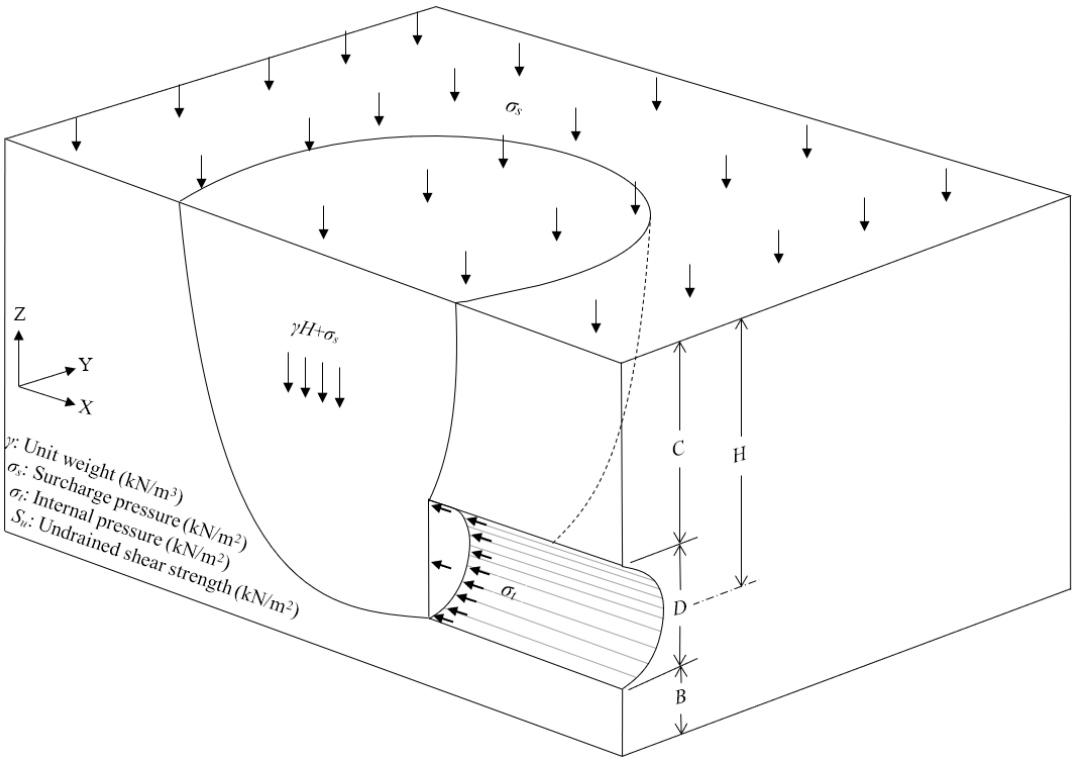

Figure 6.1. Problem Statement.

The tunnel is symmetrical around its vertical axis (z); therefore, the critical pressure calculations are based on the half of the domain of the tunnel, which is along the central axis (x). Using the *FELA* software (OptumCE 2018), rigorous upper and lower bounds of a 3D problem can be obtained efficiently using the finite element discretisation. Unlike many analytical methods, finite element limit analysis (*FELA*) does not need prior assumptions to be made in relation to the shape of the failure surface. This program was successfully used to study the stability problems of various ground structures under different loading conditions (Sloan (2013).

A typical *FELA* mesh adopted in this paper is shown in Figure 6.2. Adaptive mesh generation and refinement were used in the simulations to enable accurate limit loads

to be obtained through the use of the bounds gap error estimator (Sloan 2013). For all analyses, 5000 to 10,000 discretisation elements and three iterations for adaptive meshing were used.

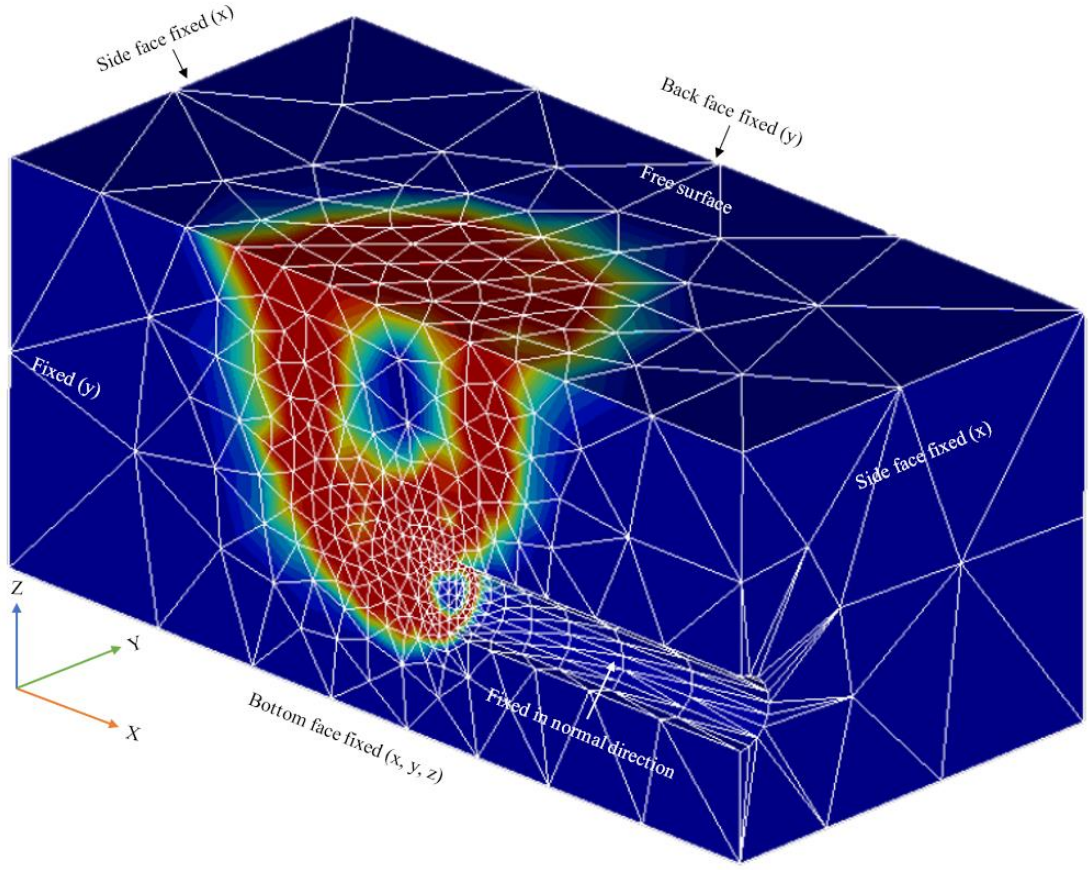

Figure 6.2. Numerical model and adaptive mesh (*C/D* = 3).

The large size of the model is essential as it ensures that the whole soil mass is simulated correctly, and the mechanism of failure does not intersect the boundaries of the model. The boundary conditions of the *FELA* mesh in Figure 6.2 are prepared such that the side surfaces are restrained in the *x*-direction, the back and the front surfaces (symmetrical plane) are restrained in the y-direction, and the ground surface is free to displace. The base is fixed in all directions. The rigid lining around the soil excavation is restrained in the normal direction to represent the smooth interface condition. For such a boundary condition, there is no transfer of shear force between the lining and the soil, and it is considered as a conservative assumption (Shiau et al. 2003; Shiau et al. 2008; Shiau et al. 2011).

Using 3D *FELA* analysis, critical internal pressures (σ_t) are computed for a number of input parameters such as (C, D, σ_s, γ, H, *and* S_u) in both blowout and collapse analyses.

The critical stability numbers (N_c) are then calculated using Equation 6.1.

$$N = \frac{\sigma_s + \gamma H - \sigma_t}{S_u} \tag{6.1}$$

This paper investigates the face stability of a 3D circular tunnel, allowing the results to be useful in design practise by making use of dimensionless ratios. The results obtained are compared and validated with the existing solutions available in the published literature as well as the two-dimensional (2D) *FELA* results by Shiau and Al-Asadi (2018).

6.3 Results and Discussion

6.3.1 Discussing N_c

3D *FELA* is used to compute the upper and the lower bounds of the minimum support pressures (σ_t) at collapse and blowout for a series of depth ratios (C/D). The critical stability numbers (N_c), as shown in Table 6.1, are determined by substituting the obtained critical support pressure σ_t into Equation 6.1.

Table 6.1. 3D N_c results (FoS = 1) in collapse and blowout (C/D = 1- 10).

C/D	Collapse		Blowout	
	3D (*LB*)	3D (*UB*)	3D (*LB*)	3D (*UB*)
1	7.339	7.634	-7.336	-7.641
2	9.490	9.845	-9.474	-9.843
3	10.842	11.276	-10.857	-11.286
4	11.845	12.319	-11.846	-12.314
5	12.589	13.163	-12.612	-13.150
6	13.272	13.816	-13.273	-13.843
7	13.795	14.411	-13.806	-14.410
8	14.317	14.910	-14.294	-14.931
9	14.734	15.370	-14.703	-15.361
10	15.094	15.771	-15.142	-15.774

The data in Table 6.1 are also graphically shown in Figure 6.3. As the depth ratio C/D increases, the value of critical stability number (N_c) also increases. Note that the gradient of the curve decreases significantly as C/D increases. Overall, the *LB* results for the critical stability number N_c are smaller than the *UB* results. The lower bound

approach is always conservative, and the "true' solution is located between the *LB* and the *UB* limits.

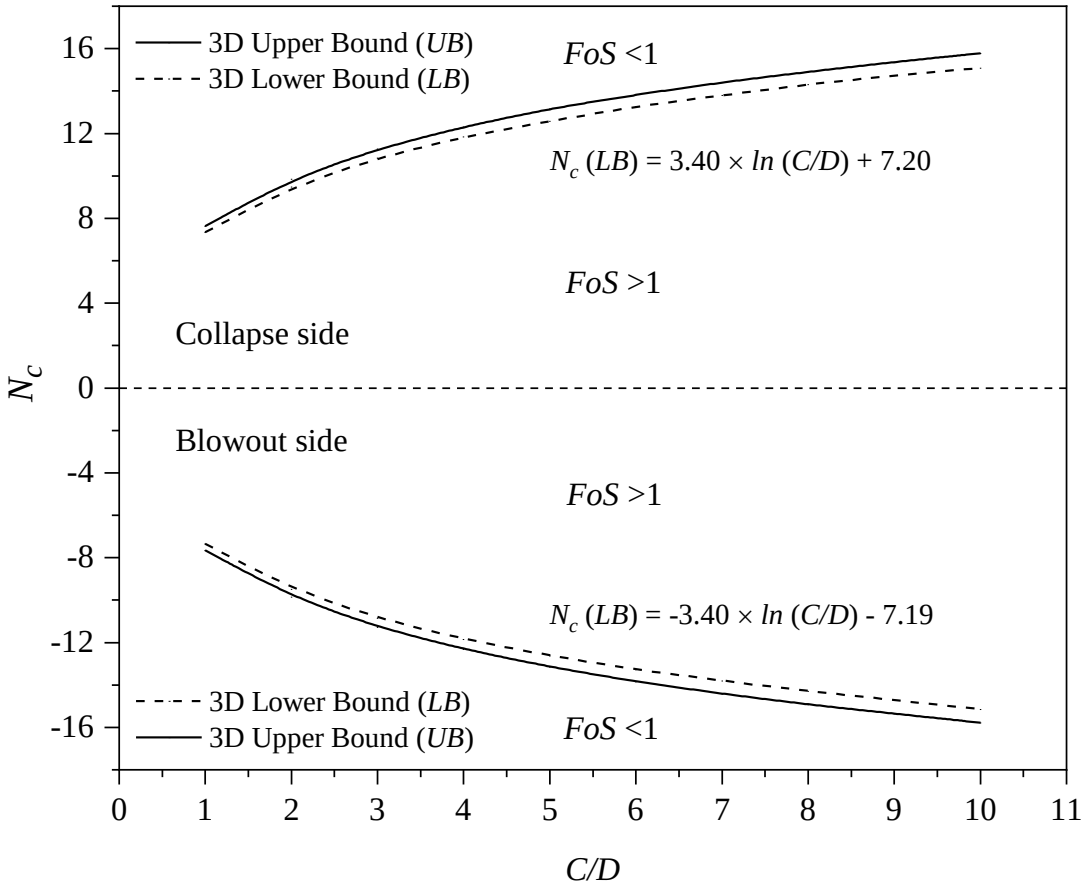

Figure 6.3. 3D N_c results (*FoS* = 1) in collapse and blowout (*C/D* = 1- 10).

The relationship between lower bound N_c and *C/D* are mathematically presented in Equations 6.2 and 6.3, respectively for collapse and blowout, with a correlation coefficient (R^2) of 0.999.

$$N_c = 3.40 \times \ln(C/D) + 7.20 \tag{6.2}$$

$$N_c = -3.40 \times \ln(C/D) - 7.19 \tag{6.3}$$

Asymmetrical form is observed for both collapse and blowout failures. The factor of safety (*FoS*) in the range between the blowout and the collapse curves is greater than one, and the maximum value of *FoS* is in the middle of the graph (*N* = 0). A designer is to ensure that the "designed" *N* value is located within the safe zone.

6.3.2 Discussing *FoS*

Shiau and Al-Asadi (2018) investigated the stability of 2D tunnel heading in undrained condition and presented practical design charts showing the relationship between *FoS* and *N* for various *C*/*D*. The authors concluded that the relationship between *FoS* and *N* is in a hyperbolic form where *FoS* and *N* are the vertical and horizontal asymptote lines, respectively.

The general Equation stated in Shiau and Al-Asadi (2018) is shown in Equation 6.4.

$$FoS = N_c / N \tag{6.4}$$

For the present 3D collapse analysis, after substituting Equations 6.1 and 6.2 into Equation 6.4, with given parameters (σ_t, σ_s, C, D, γ, H and S_u), the factor of safety (*FoS*) is calculated using Equation 6.5

$$FoS = \frac{(3.40 \times \ln(C / D) + 7.20) \times S_u}{\sigma_s + \gamma H - \sigma_t} \tag{6.5}$$

For 3D blowout analysis, Equation 6.6 can be used to calculate *FoS* by substituting Equations 6.1 and 6.3 into Equation 6.4.

$$FoS = \frac{(-3.40 \times \ln(C / D) - 7.19) \times S_u}{\sigma_s + \gamma H - \sigma_t} \tag{6.6}$$

Using Equations 6.5 and 6.6, a comprehensive 3D *FoS* (*LB* and *UB*) are presented in Tables 6.2 and 6.3 for the range of depth ratios (*C*/*D* = 1 to 10) and design stability numbers (*N* = -24 to 24).

Table 6.2. 3D *FoS* results (*LB*) for various values of *N* and *C/D* in collapse and blowout.

N	*C/D*									
	1	2	3	4	5	6	7	8	9	10
-24	0.306	0.395	0.452	0.494	0.526	0.553	0.575	0.596	0.613	0.631
-20	0.367	0.474	0.543	0.592	0.631	0.664	0.690	0.715	0.735	0.757
-16	0.459	0.592	0.679	0.740	0.788	0.830	0.863	0.893	0.919	0.946
-14	0.524	0.677	0.776	0.846	0.901	0.948	0.986	1.021	1.050	1.082
-13	0.564	0.729	0.835	0.911	0.970	1.021	1.062	1.100	1.131	1.165
-12	0.611	0.790	0.905	0.987	1.051	1.106	1.151	1.191	1.225	1.262
-11	0.667	0.861	0.987	1.077	1.147	1.207	1.255	1.299	1.337	1.377
-10	0.734	0.947	1.086	1.185	1.261	1.327	1.381	1.429	1.470	1.514
-9	0.815	1.053	1.206	1.316	1.401	1.475	1.534	1.588	1.634	1.682
-8	0.917	1.184	1.357	1.481	1.577	1.659	1.726	1.787	1.838	1.893
-7	1.048	1.353	1.551	1.692	1.802	1.896	1.972	2.042	2.100	2.163
-5	1.467	1.895	2.171	2.369	2.522	2.655	2.761	2.859	2.941	3.028
-4	1.834	2.369	2.714	2.962	3.153	3.318	3.452	3.574	3.676	3.786
-2	3.668	4.737	5.429	5.923	6.306	6.637	6.903	7.147	7.352	7.571
-1	7.336	9.474	10.857	11.846	12.612	13.273	13.806	14.294	14.703	15.142
-0.5	14.672	18.948	21.714	23.692	25.224	26.546	27.612	28.588	29.406	30.284
0	Infinity	Infinity	Infinity	Infinity	Infinity	Infinity	Infinity	Infinity	Infinity	Infinity
0.5	14.678	18.980	21.684	23.690	25.178	26.544	27.590	28.634	29.468	30.188
1	7.339	9.490	10.842	11.845	12.589	13.272	13.795	14.317	14.734	15.094
2	3.670	4.745	5.421	5.923	6.295	6.636	6.898	7.159	7.367	7.547
4	1.835	2.373	2.711	2.961	3.147	3.318	3.449	3.579	3.684	3.774
5	1.468	1.898	2.168	2.369	2.518	2.654	2.759	2.863	2.947	3.019
7	1.048	1.356	1.549	1.692	1.798	1.896	1.971	2.045	2.105	2.156
8	0.917	1.186	1.355	1.481	1.574	1.659	1.724	1.790	1.842	1.887
9	0.815	1.054	1.205	1.316	1.399	1.475	1.533	1.591	1.637	1.677
10	0.734	0.949	1.084	1.185	1.259	1.327	1.380	1.432	1.473	1.509
11	0.667	0.863	0.986	1.077	1.144	1.207	1.254	1.302	1.339	1.372
12	0.612	0.791	0.904	0.987	1.049	1.106	1.150	1.193	1.228	1.258
13	0.565	0.730	0.834	0.911	0.968	1.021	1.061	1.101	1.133	1.161
14	0.524	0.678	0.774	0.846	0.899	0.948	0.985	1.023	1.052	1.078
16	0.459	0.593	0.678	0.740	0.787	0.830	0.862	0.895	0.921	0.943
20	0.367	0.475	0.542	0.592	0.629	0.664	0.690	0.716	0.737	0.755
24	0.306	0.395	0.452	0.494	0.525	0.553	0.575	0.597	0.614	0.629

Table 6.3. 3D *FoS* results (*UB*) for various values of *N* and *C/D* in collapse and blowout.

N	*C/D*									
	1	2	3	4	5	6	7	8	9	10
-24	0.318	0.410	0.470	0.513	0.548	0.577	0.600	0.622	0.640	0.657
-20	0.382	0.492	0.564	0.616	0.658	0.692	0.721	0.747	0.768	0.789
-16	0.478	0.615	0.705	0.770	0.822	0.865	0.901	0.933	0.960	0.986
-14	0.546	0.703	0.806	0.880	0.939	0.989	1.029	1.067	1.097	1.127
-13	0.588	0.757	0.868	0.947	1.012	1.065	1.108	1.149	1.182	1.213
-12	0.637	0.820	0.941	1.026	1.096	1.154	1.201	1.244	1.280	1.315
-11	0.695	0.895	1.026	1.119	1.195	1.258	1.310	1.357	1.396	1.434
-10	0.764	0.984	1.129	1.231	1.315	1.384	1.441	1.493	1.536	1.577
-9	0.849	1.094	1.254	1.368	1.461	1.538	1.601	1.659	1.707	1.753
-8	0.955	1.230	1.411	1.539	1.644	1.730	1.801	1.866	1.920	1.972
-7	1.092	1.406	1.612	1.759	1.879	1.978	2.059	2.133	2.194	2.253
-5	1.528	1.969	2.257	2.463	2.630	2.769	2.882	2.986	3.072	3.155
-4	1.910	2.461	2.822	3.079	3.288	3.461	3.603	3.733	3.840	3.944
-2	3.821	4.922	5.643	6.157	6.575	6.922	7.205	7.466	7.681	7.887
-1	7.641	9.843	11.286	12.314	13.150	13.843	14.410	14.931	15.361	15.774
-0.5	15.282	19.686	22.572	24.628	26.300	27.686	28.820	29.862	30.722	31.548
0	Infinity	Infinity	Infinity	Infinity	Infinity	Infinity	Infinity	Infinity	Infinity	Infinity
0.5	15.268	19.690	22.552	24.638	26.326	27.632	28.822	29.820	30.740	31.542
1	7.634	9.845	11.276	12.319	13.163	13.816	14.411	14.910	15.370	15.771
2	3.817	4.923	5.638	6.160	6.582	6.908	7.206	7.455	7.685	7.886
4	1.909	2.461	2.819	3.080	3.291	3.454	3.603	3.728	3.843	3.943
5	1.527	1.969	2.255	2.464	2.633	2.763	2.882	2.982	3.074	3.154
7	1.091	1.406	1.611	1.760	1.880	1.974	2.059	2.130	2.196	2.253
8	0.954	1.231	1.410	1.540	1.645	1.727	1.801	1.864	1.921	1.971
9	0.848	1.094	1.253	1.369	1.463	1.535	1.601	1.657	1.708	1.752
10	0.763	0.985	1.128	1.232	1.316	1.382	1.441	1.491	1.537	1.577
11	0.694	0.895	1.025	1.120	1.197	1.256	1.310	1.355	1.397	1.434
12	0.636	0.820	0.940	1.027	1.097	1.151	1.201	1.243	1.281	1.314
13	0.587	0.757	0.867	0.948	1.013	1.063	1.109	1.147	1.182	1.213
14	0.545	0.703	0.805	0.880	0.940	0.987	1.029	1.065	1.098	1.127
16	0.477	0.615	0.705	0.770	0.823	0.864	0.901	0.932	0.961	0.986
20	0.382	0.492	0.564	0.616	0.658	0.691	0.721	0.746	0.769	0.789
24	0.318	0.410	0.470	0.513	0.548	0.576	0.600	0.621	0.640	0.657

The (*LB*) data in Tables 6.2 is used to prepare the design chart in Figure 6.4, where *FoS* can be determined effectively using *C/D* and *N*.

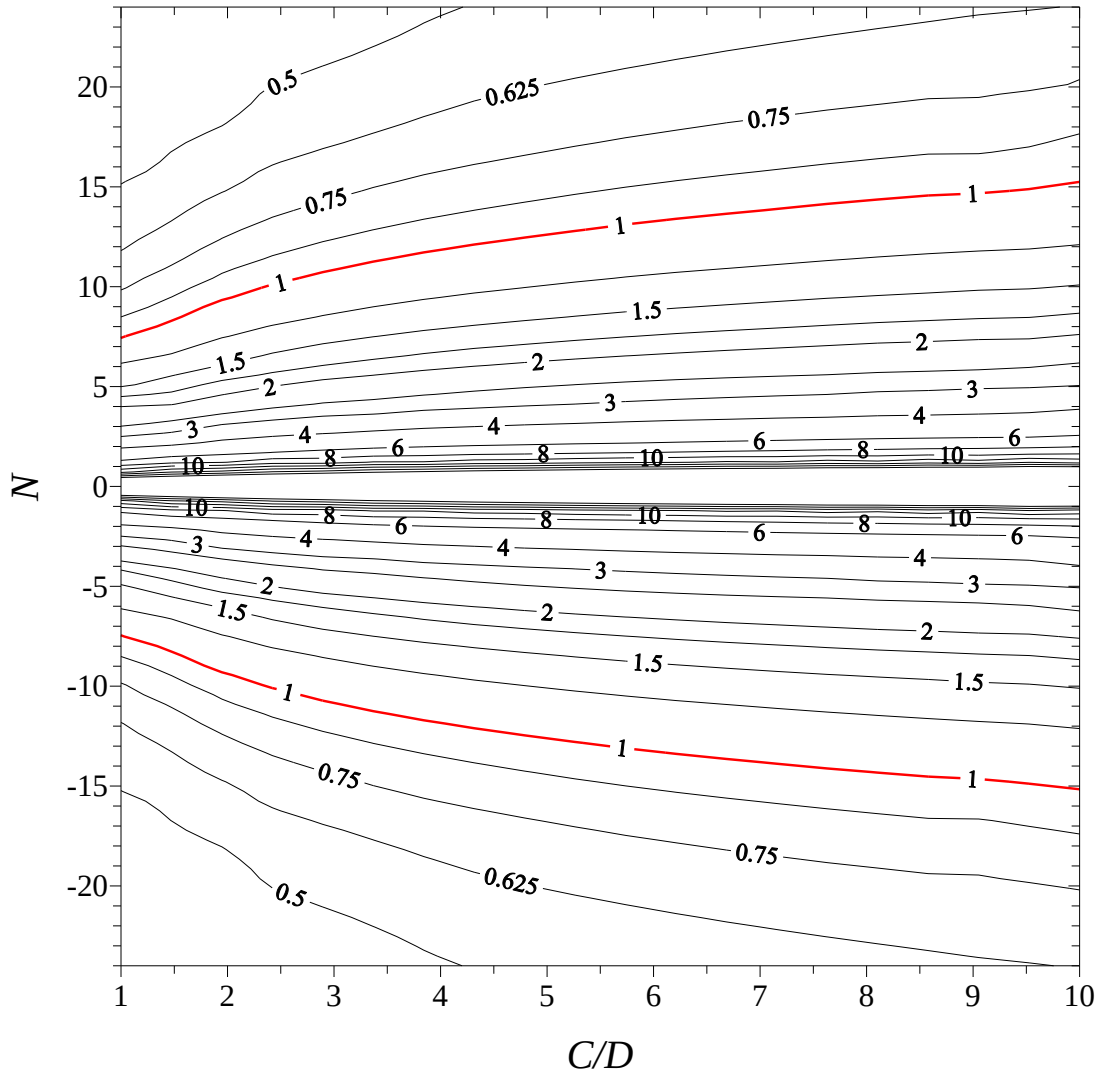

Figure 6.4. 3D *FoS* (*LB*) design chart for circular heading stability.

Figure 6.5 presents a typical plot of the *FoS* for various *N* values. This is for the depth ratio of *C*/*D* = 3. It is to be noted that when the overburden pressure ratio $((\sigma_s + \gamma H)/S_u)$ is less than the supporting pressure ratio (σ_t / S_u) the negative value of *N* indicates a blowout movement. Contrary to this, the positive value of *N* suggests that the soil moves in the collapsed condition. This occurs when the supporting pressure ratio (σ_t / S_u) is less than the overburden pressure ratio $((\sigma_s + \gamma H)/S_u)$. Noting that an impending collapse is approached where *FoS* = 1, the corresponding value of *N* is the so-called critical N_c. When the overburden pressure ratio $((\sigma_s + \gamma H)/S_u)$ is the same as the supporting pressure ratio (σ_t / S_u) *N* is equal to

zero. For such a situation, the *FoS* is infinite owing to a 'weightless' scenario of the problem.

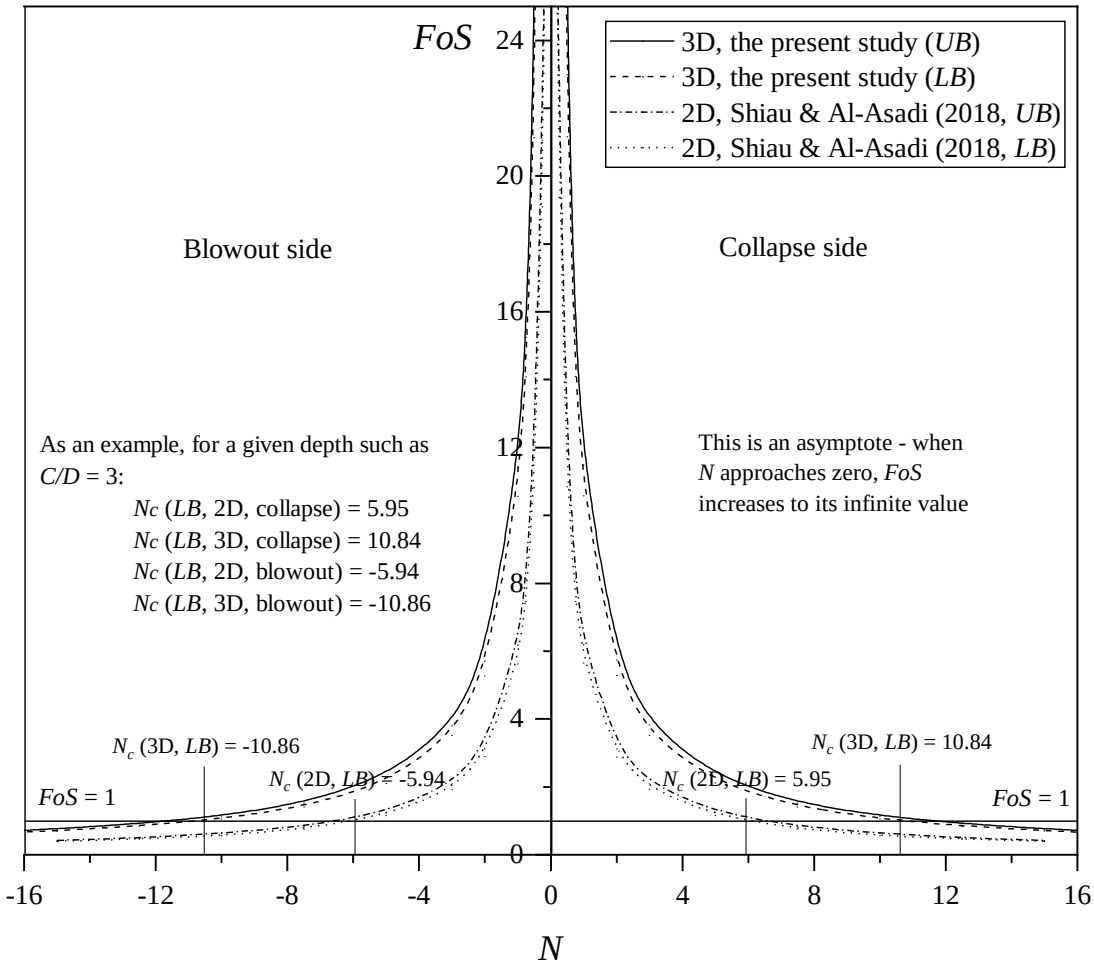

Figure 6.5. 3D *FoS* vs *N* (*C/D* = 3).

Figure 6.5 shows that a unique value can be calculated by multiplying any *N* value and the corresponding *FoS*. This unique value is the critical stability number (N_c), which corresponds to *FoS* of one. Graphically, by drawing the *FoS* = 1 horizontal line in Figure 6.5, the two intersection points give $(N_c)_{3D}$ value of 10.84 for the collapse and -10.86 for the blowout. Also, note the 2D values of $(N_c)_{2D} = \pm 5.95$ as reported in Shiau and Al-Asadi (2018).

6.3.3 Comparison of results

Figure 6.6 and Table 6.4 show a comparison of N_c results from 3D analyses of the circular tunnel of this study with those 2D solutions in Shiau and Al-Asadi (2018).

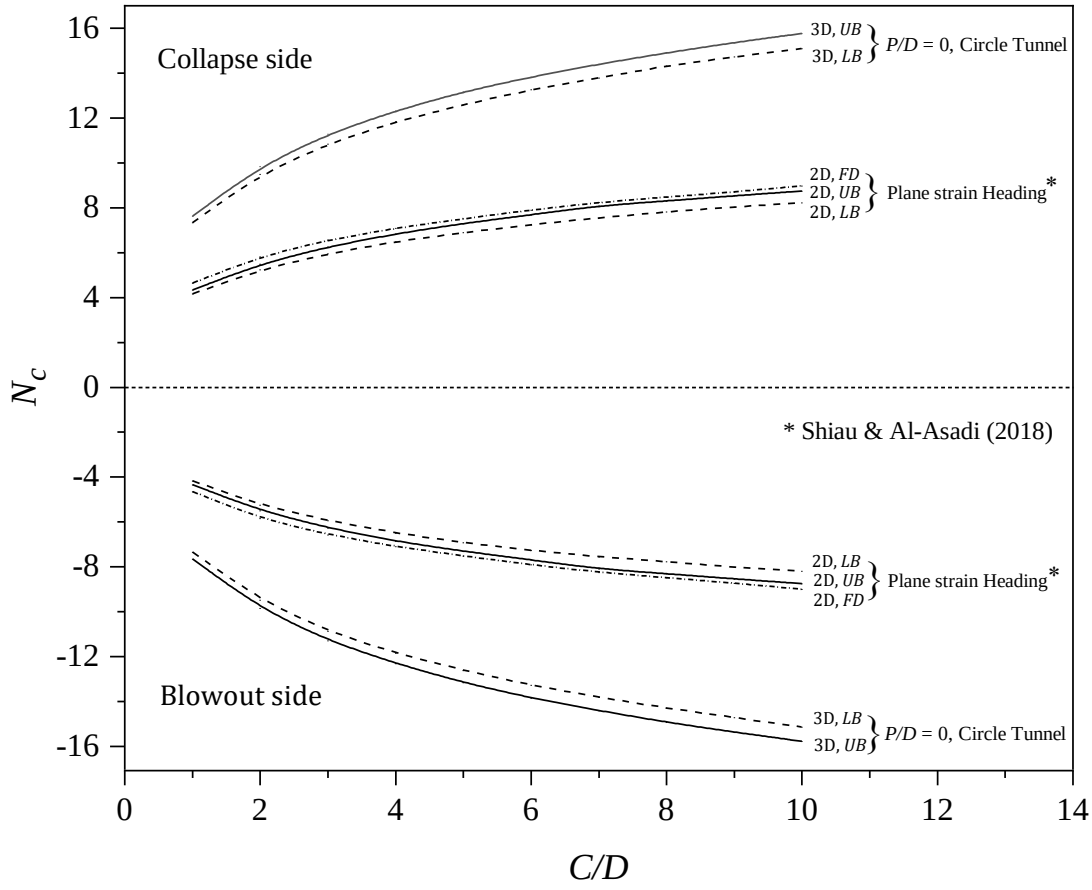

Figure 6.6. Comparison of 2D and 3D N_c results (FoS = 1) in collapse and blowout (C/D = 1- 10).

Table 6.4. Comparison of 2D and 3D N_c results in collapse and blowout (C/D = 1- 10).

C/D	Collapse				
	3D Circle (*LB*)	3D Circle (*UB*)	2D Heading (*LB*)*	2D Heading (*UB*)*	2D Heading (*FD*)*
1	7.34	7.63	4.17	4.33	4.66
2	9.49	9.85	5.25	5.50	5.81
3	10.84	11.28	5.95	6.27	6.56
4	11.85	12.32	6.49	6.84	7.10
5	12.59	13.16	6.91	7.31	7.52
6	13.27	13.82	7.24	7.68	7.90
7	13.80	14.41	7.56	8.09	8.24
8	14.32	14.91	7.82	8.31	8.47
9	14.73	15.37	8.04	8.54	8.71
10	15.09	15.77	8.22	8.75	8.98

C/D	Blowout				
	3D Circle (*LB*)	3D Circle (*UB*)	2D Heading (*LB*)*	2D Heading (*UB*)*	2D Heading (*FD*)*
1	-7.34	-7.64	-4.16	-4.33	-4.66
2	-9.47	-9.84	-5.24	-5.50	-5.84
3	-10.86	-11.29	-5.94	-6.27	-6.56
4	-11.85	-12.31	-6.50	-6.85	-7.10
5	-12.61	-13.15	-6.91	-7.31	-7.52
6	-13.27	-13.84	-7.26	-7.68	-7.90
7	-13.81	-14.41	-7.55	-8.09	-8.24
8	-14.29	-14.93	-7.76	-8.30	-8.47
9	-14.70	-15.36	-8.01	-8.54	-8.73
10	-15.14	-15.77	-8.19	-8.74	-9.00

* Shiau and Al-Asadi (2018)

As expected, the comparison appears considerable differences between 3D and 2D analyses. The 3D results are approximately 70% - 80% greater than 2D ones (Table 6.5). It can be therefore concluded that the 2D analysis produces over-conservative results and is only suitable for the preliminary stages of design.

Table 6.5. The percentage difference between 2D and 3D N_c results in collapse and blowout (*C/D* = 1 - 10).

C/D	Diffs. % between the 3D and 2D (collapse)					
	3D, *LB*	2D, *LB*	*LB*, Diffs. %	3D, *UB*	2D, *UB*	*UB*, Diffs. %
1	7.34	4.17	76.21	7.63	4.33	76.14
2	9.49	5.25	80.69	9.85	5.50	78.90
3	10.84	5.95	82.31	11.28	6.27	79.81
4	11.85	6.49	82.48	12.32	6.84	80.02
5	12.59	6.91	82.29	13.16	7.31	80.19
6	13.27	7.24	83.37	13.82	7.68	79.92
7	13.80	7.56	82.59	14.41	8.09	78.07
8	14.32	7.82	83.18	14.91	8.31	79.40
9	14.73	8.04	83.24	15.37	8.54	80.00
10	15.09	8.22	83.60	15.77	8.75	80.28

C/D	Diffs. % between the 3D and 2D (blowout)					
	3D, *LB*	2D, *LB*	*LB*, Diffs. %	3D, *UB*	2D, *UB*	*UB*, Diffs. %
1	-7.34	-4.16	76.18	-7.64	-4.33	76.34
2	-9.47	-5.24	80.77	-9.84	-5.50	78.87
3	-10.86	-5.94	82.69	-11.29	-6.27	79.97
4	-11.85	-6.50	82.36	-12.31	-6.85	79.69
5	-12.61	-6.91	82.41	-13.15	-7.31	80.01
6	-13.27	-7.26	82.87	-13.84	-7.68	80.27
7	-13.81	-7.55	82.81	-14.41	-8.09	78.12
8	-14.29	-7.76	84.20	-14.93	-8.30	79.87
9	-14.70	-8.01	83.47	-15.36	-8.54	79.89
10	-15.14	-8.19	84.79	-15.77	-8.74	80.40

It is important to compare and validate N_c results of the current study with those in published literature. The influence of the unlined length of the heading (P) on tunnel stability is presented in Figure 6.7 and Table 6.6.

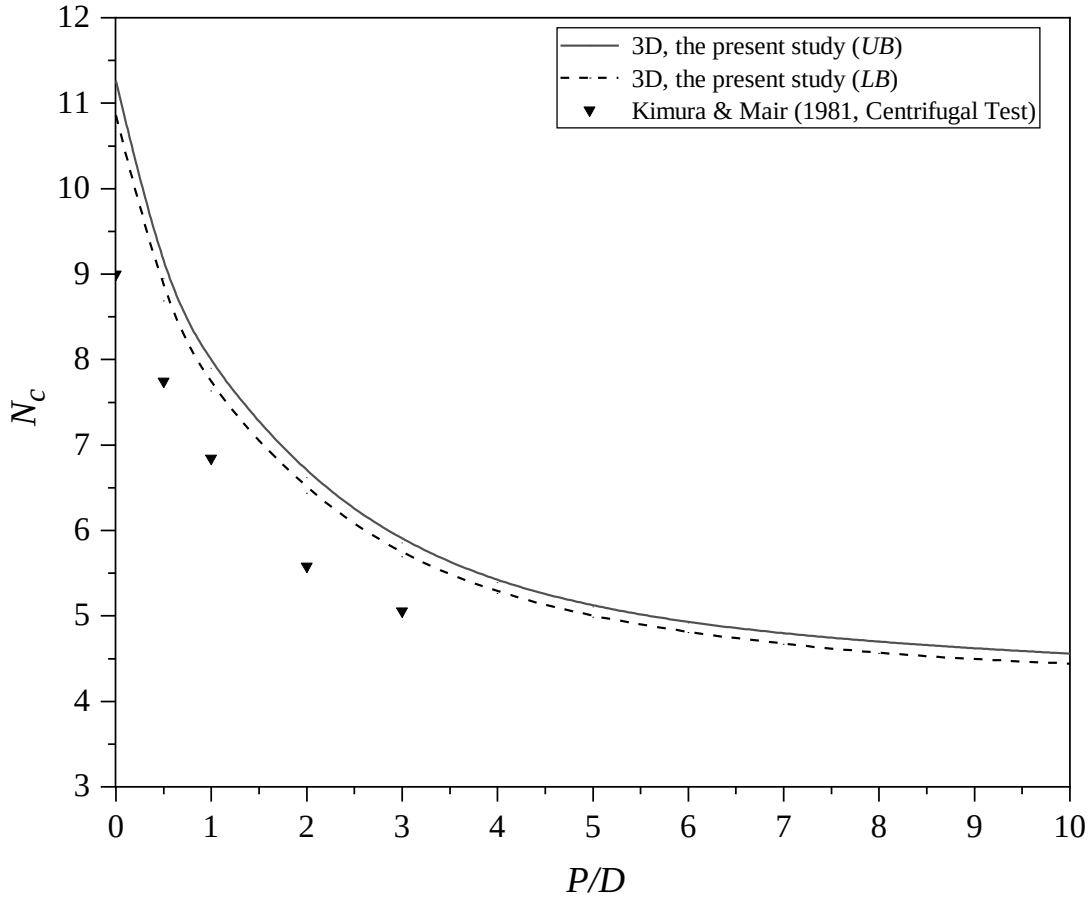

Figure 6.7. Comparison of 3D N_c results between the present study and the centrifugal test of Kimura & Mair (1981) for C/D = 3.

The present study shows a similar trend to those obtained experimentally by Kimura and Mair (1981). Note the dramatic decrease in stability (N_c) for P/D ratio from 0 to 3, meaning that relatively small differences in the critical stability number can dramatically change the required minimum internal pressure (σ_t), (Kimura & Mair 1981).

Table 6.6. Comparison of 3D N_c results between the present study and the centrifugal test of Kimura & Mair (1981) for C/D = 3.

P/D	N_c		
	3D, (*UB*)	3D, (*LB*)	Centrifugal Test, Kimura & Mair (1981)
0	11.26	10.86	9.00
0.5	8.95	8.69	7.75
1	7.90	7.64	6.85
2	6.62	6.44	5.60
3	5.86	5.69	5.10
4	5.40	5.27	--
5	5.11	4.98	--
6	4.92	4.81	--
7	4.79	4.67	--
8	4.70	4.57	--
9	4.62	4.49	--
10	4.56	4.44	--

Figure 6.8 shows the failure mechanism of a circular tunnel face with a large unlined heading ratio (P/D = 10). A general roof collapse is expected for the unlined tunnel when P/D is large.

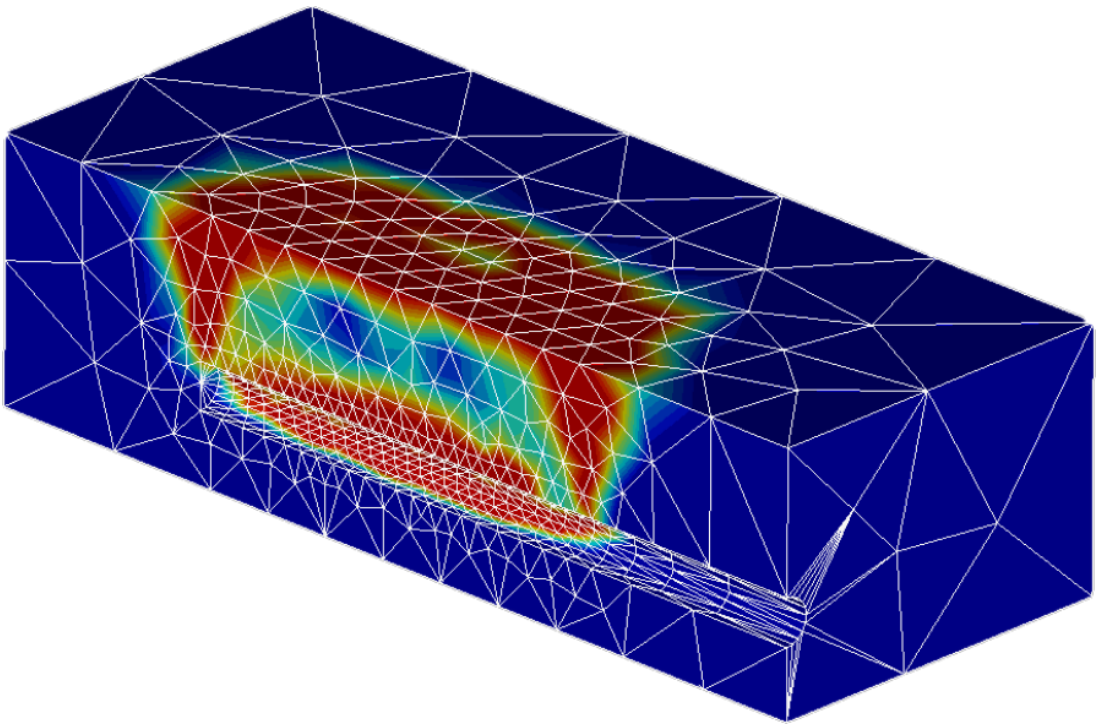

Figure 6.8. Failure mechanism and adaptive mesh for C/D = 3 and P/D = 10.

Figure 6.9 compares N_c results of this study with the analytical upper bound approach by (Mollon et al. 2013; Zhang et al. 2018) and 3D numerical analysis of Ukritchon, Yingchaloenkitkhajorn, et al. (2017).

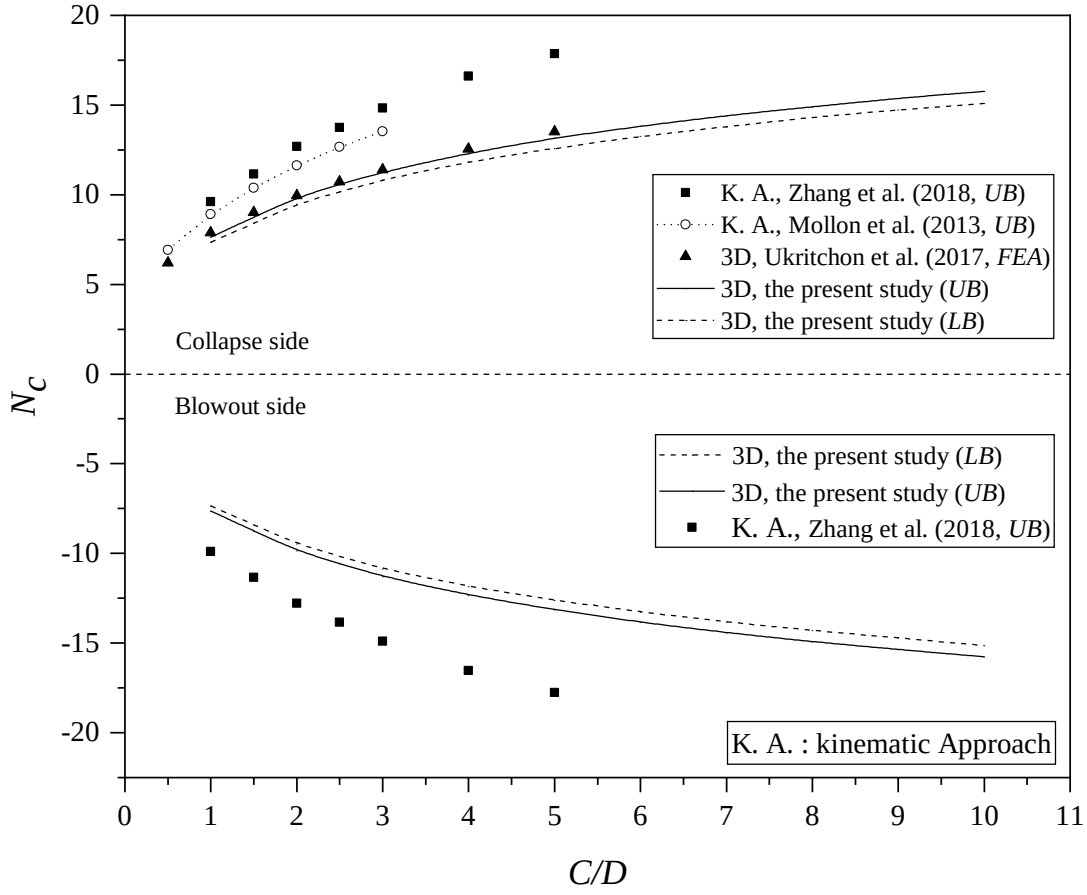

Figure 6.9. Comparison of 3D N_c results.

The analytical upper bound method requires a priori assumption in relation to the general form of the failure surface, which may yield less accurate estimates of the failure load (Sloan (2013). As seen in Figure 6.9, the analytical upper bound results are not conservative, and the difference between the *FELA* and analytical upper bound becomes greater as *C/D* increases. It is suggested that a transformation from general failure to local failure occurs as the value of *C/D* increases. The a priori assumptions of failure mechanisms in Mollon et al. (2013) and Zhang et al. (2018) need further improvement for large *C/D*. Figure 6.9 and Table 6.7 also shows that the 3D Plaxis results in Ukritchon, Yingchaloenkitkhajorn, et al. (2017) agree well with the current upper bound N_c results for collapse analysis.

Table 6.7. Comparison of 3D N_c results.

	Collapse					Blowout		
C/D	Zhang et al. (2018)	Ukritchon et al. (2017)	Mollon et al. (2013)	This study (G3, *UB*)	This study (G3, LB)	This study (G3, *LB*)	This study (G3, *UB*)	Zhang et al. (2018)
0.5	--	6.20	6.90	--	--	--	--	--
1	9.61	7.87	8.91	7.63	7.34	-7.34	-7.64	-9.90
1.5	11.14	9.02	10.39	8.74	8.41	-8.41	-8.74	-11.34
2	12.68	9.94	11.63	9.85	9.49	-9.47	-9.84	-12.78
2.5	13.75	10.72	12.67	10.56	10.17	-10.17	-10.56	-13.84
3	14.83	11.40	13.53	11.28	10.84	-10.86	-11.29	-14.90
4	16.60	12.54	--	12.32	11.85	-11.85	-12.31	-16.53
5	17.87	13.50	--	13.16	12.59	-12.61	-13.15	-17.77
6	--	--	--	13.82	13.27	-13.27	-13.84	--
7	--	--	--	14.41	13.80	-13.81	-14.41	--
8	--	--	--	14.91	14.32	-14.29	-14.93	--
9	--	--	--	15.37	14.73	-14.70	-15.36	--
10	--	--	--	15.77	15.09	-15.14	-15.77	--

Ukritchon, Keawsawasvong, et al. (2017) applied 2D and 3D finite element studies to the undrained face stability of tunnels in Bangkok clays. The non-homogeneous profile was considered as a single clay layer. Using the average undrained cohesion and unit weight, four sections of the Mass Transit Railway Authority of Thailand (MRTA), namely 23-001, 26-001, CS-8 and 7C, were analysed. Their 3D results are presented in Tables 6.8 and 6.9, together with our 3D upper and lower bounds and the analytical 3D upper bound of Mollon et al. (2013).

Table 6.8. Input parameters for the face stability analyses of Bangkok MRTA (After Ukritchon, Keawsawasvong, et al., 2017).

Section	Average unit weight, γ_{avg} (kN/m^3)	Average undrained shear strength, S_{uavg} (kPa)	Tunnel diameter, D (m)	Tunnel covered depth, C (m)
23-001	17.15	66.32	6.30	19.50
26-001	17.36	41.87	6.30	14.70
CS-8	17.37	40.50	6.30	14.35
7C	17.96	62.25	6.30	18.00

Table 6.9. Comparison of 3D *FoS* results (After Ukritchon, Keawsawasvong, et al., 2017).

Section	The factor of safety (*FoS*)				
	Face pressure σ_t (kPa)	3D, Present study (*LB*)	3D, Present study (*UB*)	3D, Ukritchon et al. (2017, *FEA*)	3D, Mollon et al. (2013, *K.A.*)
23-001	40	2.101	2.188	2.036	2.206
	60	2.229	2.321	2.157	2.326
	80	2.373	2.471	2.292	2.460
26-001	130	2.346	2.441	2.539	2.201
	155	2.725	2.835	2.906	2.486
	180	3.249	3.381	3.389	2.856
CS-8	150	2.629	2.736	2.821	2.392
	175	3.139	3.266	3.301	2.751
	200	3.894	4.051	3.965	3.236
7C	50	2.032	2.115	2.599	2.102
	100	2.395	2.493	3.047	2.430
	150	2.916	3.036	3.655	2.880

In general, the comparison shows that the results of Ukritchon, Keawsawasvong, et al. (2017) and Mollon et al. (2013) are in good agreement with our upper and lower bounds for the problems with small depth ratios $C/D \leq 3$. For large depth ratios such as $C/D > 3$, a local failure mechanism may develop, as stated before, and it is necessary to carefully validate the results when the analytical upper bound method is used.

6.4 The Extent of Surface Failure

Figures 6.10-6.12 show the |*u*| contour plots for *C/D* = 0.5, 1.0, 1.5, 2.0, 2.5 and 3.0. The absolute displacement $\left(|u| = \sqrt{u_x^2 + u_y^2}\right)$ contour plot can be used to observe failure mechanism as well as the extent of the ground surface failure. As discussed before, the actual values of the colour in the plots are not real, and they are not shown for such a perfectly plastic model.

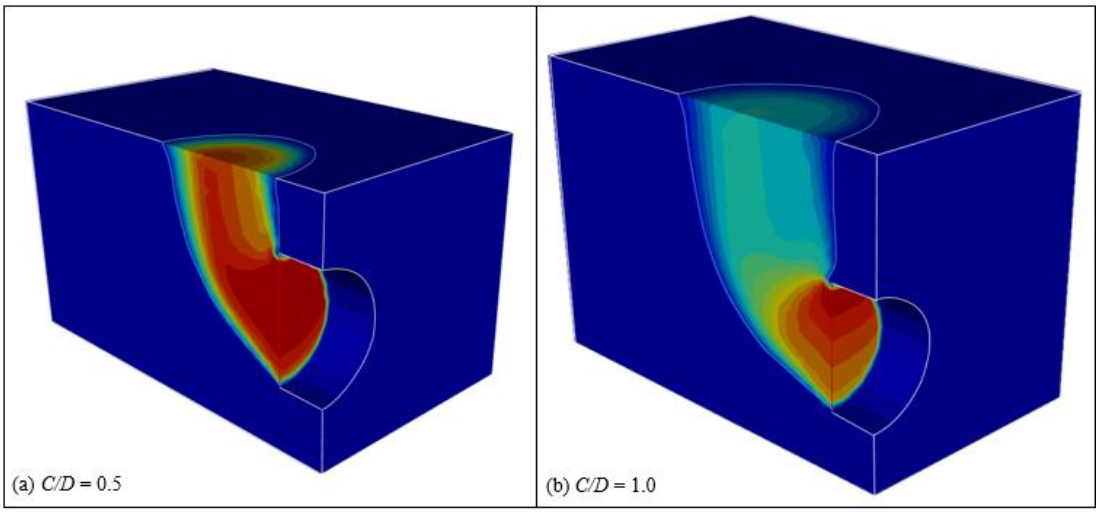

Note that the actual contour values of the plots are not important in limit analysis with the perfect plasticity theorem.

Figure 6.10. Absolute displacement (|u|) contour plots for *C/D* = 0.5 and *C/D* = 1.0.

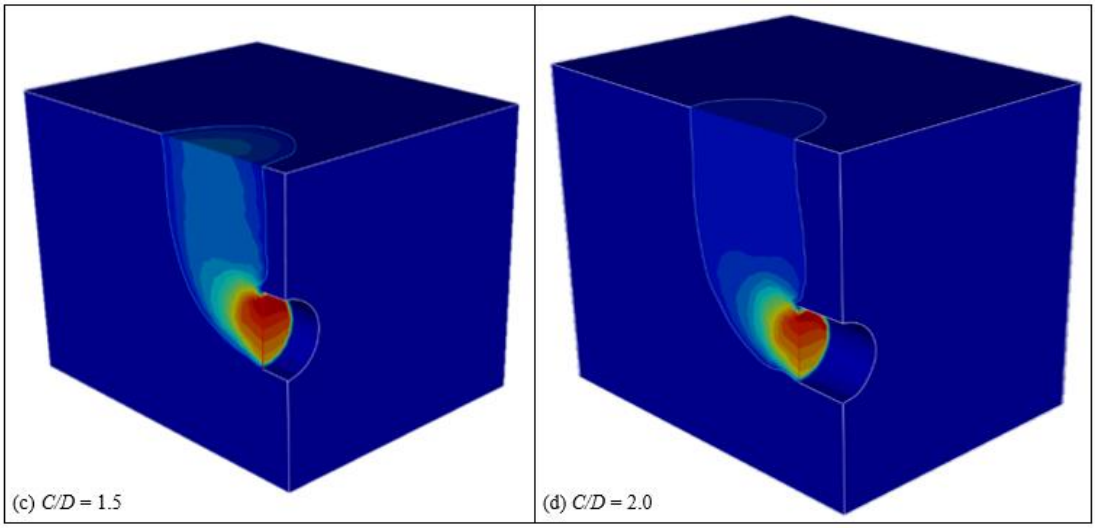

Note that the actual contour values of the plots are not important in limit analysis with the perfect plasticity theorem.

Figure 6.11. Absolute displacement (|u|) contour plots for *C/D* = 1.5 and *C/D* = 2.0.

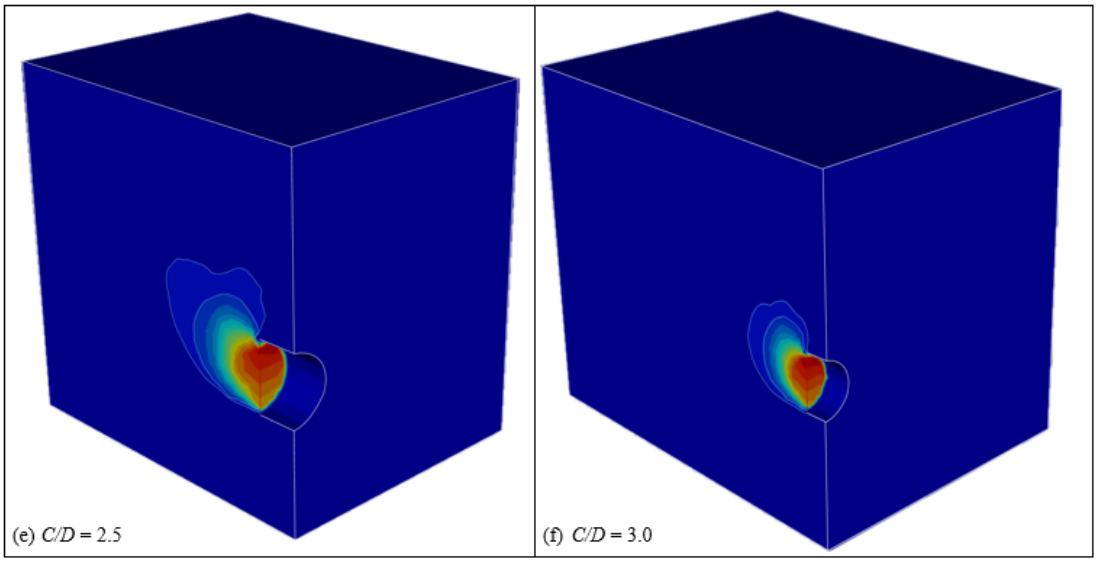

Note that the actual contour values of the plots are not important in limit analysis with the perfect plasticity theorem.

Figure 6.12. Absolute displacement (|u|) contour plots for *C/D* = 2.5 and *C/D* = 3.0.

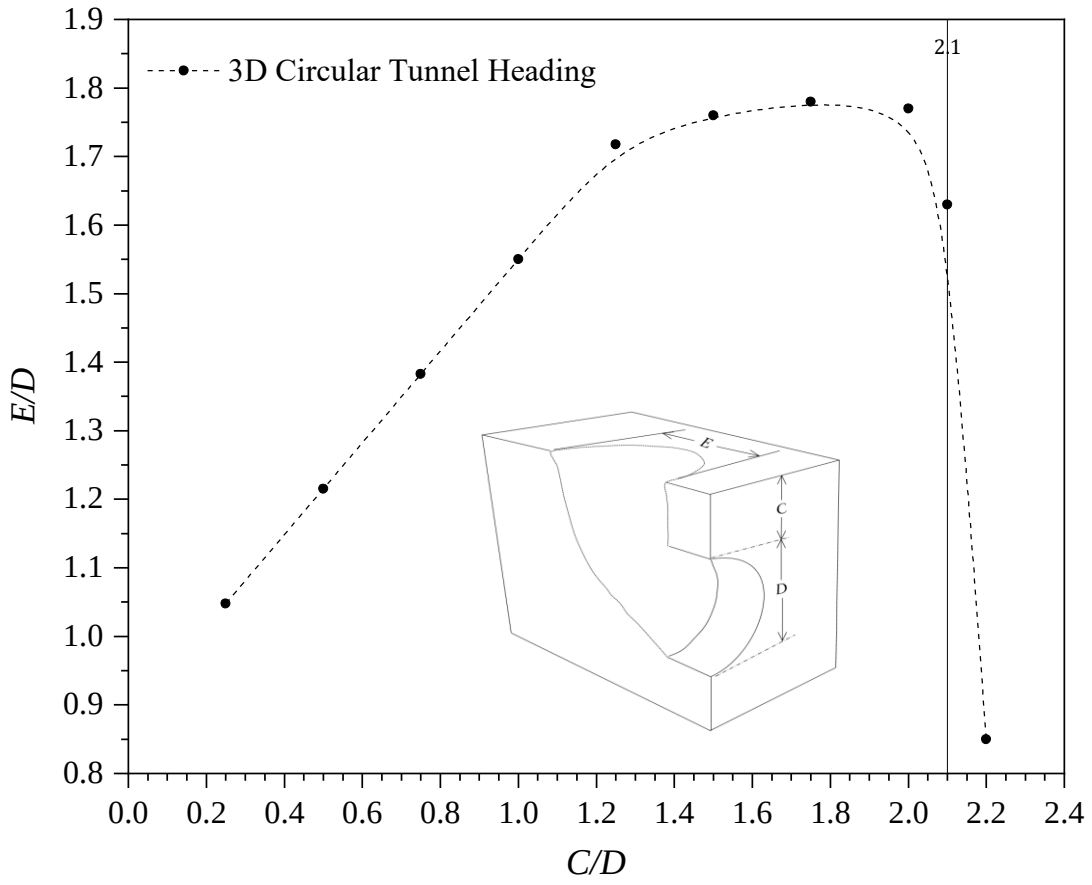

Figure 6.13. Surface failure ratio (*E/D*) vs (*C/D*).

It is interesting to see a transformation of 3D failure mechanisms from a general surface failure to a local failure as the depth ratio (*C/D*) increases in these plots.

Based on the visual inspection of the plots in Figures 6.10-6.12, Figure 6.13 shows the relationship between the surface failure extent ratio *E/D* and the corresponding depth ratio *C/D*. The data used in this figure is presented in Table 6.10. It is observed that the failure did not propagate through to the ground surface once the depth ratio is greater than 2.2. This finding is useful for the analytical upper bound, which requires a priori assumption in relation to the general form of the failure mechanism.

Table 6.10. Surface failure ratios (*E/D*) vs (*C/D*).

Depth Ratio (C/D^*)	The ratio of failure extent to tunnel diameter (E/D^*)
0.25	1.05
0.5	1.22
0.75	1.38
1	1.55
1.25	1.72
1.5	1.76
1.75	1.78
2	1.77
2.1	1.63
2.2	0.85

∗Tunnel Diameter D = 1m

6.5 Examples and Practical Uses

The key to the estimation of tunnel stability is through the use of a critical stability number N_c. The value of N_c depends on the depth ratio (*C/D*) of the problem and is irrelevant to the undrained shear strength of the soil. The usefulness of N_c is best described by some examples using the design contour chart of *LB* in Figure 6.4, which can be used to relate stability number (*N*), depth ratio (*C/D*), and factor of safety (*FoS*). Together with Equations 6.2 to 6.6, the design chart can also be used to estimate a safe working pressure to maintain the stability of the tunnel face.

6.5.1 To determine *FoS*

Given C = 20m, D = 4m, σ_t = 300 kPa, σ_s = 30 kPa, S_u = 28 kPa and γ = 18 kN/m^3, determine whether the soil movement would be in the collapse or blowout direction? What is the *FoS* for the problem?

1. $H = (C + D/2) = 22\,\text{m},\ N = (\sigma_s + \gamma H - \sigma_t)/S_u = 4.5$
2. Since $N > 0$, the resulting soil movement is in the collapse direction.
3. For collapse analysis, Equation 6.5 is used, giving *FoS* (*LB*) of 2.81.
4. For *C/D* = 5 and N = 4.5, Figure 6.4 gives an approximate *FoS* (*LB*) of 2.80.
5. Table 6.2 can also be used to determine *FoS* (*LB*) $\simeq$ 2.83 directly.

6.5.2 Analysis of a temporary unsupported tunnel heading

A decision needs to be made as to whether the tunnel would be stable for a short period of time due to machine maintenance (no internal support pressure is available). Design parameters are given as: S_u = 54 kPa, γ = 19 kN/m^3, σ_s = 65 kPa, D = 5m, C = 20m, $H = (C + D/2) = 22.5\,\text{m}$.

1. Since there is no internal heading pressure, $N = (\sigma_s + \gamma H - \sigma_t)/S_u = 9.12$
2. Given *C/D* = 4, Table 6.1 gives N_c (*LB*) of 11.85. Therefore, *FoS* (*LB*) = N_c (*LB*)/ N = 11.85/9.12 = 1.30
3. For collapse analysis, Equation 6.5 can be used, giving *FoS* (*LB*) of 1.306.
4. Using Figure 6.4, for *C/D* = 4 and N = 9.12, an approximate *FoS* (*LB*) of 1.30 is obtained. It is interesting to note that, for the same problem, the 2D analysis gives *FoS* (*LB*) of 0.71.

6.5.3 To determine face support

A TBM is used to excavate a tunnel below a central business district. It is necessary to estimate the safe operating range of the limiting face pressured (σ_t) in blowout and collapse. The given parameters are; σ_s = 216 kPa, S_u = 72 kPa, γ = 18 kN/m^3, C = 36m and D = 6m.

1. Equations 6.5 and 6.6 can be rearranged to determine the range of internal pressure (σ_t) for a specific factor of safety in collapse and blowout, respectively.
2. Given *C/D* = 6, Table 6.1 gives N_c (*LB*) = 13.272 for collapse and N_c (*LB*) = 13.273 for blowout.

3. Using Equation 6.5 and the critical collapse (FoS = 1), σ_t (*LB, Collapse*) = -37.58 kPa. The negative sign for the critical support pressure means that the tunnel is already stable (FoS > 1). Theoretically speaking, to reach a collapsed state a pulling pressure of 37.58 kPa is required (or increasing the surface pressure σ_s by 37.58 kPa).
4. Using Equation 7.6 and the critical blowout (FoS = 1), σ_t (*LB, Blowout*) = 1873.66 kPa.
5. Therefore, the safe operating range of the face support pressures is: -37.58 kPa (collapse limit) ≤ σ_t ≤ 1873.66 kPa (blowout limit).

What is the operating range for a factor of safety equal to 2.5?

6. Using Equation 6.5 with FoS = 2.5, σ_t = 535.76 kPa for collapse side.
7. Using Equation 6.6 with FoS = 2.5, σ_t = 1300.26 kPa for blowout side. Therefore, the safe operating range (FoS = 2.5): 535.76 kPa (collapse limit) ≤ σ_t ≤ 1300.26 kPa (blowout limit).

6.6 Conclusions

Three-dimensional circular tunnel face stability in cohesive soil was analysed using finite element formulation of the limit theorems. The upper and lower bound results of the critical stability number N_c of the circular tunnel were presented and consideration given to the effect of the unlined length ratio of the tunnel heading (P/D) on the stability of the tunnel.

A comparison of the 3D *FELA* solutions with those published from experimental and kinematic analysis approaches showed a good agreement among the results. In general, the 3D results are approximately 70% - 80% greater than the 2D ones. It is suggested that a 3D transformation from general failure to local failure occurs as the depth ratio increases. The finding is useful for the analytical upper bound, which requires a priori assumption in relation to the general form of the failure surface.

After the stability studies of 2D and 3D single tunnels in Chapters 4, 5 and 6, the stability of 2D and 3D twin tunnels are investigated in the next two chapters (i.e. Chapters 7 and 8) using Broms and Bennermarks' original stability number approach.

CHAPTER 7: UNDRAINED ANALYSIS OF 2D TWIN CIRCULAR TUNNELS

7.1 Introduction

The development of contemporary society and the increase of population introduce the need for more new tunnels, which often have to be constructed in congested urban areas underground. These tunnels are often constructed in parallel. The construction of twin tunnels does present some challenges for geotechnical engineers.

The 2D undrained clay twin circular tunnel models are used to determine many stability problems aligned with the construction of tunnels. This chapter will address the twin stability problem using finite element limit analysis, by rigorously commuting the upper and lower (*FoS*) bounds, and subsequently developing a factor of safety approach in developing design stability charts. Furthermore, a correlation between the individual and twin stability failure will be established. Correctly analysing the stability of underground infrastructures, such as twin circular tunnels, is crucial to prevent the collapse of such a complex assembly.

7.2 Problem Definition and Modelling Technique

Figure 7.1 shows the problem definition of an idealized 2D twin circular tunnels.

Broms and Bennermark's original stability number (N) is defined as:

$$N = \frac{\sigma_s + \gamma H - \sigma_t}{S_u} \tag{7.1}$$

Where H is the depth of the tunnel axis that is equal to $(C + D/2)$, C is the tunnel cover, D is the tunnel height, and S is the tunnel centre-to-centre distance. S_u and γ represent the undrained soil cohesion and the unit weight of the soil, respectively.

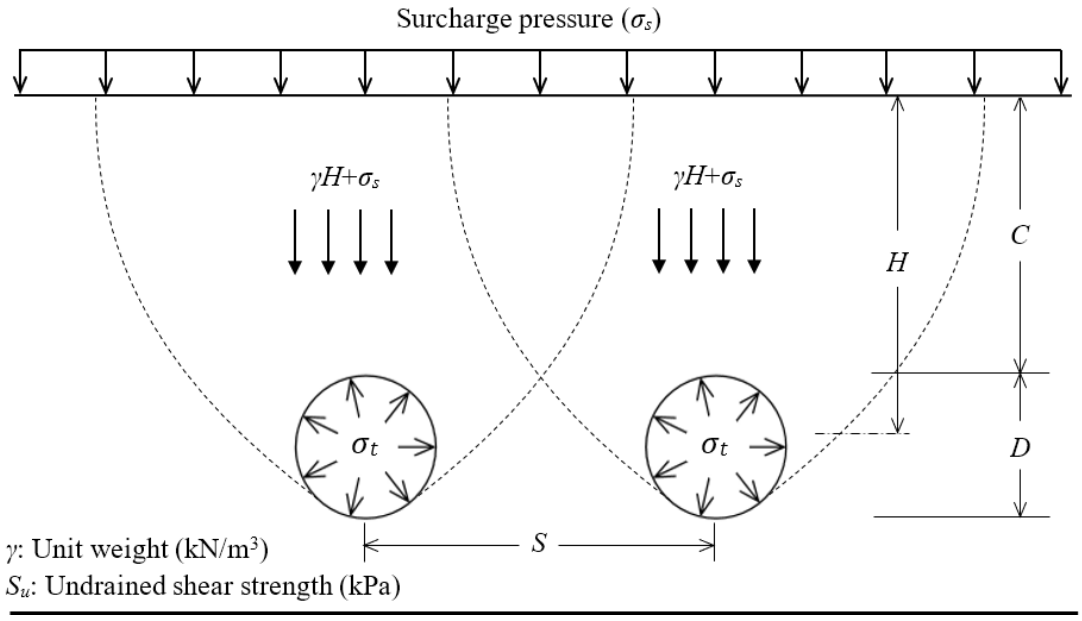

Figure 7.1. Problem Definition.

The tunnel is subjected to a normal internal pressure σ_t, while the ground surface is subjected to a vertical surcharge σ_s. These pressures, together with soil self-weight (γH) are varied to test the collapse and blowout stability of the models for various values of spacing ratio (S/D) and depth ratios (C/D).

Numerical results based on the shear strength reduction method (*SSRM*) are represented by a factor of safety (*FoS*) that is a function of the depth ratio (C/D), the spacing ratio (S/D) and the "designed" stability number (N), as shown in Equation 7.2.

$$FoS = f\left(\frac{C}{D}, \frac{S}{D}, N = \frac{\sigma_s + \gamma H - \sigma_t}{S_u}\right) \tag{7.2}$$

In practice, a "designed" stability number N (i.e. a combination of the parameters σ_s, σ_t, γ, H and S_u) can be either positive, zero or negative. It is not known whether the "designed" stability number corresponds to a tunnel failure or not. Therefore, it is necessary to compare the "designed" N value with the critical stability number N_c and calculate the corresponding factor of safety. To cover all possible scenarios of failure, the present study investigates the stability of twin tunnels by relating *FoS* to a broad range of stability numbers (N = -15 to 15), depth ratios (C/D = 2 to 10) and spacing ratios (S/D = 2 to 30).

The rigorous upper bound and lower bound factors of safety for the cases being studied are based on the limit theorems of classical plasticity (Krabbenhoft and Lyamin (2015). A full detailed description of the theory and development of this method can

be found in Sloan (2013). Details of the numerical *FELA* formulation can be found in Lyamin and Sloan (2002a, 2002b).

The *FELA* adaptive meshes used in this study are shown for *S/D* = 4, 7, and 10, respectively, in Figures 7.2 to 7.4. The boundary conditions are as follows: the ground surface is free to displace, the sides have roller boundaries, and the base is fixed. The boundary conditions are as follows: the ground surface is free to displace, the sides have roller boundaries, and the base is fixed.

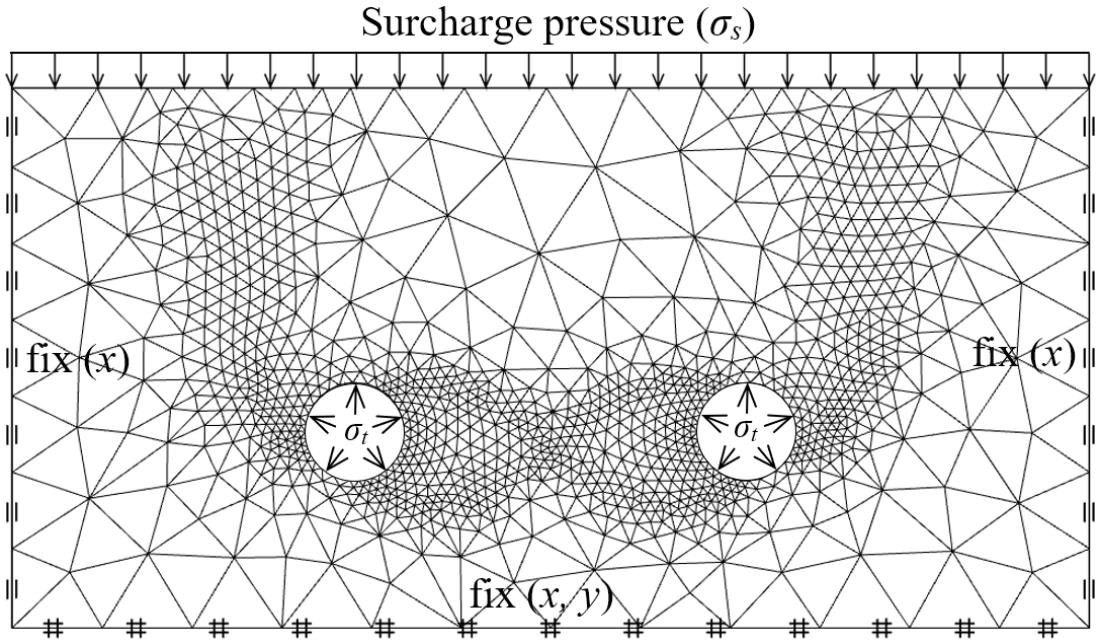

Figure 7.2. Typical adaptive mesh used for the problem (for *C/D* = 3 and *S/D* = 4).

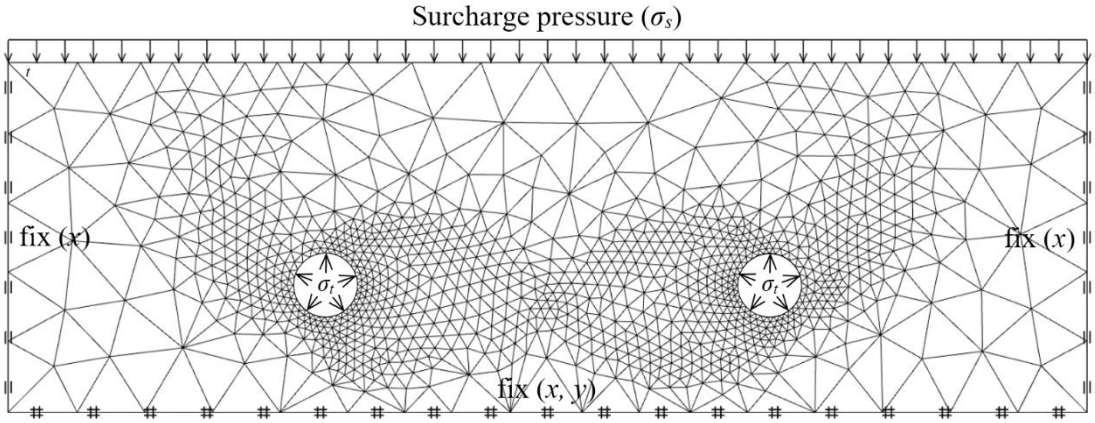

Figure 7.3. Typical adaptive mesh used for the problem (for *C/D* = 3 and *S/D* = 7).

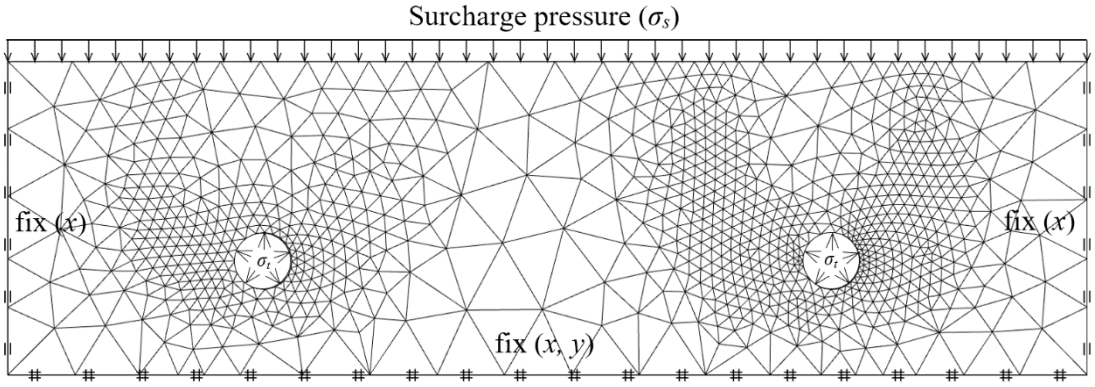

Figure 7.4. Typical adaptive mesh used for the problem (for *C/D* = 3 and *S/D* = 10).

An automatically adaptive mesh refinement was employed in both the *UB* and *LB* simulations to enable accurate limit loads to be obtained through the use of the bounds gap error estimator. Three iterations of adaptive meshing with the number of elements increasing from 1000 to 2000 were used for all analyses. The large size of the model is essential as it ensures that the entire soil mass is modelled accurately, and the failure mechanism does not intersect the boundaries of the model.

It is imprudent to rely on one single numerical model or method. Result verification is normally required. For this purpose, the finite difference (*FDM*) method, via the software *FLAC* with a built-in implementation of the strength reduction technique, was used over the same parametric range. *FISH* programming language was also developed to generate the mesh in the *FLAC* environment and solve the problems automatically (Shiau & Sams 2019).

7.3 Results and Discussion

Figures 7.5-7.7 show the full range of the results (*LB*, *UB*, and *FD*) relating to the collapse and blowout of twin tunnel models for a depth ratio of three (*C*/*D* = 3) and various spacing ratios (*S*/*D* = 4, 7 and 10). It can be seen that the curves are hyperbolic, and a pair of asymptote lines exist. The general equation for this graph was found to be $N_c = N \times FoS$. Any combination of *N* and *FoS* on this curve yields a unique N_c value, which is constant for a specific depth ratio. This N_c value is Brooms and Bennermarks' original critical stability number. For the depth ratio *C/D* = 3 and spacing ratios *S*/*D* = 4, 7 and 10, *LB* solutions give N_c = 3.27, 3.87 and 4.04 on the collapse side and N_c = -3.24, -3.85 and -4.01 on the blowout side.

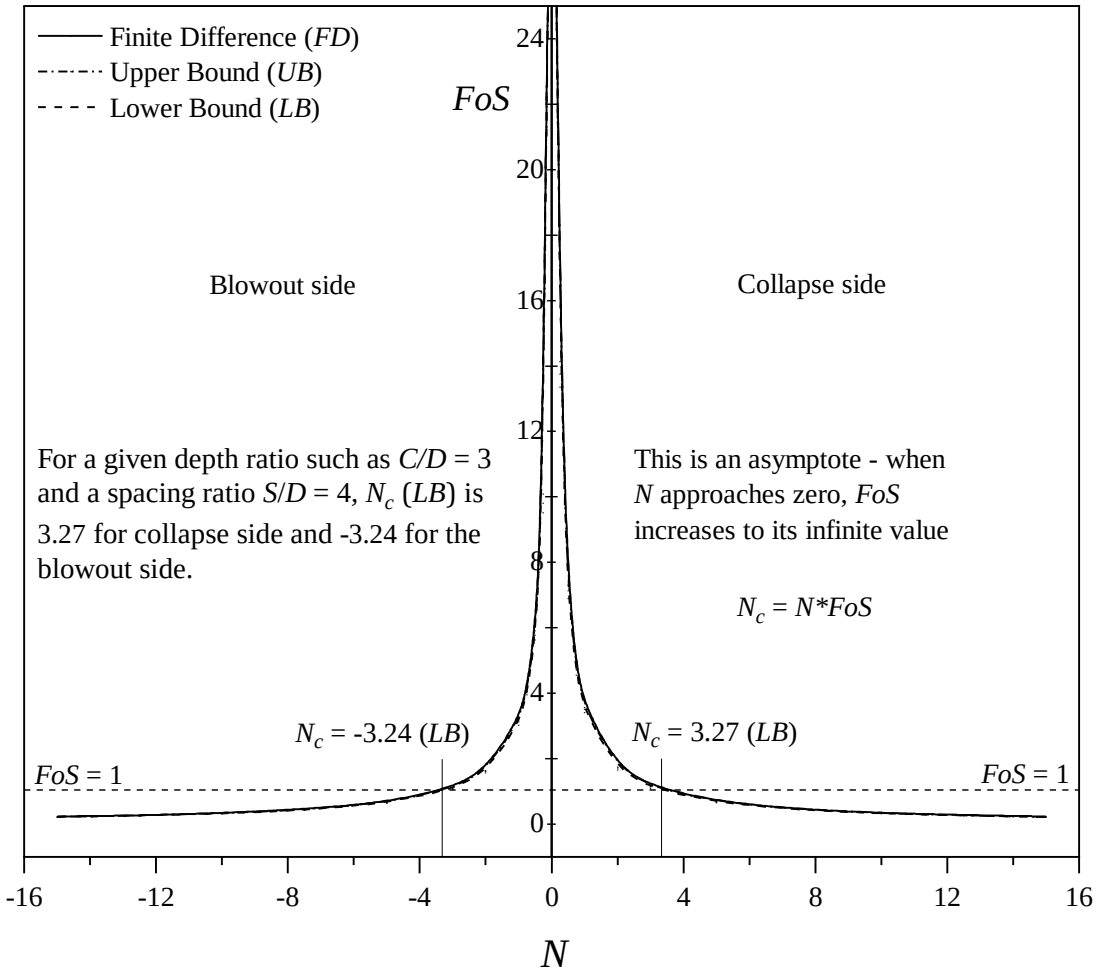

Figure 7.5. *FoS* vs. *N* for *C/D* = 3 and *S/D* = 4.

Graphically, these values can be read from the intersection points by drawing *FoS* = 1 horizontal lines. The data used to prepare these figures are shown in Tables 7.1-7.3.

Brooms and Bennermarks' stability number (*N*) consists of two parts: overburden pressure ratio $(OPR = (\sigma_s + \gamma H)/S_u)$ and supporting pressure ratio $(SPR = \sigma_t / S_u)$ The combination of these ratios would result in three situations: namely collapse (*OPR* > *SPR*), weightless (*OPR* = *SPR*), and blowout (*OPR* < *SPR*). Broms and Bennermarks' N_c Equation 7.1 can be re-arranged into a form that is more amenable to analysis, as shown in Equation 7.3.

$$\sigma_t = \sigma_s + \gamma H - N_c \times S_u \tag{7.3}$$

Using Equation 7.3, the critical supporting pressure σ_t can be determined as long as the critical stability number N_c (where *FoS* = 1) is known.

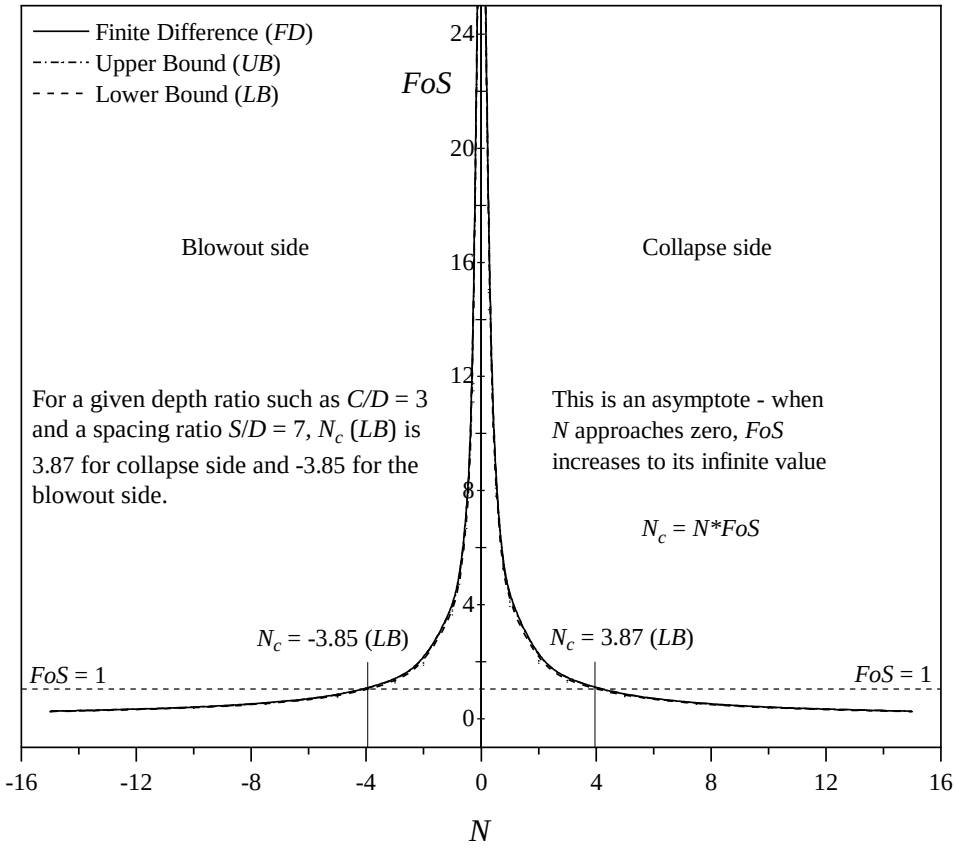

Figure 7.6. *FoS* vs. *N* for *C/D* = 3 and *S/D* = 7.

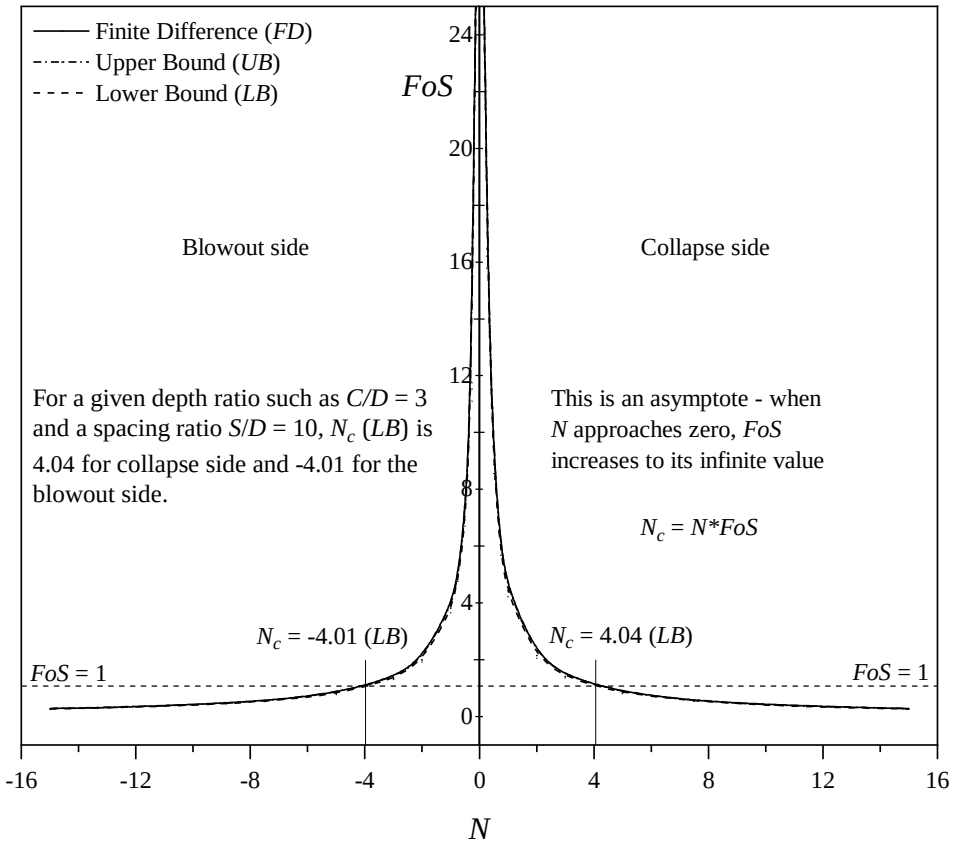

Figure 7.7. *FoS* vs. *N* for *C/D* = 3 and *S/D* = 10.

Table 7.1. *LB FoS* results vs *N* and *C/D* (Collapse and Blowout, *C/D* = 3).

	S/D									
N	1	2	3	4	5	6	7	8	9	10
-15	0.200	0.220	0.240	0.270	0.270	0.270	0.270	0.270	0.270	0.270
-12.5	0.240	0.260	0.290	0.320	0.320	0.320	0.320	0.320	0.320	0.320
-10	0.300	0.320	0.360	0.400	0.400	0.400	0.400	0.400	0.400	0.400
-7.5	0.400	0.430	0.490	0.530	0.530	0.530	0.530	0.530	0.530	0.530
-5	0.600	0.640	0.730	0.790	0.790	0.780	0.790	0.790	0.790	0.790
-4	0.711	0.811	0.913	0.996	0.995	0.994	0.994	0.992	0.995	0.994
-3	0.990	1.060	1.200	1.300	1.310	1.300	1.300	1.300	1.300	1.300
-2.5	1.138	1.297	1.462	1.593	1.592	1.591	1.591	1.587	1.593	1.591
-2	1.460	1.570	1.780	1.930	1.930	1.940	1.920	1.930	1.930	1.920
-1.5	1.897	2.162	2.436	2.655	2.653	2.652	2.652	2.645	2.654	2.652
-1	2.810	3.040	3.470	3.680	3.670	3.680	3.690	3.680	3.680	3.680
-0.75	3.650	3.950	4.510	4.750	4.770	4.760	4.760	4.760	4.760	4.770
-0.5	5.170	5.630	6.420	6.710	6.720	6.700	6.700	6.700	6.700	6.700
-0.25	8.740	9.520	10.890	11.120	11.120	11.130	11.140	11.170	11.140	11.180
0	Infinity	Infinity	Infinity	Infinity	Infinity	Infinity	Infinity	Infinity	Infinity	Infinity
0.25	13.260	13.360	13.870	14.930	15.790	15.800	15.800	15.810	15.800	15.830
0.5	6.680	6.900	7.480	8.120	8.560	8.520	8.550	8.560	8.530	8.500
0.75	4.360	4.570	5.030	5.490	5.670	5.690	8.550	5.690	5.680	5.690
1	3.240	3.410	3.780	4.120	4.230	4.230	4.220	4.230	4.220	4.230
1.5	1.918	2.182	2.448	2.687	2.690	2.685	2.686	2.688	2.694	2.692
2	1.620	1.670	1.860	2.030	2.070	2.070	2.070	2.070	2.070	2.060
2.5	1.151	1.309	1.469	1.612	1.614	1.611	1.612	1.613	1.617	1.615
3	1.030	1.110	1.240	1.360	1.370	1.360	1.360	1.370	1.370	1.370
4	0.719	0.818	0.918	1.008	1.009	1.007	1.007	1.008	1.010	1.009
5	0.620	0.660	0.740	0.810	0.810	0.810	0.810	0.810	0.810	0.810
7.5	0.410	0.440	0.490	0.540	0.540	0.540	0.540	0.540	0.540	0.540
10	0.310	0.330	0.370	0.400	0.400	0.410	0.400	0.400	0.400	0.400
12.5	0.240	0.260	0.290	0.320	0.320	0.320	0.320	0.320	0.320	0.320
15	0.200	0.220	0.240	0.270	0.270	0.270	0.270	0.270	0.270	0.270

Table 7.2. *UB FoS* results vs *N* and *C/D* (Collapse and Blowout, *C/D* = 3).

	S/D									
N	1	2	3	4	5	6	7	8	9	10
-15	0.200	0.220	0.250	0.280	0.280	0.280	0.280	0.280	0.280	0.280
-12.5	0.230	0.270	0.300	0.330	0.330	0.330	0.330	0.330	0.330	0.330
-10	0.290	0.330	0.380	0.410	0.410	0.410	0.410	0.410	0.410	0.410
-7.5	0.390	0.440	0.500	0.550	0.550	0.550	0.550	0.550	0.550	0.550
-5	0.580	0.660	0.750	0.820	0.820	0.820	0.820	0.820	0.820	0.820
-4	0.730	0.835	0.945	1.032	1.034	1.032	1.032	1.032	1.034	1.032
-3	0.950	1.100	1.250	1.350	1.350	1.350	1.350	1.350	1.350	1.350
-2.5	1.168	1.335	1.513	1.651	1.654	1.651	1.651	1.651	1.654	1.651
-2	1.410	1.620	1.850	1.990	1.990	2.000	2.000	2.000	2.000	1.990
-1.5	1.947	2.225	2.521	2.752	2.756	2.752	2.752	2.752	2.756	2.752
-1	2.690	3.140	3.590	3.810	3.810	3.810	3.810	3.810	3.810	3.810
-0.75	3.470	4.070	4.660	4.920	4.930	4.930	4.930	4.930	4.920	4.930
-0.5	4.900	5.780	6.640	6.930	6.930	6.930	6.930	6.930	6.930	6.930
-0.25	8.250	9.810	11.310	11.510	11.540	11.510	11.530	11.540	11.540	11.540
0	Infinity	Infinity	Infinity	Infinity	Infinity	Infinity	Infinity	Infinity	Infinity	Infinity
0.25	14.120	13.760	14.460	15.500	16.470	16.440	16.440	16.460	16.440	16.460
0.5	6.860	7.140	7.780	8.450	8.890	8.860	8.860	8.870	8.870	8.860
0.75	4.400	4.730	5.220	5.700	5.910	5.920	5.920	5.920	5.920	5.920
1	3.220	3.510	3.900	4.280	4.400	4.400	4.400	4.400	4.400	4.400
1.5	1.985	2.252	2.543	2.795	2.795	2.794	2.794	2.794	2.795	2.794
2	1.540	1.720	1.930	2.120	2.150	2.150	2.150	2.160	2.150	2.150
2.5	1.191	1.351	1.526	1.677	1.677	1.676	1.676	1.676	1.677	1.676
3	1.010	1.140	1.280	1.410	1.420	1.420	1.420	1.420	1.420	1.420
4	0.744	0.845	0.954	1.048	1.048	1.048	1.048	1.048	1.048	1.048
5	0.600	0.680	0.770	0.850	0.840	0.850	0.850	0.850	0.850	0.850
7.5	0.400	0.450	0.510	0.560	0.560	0.560	0.560	0.560	0.560	0.560
10	0.300	0.340	0.380	0.420	0.420	0.420	0.420	0.420	0.420	0.420
12.5	0.240	0.270	0.310	0.340	0.340	0.340	0.340	0.340	0.340	0.340
15	0.200	0.230	0.250	0.280	0.280	0.280	0.280	0.280	0.280	0.280

Table 7.3. *FD FoS* results vs *N* and *C/D* (Collapse and Blowout, *C/D* = 3).

	S/D									
N	1	2	3	4	5	6	7	8	9	10
-15	0.200	0.230	0.260	0.280	0.280	0.280	0.280	0.280	0.280	0.280
-12.5	0.240	0.270	0.310	0.330	0.330	0.330	0.330	0.330	0.330	0.330
-10	0.300	0.340	0.380	0.420	0.420	0.420	0.420	0.420	0.420	0.420
-7.5	0.400	0.450	0.510	0.550	0.550	0.550	0.550	0.550	0.550	0.550
-5	0.600	0.670	0.760	0.830	0.830	0.830	0.830	0.830	0.830	0.830
-4	0.750	0.850	0.963	1.041	1.041	1.041	1.041	1.041	1.041	1.041
-3	0.980	1.120	1.260	1.370	1.370	1.370	1.370	1.370	1.370	1.370
-2.5	1.200	1.360	1.540	1.665	1.665	1.665	1.665	1.665	1.665	1.665
-2	1.450	1.650	1.880	2.020	2.020	2.020	2.020	2.020	2.020	2.020
-1.5	2.000	2.267	2.567	2.775	2.775	2.775	2.775	2.775	2.775	2.775
-1	2.770	3.200	3.640	3.870	3.870	3.870	3.870	3.870	3.870	3.870
-0.75	3.580	4.160	4.730	5.000	5.000	5.000	5.000	5.000	5.000	5.000
-0.5	5.060	5.920	6.740	7.050	7.050	7.050	7.050	7.050	7.050	7.050
-0.25	8.520	10.090	11.490	11.760	11.760	11.760	11.760	11.760	11.760	11.760
0	Infinity	Infinity	Infinity	Infinity	Infinity	Infinity	Infinity	Infinity	Infinity	Infinity
0.25	14.53	14.14	14.68	15.45	16.21	16.71	16.71	16.70	16.70	16.71
0.5	7.060	7.320	7.890	8.460	8.960	8.970	8.980	8.980	8.980	8.980
0.75	4.520	4.830	5.290	5.690	5.980	5.980	5.980	5.980	5.990	5.980
1	3.300	3.580	3.960	4.280	4.450	4.450	4.450	4.450	4.450	4.450
1.5	2.029	2.300	2.567	2.808	2.808	2.808	2.808	2.808	2.808	2.808
2	1.580	1.750	1.960	2.140	2.170	2.170	2.170	2.170	2.170	2.170
2.5	1.218	1.380	1.540	1.685	1.685	1.685	1.685	1.685	1.685	1.685
3	1.040	1.160	1.300	1.420	1.430	1.430	1.430	1.430	1.430	1.430
4	0.761	0.863	0.963	1.053	1.053	1.053	1.053	1.053	1.053	1.053
5	0.620	0.690	0.780	0.850	0.850	0.850	0.850	0.850	0.850	0.850
7.5	0.410	0.460	0.510	0.560	0.560	0.560	0.560	0.560	0.560	0.560
10	0.310	0.340	0.380	0.420	0.420	0.420	0.420	0.420	0.420	0.420
12.5	0.240	0.280	0.310	0.340	0.340	0.340	0.340	0.340	0.340	0.340
15	0.200	0.230	0.260	0.280	0.280	0.280	0.280	0.280	0.280	0.280

Figures 7.8 and 7.9 show *LB* and *UB* results of N_c versus *S/D* for a range of depth ratios (*C/D* = 2 - 10), respectively. The data used to prepare these figures are shown in Tables 7.4-7.5. Note that the critical stability number (N_c) increases nonlinearly as *S/D* increases. The gradient of the curves decreases as values of *S/D* increase and approach to zero when there is no interaction between the tunnels (each tunnel behaves as a single isolated tunnel).

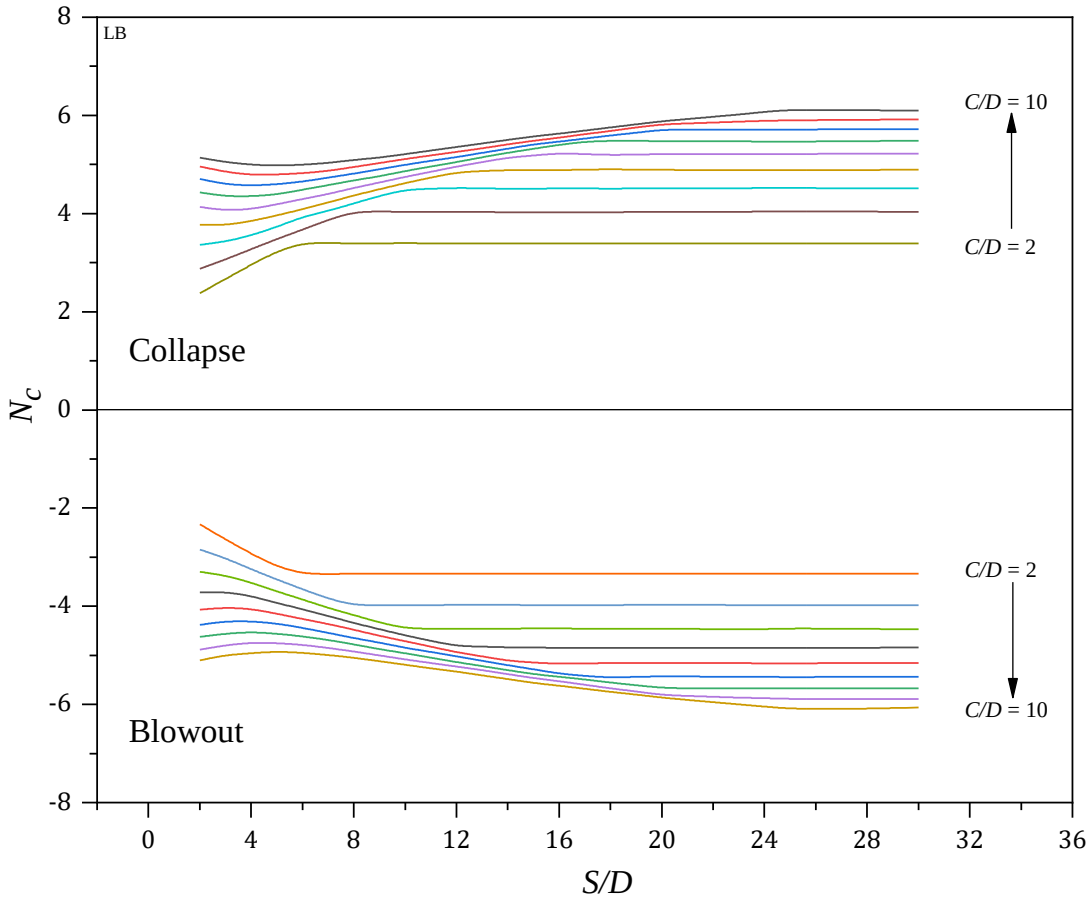

Figure 7.8. N_c results (*LB*) vs. *S/D* for *C/D* = 2 - 10 in collapse and blowout.

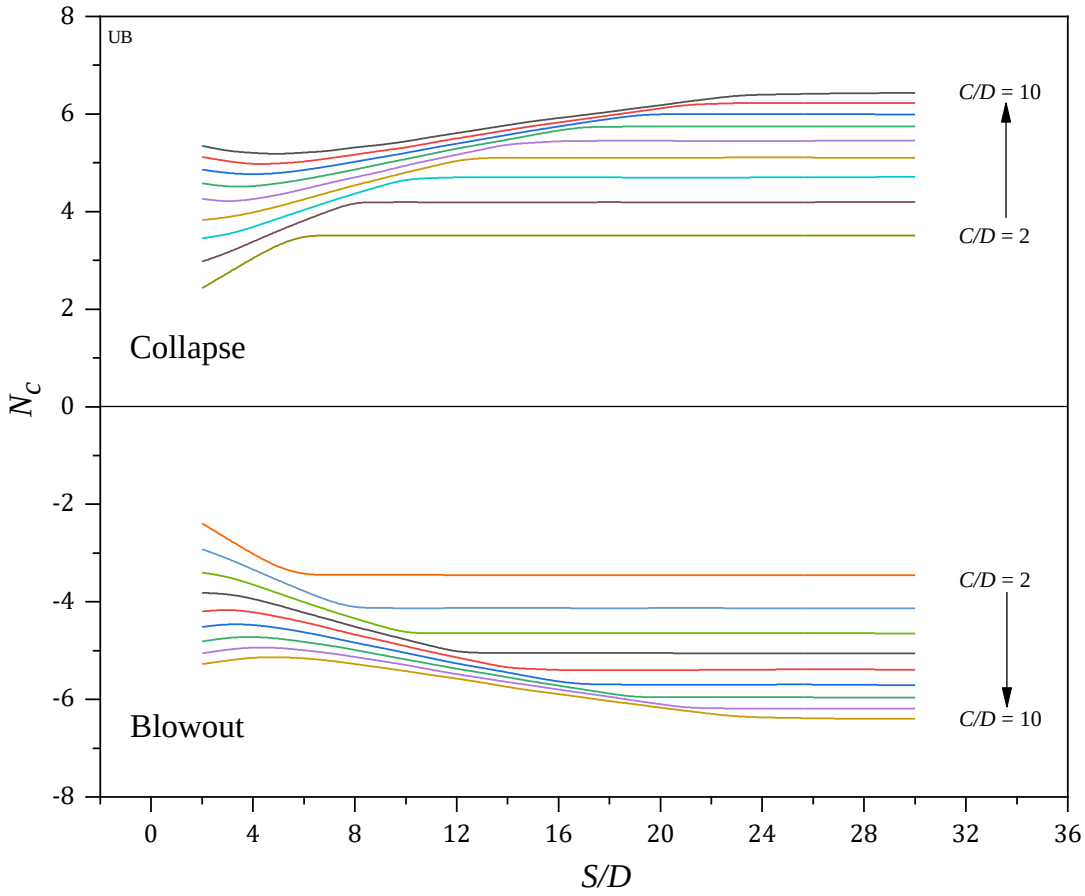

Figure 7.9. N_c results (*UB*) vs. *S/D* for *C/D* = 2 - 10 in collapse and blowout.

Table 7.4. N_c results for various *C/D* and *S/D* (*LB*, Collapse, and Blowout).

S/D	N_c, *LB* (Collapse)					N_c, *LB* (Blowout)				
	C/D					*C/D*				
	2	3	4	5	6	2	3	4	5	6
2	2.381	2.877	3.361	3.769	4.133	-2.336	-2.846	-3.305	-3.714	-4.069
3	2.67	3.061	3.424	3.759	4.059	-2.641	-3.016	-3.37	-3.712	-4.025
4	2.954	3.273	3.558	3.841	4.088	-2.928	-3.243	-3.516	-3.794	-4.054
5	3.228	3.481	3.724	3.961	4.189	-3.195	-3.454	-3.701	-3.934	-4.149
6	3.396	3.671	3.931	4.089	4.293	-3.338	-3.654	-3.86	-4.059	-4.259
7	3.401	3.87	4.055	4.226	4.394	-3.342	-3.847	-4.03	-4.198	-4.357
8	3.393	4.03	4.206	4.367	4.527	-3.341	-3.983	-4.181	-4.338	-4.482
9	3.387	4.039	4.359	4.499	4.628	-3.338	-3.983	-4.333	-4.47	-4.606
10	3.399	4.036	4.489	4.618	4.746	-3.338	-3.98	-4.451	-4.599	-4.714
11	3.394	4.037	4.504	4.729	4.853	-3.338	-3.976	-4.455	-4.706	-4.825
12	3.389	4.037	4.519	4.839	4.959	-3.337	-3.972	-4.46	-4.813	-4.936
13	3.39	4.033	4.510	4.863	5.048	-3.335	-3.973	-4.458	-4.826	-5.025
14	3.391	4.029	4.501	4.886	5.136	-3.333	-3.973	-4.456	-4.839	-5.114
15	3.389	4.028	4.508	4.887	5.182	-3.335	-3.976	-4.454	-4.844	-5.145
16	3.388	4.027	4.516	4.888	5.228	-3.338	-3.978	-4.452	-4.849	-5.177
17	3.39	4.028	4.511	4.895	5.213	-3.338	-3.978	-4.456	-4.848	-5.169
18	3.393	4.029	4.507	4.903	5.198	-3.339	-3.978	-4.46	-4.848	-5.161
19	3.393	4.03	4.509	4.897	5.206	-3.339	-3.973	-4.46	-4.849	-5.159
20	3.393	4.031	4.512	4.891	5.214	-3.339	-3.967	-4.459	-4.85	-5.157
21	3.393	4.033	4.514	4.889	5.214	-3.339	-3.97	-4.462	-4.85	-5.158
22	3.393	4.035	4.516	4.887	5.214	-3.339	-3.973	-4.465	-4.851	-5.159
23	3.393	4.037	4.518	4.885	5.214	-3.339	-3.976	-4.468	-4.851	-5.161
24	3.393	4.039	4.52	4.883	5.213	-3.339	-3.978	-4.471	-4.851	-5.162
25	3.393	4.041	4.519	4.881	5.213	-3.339	-3.981	-4.452	-4.851	-5.163
27	3.393	4.04	4.515	4.886	5.217	-3.339	-3.98	-4.46	-4.846	-5.161
30	3.393	4.038	4.512	4.893	5.22	-3.339	-3.978	-4.468	-4.837	-5.158

Table 7.4. Cont'd.

S/D	N_c, *LB* (Collapse)				N_c, *LB* (Blowout)			
	C/D				*C/D*			
	7	8	9	10	7	8	9	10
2	4.429	4.704	4.954	5.143	-4.378	-4.623	-4.889	-5.099
3	4.348	4.599	4.852	5.049	-4.301	-4.561	-4.794	-4.995
4	4.349	4.571	4.787	4.993	-4.31	-4.527	-4.738	-4.955
5	4.389	4.599	4.794	4.974	-4.351	-4.555	-4.745	-4.921
6	4.485	4.647	4.824	4.991	-4.443	-4.61	-4.789	-4.953
7	4.576	4.728	4.867	5.029	-4.539	-4.689	-4.848	-4.992
8	4.679	4.81	4.947	5.097	-4.646	-4.773	-4.919	-5.051
9	4.762	4.904	5.029	5.139	-4.744	-4.874	-5.001	-5.121
10	4.864	4.993	5.115	5.213	-4.846	-4.958	-5.089	-5.196
11	4.956	5.072	5.186	5.286	-4.934	-5.049	-5.158	-5.262
12	5.048	5.15	5.257	5.359	-5.023	-5.14	-5.228	-5.328
13	5.144	5.236	5.332	5.429	-5.113	-5.221	-5.306	-5.406
14	5.241	5.323	5.406	5.499	-5.204	-5.302	-5.383	-5.484
15	5.321	5.409	5.481	5.569	-5.288	-5.383	-5.461	-5.561
16	5.401	5.469	5.549	5.632	-5.371	-5.439	-5.53	-5.622
17	5.466	5.529	5.617	5.694	-5.418	-5.496	-5.599	-5.682
18	5.483	5.588	5.685	5.757	-5.453	-5.553	-5.668	-5.743
19	5.48	5.648	5.753	5.819	-5.439	-5.61	-5.738	-5.803
20	5.477	5.708	5.821	5.882	-5.426	-5.667	-5.807	-5.864
21	5.475	5.709	5.837	5.928	-5.43	-5.669	-5.824	-5.908
22	5.473	5.71	5.853	5.974	-5.434	-5.67	-5.842	-5.953
23	5.471	5.711	5.87	6.021	-5.438	-5.672	-5.859	-5.997
24	5.468	5.712	5.886	6.067	-5.442	-5.673	-5.876	-6.041
25	5.466	5.713	5.902	6.113	-5.446	-5.675	-5.894	-6.086
27	5.472	5.716	5.909	6.107	-5.44	-5.673	-5.894	-6.096
30	5.481	5.719	5.921	6.099	-5.438	-5.669	-5.894	-6.061

Table 7.5. N_c results for various *C/D* and *S/D* (*UB*, Collapse, and Blowout).

S/D	N_c, *UB* (Collapse)					N_c, *UB* (Blowout)				
	C/D					*C/D*				
	2	3	4	5	6	2	3	4	5	6
2	2.433	2.978	3.456	3.828	4.259	-2.392	-2.920	-3.397	-3.820	-4.198
3	2.740	3.152	3.528	3.879	4.200	-2.709	-3.110	-3.484	-3.831	-4.151
4	3.051	3.378	3.683	3.978	4.251	-3.017	-3.338	-3.641	-3.931	-4.203
5	3.331	3.604	3.859	4.103	4.341	-3.304	-3.568	-3.826	-4.070	-4.307
6	3.508	3.814	4.038	4.249	4.462	-3.449	-3.782	-4.004	-4.221	-4.416
7	3.511	4.014	4.210	4.394	4.583	-3.446	-3.985	-4.178	-4.359	-4.538
8	3.508	4.193	4.367	4.538	4.702	-3.446	-4.128	-4.341	-4.509	-4.676
9	3.508	4.191	4.521	4.671	4.816	-3.449	-4.128	-4.492	-4.638	-4.790
10	3.511	4.193	4.668	4.803	4.946	-3.448	-4.134	-4.642	-4.773	-4.908
11	3.509	4.192	4.685	4.926	5.056	-3.449	-4.131	-4.642	-4.900	-5.026
12	3.508	4.191	4.702	5.049	5.165	-3.450	-4.128	-4.642	-5.028	-5.143
13	3.508	4.191	4.701	5.103	5.273	-3.451	-4.128	-4.642	-5.047	-5.250
14	3.508	4.191	4.700	5.103	5.382	-3.452	-4.128	-4.642	-5.050	-5.358
15	3.509	4.191	4.701	5.103	5.413	-3.453	-4.128	-4.642	-5.051	-5.378
16	3.511	4.191	4.701	5.104	5.445	-3.453	-4.128	-4.642	-5.052	-5.398
17	3.509	4.192	4.703	5.105	5.448	-3.452	-4.131	-4.643	-5.052	-5.400
18	3.508	4.193	4.704	5.106	5.452	-3.450	-4.134	-4.644	-5.052	-5.401
19	3.510	4.192	4.699	5.106	5.452	-3.451	-4.131	-4.641	-5.052	-5.401
20	3.513	4.191	4.694	5.106	5.452	-3.452	-4.128	-4.638	-5.053	-5.401
21	3.513	4.191	4.695	5.106	5.451	-3.452	-4.129	-4.638	-5.053	-5.398
22	3.513	4.191	4.697	5.107	5.450	-3.452	-4.129	-4.638	-5.054	-5.395
23	3.513	4.191	4.698	5.108	5.449	-3.452	-4.129	-4.638	-5.054	-5.391
24	3.513	4.191	4.700	5.108	5.448	-3.452	-4.130	-4.638	-5.055	-5.388
25	3.513	4.191	4.701	5.109	5.447	-3.452	-4.130	-4.638	-5.056	-5.384
27	3.513	4.193	4.705	5.107	5.452	-3.452	-4.132	-4.641	-5.055	-5.387
30	3.513	4.195	4.711	5.104	5.459	-3.452	-4.134	-4.646	-5.055	-5.390

Table 7.5. Cont'd.

S/D	N_c, *UB* (Collapse)				N_c, *UB* (Blowout)			
	C/D				*C/D*			
	7	8	9	10	7	8	9	10
2	4.578	4.855	5.118	5.349	-4.516	-4.811	-5.059	-5.278
3	4.503	4.783	5.026	5.239	-4.447	-4.734	-4.980	-5.205
4	4.518	4.755	4.966	5.201	-4.468	-4.709	-4.928	-5.135
5	4.578	4.783	4.988	5.173	-4.528	-4.749	-4.936	-5.131
6	4.658	4.850	5.023	5.207	-4.624	-4.820	-4.991	-5.159
7	4.761	4.926	5.090	5.242	-4.724	-4.893	-5.052	-5.205
8	4.859	5.020	5.168	5.318	-4.841	-4.988	-5.126	-5.272
9	4.973	5.111	5.249	5.368	-4.943	-5.081	-5.212	-5.348
10	5.074	5.204	5.315	5.438	-5.045	-5.188	-5.296	-5.418
11	5.181	5.298	5.408	5.525	-5.153	-5.279	-5.389	-5.497
12	5.289	5.393	5.501	5.613	-5.261	-5.370	-5.482	-5.576
13	5.383	5.484	5.585	5.692	-5.356	-5.459	-5.562	-5.659
14	5.478	5.575	5.669	5.771	-5.451	-5.547	-5.641	-5.742
15	5.572	5.666	5.753	5.850	-5.543	-5.636	-5.721	-5.825
16	5.666	5.747	5.826	5.916	-5.636	-5.720	-5.797	-5.894
17	5.736	5.827	5.899	5.982	-5.694	-5.804	-5.872	-5.962
18	5.739	5.900	5.972	6.048	-5.694	-5.879	-5.948	-6.031
19	5.743	5.973	6.045	6.114	-5.697	-5.954	-6.023	-6.100
20	5.746	6.001	6.116	6.182	-5.700	-5.957	-6.099	-6.169
21	5.745	6.001	6.189	6.248	-5.699	-5.957	-6.174	-6.231
22	5.744	6.001	6.207	6.314	-5.698	-5.957	-6.180	-6.294
23	5.743	6.001	6.224	6.381	-5.697	-5.957	-6.186	-6.356
24	5.742	6.001	6.226	6.395	-5.696	-5.957	-6.188	-6.370
25	5.741	6.001	6.227	6.409	-5.693	-5.957	-6.189	-6.383
27	5.744	5.998	6.224	6.424	-5.698	-5.959	-6.189	-6.397
30	5.749	5.993	6.227	6.431	-5.705	-5.963	-6.189	-6.397

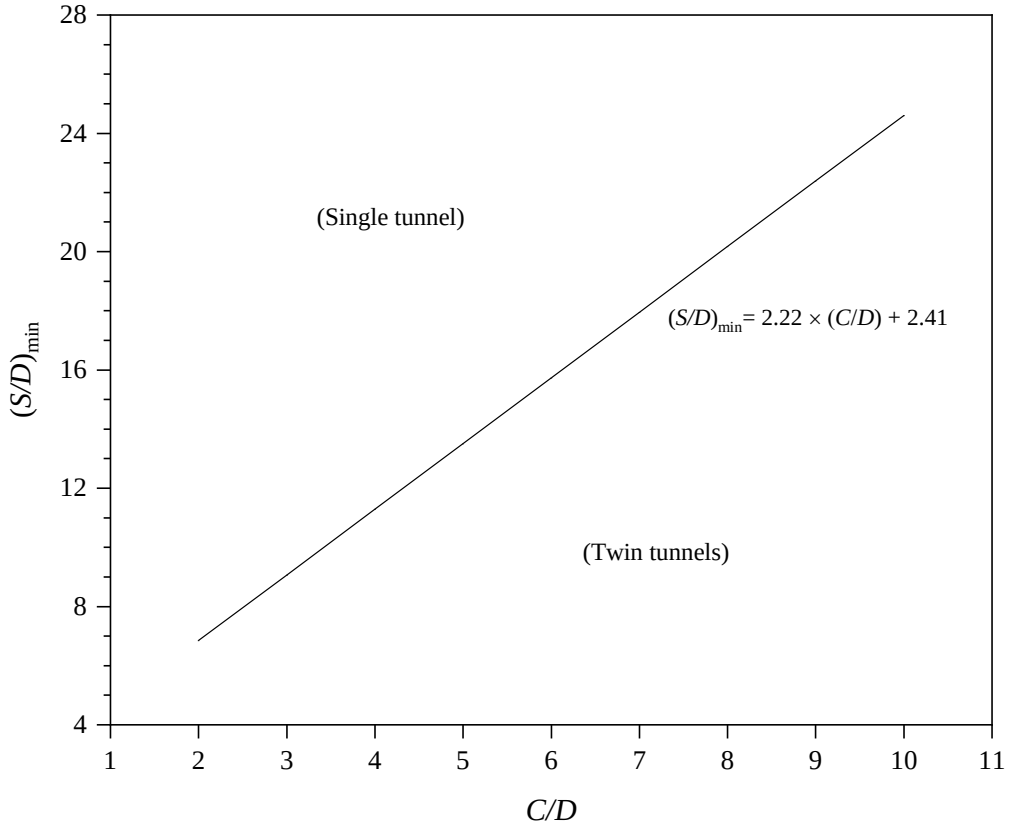

Figure 7.10. Minimum spacing ratios $(S/D)_{min}$ vs depth ratios (C/D = 2 - 10).

Figure 7.10 and Table 7.6 show the relationship between the minimum spacing ratio $(S/D)_{min}$ and the depth ratios (C/D = 2 - 10). $(S/D)_{min}$ is the minimum spacing ratio required for each tunnel to behave as a single isolated tunnel. Equations 7.4 is an accurate curve-fitting for the relationship between $(S/D)_{min}$ and C/D.

$$(S/D)_{min} = 2.22 \times (C/D) + 2.41 \quad (7.4)$$

Table 7.6. Max. N_c (*LB, UB* and *FD*) results vs. minimum spacing ratios $(S/D)_{min}$.

C/D	Twin Tunnels N_c at $(S/D)_{min}$			
	$(S/D)_{min}$	N_c (*LB*)	N_c (*UB*)	N_c (*FD*)
2	6.84	3.401	3.511	3.575
3	9.06	4.039	4.191	4.213
4	11.28	4.504	4.685	4.706
5	13.50	4.863	5.103	5.125
6	15.72	5.228	5.445	5.444
7	17.94	5.483	5.739	5.765
8	20.16	5.708	6.001	6.000
9	22.38	5.87	6.224	6.227
10	24.60	6.113	6.409	6.400

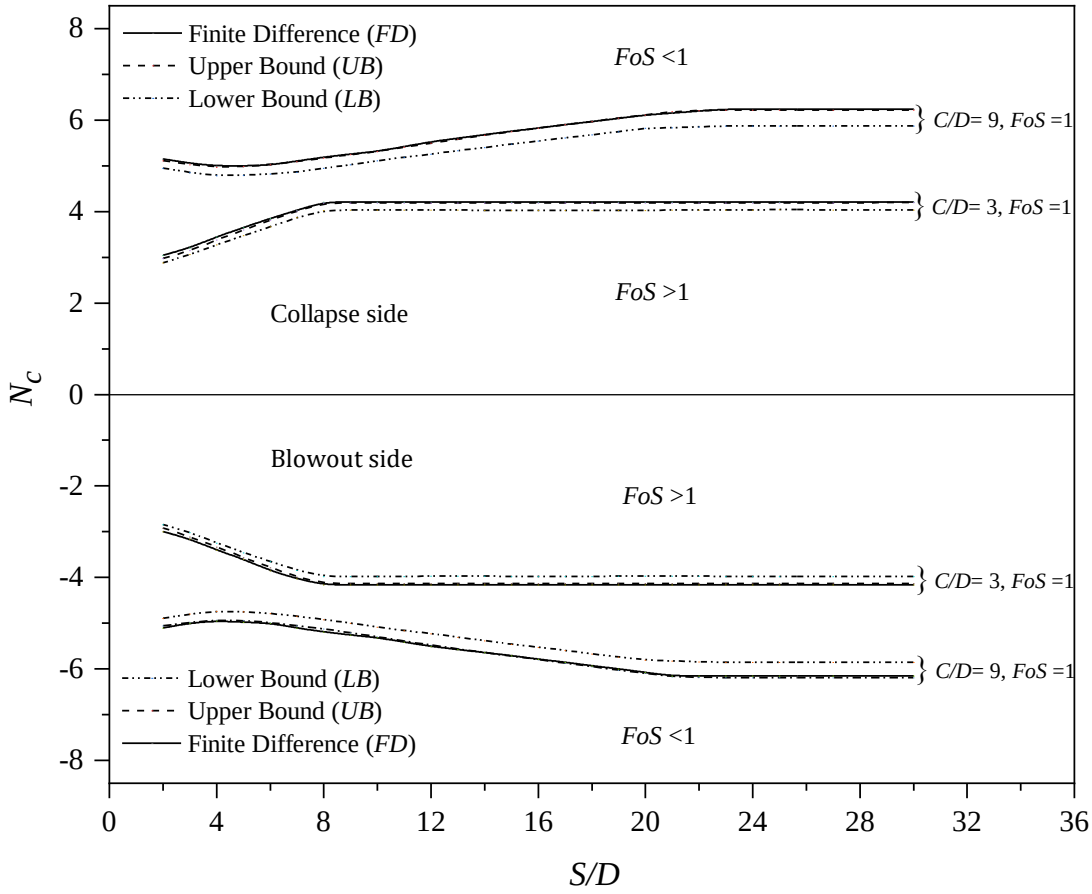

Figure 7.11. Comparison of N_c results in collapse and blowout for *C/D* = 3 and 9.

Figure 7.11 and Table 7.7 show comparisons between N_c results (*LB*, *UB*, and *FD*) for two depth ratios (*C*/*D* = 3 and 9) and a range of spacing ratios (*S*/*D* = 2-30). The *UB* and *FD* results agree well, though they are not conservative when compared to *LB*.

Table 7.7. Comparison of N_c results in collapse and blowout for C/D = 3 and C/D = 9.

S/D	Collapse						Blowout					
	C/D = 3			C/D = 9			C/D = 3			C/D = 9		
	LB	*UB*	*FD*	*LB*	*UB*	*FD*	*LB*	*UB*	*FD*	*LB*	*UB*	*FD*
2	2.88	2.98	3.04	5.15	5.12	5.15	-2.85	-2.92	-3.00	-4.89	-5.06	-5.11
3	3.06	3.15	3.21	5.04	5.03	5.04	-3.02	-3.11	-3.16	-4.79	-4.98	-4.99
4	3.27	3.38	3.45	4.99	4.97	4.99	-3.24	-3.34	-3.40	-4.74	-4.93	-4.95
5	3.48	3.60	3.65	4.99	4.99	4.99	-3.45	-3.57	-3.61	-4.75	-4.94	-4.98
6	3.67	3.81	3.85	5.03	5.02	5.03	-3.65	-3.78	-3.85	-4.79	-4.99	-4.99
7	3.87	4.01	4.03	5.11	5.09	5.11	-3.85	-3.99	-4.03	-4.85	-5.05	-5.11
8	4.03	4.19	4.21	5.19	5.17	5.19	-3.98	-4.13	-4.16	-4.92	-5.13	-5.19
9	4.04	4.19	4.21	5.25	5.25	5.25	-3.98	-4.13	-4.16	-5.00	-5.21	-5.26
10	4.04	4.19	4.21	5.32	5.32	5.32	-3.98	-4.13	-4.16	-5.09	-5.30	-5.31
11	4.04	4.19	4.21	5.41	5.41	5.41	-3.98	-4.13	-4.16	-5.16	-5.39	-5.41
12	4.04	4.19	4.21	5.51	5.50	5.51	-3.97	-4.13	-4.16	-5.23	-5.48	-5.51
13	4.03	4.19	4.21	5.59	5.59	5.59	-3.97	-4.13	-4.16	-5.31	-5.56	-5.58
14	4.03	4.19	4.21	5.68	5.67	5.68	-3.97	-4.13	-4.16	-5.38	-5.64	-5.64
15	4.03	4.19	4.21	5.76	5.75	5.76	-3.98	-4.13	-4.16	-5.46	-5.72	-5.71
16	4.03	4.19	4.21	5.83	5.83	5.83	-3.98	-4.13	-4.16	-5.53	-5.80	-5.79
17	4.03	4.19	4.21	5.90	5.90	5.90	-3.98	-4.13	-4.16	-5.60	-5.87	-5.86
18	4.03	4.19	4.21	5.97	5.97	5.97	-3.98	-4.13	-4.16	-5.67	-5.95	-5.93
19	4.03	4.19	4.21	6.04	6.05	6.04	-3.97	-4.13	-4.16	-5.74	-6.02	-6.00
20	4.03	4.19	4.21	6.12	6.12	6.12	-3.97	-4.13	-4.16	-5.81	-6.10	-6.08
21	4.03	4.19	4.21	6.14	6.19	6.14	-3.98	-4.13	-4.16	-5.82	-6.17	-6.16
22	4.03	4.19	4.21	6.16	6.21	6.16	-3.98	-4.13	-4.16	-5.84	-6.18	-6.16
23	4.03	4.19	4.21	6.18	6.22	6.18	-3.98	-4.13	-4.16	-5.86	-6.19	-6.16
24	4.03	4.19	4.21	6.18	6.22	6.18	-3.98	-4.13	-4.16	-5.86	-6.19	-6.16
25	4.03	4.19	4.21	6.18	6.22	6.18	-3.97	-4.13	-4.16	-5.86	-6.19	-6.16
27	4.03	4.19	4.21	6.18	6.22	6.18	-3.97	-4.13	-4.16	-5.86	-6.19	-6.16
30	4.03	4.19	4.21	6.18	6.22	6.18	-3.97	-4.13	-4.16	-5.86	-6.19	-6.16

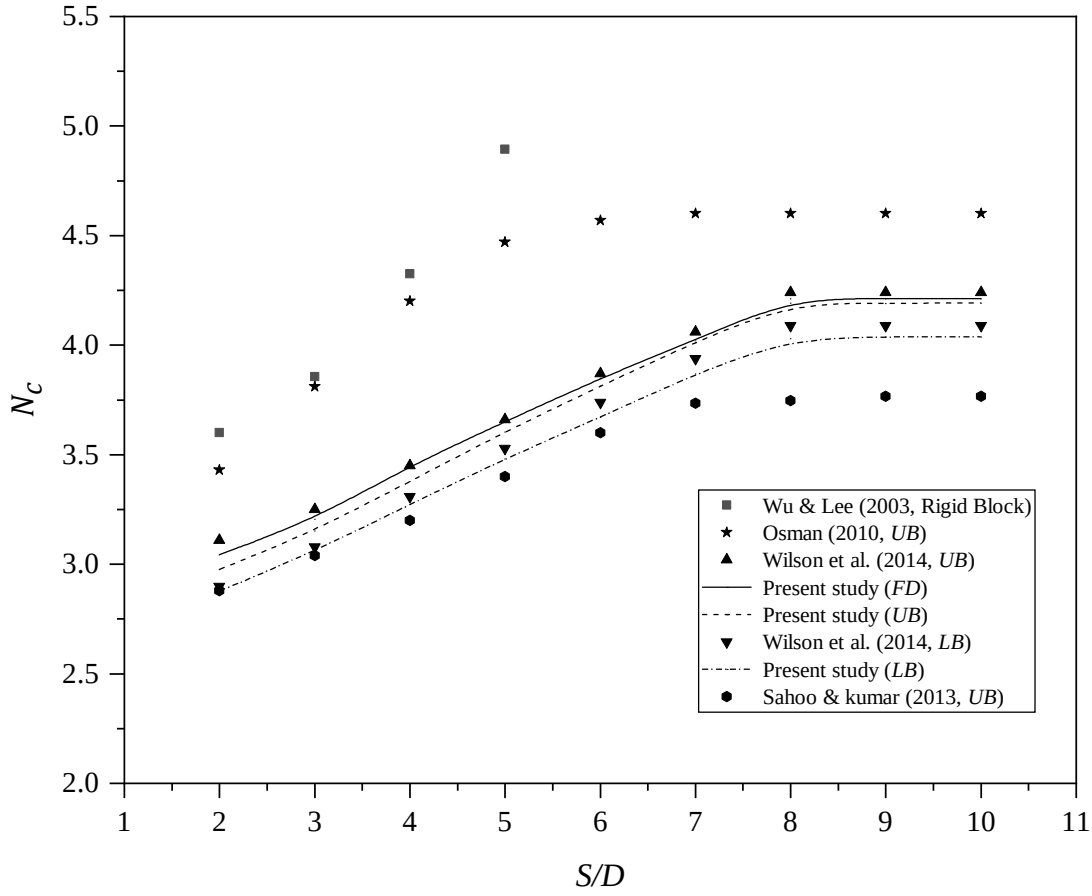

Figure 7.12. Comparison of N_c between the present study and published solutions (*C/D* = 3).

Figure 7.12 and Table 7.8 show a comparison of the N_c results obtained by the present study and those in published literature. The results of this study agree well with those of Wilson et al. (2014).

The present *UB* solution has been significantly improved owing to the use of adaptive mesh. The results from Sahoo and Kumar (2013) are conservative, while the comparison between the present numerical *UB* results and those from Osman (2010) and Wu and Lee (2003) using analytical *UB* shows very high variation. It is not surprising to see that the rigid block *UB* yields an unsafe solution and hence should not be used in practice.

Table 7.8. Comparison of N_c with published solutions (C/D = 3 and S/D = 2 - 10).

S/D	Wu & Lee (2003) R. Block (*UB*)	Osman (2010) R. Block (*UB*)	Wilson et al. (2014) *FELA* (*UB*)	Present study *FDM*	Present study *FELA* (*UB*)	Wilson et al. (2014) *FELA* (*LB*)	Present study *FELA* (*LB*)	Sahoo and Kumar (2013) *FELA* (*UB*)
2	3.6	3.43	3.11	3.04	2.94	2.90	2.92	2.88
3	3.9	3.81	3.25	3.21	3.12	3.08	3.09	3.04
4	4.3	4.20	3.45	3.45	3.34	3.31	3.31	3.20
5	4.9	4.47	3.66	3.65	3.56	3.53	3.51	3.40
6	-	4.57	3.87	3.85	3.78	3.74	3.75	3.60
7	-	4.60	4.06	4.03	3.98	3.94	3.93	3.74
8	-	4.60	4.24	4.21	4.14	4.09	4.08	3.75
9	-	4.60	4.24	4.21	4.14	4.09	4.09	3.77
10	-	4.60	4.24	4.21	4.14	4.09	4.08	3.77

7.4 Failure Mechanism

On the left-hand side of Figures 7.13 to 7.15, the absolute displacement contour plots are presented for C/D = 3 with various spacing ratio (S/D = 4, 8, 9). As discussed before, the absolute displacement $\left(|u| = \sqrt{u_x^2 + u_y^2}\right)$ plots are useful to give an overall indication of failure mechanism and the ground surface failure extent while the actual values of the displacement are not real.

Also shown on the right-hand side of Figures 7.13 to 7.15 are the displacement vector plots. The vector plot is useful as both the magnitude and direction of soil movement can be observed.

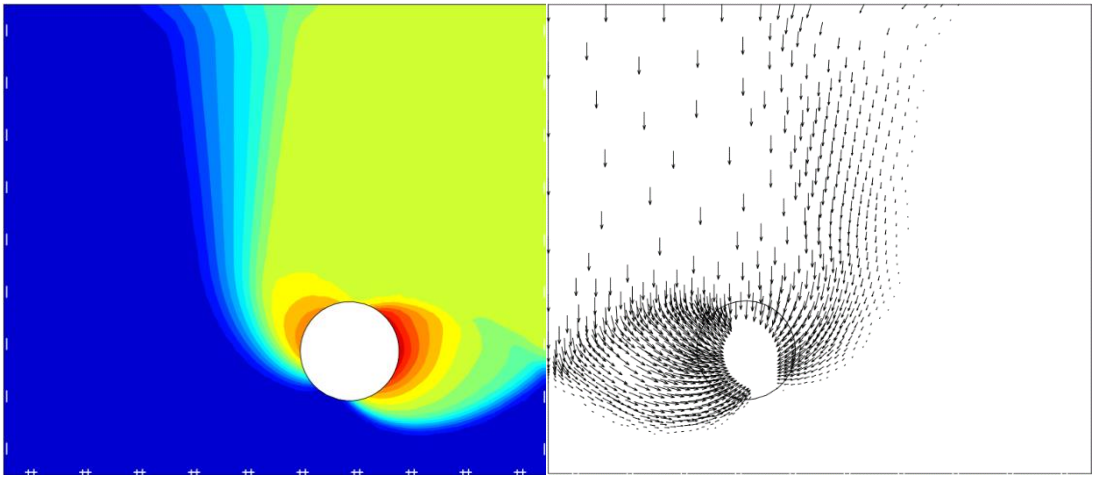

Note that the actual contour values of the plots are not important in limit analysis with the perfect plasticity theorem.

Figure 7.13. Absolute displacement ($|u|$) contour and velocity plots for C/D = 3 and S/D = 4.

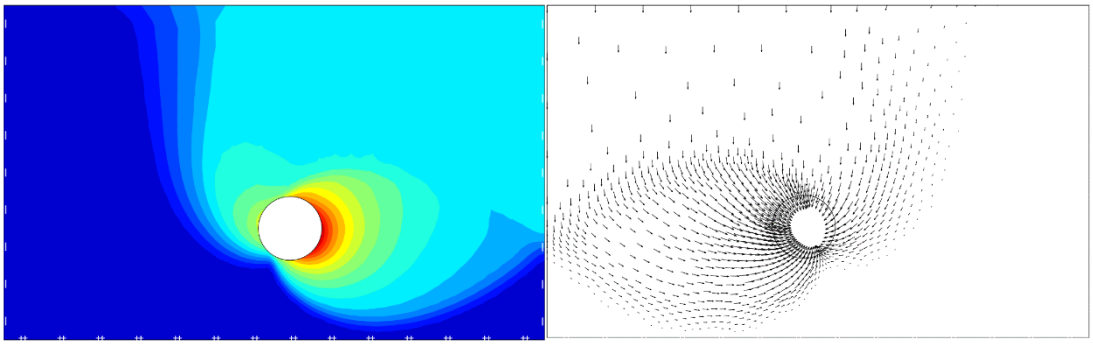

Note that the actual contour values of the plots are not important in limit analysis with the perfect plasticity theorem.

Figure 7.14. Absolute displacement ($|u|$) contour and velocity plots for C/D = 3 and S/D = 8.

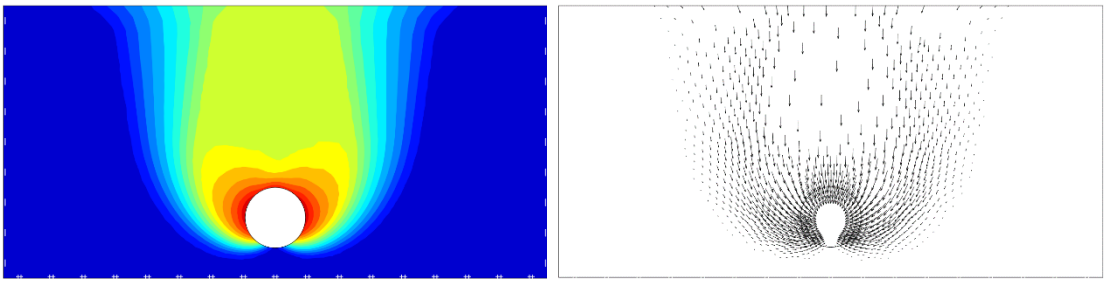

Note that the actual contour values of the plots are not important in limit analysis with the perfect plasticity theorem.

Figure 7.15. Absolute displacement ($|u|$) contour and velocity plots for C/D = 3 and S/D = 9.

Note that these are symmetrical plots; only half of the domain is presented. As expected, there are obvious differences in the failure shape when the spacing ratio S/D increases. A simple and direct observation is that the overlapping effects of twin tunnels disappear at S/D = 9, where a single tunnel failure mechanism is achieved. At this point, the corresponding S/D is the minimum spacing ratio $(S/D)_{min}$ required to eliminate the interaction effect between the tunnels, where each tunnel behaves as a single isolated tunnel. For all C/D, the failure zone gets wider for increasing depth ratios. Floor heaving is most severe for deep cases but reduces for shallow cases (small C/D). It is also interesting to see a second failure surface occurring between the two tunnels when the spacing ratio S/D is small (see Figures 7.13 and 7.14).

Another set of plots are presented in Figures 7.16-7.18 for a larger depth ratio of C/D = 6 with various spacing ratio (S/D = 10, 15, 16).

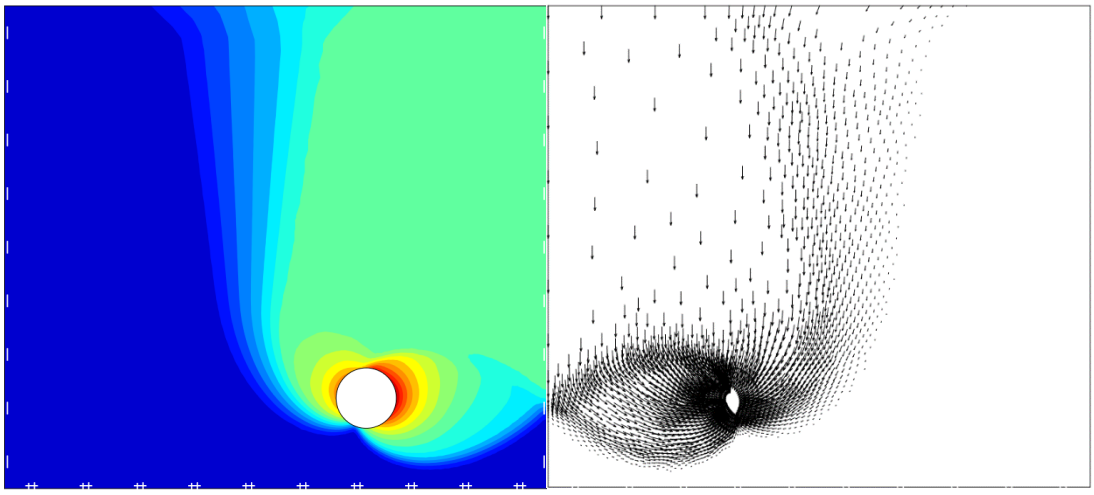

Note that the actual contour values of the plots are not important in limit analysis with the perfect plasticity theorem.

Figure 7.16. Absolute displacement ($|u|$) contour and velocity plots for C/D = 6 and S/D = 6.

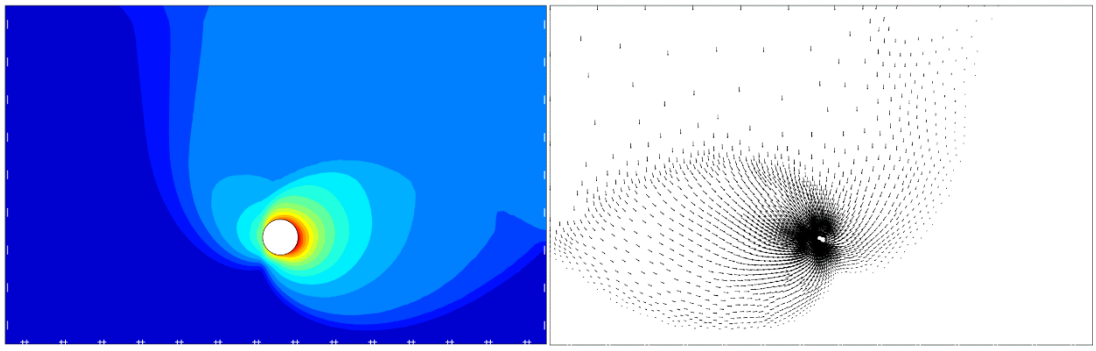

Note that the actual contour values of the plots are not important in limit analysis with the perfect plasticity theorem.

Figure 7.17. Absolute displacement ($|u|$) contour and velocity plots for C/D = 6 and S/D = 15.

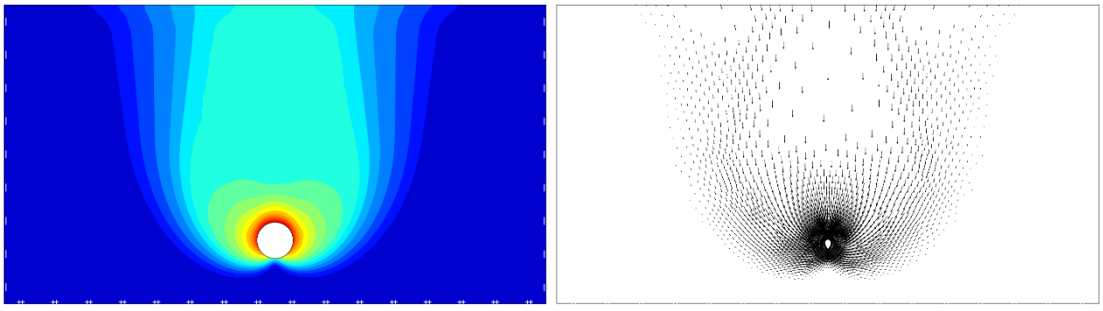

Note that the actual contour values of the plots are not important in limit analysis with the perfect plasticity theorem.

Figure 7.18. Absolute displacement ($|u|$) contour and velocity plots for C/D = 6 and S/D = 16.

7.5 Example and Practical Uses

The usefulness of this study is best demonstrated through examples. Since the lower bound theorem offers a safe assessment of the critical stability number, the calculations of the examples are based on *LB* results.

7.5.1 Example

Two side-by-side tunnels are planned to be 30 metres apart (centre-to-centre) and are assumed to be bored simultaneously. The tunnel boring machines have a diameter (D) of 6.0m and are buried at a depth (C) of 18m in an undrained clayey soil with properties S_u = 27kPa, $\phi_u = 0°$ and γ = 18 kN/m^3. The site is assumed to be a Greenfield $(\sigma_s = 0)$. The dimensionless ratios are calculated as C/D = 3 and S/D = 5. With Table 7.4, it is found that the *LB* critical stability number (N_c) is approximately 3.48. Therefore,

$$FoS = N_c / N = 3.48 / ((0 + 18 \times 21 - 0) / 27) = 0.249$$

Using (N_c = 3.48) and Equation 7.3, the internal tunnel pressure required for FoS = 1 is calculated as 284.04 kPa.

With S/D = 5, the *LB* critical stability number is (N_c = 3.48). For a depth ratio C/D = 3, the maximum stability number (N_c = 4.04) occurs at S/D = 9 for a single tunnel response (Table 7.4 or Equation 7.4). Therefore, the reduction % in stability number due to twin tunnel effect is approximately 14.8 %.

7.6 Conclusions

This chapter has successfully investigated the stability of twin circular tunnels. Both upper and lower FoS bounds were calculated for a wide ranges of stability numbers (N = -15 to 15), depth ratios (C/D = 2 - 10) and spacing ratios (S/D = 2 - 30). The obtained numerical upper and lower bounds are generally within a few per cents of one another, with the true solution lying between the two bounds. A unique critical stability number (N_c) was presented by multiplying the "designed" stability number and the corresponding FoS for each depth ratio. The variation of N_c has been studied as a function of C/D and S/D and the minimum spacing ratios required to avoid twin tunnel interaction determined for uses in practical designs.

A full 3D analysis of twin tunnel headings is presented next in Chapter 8.

CHAPTER 8: UNDRAINED ANALYSIS OF 3D TWIN CIRCULAR TUNNELS

8.1 Introduction

In comparison to the 3D single circular tunnel investigated in Chapter 6, the effect of the centre-to-centre distance appears as a new problem parameter and plays a key factor in the behaviour of twin circular tunnels.

This chapter addresses the 3D twin tunnels stability problem using finite element limit analysis. Rigorous solutions of the upper and lower bounds of the critical pressure (σ_t) in collapse and blowout are determined, and subsequently, the factor of safety calculated using Brooms and Bennermarks' critical stability number (N_c). Furthermore, a correlation between the individual and twin stability failure is established.

The results are presented as dimensionless stability charts for use by practising engineers, and the actual tunnel stability numbers closely bracket the true solution from above and below.

Correctly analysing the stability of underground infrastructures, such as twin circular tunnels, is crucial to prevent the collapse of such a complex assembly.

8.2 Problem Definition and Modelling Technique

Figure 8.1 shows the problem definition of 3D twin circular tunnels. The undrained shear strength (S_u), and the unit weight (γ) describe soil properties used for an elastic-perfectly plastic Tresca material, while the tunnels are of diameter (D), cover depth (C) above the crown of the tunnels and centre-to-centre distance (S) between the tunnels. The undrained stability of twin tunnels is described by a stability number (N) that was originally stated in Broms and Bennermark (1967). The twin tunnel stability number (N) is a function of the depth ratio (C/D) and the spacing ratio (S/D), and it is defined as shown in Equation 8.1.

$$N = \frac{\sigma_s + \gamma H - \sigma_t}{S_u} \tag{8.1}$$

Where σ_s is the possible surcharge loading acting on the ground surface, σ_t is the uniform pressure applied to the tunnel face and H is the depth of the tunnel axis that is equal to $(C + D/2)$.

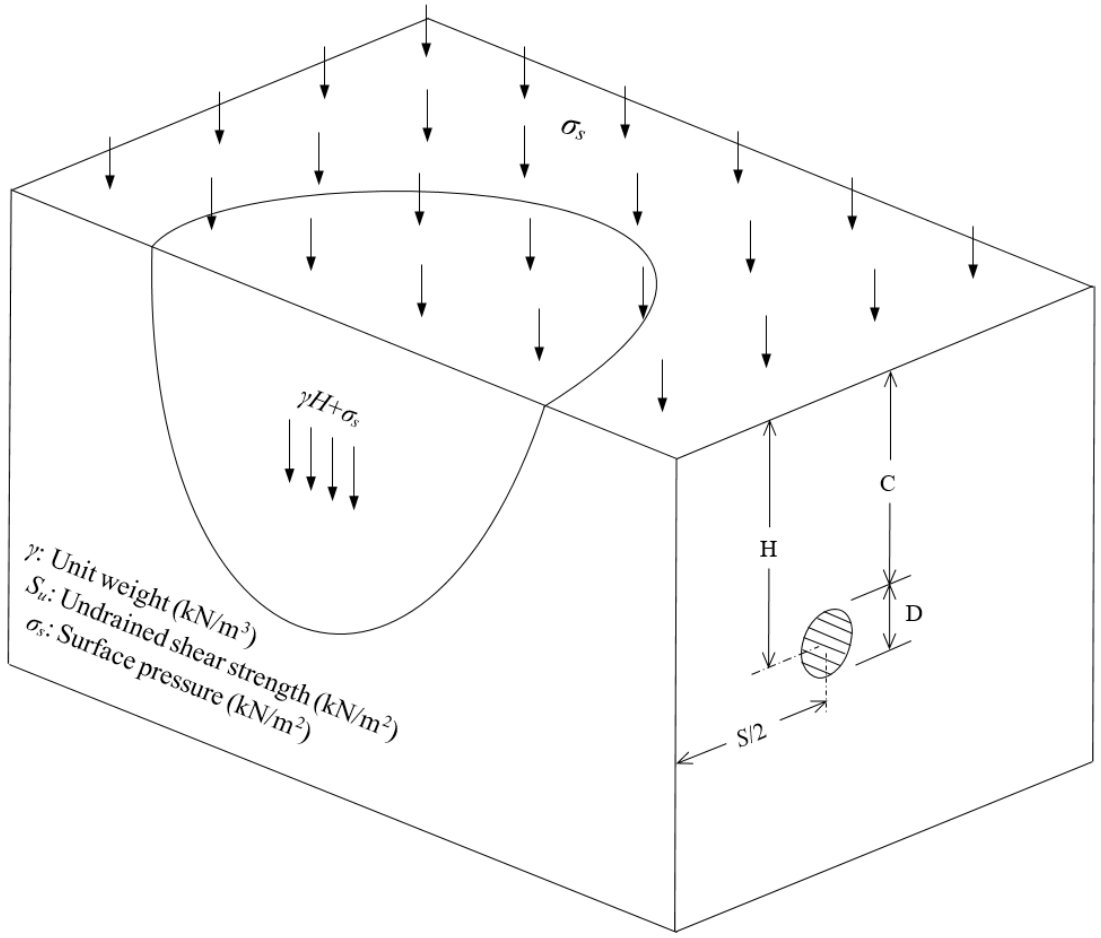

Figure 8.1. Problem definition.

Broms and Bennermarks' original stability number has been successfully applied to a number of two-dimensional soil stability problems (Shiau, Lamb, et al. 2016; Shiau, Sams, et al. 2016; Shiau & Al-Asadi 2018; Shiau & Sams 2019).

The present twin tunnels problem is symmetrical about the vertical plane, which passes through the centerline of the distance between tunnels centres. Therefore, the failure load and the stability number calculations are based on one half of the total domain size. It is essential to use a large mesh size as it ensures that the entire soil mass is unaffected by the boundaries of the model. The boundary conditions of the *FELA* model are as follows: the ground surface is free to displace, the side surfaces are restrained in the *x*-direction, while the back and the front surfaces (symmetrical plane) are restrained in the y-direction. The base is fixed in all directions. The rigid lining

around the soil excavation is restrained in the normal direction to represent the smooth interface condition. A typical 3D *FELA* adaptive mesh used for *C/D* = 3 is shown in Figure 8.2. An automatically adaptive mesh refinement was employed in both the *UB* and *LB* simulations. Three iterations of adaptive meshing with the number of elements increasing from 5000 to 10000 were used for all analyse.

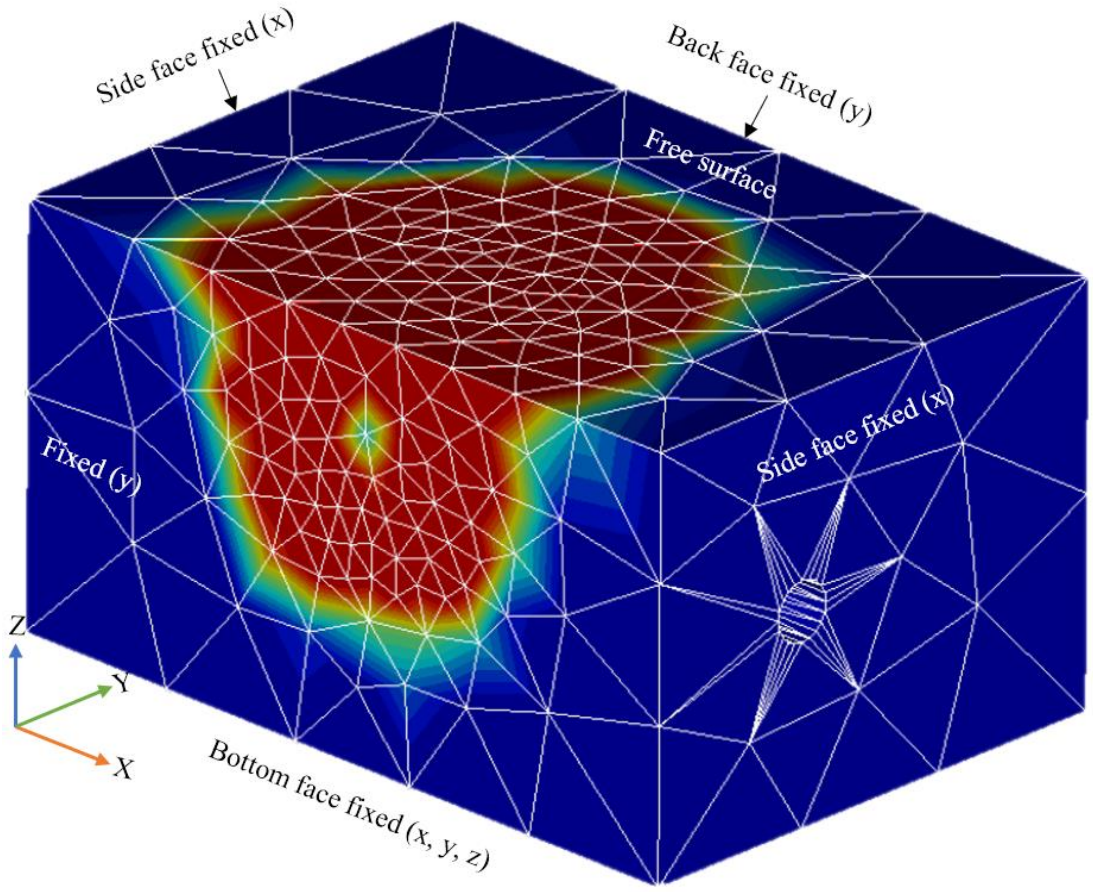

Figure 8.2. A typical adaptive mesh with boundary conditions and failure mechanism (*C/D* = 3 and *S/D* = 4).

The numerical simulations presented in this study make use of recently developed 3D finite element limit analysis (OptumCE 2018). This technique can accurately determine the limit load of a 3D problem with the power of finite element discretisation and the bounding capability of lower and upper bound plastic limit theorems (Sloan 2013). Using the limit analysis of 3D *FELA* and the undrained stability number in Equation 8.1, critical internal pressures (σ_t) are optimised for various material parameters such as (σ_s, γ, *H, and* S_u), depth ratios (*C/D*) and spacing ratios (*S/D*) in both collapse and blowout scenarios. Shown in Figure 8.2 is also a plot of the failure mechanism for (*C/D* = 3 and *S/D* = 4) using the contours of *UB* power dissipation.

Noting that this is the symmetrical model for a close twin tunnel (S/D = 4), the resulting surface failure area resembles an elliptical shape due to the twin tunnel effects.

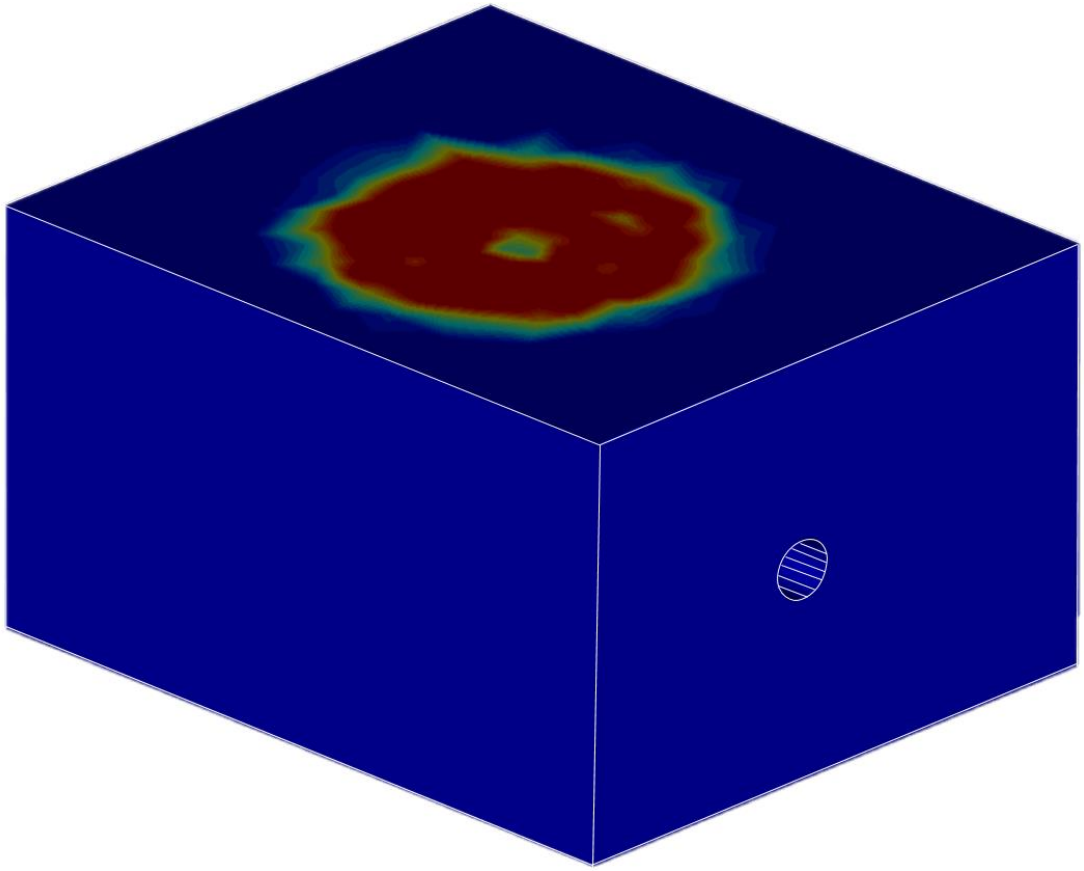

Figure 8.3. A typical single tunnel response for large twin tunnel spacing (symmetrical *UB* shear dissipation plot for C/D = 3 and S/D = 9).

Another plot of the failure mechanism for (C/D = 3 and S/D = 9) is shown in Figure 8.3. Due to the large value of S/D, it is not surprising to see a single tunnel response with a near-circular failure surface.

8.3 Results and Discussion

For various centre-to-centre spacing ratio (S/D) between the twin tunnels, the stability is expressed in terms of Broms and Bennermark's critical stability number (N_c) in both the collapse and blowout analyses. The obtained upper and lower bound N_c numbers at collapse and blowout are presented in Table 8.1 for each depth ratio (C/D) in a series of spacing ratio (S/D). These results were used to produce stability Figures 8.4 - 8.6, showing the relationship between N_c and S/D for various depth ratios (C/D = 2 - 10).

Table 8.1. Complete N_c values in collapse and blowout (*LB* and *UB* for *C*/*D* = 2- 10 and various *S*/*D*).

C/D	*S/D*	Collapse			Blowout		
		LB	*UB*	*Diff. %*	*LB*	*UB*	*Diff. %*
2	2	8.465	8.964	5.726	-8.514	-8.959	5.094
	3	8.886	9.397	5.590	-8.897	-9.380	5.285
	4	9.253	9.770	5.436	-9.249	-9.796	5.744
	5	9.364	9.925	5.817	-9.350	-9.919	5.906
	6	9.364	9.925	5.817	-9.350	-9.919	5.906
	7	9.364	9.925	5.817	-9.350	-9.919	5.906
3	2	9.608	10.163	5.614	-9.627	-10.172	5.505
	3	9.903	10.461	5.480	-9.897	-10.454	5.474
	4	10.156	10.767	5.840	-10.151	-10.774	5.955
	5	10.400	11.057	6.124	-10.427	-11.051	5.811
	6	10.635	11.296	6.028	-10.632	-11.292	6.021
	7	10.703	11.358	5.938	-10.682	-11.346	6.029
	8	10.703	11.358	5.938	-10.682	-11.346	6.029
	9	10.703	11.358	5.938	-10.682	-11.346	6.029
4	2	10.543	11.154	5.632	-10.539	-11.139	5.536
	3	10.698	11.329	5.729	-10.694	-11.336	5.828
	4	10.901	11.550	5.781	-10.887	-11.554	5.944
	5	11.117	11.768	5.689	-11.128	-11.758	5.506
	6	11.311	12.000	5.911	-11.335	-12.000	5.700
	7	11.502	12.205	5.931	-11.512	-12.209	5.877
	8	11.613	12.381	6.402	-11.630	-12.365	6.126
	9	11.654	12.410	6.283	-11.670	-12.392	6.001
	10	11.654	12.410	6.283	-11.670	-12.392	6.001
	12	11.654	12.410	6.283	-11.670	-12.392	6.001
	14	11.654	12.410	6.283	-11.670	-12.392	6.001
5	2	11.299	11.940	5.517	-11.290	-11.944	5.630
	3	11.365	12.019	5.594	-11.368	-12.020	5.576
	4	11.500	12.198	5.891	-11.501	-12.217	6.038
	5	11.673	12.385	5.919	-11.659	-12.407	6.216
	6	11.833	12.572	6.056	-11.838	-12.597	6.212
	7	12.020	12.762	5.988	-12.034	-12.758	5.841
	8	12.190	12.936	5.938	-12.199	-12.938	5.880
	9	12.350	13.100	5.894	-12.330	-13.097	6.033
	10	12.460	13.222	5.934	-12.406	-13.199	6.194
	12	12.460	13.222	5.934	-12.407	-13.231	6.428
	12	12.460	13.222	5.934	-12.407	-13.231	6.428
	14	12.460	13.222	5.934	-12.407	-13.231	6.428

Table 8.1. Cont'd.

C/D	*S/D*	Collapse			Blowout		
		LB	*UB*	*Diff. %*	*LB*	*UB*	*Diff. %*
6	2	11.918	12.661	6.046	-11.986	-12.677	5.604
	3	11.940	12.679	6.003	-11.974	-12.669	5.641
	4	12.010	12.770	6.134	-12.045	-12.793	6.023
	5	12.158	12.917	6.054	-12.156	-12.926	6.140
	6	12.298	13.070	6.086	-12.288	-13.087	6.298
	7	12.448	13.246	6.212	-12.450	-13.257	6.278
	8	12.606	13.417	6.233	-12.616	-13.419	6.169
	9	12.733	13.568	6.350	-12.763	-13.567	6.107
	10	12.877	13.714	6.295	-12.892	-13.706	6.121
	12	13.046	13.912	6.425	-13.070	-13.908	6.212
	14	13.046	13.912	6.425	-13.070	-13.908	6.212
7	2	12.545	13.232	5.330	-12.533	-13.253	5.584
	3	12.520	13.222	5.454	-12.502	-13.226	5.628
	4	12.572	13.290	5.553	-12.518	-13.320	6.208
	5	12.658	13.411	5.777	-12.617	-13.432	6.257
	6	12.767	13.535	5.840	-12.733	-13.548	6.202
	7	12.885	13.678	5.971	-12.850	-13.672	6.199
	8	13.020	13.826	6.005	-12.990	-13.810	6.119
	9	13.145	13.961	6.021	-13.131	-13.946	6.020
	10	13.275	14.093	5.978	-13.276	-14.082	5.892
	12	13.480	14.341	6.190	-13.483	-14.334	6.119
	14	13.598	14.512	6.503	-13.592	-14.504	6.492
	16	13.598	14.512	6.503	-13.592	-14.504	6.492
8	2	13.016	13.741	5.419	-13.028	-13.762	5.480
	3	12.980	13.706	5.441	-12.982	-13.700	5.382
	4	13.000	13.764	5.709	-12.983	-13.756	5.782
	5	13.072	13.854	5.809	-13.029	-13.861	6.188
	6	13.138	13.971	6.146	-13.140	-13.970	6.123
	7	13.237	14.088	6.229	-13.255	-14.076	6.008
	8	13.352	14.204	6.184	-13.376	-14.195	5.941
	9	13.486	14.322	6.013	-13.483	-14.314	5.979
	10	13.595	14.446	6.070	-13.608	-14.422	5.808
	12	13.817	14.682	6.070	-13.830	-14.645	5.724
	14	13.990	14.883	6.186	-13.987	-14.871	6.127
	16	14.025	14.995	6.685	-14.060	-15.011	6.543
	18	14.025	14.995	6.685	-14.060	-15.011	6.543
	20	14.025	14.995	6.685	-14.060	-15.011	6.543

Table 8.1. Cont'd.

C/D	*S/D*	Collapse			Blowout		
		LB	*UB*	*Diff. %*	*LB*	*UB*	*Diff. %*
9	2	13.477	14.211	5.302	-13.464	-14.203	5.342
	3	13.366	14.171	5.847	-13.353	-14.156	5.838
	4	13.345	14.166	5.969	-13.343	-14.144	5.828
	5	13.358	14.190	6.040	-13.380	-14.180	5.806
	6	13.390	14.252	6.237	-13.435	-14.239	5.811
	7	13.458	14.322	6.220	-13.520	-14.324	5.775
	8	13.570	14.423	6.094	-13.606	-14.420	5.809
	9	13.702	14.563	6.092	-13.719	-14.555	5.914
	10	13.828	14.712	6.195	-13.852	-14.700	5.940
	12	14.074	15.000	6.370	-14.103	-14.974	5.991
	14	14.290	15.226	6.342	-14.300	-15.215	6.200
	16	14.358	15.287	6.267	-14.441	-15.379	6.291
	18	14.425	15.347	6.194	-14.487	-15.475	6.595
	20	14.425	15.347	6.194	-14.487	-15.475	6.595
	22	14.425	15.347	6.194	-14.487	-15.475	6.595
	24	14.425	15.347	6.194	-14.487	-15.475	6.595
	26	14.425	15.347	6.194	-14.487	-15.475	6.595
	28	14.425	15.347	6.194	-14.487	-15.475	6.595
10	2	13.821	14.634	5.714	-13.810	-14.644	5.862
	3	13.717	14.580	6.100	-13.750	-14.594	5.955
	4	13.720	14.581	6.085	-13.740	-14.588	5.987
	5	13.764	14.624	6.059	-13.772	-14.622	5.987
	6	13.830	14.699	6.092	-13.835	-14.700	6.063
	7	13.890	14.783	6.229	-13.900	-14.782	6.150
	8	13.963	14.869	6.285	-13.982	-14.883	6.243
	9	14.056	14.961	6.238	-14.078	-14.972	6.155
	10	14.146	15.053	6.213	-14.162	-15.076	6.252
	12	14.320	15.244	6.251	-14.350	-15.266	6.186
	14	14.524	15.441	6.120	-14.547	-15.459	6.079
	16	14.687	15.648	6.336	-14.696	-15.665	6.383
	18	14.805	15.855	6.849	-14.785	-15.839	6.883
	20	14.851	15.855	6.539	-14.811	-15.847	6.758
	22	14.851	15.855	6.539	-14.811	-15.847	6.758
	24	14.851	15.855	6.539	-14.811	-15.847	6.758
	26	14.851	15.855	6.539	-14.811	-15.847	6.758
	28	14.851	15.855	6.539	-14.811	-15.847	6.758
	30	14.851	15.855	6.539	-14.811	-15.847	6.758

8.3.1 Discussing S/D, N_c and $(S/D)_{min}$

The limit analysis is most useful when both the upper and lower bounds are calculated to bracket the exact collapse load. Figure 8.4 presents upper and lower bound N_c values for various values of S/D and C/D. Note that the finite element upper and lower bounds for the most depth ratios (C/D = 2- 10) lie within a few per cent (5% - 7%) of each other. Although the current bounding % is considered to be accurate for practical applications, it can be further reduced by refining the meshes to gain a more accurate set of bounds (Sloan 2013).

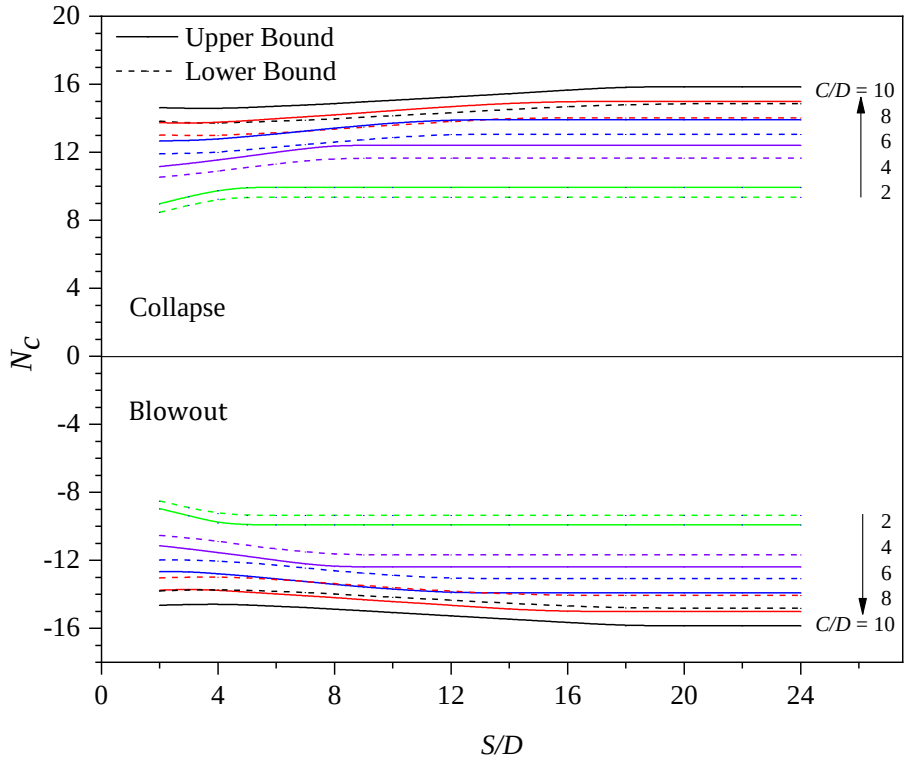

Figure 8.4. N_c versus S/D (*LB* and *UB*, C/D = 2 - 10, in collapse and blowout).

It is important to study the effect of spacing ratio (S/D) on the critical stability number N_c. Figure 8.5 presents the lower bound N_c values for various S/D and C/D values, while the upper bound ones are presented in Figure 8.6. These figures show that the critical stability number (N_c) increases nonlinearly as S/D increases until it approaches a constant value, which indicates that the twin tunnels stability is unaffected by the tunnel spacing. At this point, the stability responses are identical to those of corresponding single tunnel and the stability number is at its maximum value. It is also noted that the corresponding S/D is the minimum spacing ratio $(S/D)_{min}$ required to eliminate the overlapping effect between the tunnels.

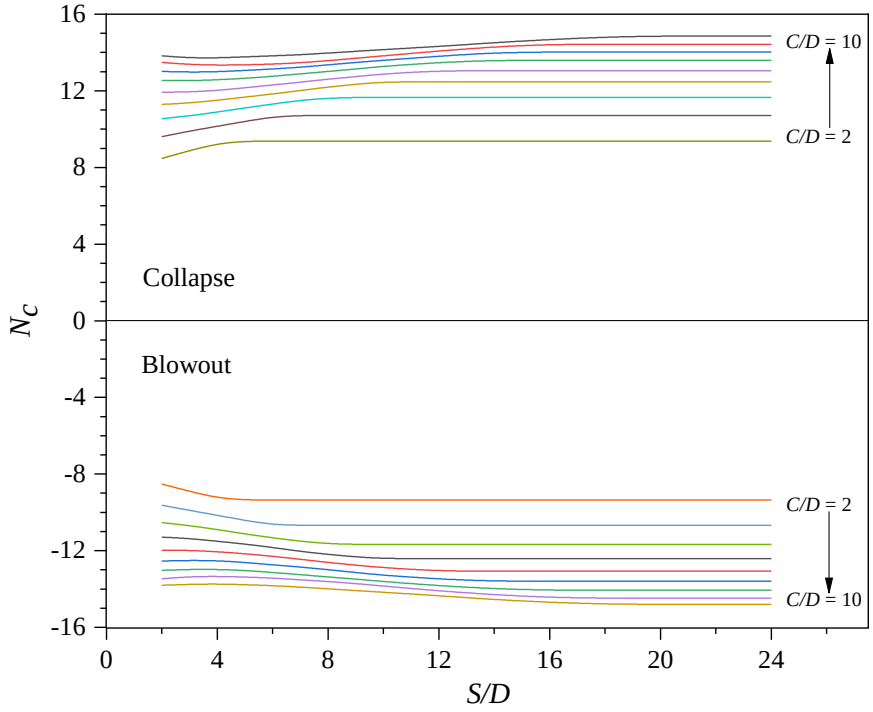

Figure 8.5. N_c versus S/D (*LB* only, C/D = 2 - 10, in collapse and blowout).

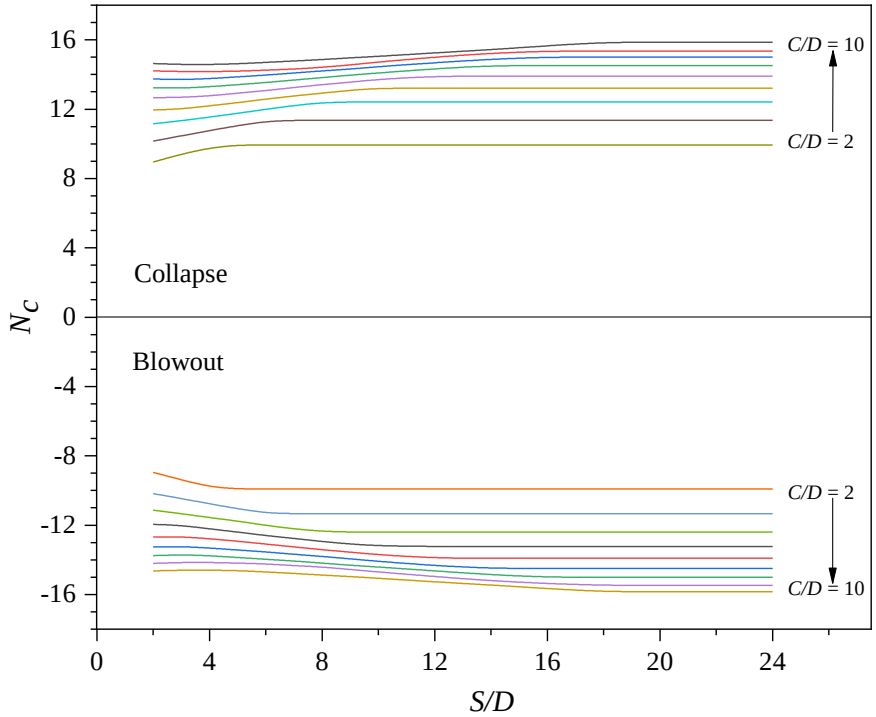

Figure 8.6. N_c versus S/D (*UB* only, C/D = 2 - 10, in collapse and blowout).

Since the lower bound theorem offers a conservative assessment in soil stability, the *LB* results (Table 8.1 and Figure 8.5) are used to define the minimum spacing ratios $(S/D)_{min}$ for various depth ratios C/D. This is shown in Figure 8.7. A linear relationship is observed between C/D and $(S/D)_{min}$. The linear line separates two zones: one being

the single tunnel (unaffected by the tunnel spacing) and the other is the zone with twin tunnels effects. Equations 8.2 is an accurate curve-fitting for the relationship between $(S/D)_{min}$ and C/D, with a correlation coefficient (R^2) of 0.999.

$$(S/D)_{min} = 1.85 \times (C/D) + 1.20 \quad (8.2)$$

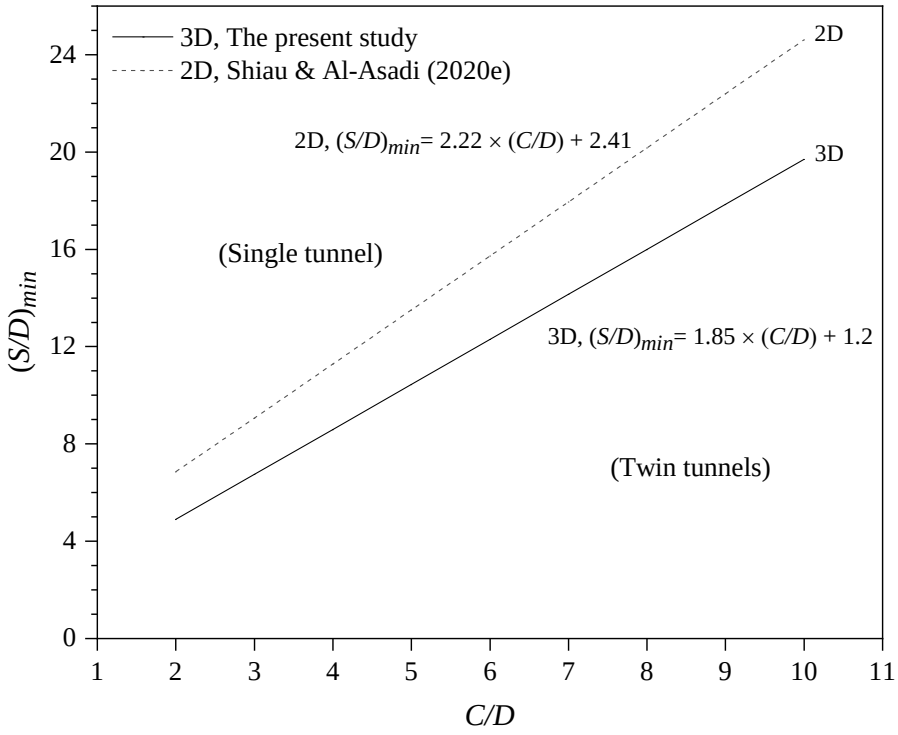

Figure 8.7. Minimum spacing ratios $(S/D)_{min}$ vs depth ratios (C/D = 2 - 10).

Also plotted in Figure 8.7 is the 2D results of Shiau & Al-Asadi (2020e) for the purpose of results comparison. It is to be noted that the minimum 2D spacing ratios $(S/D)_{min}$ are consistently greater than those of 3D by 20%-30%.

8.3.2 Discussing *FoS*

Broms and Bennermarks' critical stability number (N_c) represents a factor of safety of unity in conventional geotechnical designs. In general, the practising engineers prefer the safety factor approach as it is a familiar quantity that can be used to determine soil stability directly. Based on their 2D undrained stability analysis, Shiau and Al-Asadi (2018) proposed an equation $(FoS = N_c / N)$ to relate factors of safety to a wide range of "designed" stability number (N) for known values of N_c.

For the depth ratio of C/D = 3, Tables 8.2 - 8.3 produce the factors of safety results (*LB* and *UB*) for a broad range of "designed" stability numbers (N = - 24 + 24) and S/D using Shiau and Al-Asadi's equation.

Table 8.2. *FoS* vs *N* (*C/D* = 3 and *S/D* = 2 - 12, *LB*).

N	*S/D* (*LB*)								
	2	3	4	5	6	7	8	9	10
-24	0.401	0.412	0.423	0.434	0.443	0.445	0.445	0.445	0.445
-20	0.481	0.495	0.508	0.521	0.532	0.534	0.534	0.534	0.534
-16	0.602	0.619	0.634	0.652	0.665	0.668	0.668	0.668	0.668
-14	0.688	0.707	0.725	0.745	0.759	0.763	0.763	0.763	0.763
-13	0.741	0.761	0.781	0.802	0.818	0.822	0.822	0.822	0.822
-12	0.802	0.825	0.846	0.869	0.886	0.890	0.890	0.890	0.890
-11	0.875	0.900	0.923	0.948	0.967	0.971	0.971	0.971	0.971
-10	0.963	0.990	1.015	1.043	1.063	1.068	1.068	1.068	1.068
-9	1.070	1.100	1.128	1.159	1.181	1.187	1.187	1.187	1.187
-8	1.203	1.237	1.269	1.303	1.329	1.335	1.335	1.335	1.335
-7	1.375	1.414	1.450	1.490	1.519	1.526	1.526	1.526	1.526
-5	1.925	1.979	2.030	2.085	2.126	2.136	2.136	2.136	2.136
-4	2.407	2.474	2.538	2.607	2.658	2.671	2.671	2.671	2.671
-2	4.814	4.949	5.076	5.214	5.316	5.341	5.341	5.341	5.341
-1	9.627	9.897	10.151	10.427	10.632	10.682	10.682	10.682	10.682
-0.5	19.254	19.794	20.302	20.854	21.264	21.364	21.364	21.364	21.364
0	Infinity	Infinity	Infinity	Infinity	Infinity	Infinity	Infinity	Infinity	Infinity
0.5	19.216	19.806	20.312	20.800	21.270	21.406	21.406	21.406	21.406
1	9.608	9.903	10.156	10.400	10.635	10.703	10.703	10.703	10.703
2	4.804	4.952	5.078	5.200	5.318	5.352	5.352	5.352	5.352
4	3.203	3.301	3.385	3.467	3.545	3.568	3.568	3.568	3.568
5	2.402	2.476	2.539	2.600	2.659	2.676	2.676	2.676	2.676
7	1.373	1.415	1.451	1.486	1.519	1.529	1.529	1.529	1.529
8	1.201	1.238	1.270	1.300	1.329	1.338	1.338	1.338	1.338
9	1.068	1.100	1.128	1.156	1.182	1.189	1.189	1.189	1.189
10	0.961	0.990	1.016	1.040	1.064	1.070	1.070	1.070	1.070
11	0.873	0.900	0.923	0.945	0.967	0.973	0.973	0.973	0.973
12	0.801	0.825	0.846	0.867	0.886	0.892	0.892	0.892	0.892
13	0.739	0.762	0.781	0.800	0.818	0.823	0.823	0.823	0.823
14	0.686	0.707	0.725	0.743	0.760	0.765	0.765	0.765	0.765
16	0.601	0.619	0.635	0.650	0.665	0.669	0.669	0.669	0.669
20	0.480	0.495	0.508	0.520	0.532	0.535	0.535	0.535	0.535
24	0.400	0.413	0.423	0.433	0.443	0.446	0.446	0.446	0.446

Table 8.3. *FoS* vs *N* (*C*/*D* = 3 and *S*/*D* = 2 - 12, *UB*).

N	*S/D* (*UB*)								
	2	3	4	5	6	7	8	9	10
-24	0.424	0.436	0.449	0.460	0.471	0.473	0.473	0.473	0.473
-20	0.509	0.523	0.539	0.553	0.565	0.567	0.567	0.567	0.567
-16	0.636	0.653	0.673	0.691	0.706	0.709	0.709	0.709	0.709
-14	0.727	0.747	0.770	0.789	0.807	0.810	0.810	0.810	0.810
-13	0.782	0.804	0.829	0.850	0.869	0.873	0.873	0.873	0.873
-12	0.848	0.871	0.898	0.921	0.941	0.946	0.946	0.946	0.946
-11	0.925	0.950	0.979	1.005	1.027	1.031	1.031	1.031	1.031
-10	1.017	1.045	1.077	1.105	1.129	1.135	1.135	1.135	1.135
-9	1.130	1.162	1.197	1.228	1.255	1.261	1.261	1.261	1.261
-8	1.272	1.307	1.347	1.381	1.412	1.418	1.418	1.418	1.418
-7	1.453	1.493	1.539	1.579	1.613	1.621	1.621	1.621	1.621
-5	2.034	2.091	2.155	2.210	2.258	2.269	2.269	2.269	2.269
-4	2.543	2.614	2.694	2.763	2.823	2.837	2.837	2.837	2.837
-2	5.086	5.227	5.387	5.526	5.646	5.673	5.673	5.673	5.673
-1	10.172	10.454	10.774	11.051	11.292	11.346	11.346	11.346	11.346
-0.5	20.344	20.908	21.548	22.102	22.584	22.692	22.692	22.692	22.692
0	Infinity	Infinity	Infinity	Infinity	Infinity	Infinity	Infinity	Infinity	Infinity
0.5	20.326	20.922	21.534	22.114	22.592	22.716	22.716	22.716	22.716
1	10.163	10.461	10.767	11.057	11.296	11.358	11.358	11.358	11.358
2	5.082	5.231	5.384	5.529	5.648	5.679	5.679	5.679	5.679
4	3.388	3.487	3.589	3.686	3.765	3.786	3.786	3.786	3.786
5	2.541	2.615	2.692	2.764	2.824	2.840	2.840	2.840	2.840
7	1.452	1.494	1.538	1.580	1.614	1.623	1.623	1.623	1.623
8	1.270	1.308	1.346	1.382	1.412	1.420	1.420	1.420	1.420
9	1.129	1.162	1.196	1.229	1.255	1.262	1.262	1.262	1.262
10	1.016	1.046	1.077	1.106	1.130	1.136	1.136	1.136	1.136
11	0.924	0.951	0.979	1.005	1.027	1.033	1.033	1.033	1.033
12	0.847	0.872	0.897	0.921	0.941	0.947	0.947	0.947	0.947
13	0.782	0.805	0.828	0.851	0.869	0.874	0.874	0.874	0.874
14	0.726	0.747	0.769	0.790	0.807	0.811	0.811	0.811	0.811
16	0.635	0.654	0.673	0.691	0.706	0.710	0.710	0.710	0.710
20	0.508	0.523	0.538	0.553	0.565	0.568	0.568	0.568	0.568
24	0.423	0.436	0.449	0.461	0.471	0.473	0.473	0.473	0.473

Note that the "designed" stability number is a combination of the known design parameters such as σ_s, γ, H, σ_t, and S_u (see Equation 8.1). Graphically, these data are plotted in Figures 8.8 - 8.10 for C/D = 3 and various S/D (4, 7 and 10).

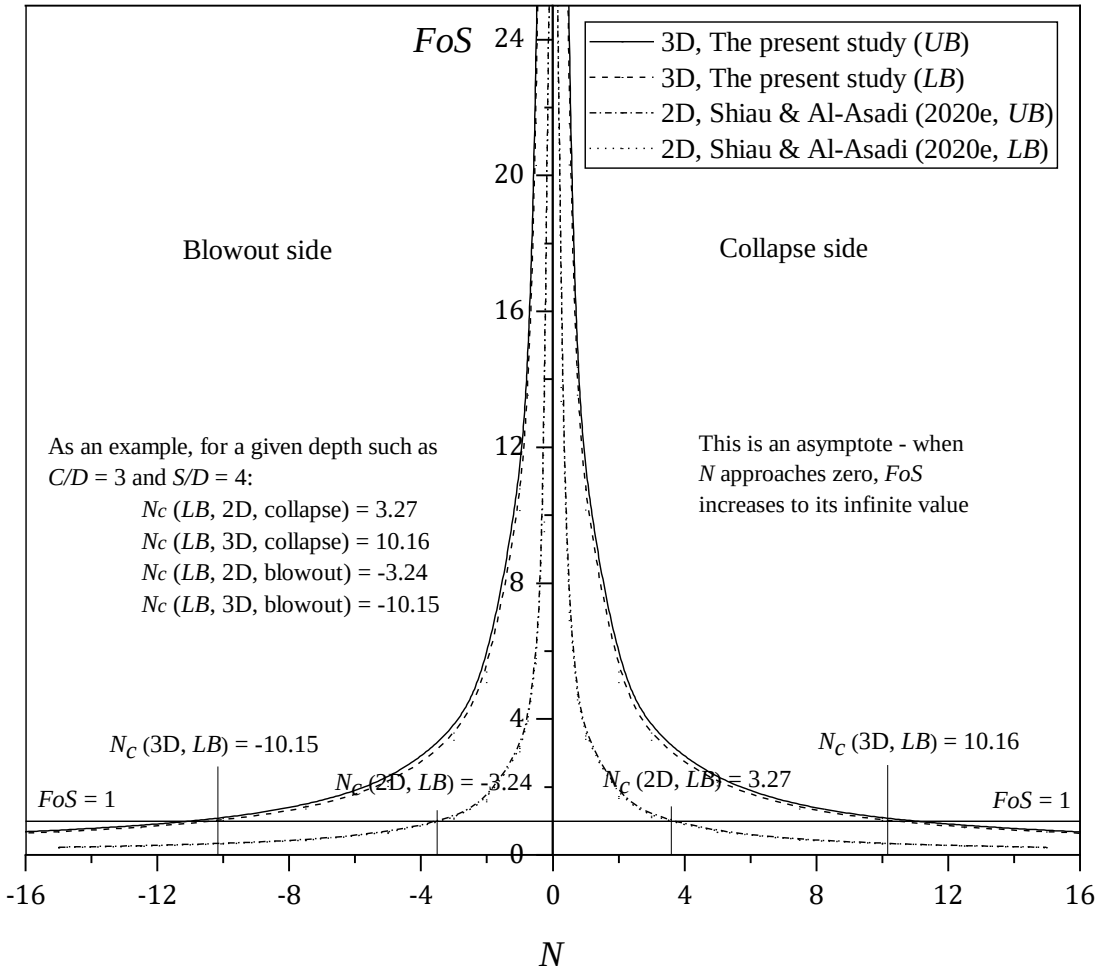

Figure 8.8. *FoS* vs *N* for *C*/*D* = 3 and *S*/*D* = 4.

It can be seen that a pair of asymptote lines exist for collapse and blowout scenarios. The curves are hyperbolic, meaning that any combination of *N* and *FoS* on this curve yields a unique N_c value. This N_c value is constant for a specific depth ratio. For the spacing ratio *S/D* = 4 (Figure 8.8), *LB* solutions give N_c = +10.16 on the collapse side and N_c = -10.15 on the blowout side. These two values can be read from the intersection points by drawing a *FoS* = 1 horizontal line on the figure.

Figures 8.8 - 8.10 also compare the current 3D results with those 2D ones in Shiau and Al-Asadi (2020e). For a given "design" *N* value, the 2D analysis produces lower factors of safety than those in 3D analysis, indicating that 2D analysis is a conservative method in comparison to the 3D analysis.

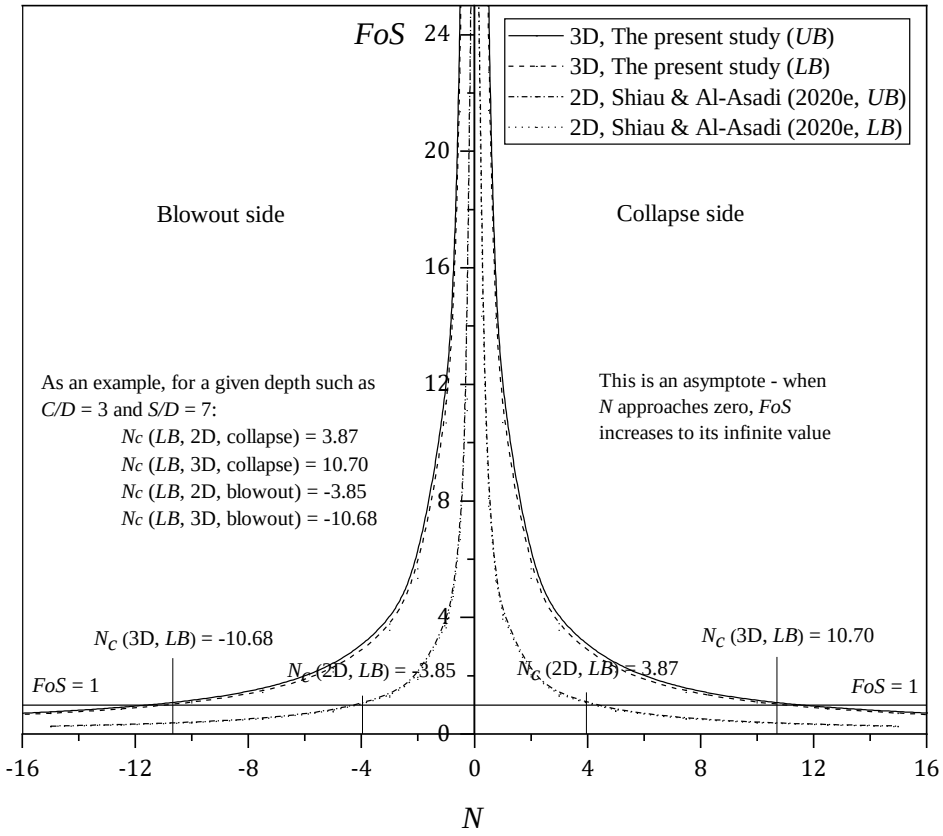

Figure 8.9. *FoS* vs *N* for *C/D* = 3 and *S/D* = 7.

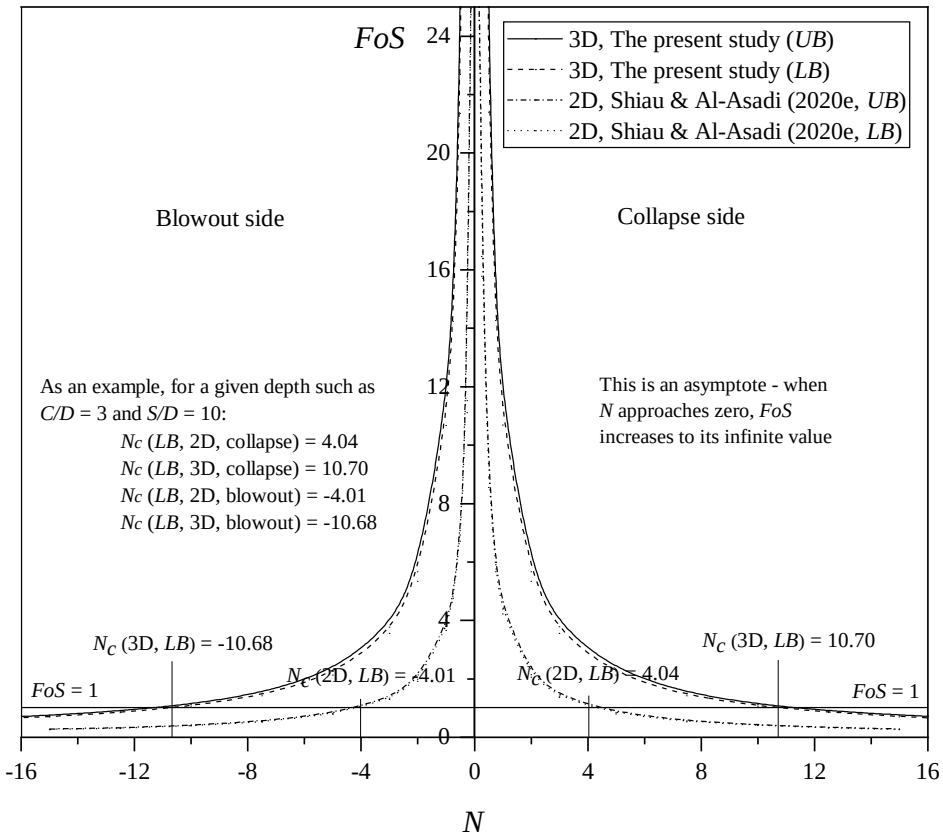

Figure 8.10. *FoS* vs *N* for *C*/*D* = 3 and *S*/*D* = 10.

8.3.3 Comparison of results

It is crucial to compare and validate N_c results obtained by the present study with those in published literature. The comparisons are necessary to ensure that findings from this paper and the conclusions drawn are relevant and reliable. To the authors' best knowledge, perhaps due to the technical difficulty in studying 3D twin tunnels, no published literature can be found in relation to the 3D heading stability of twin tunnels. It was decided that the current 3D results be compared with available 2D twin tunnel results. Figure 8.11 shows a comparison between the present 3D study and those 2D *FELA* results by Shiau and Al-Asadi (2020e).

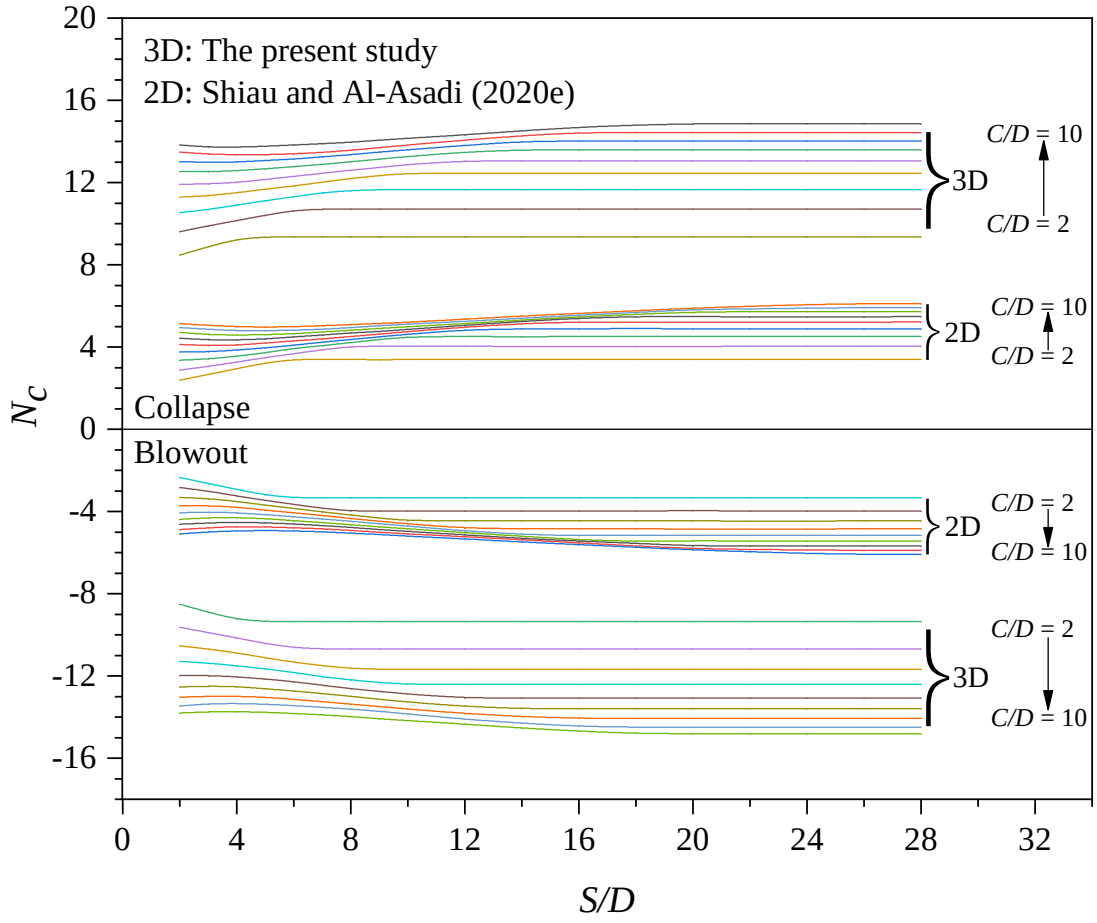

Figure 8.11. Comparison of 2D and 3D N_c results (*LB*) for various depth ratios and spacing ratios in collapse and blowout.

Figure 8.11 suggests that there is a significant variance between the 3D and 2D results. In general, the 3D stability results are approximately 2.5 fold higher than those in the 2D analysis. Noting that the use of 3D analysis produces realistic stability results, they are less conservative than 2D analysis.

Figure 8.12 shows a comparison of current 3D results with some existing 2D solutions for the depth ratio *C/D* of three. Noting that the 3D results are significantly greater than the 2D results, the variations are mostly attributed to the differences in the two types of problems. The twin tunnels are assumed to be unlined and infinitely long in the plane strain 2D analysis, while the 3D analysis of twin tunnel is for the close face heading scenario.

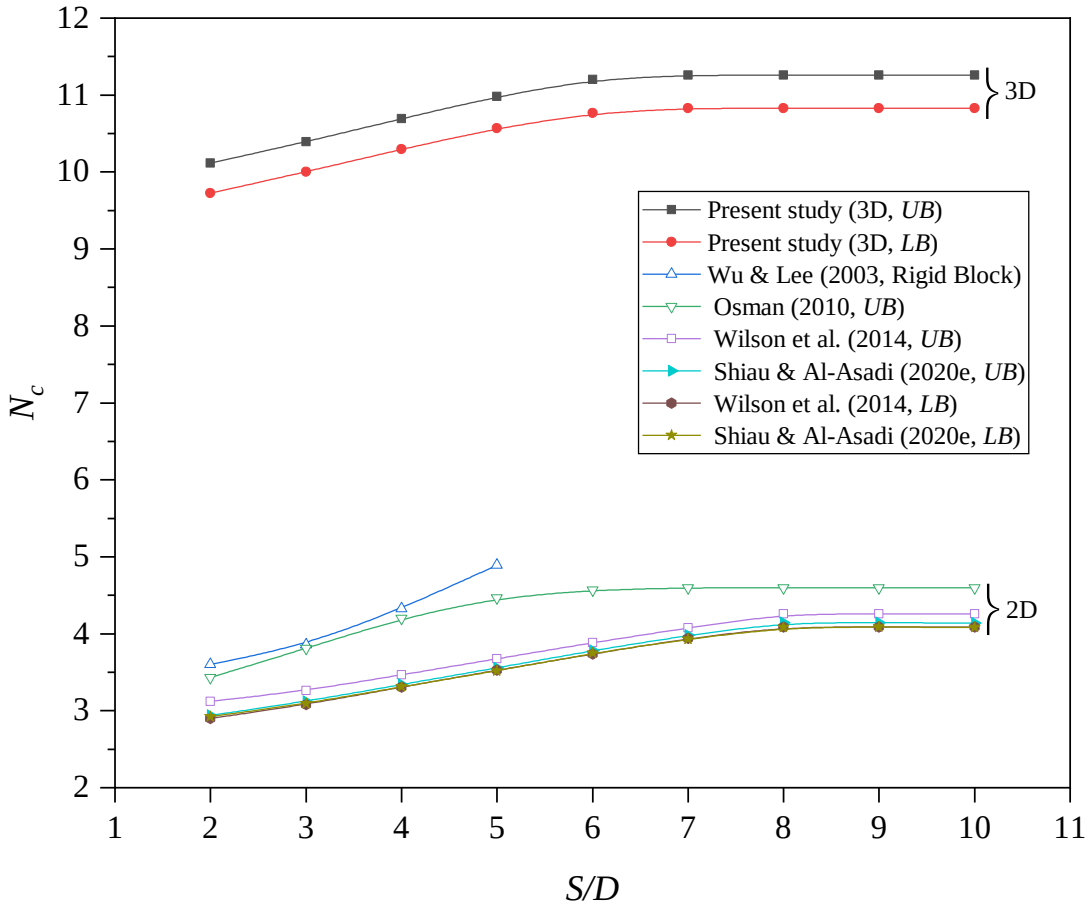

Figure 8.12. Comparison of 3D N_c results with the available 2D solutions in the literature.

Having said that, the 2D twin tunnel analysis yields conservative results in comparison with those in the 3D analysis, and it can be used in the preliminary stage of lining designs. Nevertheless, the current 3D results shall be used for the estimation of heading pressure and ground settlement during the construction stage.

8.4 Failure Mechanism

As in the previous chapter for 2D twin tunnels, shown in Figure 8.13 is asymmetrical plot of failure mechanisms using the contour of the absolute displacement $\left(|u| = \sqrt{u_x^2 + u_y^2}\right)$ for *C/D* = 2 and various spacing ratio (*S/D* = 2 - 5). These plots show the overlapping effect between the 3D tunnel headings. Note that the 3D twin tunnel effect decreases as the spacing ratio (*S/D*) increase. This effect approaches to none when there is no interaction between the tunnels (Figure 8.13d). At this point, the corresponding *S/D* is the minimum spacing ratio $(S/D)_{min}$ required to eliminate the interaction effect between the tunnels, where each tunnel behaves as a single isolated tunnel. It is interesting to see the perfect circle predicted for the ground surface failure extent in the plot. On the other hand, due to the 3D twin effects, the ground surface failure extent resembles the outline of an ellipse (Figure 8.13a, b and c).

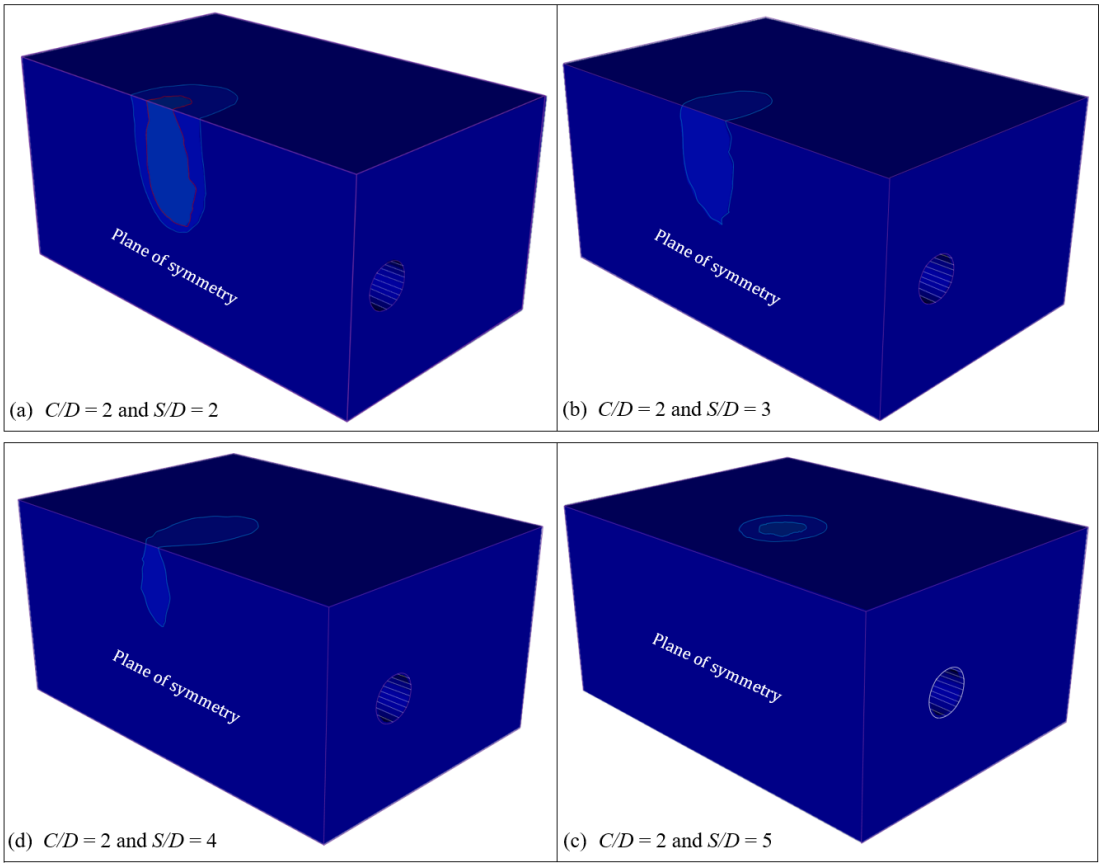

Note that the actual contour values of the plots are not important in limit analysis with the perfect plasticity theorem.

Figure 8.13. Absolute displacement ($|u|$) contour and velocity plots for *C/D* = 2 and various spacing ratio (*S/D* = 2 - 5).

8.5 An Illustrated Example

It is known that lower bound solutions provide a safe assessment of the critical stability number N_c. Therefore, the following example is based on the use of *LB* results. The design tables and equations produced in the paper can be used to estimate a safe working pressure to maintain the stability of the tunnel faces.

8.5.1 Evaluation of a twin tunnel heading stability in cohesive soil

Two side-by-side tunnels are planned to be 30 metres apart (centre-to-centre) and are assumed to be bored simultaneously.

The tunnel boring machines have a diameter (D) of 6.0m and are buried at a depth of 18m (C) in an undrained clayey soil with the soil properties S_u = 27kPa, $\phi_u = 0°$ and γ = 18 kN/m^3. The site is assumed to be a Greenfield without surface pressure ($\sigma_s = 0$).

8.5.2 To determine *FoS* for the unsupported face of the tunnel ($\sigma_t = 0$)

The dimensionless ratios are calculated as C/D = 3 and S/D = 5. With Table 8.1, it is found that the *LB* critical stability number (N_c) is approximately 10.4. Therefore,

$$FoS = N_c / N = 10.4 / ((0 + 18 \times 21 - 0) / 27) = 0.743$$

8.5.3 To determine the critical tunnel pressure to avoid collapse (*FoS* = 1)

Using (N_c = 10.4) in Equation 8.1, the minimum internal tunnel pressure to avoid collapse is $\sigma_t = \sigma_s + \gamma H - \frac{N_c \times S_u}{FoS} = 0 + 18 \times 21 - \frac{10.4 \times 27}{1} = 97.2$ kPa.

8.5.4 To determine the reduction % of N_c due to twin effects

For a depth ratio C/D = 3, the maximum stability number (N_c = 10.7) occurs at $S/D \simeq$ 7 for a single tunnel response (see Table 8.1 or Equation 8.2). For the current example with S/D = 5, the *LB* critical stability number is (N_c = 10.4). Therefore, the reduction % in the stability number due to the twin tunnel effect is approximately 2.84 %.

8.6 Conclusion

Three-dimensional heading stability of two parallel circular tunnel faces has been investigated in collapse and blowout scenarios using finite element limit analyses and Broms and Bennermarks' critical stability numbers N_c. The current numerical upper

and lower bounds of N_c are generally within a few per cents of one another, with the true solution lying between the two bounds. The critical stability number N_c, that is a function of the depth ratio C/D and the spacing ratio S/D can be used to estimate the working pressures required for a given factor of safety.

Based on the observation of the failure mechanism and the N_c results for each increase in the spacing ratio S/D, an equation was derived to calculate the critical spacing $(S/D)_{min}$ required for a single tunnel response (i.e. without overlapping effects). To the author's best knowledge, there is no published literature on the 3D heading stability investigation of twin tunnels. The presented numerical results in this paper are valuable for practical engineers.

Chapters 4-8 (Part A) have successfully studied the undrained stability of five tunnel configurations (i.e. 2D heading, 2D circle, 3D circle, 2D twin circle and 3D twin circle). Drained analysis of the five tunnel configurations using the tunnel stability factor approach is presented next in Part B (chapters 9-13).

PART B:

DRAINED ANALYSIS

(Chapters 9 - 13)

CHAPTER 9: DRAINED ANALYSIS OF 2D TUNNEL HEADING

9.1 Introduction

One of the main problems when constructing a tunnel is to ensure the stability of the tunnel heading. Ensuring tunnel face stability is directly related to the safe and successful construction of the underground structure.

This chapter discusses the stability of an idealised tunnel heading in drained soil conditions. The primary method adopted is a conventional equation based on the soil property and stability factors, analogous to the bearing capacity factors (N_c, N_s and N_γ) of strip footings. The heading is rigidly supported along its length, while the face is subjected to internal pressure, and free to move. The problem approximates a longwall in an underground excavation. This model can also be assumed to be the longitudinal section of a tunnel.

The finite element limit analysis (*FELA*) is employed to determine rigorous upper bound (*UB*) and lower bound (*LB*) solutions of stability factors (F_c, F_s and F_γ), which are functions of the depth ratio (*C/D*) and soil internal friction angle (ϕ), for a wide range of heading configurations and stability scenarios. The obtained results are compared and validated by using the finite-difference analysis as well as other available published results in the literature. A number of examples are illustrated on how to use the factors to estimate tunnel heading pressures.

9.2 Problem Definition and Modelling Technique

Finite element limit analysis is the numerical computational method of limit analysis that employs the classical plasticity theorems with the concept of finite element and mathematical programming (Sloan (2013). It is particularly powerful when upper bound (*UB*) and lower bound (*LB*) estimates are calculated together so that the true collapse load is bracketed. The difference between the two limits then provides an exact measure of the discretization error in the solution and can be used to refine the

meshes until a suitably accurate estimate of the collapse load is found. The initial developments using linear programming are in (Sloan 1988b, 1989). The newer developments are based on a much faster nonlinear programming formulation by (Lyamin & Sloan 2002b, 2002a) and Krabbenhoft et al. (2005 and 2007). The underlying bound theorems assume a rigid-perfectly plastic material with associated plasticity, i.e. the dilation angle was assumed to equal to the friction angle. The details of limit analysis and *FELA* can be found in Sloan (2013).

Recently, the *FELA* software, *OptumG2* (OptumCE 2017) has been successfully applied to solve a variety of drained and undrained stability problems in geotechnical engineering. Consequently, it was chosen in this study to compute the stability factors (F_c, F_s and F_γ) for the calculation of minimum heading support pressures by using Equation 9.1.

$$\sigma_t = -cF_c + \sigma_s F_s + \gamma D F_\gamma \tag{9.1}$$

The layout of the plane strain heading stability problem is shown in Figure 9.1. The heading has a height D and soil cover C. The ground surface is subject to a vertical surcharge σ_s. The face of the heading is free to move and is subject to normal stress (σ_t) in order to induce collapse or blowout failure (depending on the load direction).

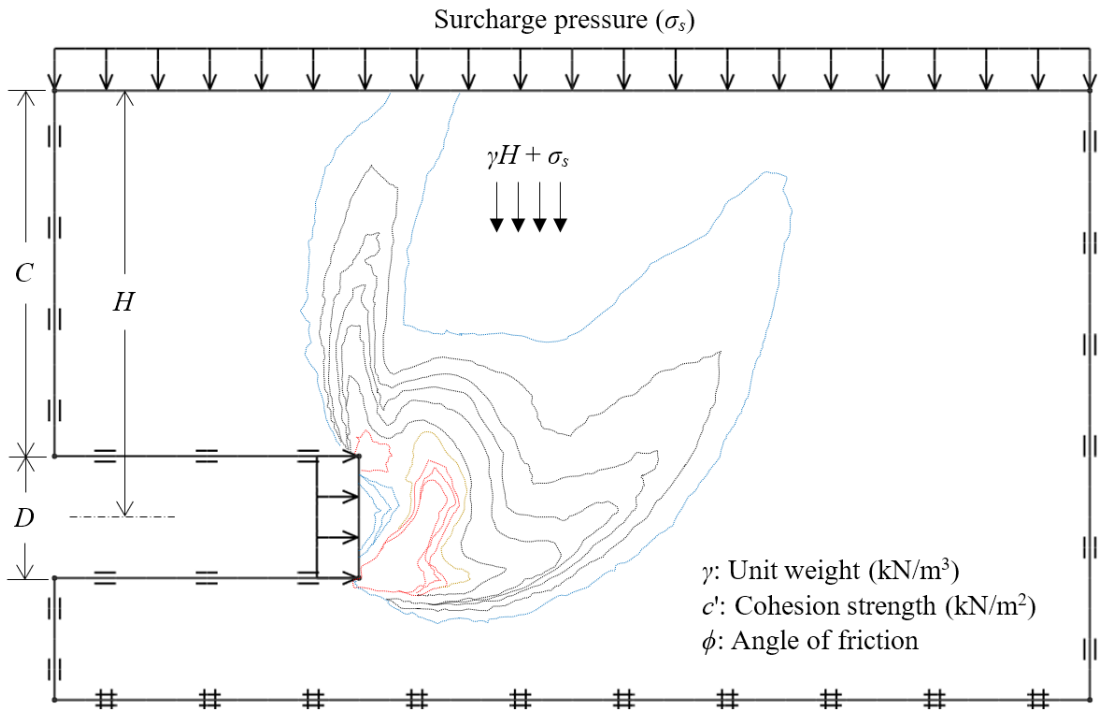

Figure 9.1. Problem definition.

The problem is similar to a longwall mining or any flat wall in an underground excavation with an infinitely long flat wall. Therefore, the assumption of 2D plane strain is valid for the analysis as, in practice, the length of the longwall mining is about 10,000 ft - 15,000 ft (Thakur 2014).

Figure 9.2 shows a typical *FELA* mesh and the boundary conditions used in the analysis. In both upper and lower bound calculations, the soil mass was discretised as triangular elements and modelled as Mohr-Coulomb material with the associated flow rule. For all analyses, 1000 to 2000 discretisation elements and three iterations for adaptive meshing were used. The boundary condition of the problem was defined such that the bottom boundary of the model was fixed in both vertical and horizontal directions, while the left and the right boundary of the problem was allowed to move only in the vertical direction. A smooth rigid lining along the tunnel length is achieved by constraining the movement in the vertical direction only.

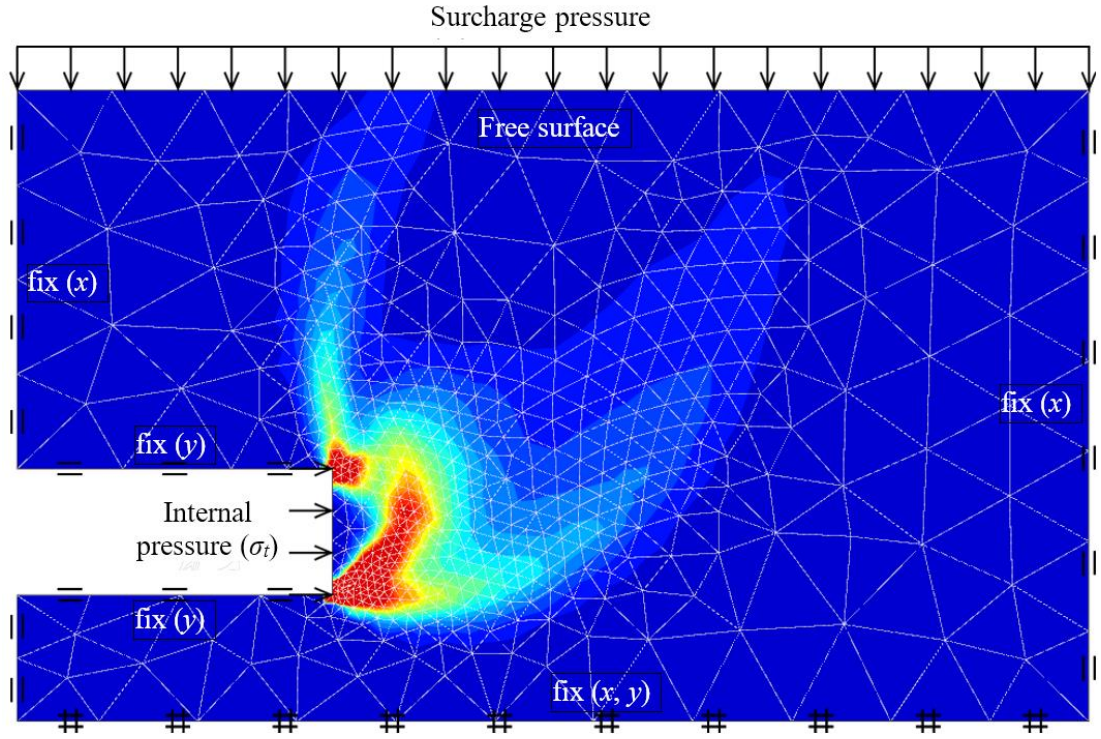

Figure 9.2. A typical adaptive mesh used for the problem.

The normal stress (i.e. internal pressure σ_t) is optimised in both upper and lower bound simulations to compute the bound solution of the stability factors (F_c, F_s and F_γ). The size of the problem domains was chosen to be large enough so that the plastic yielding zone was contained within the domain. The *UB* and *LB* solutions of the limiting pressure σ_t are solved by employing the second-order cone programming (Krabbenhøft

et al. (2007). An automatically adaptive mesh refinement was employed in both the *UB* and *LB* simulations to compute the tight *UB* and *LB* solutions. Using the load multiplier method, the numerical results of tunnel stability factors (F_c, F_s and F_γ) are obtained for tunnel heading in the cohesive-frictional soil. The principles of these calculations using Equation (9.2) are as follows.

1. To determine F_c, both $\gamma = 0$ and $\sigma_s = 0$ are used in the analysis. F_c is then calculated using the equation $\sigma_t = -c' F_c$.
2. To determine F_s, both $\gamma = 0$ and $c' = 0$ are used in the analysis. F_s is then calculated using the equation $\sigma_t = \sigma_s F_s$.
3. To determine F_γ, both $c' = 0$ and $\sigma_s = 0$ are used in the analysis. F_γ is then calculated using the equation $\sigma_t = \gamma D F_\gamma$.

Using the principle of superposition, the minimum support pressure σ_t at collapse is determined for a wide range of soil parameters (ϕ = 0˚ - 40˚) and depth ratios ($C/D = 1-10$).

9.3 Discussing the Tunnel Stability Factors (F_c, F_s and F_γ)

Numerical analyses were performed to calculate the upper bound (*UB*) and the lower bound (*LB*) limits of the stability factors (F_γ, F_s and F_c) for various depth ratios (*C/D* = 1 - 10) and angles of internal friction (ϕ = 0˚- 40˚). The obtained tunnel stability factors are presented in Tables 9.1 to 9.3 and Figures 9.3 to 9.5.

9.3.1 The stability factor for cohesion, F_c

Given no surcharge load ($\sigma_s = 0$) and an idealised weightless soil ($\gamma = 0$) a total of 820 *FELA* were performed to calculate the cohesion stability factors F_c using $F_c = -\sigma_t / c'$. Figure 9.3 shows that the greater the *C/D* value is, the greater the F_c factor is. F_c decreases as ϕ increases for all values of *C/D*. The effect of soil cohesion diminishes as the soil friction angle increases. It is interesting to see that all curves merge into a single line at approximately ϕ = 30 degree, indicating that the F_c factor is independent of *C/D* values for ϕ > 30°. Double logarithmic regression analysis was employed to develop Equation 9.2 using *LB* results. The equation has a correlation coefficient (R^2) = 0.996.

Table 9.1. F_c vs ϕ for various depth ratios (C/D = 1 - 10, ϕ = 0˚- 40˚, *UB* and *LB*).

	F_c									
	C/D = 1		C/D = 2		C/D = 3		C/D = 4		C/D = 5	
ϕ	*LB*	*UB*	*LB*	*UB*	*LB*	*UB*	*LB*	*UB*	*LB*	*UB*
0	4.178	4.326	5.236	5.496	5.963	6.260	6.509	6.844	6.920	7.295
1	4.083	4.224	5.096	5.326	5.738	6.030	6.247	6.551	6.622	6.960
2	3.992	4.131	4.944	5.153	5.562	5.797	5.996	6.276	6.352	6.638
3	3.901	4.031	4.794	4.989	5.349	5.573	5.738	6.003	6.046	6.328
4	3.794	3.935	4.636	4.823	5.137	5.351	5.504	5.731	5.775	6.025
5	3.712	3.835	4.485	4.659	4.960	5.137	5.267	5.473	5.515	5.738
6	3.624	3.739	4.342	4.496	4.761	4.929	5.032	5.226	5.256	5.456
7	3.510	3.645	4.194	4.335	4.577	4.723	4.820	4.988	5.014	5.189
8	3.441	3.548	4.045	4.179	4.392	4.526	4.608	4.757	4.779	4.930
9	3.337	3.450	3.902	4.023	4.218	4.334	4.409	4.538	4.541	4.683
10	3.255	3.354	3.764	3.873	4.041	4.147	4.200	4.323	4.328	4.450
11	3.174	3.259	3.631	3.728	3.873	3.968	4.019	4.117	4.119	4.225
12	3.071	3.164	3.501	3.584	3.712	3.794	3.835	3.923	3.924	4.011
13	2.994	3.070	3.372	3.445	3.555	3.626	3.661	3.737	3.738	3.810
14	2.898	2.977	3.240	3.310	3.406	3.465	3.495	3.559	3.563	3.619
15	2.820	2.884	3.116	3.180	3.257	3.312	3.333	3.390	3.393	3.440
16	2.723	2.794	2.999	3.052	3.120	3.165	3.183	3.229	3.227	3.270
17	2.643	2.704	2.883	2.929	2.986	3.024	3.037	3.077	3.075	3.110
18	2.565	2.616	2.770	2.811	2.860	2.891	2.900	2.933	2.932	2.960
19	2.484	2.529	2.664	2.698	2.734	2.763	2.770	2.797	2.796	2.818
20	2.403	2.445	2.559	2.588	2.618	2.642	2.647	2.669	2.666	2.685
21	2.325	2.361	2.458	2.483	2.507	2.527	2.531	2.548	2.545	2.560
22	2.247	2.279	2.361	2.382	2.401	2.417	2.420	2.434	2.432	2.443
23	2.170	2.200	2.269	2.286	2.301	2.313	2.316	2.326	2.325	2.334
24	2.095	2.123	2.179	2.194	2.205	2.215	2.217	2.225	2.224	2.231
25	2.027	2.049	2.094	2.106	2.115	2.123	2.124	2.130	2.129	2.134
26	1.953	1.976	2.013	2.022	2.029	2.035	2.036	2.040	2.039	2.043
27	1.891	1.905	1.935	1.942	1.947	1.952	1.952	1.956	1.955	1.958
28	1.823	1.837	1.860	1.866	1.870	1.873	1.874	1.876	1.876	1.878
29	1.760	1.771	1.789	1.794	1.796	1.799	1.799	1.801	1.801	1.802
30	1.698	1.707	1.721	1.725	1.727	1.729	1.729	1.730	1.730	1.731
31	1.638	1.646	1.657	1.659	1.661	1.662	1.662	1.663	1.663	1.664
32	1.581	1.587	1.595	1.597	1.598	1.599	1.599	1.600	1.599	1.600
33	1.526	1.530	1.536	1.538	1.538	1.539	1.539	1.539	1.539	1.540
34	1.472	1.476	1.480	1.481	1.481	1.482	1.482	1.482	1.482	1.482
35	1.420	1.423	1.421	1.427	1.426	1.428	1.427	1.428	1.428	1.428
36	1.371	1.373	1.375	1.376	1.376	1.376	1.376	1.376	1.376	1.376
37	1.323	1.325	1.326	1.327	1.327	1.327	1.327	1.327	1.327	1.327
38	1.277	1.279	1.279	1.280	1.280	1.280	1.280	1.280	1.280	1.280
39	1.233	1.234	1.235	1.235	1.235	1.235	1.235	1.235	1.235	1.235
40	1.190	1.191	1.192	1.192	1.192	1.192	1.192	1.192	1.192	1.192

Table 9.1. Cont'd.

	F_c									
	C/D = 6		C/D = 7		C/D = 8		C/D = 9		C/D = 10	
ϕ	*LB*	*UB*	*LB*	*UB*	*LB*	*UB*	*LB*	*UB*	*LB*	*UB*
0	7.257	7.671	7.573	7.991	7.845	8.262	8.036	8.516	8.251	8.737
1	6.934	7.295	7.208	7.581	7.442	7.822	7.617	8.038	7.820	8.237
2	6.629	6.934	6.853	7.183	7.045	7.404	7.194	7.592	7.381	7.750
3	6.282	6.582	6.508	6.806	6.685	6.995	6.836	7.154	6.977	7.303
4	5.977	6.251	6.197	6.446	6.328	6.610	6.445	6.742	6.575	6.867
5	5.686	5.930	5.868	6.098	6.006	6.237	6.104	6.353	6.222	6.451
6	5.427	5.626	5.570	5.767	5.689	5.884	5.777	5.983	5.874	6.067
7	5.154	5.336	5.273	5.453	5.386	5.553	5.449	5.639	5.534	5.709
8	4.892	5.055	4.999	5.157	5.091	5.241	5.152	5.309	5.228	5.371
9	4.659	4.789	4.741	4.878	4.817	4.944	4.879	5.002	4.925	5.050
10	4.421	4.539	4.499	4.608	4.563	4.666	4.604	4.715	4.650	4.754
11	4.205	4.303	4.267	4.359	4.316	4.405	4.349	4.446	4.389	4.478
12	3.993	4.075	4.047	4.122	4.089	4.162	4.117	4.195	4.140	4.221
13	3.795	3.864	3.836	3.902	3.871	3.932	3.893	3.961	3.920	3.981
14	3.606	3.663	3.638	3.693	3.666	3.719	3.686	3.742	3.708	3.757
15	3.427	3.474	3.454	3.500	3.477	3.520	3.494	3.537	3.509	3.550
16	3.258	3.298	3.279	3.318	3.301	3.334	3.313	3.347	3.326	3.358
17	3.102	3.132	3.119	3.148	3.133	3.161	3.143	3.171	3.152	3.179
18	2.951	2.977	2.966	2.989	2.978	2.999	2.986	3.007	2.993	3.013
19	2.811	2.831	2.823	2.841	2.832	2.849	2.837	2.855	2.844	2.859
20	2.679	2.696	2.688	2.703	2.695	2.709	2.701	2.713	2.705	2.717
21	2.555	2.569	2.563	2.574	2.568	2.578	2.572	2.582	2.575	2.584
22	2.440	2.449	2.445	2.454	2.449	2.457	2.452	2.460	2.452	2.461
23	2.331	2.338	2.335	2.341	2.338	2.344	2.340	2.346	2.342	2.347
24	2.228	2.234	2.231	2.236	2.233	2.238	2.235	2.239	2.236	2.240
25	2.132	2.136	2.134	2.138	2.136	2.139	2.137	2.140	2.138	2.141
26	2.042	2.045	2.043	2.046	2.045	2.047	2.045	2.047	2.046	2.048
27	1.957	1.959	1.958	1.960	1.959	1.960	1.960	1.961	1.960	1.961
28	1.877	1.879	1.878	1.879	1.878	1.879	1.879	1.880	1.879	1.880
29	1.802	1.803	1.802	1.803	1.802	1.803	1.803	1.803	1.803	1.804
30	1.730	1.731	1.731	1.731	1.731	1.732	1.731	1.732	1.731	1.732
31	1.663	1.664	1.664	1.664	1.664	1.664	1.664	1.664	1.664	1.664
32	1.600	1.600	1.600	1.600	1.600	1.600	1.600	1.600	1.600	1.600
33	1.539	1.540	1.540	1.540	1.540	1.540	1.540	1.540	1.540	1.540
34	1.482	1.482	1.482	1.483	1.482	1.483	1.482	1.483	1.482	1.483
35	1.428	1.428	1.428	1.428	1.428	1.428	1.428	1.428	1.428	1.428
36	1.376	1.376	1.376	1.376	1.376	1.376	1.376	1.376	1.376	1.376
37	1.327	1.327	1.327	1.327	1.327	1.327	1.327	1.327	1.327	1.327
38	1.280	1.280	1.280	1.280	1.280	1.280	1.280	1.280	1.280	1.280
39	1.235	1.235	1.235	1.235	1.235	1.235	1.235	1.235	1.235	1.235
40	1.192	1.192	1.192	1.192	1.192	1.192	1.192	1.192	1.192	1.192

Table 9.2. F_s vs ϕ for various depth ratios (C/D = 1 - 10, ϕ = 0˚- 40˚, *UB* and *LB*).

	F_s									
	C/D = 1		C/D = 2		C/D = 3		C/D = 4		C/D = 5	
ϕ	*LB*	*UB*	*LB*	*UB*	*LB*	*UB*	*LB*	*UB*	*LB*	*UB*
0	0.996	0.996	0.995	0.995	0.994	0.994	0.993	0.993	0.993	0.993
1	0.925	0.922	0.906	0.902	0.894	0.889	0.885	0.879	0.878	0.872
2	0.857	0.852	0.822	0.815	0.8	0.792	0.785	0.775	0.772	0.762
3	0.792	0.785	0.744	0.734	0.714	0.702	0.694	0.679	0.677	0.662
4	0.731	0.721	0.671	0.658	0.635	0.62	0.61	0.594	0.59	0.573
5	0.671	0.661	0.603	0.588	0.561	0.545	0.534	0.516	0.512	0.492
6	0.616	0.603	0.54	0.523	0.495	0.477	0.466	0.445	0.442	0.421
7	0.564	0.549	0.481	0.463	0.433	0.415	0.403	0.383	0.379	0.358
8	0.513	0.498	0.427	0.409	0.378	0.359	0.348	0.327	0.323	0.302
9	0.468	0.45	0.378	0.359	0.328	0.309	0.297	0.277	0.276	0.254
10	0.423	0.405	0.333	0.313	0.283	0.265	0.255	0.233	0.233	0.211
11	0.38	0.363	0.291	0.272	0.244	0.225	0.215	0.196	0.195	0.175
12	0.344	0.324	0.252	0.235	0.207	0.19	0.181	0.162	0.162	0.143
13	0.305	0.288	0.218	0.201	0.176	0.159	0.151	0.134	0.133	0.116
14	0.273	0.255	0.189	0.171	0.147	0.133	0.125	0.109	0.108	0.094
15	0.241	0.224	0.162	0.145	0.124	0.109	0.104	0.088	0.088	0.075
16	0.216	0.196	0.137	0.122	0.102	0.089	0.084	0.071	0.071	0.059
17	0.188	0.171	0.116	0.101	0.084	0.072	0.069	0.056	0.057	0.046
18	0.164	0.147	0.097	0.084	0.068	0.058	0.055	0.044	0.044	0.035
19	0.142	0.127	0.08	0.068	0.056	0.046	0.043	0.034	0.034	0.027
20	0.123	0.108	0.066	0.056	0.045	0.036	0.034	0.026	0.027	0.02
21	0.105	0.091	0.054	0.044	0.035	0.028	0.026	0.02	0.02	0.015
22	0.09	0.077	0.044	0.035	0.027	0.021	0.02	0.014	0.015	0.01
23	0.077	0.064	0.035	0.027	0.021	0.016	0.015	0.01	0.011	0.007
24	0.065	0.052	0.028	0.021	0.016	0.011	0.011	0.007	0.008	0.005
25	0.053	0.043	0.021	0.016	0.012	0.008	0.008	0.005	0.005	0.003
26	0.044	0.034	0.016	0.012	0.008	0.005	0.005	0.003	0.003	0.001
27	0.035	0.028	0.012	0.008	0.006	0.003	0.003	0.001	0.002	0
28	0.029	0.022	0.009	0.006	0.004	0.002	0.002	0.001	0.001	0
29	0.023	0.017	0.007	0.004	0.002	0.001	0.001	0	0	0
30	0.018	0.013	0.005	0.002	0	0	0	0	0	0
31	0.014	0.009	0.003	0	0	0	0	0	0	0
32	0.011	0.007	0.002	0	0	0	0	0	0	0
33	0.008	0.005	0	0	0	0	0	0	0	0
34	0.006	0.003	0	0	0	0	0	0	0	0
35	0.004	0.002	0	0	0	0	0	0	0	0
36	0.003	0	0	0	0	0	0	0	0	0
37	0	0	0	0	0	0	0	0	0	0
38	0	0	0	0	0	0	0	0	0	0
39	0	0	0	0	0	0	0	0	0	0
40	0	0	0	0	0	0	0	0	0	0

Table 9.2. Cont'd.

	F_s									
	C/D = 6		C/D = 7		C/D = 8		C/D = 9		C/D = 10	
ϕ	*LB*	*UB*	*LB*	*UB*	*LB*	*UB*	*LB*	*UB*	*LB*	*UB*
0	0.993	0.992	0.992	0.992	0.992	0.992	0.992	0.991	0.992	0.991
1	0.872	0.865	0.867	0.86	0.862	0.856	0.859	0.852	0.856	0.848
2	0.762	0.751	0.754	0.742	0.747	0.734	0.742	0.727	0.735	0.722
3	0.664	0.648	0.652	0.637	0.643	0.626	0.635	0.618	0.627	0.61
4	0.576	0.557	0.56	0.543	0.551	0.531	0.543	0.522	0.534	0.513
5	0.497	0.475	0.481	0.46	0.469	0.448	0.46	0.438	0.449	0.429
6	0.424	0.403	0.409	0.388	0.396	0.376	0.387	0.365	0.377	0.356
7	0.362	0.34	0.347	0.325	0.334	0.313	0.325	0.302	0.315	0.293
8	0.307	0.284	0.293	0.27	0.279	0.258	0.271	0.249	0.26	0.24
9	0.257	0.237	0.244	0.223	0.232	0.212	0.222	0.203	0.215	0.195
10	0.216	0.195	0.202	0.183	0.191	0.173	0.184	0.164	0.175	0.157
11	0.178	0.159	0.166	0.148	0.156	0.139	0.15	0.131	0.144	0.125
12	0.148	0.13	0.136	0.12	0.127	0.111	0.121	0.104	0.114	0.099
13	0.12	0.104	0.111	0.095	0.103	0.088	0.097	0.082	0.091	0.077
14	0.097	0.083	0.089	0.076	0.082	0.069	0.077	0.063	0.072	0.059
15	0.078	0.066	0.071	0.059	0.065	0.053	0.06	0.049	0.056	0.045
16	0.062	0.051	0.056	0.045	0.05	0.041	0.047	0.037	0.043	0.034
17	0.048	0.039	0.044	0.034	0.039	0.03	0.036	0.027	0.033	0.025
18	0.038	0.03	0.033	0.026	0.029	0.023	0.027	0.02	0.024	0.018
19	0.029	0.022	0.025	0.019	0.022	0.016	0.02	0.014	0.018	0.013
20	0.022	0.016	0.019	0.013	0.016	0.011	0.014	0.01	0.013	0.008
21	0.017	0.011	0.014	0.009	0.012	0.008	0.01	0.006	0.009	0.005
22	0.012	0.008	0.01	0.006	0.008	0.005	0.007	0.004	0.006	0.003
23	0.008	0.005	0.007	0.004	0.005	0.003	0.004	0.002	0.004	0.002
24	0.006	0.003	0.004	0.002	0.003	0.001	0.003	0.001	0.002	0
25	0.004	0.002	0.003	0.001	0.002	0	0	0	0	0
26	0.002	0	0	0	0	0	0	0	0	0
27	0	0	0	0	0	0	0	0	0	0
28	0	0	0	0	0	0	0	0	0	0
29	0	0	0	0	0	0	0	0	0	0
30	0	0	0	0	0	0	0	0	0	0
31	0	0	0	0	0	0	0	0	0	0
32	0	0	0	0	0	0	0	0	0	0
33	0	0	0	0	0	0	0	0	0	0
34	0	0	0	0	0	0	0	0	0	0
35	0	0	0	0	0	0	0	0	0	0
36	0	0	0	0	0	0	0	0	0	0
37	0	0	0	0	0	0	0	0	0	0
38	0	0	0	0	0	0	0	0	0	0
39	0	0	0	0	0	0	0	0	0	0
40	0	0	0	0	0	0	0	0	0	0

Table 9.3. F_γ vs ϕ for various depth ratios (C/D = 1 - 10, ϕ = 0˚- 40˚, *UB* and *LB*).

	F_γ									
	C/D = 1		C/D = 2		C/D = 3		C/D = 4		C/D = 5	
ϕ	*LB*	*UB*	*LB*	*UB*	*LB*	*UB*	*LB*	*UB*	*LB*	*UB*
0	1.665	1.652	2.622	2.628	3.661	3.633	4.661	4.632	5.621	5.634
1	1.571	1.556	2.444	2.441	3.364	3.331	4.246	4.208	5.101	5.079
2	1.481	1.465	2.275	2.265	3.088	3.050	3.872	3.818	4.625	4.568
3	1.395	1.378	2.115	2.098	2.830	2.789	3.506	3.452	4.171	4.097
4	1.313	1.295	1.963	1.940	2.587	2.544	3.177	3.117	3.757	3.672
5	1.238	1.217	1.820	1.794	2.367	2.316	2.885	2.811	3.382	3.283
6	1.160	1.142	1.687	1.650	2.161	2.109	2.612	2.532	3.040	2.929
7	1.087	1.070	1.555	1.519	1.972	1.915	2.359	2.275	2.724	2.607
8	1.021	1.003	1.437	1.398	1.796	1.736	2.124	2.039	2.432	2.316
9	0.958	0.939	1.326	1.284	1.634	1.573	1.916	1.824	2.168	2.052
10	0.901	0.880	1.221	1.178	1.485	1.422	1.726	1.631	1.932	1.819
11	0.845	0.823	1.123	1.080	1.347	1.283	1.543	1.451	1.717	1.606
12	0.792	0.769	1.033	0.989	1.218	1.157	1.382	1.295	1.521	1.416
13	0.741	0.718	0.948	0.904	1.101	1.042	1.237	1.153	1.350	1.248
14	0.695	0.670	0.872	0.826	0.995	0.937	1.106	1.025	1.199	1.099
15	0.649	0.624	0.797	0.754	0.901	0.843	0.988	0.911	1.059	0.965
16	0.606	0.582	0.732	0.689	0.816	0.759	0.887	0.810	0.943	0.849
17	0.565	0.542	0.670	0.628	0.736	0.684	0.793	0.722	0.835	0.753
18	0.528	0.504	0.614	0.573	0.665	0.614	0.712	0.643	0.744	0.665
19	0.492	0.469	0.561	0.522	0.604	0.554	0.637	0.575	0.663	0.590
20	0.459	0.436	0.516	0.478	0.551	0.500	0.570	0.515	0.589	0.524
21	0.429	0.406	0.472	0.437	0.499	0.454	0.514	0.462	0.527	0.471
22	0.399	0.377	0.434	0.401	0.452	0.411	0.466	0.417	0.473	0.421
23	0.373	0.351	0.400	0.368	0.412	0.375	0.420	0.377	0.429	0.380
24	0.346	0.327	0.368	0.339	0.377	0.343	0.383	0.343	0.390	0.342
25	0.323	0.304	0.339	0.312	0.346	0.314	0.352	0.313	0.355	0.312
26	0.345	0.283	0.315	0.289	0.319	0.289	0.323	0.286	0.324	0.287
27	0.282	0.264	0.290	0.267	0.293	0.267	0.295	0.264	0.298	0.265
28	0.264	0.246	0.269	0.249	0.272	0.247	0.274	0.247	0.276	0.245
29	0.247	0.231	0.251	0.230	0.252	0.229	0.254	0.228	0.256	0.227
30	0.231	0.216	0.233	0.216	0.235	0.214	0.237	0.212	0.238	0.209
31	0.217	0.203	0.218	0.201	0.219	0.200	0.221	0.198	0.222	0.195
32	0.203	0.190	0.204	0.188	0.205	0.187	0.207	0.185	0.208	0.183
33	0.191	0.178	0.191	0.177	0.192	0.175	0.194	0.173	0.195	0.171
34	0.179	0.167	0.179	0.166	0.180	0.164	0.182	0.161	0.183	0.158
35	0.168	0.158	0.169	0.156	0.169	0.154	0.171	0.152	0.172	0.146
36	0.159	0.148	0.159	0.146	0.159	0.145	0.161	0.141	0.162	0.141
37	0.150	0.139	0.150	0.138	0.150	0.136	0.152	0.133	0.153	0.132
38	0.141	0.131	0.141	0.129	0.141	0.126	0.143	0.125	0.144	0.124
39	0.133	0.123	0.133	0.122	0.133	0.118	0.135	0.117	0.135	0.115
40	0.125	0.116	0.126	0.115	0.126	0.112	0.128	0.110	0.128	0.108

Table 9.3 Cont'd.

	F_γ									
	C/D = 6		*C/D* = 7		*C/D* = 8		*C/D* = 9		*C/D* = 10	
ϕ	*LB*	*UB*	*LB*	*UB*	*LB*	*UB*	*LB*	*UB*	*LB*	*UB*
0	6.650	6.627	7.631	7.630	8.639	8.625	9.637	9.617	10.606	10.616
1	5.986	5.941	6.841	6.811	7.706	7.659	8.588	8.507	9.419	9.357
2	5.369	5.310	6.111	6.042	6.851	6.768	7.584	7.487	8.323	8.210
3	4.819	4.733	5.456	5.355	6.088	5.968	6.715	6.581	7.325	7.187
4	4.317	4.215	4.863	4.737	5.399	5.255	5.930	5.769	6.456	6.278
5	3.854	3.743	4.323	4.182	4.766	4.614	5.217	5.039	5.659	5.466
6	3.431	3.315	3.829	3.686	4.209	4.037	4.580	4.387	4.960	4.722
7	3.050	2.930	3.387	3.234	3.694	3.527	4.021	3.811	4.316	4.082
8	2.703	2.581	2.979	2.832	3.239	3.070	3.511	3.299	3.749	3.512
9	2.408	2.271	2.634	2.471	2.847	2.660	3.064	2.845	3.257	3.013
10	2.118	1.991	2.306	2.154	2.493	2.309	2.639	2.451	2.814	2.590
11	1.871	1.745	2.027	1.869	2.170	1.994	2.301	2.107	2.428	2.215
12	1.651	1.524	1.777	1.624	1.887	1.722	2.000	1.807	2.077	1.892
13	1.458	1.332	1.548	1.409	1.645	1.484	1.721	1.553	1.793	1.614
14	1.274	1.163	1.352	1.220	1.417	1.280	1.484	1.331	1.538	1.374
15	1.120	1.015	1.188	1.064	1.235	1.104	1.286	1.143	1.327	1.170
16	0.986	0.889	1.031	0.920	1.067	0.953	1.108	0.983	1.138	1.002
17	0.868	0.777	0.903	0.801	0.928	0.826	0.965	0.846	0.987	0.861
18	0.766	0.684	0.790	0.700	0.808	0.717	0.841	0.730	0.849	0.745
19	0.676	0.601	0.700	0.614	0.714	0.627	0.732	0.634	0.732	0.645
20	0.601	0.533	0.619	0.543	0.631	0.548	0.639	0.553	0.646	0.556
21	0.537	0.476	0.547	0.479	0.548	0.482	0.563	0.483	0.570	0.488
22	0.479	0.424	0.488	0.429	0.492	0.427	0.501	0.423	0.503	0.433
23	0.432	0.382	0.435	0.381	0.439	0.382	0.448	0.372	0.448	0.384
24	0.391	0.347	0.395	0.346	0.399	0.345	0.396	0.342	0.397	0.345
25	0.354	0.316	0.359	0.315	0.362	0.314	0.359	0.310	0.363	0.315
26	0.323	0.289	0.326	0.287	0.328	0.287	0.329	0.276	0.329	0.285
27	0.298	0.264	0.300	0.263	0.300	0.262	0.303	0.260	0.301	0.260
28	0.276	0.244	0.276	0.244	0.277	0.242	0.278	0.236	0.277	0.241
29	0.257	0.222	0.256	0.224	0.257	0.223	0.258	0.216	0.256	0.224
30	0.239	0.206	0.238	0.209	0.238	0.209	0.240	0.203	0.239	0.207
31	0.222	0.192	0.222	0.195	0.223	0.195	0.224	0.190	0.222	0.193
32	0.207	0.181	0.207	0.183	0.209	0.182	0.208	0.178	0.209	0.182
33	0.194	0.169	0.194	0.172	0.195	0.171	0.195	0.161	0.195	0.170
34	0.182	0.158	0.183	0.160	0.183	0.160	0.183	0.151	0.183	0.158
35	0.171	0.147	0.171	0.151	0.173	0.150	0.172	0.141	0.173	0.150
36	0.160	0.138	0.162	0.141	0.162	0.141	0.162	0.136	0.162	0.139
37	0.151	0.131	0.152	0.133	0.153	0.133	0.153	0.128	0.153	0.132
38	0.143	0.122	0.143	0.124	0.144	0.125	0.143	0.121	0.144	0.118
39	0.134	0.115	0.135	0.117	0.136	0.114	0.135	0.114	0.136	0.112
40	0.127	0.108	0.128	0.110	0.129	0.107	0.128	0.107	0.128	0.108

$$F_c = -0.24 \times \ln(C/D) + 1.11 + (-0.49 \times \ln(C/D) + 1.18) \times \ln(\tan\phi) \quad (9.2)$$

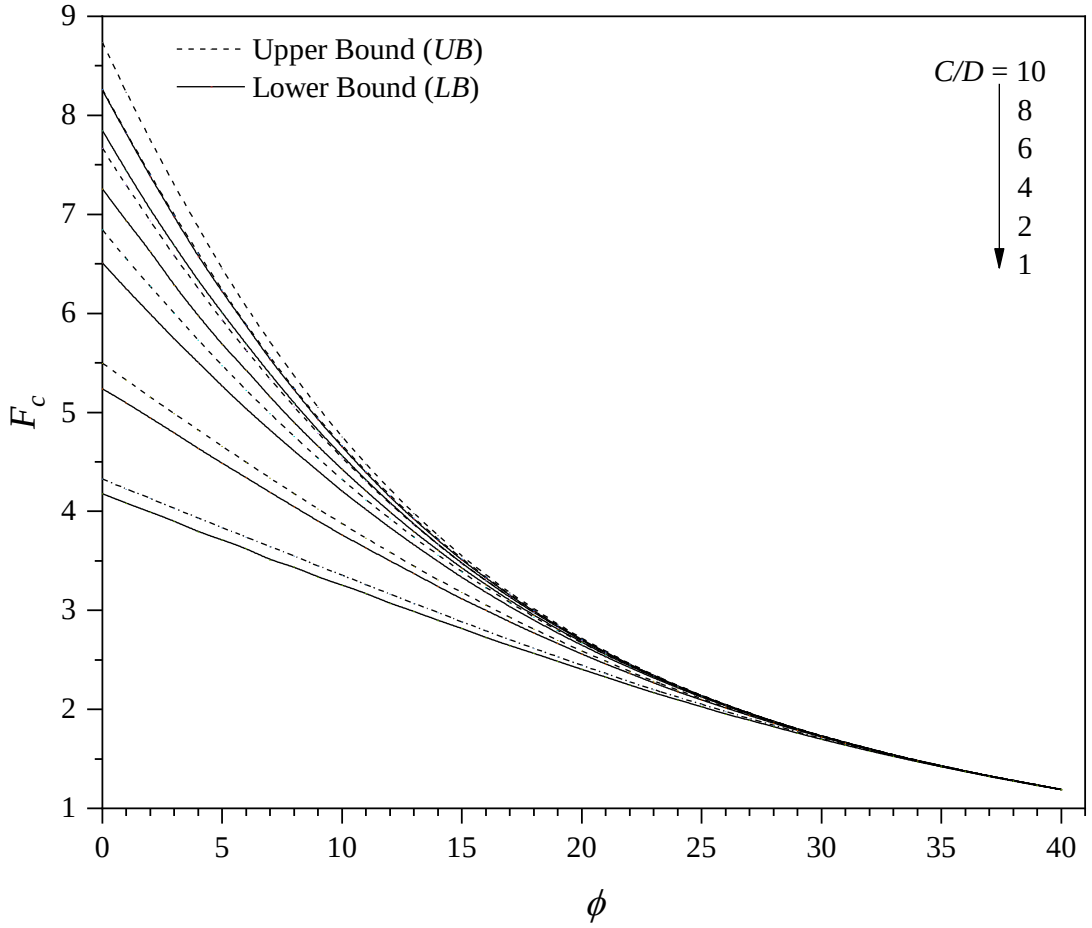

Figure 9.3. F_c vs ϕ for various depth ratios (C/D = 1 - 10, ϕ = 0˚- 40˚, *UB* and *LB*).

For ϕ > 30°, Equation 9.3 gives the best fit. This equation was obtained by using double regression analysis (power and logarithmic) with a correlation coefficient (R^2) = 0.997.

$$F_c = 1.017 \times (C/D)^{-0.008} \times (\tan\phi)^{-0.034 \times \ln(C/D) - 0.926} \quad (9.3)$$

9.3.2 The stability factor for surcharge, F_s

Given no cohesion $(c' = 0)$ and an idealised weightless soil $(\gamma = 0)$, a total of 820 *FELA* were performed to calculate the surcharge stability factors F_s using $F_s = \sigma_t / \sigma_s$. Figure 9.4 shows that the maximum value of the surcharge stability factor (F_s) is equal to one. This occurs when the internal friction angle (ϕ) of the soil is equal to zero. For such an undrained case, there is no volume loss during plastic shearing and the stability results are independent of the loading direction (Shiau & Hassan 2019; Shiau & Sams 2019). With increasing angle of internal friction ϕ, the value of F_s decreases and

merges into one line at ϕ = 35 degree where F_s approaches to zero. The surcharge pressure σ_s has very little contribution to the internal heading pressure when the value of ϕ is large.

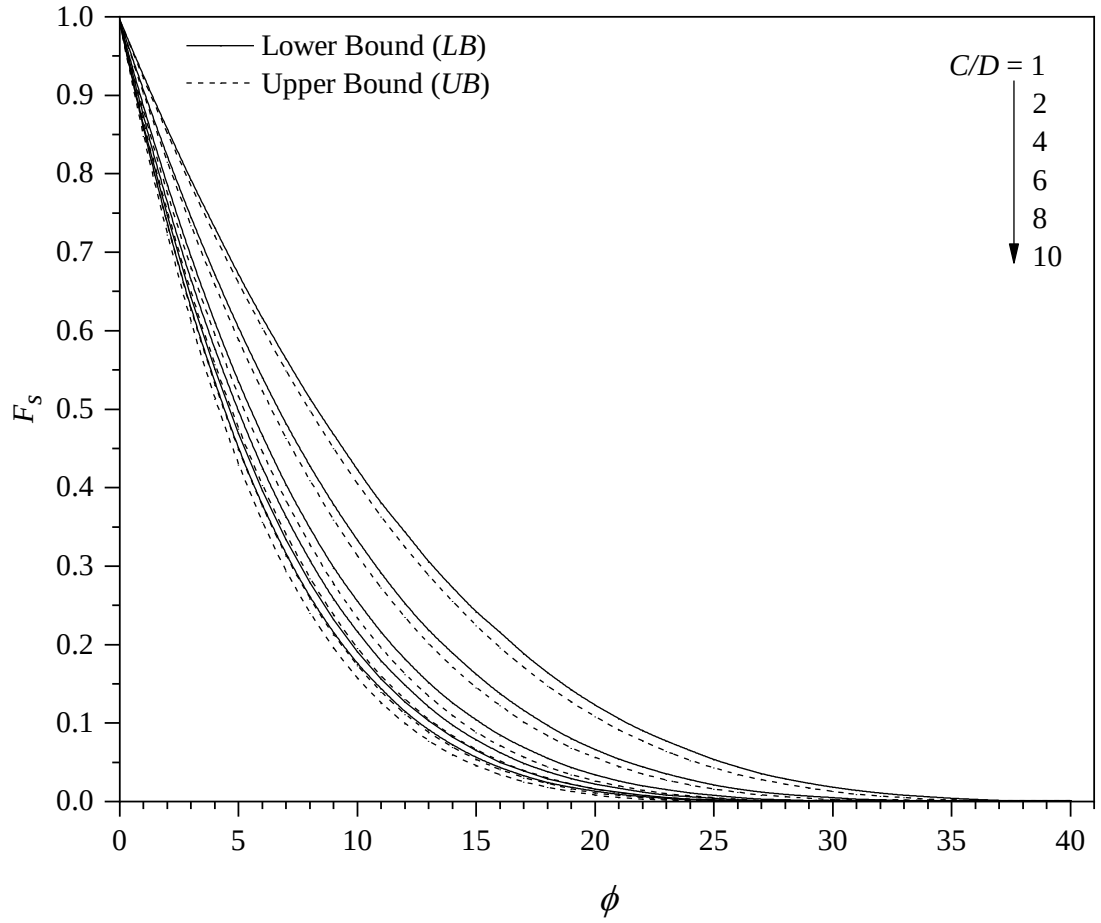

Figure 9.4. F_s vs ϕ for various depth ratios (C/D = 1 - 10, ϕ = 0˚- 40˚, *UB* and *LB*).

A double regression analysis (exponential and logarithmic) was employed to develop Equation 9.4 using *LB* results. It gives a correlation coefficient (R^2) = 0.991.

$$F_s = (0.056 \times (C/D) + 1.163) \times e^{(-3.33 \times \ln(C/D) - 5.973) \times \tan\phi} \quad (9.4)$$

9.3.3 The stability factor for unit weight, F_γ

Given no cohesion $(c' = 0)$ and no surcharge $(\sigma_s = 0)$ a total of 820 *FELA* were performed to calculate the unit weight stability factors F_γ using $F_\gamma = \sigma_t / \gamma D$.

Figure 9.5 shows that F_γ has a maximum value of (C/D + 0.5) at ϕ = 0˚ and decreases dramatically as the soil friction angle ϕ increases due to the development of soil arching.

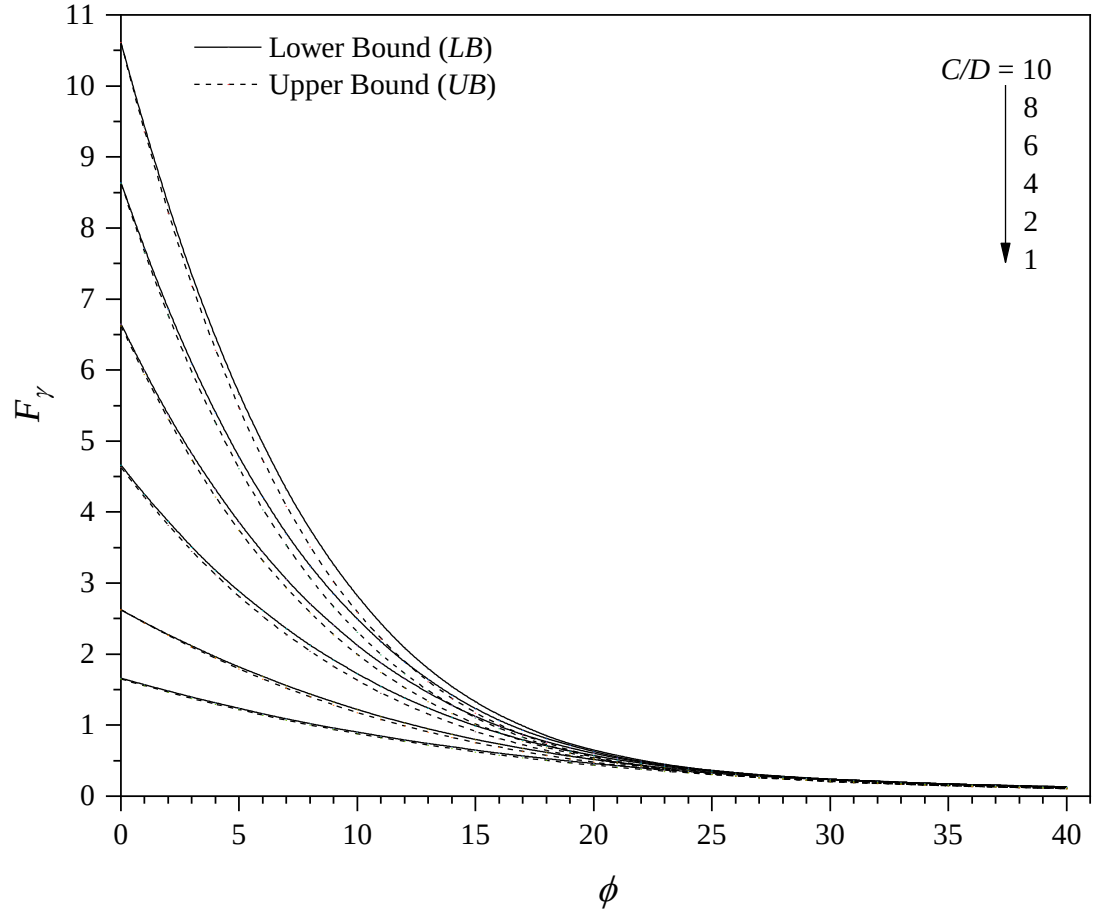

Figure 9.5. F_γ vs ϕ for various depth ratios (C/D = 1 - 10, ϕ = 0˚- 40˚, *UB* and *LB*).

The effect of unit weight (or the overburden pressure) is reduced as the soil friction angle increases due to the presence of soil arching. All *C/D* curves merge into a single line at approximately ϕ = 25 degree.

F_γ factor is independent of *C/D* for $\phi \geq 25°$. On the other note, for $\phi < 25°$, Figure 9.5 shows that the greater the *C/D* value is, the greater the F_γ factor is.

Double regression analysis (exponential and logarithmic) was employed to develop Equation 9.5 using *LB* results. It has a correlation coefficient (R^2) = 0.983.

$$F_\gamma = (-0.016 \times \ln(C/D) + 0.143) \times (\tan\phi)^{-0.347 \times \ln(C/D) + 0.994} \quad (9.5)$$

Equation 9.6 gives the best fit for $\phi \geq 25°$. This equation was obtained by using double regression analysis (power and logarithmic) with a correlation coefficient (R^2) = 0.999.

$$F_\gamma = (-0.0004 \times \ln(C/D) + 0.094) \times (\tan\phi)^{-0.059 \times \ln(C/D) + 1.635} \quad (9.6)$$

9.4 Comparison of Results

Figure 9.6 shows a comparison of the stability factor F_c with published results. The available solutions for the comparison are for $\phi > 20^{\circ}$.

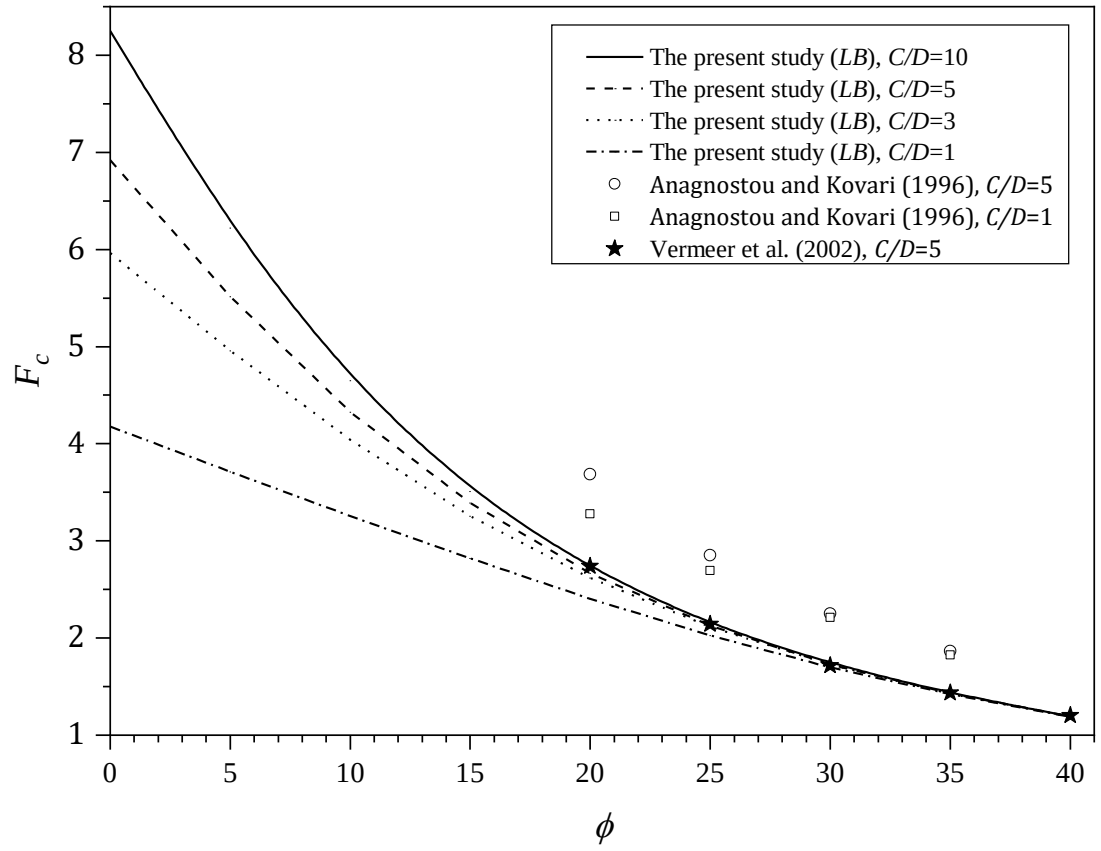

Figure 9.6. Comparison of cohesion stability factor (F_c).

The F_c results of Vermeer et al. (2002) are based on 3D finite element analysis and is only available for a depth ratio of C/D = 5. It can be seen that their results agree well with the present study of lower bound results (for $\phi > 20^{\circ}$). On the other hand, the F_c results of limit equilibrium method by Anagnostou and Kovári (1996) are significantly greater than the lower bound results for both C/D = 1 and C/D = 5. Their sliding wedge model provides an un-conservative solution for the tunnel heading problem, and hence it should be used with care in practice.

Figure 9.7 shows a comparison of the surcharge stability factor (F_s) with published results. The only available results for comparison purpose are the experimental solutions provided by Atkinson and Mair (1981).

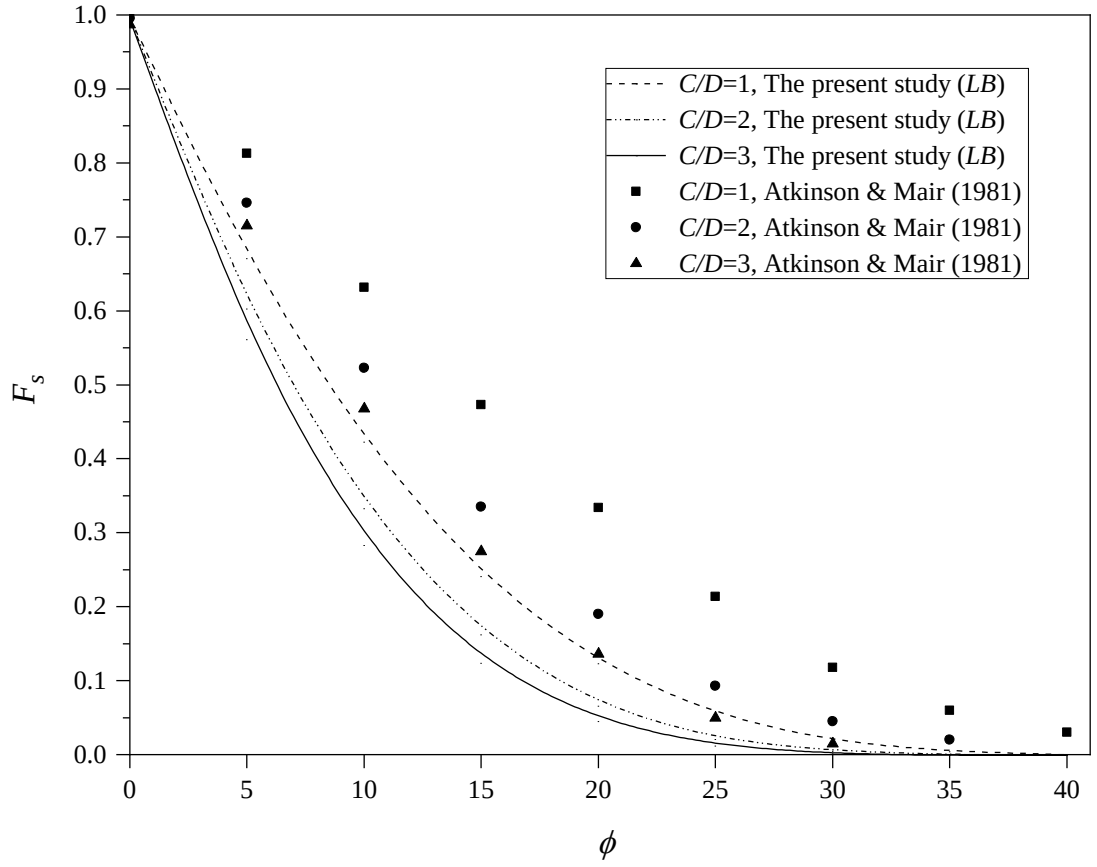

Figure 9.7. Comparison of surcharge stability factor (F_s).

They are for depth ratios of $C/D \leq 3$ and are based on model tests. Overall, there is a good agreement in the trend of all curves despite that their results are conservative

The unit weight stability factor (F_γ) were discussed by Atkinson and Potts (1977), Atkinson and Mair (1981), Leca and Dormieux (1990), Anagnostou and Kovári (1996) and Vermeer et al. (2002). It was concluded that the values of F_γ depend only on the angle of internal friction (ϕ) and are independent of the depth of the tunnel. This conclusion was merely based on the study of shallow tunnels with $\phi > 25^\circ$.

Figure 9.8 shows a comparison within this range of $\phi > 25^\circ$. It can be seen from Figure 9.8 that the results from the sliding wedge model by Anagnostou and Kovári (1996) agrees well with the present study using *FELA*. However, the results of Atkinson and Mair (1981) are located above the *FELA* results while those of Leca and Dormieux (1990) and Vermeer et al. (2002) below the *FELA* results. Note that this comparison is for $\phi > 25^\circ$.

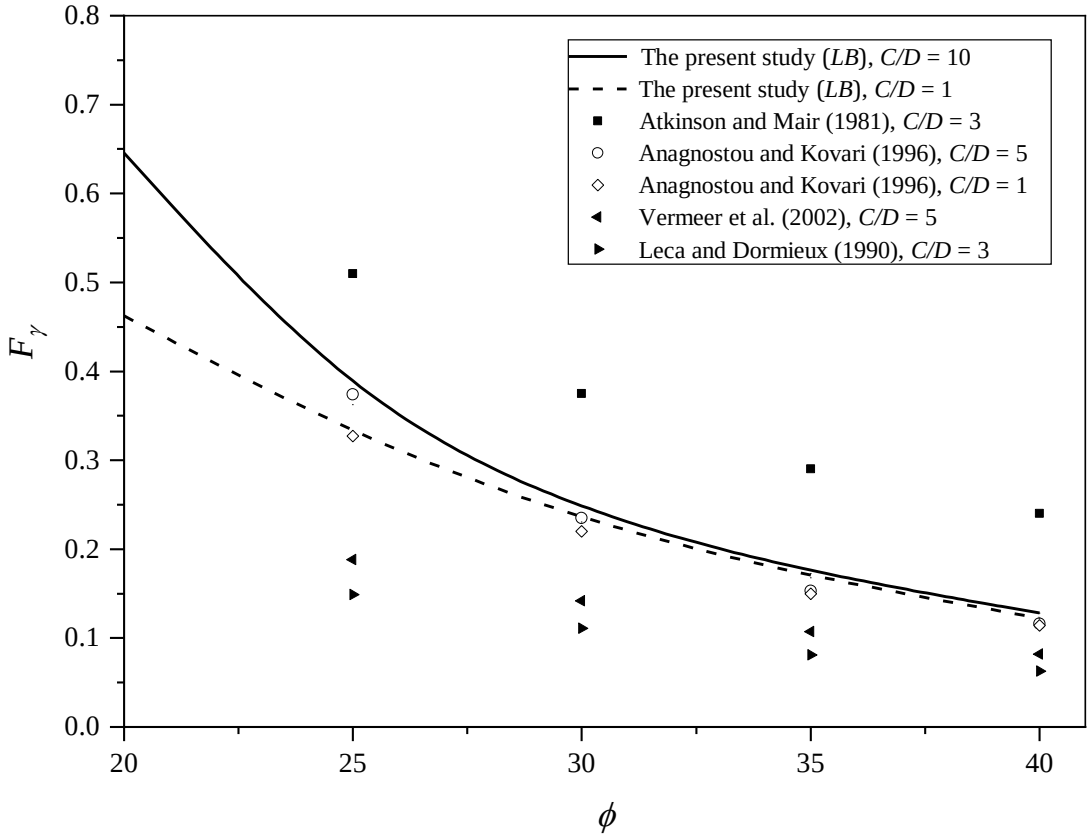

Figure 9.8. Comparison of self-weight stability factor (F_γ) (after Vermeer et al. 2002).

Interestingly, this comparison becomes insignificant were the results plotted in Figure 9.5, which covers a broad range of internal friction ($\phi = 0^\circ$- 40°) and depth ratios (C/D = 1 - 10).

9.5 Examples and practical Uses

Relying on one single numerical method is usually not convincing, and result verifications are normally required. For this purpose, the finite difference method (*FDM*) via the software package *FLAC* and the pressure relaxation method (Shiau & Kemp 2013; Shiau et al. 2014)) has also been used for comparison purpose in the following examples. Since the lower bound theorem offers a safe assessment of the limit pressure for a stability problem, Equations (9.2 to 9.6) have been derived based on *LB* results. These results can assist designers and practising engineers in the safe evaluation of tunnel heading stability.

9.5.1 Stability analysis of a tunnel heading in cohesive soil

A tunnel boring machine has a height (D) of 6.0m in cohesive material with a unit weight (γ) of 18 kN/m^3 and cohesion (c) of 45 kPa. The internal friction angle $\phi = 0^\circ$. The site is assumed to be located in a developed area, and the surface pressure (σ_s) is 40 kPa. The soil cover (C) above the tunnel boring machine is 18m. Determine the minimum support pressure (σ_t) at collapse.

- For C/D = 3 and $\phi = 0^\circ$, Tables 9.1-9.3 give LB values of F_c = 5.963, F_s = 0.994 and F_γ = 3.661, and UB values of F_c = 6.26, F_s = 0.994 and F_γ = 3.633.
- Using Equation 9.1, σ_t (LB) = 166.8 kPa and σ_t (UB) = 150.4 kPa.
- A *FELA* analysis of this case gives σ_t (LB) = 153.4 kPa and σ_t (UB) = 140.3 kPa.
- A *FDM* analysis using pressure relaxation method gives σ_t (FDM) = 143.1 kPa.
- A positive value of σ_t indicates that an internal support pressure is required to maintain tunnel stability. This belongs to the class of "active" failure. The lower bound (LB) support pressure is always greater than the upper bound (UB) one.

9.5.2 Stability analysis of a tunnel heading in cohesive-frictional soil

A planned tunnel has a height (D) of 6m and a cover depth (C) of 24m. The soil is found to be cohesive-frictional with a unit weight (γ) of 18 kN/m^3, angle of internal friction (ϕ) of 35° and cohesion (c) of 54 kPa. Determine the critical internal pressure (σ_t) when the surcharge pressure (σ_s) is zero.

- For C/D = 4 and $\phi = 35^\circ$, Tables 9.1-9.3 gives LB values of F_c = 1.427, F_s = 0.0 and F_γ = 0.171, and UB values of F_c = 1.428, F_s = 0.0 and F_γ = 0.152.
- Using Equation 9.1, σ_t (LB) = -58.59 kPa and σ_t (UB) = -60.69 kPa.
- A *FELA* analysis of this case gives σ_t (LB) = -58.7 kPa and σ_t (UB) = -60.7kPa.
- A *FDM* analysis using pressure relaxation method gives σ_t (FDM) = -59.3 kPa.
- A negative value of σ_t indicates that an internal "pulling" pressure is required in order to reach a collapsed state. In other words, the tunnel will remain stable without any internal pressure.
- This belongs to the class of "passive" failure. The upper bound (UB) pressure is always greater than the lower bound (LB) one.

9.5.3 Stability analysis of a tunnel heading in cohesionless soil

It is proposed to excavate a tunnel in greenfield conditions (σ_s = 0) through a cohesionless soil (c = 0 kPa, ϕ = 35˚ and γ = 18 kN/m^3). The tunnel has a height (D) of 6m and a soil cover (C) of 18 m. Determine the critical internal support pressure.

- For the greenfield condition (σ_s = 0) with C/D = 3 and ϕ = 35˚, Table 9.3 gives LB value of F_γ = 0.169 and UB value of F_γ = 0.154.
- Using Equation 9.2, σ_t (LB) = 18.25 kPa and σ_t (UB) = 16.63 kPa.
- A *FELA* analysis of this case gives σ_t (LB) = 18.27 kPa and σ_t (UB) = 16.67 kPa.
- A *FDM* analysis using pressure relaxation method gives σ_t (FDM) = 16.59 kPa.
- In cohesionless soil, a positive internal pressure σ_t (support pressure) is always required to maintain tunnel stability and prevent collapse regardless of the value of the internal friction (ϕ).

9.6 Conclusion

In order to study the face stability of tunnel heading in cohesive-frictional soils, numerical simulations through finite element limit analyses were performed. A series of parametric studies for different soils (ϕ = 0˚- 40˚) and various depth ratios (C/D = 1 - 10) were studied to calculate the tunnel stability factors (F_c, F_s and F_γ). Examples were illustrated on how to use the factors to estimate limit support pressures, and they were favourably compared with those obtained from the pressure relaxation method using finite difference method. The following conclusions are drawn:

1. Unlike the traditional bearing capacity factors (N_c, N_s and N_γ), the tunnel stability factors (F_c, F_s and F_γ) are functions of the soil friction angle ϕ and the depth ratio (C/D).
2. The cohesion stability factor (F_c) increases as the depth ratio (C/D) increases, but it decreases as the soil friction angle ϕ increases. The F_c curves for various C/D merge into a single line at approximately ϕ = 30˚.
3. The surcharge stability factor (F_s) decreases nonlinearly as the soil friction angle ϕ increases. F_s has a maximum value of one at ϕ = 0˚ and a minimum value of zero at approximately ϕ = 35˚ for all depth ratios (C/D). In general, the effect of

surcharge load (σ_s) diminishes as the soil friction angle increases due to the development of soil arching.

4. The unit weight stability factor (F_γ) increases as the depth ratio (C/D) increases. F_γ has a maximum value of (C/D + 0.5) at $\phi = 0^\circ$ and decreases dramatically as the soil friction angle ϕ increases due to the development of soil arching. The F_γ curves merge into a single line at approximately $\phi = 25^\circ$.

The finite element limit analysis is useful as both upper and lower bounds are calculated and they bracket the actual collapse load from above and below, which provides confidence to the end-users in using the design tables, equations and charts.

Using the novel tunnel stability factor approach, 2D single circular tunnels are studied next in Chapter 10.

CHAPTER 10: DRAINED ANALYSIS OF 2D SINGLE CIRCULAR TUNNEL

10.1 Introduction

Chapter 9, the stability of plane strain tunnel heading was addressed. This chapter discusses another stability problem of an idealised circular tunnel in drained soil conditions. The problem approximates the stability of a very long unlined circular tunnel, to determine the radial pressure a cylindrical tunnel shield must resist. This case is equivalent to a long cylindrical cavity. Failure of the tunnel in collapse is initiated by different combinations of overburden pressure and internal radial pressure.

The focus of this chapter is to assess the stability of unlined circular tunnel problem by using stability factors (F_c, F_s and F_γ) for the calculation of minimum radial support pressures to achieve stability. The primary method adopted in the analyses is a conventional equation based on the soil property and stability factors, analogous to the bearing capacity factors (N_c, N_s and N_γ) of strip footings.

The finite element limit analysis (*FELA*) is employed to determine rigorous upper bound (*UB*) and lower bound (*LB*) solutions of stability factors (F_c, F_s and F_γ), which are functions of the depth ratio (*C/D*) and soil internal friction angle (ϕ). The obtained results are compared and validated by using the available published results in the literature. A number of examples are illustrated on how to use the factors to estimate internal tunnel support pressures.

10.2 Problem Definition and Methodology

Finite element limit analysis is the numerical computational method of limit analysis that employs the classical plasticity theorems with the concept of finite element and mathematical programming (Sloan (2013). It is particularly powerful when upper bound (*UB*) and lower bound (*LB*) estimates are calculated together so that the true collapse load is bracketed. The difference between the two limits then provides an exact measure of the discretisation error in the solution and can be used to refine the

meshes until a suitably accurate estimate of the collapse load is found (Lyamin & Sloan 2002b, 2002a). The initial developments using linear programming are in (Sloan 1988b, 1989). The newer developments are based on a much faster nonlinear programming formulation by (Lyamin & Sloan 2002b, 2002a) and (Krabbenhøft et al. 2005; Krabbenhøft et al. 2007). The underlying bound theorems assume a rigid-perfectly plastic material with associated plasticity, i.e. the dilation angle was assumed to equal to the friction angle. The details of limit analysis and *FELA* can be found in Sloan (2013). Recently, the *FELA* has been successfully applied to solve a variety of drained and undrained stability problems in geotechnical engineering (Keawsawasvong & Ukritchon 2017; Ukritchon & Keawsawasvong 2017; Shiau & Al-Asadi 2020a, 2020b, 2020c). Consequently, *OptumG2* (OptumCE 2017) was chosen in this study to compute the stability factors F_c, F_s and F_γ for the calculation of minimum heading support pressures by using Equation 10.1.

$$\sigma_t = -cF_c + \sigma_s F_s + \gamma D F_\gamma \tag{10.1}$$

The layout of the plane strain heading stability problem is shown in Figure 10.1. The tunnel has a diameter (D), cover depth (C) above its crown and axis depth (H) below the ground surface. The ground surface is horizontal and subject to a vertical surcharge (σ_s), while the normal internal pressure of the tunnel is (σ_t).

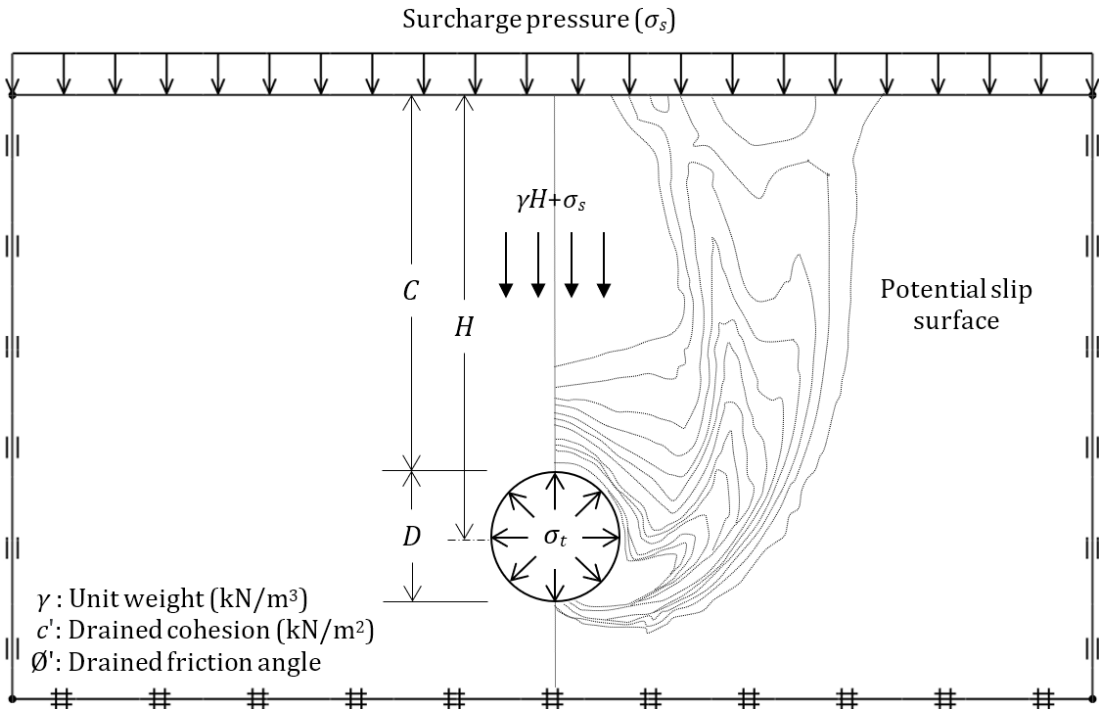

Figure 10.1. Problem Definition.

Because the geometry of the problem is assumed to be a very long unlined circular tunnel, a plane strain condition was adopted (Shiau & Sams 2019).

Figure 10.2 shows a typical *FELA* mesh used in the analysis. In both upper and lower bound calculations, the soil mass was discretised as triangular elements and modelled as Mohr-Coulomb material with the associated flow rule.

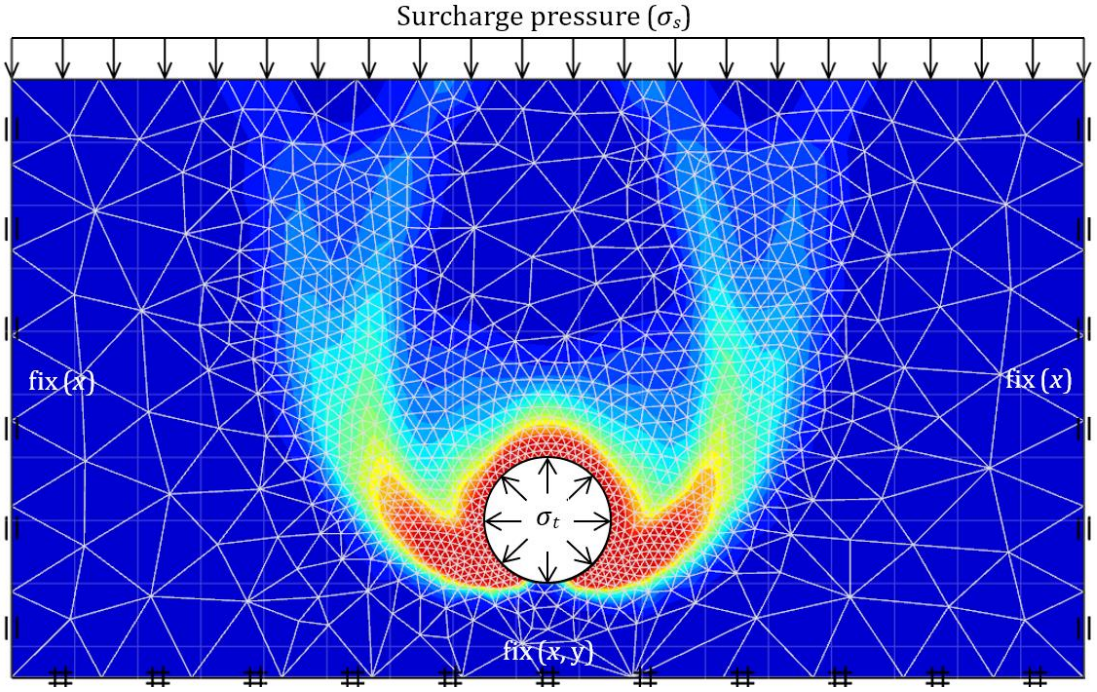

Figure 10.2. Numerical model, boundary condition and adaptive mesh for *OptumG2*.

The boundary condition of the problem was defined such that the bottom boundary of the model was fixed in both vertical and horizontal directions, while the left and the right boundary of the problem was allowed to move only in the vertical direction.

The size of the problem domains was chosen to be large enough so that the plastic yielding zone was contained within the domain. The *UB* and *LB* solutions of the limiting pressure σ_t are solved by employing the second-order cone programming (Krabbenhøft et al. (2007).

An automatically adaptive mesh refinement was employed in both the *UB* and *LB* simulations to compute the tight *UB* and *LB* solutions. Using the load multiplier method, the numerical results of tunnel stability factors (F_c, F_s and F_γ) are obtained for estimating the minimum support pressure (σ_t) at collapse.

10.3 Results and Discussion

Wide ranges of tunnel cover-to-diameter ratios (*C/D* = 1 - 10) and angles of internal friction (ϕ = 0˚- 40˚) have been studied. The obtained results of the stability factors (F_c, F_s and F_γ) are presented in Tables 10.1 to 10.6 and Figures 10.3 to 10.5.

For all stability factors (F_c, F_s and F_γ) presented in this study, there are good agreements between the upper and the lower bounds results, and the limits of each stability factor are within a few percentages from each other.

As discussed in Sloan (2013), using both upper bound and lower bound of the finite element limit analysis, it is not difficult to explore the modelling error from the other sources of error, and the real solution can be estimated with high accuracy.

10.3.1 The stability factor for cohesion, F_c

Assuming no surface load ($\sigma_s = 0$) and a weightless soil ($\gamma = 0$) equation 10.1 reduces to $\sigma_t = -c' F_c$. Using a constant value of cohesion *c*, a total of 820 *FELA* runs was conducted to obtain the upper and lower bounds results of σ_t. The cohesion stability factor (F_c) is then calculated as $F_c = -(\sigma_t / c')$. This is done for (ϕ = 0˚- 40˚) and (*C/D* = 1 - 10), as shown in Tables 10.1 and 10.2 and Figure 10.3.

Table 10-1.F_c vs ϕ (LB) for various depth ratios (C/D = 1 - 10).

ϕ	C/D (F_c, LB)									
	1	2	3	4	5	6	7	8	9	10
0	2.412	3.411	4.079	4.555	4.931	5.281	5.559	5.799	6.028	6.211
1	2.399	3.357	3.980	4.453	4.800	5.112	5.372	5.602	5.797	5.977
2	2.380	3.310	3.898	4.336	4.670	4.955	5.187	5.398	5.576	5.741
3	2.352	3.255	3.818	4.226	4.532	4.800	5.017	5.206	5.371	5.511
4	2.335	3.207	3.731	4.104	4.401	4.641	4.839	5.017	5.163	5.295
5	2.320	3.137	3.645	3.997	4.269	4.490	4.678	4.823	4.957	5.081
6	2.296	3.089	3.558	3.888	4.136	4.337	4.503	4.643	4.763	4.860
7	2.268	3.028	3.476	3.779	4.007	4.188	4.334	4.467	4.577	4.658
8	2.244	2.969	3.384	3.667	3.875	4.045	4.178	4.289	4.388	4.467
9	2.225	2.913	3.297	3.56	3.746	3.893	4.014	4.121	4.205	4.282
10	2.203	2.850	3.211	3.456	3.627	3.762	3.868	3.957	4.033	4.097
11	2.174	2.792	3.126	3.34	3.498	3.622	3.720	3.795	3.863	3.918
12	2.145	2.734	3.041	3.237	3.376	3.490	3.570	3.645	3.702	3.750
13	2.119	2.673	2.955	3.134	3.264	3.357	3.430	3.494	3.543	3.587
14	2.090	2.612	2.871	3.035	3.148	3.232	3.295	3.352	3.395	3.430
15	2.062	2.548	2.784	2.934	3.035	3.107	3.165	3.213	3.251	3.282
16	2.029	2.486	2.703	2.837	2.924	2.987	3.039	3.078	3.110	3.138
17	1.999	2.425	2.619	2.740	2.815	2.875	2.916	2.952	2.978	3.001
18	1.966	2.365	2.537	2.643	2.712	2.761	2.799	2.828	2.851	2.870
19	1.934	2.302	2.459	2.553	2.613	2.655	2.687	2.711	2.729	2.744
20	1.902	2.24	2.379	2.465	2.515	2.551	2.577	2.598	2.614	2.627
21	1.870	2.179	2.308	2.377	2.421	2.451	2.473	2.491	2.503	2.513
22	1.833	2.117	2.233	2.292	2.330	2.355	2.374	2.388	2.398	2.406
23	1.800	2.057	2.159	2.210	2.242	2.263	2.279	2.289	2.298	2.305
24	1.764	1.998	2.085	2.130	2.156	2.175	2.187	2.197	2.203	2.209
25	1.727	1.938	2.016	2.054	2.075	2.09	2.101	2.108	2.113	2.117
26	1.690	1.883	1.948	1.979	1.998	2.009	2.018	2.023	2.028	2.031
27	1.652	1.825	1.882	1.908	1.922	1.932	1.939	1.943	1.946	1.949
28	1.618	1.769	1.816	1.838	1.851	1.858	1.863	1.867	1.869	1.871
29	1.580	1.713	1.754	1.772	1.782	1.788	1.791	1.794	1.796	1.797
30	1.541	1.659	1.693	1.708	1.715	1.720	1.723	1.725	1.727	1.727
31	1.504	1.606	1.635	1.646	1.652	1.656	1.658	1.659	1.660	1.661
32	1.465	1.554	1.578	1.586	1.591	1.594	1.596	1.597	1.598	1.598
33	1.427	1.503	1.523	1.530	1.534	1.536	1.537	1.538	1.538	1.538
34	1.390	1.455	1.47	1.475	1.478	1.480	1.481	1.481	1.481	1.482
35	1.351	1.407	1.419	1.423	1.425	1.426	1.427	1.427	1.427	1.428
36	1.314	1.360	1.370	1.373	1.374	1.375	1.376	1.376	1.376	1.376
37	1.276	1.315	1.322	1.325	1.326	1.326	1.326	1.327	1.327	1.327
38	1.239	1.271	1.277	1.278	1.279	1.279	1.280	1.280	1.280	1.280
39	1.202	1.228	1.233	1.234	1.234	1.235	1.235	1.235	1.235	1.235
40	1.166	1.187	1.190	1.191	1.191	1.192	1.192	1.192	1.192	1.192

Table 10-2. F_c vs ϕ (*UB*) for various depth ratios (*C/D* = 1 - 10).

ϕ	*C/D* (F_c, *UB*)									
	1	2	3	4	5	6	7	8	9	10
0	2.443	3.469	4.144	4.65	5.052	5.389	5.675	5.925	6.148	6.349
1	2.426	3.415	4.058	4.533	4.909	5.220	5.486	5.717	5.921	6.104
2	2.406	3.361	3.971	4.418	4.767	5.055	5.300	5.509	5.696	5.863
3	2.386	3.306	3.883	4.301	4.628	4.892	5.114	5.308	5.478	5.627
4	2.366	3.249	3.795	4.185	4.487	4.731	4.935	5.110	5.262	5.398
5	2.345	3.192	3.707	4.070	4.348	4.571	4.757	4.916	5.052	5.174
6	2.322	3.134	3.617	3.955	4.212	4.414	4.583	4.726	4.849	4.958
7	2.299	3.074	3.529	3.841	4.076	4.260	4.412	4.541	4.651	4.748
8	2.276	3.015	3.439	3.728	3.942	4.110	4.246	4.359	4.458	4.543
9	2.250	2.955	3.350	3.615	3.811	3.961	4.083	4.185	4.271	4.346
10	2.225	2.892	3.261	3.505	3.681	3.816	3.925	4.014	4.091	4.157
11	2.199	2.830	3.172	3.394	3.553	3.674	3.771	3.851	3.917	3.974
12	2.171	2.769	3.084	3.286	3.429	3.536	3.621	3.690	3.748	3.798
13	2.143	2.707	2.996	3.179	3.306	3.401	3.476	3.537	3.586	3.629
14	2.114	2.643	2.909	3.073	3.187	3.271	3.336	3.389	3.431	3.467
15	2.084	2.580	2.822	2.970	3.071	3.144	3.200	3.245	3.282	3.313
16	2.054	2.517	2.737	2.869	2.957	3.021	3.069	3.108	3.139	3.165
17	2.022	2.453	2.653	2.769	2.847	2.902	2.944	2.976	3.002	3.024
18	1.989	2.391	2.570	2.673	2.740	2.788	2.823	2.850	2.872	2.890
19	1.957	2.327	2.488	2.578	2.636	2.677	2.706	2.729	2.747	2.762
20	1.923	2.264	2.408	2.486	2.536	2.570	2.595	2.614	2.628	2.640
21	1.889	2.201	2.329	2.397	2.439	2.468	2.488	2.504	2.516	2.525
22	1.854	2.139	2.252	2.310	2.346	2.370	2.386	2.399	2.408	2.416
23	1.818	2.077	2.176	2.226	2.256	2.275	2.289	2.299	2.307	2.313
24	1.781	2.016	2.102	2.144	2.169	2.185	2.196	2.204	2.210	2.215
25	1.745	1.956	2.030	2.066	2.086	2.099	2.108	2.114	2.119	2.122
26	1.707	1.897	1.960	1.990	2.006	2.017	2.023	2.028	2.032	2.034
27	1.670	1.838	1.892	1.916	1.930	1.938	1.943	1.947	1.950	1.952
28	1.632	1.780	1.826	1.846	1.856	1.863	1.867	1.870	1.872	1.873
29	1.593	1.724	1.762	1.778	1.786	1.791	1.794	1.796	1.798	1.799
30	1.555	1.669	1.700	1.713	1.719	1.723	1.725	1.727	1.728	1.729
31	1.516	1.615	1.640	1.650	1.655	1.658	1.660	1.661	1.662	1.662
32	1.477	1.562	1.582	1.590	1.594	1.596	1.597	1.598	1.599	1.599
33	1.438	1.510	1.527	1.533	1.536	1.537	1.538	1.538	1.539	1.539
34	1.399	1.460	1.473	1.478	1.480	1.481	1.481	1.482	1.482	1.482
35	1.360	1.411	1.421	1.425	1.426	1.427	1.427	1.428	1.428	1.428
36	1.322	1.364	1.372	1.374	1.375	1.376	1.376	1.376	1.376	1.376
37	1.283	1.318	1.324	1.326	1.326	1.327	1.327	1.327	1.327	1.327
38	1.246	1.273	1.278	1.279	1.279	1.280	1.280	1.280	1.280	1.280
39	1.208	1.230	1.233	1.234	1.235	1.235	1.235	1.235	1.235	1.235
40	1.171	1.189	1.191	1.191	1.192	1.192	1.192	1.192	1.192	1.192

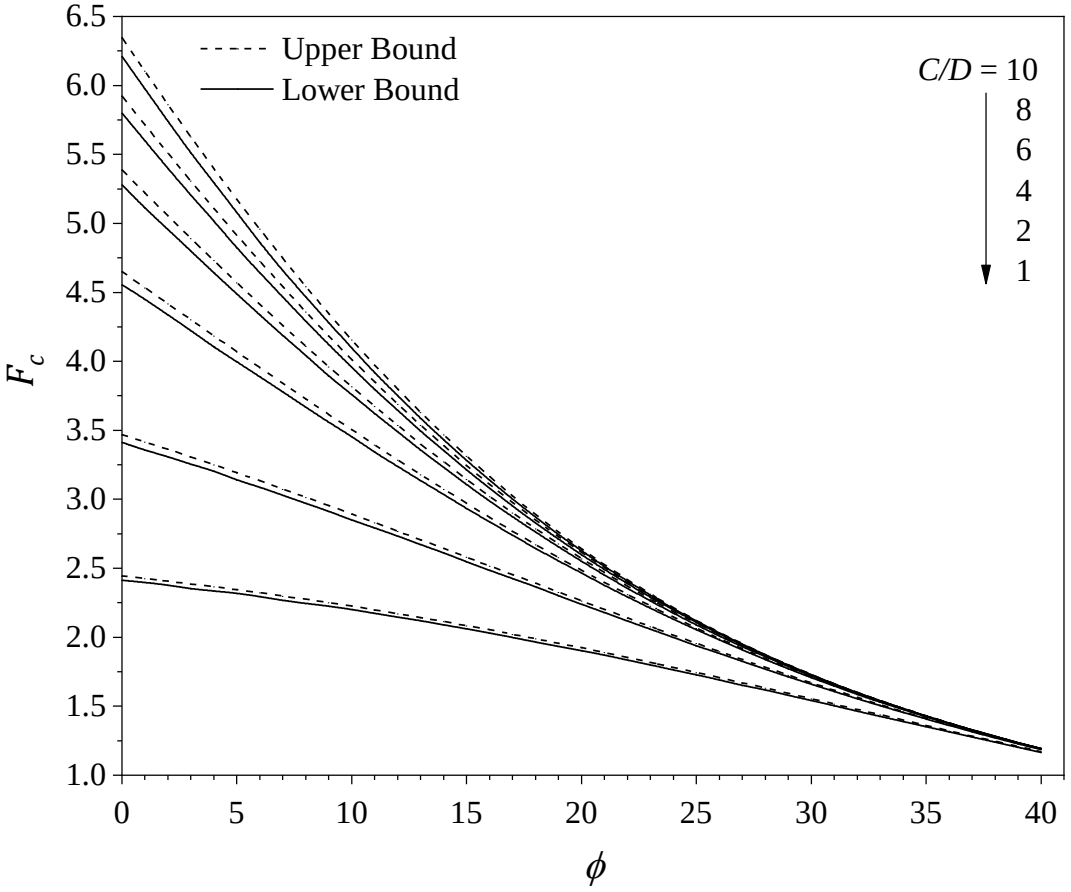

Figure 10.3. F_c vs ϕ (*UB* and *LB*) for various depth ratios (*C/D* = 1 - 10).

Figure 10.3 shows that for all *C/D* ratios, the cohesion stability factor F_c decreases with the increasing of ϕ. It is to be noted that all curves of F_c merge in one line at approximate ϕ of 35 ˚ and F_c reaches a minimum value of 1.19 at $\phi = 40$˚. Noting that F_c increases with increasing *C/D*, the effect of the *C/D* ratio on F_c is significant for ϕ < 20 ˚. A double regression analysis (exponential and logarithmic) was employed to develop Equation 10.2 using the lower bound F_c results. The Equation has a correlation coefficient (R^2) = 0.995.

$$F_c = (1.558 \times \ln(C/D) + 2.641) \times e^{((-0.01 \times \ln(C/D) - 0.02) \times \phi)} \quad (10.2)$$

10.3.2 The stability factor for surcharge, F_s

Assuming a cohesionless soil $(c' = 0)$ and a weightless soil $(\gamma = 0)$, Equation 10.1 reduces to $\sigma_t = \sigma_s F_s$. Using a constant value of surface load σ_s, a total of 820 *FELA* runs was conducted to obtain the upper and lower bounds results of the surcharge

stability factor (F_s) is then calculated as $F_s = (\sigma_t / \sigma_s)$. This is done for ($\phi$ = 0˚- 40˚) and (C/D = 1 - 10), as shown in Tables 10.3-10.4 and Figure 10.4.

Table 10-3. F_s vs ϕ (LB) for various depth ratios (C/D = 1 - 10).

ϕ	C/D (F_s, LB)									
	1	2	3	4	5	6	7	8	9	10
0	0.998	0.997	0.996	0.995	0.995	0.995	0.994	0.994	0.994	0.994
1	0.956	0.938	0.927	0.918	0.911	0.906	0.901	0.897	0.893	0.89
2	0.915	0.881	0.860	0.844	0.832	0.822	0.813	0.806	0.800	0.794
3	0.874	0.826	0.796	0.774	0.758	0.744	0.732	0.722	0.713	0.705
4	0.834	0.773	0.735	0.709	0.688	0.671	0.657	0.644	0.634	0.625
5	0.795	0.722	0.677	0.646	0.622	0.603	0.586	0.573	0.561	0.550
6	0.756	0.673	0.623	0.588	0.561	0.54	0.522	0.507	0.494	0.484
7	0.719	0.625	0.570	0.532	0.504	0.482	0.463	0.447	0.433	0.423
8	0.682	0.580	0.521	0.481	0.452	0.428	0.409	0.393	0.379	0.368
9	0.646	0.536	0.474	0.432	0.403	0.379	0.36	0.344	0.330	0.318
10	0.609	0.494	0.430	0.387	0.357	0.333	0.314	0.299	0.285	0.274
11	0.575	0.454	0.389	0.347	0.316	0.292	0.273	0.258	0.245	0.234
12	0.542	0.416	0.351	0.308	0.279	0.254	0.237	0.221	0.210	0.199
13	0.508	0.381	0.315	0.273	0.243	0.222	0.205	0.190	0.178	0.168
14	0.477	0.346	0.281	0.240	0.212	0.191	0.176	0.161	0.150	0.141
15	0.446	0.315	0.251	0.211	0.184	0.164	0.149	0.136	0.126	0.117
16	0.416	0.285	0.222	0.184	0.159	0.14	0.126	0.114	0.105	0.097
17	0.387	0.256	0.197	0.160	0.137	0.118	0.105	0.095	0.086	0.079
18	0.359	0.229	0.173	0.138	0.116	0.100	0.088	0.078	0.071	0.065
19	0.332	0.205	0.151	0.118	0.098	0.083	0.072	0.064	0.057	0.052
20	0.306	0.182	0.132	0.100	0.082	0.069	0.060	0.052	0.046	0.041
21	0.280	0.162	0.112	0.085	0.068	0.057	0.048	0.041	0.037	0.033
22	0.258	0.143	0.096	0.072	0.056	0.046	0.038	0.033	0.029	0.025
23	0.234	0.125	0.081	0.060	0.046	0.037	0.031	0.026	0.022	0.019
24	0.213	0.108	0.069	0.050	0.038	0.030	0.024	0.020	0.017	0.015
25	0.193	0.094	0.058	0.040	0.030	0.023	0.018	0.015	0.012	0.011
26	0.174	0.080	0.048	0.033	0.024	0.018	0.014	0.011	0.009	0.008
27	0.157	0.068	0.039	0.026	0.019	0.014	0.010	0.008	0.006	0.005
28	0.138	0.057	0.032	0.021	0.014	0.010	0.008	0.006	0.004	0.003
29	0.123	0.049	0.026	0.016	0.011	0.007	0.005	0.004	0.003	0.002
30	0.109	0.041	0.021	0.012	0.008	0.005	0.003	0.002	0.002	0.001
31	0.095	0.033	0.016	0.009	0.006	0.003	0.002	0.001	0.001	0
32	0.084	0.027	0.012	0.007	0.004	0.002	0.001	0	0	0
33	0.072	0.022	0.009	0.005	0.003	0.001	0	0	0	0
34	0.062	0.018	0.007	0.003	0.001	0	0	0	0	0
35	0.052	0.013	0.005	0.002	0.001	0	0	0	0	0
36	0.044	0.011	0.003	0.001	0	0	0	0	0	0
37	0.037	0.008	0.002	0	0	0	0	0	0	0
38	0.030	0.006	0.001	0	0	0	0	0	0	0
39	0.026	0.004	0.001	0	0	0	0	0	0	0
40	0.020	0.003	0	0	0	0	0	0	0	0

Table 10-4. F_s vs ϕ (*UB*) for various depth ratios (*C/D* = 1 - 10).

ϕ	*C/D* (F_s, *UB*)									
	1	2	3	4	5	6	7	8	9	10
0	0.998	0.997	0.996	0.995	0.995	0.995	0.994	0.994	0.994	0.994
1	0.955	0.937	0.925	0.916	0.909	0.904	0.899	0.895	0.891	0.887
2	0.914	0.879	0.857	0.841	0.829	0.818	0.810	0.802	0.795	0.789
3	0.873	0.823	0.793	0.770	0.753	0.739	0.727	0.716	0.708	0.699
4	0.832	0.770	0.731	0.703	0.682	0.664	0.65	0.638	0.627	0.617
5	0.793	0.718	0.672	0.640	0.615	0.595	0.579	0.565	0.553	0.542
6	0.754	0.668	0.616	0.580	0.553	0.532	0.514	0.499	0.486	0.474
7	0.715	0.619	0.563	0.524	0.496	0.473	0.454	0.438	0.424	0.412
8	0.678	0.573	0.513	0.472	0.442	0.418	0.399	0.383	0.369	0.357
9	0.641	0.529	0.466	0.424	0.393	0.369	0.349	0.333	0.319	0.307
10	0.605	0.487	0.422	0.379	0.347	0.323	0.304	0.288	0.275	0.263
11	0.570	0.447	0.380	0.337	0.306	0.282	0.263	0.248	0.235	0.224
12	0.536	0.409	0.341	0.298	0.268	0.245	0.227	0.212	0.199	0.189
13	0.503	0.372	0.305	0.263	0.233	0.211	0.194	0.180	0.168	0.159
14	0.471	0.338	0.272	0.231	0.202	0.181	0.165	0.152	0.141	0.132
15	0.439	0.306	0.241	0.201	0.174	0.155	0.139	0.127	0.117	0.109
16	0.409	0.276	0.212	0.174	0.149	0.131	0.117	0.106	0.097	0.089
17	0.380	0.247	0.186	0.151	0.127	0.110	0.097	0.087	0.079	0.073
18	0.352	0.221	0.162	0.129	0.107	0.092	0.080	0.071	0.064	0.058
19	0.324	0.196	0.141	0.110	0.090	0.076	0.065	0.058	0.051	0.046
20	0.298	0.174	0.121	0.093	0.074	0.062	0.053	0.046	0.041	0.036
21	0.273	0.153	0.104	0.078	0.061	0.050	0.042	0.036	0.032	0.028
22	0.249	0.134	0.088	0.064	0.050	0.040	0.033	0.028	0.025	0.022
23	0.227	0.116	0.074	0.053	0.040	0.032	0.026	0.022	0.019	0.016
24	0.205	0.100	0.062	0.043	0.032	0.025	0.020	0.017	0.014	0.012
25	0.185	0.086	0.051	0.035	0.025	0.019	0.015	0.012	0.010	0.008
26	0.166	0.073	0.042	0.028	0.020	0.015	0.011	0.009	0.007	0.006
27	0.148	0.062	0.034	0.022	0.015	0.011	0.008	0.006	0.005	0.004
28	0.131	0.051	0.027	0.017	0.011	0.008	0.006	0.004	0.003	0.002
29	0.115	0.043	0.022	0.013	0.008	0.005	0.004	0.003	0.002	0.001
30	0.101	0.035	0.017	0.009	0.006	0.004	0.002	0.001	0.001	0
31	0.088	0.028	0.013	0.007	0.004	0.002	0.001	0	0	0
32	0.076	0.023	0.010	0.005	0.002	0.001	0	0	0	0
33	0.065	0.018	0.007	0.003	0.001	0	0	0	0	0
34	0.055	0.014	0.005	0.002	0.001	0	0	0	0	0
35	0.046	0.010	0.003	0.001	0	0	0	0	0	0
36	0.039	0.008	0.002	0	0	0	0	0	0	0
37	0.032	0.006	0.001	0	0	0	0	0	0	0
38	0.026	0.004	0	0	0	0	0	0	0	0
39	0.021	0.002	0	0	0	0	0	0	0	0
40	0.016	0.001	0	0	0	0	0	0	0	0

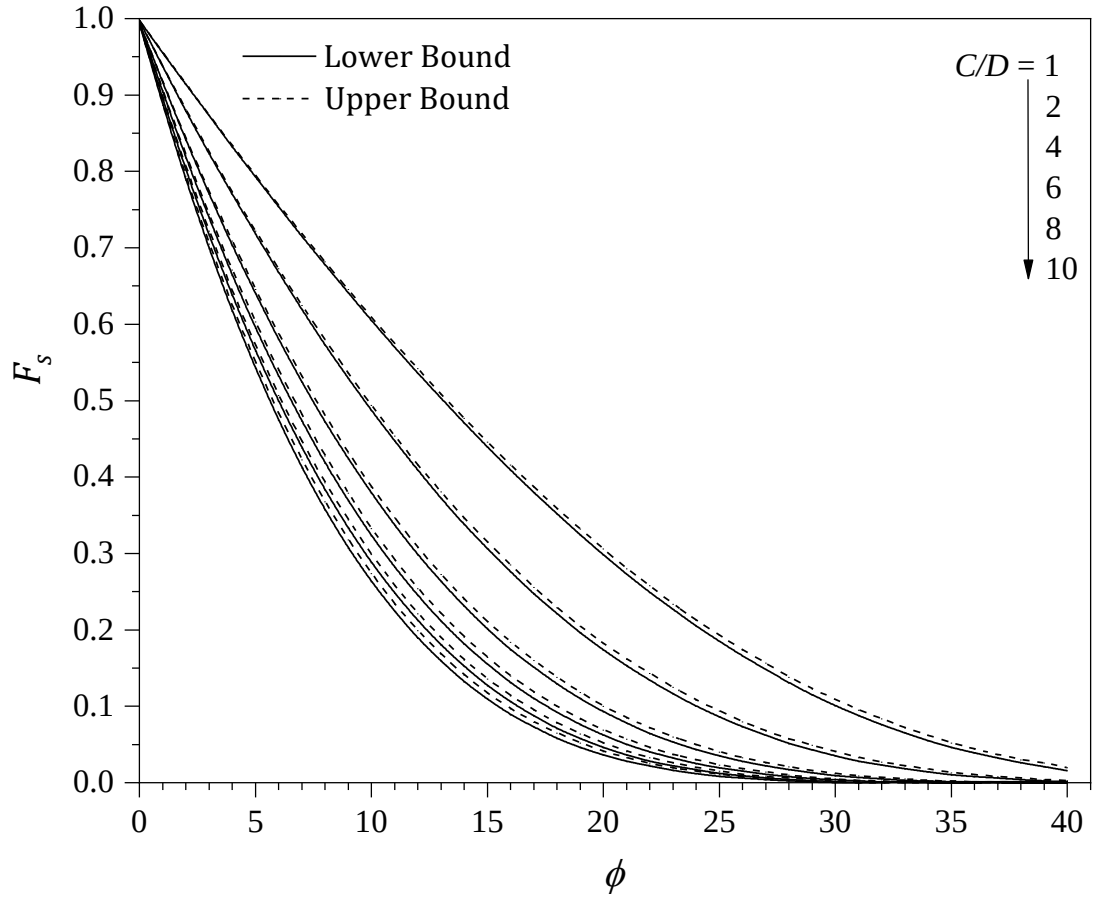

Figure 10.4. F_s vs ϕ (*UB* and *LB*) for various depth ratios (*C/D* = 1 - 10).

Figure 10.4 shows that, for all *C/D* ratios, the surcharge stability factor F_s decreases with the increasing of ϕ. Noting that F_s has a minimum value of zero at $\phi = 40^\circ$, the effect of surcharge loading is practically none when the soil friction angle ϕ is large. This is due to the strong material arching for soils with large ϕ (Shiau & Al-Asadi 2020b, 2020c). On the other hand, F_s has a maximum value of one at $\phi = 0^\circ$ (i.e. undrained clay). Different level of the *C/D* effect on F_s can be observed for $0^\circ < \phi < 40^\circ$. Take $\phi = 15^\circ$ for example, the deeper the tunnel is, the smaller the F_s (surcharge effect) is.

A double regression analysis (exponential and logarithmic) was employed to develop Equation 10.3 using the lower bound F_s results. Equation 10.3 has a correlation coefficient (R^2) = 0.991.

$$F_s = (0.082 \times (C/D) + 1.150) \times e^{((-0.061 \times \ln(C/D) - 0.065) \times \phi)} \quad (10.3)$$

10.3.3 The stability factor for unit weight, F_γ

To investigate the unit weight stability factor (F_γ) and its effect on the tunnel stability, both the cohesion (c') and the surface load (σ_s) are set to zero. Equation 10.1 now reduces to $\sigma_t = \gamma D F_\gamma$. Using constant values of γ and D, a total of 820 *FELA* runs was conducted to obtain the upper and lower bounds results of σ_t. The unit weight stability factor (F_γ) is then calculated as $F_\gamma = (\sigma_t/\gamma D)$. This is done for ($\phi$ = 0˚- 40˚) and (C/D = 1 - 10), as shown in Figure 10.5 and Tables 10.5-10.6.

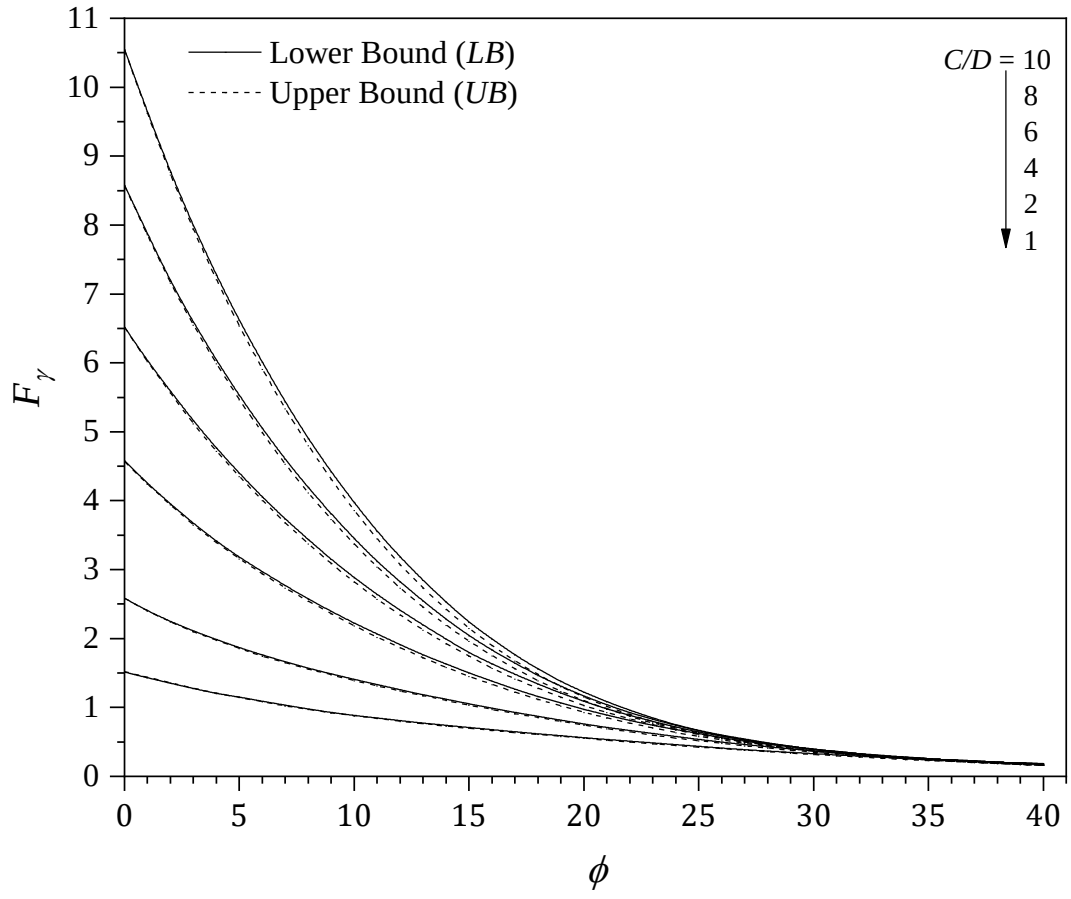

Figure 10.5. F_γ vs ϕ (*UB* and *LB*) for various depth ratios (C/D = 1 - 10).

Figure 10.5 shows that F_γ has a maximum value of (C/D + 0.5) at ϕ = 0˚ (i.e. undrained clay). A dramatic decline in F_γ with the increasing ϕ is observed for all curves. The value of F_γ is very sensitive to the increase of ϕ value due to the soil arching effect. Most C/D curves merge into one line at approximately $\phi \geq 25$˚. For $C/D \leq 2$, the curves merge at $\phi \geq 30$˚. This is because the shallow depths provide smaller soil arching support.

Table 10-5. F_γ vs ϕ (*LB*) for various depth ratios (*C/D* = 1 - 10).

ϕ	*C/D* (*Fγ*, *LB*)									
	1	2	3	4	5	6	7	8	9	10
0	1.521	2.582	3.549	4.580	5.545	6.518	7.515	8.581	9.526	10.547
1	1.431	2.405	3.312	4.249	5.141	6.034	6.932	7.884	8.773	9.651
2	1.352	2.249	3.095	3.954	4.774	5.589	6.391	7.187	7.977	8.766
3	1.275	2.109	2.901	3.671	4.421	5.158	5.880	6.592	7.291	7.993
4	1.199	1.983	2.711	3.411	4.090	4.762	5.404	6.037	6.663	7.274
5	1.151	1.867	2.541	3.184	3.803	4.400	4.965	5.527	6.070	6.618
6	1.104	1.754	2.378	2.965	3.522	4.045	4.552	5.037	5.521	5.995
7	1.034	1.658	2.233	2.765	3.258	3.725	4.175	4.601	5.017	5.422
8	0.973	1.566	2.094	2.571	3.007	3.419	3.817	4.189	4.545	4.893
9	0.926	1.482	1.962	2.388	2.776	3.142	3.485	3.797	4.108	4.399
10	0.882	1.403	1.833	2.212	2.558	2.874	3.165	3.448	3.715	3.962
11	0.842	1.327	1.719	2.056	2.358	2.627	2.879	3.114	3.342	3.550
12	0.804	1.252	1.603	1.901	2.161	2.396	2.610	2.813	2.997	3.176
13	0.769	1.181	1.493	1.754	1.985	2.181	2.357	2.528	2.691	2.828
14	0.735	1.114	1.395	1.624	1.819	1.985	2.140	2.274	2.397	2.523
15	0.704	1.049	1.291	1.493	1.661	1.800	1.932	2.047	2.144	2.233
16	0.673	0.986	1.202	1.375	1.511	1.625	1.738	1.832	1.912	1.984
17	0.644	0.927	1.117	1.261	1.374	1.477	1.561	1.635	1.705	1.762
18	0.614	0.868	1.032	1.154	1.252	1.335	1.400	1.460	1.513	1.561
19	0.586	0.814	0.954	1.058	1.137	1.197	1.257	1.309	1.338	1.375
20	0.559	0.762	0.880	0.970	1.028	1.074	1.125	1.164	1.194	1.212
21	0.533	0.712	0.812	0.885	0.931	0.982	1.009	1.036	1.057	1.076
22	0.507	0.663	0.749	0.806	0.845	0.881	0.904	0.924	0.937	0.954
23	0.481	0.619	0.687	0.737	0.771	0.793	0.812	0.823	0.837	0.844
24	0.458	0.577	0.631	0.671	0.691	0.714	0.728	0.735	0.750	0.749
25	0.433	0.535	0.582	0.612	0.626	0.647	0.654	0.656	0.662	0.668
26	0.410	0.494	0.536	0.558	0.574	0.584	0.589	0.589	0.594	0.591
27	0.389	0.460	0.491	0.508	0.518	0.525	0.531	0.531	0.533	0.532
28	0.367	0.428	0.450	0.466	0.471	0.477	0.480	0.481	0.478	0.477
29	0.349	0.394	0.417	0.426	0.433	0.432	0.435	0.435	0.432	0.432
30	0.327	0.366	0.382	0.390	0.391	0.390	0.397	0.395	0.397	0.395
31	0.308	0.341	0.352	0.358	0.358	0.361	0.360	0.359	0.364	0.356
32	0.290	0.315	0.323	0.328	0.328	0.329	0.330	0.328	0.327	0.326
33	0.272	0.291	0.298	0.301	0.302	0.301	0.302	0.301	0.301	0.299
34	0.256	0.269	0.274	0.277	0.278	0.276	0.277	0.278	0.278	0.275
35	0.240	0.249	0.255	0.256	0.258	0.255	0.256	0.257	0.257	0.254
36	0.225	0.231	0.235	0.237	0.237	0.238	0.237	0.237	0.238	0.237
37	0.210	0.216	0.220	0.220	0.219	0.221	0.221	0.219	0.220	0.219
38	0.197	0.200	0.204	0.204	0.206	0.207	0.203	0.204	0.204	0.208
39	0.182	0.187	0.190	0.193	0.194	0.194	0.192	0.193	0.190	0.191
40	0.172	0.175	0.176	0.181	0.181	0.181	0.181	0.181	0.181	0.181

Table 10-6. F_γ vs ϕ (*UB*) for various depth ratios (*C/D* = 1 - 10).

ϕ	*C/D* (*Fγ*, *UB*)									
	1	2	3	4	5	6	7	8	9	10
0	1.514	2.583	3.555	4.572	5.543	6.517	7.552	8.572	9.521	10.543
1	1.436	2.402	3.309	4.237	5.130	6.019	6.950	7.865	8.747	9.626
2	1.355	2.242	3.087	3.940	4.756	5.563	6.363	7.157	7.945	8.728
3	1.279	2.099	2.887	3.647	4.390	5.119	5.838	6.546	7.245	7.936
4	1.208	1.972	2.694	3.391	4.064	4.719	5.360	5.987	6.603	7.209
5	1.148	1.853	2.522	3.157	3.763	4.349	4.915	5.468	6.007	6.535
6	1.096	1.743	2.360	2.935	3.479	3.999	4.498	4.981	5.450	5.907
7	1.027	1.646	2.212	2.731	3.215	3.673	4.111	4.531	4.936	5.329
8	0.967	1.555	2.072	2.537	2.967	3.369	3.750	4.113	4.461	4.798
9	0.919	1.470	1.939	2.354	2.733	3.084	3.413	3.724	4.020	4.306
10	0.876	1.389	1.813	2.181	2.512	2.817	3.099	3.365	3.615	3.856
11	0.836	1.311	1.692	2.017	2.305	2.568	2.808	3.033	3.244	3.444
12	0.798	1.237	1.577	1.863	2.112	2.335	2.539	2.727	2.904	3.069
13	0.762	1.166	1.468	1.716	1.930	2.121	2.291	2.448	2.593	2.728
14	0.729	1.097	1.364	1.579	1.762	1.921	2.063	2.193	2.310	2.419
15	0.697	1.031	1.266	1.450	1.604	1.737	1.856	1.959	2.055	2.142
16	0.666	0.968	1.172	1.330	1.459	1.568	1.664	1.748	1.826	1.895
17	0.636	0.907	1.085	1.218	1.325	1.413	1.491	1.558	1.618	1.672
18	0.607	0.849	1.002	1.113	1.201	1.272	1.334	1.387	1.433	1.475
19	0.579	0.794	0.924	1.016	1.087	1.144	1.193	1.233	1.269	1.301
20	0.551	0.741	0.851	0.926	0.983	1.028	1.065	1.097	1.123	1.147
21	0.524	0.691	0.783	0.844	0.89	0.923	0.952	0.975	0.995	1.013
22	0.498	0.643	0.719	0.769	0.803	0.829	0.851	0.868	0.882	0.895
23	0.473	0.598	0.661	0.699	0.725	0.745	0.76	0.773	0.783	0.792
24	0.448	0.555	0.606	0.636	0.656	0.67	0.681	0.689	0.697	0.702
25	0.424	0.515	0.555	0.578	0.593	0.603	0.610	0.616	0.621	0.625
26	0.401	0.478	0.509	0.526	0.536	0.544	0.549	0.553	0.555	0.557
27	0.379	0.442	0.467	0.479	0.486	0.491	0.494	0.497	0.499	0.500
28	0.357	0.409	0.428	0.437	0.442	0.445	0.447	0.448	0.449	0.450
29	0.336	0.379	0.392	0.399	0.402	0.404	0.405	0.405	0.406	0.407
30	0.316	0.350	0.360	0.364	0.366	0.367	0.368	0.368	0.368	0.369
31	0.297	0.324	0.331	0.333	0.335	0.335	0.336	0.335	0.336	0.336
32	0.279	0.300	0.304	0.306	0.307	0.307	0.307	0.307	0.307	0.307
33	0.261	0.277	0.28	0.281	0.282	0.282	0.282	0.282	0.281	0.281
34	0.245	0.256	0.258	0.259	0.259	0.259	0.259	0.259	0.259	0.259
35	0.229	0.237	0.239	0.239	0.239	0.239	0.238	0.239	0.239	0.238
36	0.214	0.220	0.221	0.221	0.221	0.221	0.221	0.220	0.220	0.220
37	0.200	0.204	0.204	0.204	0.204	0.204	0.204	0.204	0.204	0.204
38	0.187	0.189	0.189	0.189	0.189	0.189	0.189	0.189	0.189	0.189
39	0.174	0.176	0.176	0.176	0.176	0.176	0.175	0.175	0.175	0.175
40	0.163	0.164	0.163	0.163	0.163	0.163	0.163	0.163	0.163	0.162

Noting that underground excavations in cohesionless soils (i.e. dry sand) are unstable and internal support pressure is always needed regardless of how high the value of internal friction angle is. It is interesting to note that, for all depth ratios *C/D*, F_γ (*LB*) has a minimum value of (0.18) at $\phi = 40^\circ$.

A double regression analysis (exponential and logarithmic) was employed to develop Equation 10.4 using the lower bound F_s results. Equation 10.4 has a correlation coefficient (R^2) = 0.999.

$$F_\gamma = 1.521 \times (C/D)^{0.860} \times e^{((-0.024 \times \ln(C/D) - 0.051) \times \phi)} \quad (10.4)$$

10.4 Comparison of Results

Finite element limit analysis provides a comparison between the upper and lower limits, which can be used to verify the results and increase the user confidence. However, by comparing the upper and lower bounds with other available solutions does increase the credibility of the study and the feasibility of implementing it in practice.

10.4.1 Comparison with a plane strain tunnel heading

Within the same parametric study (*C/D* = 1 - 10 and $\phi = 0^\circ$ - 40°), Figures 10.6-10.8 show comparisons of tunnel stability factors (F_c, F_s and F_γ) between the present study and the plain strain tunnel heading in Shiau and Al-Asadi (2020b).

The comparisons show the same trend: i.e. the stability factors decrease with the increasing of the internal friction angle. In general, circular tunnel stability factors are consistently higher than tunnel heading stability factors. This indicates that the stability of the circular tunnel is more critical than the stability of the tunnel heading. In other words, the support pressure required to maintain the stability of the circular tunnel is higher than that in tunnel heading for the same soil properties and depth ratios. This difference is due to the variance in geometry between the two cases. The circular tunnel is an unlined cylindrical cavity with infinite length, while the tunnel heading has a long unsupported vertical face. Therefore, the geometric arching of the tunnel heading is greater than that for the unlined circular tunnel.

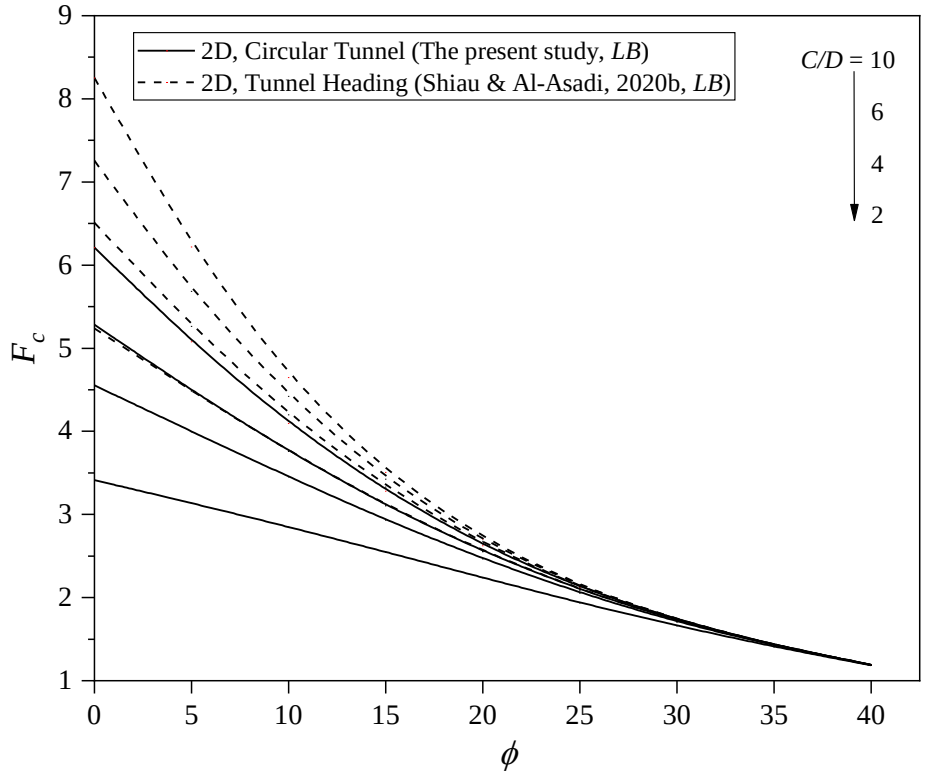

Figure 10.6. Comparison F_c (*LB*) of this study with that for tunnel heading (Shiau and Al-Asadi, 2020b).

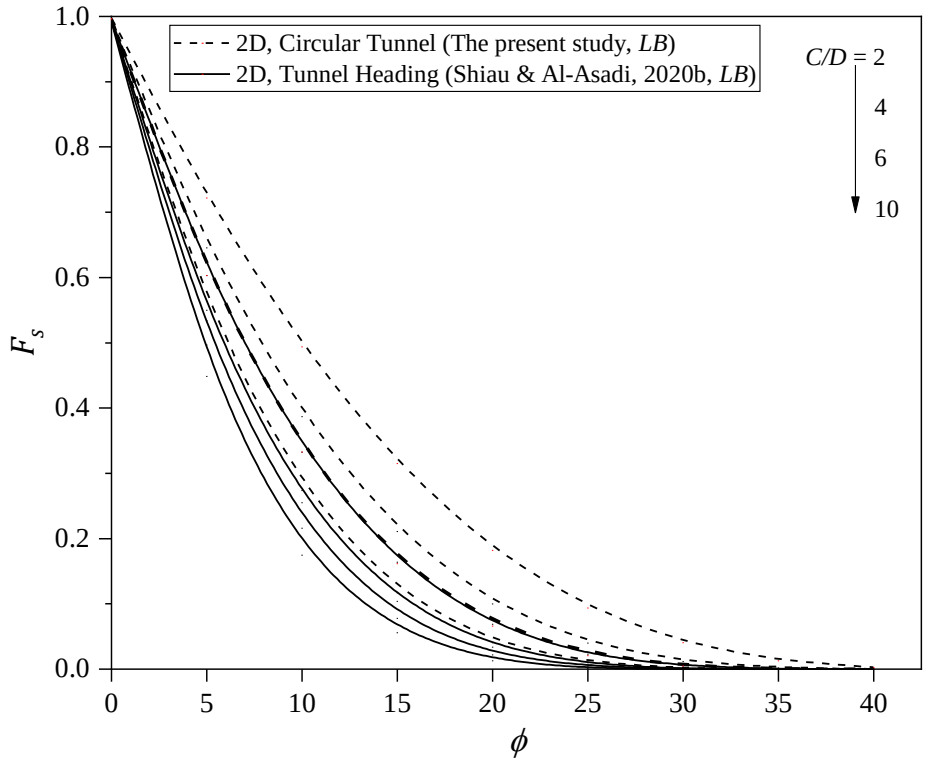

Figure 10.7. Comparison F_s (*LB*) of this study with that for tunnel heading (Shiau and Al-Asadi, 2020b).

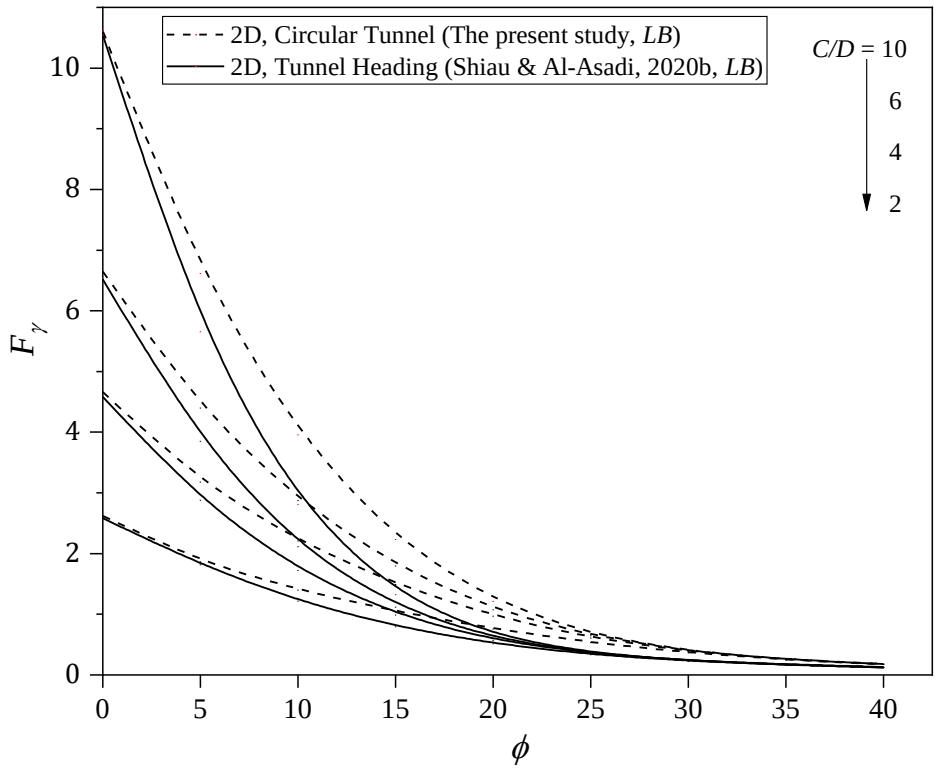

Figure 10.8. Comparison F_γ (*LB*) of this study with that for tunnel heading (Shiau and Al-Asadi, 2020b).

10.4.2 Comparison with a 2D circular tunnel heading

Figures 10.9-10.10 compares the critical pressure ratio $(-\sigma_t / c')$. between (Lyamin & Sloan 2000) and the present study. In (Lyamin & Sloan 2000), a dimensionless critical pressure ratio $(-\sigma_t / c')$. was presented. Their study did not produce stability factors for a direct comparison. Unlike our stability factor approach, their solution is only suitable for cohesive-frictional soil with cohesion greater than zero (cannot be used for cohesionless soil) and for shallow depth ratios ($C/D \leq 5$).

The comparison was achieved by assuming both of the surcharge pressure (σ_s) and the unit weight of the soil (γ) are equal to zero. Therefore, the cohesion stability factor is equal to $(-\sigma_t / c')$. The comparisons show a very good agreement between the two studies for *LB* and *UB* analyses.

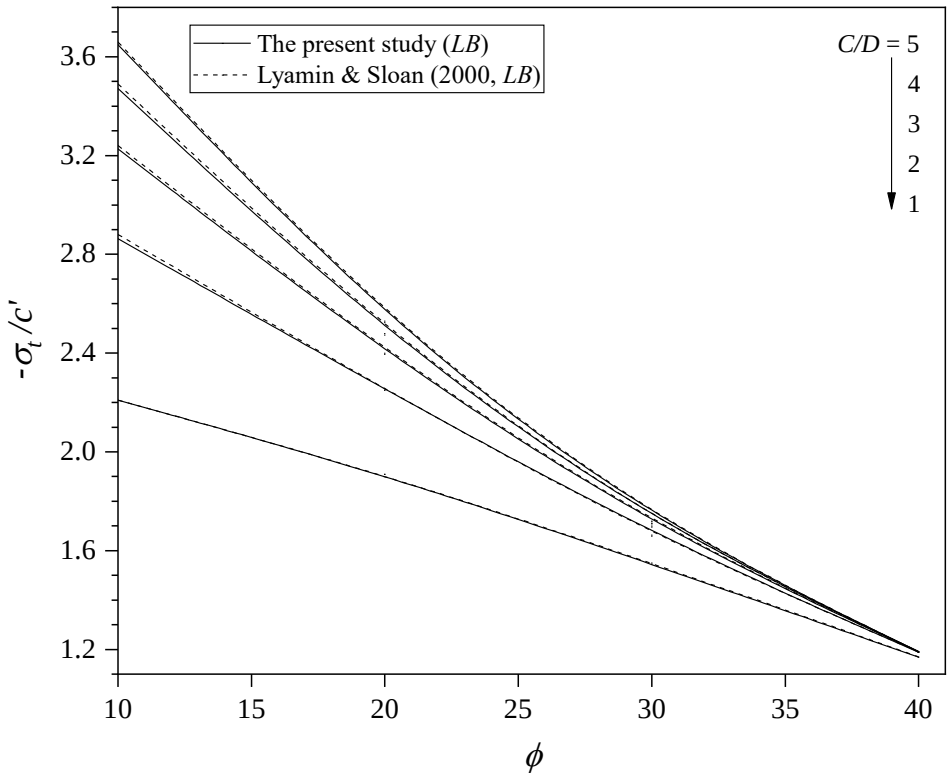

Figure 10.9. Comparison of ($-\sigma_t/c'$, *LB*) of this study with that for circular tunnel from (Lyamin and Sloan, 2000).

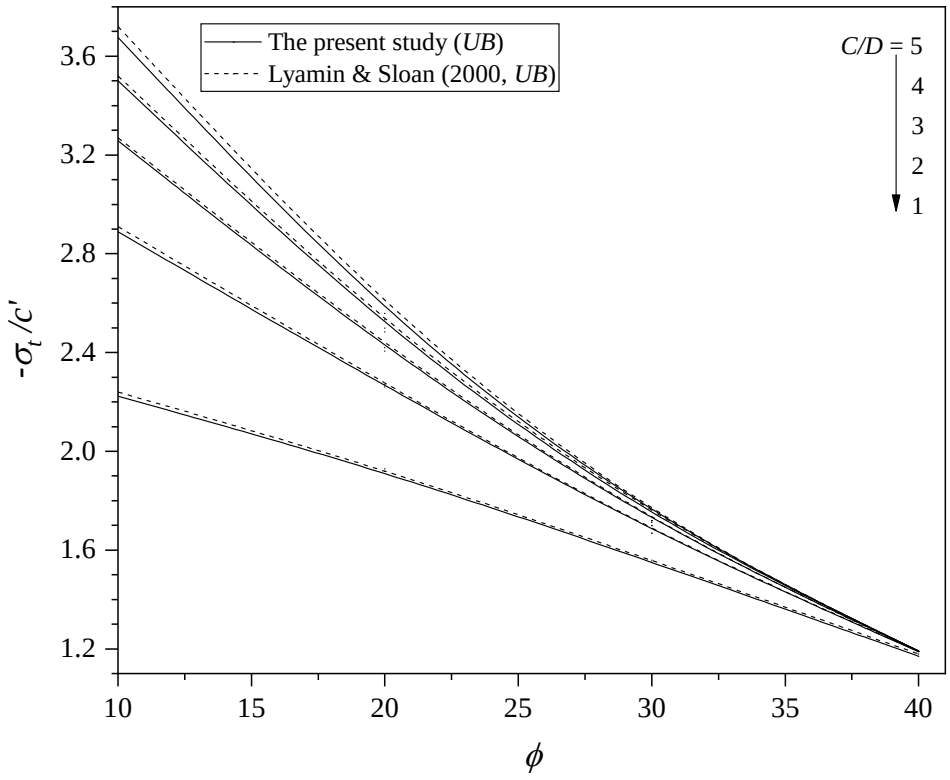

Figure 10.10. Comparison of ($-\sigma_t/c'$, *UB*) of this study with that for circular tunnel from (Lyamin and Sloan, 2000).

10.5 Examples

A circular tunnel in greenfield conditions (σ_s = 0) has a diameter of 6m and a cover depth of 18m. The soil is found to be cohesionless (c' = 0) with a unit weight of 18 kN/m^3 and an angle of internal friction of 22˚.

For C/D = 3 and ϕ = 22˚, Tables 10.1, 10.3 and 10.5 give lower bound F_c = 2.233, F_s = 0.096 and F_γ = 0.749. Equations 10.2 to 10.4 give lower bound F_c = 2.226, F_s = 0.096 and F_γ = 0.724.

10.5.1 Minimum support pressure to maintain stability

Equation 10.1 reduces to $\sigma_t = \gamma D F_\gamma$. for such a cohesionless soil without surcharge (c' and σ_s are equal to zero). Substituting γ, D, and F_γ into the equation, σ_t = 80.89 kPa (using tables) is the minimum support pressure to maintain soil stability for the cohesionless soil with ϕ = 22˚.

10.5.2 Minimum cohesion to maintain stability

The minimum cohesion required to maintain stability without internal support pressure (σ_t = 0) can be estimated using $\sigma_t = 0 = (-cF_c + \gamma D F_\gamma) = (-c \times 2.233 + 18 \times 6 \times 0.749)$. Therefore c is calculated as 36.23 kPa. This is approximately equal to (36.23/γD) = 33.55% of (γD) value for this case when ϕ = 22˚.

10.5.3 Effect of the depth ratios (*C/D* = 3, 6 and 8)

For the same example but the angle of internal friction is 40˚, determine the critical support pressure for the three depth ratios C/D = 3, 6 and 8.

Using Tables 10.1, 10.3, and 10.5, the lower bound stability factors for the three depth ratios of ϕ = 40˚ are:

For C/D = 3: F_c = 1.190, Fs = 0 and F_γ = 0.176; σ_t = 19.01 kPa

For C/D = 6: F_c = 1.192, Fs = 0 and F_γ = 0.181; σ_t = 19.55 kPa

For C/D = 8: F_c = 1.192, Fs = 0 and F_γ = 0.181; σ_t = 19.55 kPa

The above calculations have shown that the support pressures are independent of the depths for a large value of soil friction angle. This is due to the effect of material arching as discussed before.

10.6 Conclusion

Numerical simulations through finite element limit analyses were performed to study the stability of a circular tunnel in cohesive-frictional soil. Parametric studies for various depth ratios (C/D = 1 - 10) and internal friction angles (ϕ = 0˚- 40˚) were achieved to calculate the lower and upper bound tunnel stability factors (F_c, F_s and F_γ). The upper and lower bounds of each factor are in a good agreement with only a few percentages of each other. The results were also favourably compared with those existing solutions in the literature. Some examples are used to illustrate the usefulness of the factors. The following conclusions are drawn based on this study:

1. The tunnel stability factors (F_c, F_s and F_γ) are functions of the soil friction angle ϕ and the depth ratio (C/D).
2. The cohesion stability factor (F_c) increases as the depth ratio (C/D) increases, but it decreases as the soil friction angle ϕ increases. The F_c curves merge into a single line at approximately ϕ = 35 ˚, and F_c reaches a minimum value of 1.19 at ϕ = 40˚.
3. The surcharge stability factor (F_s) decreases nonlinearly as the soil friction angle ϕ increases. F_s has a maximum value of one at ϕ = 0˚ (i.e. undrained clay) and a minimum value of zero at approximately ϕ = 40˚. In general, the effect of surcharge load (σ_s) diminishes as the soil friction angle increases due to the development of soil arching.
4. The unit weight stability factor (F_γ) has a maximum value of (C/D + 0.5) at ϕ = 0˚ (i.e. undrained clay) and decreases dramatically as the soil friction angle ϕ increases due to the development of soil arching. The deeper the tunnel is, the larger the F_γ (unit weight effect) is. Most C/D curves merge into one line at approximately $\phi \geq 25$˚. For $C/D \leq 2$, the curves merge at $\phi \geq 30$˚.

The finite element limit analysis is useful as both upper and lower bounds are calculated and they bracket the actual collapse load from above and below, which provides confidence to the end-users in using the design tables, equations and charts.

A full 3D circular tunnel in the drained condition is studied next in Chapter 11 using the developed tunnel stability factors approach.

CHAPTER 11: DRAINED ANALYSIS OF 3D SINGLE CIRCULAR TUNNEL

11.1 Introduction

In the previous chapters, the drained stability of plane strain tunnel heading and plane strain circular tunnel was investigated by using tunnel stability factors approach. Tunnel stability is an inherently three-dimensional problem and therefore requires a full 3D analysis. Two-dimensional (2D) results may be misleading, although they always result in a conservative design. Thus, this chapter will discuss the three-dimensional stability problem of a circular tunnel in cohesive-frictional soil under drained conditions.

Following the superposition principle of the traditional bearing capacity equations, this chapter focuses on tunnel face stability analysis in cohesive-frictional soil by using the 3D *FELA* technique. The purpose of the study is to achieve an accurate and realistic assessment of the limit support pressure of the tunnel face, by bracketing the upper and lower values of the tunnel stability factors (F_c, F_s and F_γ).

These factors are functions of the depth ratio (*C/D*) and soil internal friction angle (ϕ). The obtained results are compared and validated by using the available published results in the literature. A number of examples are illustrated on how to use the factors to estimate internal tunnel support pressures.

11.2 Methodology and Problem Definition

Finite element limit analysis (*FELA*) is the numerical computational method of limit analysis that employs the classical plasticity theorems with the concept of finite element and mathematical programming (Sloan 2013). The underlying bound theorems assume a perfectly plastic material with associated flow rule, i.e. the dilation angle is assumed to be equal to the friction angle. It is particularly powerful when the upper bound (*UB*) and lower bound (*LB*) estimates are calculated together as the two limits provide a measure of the discretisation error in the solution. The initial

developments using linear programming are in (Sloan 1988b, 1989). The newer developments are based on a much faster nonlinear programming formulation by (Lyamin & Sloan 2002b, 2002a) and (Krabbenhøft et al. 2005; Krabbenhøft et al. 2007). Most of the available 3D numerical simulations such as the Finite Element Method (*FEM*), the Finite Difference Method (*FDM*) and the Discrete Element Method (*DEM*) are considered very time consuming for simulating the failure of a 3D tunnel face. The new development of 3D *FELA* technique has been successfully applied to solve a variety of drained and undrained stability problems in geotechnical engineering (Sloan 2013; Shiau & Al-Asadi 2020a, 2020c, 2020d). Consequently, *OptumG3* (OptumCE 2018) was chosen in this study to compute the rigorous upper and lower bounds of the tunnel stability factors (F_c, F_s and F_γ).

Figure 11.1 shows the problem definition of a three-dimensional half-circular tunnel. The soil medium is considered as a perfectly plastic Mohr-Coulomb material with a cohesion of c' and an angle of internal friction ϕ. The tunnel has a diameter (D), cover depth (C) and axis depth (H) from the ground surface.

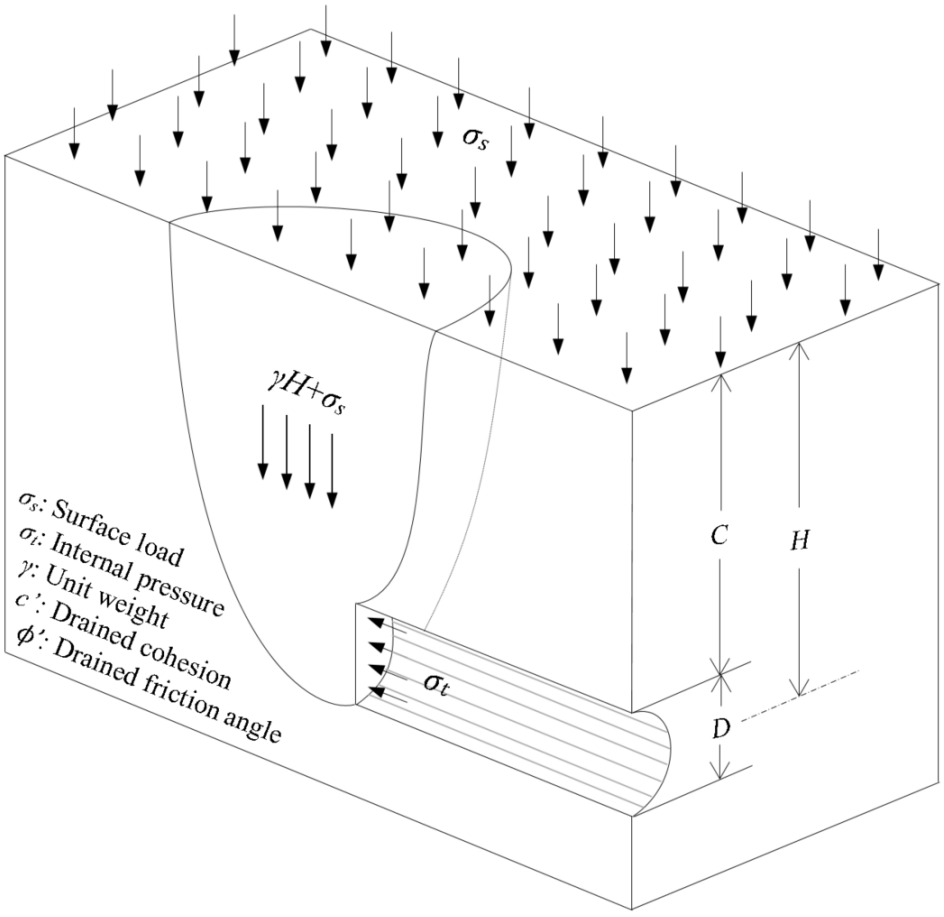

Figure 11.1. Problem definition (C/D = 3).

σ_t is a normal uniform pressure on the face of the tunnel, and σ_s is a vertical surcharge pressure on the ground surface.

As symmetrical tunnels are considered, the stability factor calculations are based on half a circular tunnel, which is cut lengthwise along the central axis. The tunnel has a diameter *D*, and soil cover *C*. The ground surface is subject to a vertical surcharge (σ_s). Using Equation 11.1, the internal pressure (σ_t) is optimised in both upper and lower bound analyses to compute the bound solution of the stability factors (F_c, F_s and F_γ).

$$\sigma_t = -cF_c + \sigma_s F_s + \gamma D F_\gamma \tag{11.1}$$

A typical *FELA* adaptive mesh used in this study is shown in Figure 11.2. An automatically adaptive mesh refinement was employed in both the *UB* and *LB* simulations to enable accurate limits to be obtained through the use of an exact error estimate. Three iterations of adaptive meshing with the initial number of elements increasing from 5000 to10000 were used in all analyses.

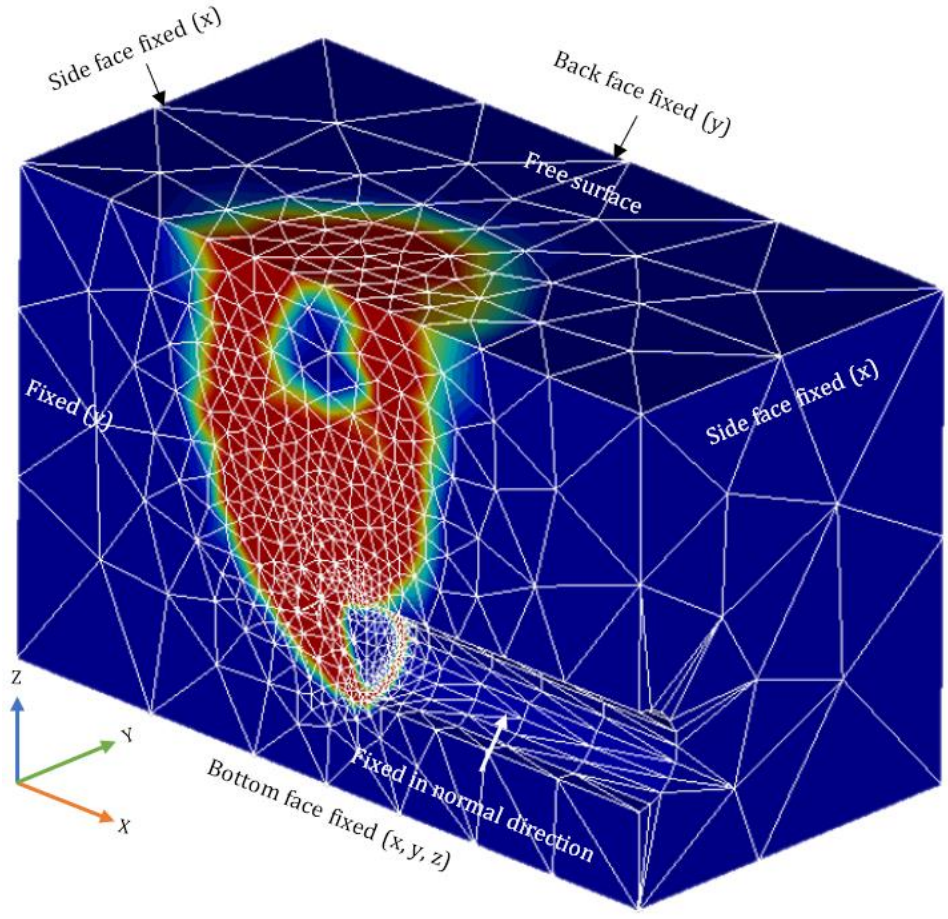

Figure 11.2. Numerical model and adaptive mesh (*C/D* = 3).

The boundary conditions of 3D *FELA* mesh are presented in Figure 11.2. The ground surface is free to displace and the side surfaces, including the symmetrical surface, have roller boundaries (i.e. restrained in the normal direction). The base is fixed in all directions and the rigid lining around the soil excavation is restrained in the normal direction to represent the nature of the lining supports. The tunnel linings are assumed to be smooth and there is no transfer of shear force between the lining and the soil. Using the load multiplier method in *FELA*, the tunnel internal pressure (σ_t) is optimised in both upper and lower bound analyses for a circular tunnel heading in cohesive-frictional soil under various depth ratios (*C/D*) and angles of internal friction (ϕ). The finite-element limit analysis does not require assumptions to be made about the mode of failure and uses only shear strength parameters that are familiar to geotechnical engineers (Sloan 2013). This has the advantage over the displacement finite-element method in geotechnical stability analysis, which requires not only the conventional strength parameters but also the deformation parameters (Poisson's ratio and elastic modulus). The principles of calculating the stability factors (F_c, F_s and F_γ) using equation (11.1) are as follows:

1. F_c is calculated using $\sigma_t = -c' F_c.$, while $\gamma = 0$ and $\sigma_s = 0$ are used in the analysis.
2. To determine F_s, both $\gamma = 0$ and $c' = 0$ are used in the analysis. F_s is then calculated using $\sigma_t = \sigma_s F_s$.
3. To determine F_γ, both $c' = 0$ and $\sigma_s = 0$ are used in the analysis. F_γ is then calculated using $\sigma_t = \gamma D F_\gamma$.

By using the principle of superposition, the minimum support pressure σ_t at collapse can then be estimated for various soil parameters (ϕ) and depth ratios (*C/D*) using the stability factors (F_c, F_s and F_γ) produced in this paper.

11.3 Discussing the Tunnel Stability Factors (F_c, F_s and F_γ)

Numerical analyses were performed to calculate the upper bound (*UB*) and the lower bound (*LB*) limits of the stability factors (F_c, F_s and F_γ) for various depth ratios (*C/D* = 1 - 10) and angles of internal friction (ϕ = 0˚ - 40˚). The comprehensive solutions of (F_c, F_s and F_γ) are presented in Tables 11.1-11.3 and Figures 11.3-11.6.

Table 11-1. F_c vs ϕ for various depth ratios (C/D = 1 - 10, *UB* and *LB*).

	F_c									
	C/D = 1		C/D = 2		C/D = 3		C/D = 4		C/D = 5	
ϕ	*LB*	*UB*	*LB*	*UB*	*LB*	*UB*	*LB*	*UB*	*LB*	*UB*
0	6.940	7.821	9.196	10.041	10.552	11.469	11.546	12.516	12.246	13.361
1	6.616	7.378	8.656	9.304	9.776	10.548	10.548	11.415	11.235	12.097
2	6.305	7.023	8.093	8.670	9.115	9.706	9.710	10.433	10.228	10.971
3	6.007	6.633	7.563	8.089	8.410	8.918	8.952	9.485	9.338	9.928
4	5.723	6.300	7.072	7.533	7.780	8.223	8.233	8.675	8.545	9.035
5	5.449	5.965	6.668	7.008	7.206	7.574	7.591	7.947	7.842	8.218
6	5.188	5.656	6.236	6.542	6.689	6.991	7.002	7.279	7.196	7.487
7	4.940	5.348	5.842	6.092	6.216	6.466	6.456	6.690	6.632	6.847
8	4.700	5.055	5.475	5.686	5.779	5.980	5.978	6.155	6.113	6.276
9	4.475	4.791	5.131	5.311	5.390	5.541	5.539	5.678	5.639	5.771
10	4.259	4.542	4.823	4.961	5.025	5.145	5.141	5.248	5.217	5.315
11	4.054	4.291	4.531	4.642	4.690	4.789	4.786	4.864	4.838	4.916
12	3.860	4.075	4.265	4.350	4.386	4.461	4.461	4.523	4.496	4.555
13	3.675	3.858	4.013	4.083	4.112	4.165	4.165	4.210	4.195	4.238
14	3.500	3.658	3.777	3.838	3.858	3.901	3.898	3.931	3.919	3.951
15	3.333	3.469	3.570	3.612	3.627	3.658	3.656	3.680	3.674	3.694
16	3.178	3.291	3.369	3.404	3.414	3.439	3.436	3.455	3.449	3.465
17	3.030	3.129	3.187	3.214	3.221	3.239	3.237	3.249	3.246	3.257
18	2.891	2.974	3.018	3.040	3.043	3.057	3.055	3.065	3.061	3.070
19	2.759	2.828	2.862	2.878	2.882	2.891	2.889	2.896	2.894	2.900
20	2.634	2.693	2.718	2.729	2.732	2.738	2.738	2.742	2.741	2.745
21	2.517	2.559	2.584	2.593	2.594	2.600	2.599	2.601	2.600	2.604
22	2.408	2.442	2.462	2.467	2.469	2.472	2.471	2.473	2.472	2.473
23	2.304	2.306	2.335	2.340	2.340	2.343	2.342	2.344	2.343	2.343
24	2.207	2.216	2.240	2.243	2.243	2.245	2.244	2.246	2.244	2.245
25	2.114	2.121	2.140	2.143	2.142	2.143	2.143	2.144	2.143	2.144
26	2.028	2.033	2.047	2.049	2.048	2.049	2.049	2.050	2.050	2.050
27	1.945	1.948	1.960	1.962	1.962	1.962	1.962	1.962	1.962	1.962
28	1.868	1.868	1.879	1.880	1.880	1.880	1.880	1.880	1.880	1.880
29	1.794	1.793	1.803	1.804	1.803	1.804	1.804	1.804	1.804	1.804
30	1.724	1.725	1.731	1.732	1.732	1.732	1.732	1.732	1.732	1.732
31	1.658	1.660	1.664	1.664	1.664	1.664	1.664	1.664	1.664	1.664
32	1.596	1.596	1.600	1.600	1.600	1.600	1.600	1.600	1.600	1.600
33	1.536	1.537	1.539	1.540	1.540	1.540	1.539	1.540	1.540	1.540
34	1.480	1.480	1.482	1.482	1.482	1.482	1.482	1.482	1.482	1.482
35	1.426	1.426	1.428	1.428	1.428	1.428	1.428	1.428	1.428	1.428
36	1.375	1.375	1.376	1.376	1.376	1.376	1.376	1.376	1.376	1.376
37	1.326	1.326	1.327	1.327	1.327	1.327	1.327	1.327	1.327	1.327
38	1.279	1.280	1.280	1.279	1.280	1.280	1.280	1.280	1.280	1.280
39	1.234	1.235	1.235	1.235	1.235	1.235	1.235	1.235	1.235	1.235
40	1.191	1.191	1.192	1.192	1.192	1.192	1.192	1.192	1.192	1.192

Table 11.1. Cont'd.

	F_c									
	C/D = 6		*C/D* = 7		*C/D* = 8		*C/D* = 9		*C/D* = 10	
ϕ	*LB*	*UB*	*LB*	*UB*	*LB*	*UB*	*LB*	*UB*	*LB*	*UB*
0	13.272	13.834	13.795	14.411	14.317	14.910	14.734	15.379	15.094	15.771
1	11.681	12.660	12.128	13.100	12.467	13.523	12.757	13.869	13.076	14.215
2	10.623	11.395	10.952	11.737	11.241	12.077	11.523	12.346	11.689	12.585
3	9.652	10.266	9.934	10.557	10.183	10.801	10.384	11.011	10.513	11.192
4	8.824	9.311	9.006	9.513	9.197	9.685	9.356	9.841	9.464	9.984
5	8.042	8.416	8.218	8.576	8.359	8.725	8.468	8.850	8.565	8.947
6	7.363	7.649	7.489	7.773	7.582	7.879	7.669	7.960	7.756	8.037
7	6.747	6.976	6.833	7.057	6.928	7.142	6.983	7.199	7.042	7.257
8	6.198	6.366	6.286	6.434	6.327	6.493	6.375	6.531	6.410	6.571
9	5.710	5.836	5.768	5.884	5.804	5.929	5.840	5.960	5.874	5.985
10	5.275	5.364	5.316	5.399	5.345	5.430	5.377	5.452	5.389	5.491
11	4.877	4.952	4.913	4.974	4.932	4.997	4.952	5.019	4.963	5.037
12	4.529	4.581	4.552	4.600	4.568	4.612	4.584	4.629	4.592	4.628
13	4.218	4.257	4.232	4.266	4.246	4.276	4.252	4.279	4.261	4.322
14	3.938	3.964	3.948	3.969	3.954	3.976	3.963	3.982	3.967	3.985
15	3.684	3.702	3.692	3.707	3.699	3.711	3.701	3.715	3.705	3.717
16	3.456	3.469	3.463	3.473	3.465	3.475	3.469	3.478	3.471	3.479
17	3.250	3.261	3.255	3.262	3.257	3.264	3.260	3.263	3.261	3.266
18	3.064	3.071	3.068	3.071	3.070	3.074	3.071	3.074	3.071	3.075
19	2.897	2.900	2.898	2.901	2.899	2.900	2.900	2.901	2.900	2.902
20	2.742	2.745	2.743	2.745	2.743	2.746	2.744	2.746	2.745	2.746
21	2.602	2.603	2.602	2.603	2.602	2.605	2.603	2.604	2.603	2.604
22	2.473	2.474	2.473	2.474	2.474	2.474	2.474	2.474	2.474	2.474
23	2.343	2.344	2.343	2.344	2.343	2.343	2.343	2.344	2.343	2.344
24	2.245	2.246	2.245	2.246	2.245	2.246	2.246	2.245	2.245	2.246
25	2.144	2.143	2.144	2.144	2.144	2.144	2.144	2.144	2.144	2.144
26	2.050	2.049	2.050	2.050	2.050	2.050	2.050	2.050	2.050	2.050
27	1.962	1.962	1.962	1.962	1.962	1.962	1.962	1.962	1.962	1.962
28	1.880	1.880	1.880	1.881	1.880	1.881	1.880	1.881	1.880	1.881
29	1.804	1.804	1.804	1.804	1.804	1.804	1.804	1.804	1.804	1.804
30	1.732	1.732	1.732	1.732	1.732	1.732	1.732	1.732	1.732	1.732
31	1.664	1.664	1.664	1.664	1.664	1.664	1.664	1.664	1.664	1.664
32	1.600	1.600	1.600	1.600	1.600	1.600	1.600	1.600	1.600	1.600
33	1.540	1.540	1.540	1.540	1.540	1.540	1.540	1.540	1.540	1.540
34	1.482	1.482	1.482	1.482	1.482	1.482	1.482	1.482	1.482	1.482
35	1.428	1.428	1.428	1.428	1.428	1.428	1.428	1.428	1.428	1.428
36	1.376	1.376	1.376	1.376	1.376	1.376	1.376	1.376	1.376	1.376
37	1.327	1.327	1.327	1.327	1.327	1.327	1.327	1.327	1.327	1.327
38	1.280	1.280	1.280	1.280	1.280	1.280	1.280	1.280	1.280	1.280
39	1.235	1.235	1.235	1.235	1.235	1.235	1.235	1.235	1.235	1.235
40	1.191	1.192	1.191	1.192	1.192	1.191	1.192	1.192	1.192	1.192

Table 11-2. F_s vs ϕ for various depth ratios (C/D = 1 - 10, *UB* and *LB*).

	F_s									
	C/D = 1		C/D = 2		C/D = 3		C/D = 4		C/D = 5	
ϕ	*LB*	*UB*	*LB*	*UB*	*LB*	*UB*	*LB*	*UB*	*LB*	*UB*
0	0.993	0.992	0.991	0.990	0.989	0.989	0.988	0.988	0.988	0.987
1	0.874	0.863	0.841	0.828	0.820	0.806	0.805	0.789	0.794	0.777
2	0.766	0.748	0.708	0.688	0.675	0.651	0.651	0.626	0.633	0.607
3	0.669	0.645	0.596	0.569	0.552	0.523	0.522	0.493	0.501	0.469
4	0.581	0.553	0.497	0.465	0.448	0.417	0.418	0.384	0.392	0.360
5	0.504	0.473	0.412	0.378	0.361	0.329	0.330	0.297	0.305	0.273
6	0.433	0.401	0.337	0.307	0.290	0.257	0.257	0.228	0.235	0.204
7	0.371	0.338	0.277	0.247	0.231	0.200	0.201	0.172	0.178	0.152
8	0.315	0.284	0.225	0.196	0.182	0.154	0.154	0.129	0.136	0.111
9	0.270	0.236	0.182	0.154	0.141	0.116	0.117	0.094	0.100	0.080
10	0.225	0.194	0.146	0.120	0.109	0.087	0.088	0.069	0.073	0.057
11	0.188	0.161	0.114	0.093	0.084	0.064	0.066	0.049	0.054	0.040
12	0.157	0.131	0.090	0.070	0.063	0.047	0.048	0.035	0.038	0.027
13	0.131	0.105	0.070	0.053	0.046	0.034	0.034	0.024	0.026	0.018
14	0.109	0.085	0.053	0.040	0.034	0.023	0.024	0.016	0.018	0.011
15	0.087	0.066	0.041	0.028	0.024	0.016	0.017	0.010	0.012	0.006
16	0.069	0.052	0.031	0.020	0.017	0.010	0.011	0.006	0.008	0.003
17	0.057	0.040	0.023	0.014	0.012	0.006	0.007	0.003	0.004	0.001
18	0.044	0.031	0.016	0.009	0.008	0.004	0.004	0.001	0.002	0
19	0.034	0.023	0.011	0.006	0.005	0.001	0.002	0	0	0
20	0.027	0.017	0.007	0.003	0.003	0	0.001	0	0	0
21	0.021	0.012	0.005	0.002	0.001	0	0	0	0	0
22	0.015	0.008	0.005	0.002	0	0	0	0	0	0
23	0.011	0.005	0.003	0	0	0	0	0	0	0
24	0.009	0.003	0.002	0	0	0	0	0	0	0
25	0.006	0.002	0	0	0	0	0	0	0	0
26	0.004	0.001	0	0	0	0	0	0	0	0
27	0.003	0	0	0	0	0	0	0	0	0
28	0.001	0	0	0	0	0	0	0	0	0
29	0	0	0	0	0	0	0	0	0	0
30	0	0	0	0	0	0	0	0	0	0
31	0	0	0	0	0	0	0	0	0	0
32	0	0	0	0	0	0	0	0	0	0
33	0	0	0	0	0	0	0	0	0	0
34	0	0	0	0	0	0	0	0	0	0
35	0	0	0	0	0	0	0	0	0	0
36	0	0	0	0	0	0	0	0	0	0
37	0	0	0	0	0	0	0	0	0	0
38	0	0	0	0	0	0	0	0	0	0
39	0	0	0	0	0	0	0	0	0	0
40	0	0	0	0	0	0	0	0	0	0

Table 11.2. Cont'd.

	F_s									
	C/D = 6		*C/D* = 7		*C/D* = 8		*C/D* = 9		*C/D* = 10	
ϕ	*LB*	*UB*	*LB*	*UB*	*LB*	*UB*	*LB*	*UB*	*LB*	*UB*
0	0.987	0.986	0.987	0.985	0.986	0.985	0.986	0.985	0.986	0.984
1	0.785	0.767	0.776	0.758	0.771	0.756	0.766	0.743	0.760	0.738
2	0.617	0.590	0.608	0.578	0.596	0.567	0.587	0.558	0.578	0.549
3	0.482	0.452	0.470	0.436	0.459	0.422	0.448	0.411	0.438	0.403
4	0.375	0.340	0.358	0.325	0.348	0.311	0.336	0.300	0.328	0.292
5	0.287	0.255	0.272	0.241	0.261	0.228	0.250	0.219	0.242	0.209
6	0.219	0.189	0.205	0.176	0.193	0.163	0.185	0.155	0.177	0.147
7	0.165	0.138	0.152	0.126	0.144	0.116	0.136	0.109	0.128	0.102
8	0.122	0.099	0.112	0.089	0.103	0.079	0.096	0.075	0.091	0.071
9	0.090	0.070	0.081	0.062	0.075	0.055	0.068	0.050	0.064	0.046
10	0.064	0.049	0.058	0.042	0.053	0.037	0.047	0.033	0.044	0.029
11	0.046	0.033	0.040	0.028	0.037	0.024	0.033	0.021	0.029	0.018
12	0.032	0.022	0.027	0.018	0.024	0.015	0.021	0.013	0.019	0.010
13	0.022	0.013	0.018	0.011	0.016	0.008	0.014	0.007	0.012	0.005
14	0.014	0.008	0.011	0.006	0.009	0.004	0.008	0.003	0.007	0.002
15	0.009	0.004	0.007	0.003	0.006	0.001	0.004	0.001	0.003	0
16	0.005	0.002	0.003	0.001	0.003	0	0.002	0	0.001	0
17	0.003	0	0.002	0	0.001	0	0	0	0	0
18	0.001	0	0	0	0	0	0	0	0	0
19	0	0	0	0	0	0	0	0	0	0
20	0	0	0	0	0	0	0	0	0	0
21	0	0	0	0	0	0	0	0	0	0
22	0	0	0	0	0	0	0	0	0	0
23	0	0	0	0	0	0	0	0	0	0
24	0	0	0	0	0	0	0	0	0	0
25	0	0	0	0	0	0	0	0	0	0
26	0	0	0	0	0	0	0	0	0	0
27	0	0	0	0	0	0	0	0	0	0
28	0	0	0	0	0	0	0	0	0	0
29	0	0	0	0	0	0	0	0	0	0
30	0	0	0	0	0	0	0	0	0	0
31	0	0	0	0	0	0	0	0	0	0
32	0	0	0	0	0	0	0	0	0	0
33	0	0	0	0	0	0	0	0	0	0
34	0	0	0	0	0	0	0	0	0	0
35	0	0	0	0	0	0	0	0	0	0
36	0	0	0	0	0	0	0	0	0	0
37	0	0	0	0	0	0	0	0	0	0
38	0	0	0	0	0	0	0	0	0	0
39	0	0	0	0	0	0	0	0	0	0
40	0	0	0	0	0	0	0	0	0	0

Table 11-3. F_γ vs ϕ for various depth ratios (C/D = 1 - 10, *UB* and *LB*).

	F_γ									
	C/D = 1		C/D = 2		C/D = 3		C/D = 4		C/D = 5	
ϕ	*LB*	*UB*	*LB*	*UB*	*LB*	*UB*	*LB*	*UB*	*LB*	*UB*
0	1.667	1.682	2.652	2.646	3.628	3.620	4.601	4.613	5.581	5.638
1	1.524	1.520	2.331	2.344	3.150	3.113	3.949	3.888	4.719	4.697
2	1.387	1.370	2.050	2.049	2.731	2.665	3.356	3.283	3.978	3.870
3	1.260	1.237	1.833	1.780	2.354	2.280	2.857	2.756	3.336	3.210
4	1.145	1.114	1.615	1.558	2.039	1.947	2.433	2.320	2.813	2.650
5	1.040	1.005	1.426	1.368	1.765	1.672	2.068	1.944	2.357	2.192
6	0.947	0.909	1.264	1.199	1.530	1.437	1.758	1.642	1.978	1.826
7	0.862	0.823	1.119	1.056	1.323	1.228	1.503	1.386	1.662	1.514
8	0.784	0.745	0.991	0.930	1.152	1.060	1.281	1.169	1.399	1.259
9	0.716	0.677	0.879	0.813	1.021	0.912	1.096	0.979	1.171	1.050
10	0.655	0.614	0.781	0.715	0.869	0.788	0.943	0.844	0.996	0.881
11	0.598	0.557	0.699	0.638	0.761	0.684	0.807	0.719	0.851	0.745
12	0.548	0.509	0.621	0.567	0.668	0.597	0.700	0.618	0.727	0.632
13	0.500	0.465	0.557	0.508	0.589	0.524	0.609	0.537	0.626	0.539
14	0.460	0.424	0.500	0.453	0.521	0.465	0.538	0.470	0.548	0.475
15	0.421	0.390	0.453	0.406	0.466	0.419	0.472	0.415	0.478	0.419
16	0.390	0.357	0.411	0.366	0.417	0.374	0.420	0.372	0.427	0.372
17	0.359	0.330	0.373	0.334	0.377	0.335	0.382	0.334	0.383	0.331
18	0.333	0.303	0.341	0.304	0.341	0.303	0.342	0.300	0.346	0.301
19	0.305	0.281	0.315	0.278	0.316	0.281	0.312	0.272	0.313	0.273
20	0.284	0.258	0.287	0.258	0.288	0.256	0.285	0.256	0.288	0.251
21	0.262	0.238	0.267	0.234	0.266	0.237	0.266	0.233	0.264	0.233
22	0.245	0.221	0.246	0.210	0.244	0.222	0.246	0.216	0.246	0.210
23	0.229	0.206	0.230	0.200	0.229	0.202	0.230	0.194	0.229	0.199
24	0.213	0.191	0.214	0.185	0.214	0.187	0.213	0.187	0.214	0.186
25	0.200	0.179	0.201	0.175	0.198	0.174	0.199	0.174	0.200	0.175
26	0.188	0.167	0.187	0.160	0.186	0.161	0.186	0.157	0.185	0.155
27	0.175	0.155	0.176	0.151	0.174	0.155	0.174	0.156	0.176	0.153
28	0.165	0.145	0.165	0.140	0.165	0.144	0.165	0.146	0.163	0.143
29	0.155	0.135	0.155	0.134	0.154	0.137	0.154	0.136	0.155	0.130
30	0.147	0.127	0.145	0.128	0.145	0.124	0.146	0.128	0.145	0.128
31	0.138	0.119	0.138	0.120	0.138	0.119	0.138	0.120	0.137	0.118
32	0.131	0.110	0.130	0.107	0.129	0.113	0.129	0.113	0.129	0.109
33	0.123	0.103	0.123	0.101	0.122	0.105	0.121	0.106	0.121	0.101
34	0.116	0.097	0.116	0.096	0.115	0.095	0.116	0.099	0.115	0.099
35	0.109	0.091	0.109	0.090	0.109	0.094	0.108	0.092	0.109	0.092
36	0.103	0.085	0.102	0.085	0.102	0.086	0.103	0.089	0.103	0.087
37	0.098	0.079	0.097	0.080	0.096	0.082	0.097	0.079	0.098	0.077
38	0.092	0.075	0.092	0.075	0.091	0.078	0.091	0.077	0.091	0.078
39	0.087	0.070	0.086	0.069	0.087	0.071	0.086	0.068	0.086	0.068
40	0.082	0.065	0.081	0.069	0.081	0.067	0.081	0.065	0.081	0.066

Table 11.3 Cont'd.

	F_γ									
	C/D = 6		*C/D* = 7		*C/D* = 8		*C/D* = 9		*C/D* = 10	
ϕ	*LB*	*UB*	*LB*	*UB*	*LB*	*UB*	*LB*	*UB*	*LB*	*UB*
0	6.611	6.594	7.598	7.580	8.578	8.555	9.565	9.529	10.570	10.510
1	5.527	5.437	6.300	6.191	7.066	6.930	7.827	7.667	8.592	8.404
2	4.585	4.450	5.172	5.019	5.767	5.566	6.344	6.110	6.916	6.641
3	3.810	3.636	4.262	4.048	4.710	4.455	5.136	4.852	5.565	5.250
4	3.159	2.968	3.494	3.277	3.846	3.577	4.173	3.853	4.471	4.122
5	2.632	2.432	2.883	2.662	3.140	2.855	3.357	3.067	3.570	3.225
6	2.179	1.989	2.360	2.135	2.541	2.266	2.711	2.411	2.868	2.545
7	1.808	1.621	1.935	1.744	2.061	1.810	2.185	1.906	2.301	2.005
8	1.503	1.332	1.594	1.407	1.688	1.463	1.771	1.524	1.836	1.578
9	1.236	1.104	1.313	1.149	1.383	1.173	1.434	1.202	1.485	1.262
10	1.051	0.916	1.092	0.940	1.129	0.955	1.173	0.985	1.198	1.014
11	0.886	0.759	0.908	0.779	0.933	0.792	0.966	0.789	0.989	0.823
12	0.752	0.643	0.766	0.656	0.785	0.659	0.805	0.674	0.809	0.662
13	0.643	0.542	0.652	0.564	0.663	0.557	0.670	0.555	0.694	0.564
14	0.559	0.468	0.560	0.480	0.574	0.472	0.582	0.483	0.573	0.480
15	0.484	0.418	0.486	0.421	0.495	0.411	0.496	0.422	0.498	0.419
16	0.429	0.364	0.433	0.364	0.435	0.353	0.434	0.362	0.432	0.371
17	0.383	0.328	0.386	0.335	0.385	0.322	0.388	0.330	0.387	0.327
18	0.348	0.296	0.347	0.298	0.347	0.282	0.349	0.291	0.347	0.290
19	0.314	0.275	0.315	0.274	0.316	0.271	0.317	0.272	0.313	0.271
20	0.290	0.252	0.290	0.256	0.291	0.225	0.292	0.229	0.289	0.251
21	0.267	0.231	0.267	0.233	0.266	0.227	0.276	0.214	0.263	0.213
22	0.247	0.212	0.249	0.210	0.247	0.208	0.249	0.201	0.248	0.209
23	0.230	0.198	0.227	0.200	0.228	0.194	0.228	0.197	0.226	0.193
24	0.214	0.187	0.214	0.182	0.213	0.187	0.212	0.184	0.211	0.182
25	0.200	0.174	0.199	0.172	0.199	0.165	0.198	0.173	0.196	0.168
26	0.186	0.162	0.185	0.163	0.185	0.157	0.185	0.152	0.184	0.155
27	0.176	0.148	0.176	0.145	0.175	0.153	0.175	0.146	0.173	0.154
28	0.164	0.136	0.164	0.141	0.164	0.135	0.163	0.135	0.164	0.136
29	0.153	0.124	0.156	0.131	0.154	0.123	0.155	0.129	0.156	0.131
30	0.146	0.120	0.146	0.120	0.146	0.118	0.146	0.112	0.142	0.122
31	0.136	0.115	0.137	0.114	0.137	0.114	0.136	0.115	0.135	0.115
32	0.130	0.110	0.129	0.111	0.128	0.104	0.127	0.114	0.129	0.104
33	0.122	0.104	0.123	0.097	0.121	0.091	0.123	0.103	0.122	0.100
34	0.114	0.096	0.115	0.091	0.114	0.083	0.115	0.095	0.115	0.089
35	0.109	0.087	0.108	0.088	0.108	0.087	0.108	0.090	0.107	0.087
36	0.103	0.088	0.102	0.083	0.103	0.090	0.102	0.084	0.104	0.080
37	0.096	0.081	0.096	0.078	0.096	0.083	0.096	0.080	0.097	0.078
38	0.091	0.070	0.091	0.071	0.091	0.072	0.091	0.075	0.094	0.077
39	0.086	0.069	0.087	0.061	0.085	0.068	0.086	0.065	0.086	0.063
40	0.082	0.066	0.081	0.065	0.081	0.059	0.081	0.060	0.081	0.066

11.3.1 The stability factor for cohesion, F_c

Given no surcharge load $(\sigma_s = 0)$ and an idealised weightless soil $(\gamma = 0)$, a total of 820 *FELAs* were performed to calculate the cohesion stability factors F_c using $F_c = -(\sigma_t / c')$. Figure 11.3 shows that, for all depth ratios (*C/D* =1 - 10), the cohesion stability factor (F_c) decreases as the angle of friction (ϕ) increases.

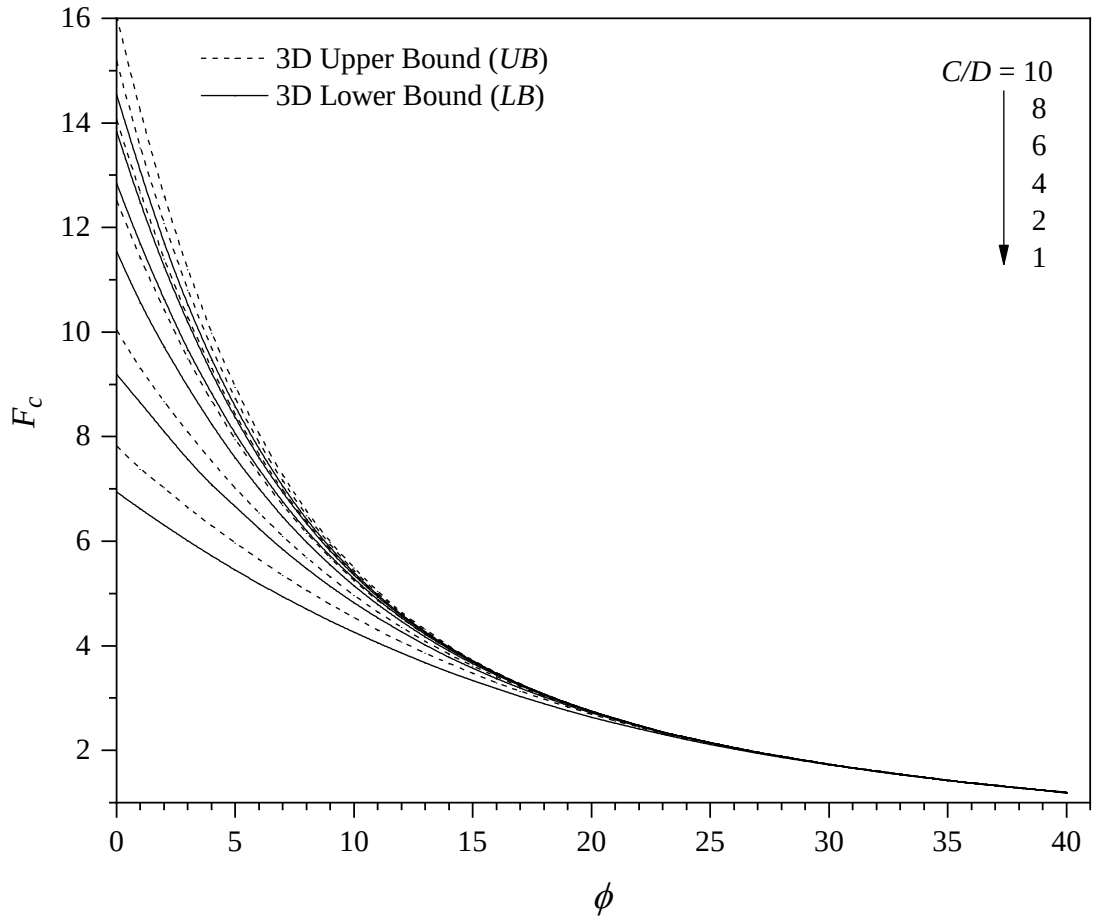

Figure 11.3. F_c vs ϕ for various depth ratios (*C/D* = 1 - 10, *UB* and *LB*).

For ϕ = 0˚, Figure 11.4 presents the relationship between F_c and *C/D*. The two curves are for the upper and lower bound solutions respectively and are best fitted with the Equations (11.2) and (11.3).

$$F_c(UB) = 3.569 \times \ln(C / D) + 7.464 \tag{11.2}$$

$$F_c(LB) = 3.398 \times \ln(C / D) + 7.199 \tag{11.3}$$

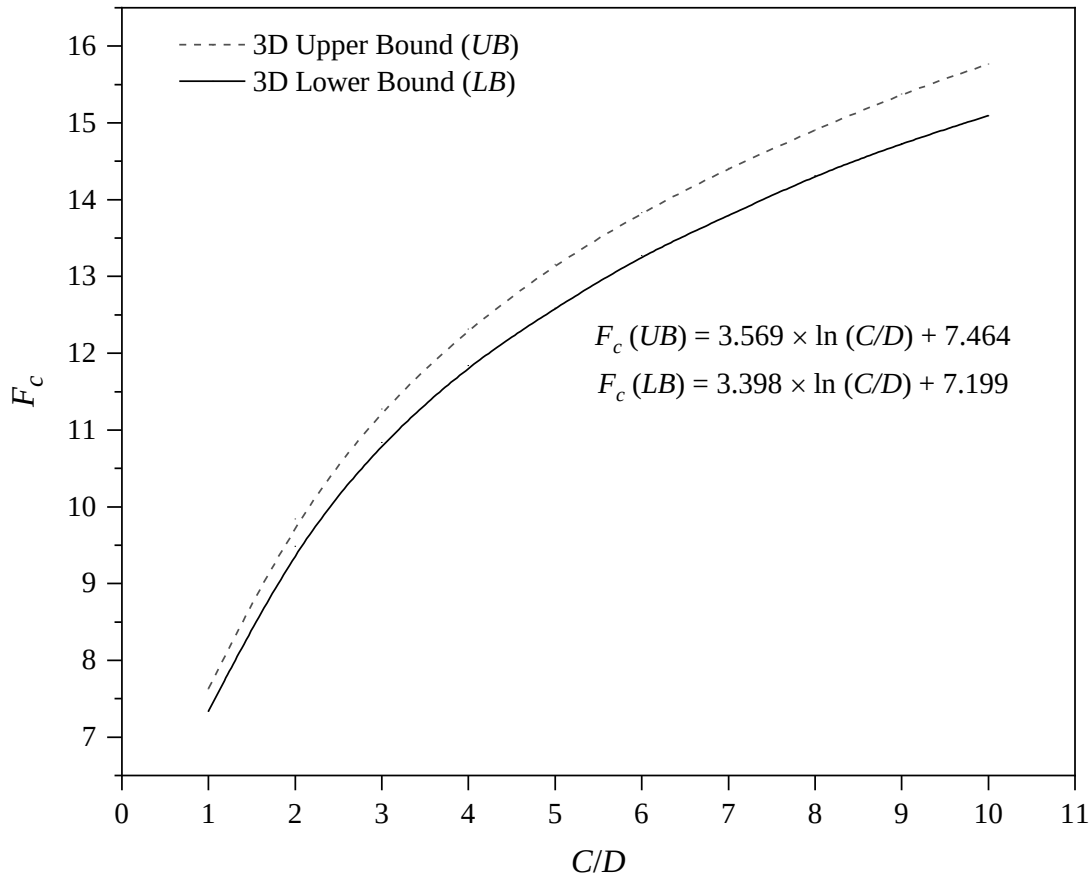

Figure 11.4. F_c vs C/D for $\phi = 0^{\circ}$.

Figure 11.3 can be divided into three distinct zones with the discussions as follow:

For ϕ =1˚ - 10˚, F_c decreases dramatically as ϕ increases for all depth ratios (C/D). Power and logarithmic regression analyses were employed to develop Equation (11.4) using *LB* results. The equation has a correlation coefficient (R^2) = 0.999.

$$F_c = (3.107 \times \ln(C/D) + 7.007 \times e^{((-1.214 \times \ln(C/D) + 2.828) \times \tan\phi)} \quad (11.4)$$

For ϕ =11-20, F_c decreases moderately as ϕ increases. Double power and logarithmic regressions analyses were employed to develop Equation (11.5) using *LB* results. It is the best fit for the data in this range with a correlation coefficient (R^2) = 0.951.

$$F_c = (1.298 \times \ln(C/D)^{-0.096}) \times (\tan\phi)^{(-0.106 \times \ln(C/D) - 0.727)} \quad (11.5)$$

For $\phi = 21^{\circ}$ - 40˚, F_c decreases gradually as ϕ increases. In this range, all curves merge into a single line at approximately $\phi = 21^{\circ}$, indicating that the F_c factor is independent of C/D values for $\phi > 20^{\circ}$. Using *LB* results, Equation (11.6) has a correlation coefficient (R^2) = 1.

$$F_c = (\tan\phi)^{-1} \quad (11.6)$$

11.3.2 The stability factor for surcharge, F_s

Given no cohesion $(c'=0)$ and an idealised weightless soil $(\gamma=0)$, a total of 820 *FELAs* were performed to calculate the surcharge stability factors using $F_s=(\sigma_t/\sigma_s)$. Figure 11.5 shows the relationship between the surcharge stability factor (F_s) and the angle of the internal friction of the soil (ϕ).

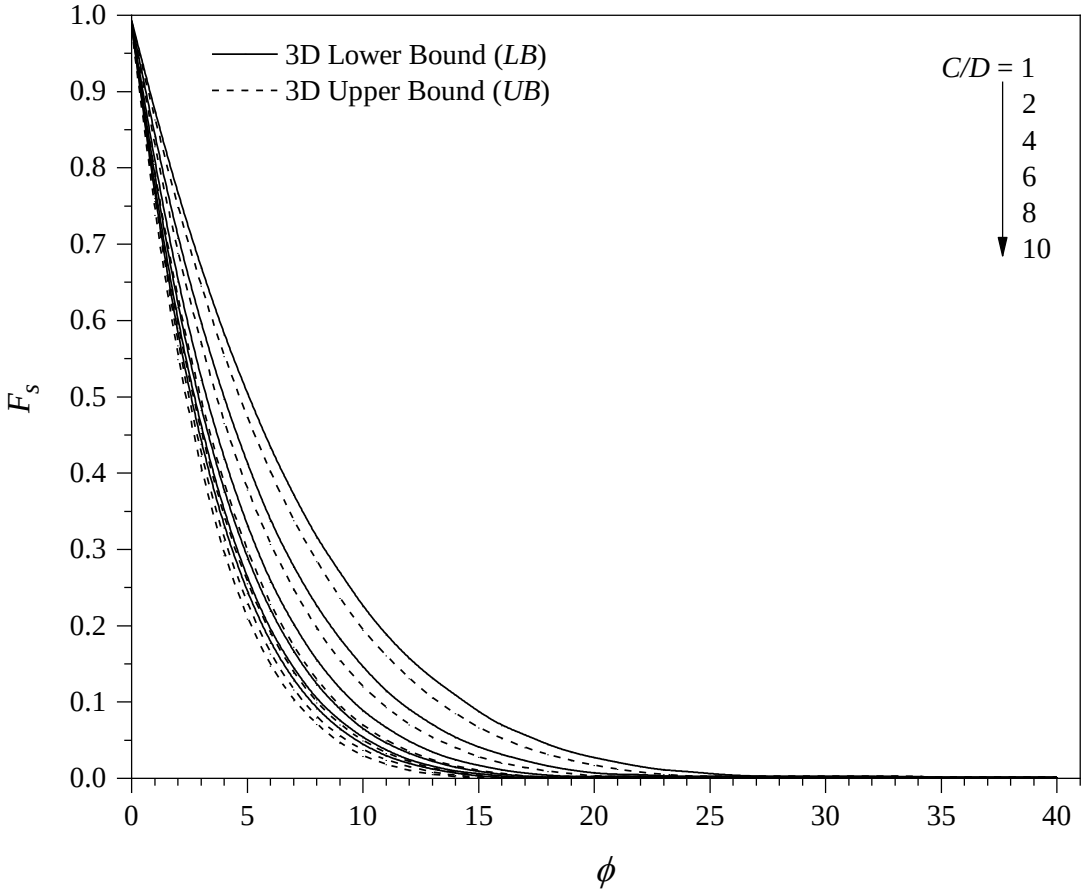

Figure 11.5. F_s vs ϕ for various depth ratios (*C/D* = 1 - 10, *UB* and *LB*).

There is a unique curve for each depth ratio (*C/D*), and all the curves have the same maximum value of one (F_s = 1) when ϕ = 0˚. With an increasing angle of internal friction ϕ, the value of F_s decreases dramatically. A 50% reduction of F_s is observed at a small ϕ = 3˚- 5˚ (ϕ = 3˚ for *C/D* = 10 and ϕ = 5˚ for *C/D* = 1). Note that F_s approaches zero when ϕ > 15˚ (for deep tunnels, *C/D* > 4) and ϕ > 20˚ (for shallow tunnels, *C/D* < 2). It is interesting to see that the surcharge pressure σ_s has little contribution to the internal tunnel face pressure for ϕ > 20˚. This may be attributed to the development of soil arching in greater soil internal friction angles.

Double exponential and logarithmic regressions analyses were employed to develop Equation 11.7 using *LB* results of F_s. The equation has a correlation coefficient (R^2) = 0.992.

$$F_s = (0.034 \times (C/D) + 1.069 \times e^{(-5.081 \times \ln(C/D) - 8.647) \times \tan\phi} \quad (11.7)$$

11.3.3 The stability factor for soil weight, F_γ

Given no cohesion $(c' = 0)$ and no surcharge $(\sigma_s = 0)$ a total of 820 *FELAs* were performed to calculate the soil weight stability factors F_γ using $F_\gamma = \sigma_t / \gamma D$.

Figure 11.6 shows that F_γ has a maximum value of approximately (*C/D* + 0.5) at ϕ = 0˚ and decreases dramatically as the friction angle (ϕ) increases.

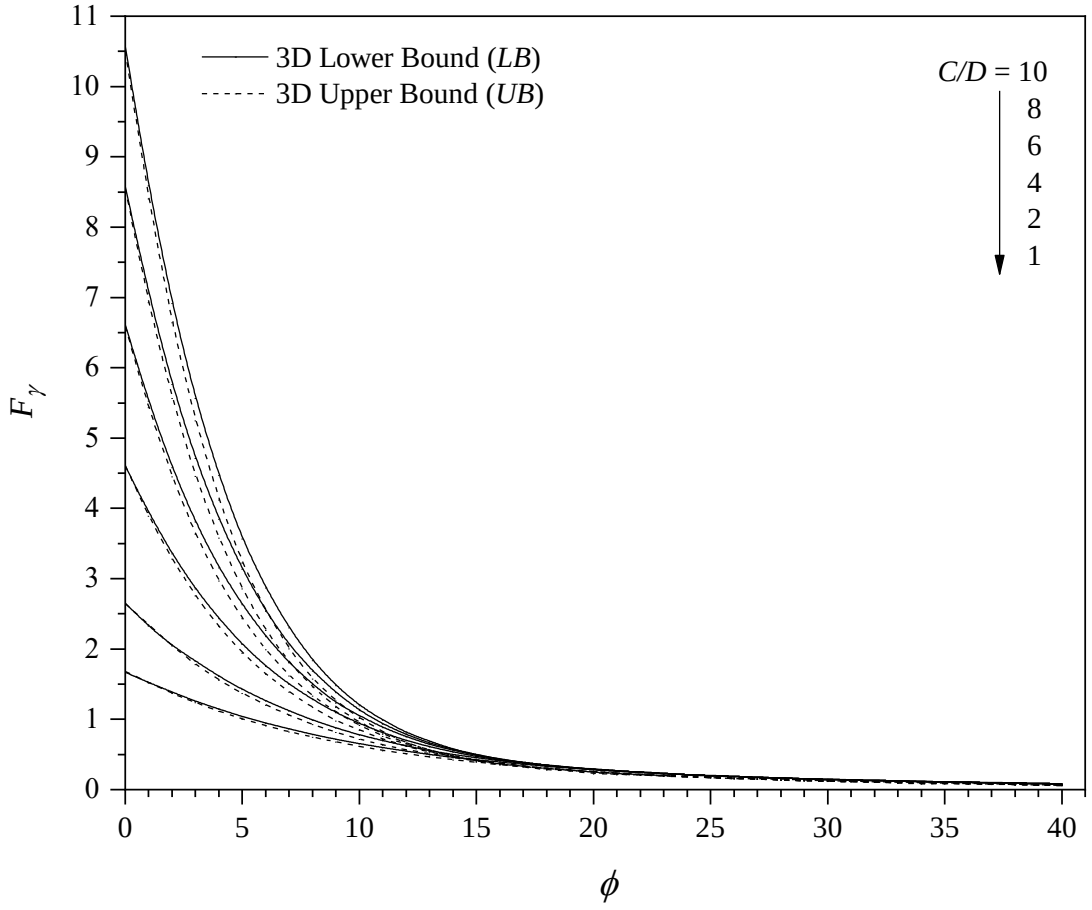

Figure 11.6. F_γ vs ϕ for various depth ratios (*C/D* = 1 - 10, *UB* and *LB*).

Also note that the larger the *C/D* value is, the greater the F_γ factor is. For ϕ = 0˚ -17˚ a double regression analysis (power and logarithmic) was employed to develop Equation (11.8) using *LB* results. Equation (11.8) has a correlation coefficient (R^2) = 0.992.

$$F_\gamma = (0.861 \times \ln(C/D) + 0.802) \times e^{(-2.673 \times \ln(C/D) - 4.732) \times \tan\phi} \quad (11.8)$$

Owing to the presence of soil arching ($\phi \neq 0^\circ$), all *C/D* curves merge into a single line at approximately $\phi = 17^\circ$. It is interesting to know that F_γ is independent of *C/D* for $\phi \geq 17^\circ$ and Equation (11.9) is the best fit for F_γ in this range with a correlation coefficient (R^2) = 0.995.

$$F_\gamma = 0.064 \times (\tan\phi)^{-1.517} \quad (11.9)$$

11.4 Comparison of Results (F_c, F_s and F_γ)

11.4.1 Comparison with published results

Figure 11.7 shows a comparison of the stability factor F_c with published results. The available solutions for the comparison are mostly for ϕ greater than 20˚.

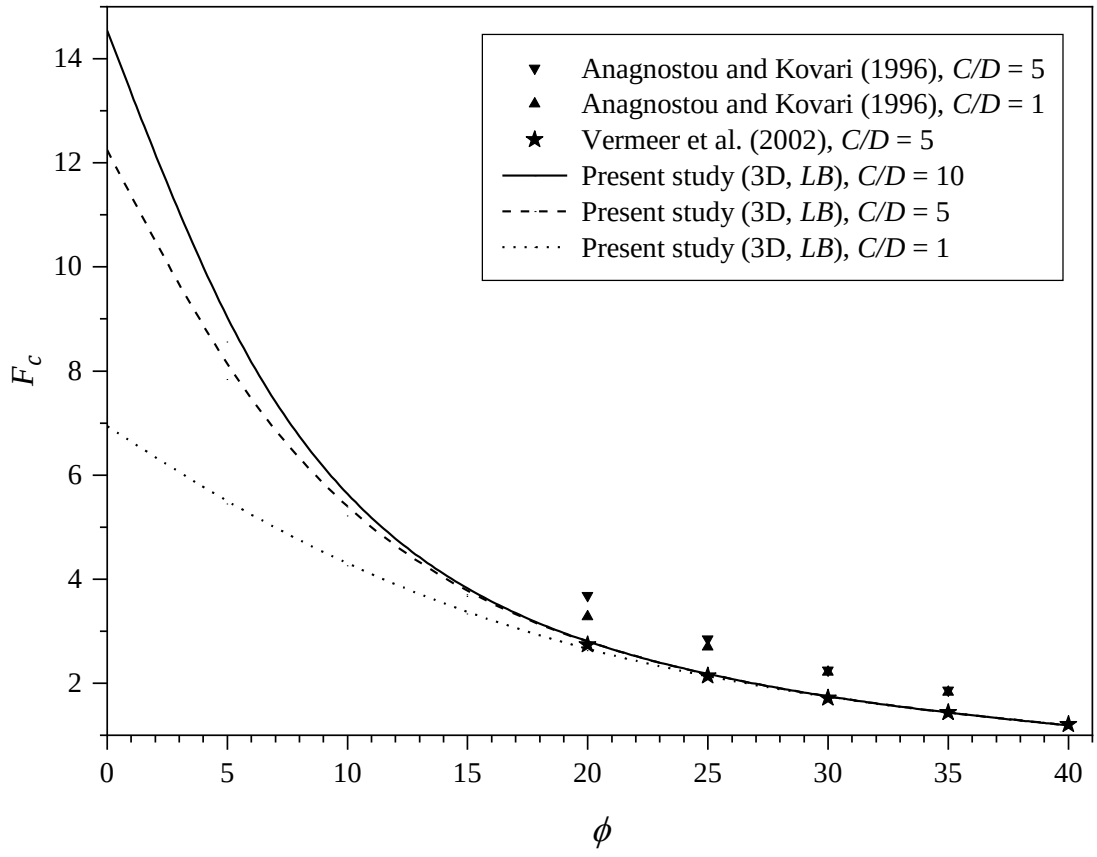

Figure 11.7. Comparison of cohesion stability factor (F_c).

The F_c results of Vermeer et al. (2002) are based on 3D displacement finite element analysis and is only available for a depth ratio of *C/D* = 5 and ϕ >20˚. It can be seen that their results agree well with the present study of 3D lower bound results and, as

discussed before, there is no effective difference between 2D and 3D analyses when $\phi > 20^{\circ}$. On the other hand, F_c results using the limit equilibrium method by Anagnostou and Kovári (1996) are greater than the lower bound results. Their sliding wedge model provides an un-conservative solution for the tunnel heading problem, and hence it should be used with caution in practice.

Figure 11.8 shows a comparison of the surcharge stability factor (F_s) with published results.

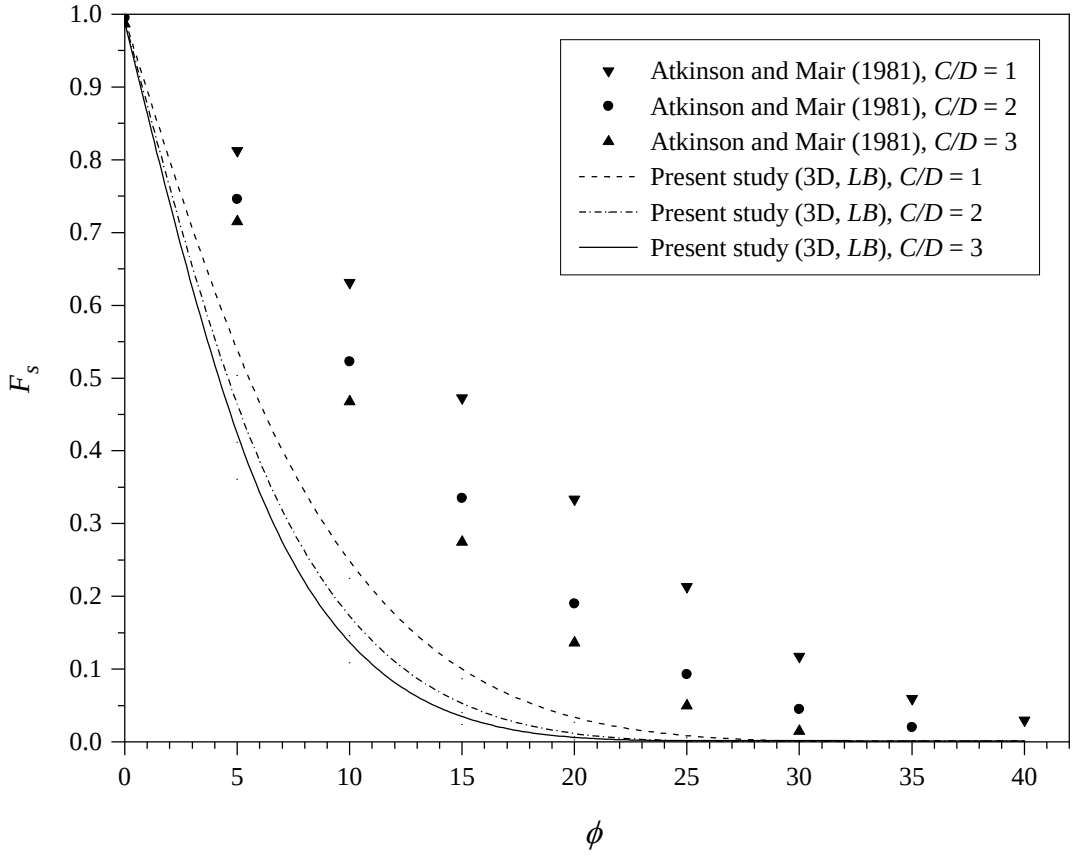

Figure 11.8. Comparison of surcharge stability factor (F_s).

The only available results for comparison are the experimental solutions for depth ratios of $C/D \leq 3$ by Atkinson and Mair (1981). Overall, there is good agreement in the trend of all curves despite their results being highly conservative.

The soil weight stability factor (F_γ) was discussed by Atkinson and Potts (1977), Atkinson and Mair (1981), Leca and Dormieux (1990), Anagnostou and Kovári (1996) and Vermeer et al. (2002). It was concluded in these studies that the values of F_γ are independent of the depth of the tunnel. This conclusion was reached based on the study

of shallow tunnels with $\phi > 20^{\circ}$. Figure 11.9 shows a comparison of F_{γ} between the 3D *FELA* studies and those published results for $\phi = 20^{\circ}$ - 40°.

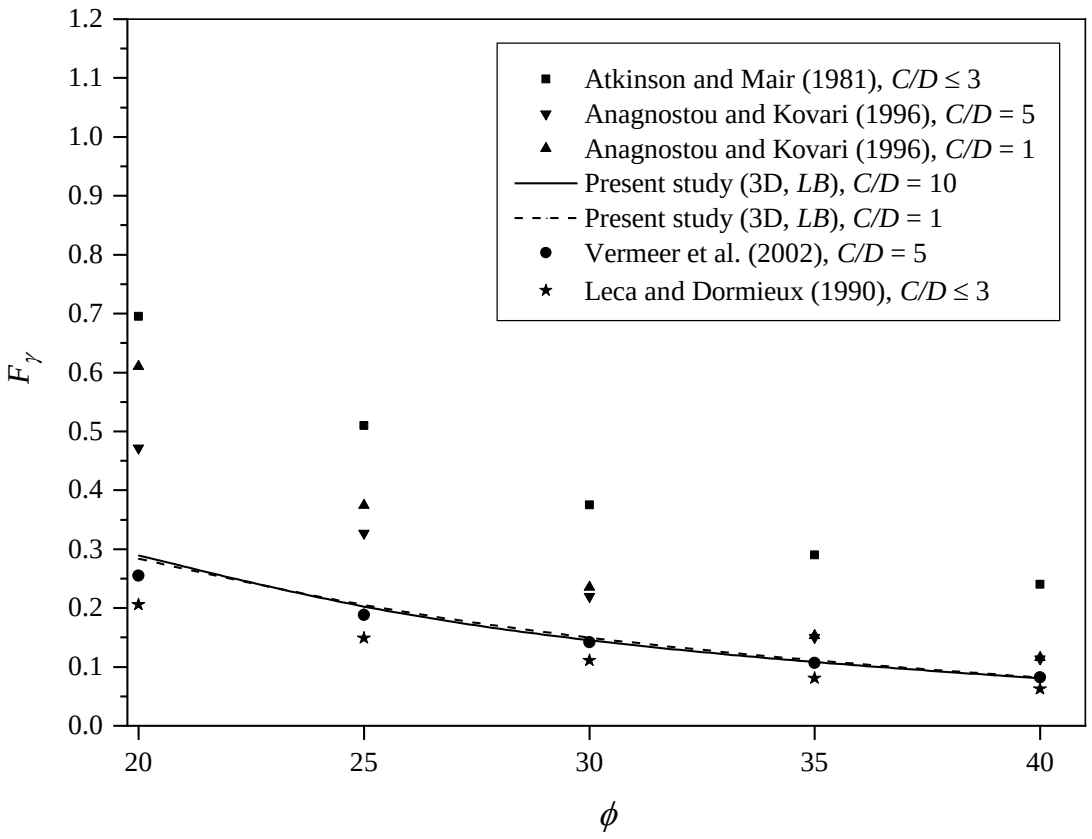

Figure 11.9. Comparison of soil weight stability factor (F_{γ}) (after Vermeer et al., 2002).

As discussed in Figure 11.6, all *C/D* curves merge into a single line at approximately $\phi = 17^{\circ}$. Therefore, it is not surprising to see from Figure 11.9 that very little difference of F_{γ} is observed between the two *FELA* curves (i.e. *C/D* = 1 and *C/D* = 10). Note that the results reported by Vermeer et al. (2002) are very close to our 3D *FELA LB*. On the other hand, the analytical upper bounds reported by Leca and Dormieux (1990) are about 25% below our *FELA LB* results, while those of Atkinson and Mair (1981) and Anagnostou and Kovári (1996) are more conservative. This comparison is for $20^{\circ} < \phi < 40^{\circ}$. Should these data be plotted in Figure 11.6, which covers a broad range of internal frictions ($\phi = 0^{\circ}$- 40°) and depth ratios (*C/D* = 1 - 10), the differences are shown in Figure 11.9 become insignificant.

11.4.2 Comparison with experimental results

Figure 11.10 shows a comparison of the normalised face pressures ($\sigma_t/\gamma D$) at collapse between the experimental results and other published solutions (after Kirsch (2010).

The experimental tunnel has a diameter D = 10m and a soil cover C = 10m in sandy soil with a variation of friction angle ϕ between 30˚ and 42˚. The 3D upper and lower bound solutions of the present study are added to Figure 11.10. Note that, with $c' = 0$ and $\sigma_s = 0$, $F_\gamma = \sigma_t / \gamma D$ (see Equation 11.1).

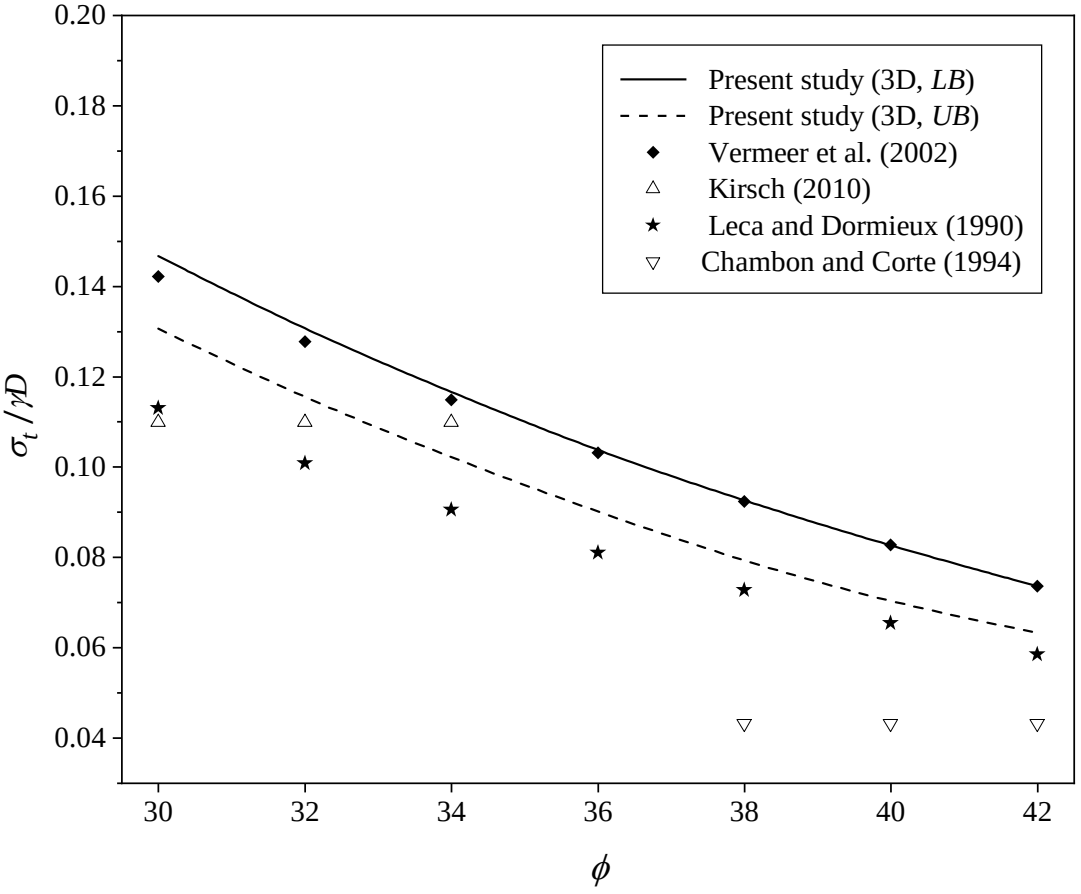

Figure 11.10. Comparison with various studies (after Kirsch, 2010).

The experimental results of ϕ = 30˚, 32˚ and 34˚ by Kirsch (2010) show a horizontal line, which is similar to the experimental results of ϕ = 38˚, 40° and 42° by Chambon & Corte (1994). The difference between current 3D *FELA* and these experimental results varies despite the small values of $(F_\gamma = \sigma_t / \gamma D)$ in the figure. Close agreement is found between the *LB* results and the 3D *FEM* results by Vermeer et al. (2002). Numerical results of Leca and Dormieux (1990) are also reasonably close to the *UB* results. Note that for the problem of "support" pressure, *LB* provides conservative estimation and are greater than *UB*.

11.5 Examples and Practical Uses

Since the lower bound theorem offers a safe assessment of the limit pressure for a stability problem, Equations (11.4-11.9) have been derived based on *LB* results. These results can assist designers and practising engineers in the safety evaluation of tunnel face stability.

11.5.1 Stability analysis of a tunnel face in cohesionless soil

It is proposed to excavate a tunnel in the greenfield condition (σ_s = 0) through a cohesionless soil ($c' = 0$ kPa, ϕ = 35˚ and γ = 18 kN/m^3). The tunnel has a diameter (*D*) of 6m and a soil cover (*C*) of 18m. Determine the critical internal support pressure.

- For the greenfield condition ($\sigma_s = 0$) with *C/D* = 3 and ϕ = 35˚, Table 11.3 gives *LB* value of F_γ = 0.109. Equation (11.9) also gives *LB* value of F_γ = 0.109.
- Equation (11.1) is used to calculate the critical pressure, σ_t (*LB*) = 11.772 kPa. An actual 3D *FELA* analysis gives σ_t (*LB*) = 11.775 kPa.
- In cohesionless soil, a positive internal pressure σ_t (support pressure) is always required to prevent tunnel collapse regardless of the value of internal friction (ϕ). This case belongs to the class of "active" failure where *LB* pressures are always greater than *UB* ones.

11.5.2 Stability analysis of a tunnel face in cohesive-frictional soil

A planned tunnel has a diameter (*D*) of 6m and a cover depth (*C*) of 24m. The soil is found to be cohesive-frictional with a unit weight (γ) of 18 kN/m^3, angle of internal friction (ϕ) of 35˚ and cohesion (*c*) of 54 kPa. Determine the critical internal pressure (σ_t) when the surcharge pressure (σ_s) is zero.

- For *C/D* = 4 and ϕ = 35˚, Tables 11.1-11.3 gives *LB* values of (F_c = 1.428, F_s = 0 and F_γ = 0.108) and *UB* values of (F_c = 1.428, F_s = 0 and F_γ = 0.092).
- Using Equation (11.1), σ_t (*LB*) = -65.448 kPa and σ_t (*UB*) = -67.176 kPa.
- An actual 3D *FELA* analysis gives σ_t (*LB*) = -65.438 kPa and σ_t (*UB*) = -67.834 kPa.
- The negative value of σ_t indicates that an internal "pulling" pressure is required to reach a collapse state. In other words, the tunnel will remain stable without any internal "pulling" pressure. This case belongs to the class of "passive" failure where *UB* pressures are always greater than *LB* ones.

11.6 Conclusion

In order to study the face stability of circular tunnels in cohesive-frictional soil, numerical simulations were conducted using the 3D finite element limit analyses. A series of parametric studies for different soils (ϕ = 0˚- 40˚) and various depth ratios (C/D = 1 - 10) were performed and the tunnel stability factors (F_c, F_s and F_γ) were calculated. Examples were provided, demonstrating how to use the factors to estimate internal support pressures. The following conclusions are drawn:

1. Unlike the traditional bearing capacity factors (N_c, N_s and N_γ), the tunnel stability factors (F_c, F_s and F_γ) are functions of both the soil friction angle ϕ and the depth ratio (C/D). The equation for estimating the tunnel face support pressures is $\sigma_t = -c\ F_c + \sigma_s\ F_s + \gamma D F_\gamma$
2. The cohesion stability factor (F_c) increases as the depth ratio (C/D) increases, but it decreases as the soil friction angle ϕ increases. The F_c curves for various C/D merge into a single line at approximately ϕ = 21˚.
3. The surcharge stability factor (F_s) decreases nonlinearly as the soil friction angle ϕ increases. For all depth ratios (C/D), F_s has a maximum value of one at ϕ =0˚ and a minimum value of zero when ϕ > 20˚. In general, the effect of surcharge load (σ_s) diminishes as the soil friction angle increases due to the development of soil arching.
4. The soil weight stability factor (F_γ) increases as the depth ratio (C/D) increases. F_γ has a maximum value of (C/D + 0.5) at ϕ = 0˚ and decreases dramatically as the soil friction angle ϕ increases due to the development of soil arching. The F_γ curves merge into a single line at approximately ϕ =17˚.

Similar to the undrained study in Part A, both 2D and 3D twin tunnels are studied in drained condition using the tunnel stability factors approach in Chapters 12 and 13.

CHAPTER 12: DRAINED ANALYSIS OF 2D TWIN CIRCULAR TUNNELS

12.1 Introduction

In the previous chapters, the stability of single circular tunnels was studied. This chapter presents the stability problem of twin circular tunnels drive side-by-side in drained cohesive-frictional soil. Unlike the case of a single tunnel, the centre-to-centre distance between the twin tunnels appears as a new parameter that must be considered in twin tunnel stability.

Similar to the bearing capacity equation proposed by Terzaghi, the proposed method is based on the three stability factors that are functions of the soil internal friction angle and the tunnel depth ratio. Two-dimensional finite element limit analysis (*FELA*) is employed to determine rigorous upper bound (*UB*) and lower bound (*LB*) solutions of the tunnel stability factors (F_c, F_s and F_γ).

The variations of the stability factors with tunnels' spacing ratio are established for various depth ratios (*C/D*) and soil internal friction angles (ϕ). For practical suitability, the results are presented in the form of dimensionless stability charts with the actual tunnel stability factors closely bracketed from above and below using upper and lower bound methods. As an extra validation, the results are compared with available solutions reported in the literature.

12.2 Problem Definition and Methodology

Finite element limit analysis (*FELA*) is a novel computational method of limit analysis. It employs the classical plasticity theorems with the concept of finite element and mathematical programming (either linear or nonlinear programming). When upper bound (*UB*) and lower bound (*LB*) estimates are calculated together, a true collapse load is bracketed. The difference between the two limits provides an exact measure of the discretisation error in the solution (Lyamin & Sloan 2002a, 2002b; Sloan 2013).

Recently, the *FELA* software, *OptumG2* (OptumCE 2017), has been successfully applied to solve a variety of drained and undrained stability problems in geotechnical engineering (Keawsawasvong & Ukritchon 2017; Ukritchon & Keawsawasvong 2017; Shiau & Al-Asadi 2018, 2020b). Consequently, it was chosen in this study to compute the stability factors (F_c, F_s and F_γ) that can be used in a traditional formula, as shown in Equation 12.1.

$$\sigma_t = -cF_c + \sigma_s F_s + \gamma D F_\gamma \tag{12.1}$$

The initial developments of the *FELA* were by using linear programming (Sloan 1988b, 1989). The newer developments are based on a much faster nonlinear programming formulation by (Lyamin & Sloan 2002b, 2002a) and (Krabbenhøft et al. 2005; Krabbenhøft et al. 2007). The underlying bound theorems assume a rigid-perfectly plastic material with associated plasticity. The details of limit analysis and *FELA* can be found in Sloan (2013), and they will not be repeated here.

The layout of the unlined twin tunnels stability problem is shown in Figure 12.1. The tunnels have a diameter D and soil cover C. The ground surface is horizontal and subject to a vertical surcharge σ_s, while the internal uniform support pressure is represented by σ_t. Since the tunnels are unlined with infinite length, a plane strain condition was adopted (Shiau & Sams 2019).

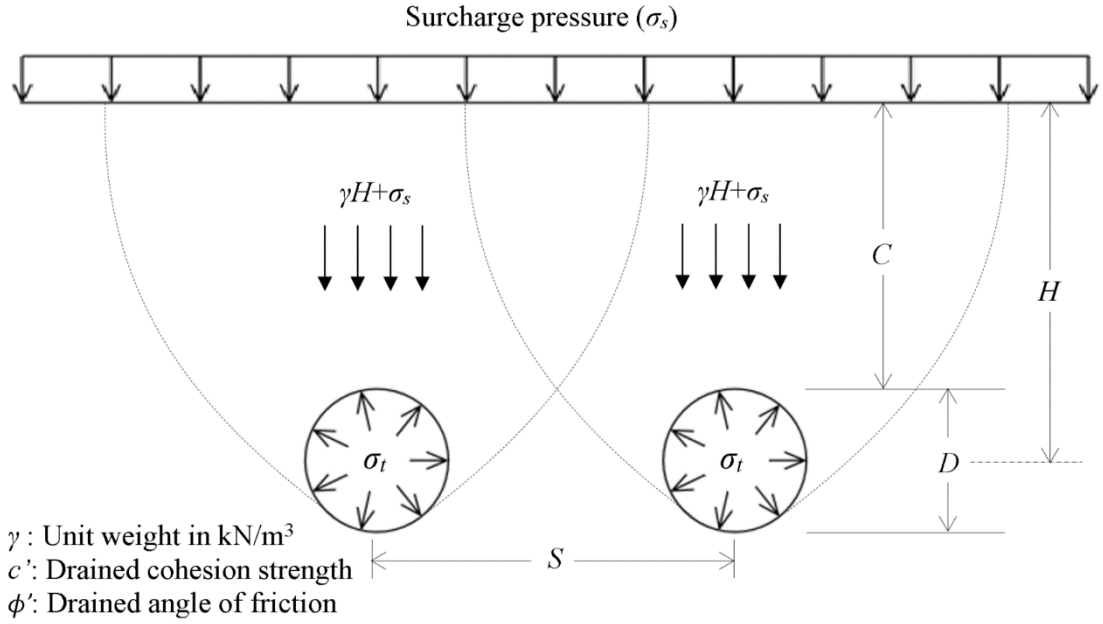

Figure 12.1. Statement of the problem.

Figure 12.2 shows a typical *FELA* half mesh used in the analysis for (*C/D* = 2 and *S/D* = 3). In both upper and lower bound calculations, the soil mass was discretised as triangular elements and modelled as Mohr-Coulomb material with the associated flow rule.

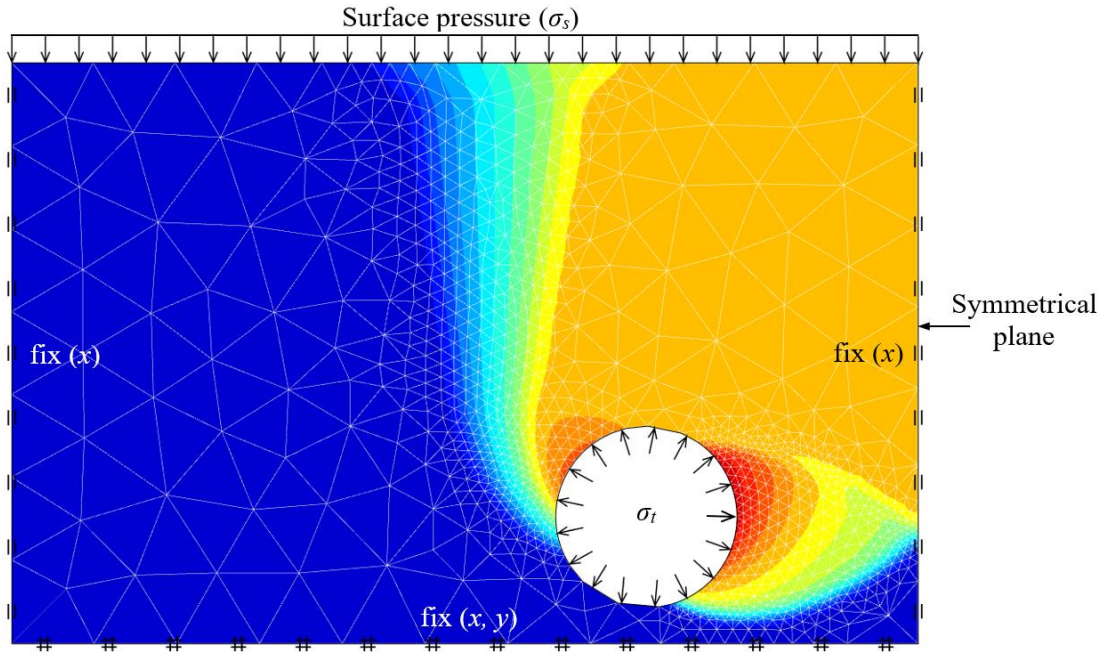

Figure 12.2. Adaptive mesh (half) and absolute displacement (|u|) contour plot for the twin tunnel problem (*C/D* = 2 and *S/D* = 3).

The boundary condition of the problem was defined such that the bottom boundary of the model be fixed in both vertical and horizontal directions, while the left and the right boundary of the problem was allowed to move only in the vertical direction. Note that the right-hand side boundary is the plane of symmetry. The size of the problem domains was chosen to be large enough so that the plastic yielding zone was contained within the domain.

An automatically adaptive mesh refinement was employed in both the *UB* and *LB* simulations to compute the tight *UB* and *LB* solutions. It is interesting to see the adaptive mesh created using the latest *FELA* program, which was so generated in such a way that it follows exactly the potential slip surface of the failure mechanism. The mechanism transforms from the twin effects to a non-twin effect of a single tunnel. This can be seen in Figures 12.3-12.4 where (*S/D* = 5 and *S/D* = 7).

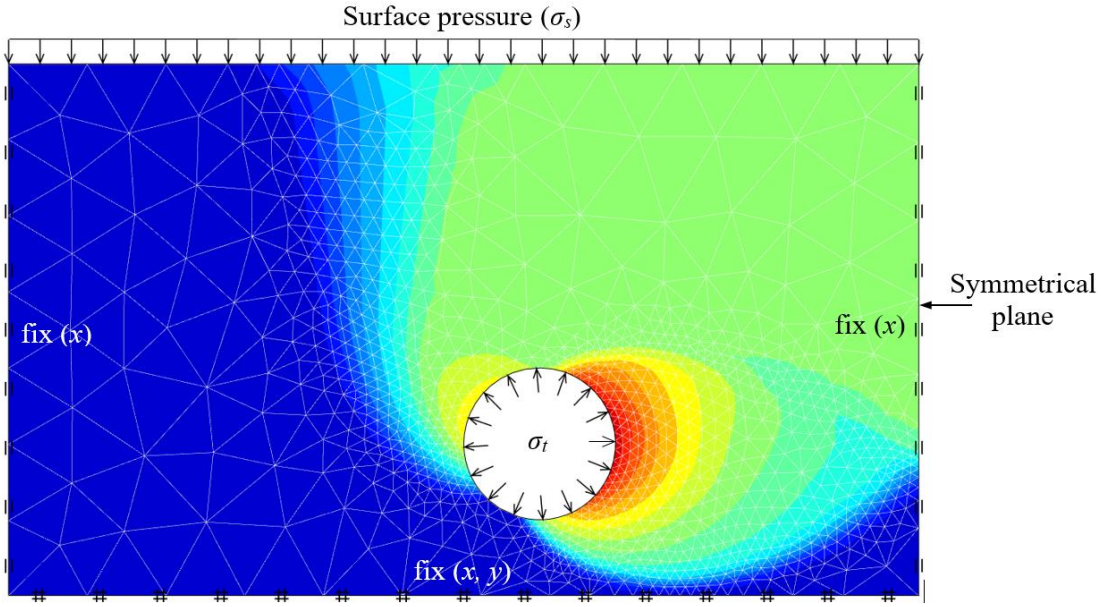

Figure 12.3. Adaptive mesh (half) and absolute displacement (|u|) contour plot for the twin tunnels problem (*C/D* = 2 and *S/D* = 5).

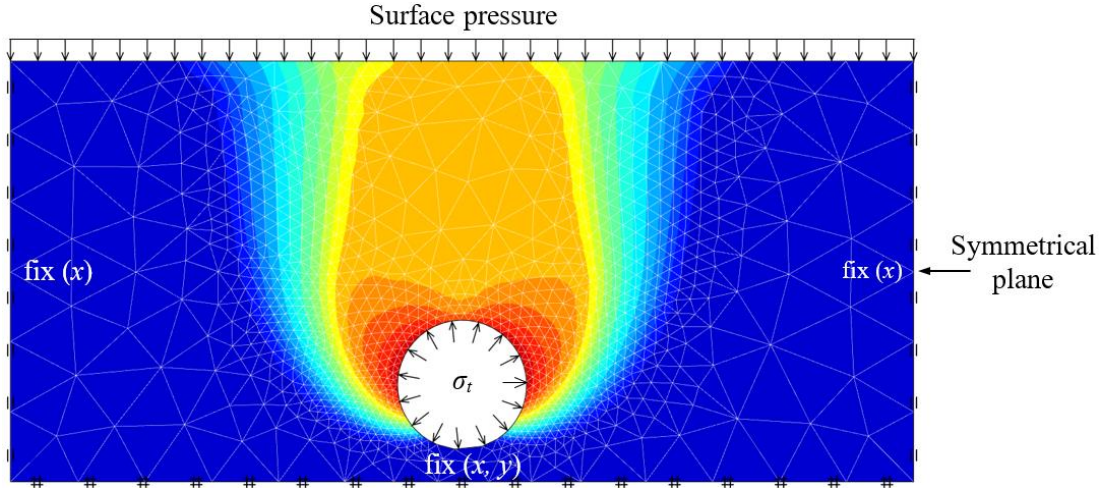

Figure 12.4. Adaptive mesh (half) and absolute displacement (|u|) contour plot for the twin tunnels problem (*C/D* = 2 and *S/D* = 7).

Approximately 40,836 *FELA* analyses were performed to calculate the stability factors (F_c, F_s and F_γ) for a wide range of soil parameters (ϕ = 0˚- 40˚), spacing ratios (*S/D* = 2 - 28) and depth ratios (*C/D* = 2 - 10). The principles in the calculations of the three factors are as follows: (1) both $\gamma = 0$ and $\sigma_s = 0$ are used in the analysis to determine F_c, which can be calculated using the equation $\sigma_t = -c' F_c$; (2) both $\gamma = 0$ and $c' = 0$ are adopted in the analysis and F_s is calculated using the equation $\sigma_t = \sigma_s F_s$; (3) both $c' = 0$ and $\sigma_s = 0$ are used in the analysis so that F_γ can be determined using the

equation $\sigma_t = \gamma D F_\gamma$. Similar to the superposition principle of the traditional bearing capacity equations, the minimum support pressures σ_t at collapse can be determined using equation (12.1) with the produced twin tunnel stability factors in this chapter.

12.3 Discussing the Twin Tunnel Stability Factors (F_c, F_s and F_γ)

Numerical analyses were performed to calculate the upper and the lower bounds limits of the stability factors (F_c, F_s and F_γ) for various depth ratios (C/D = 2 - 10), spacing ratios (S/D = 2 - 28) and angles of internal friction (ϕ = 0˚ - 40˚). The effect of the parameters C/D, S/D and ϕ on the tunnel stability factors are presented in Figures 12.5-12.7, 12.9-12.20, and they are discussed below.

12.3.1 F_c, F_s and F_γ in undrained condition (ϕ = 0˚)

Figure 12.5 shows that F_c is a function of the depth ratio (C/D) and the spacing ratio (S/D). F_c increases with the increasing of C/D. For each C/D, F_c increases nonlinearly as S/D increases until it reaches a constant value, which indicates that the twin tunnels stability is unaffected by the tunnel spacing.

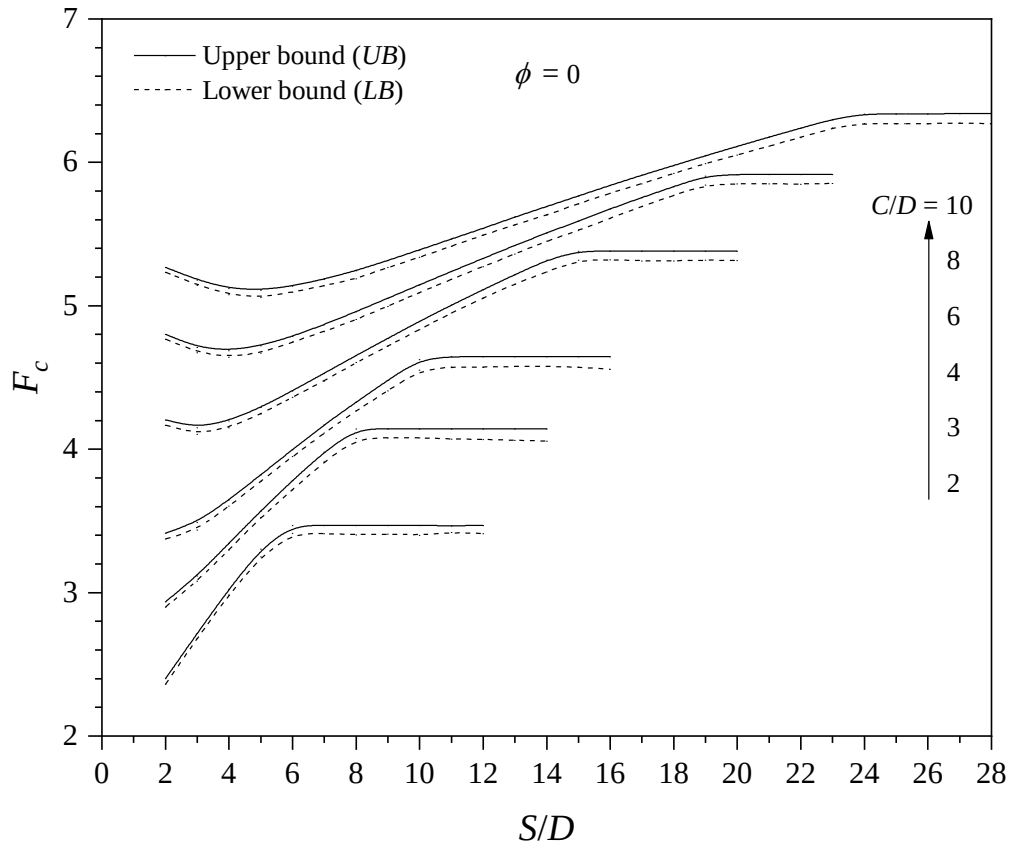

Figure 12.5. F_c vs S/D and various C/D (ϕ = 0˚).

At this point, the stability responses are identical to those of corresponding single tunnels, and the stability factor (F_c) are at their maximum values. The corresponding *S/D* to the first constant value of F_c is the minimum spacing ratio $(S/D)_{min}$ required to eliminate the interaction effect between the twin tunnels. It is interesting to see that the minimum value of F_c is not always at the closest spacing ratio but at the spacing ratio of 3-4, in particular for deep cases ($C/D \geq 6$).

For F_s in undrained condition ($\phi = 0^\circ$), Figure 12.6 shows that the factor F_s has a constant value of unity no matter what values of *C/D* and *S/D* are. This finding is understandable for such cases in the undrained condition where no volume loss occurs during plastic shearing.

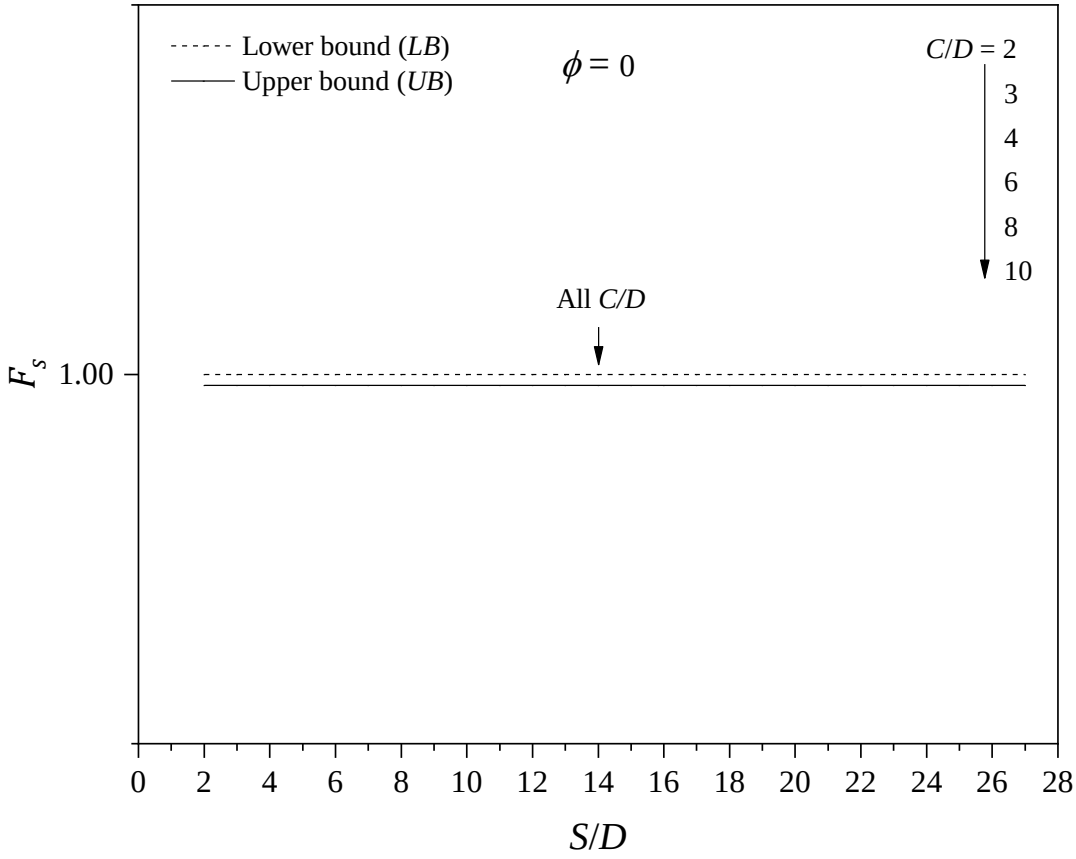

Figure 12.6. F_s vs *S/D* and various *C/D* ($\phi = 0^\circ$).

For F_γ in the undrained condition ($\phi = 0^\circ$), Figure 12.7 shows that the factor F_γ is a function of *C/D* only. The value of *S/D* does not affect the factor $F_{\gamma.}$ Indeed, the unit weight effect displays the same trend as the surcharge in an undrained condition. In general, $F_\gamma = (C/D + 0.5)$. The larger the *C/D* value is, the larger the factor F_γ is. This

finding is the same as in Shiau and Al-Asadi (2020b, 2020c) for 2D and 3D tunnel heading studies.

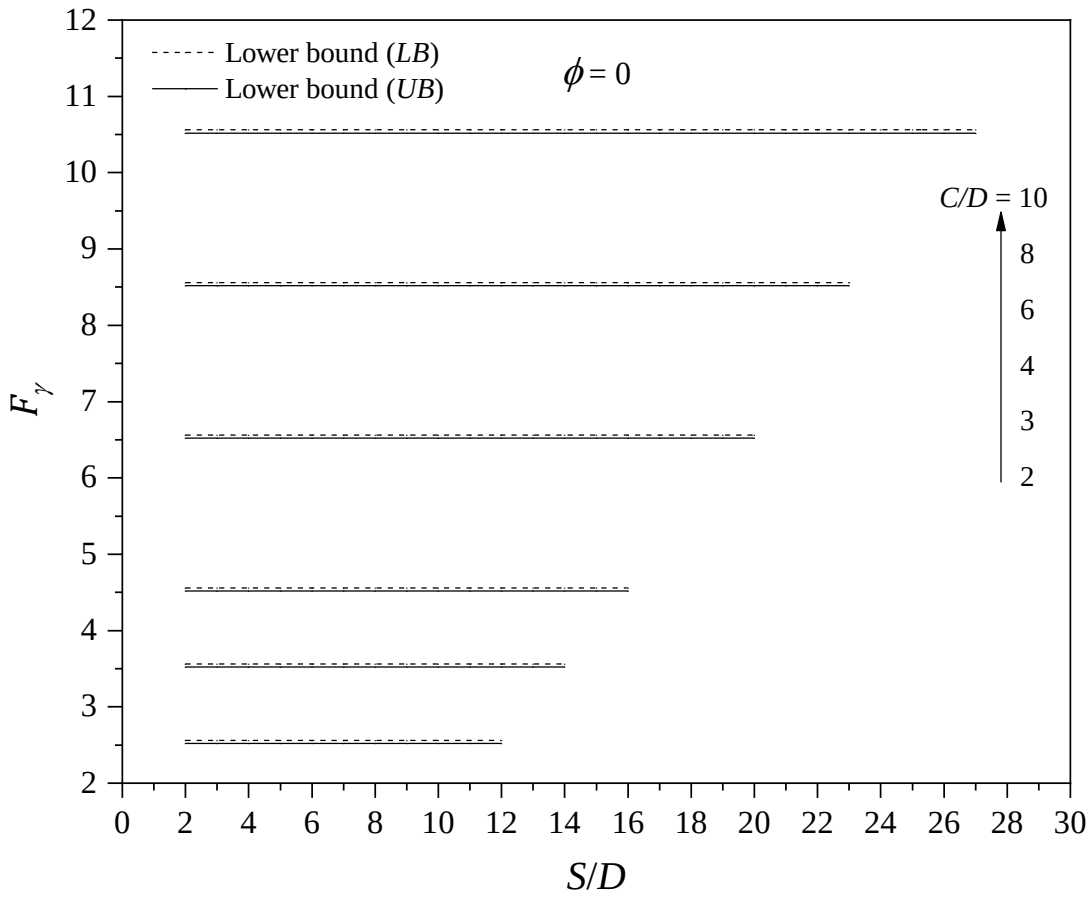

Figure 12.7. F_γ vs S/D and various C/D ($\phi = 0^\circ$).

Figure 12.8 shows the minimum spacing ratios $(S/D)_{min}$ for various depth ratios (C/D). A linear relationship is observed between C/D and $(S/D)_{min}$. The line separates two zones; one being the single tunnel (unaffected by the tunnel spacing) and the other is the zone with twin tunnels effects. Equations 2 is an accurate curve-fitting for the relationship between $(S/D)_{min}$ and C/D, with a correlation coefficient (R^2) of 0.999.

$$(S/D)_{min} = 2.285 \times (C/D) + 1.15 \quad (2)$$

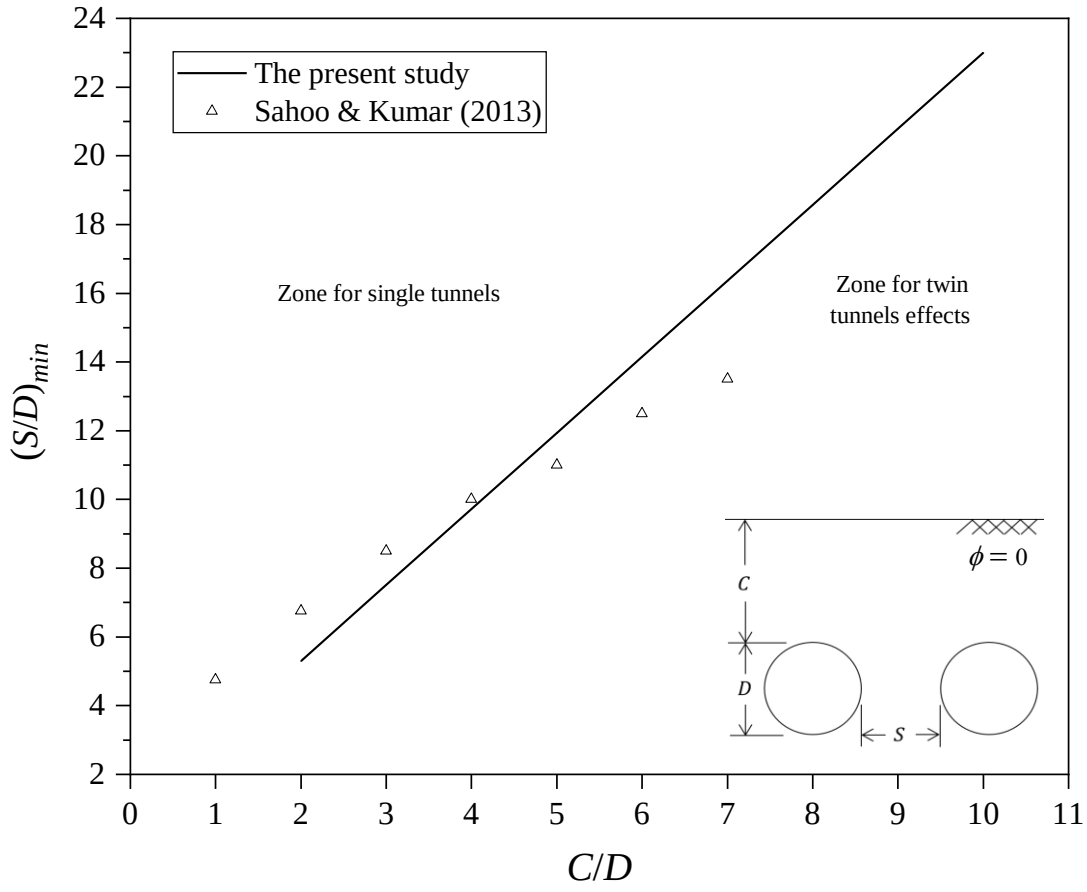

Figure 12.8. Comparison of the minimum spacing ratio $(S/D)_{min}$ required to eliminate the interaction between the tunnels ($\phi = 0^{\circ}$).

12.3.2 F_c, F_s and F_γ in drained condition ($\phi > 0^{\circ}$)

In contrary to undrained condition, Figures 12.9 - 12.20 (for $\phi > 0^{\circ}$ drained analysis) show that all the stability factors are a function of the angle of internal friction (ϕ), depth ratio (C/D) and spacing ratio (S/D).

Figures 12.9 - 12.12 (ϕ = 10 $^{\circ}$, 20 $^{\circ}$, 30 $^{\circ}$ and 40° respectively) show that F_c increases with the increasing of C/D. For each C/D, F_c increases nonlinearly as S/D increases until it reaches a constant value, which indicates that no interactions occur between the tunnels. However, for high friction angles ($\phi > 30^{\circ}$), both C/D and S/D have little effects on the results of F_c in particular for large depth ratios ($C/D > 5$). Also, note that the minimum spacing ratios $(S/D)_{min}$ decrease with the increasing of ϕ.

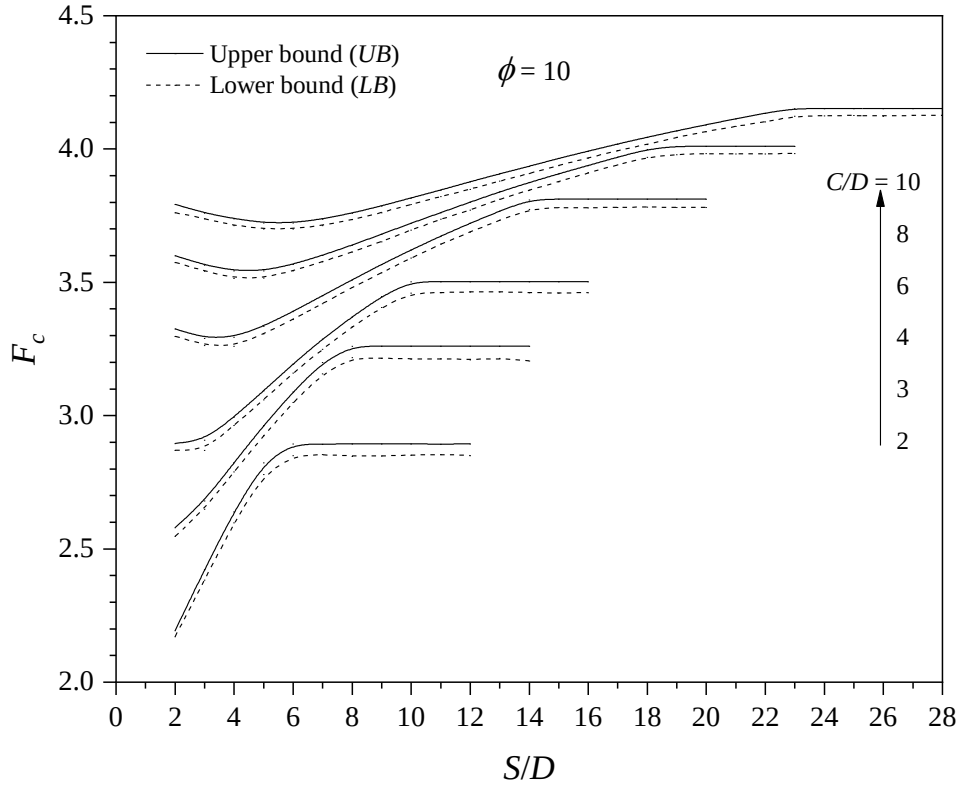

Figure 12.9. F_c vs S/D and various C/D (ϕ = 10˚).

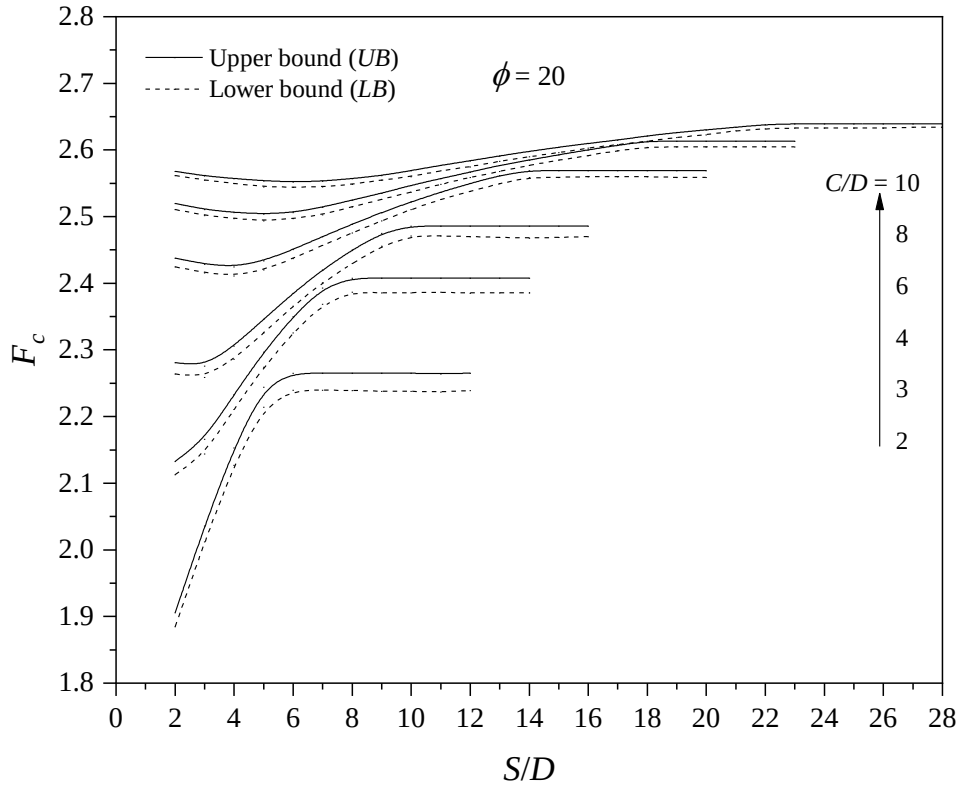

Figure 12.10. F_c vs S/D and various C/D (ϕ = 20˚).

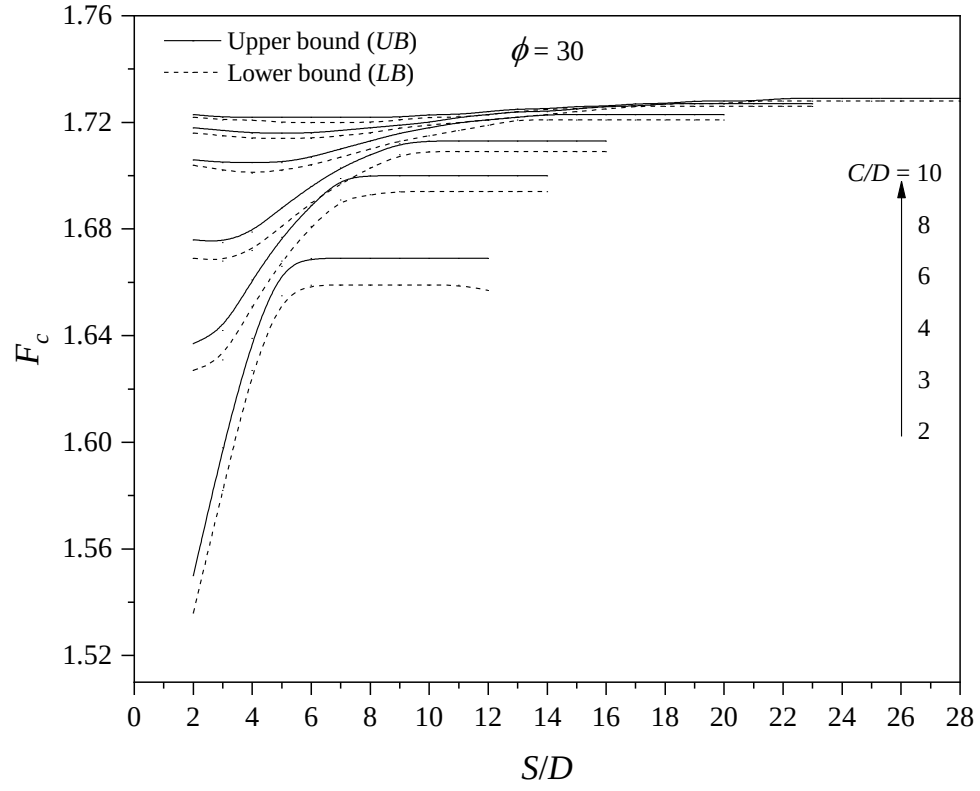

Figure 12.11. F_c vs *S/D* and various *C/D* (ϕ = 30˚).

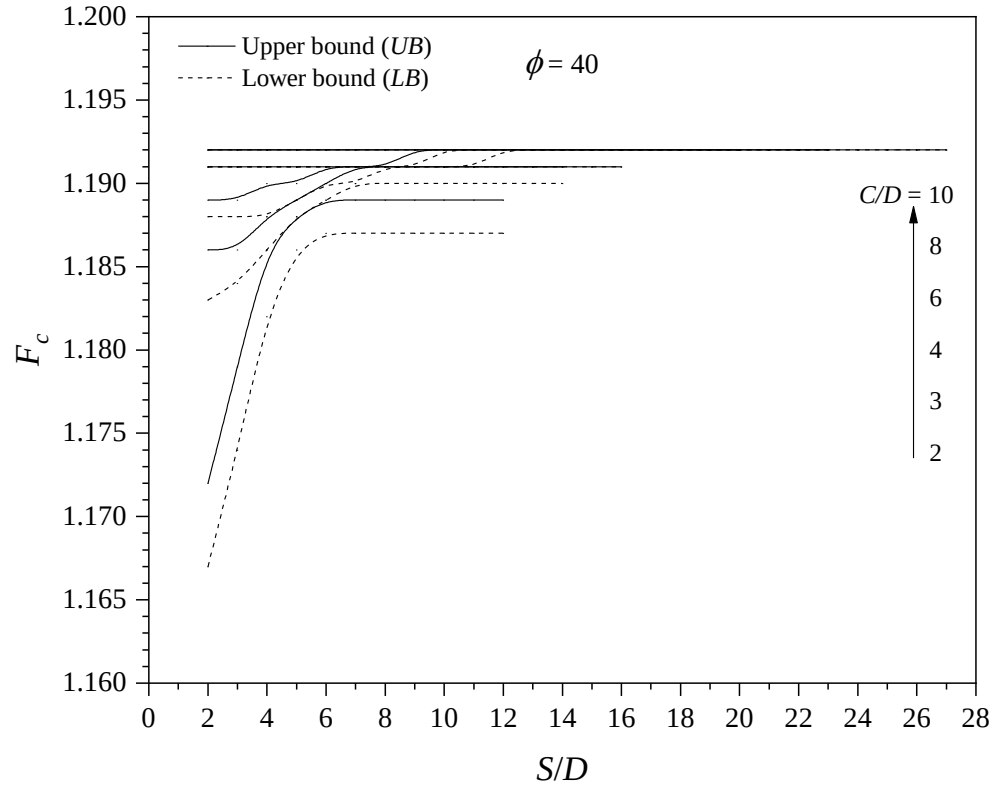

Figure 12.12. F_c vs *S/D* and various *C/D* (ϕ = 40˚).

With regards to F_s, Figures 12.13 - 12.16 (ϕ = 10˚, 20˚, 30˚ and 40˚ respectively) show that the surcharge stability factor (F_s) decreases with the increasing of *C/D*. In general, F_s decreases with the increasing of *S/D* until it reaches a constant value, indicating no interference occurs between twin tunnels. Also, F_s decreases with the increasing of ϕ and the effect of *C/D* and *S/D* diminishes when ϕ > 20˚. Figure 12.16 shows that, for all *C/D* values, F_s = 0 when ϕ = 40˚.

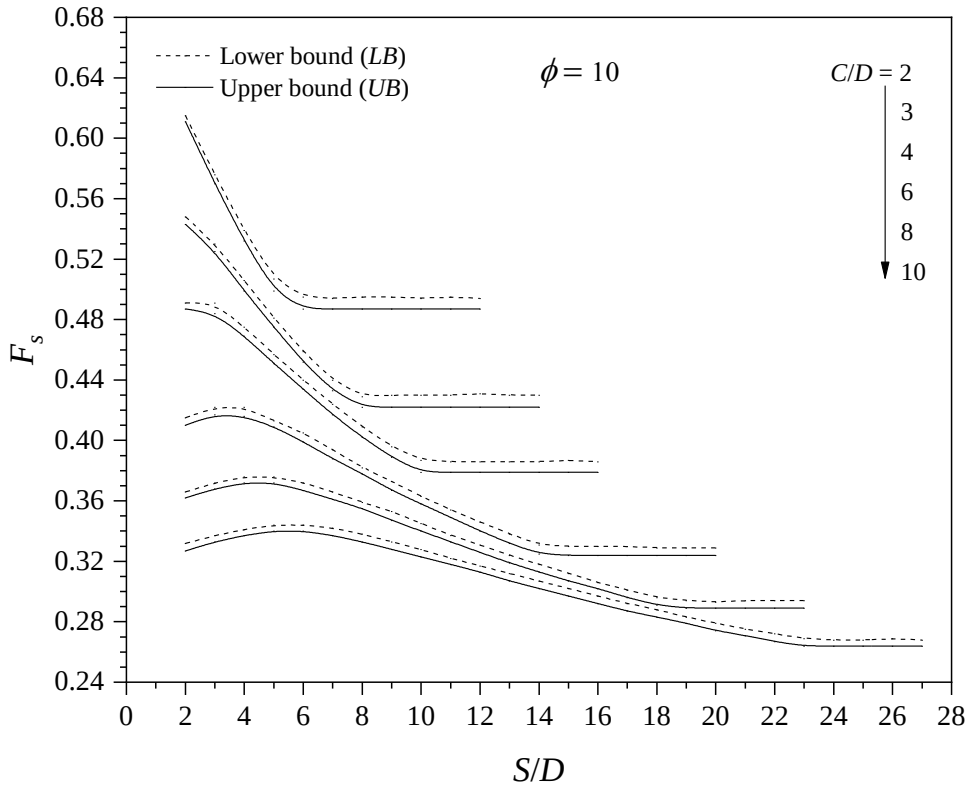

Figure 12.13. F_s vs *S/D* and various *C/D* (ϕ = 10˚).

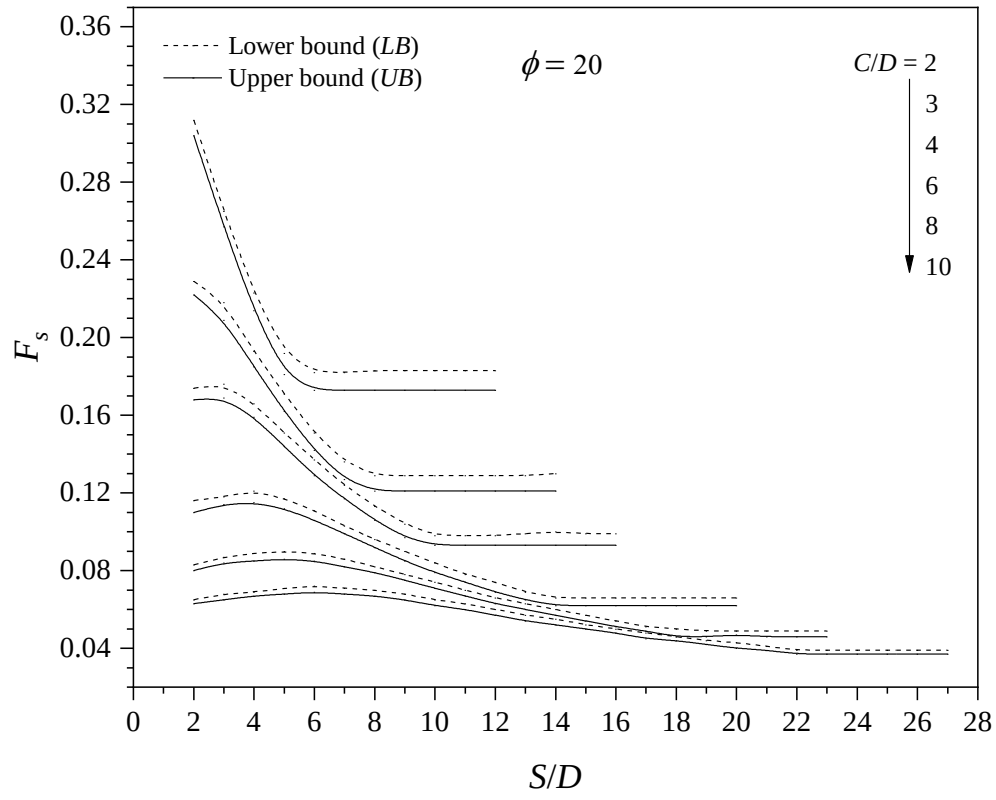

Figure 12.14. F_s vs *S/D* and various *C/D* (ϕ = 20˚).

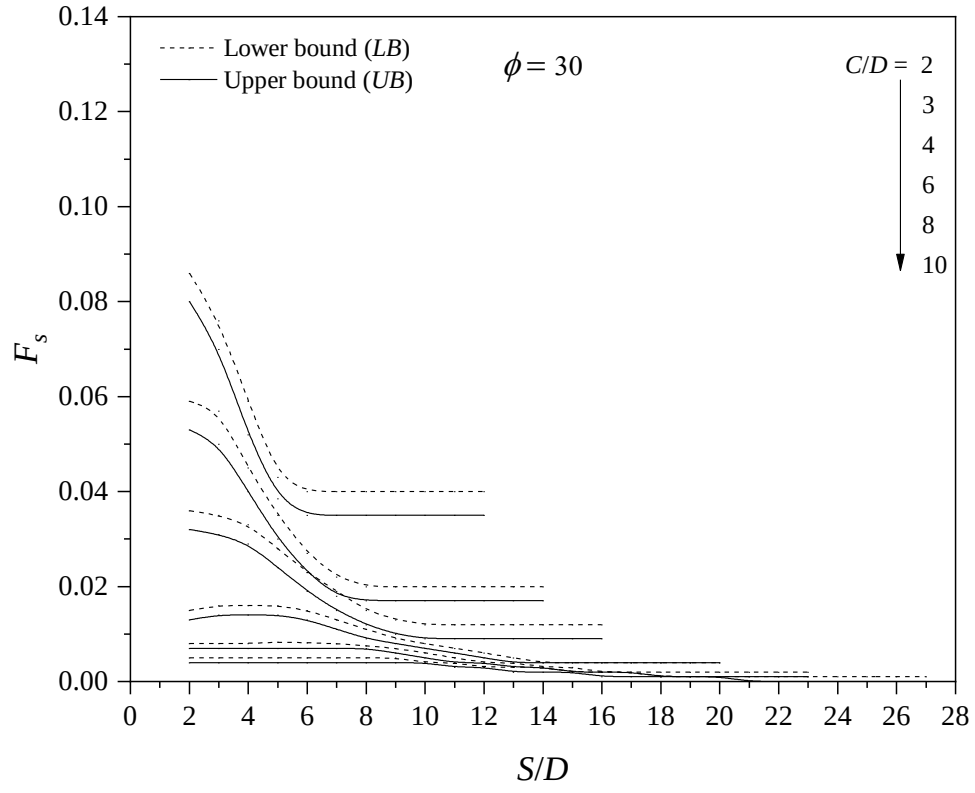

Figure 12.15. F_s vs *S/D* and various *C/D* (ϕ = 30˚).

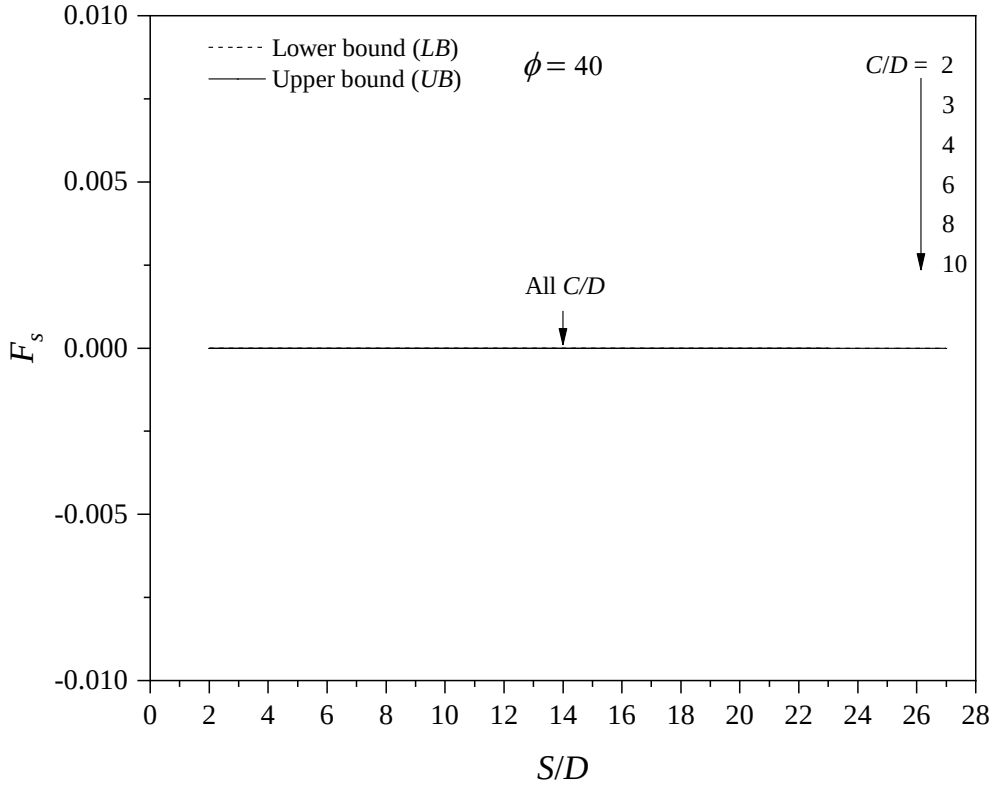

Figure 12.16. F_s vs *S/D* and various *C/D* (ϕ = 40˚).

Finally, for the factor F_γ, Figures 12.17-12.20 (ϕ = 10˚, 20˚, 30˚ and 40˚ respectively) show that the unit weight stability factor (F_γ) increases with the increasing of *C/D*. Similar to F_s, the unit weight stability factor (F_γ) increases with the decreasing of *S/D* below the minimum spacing ratios $(S/D)_{min}$. Also, F_γ decreases with increasing of ϕ, due to the material arching. It is noted that a minimum value of $F_\gamma \simeq 0.181$ is obtained for ϕ = 40˚ irrespective of *C/D* values (see Figure 12.20).

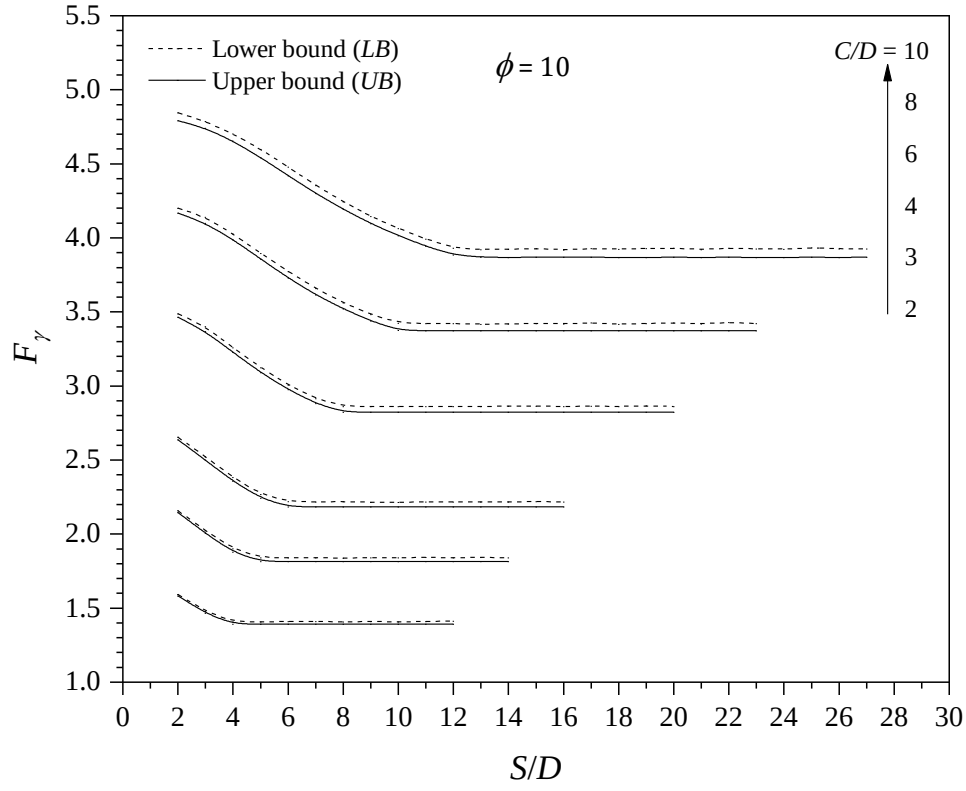

Figure 12.17. F_γ vs *S/D* and various *C/D* (ϕ = 10˚).

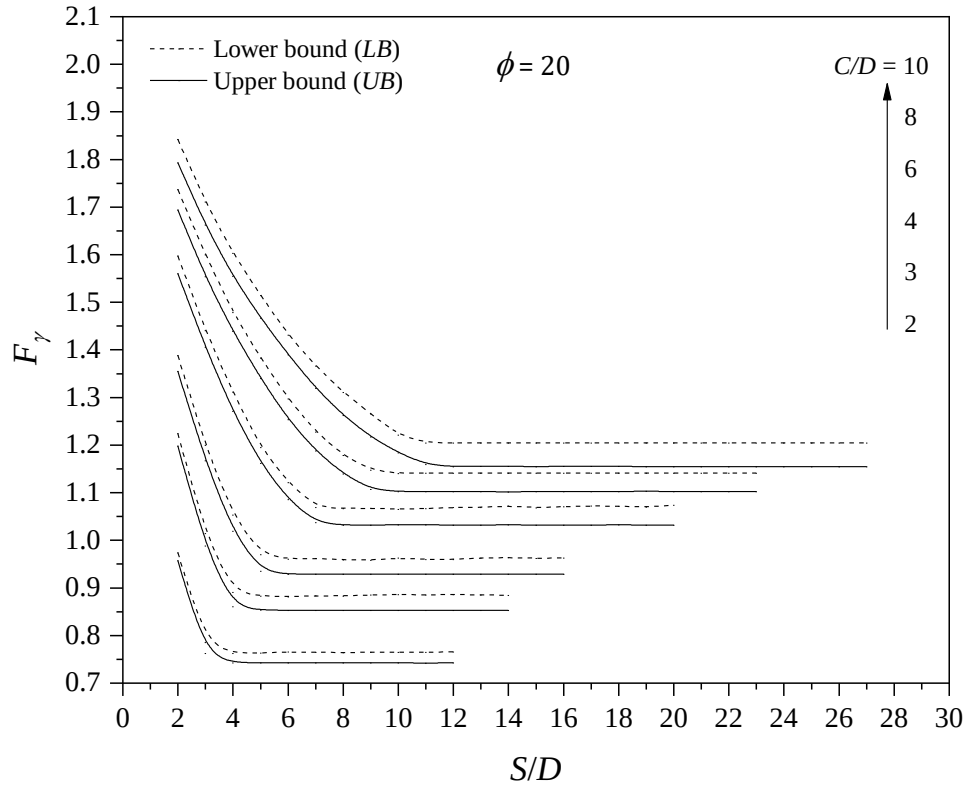

Figure 12.18. F_γ vs *S/D* and various *C/D* (ϕ = 20˚).

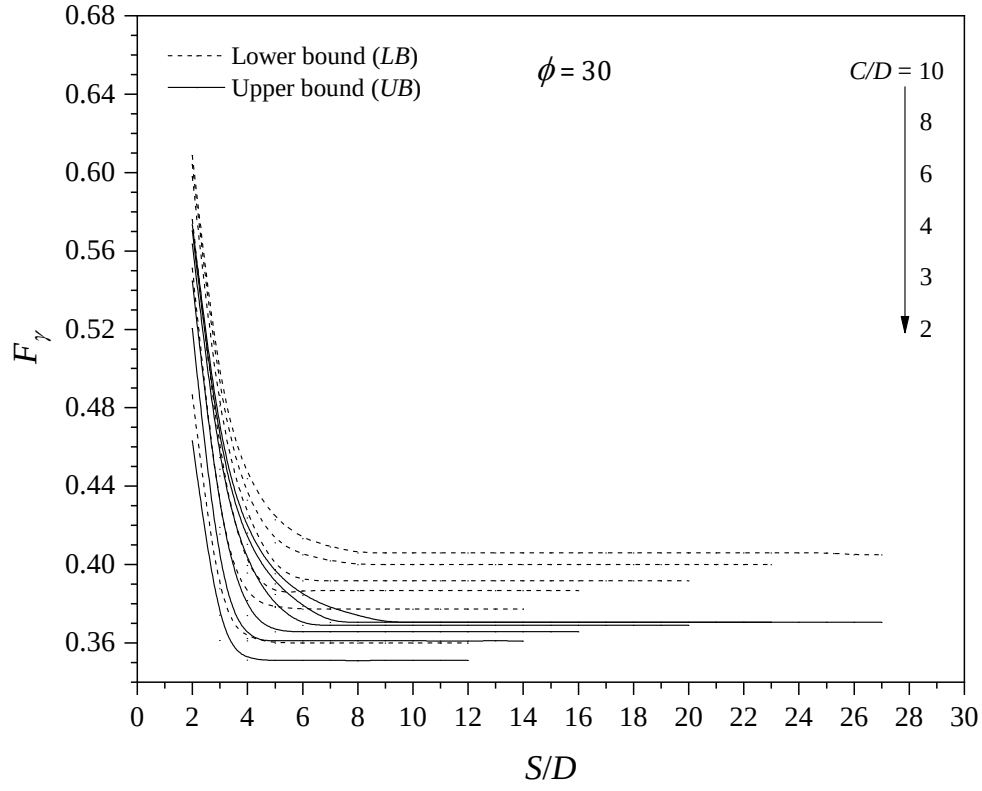

Figure 12.19. F_γ vs *S/D* and various *C/D* (ϕ = 30˚).

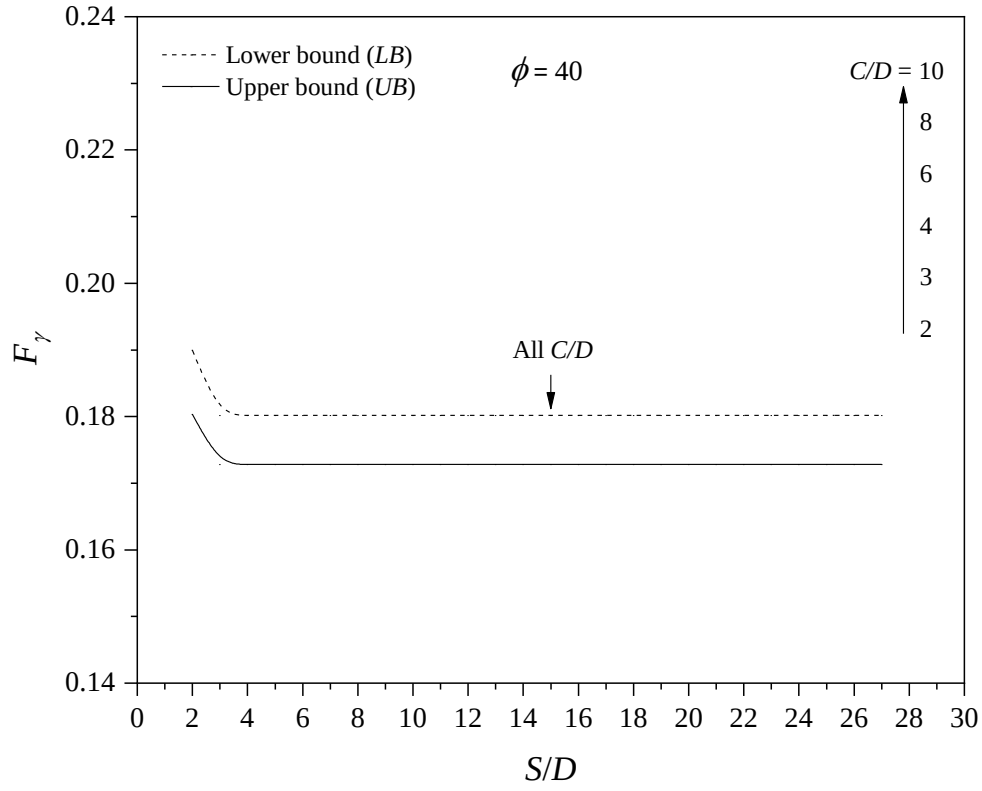

Figure 12.20. F_γ vs *S/D* and various *C/D* (ϕ = 40˚).

12.4 Comparison of Results

Following Sahoo and Kumar (2013), Figure 12.21 and Table 12.1 show a comparison of the stability results of this study with those of (Osman 2010; Sahoo & Kumar 2013; Wilson et al. 2014, 2015) for a depth ratio of five (C/D = 5). A different expression for the stability ($N = \gamma_{max}H/c$) was used in Sahoo and Kumar (2013) for undrained clay. To make the comparison, both (F_c and F_γ) factor for C/D = 5 are used to reproduce the corresponding ($N = \gamma_{max}H/c$).

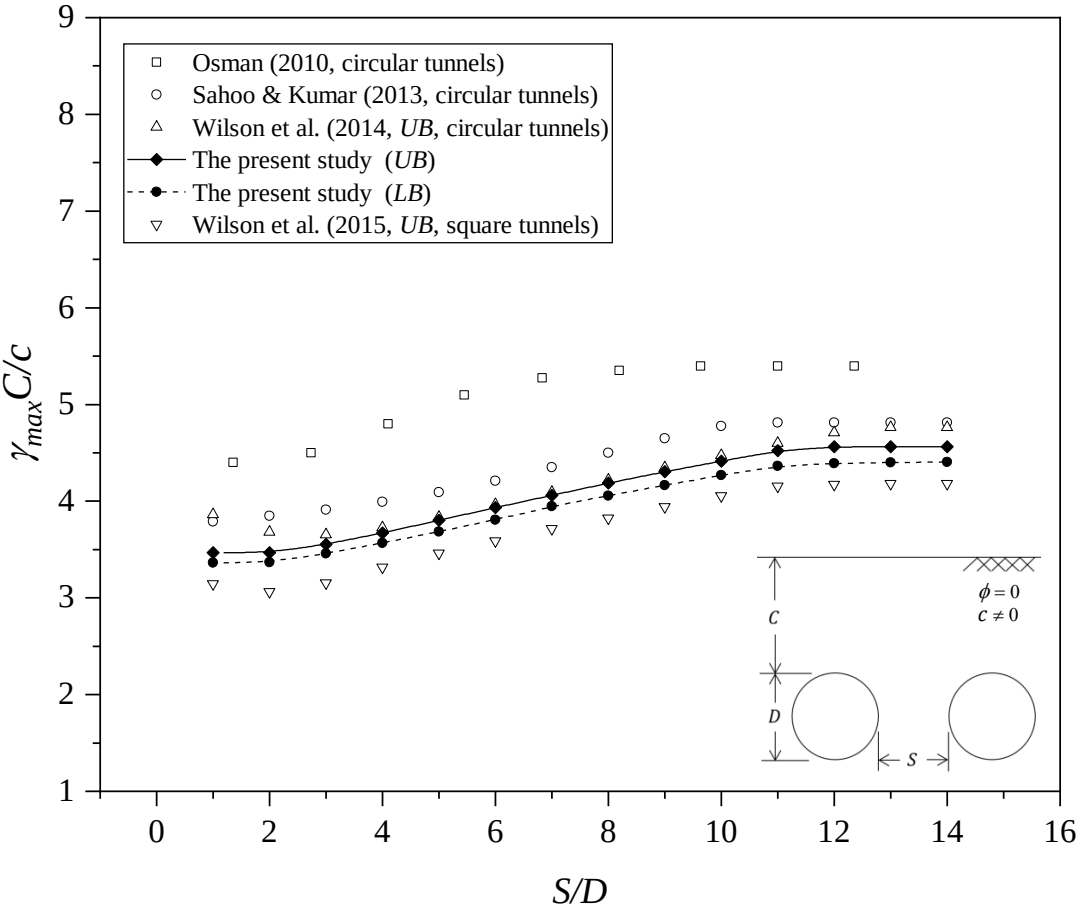

Figure 12.21. Comparison of the $\gamma_{max}C/c$ results with those available in the literature for twin tunnels (C/D = 5 and $\phi = 0^\circ$, after Sahoo and Kumar, 2013).

The comparisons in Figure 12.21 show good agreements with the results of (Wilson et al. 2014, 2015) for twin circular and square tunnels in view of the same minimum spacing ratios $(S/D)_{min}$ =12. However, the upper bound results for square twin tunnels of Wilson et al. (2015) are below the lower bound results of this study (twin circular tunnels). This indicates that the stability of the twin square tunnels is more critical than that for twin circular tunnels. Results of Sahoo and Kumar (2013) are consistently 6%

higher than the upper and lower bounds of this paper. However, the rigid block mechanism of Osman (2010) produced results that are approximately 30% - 40% greater than the current upper and lower bounds. Osman's failure mechanism shall be further improved so that the results can be used with confidence.

Table 12-1. Comparison of the $\gamma_{max}C/c$ results with those available in the literature for twin tunnels (C/D = 5 and $\phi = 0^{\circ}$, after Sahoo and Kumar, 2013).

S/D	Osman (2010) *UB,* circular tunnels	Sahoo & Kumar (2013) *UB,* circular tunnels	Wilson et al. (2014) *UB,* circular tunnels	The present study (*UB*)	The present study (*LB*)	Wilson et al. (2015) *UB,* Square tunnels
1.00	--	3.79	3.86	3.47	3.36	3.15
1.36	4.40	--	--	--	--	--
2.00	--	3.85	3.68	3.47	3.37	3.06
2.74	4.50	--	--	--	--	--
3.00	--	3.91	3.65	3.55	3.46	3.15
4.00	--	3.99	3.73	3.67	3.57	3.32
4.10	4.80	--	--	--	--	--
5.00	--	4.09	3.84	3.80	3.69	3.46
5.45	5.10	--	--	--	--	--
6.00	--	4.21	3.96	3.93	3.81	3.59
6.83	5.27	--	--	--	--	--
7.00	--	4.35	4.09	4.06	3.95	3.72
8.00	--	4.50	4.22	4.19	4.06	3.83
8.19	5.35	--	--	--	--	--
9.00	--	4.65	4.35	4.30	4.17	3.95
9.63	5.40	--	--	--	--	--
10.00	--	4.78	4.47	4.41	4.27	4.05
11.00	5.40	4.81	4.60	4.52	4.36	4.15
12.00	--	4.81	4.71	4.56	4.39	4.17
12.36	5.40	--	--	--	--	--
13.00	--	4.81	4.76	4.56	4.40	4.18
14.00	--	4.81	4.76	4.56	4.41	4.18

Figure 12.8 shows a comparison of the minimum spacing ratio $(S/D)_{min}$ of the present study and those of Sahoo and Kumar (2013) for various depth ratios (C/D). In general, the comparison shows a good agreement for shallow depth ratios. For deep tunnels (C/D > 5), larger differences are observed between the two methods. This could be attributed to the inaccuracy in the assumed rigid blocks for deep cases in Sahoo and Kumar (2013).

To the authors' knowledge, there are no published results of stability factors for twin tunnels. Therefore, no other comparisons can be made at this stage. Having said that, *FELA* is most useful when both the upper and lower bounds are calculated to bracket the true collapse load from above and below (Sloan 2013). The numerical upper and lower bounds of this study are generally within a few per cent of one another, with the true solution lying between the two bounds. These results are valuable and can be used for comparison by future researchers.

12.5 A Simple Example

Tunnel stability factors are useful in practice for preliminary design as they provide a quick calculation of the supporting pressure of the tunnels. In this paper, the variation of the stability factors with tunnels' spacing ratio (S/D) has been established for a series of depth ratios (C/D = 2 - 10) and angle of internal friction (ϕ = 0˚ - 40˚). The usefulness of these stability factors is best demonstrated through the use of examples.

***Example**:* Two side-by-side tunnels are planned to be 20 metres apart (centre-to-centre) and are assumed to be bored simultaneously. The tunnels have a diameter (D) of 4.0 m and are buried at a depth of 12m (C) in a cohesive-frictional soil with properties c' = 27 kPa, ϕ = 10° and γ = 18 kN/m^3. The site is assumed to be a Greenfield, so no surface pressure is assumed ($\sigma_s = 0$). The following procedures can be used to determine the minimum tunnel internal pressure (σ_t) to prevent collapse.

1. Calculate the dimensionless ratios: C/D = 3 and S/D = 5.
2. With Figures 12.9, 12.13 and 12.17 (for ϕ = 10˚), it was found that the *LB* stability factors are F_c = 2.92, F_s = 0.48 and F_γ = 1.85.
3. Using equation (12.1), the critical internal tunnel pressure to avoid collapse is

$$\sigma_t = -27 \times 2.92 + 0 + 18 \times 4 \times 1.85 = 54.36 \text{ kPa}$$

12.6 Conclusions

The stability of twin circular tunnels horizontally aligned in cohesive–frictional soil was investigated by using finite element limit analysis (*FELA*). A series of parametric studies for a wide range of angles of internal friction (ϕ = 0˚- 40˚), various depth ratios (C/D = 2 - 10) and spacing ratios (S/D = 2 - 28) were conducted to calculate the bounds

of the stability factors (F_c, F_s and F_γ). An example was illustrated on how to use the factors to estimate limit support pressures. The following conclusions are drawn:

1. For undrained conditions, the stability factor F_c is a function of the depth ratio (C/D), and the spacing ratio (S/D) while the stability factor F_γ is a function of the depth ratio (C/D) only i.e. F_γ = (C/D + 0.5). Also, note that, in the undrained condition, the stability factor F_s has a value of unity and is independent of (C/D) and (S/D).

2. It has been observed that the minimum spacing ratio ((S/D)$_{min}$) required to eliminate the interference effect of the twin tunnels increases with the increasing of the depth ratio (C/D). An equation has been derived for the determination of (S/D)$_{\text{min}}$ for the undrained condition, which is considered as the worst scenario of the whole study.

3. The proposed equation for estimating the tunnel critical support pressures is $\sigma_t = -cF_c + \sigma_s F_s + \gamma D F_\gamma$.

4. For drained conditions, these stability factors depend on the soil friction angle (ϕ), the depth ratio (C/D) and the spacing ratio (S/D). Due to the soil arching effects, the factors decrease with the increasing of ϕ. However, for large values of ϕ such as 40 degrees in this study, the stability factors are independent of the depth ratio (C/D) and the spacing ratio (S/D).

5. The finite element limit analysis is robust and computationally efficient. It is useful as both upper and lower bounds are calculated, providing great confidence to the end-users in using the tunnel stability factors.

A full 3D study of twin tunnels stability in the drained condition is presented in the very final technical chapter next in Chapter 13.

CHAPTER 13: DRAINED ANALYSIS OF 3D TWIN CIRCULAR TUNNELS

13.1 Introduction

In cohesive-frictional soil, the weight of the soil is small when it is compared with the soil arching developed due to the internal friction angle of soil. The failure study of the shield or the permanent lining has become insignificant, and the most obvious possibility of instability arises from the tunnel face, which is normally unsupported or supported by insufficient air or bentonite slurry pressure.

In the previous chapter, the stability of 2D twin tunnels in drained soil conditions was investigated by using tunnel stability factors approach. Tunnel stability is an inherently three-dimensional problem and therefore requires a full 3D analysis. This chapter discusses the three-dimensional stability problem of twin circular tunnels in cohesive-frictional soil under drained conditions. The minimum supporting pressure required to maintain the face stability of twin circular tunnels aligned horizontally in drained cohesive-frictional soil is studied using a stability factor approach. The primary concept adopted is the use of a conventional equation that is analogous to the bearing capacity factors (N_c, N_s and N_γ) in Terzaghi's bearing capacity equation. Three-dimensional finite element limit analysis (*FELA*) is employed to perform the analysis. For various spacing ratios (*S/D*) between the tunnels, the stability of tunnels is expressed in terms of non-dimensional tunnel stability factors (F_c, F_s and F_γ). The variation of the stability factors with tunnels' spacing ratios have been established for different combinations of depth ratio (*C/D*) and soil internal friction angle (ϕ).

For practical suitability, the results are presented in the form of dimensionless stability charts and tables with the tunnel stability factors closely bracketed from above and below using the rigorous upper and lower bound solutions.

13.2 Problem Statement and Modeling Technique

The centre-to-centre distance (*S*) plays a key role in twin tunnel stability. When the distance (*S*) is small, the stress field around each tunnel overlaps and the interactions of two tunnel become important in stability design. Figure 13.1 shows the problem definition of twin circular tunnels in three-dimension. The ground is modelled as a uniform Mohr-Coulomb material with cohesion (c'), friction angle (ϕ), and unit weight (γ). The tunnels have a diameter (*D*), cover depth (*C*) above the crown of the tunnel and separated by a centre-to-centre distance (*S*). σ_s is the surcharge applied to the ground surface, and σ_t is the internal tunnel pressure.

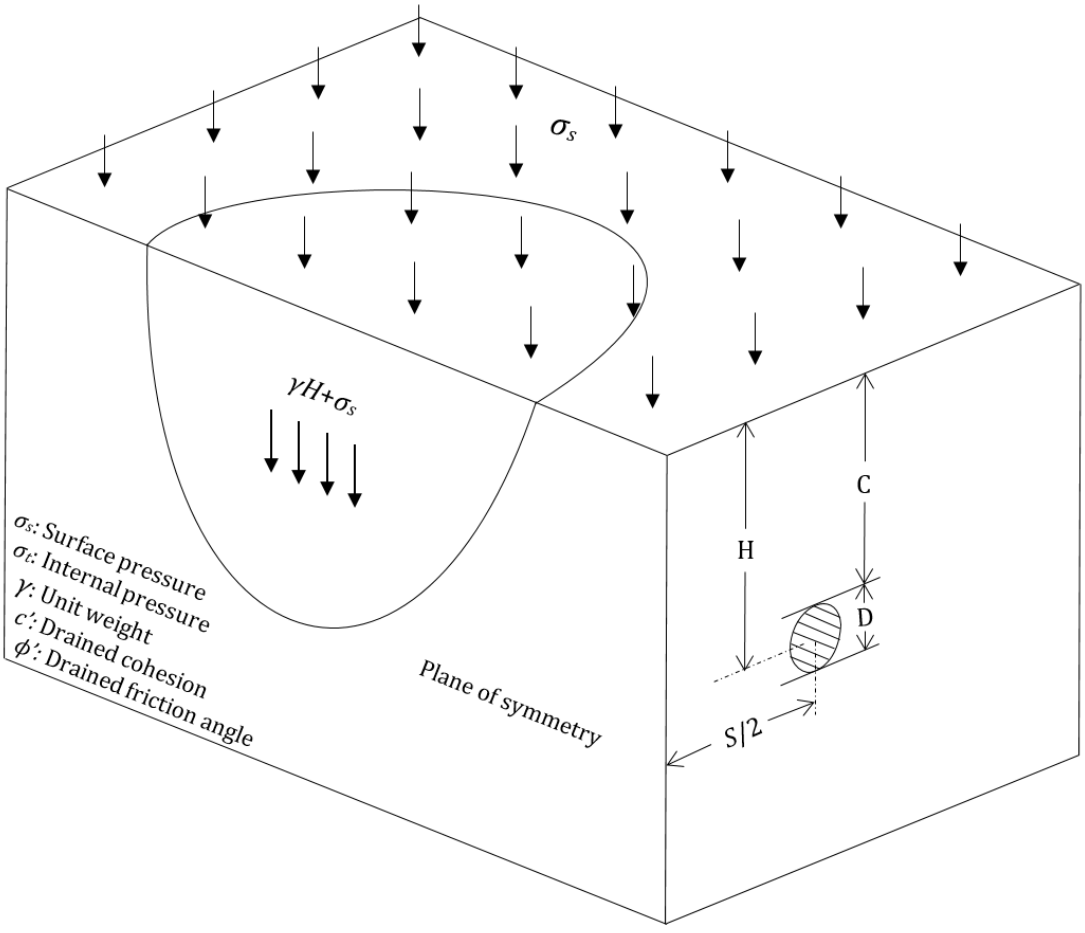

Figure 13.1. Problem Definition.

As the problem of twin tunnels is symmetrical about the vertical plane. Since it passes through the centerline of the distance between tunnels centres, the numerical calculations are based on one half of the total domain size.

Typical *FELA* adaptive meshes and boundary conditions used in this study are shown in Figures 13.2-13.3 (*S*/*D* = 4 and 8). An automatically adaptive mesh refinement was

employed in both the *UB* and *LB* simulations to enable accurate limit loads to be obtained through the use of the bounds gap error estimator (Sloan 2013). Three iterations of adaptive meshing with the number of elements increasing from 5000 to 10000 were used for all analyses.

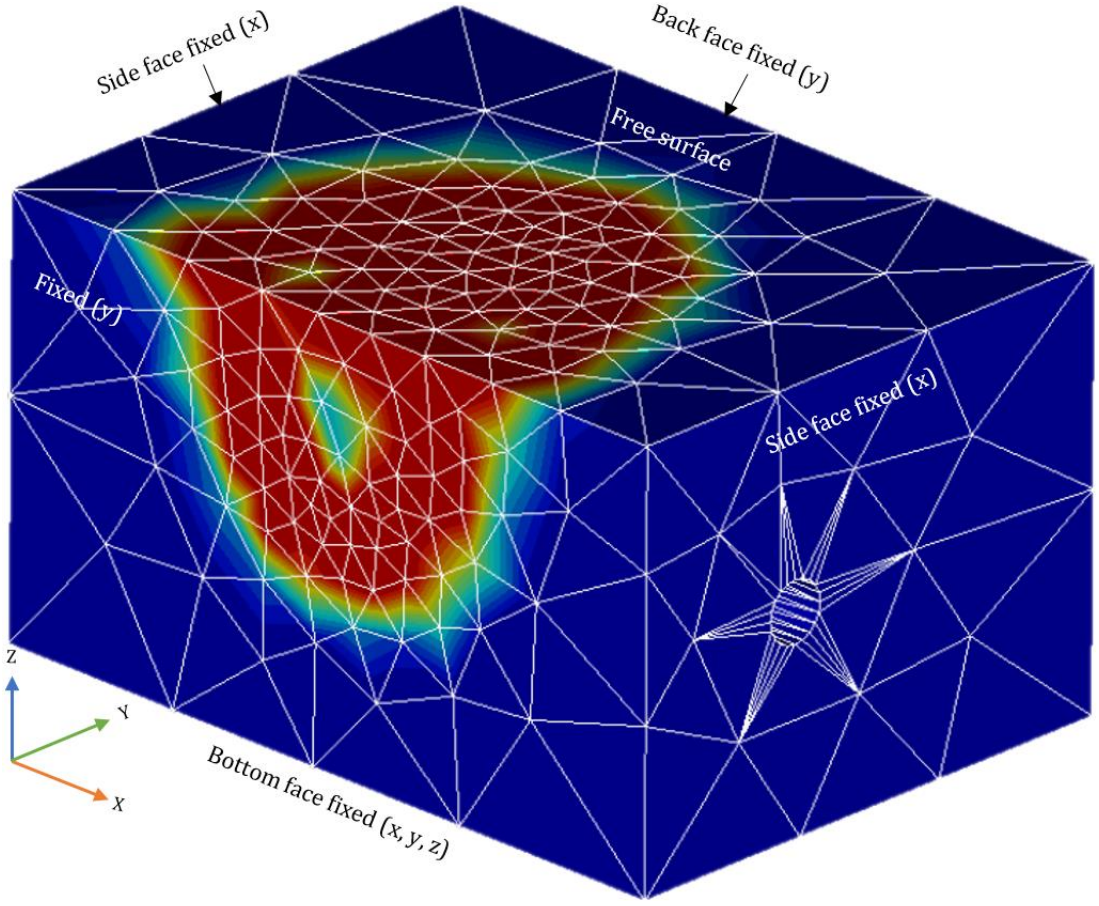

Figure 13.2. A typical adaptive mesh with boundary conditions and failure mechanism plot showing twin tunnel effects (C/D = 3 and S/D = 4).

The large size of the model is essential as it ensures that the entire soil mass is modelled accurately, and the failure mechanism does not intersect the boundaries of the model. The boundary conditions of the numerical models in Figures 13.2 and 13.3 are as follows: the ground surface is free to displace, the side surfaces are restrained in the x-direction, while the back and the front surfaces (symmetrical plane) are restrained in the y-direction. The base is fixed in all directions. The rigid lining around the soil excavation is restrained in the normal direction to represent the smooth interface condition. For such a boundary condition, there is no transfer of shear force between the lining and the soil.

Shown in Figure 13.2 is also a plot of the failure mechanism using the contours of *UB* power dissipation. Noting that this is the symmetrical model for a close twin tunnel (*C/D* = 3 and *S/D* = 4), the resulting surface failure area resembles an elliptical shape due to the twin tunnel effects.

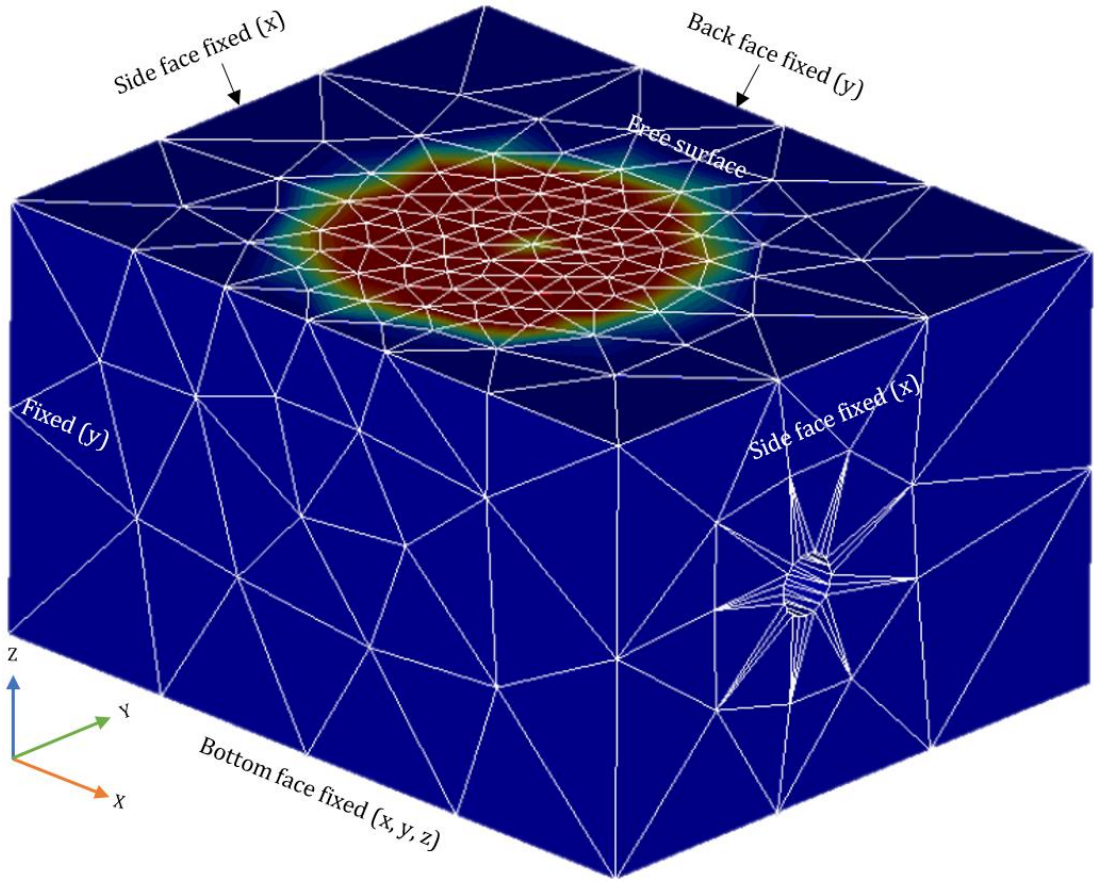

Figure 13.3. A typical adaptive mesh with boundary conditions and failure mechanism plot showing a single tunnel response (*C*/*D* = 3 and *S*/*D* = 8).

Another plot of the failure mechanism for (*C/D* = 3 and *S/D* = 8) is shown in Figure 13.3. Due to the large value of *S/D*, it is not surprising to see a single tunnel response with a near-circular failure surface.

The numerical simulations presented in this study are based on the state of the art *FELA* software (OptumCE 2018). This software can accurately determine the limits of 2D and 3D stability problems with the power of finite element discretisation and the bounding capability of lower and upper bound plastic limit theorems. Furthermore, it has been successfully applied to solve various stability problems in underground stability problems (Keawsawasvong & Ukritchon 2017; Ukritchon & Keawsawasvong 2017; Shiau & Al-Asadi 2018, 2020a, 2020b, 2020c).

Approximately 27,666 *FELA* analyses were performed to calculate the stability factors (F_c, F_s and F_γ) for a wide range of soil parameters (ϕ = 0˚- 40˚), spacing ratios (*S/D* = 2 - 28) and depth ratios (*C/D* = 2 - 10). The principles in the calculations of the three factors are as follows: (1) both $\gamma = 0$ and $\sigma_s = 0$ are used in the analysis to determine F_c, which can be calculated using the equation $\sigma_t = -c' F_c.$; (2) both $\gamma = 0$ and $c' = 0$ are adopted in the analysis and F_s is calculated using the equation $\sigma_t = \sigma_s F_s.$; (3) both $c' = 0$ and $\sigma_s = 0$ are used in the analysis so that F_γ can be determined using the equation $\sigma_t = \gamma D F_\gamma$.

Similar to the superposition principle of the traditional bearing capacity equations, the minimum support pressures σ_t at collapse can be determined using Equation (13.1) with the produced twin tunnel stability factors in this paper. The use of dimensionless ratios allows the results of this study to be useful in design practice.

13.3 Discussing the Twin Tunnel Stability Factors (F_c, F_s and F_γ)

Three-dimensional finite element limit analyses (*FELA*) were performed to calculate the upper and the lower bounds limits of the stability factors (F_c, F_s and F_γ) for various depth ratios (*C/D* = 2-10), spacing ratios (*S/D* = 2 - 28) and angle of internal friction (ϕ = 0˚ - 40˚). The effects of the parameters *C/D*, *S/D* and ϕ on the tunnel stability factors (F_c, F_s and F_γ) are presented in Figures 13.4 - 13.6 and Figures 13.8 - 13.18.

13.3.1 F_c, F_s and F_γ in undrained condition (ϕ = 0˚)

Figure 13.4 shows that F_c is a function of the depth ratio (*C/D*) and the spacing ratio (*S/D*). F_c increases with the increasing of *C/D*. For each depth ratio, F_c increases nonlinearly as *S/D* increases until it reaches a constant value. At this point, the stability factor (F_c) is at its maximum value, and the twin tunnels stability is unaffected by the tunnel spacing. The corresponding *S/D* to the first constant value of F_c is the minimum spacing ratio $(S/D)_{min}$, which is a critical spacing ratio separating twin tunnels and single tunnel effects.

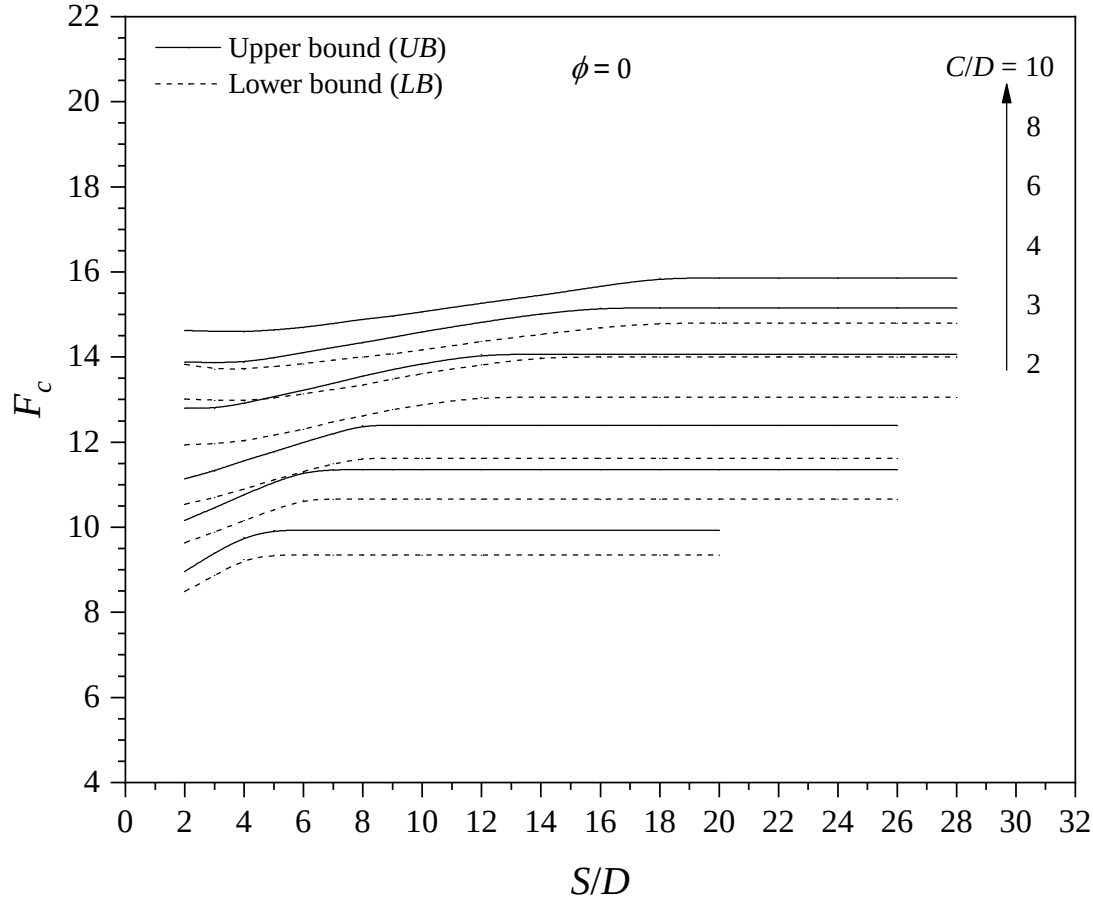

Figure 13.4. 3D F_c vs *S/D* and various *C/D* ($\phi = 0^{\circ}$).

Figure 13.5 shows that the factor F_s has a constant value of unity no matter what values of *C/D* and *S/D* are. This finding is understandable for soils in undrained condition ($\phi = 0^{\circ}$) where the stability is independent of the loading direction due to zero volume loss during plastic shearing (Shiau & Sams 2019).

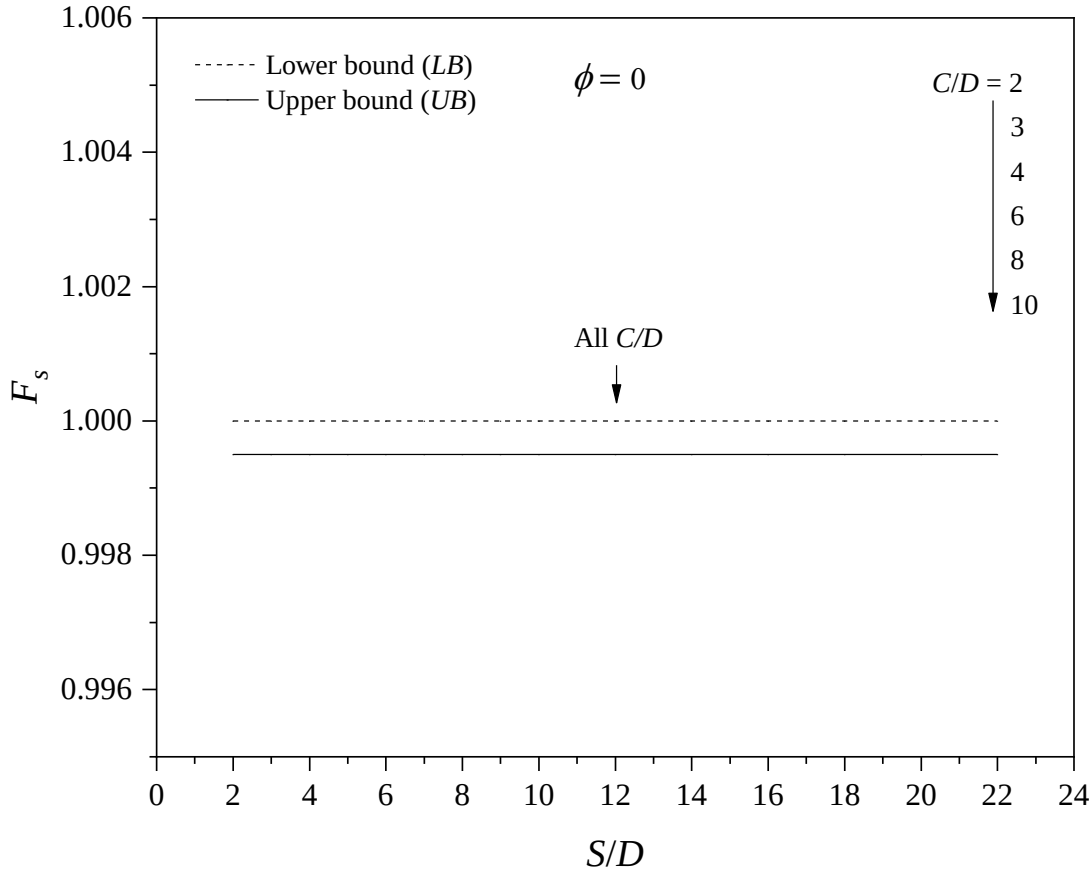

Figure 13.5. 3D F_s vs *S/D* and various *C/D* ($\phi = 0^{\circ}$).

For F_γ in the undrained condition ($\phi = 0^{\circ}$), Figure 13.6 shows that the value of *S/D* does not affect the factor F_γ, which is a function of *C/D* only. Indeed, the unit weight effect displays the same trend as the surcharge effect, except that now $F_\gamma = (C/D + 0.5)$ for all values of *S/D*. The larger the *C/D* value is, the larger the factor F_γ is. This finding is the same as in (Shiau & Al-Asadi 2020c) for the 3D single circular tunnel stability in cohesive-frictional soil under undrained condition using tunnel stability factors approach.

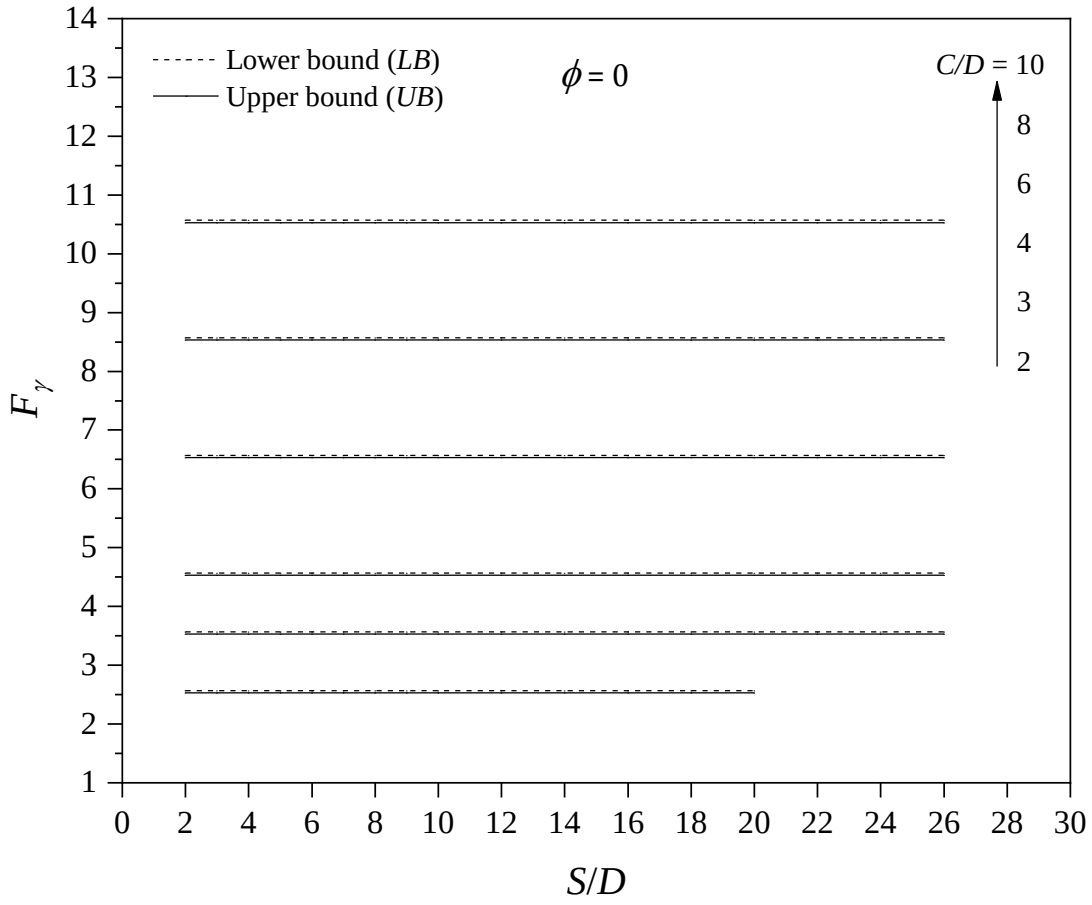

Figure 13.6. 3D F_γ vs *S/D* and various *C/D* ($\phi = 0^\circ$).

Figure 13.7 shows the minimum spacing ratios $(S/D)_{min}$ for various depth ratios (*C*/*D*). A linear relationship is observed between *C*/*D* and $(S/D)_{min}$. When the spacing ratio is less than $(S/D)_{min}$, it is necessary to study the twin tunnel interaction effects. Once the spacing ratio is equal to or larger than $(S/D)_{min}$, the stability of each of the tunnels is essentially identical to those of corresponding single tunnel. The results of $(S/D)_{min}$ for various depth ratios, which presented in Figure 13.7, can also be calculated using Equation 13.2.

$$(S/D)_{min} = 1.8 \times (C/D) + 1.0 \tag{13.2}$$

More discussions of Figure 13.7 are also presented in the comparison section.

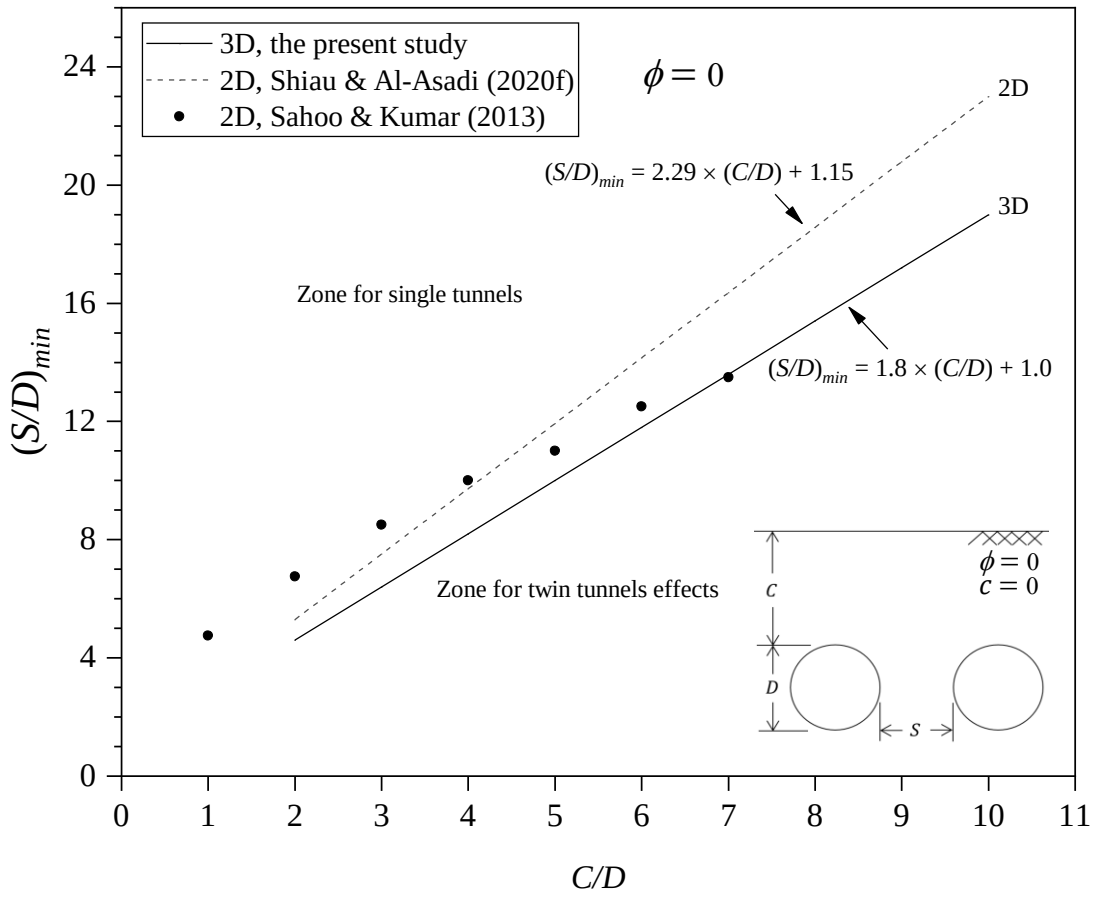

Figure 13.7. Comparison of the minimum spacing ratio $(S/D)_{min}$ required to eliminate the interaction between the tunnels.

13.3.2 F_c, F_s and F_γ in drained condition ($\phi > 0^\circ$)

Figures 13.8-13.18 (for $\phi > 0^\circ$, drained analysis) show that all the stability factors are functions of the angle of internal friction (ϕ), depth ratio (C/D) and spacing ratio (S/D). This is in contrary to the undrained condition ($\phi = 0^\circ$).

Figures 13.8-13.9 ($\phi = 10^\circ$ and 20°) show that F_c increases with the increasing of C/D. For each C/D, F_c increases nonlinearly as S/D increases until it reaches a constant value, which indicates that no interactions between the tunnels. However, for high friction angles ($\phi \geq 20$, see Figures 13.10 and 13.11), both C/D and S/D have negligible effects on the results of F_c. In general, F_c decreases as ϕ increases from 10° to 40°. Also, note that for the range of ϕ between zero and twenty degrees ($0^\circ < \phi < 20^\circ$), the minimum spacing ratios $(S/D)_{min}$ decrease with the increasing of the angle of internal friction.

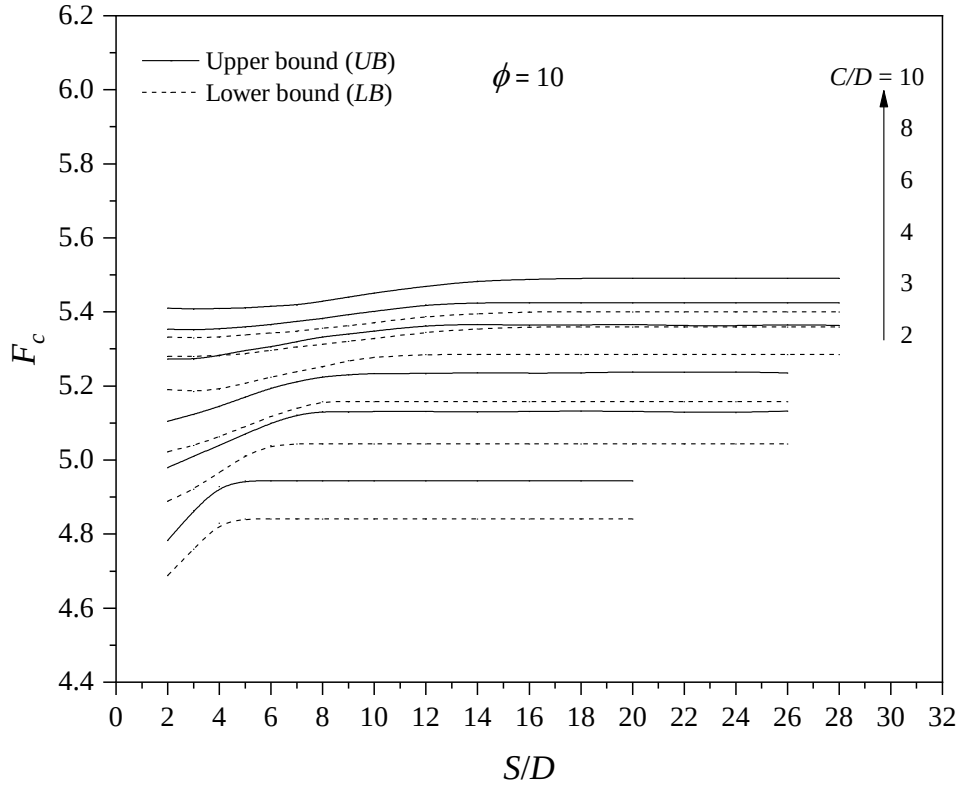

Figure 13.8. 3D F_c vs S/D and various C/D (ϕ = 10˚).

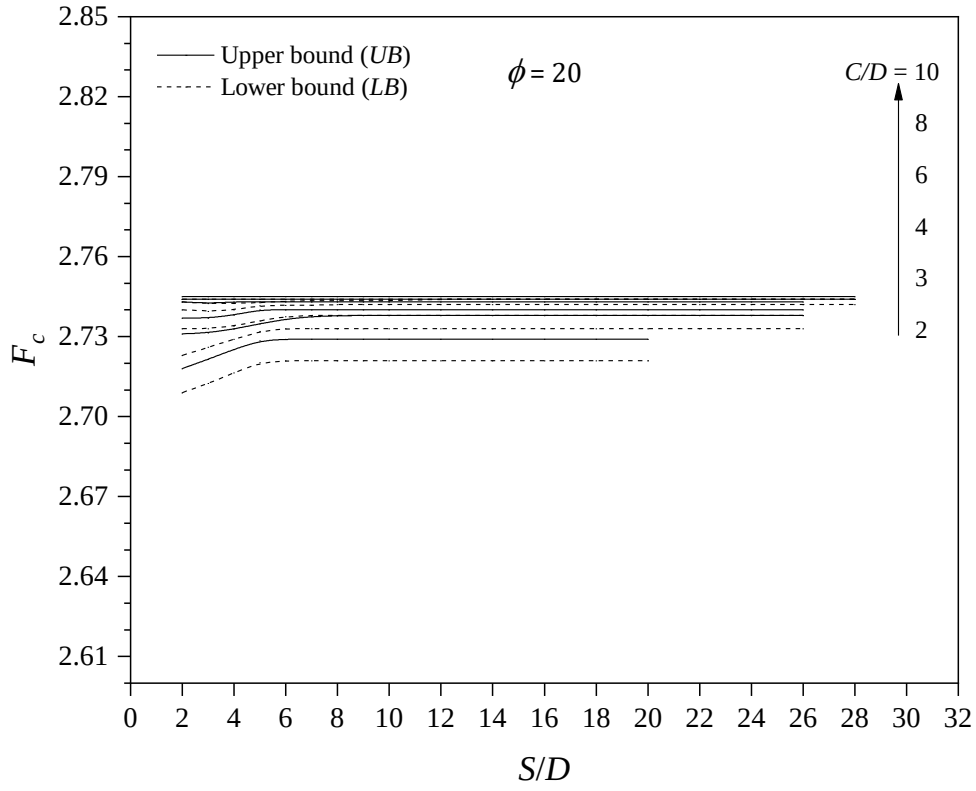

Figure 13.9. 3D F_c vs S/D and various C/D (ϕ = 20˚).

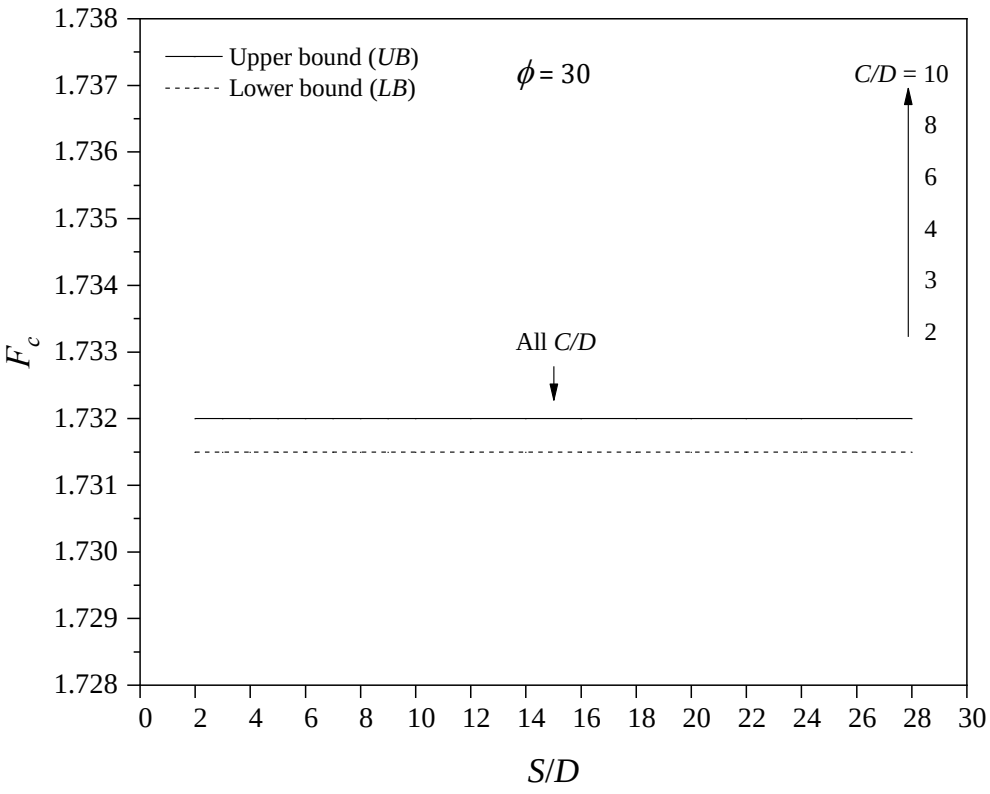

Figure 13.10. 3D F_c vs *S/D* and various *C/D* (ϕ = 30˚).

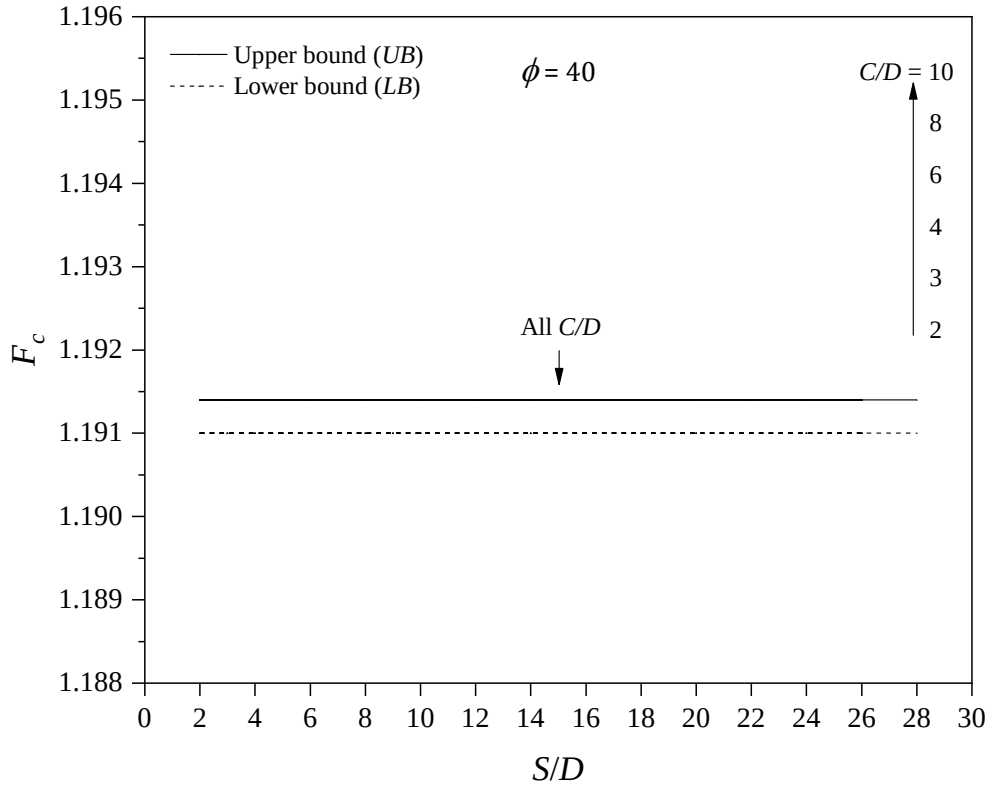

Figure 13.11. 3D F_c vs *S/D* and various *C/D* (ϕ = 40˚).

With regards to F_s, Figure 13.12 (ϕ = 10˚) shows that the surcharge stability factor (F_s) decreases with the increasing of *C/D*. It is interesting to see that the diminishing effect of the depth ratio (*C/D*) on (F_s) when ϕ increases from 10˚ to 40˚. This can be seen from Figures 13.13 - 13.14 ($\phi = 20^{\circ}$ and $\phi \geq 25^{\circ}$). It is to be noted that F_s decreases with the increasing of *S/D* until it reaches a constant value, although the actual F_s values are very small.

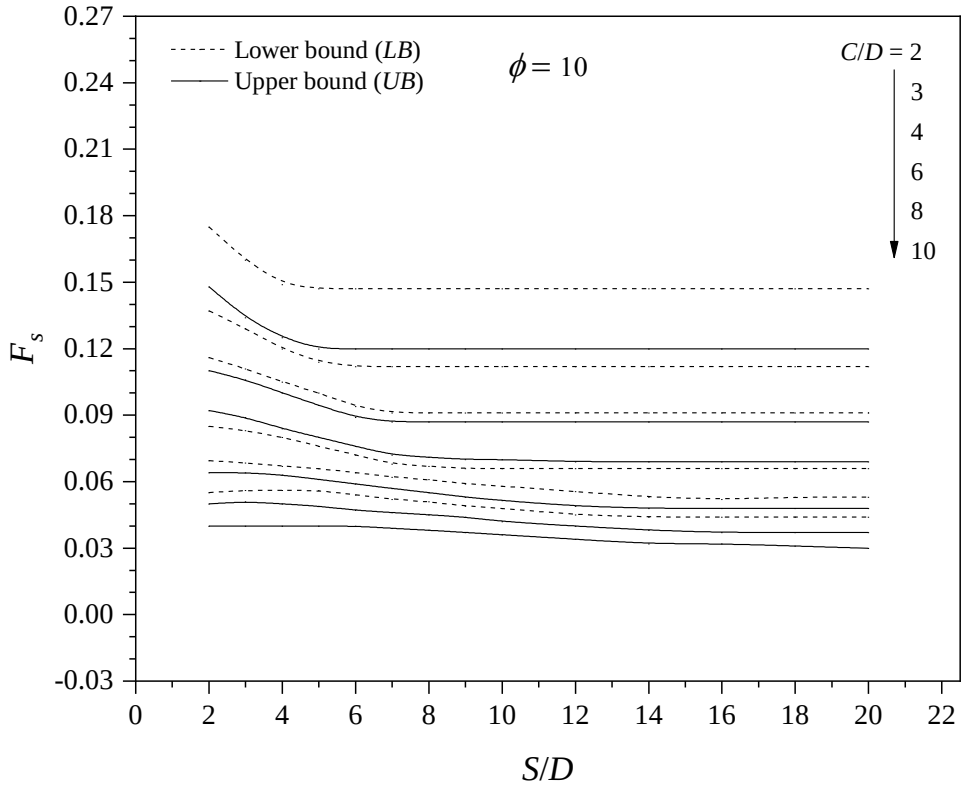

Figure 13.12. 3D F_s vs *S/D* and various *C/D* (ϕ = 10˚).

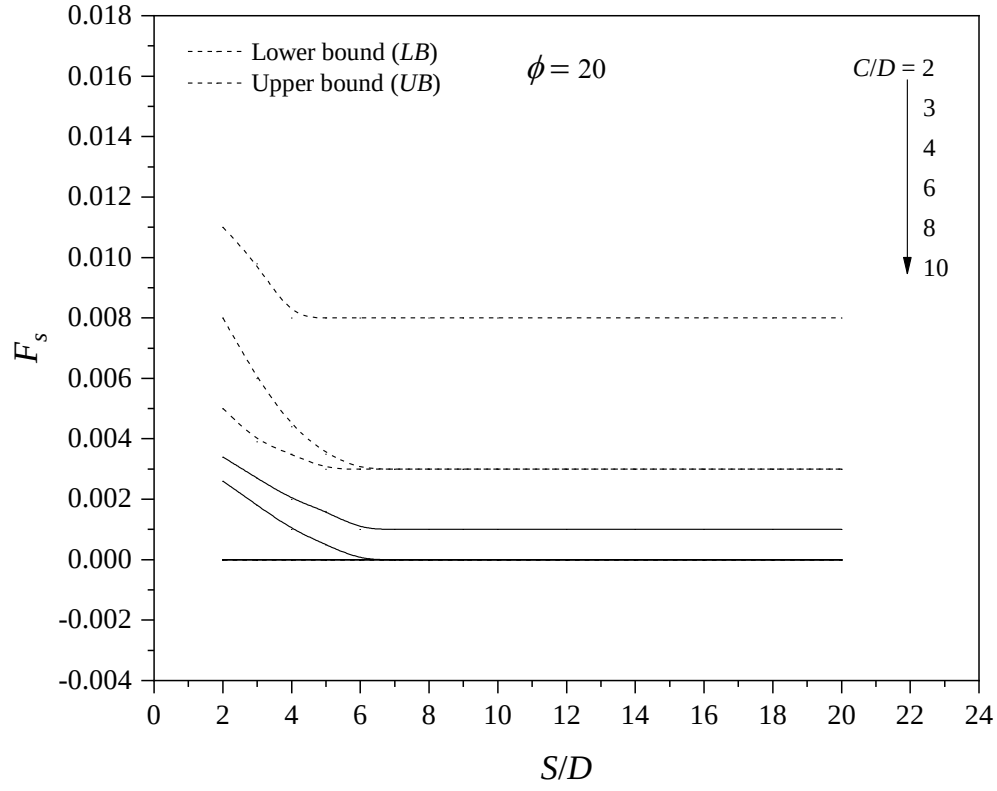

Figure 13.13. 3D F_s vs S/D and various C/D (ϕ = 20°).

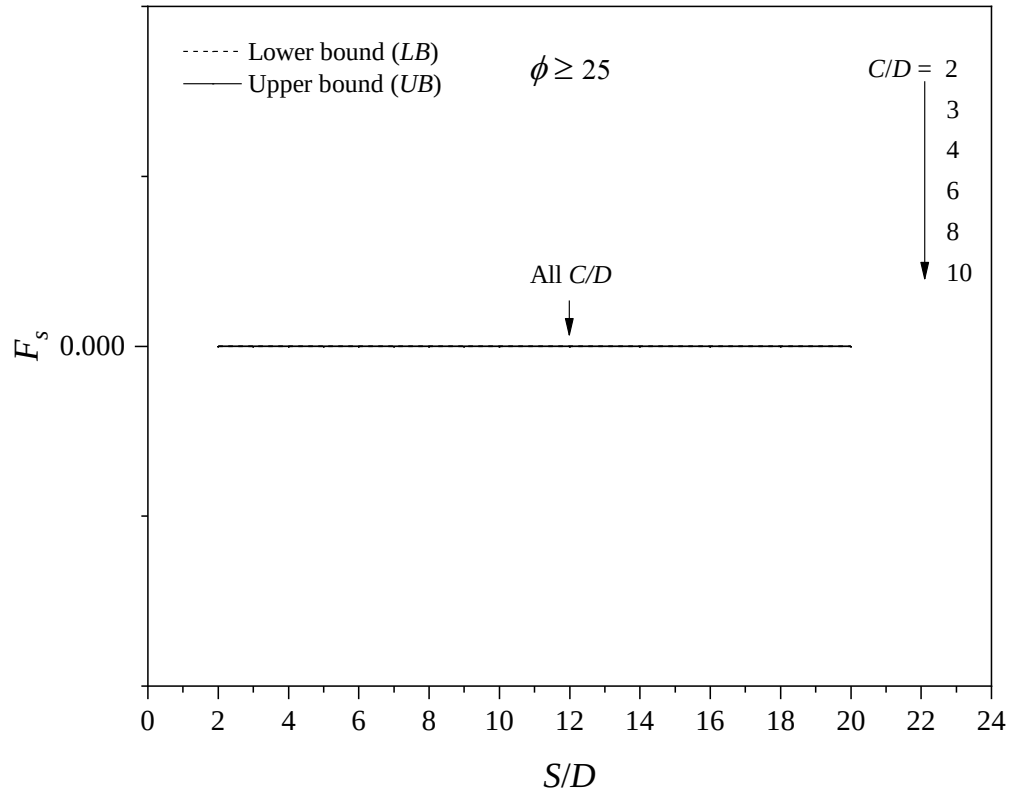

Figure 13.14. 3D F_s vs S/D and various C/D ($\phi \geq 25°$).

Finally, for the factor F_γ, Figure 13.15 (ϕ = 10˚) shows that the unit weight stability factor (F_γ) increases with the increasing of *C/D*. Similar to F_s, the unit weight stability factor (F_γ) decreases with the increasing of *S/D* until it reaches a constant value. Also, F_γ decreases dramatically with the increasing of ϕ due to the developing of a stress arch that could carry the overburden pressure, and the tunnel stability becomes independent of the geometries (*C/D*) and (*S/D*). This can be seen in Figures 13.16-13.18. It is also noted that F_γ has a minimum value of 0.08 when ϕ = 40˚.

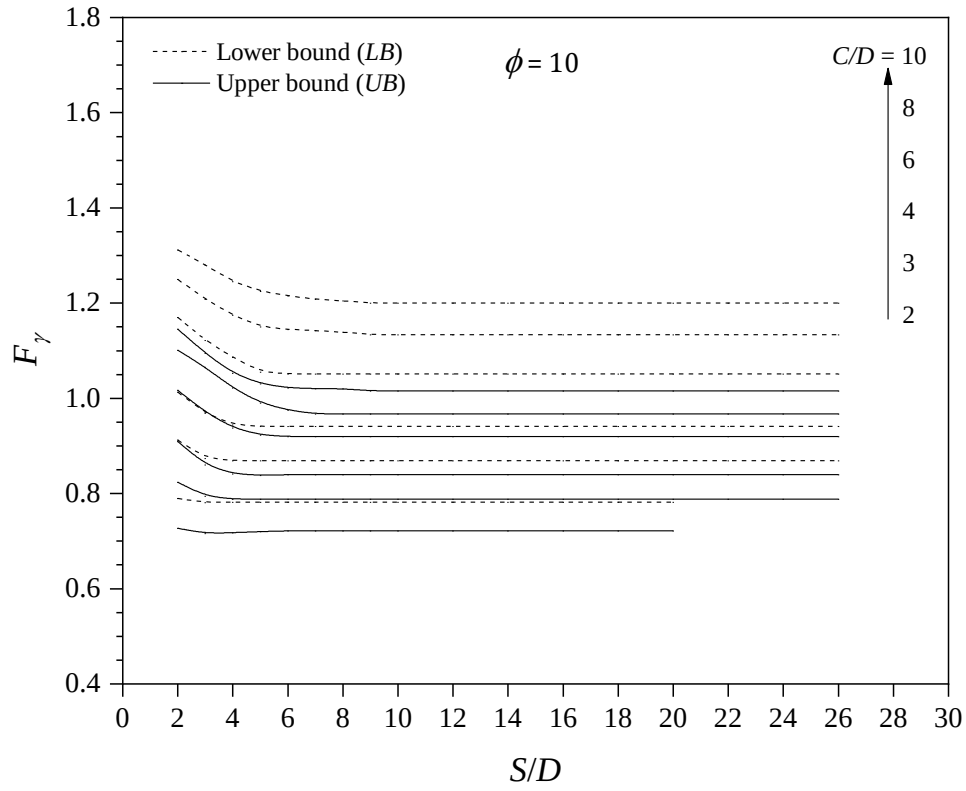

Figure 13.15. 3D F_γ vs *S/D* and various *C/D* (ϕ = 10˚).

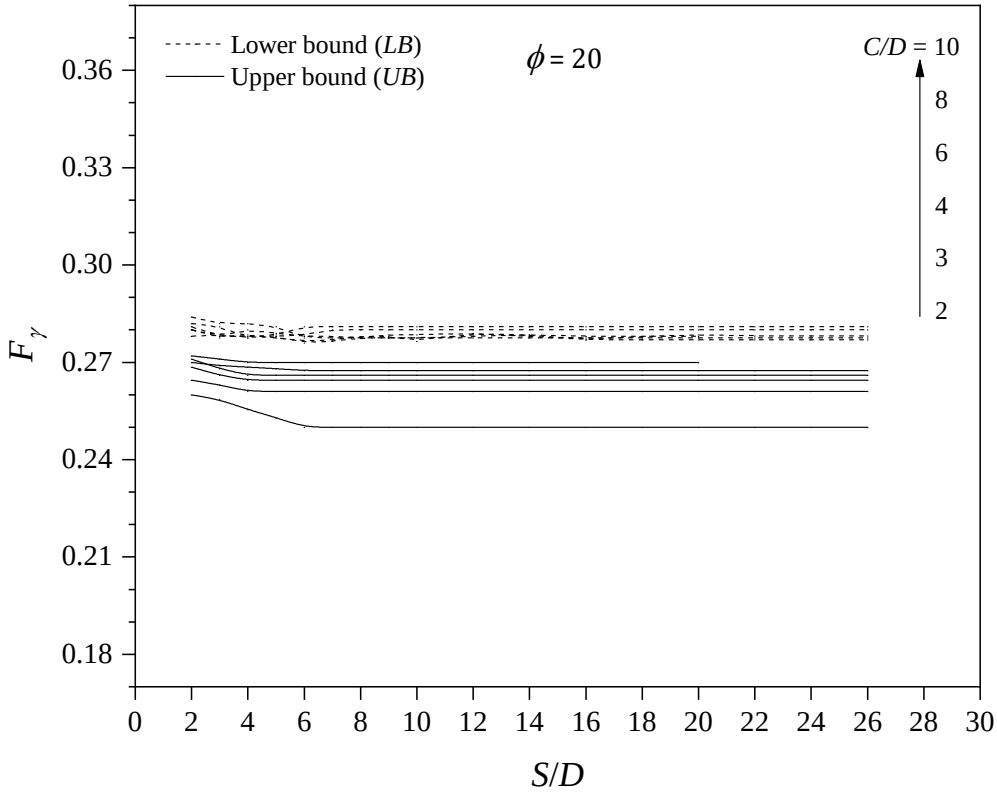

Figure 13.16. 3D F_γ vs *S/D* and various *C/D* (ϕ = 20˚).

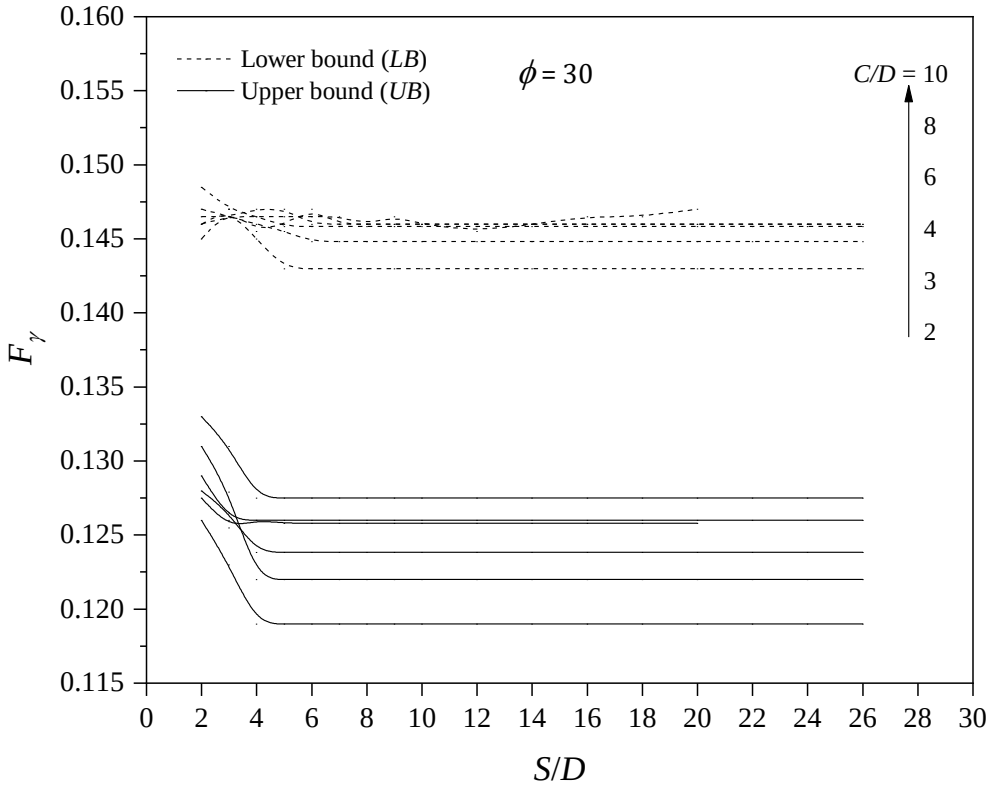

Figure 13.17. 3D F_γ vs *S/D* and various *C/D* (ϕ = 30˚).

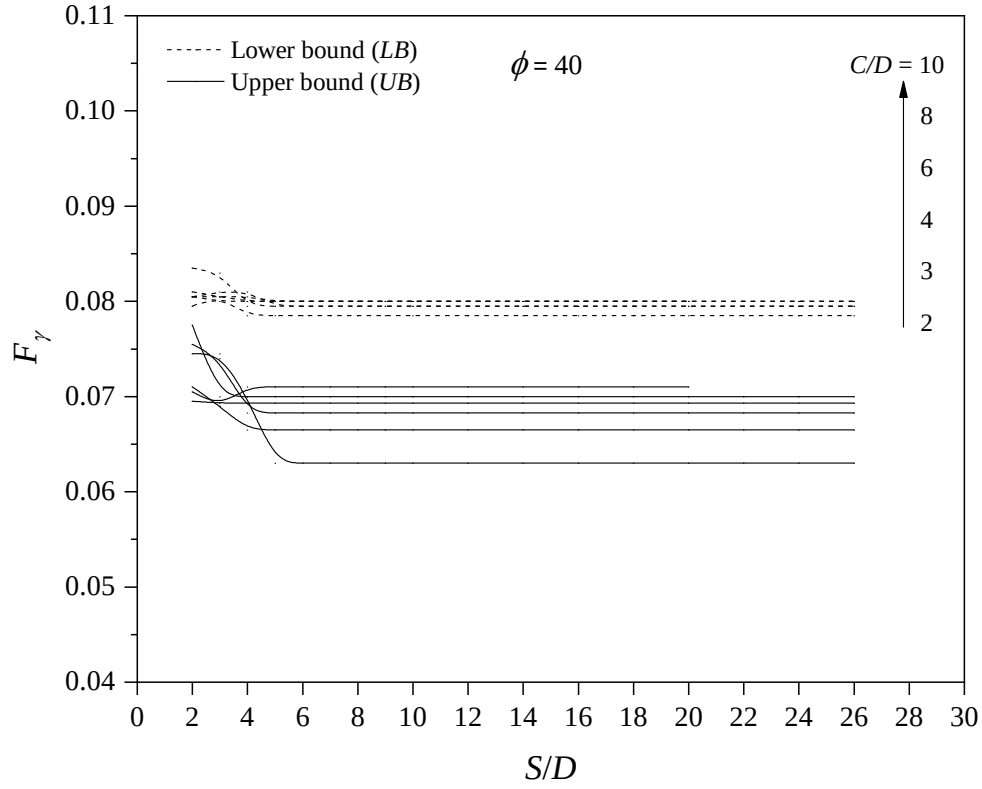

Figure 13.18. 3D F_γ vs *S/D* and various *C/D* (ϕ = 40˚).

13.4 Comparison of Results

FELA is most useful when both the upper and lower bounds are calculated to bracket the true collapse load from above and below. This allows an accurate measure of the error in the solution to be computed. Figures 13.4-13.6 and Figures 13.8-13.18 show that the numerical upper and lower bounds are generally within a few per cents of one another, with the true solution lying between the two bounds. The confidence level in producing these results are extremely high even though very few literatures can be found in relation to 2D and 3D twin tunnels in cohesive-frictional soil. Therefore, the comparison will be made with the available 2D and 3D results of twin tunnels under undrained conditions (ϕ = 0˚). Table 13.1 and Figure 13.19 show a comparison between the present results and those by (Sahoo & Kumar 2013; Wilson et al. 2014; Shiau & Al-Asadi 2020a,2020f). The Figure presents an excellent agreement between the results of this study (tunnel stability factor approach) and the 3D stability results of twin tunnels in cohesive soil using Broms and Bennermarks' original stability number approach by (Shiau & Al-Asadi 2020a). However, Figure 13.19 highlights a significant variance between the 3D and 2D results.

Table 13-1. Comparison of the $\gamma_{max}C/c$ results with those available in the literature for twin tunnels (C/D = 5 and ϕ = 0˚, after Sahoo and Kumar, 2013).

S/D	The present study (3D, *UB*)	The present study (3D, *LB*)	Shiau & Al-Asadi (2020a), (3D, *UB*)	Shiau & Al-Asadi (2020a), (3D, *LB*)	Sahoo & Kumar (2013), (2D, *UB*)	Wilson et al. (2014), (2D, *UB*)	Shiau & Al-Asadi (2020f), (2D, *UB*)	Shiau & Al-Asadi (2020f), (2D, *LB*)
1	10.93	10.22	10.85	10.27	3.79	3.86	3.47	3.36
2	10.97	10.26	10.93	10.33	3.85	3.68	3.47	3.37
3	11.10	10.37	11.09	10.45	3.91	3.65	3.55	3.46
4	11.30	10.52	11.26	10.61	3.99	3.73	3.67	3.57
5	11.50	10.68	11.43	10.76	4.09	3.84	3.80	3.69
6	11.70	10.87	11.60	10.93	4.21	3.96	3.93	3.81
7	11.88	11.05	11.76	11.08	4.35	4.09	4.06	3.95
8	12.02	11.16	11.91	11.23	4.50	4.22	4.19	4.06
9	12.10	11.19	12.02	11.33	4.65	4.35	4.30	4.17
10	12.12	11.19	12.02	11.33	4.78	4.47	4.41	4.27
11	12.12	11.19	12.02	11.33	4.81	4.60	4.52	4.36
12	12.12	11.19	12.02	11.33	4.81	4.71	4.56	4.39
13	12.12	11.19	12.02	11.33	4.81	4.76	4.56	4.40
14	12.12	11.19	12.02	11.33	4.81	4.76	4.56	4.41

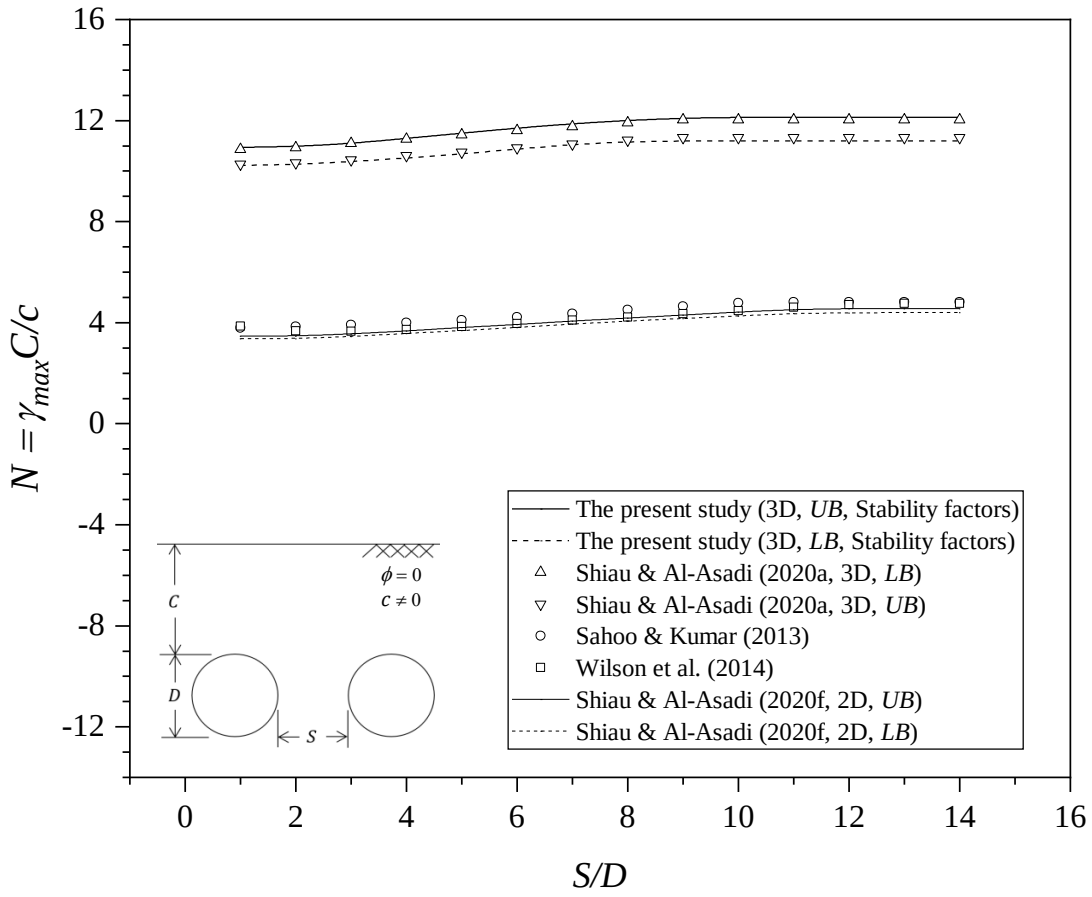

Figure 13.19. Comparison of the $\gamma_{max}C/c$ results with those available in the literature for twin tunnels (C/D = 5 and ϕ = 0˚, after Sahoo and Kumar, 2013).

In general, the 3D stability results are approximately 2.5-3.0 fold higher than those in the 2D analysis. It can be concluded that the 2D analysis produces over-conservative results and is only suitable for the preliminary stages of design.

Also, Figure 13.7 shows a comparison of the minimum spacing ratio $(S/D)_{min}$ of the present study and those of Sahoo and Kumar (2013) and (Shiau & Al-Asadi 2020f) for various depth ratios (C/D). Generally, the comparison shows that the results of the 2D analyses are conservative compared to the results of the 3D analysis.

13.5 An Example

The produced figures and tables for the stability factors (F_c, F_s and F_γ) can be used to estimate the critical pressure to maintain the stability of the headings of 3D twin tunnels. The usefulness of these stability factors is best demonstrated through the example below.

Example: Two side-by-side tunnels are planned to be 30 metres apart (centre-to-centre) and are assumed to be bored simultaneously. The tunnels have a diameter (D) of 6.0 m and are buried at a depth of 18m (C) in a cohesive-frictional soil with properties c' = 15 kPa, $\phi = 10^\circ$ and γ = 18 kN/m3. The site is assumed to be a greenfield (σ_s = 0). The following procedures can be used to determine the minimum internal pressure (σ_t) to prevent collapse.

1. Calculate the dimensionless ratios: C/D = 3 and S/D = 5.
2. With Figures 13.8, 13.12 and 13.15 (for C/D = 3, S/D = 5 and $\phi = 10^\circ$), it was found that the *LB* stability factors are F_c =5.01, F_s = 0.116 and F_γ = 0.870.
3. Using Equation (13.1), the minimum internal supporting tunnel pressure (σ_t) to present collapse is

   $$\sigma_t = -cF_c + \sigma_s F_s + \gamma D F_\gamma = -15 \times 5.01 + 0 + 18 \times 6 \times 0.870 = 18.81 \text{ kPa.}$$

What is the required critical pressure when $\phi = 20^\circ$?

1. With Figures 13.9, 13.13 and 13.16 (for C/D = 3, S/D = 5 and $\phi = 20^\circ$), it was found that the *LB* stability factors are F_c = 2.73, F_s = 0.003 and F_γ = 0.278.
2. Using Equation (13.1), the minimum internal supporting tunnel pressure (σ_t) to induce collapse is

   $$\sigma_t = -cF_c + \sigma_s F_s + \gamma D F_\gamma = -15 \times 2.73 + 0 + 18 \times 6 \times 0.278 = -10.93 \text{ kPa.}$$

3. A negative value of σ_t indicates that the tunnel requires a pulling pressure to reach a collapsed state. In other words, the tunnel will remain stable without any internal pressure.

13.6 Conclusions

The stability of twin circular tunnels horizontally aligned in cohesive–frictional soil has been studied using 3D finite element limit analysis. A series of parametric studies for a wide range of internal soil friction (ϕ = 0˚- 40˚), depth ratios (C/D = 2 - 10) and spacing ratios (S/D = 2 - 28) were conducted to calculate the tunnel stability factors (F_c, F_s and F_γ). An example was illustrated on how to use the factors to estimate limit support pressures. The following conclusions are drawn:

1. The equation for estimating the tunnel critical support pressures of 3D twin tunnels is: $\sigma_t = -cF_c + \sigma_s F_s + \gamma D F_\gamma$.
2. For the undrained condition (ϕ = 0˚), the stability factor F_c is a function of the spacing ratio (S/D) and the depth ratio (C/D), while the stability factors F_s and F_γ are independent of (S/D) and have constant values of F_s = 1 and F_γ = (C + 0.5), respectively.
3. For drained condition, the stability factors are functions of the angle of internal friction (ϕ), depth ratio (C/D) and spacing ratio (S/D). In general, the factors decrease with the increasing of ϕ. For $\phi \geq 20$˚, owing to the developing of soil arching, the stability factors are independent of the depth ratio (C/D) and the spacing ratio (S/D).

Three-dimensional finite element limit analysis is robust and computationally efficient. It is useful as both upper and lower bounds are calculated, providing great confidence to the end-users in using the tunnel stability factors. The proposed tunnel stability factor approach to estimate tunnel face pressures, similar to the bearing capacity problem, is convenient and effective for practical engineers.

This is the very final technical chapter of the thesis, which provides a comprehensive study of undrained (Part A) and drained (Part B) analyses for five tunnel geometries. Chapter 14 concludes the thesis study with new research contributions. Future work is also recommended.

CHAPTER 14: CONCLUSIONS AND RECOMMENDATIONS

14.1 Summary

The thesis has successfully investigated the undrained and drained stability of five tunnel configurations (i.e. 2D heading, 2D circle, 3D circle, 2D twin circles and 3D twin circles). Finite element limit analysis (*FELA*) is used to determine lower and upper bound stability limits for a range of various geometrical and material scenarios. The thesis is divided into two parts.

Part A (Chapters 4-8): This part focuses on undrained stability analysis. The method used to check the stability of a tunnel face is based on the so-called Broms and Bennermarks' original stability number (N). For the 2D undrained analyses, the safety factors were calculated using the shear strength reduction method in *FELA* and finite difference method in *FLAC*, while for the 3D undrained analysis, the critical supporting pressure values were calculated using the load multiplier method in *FELA*.

To the author's best knowledge, it is the first to use Broms and Bennermarks' original stability number with shear strength reduction method in the stability analysis of underground openings. Comprehensive design charts, tables, and equations have been produced for various tunnel shapes (i.e. 2D heading, 2D circle, 3D circle, 2D twin circles and 3D twin circles) with wide ranges of stability numbers (N), factor of safety (*FoS*) and depth ratios (C/D =1-10). These results can be used to determine the safe operating range for the pressure that can be applied to the tunnel excavation face by a tunnel boring machine during construction.

Part B (Chapters 9-13): Following the superposition principle of the bearing capacity equations, this part focuses on the drained analysis using tunnel stability factors (F_c, F_s and F_γ). This approach is convenient for stability analysis of underground openings with a wide range of depth ratios (C/D = 1 - 10) in the more general case of a cohesive and/or frictional soil (ϕ = 0 - 40˚). Tunnel stability factors allow a quick calculation of the critical collapse pressure, which is useful for practical purposes. This can be

performed by a simple application of a traditional equation (analogous to Terzaghi's bearing capacity equation) using the superposition principle.

To the author's best knowledge, this thesis is the first to use the advanced *FELA* with the tunnel stability factor approach in the stability analysis of underground openings and to produce comprehensive results of the three stability factors (F_c, F_s and F_γ) for a wide range of design parameters of the following five tunnel configurations:

- Two-dimensional tunnel heading (Chapter 9)
- Two-dimensional circular tunnel (Chapter 10)
- Three-dimensional circular tunnel heading (Chapter 11)
- Two-dimensional twin circular tunnels (Chapter 12)
- Three-dimensional twin circular tunnel heading (Chapter 13)

The key conclusions for each chapter are presented as follows:

14.2 Key conclusions in Chapter 4

The following main conclusions were drawn based on the two-dimensional analysis of tunnel heading in cohesive undrained soil.

1. The relationship between the factor of safety (*FoS*) and the stability number (*N*), for any given depth ratio (*C/D*), was represented by a pair of identical hyperbolic curves. One curve relating to failure due to the collapse mechanism and the other relating to failure due to the blowout mechanism.
2. Any combination of *N* and *FoS* on these curves yield a unique critical stability number (N_c) value, which is a function of the depth ratio and increases nonlinearly as *C/D* increases.
3. For all cases analysed, it was found that the optimum factor of safety occurs at a stability number of zero, where the internal tunnel pressure equal to the overburden stress.
4. In the 2D analysis of tunnel heading in a cohesive soil, the study showed that the failure of the tunnel face propagates to the ground surface and failure extent ratio increases linearly as *C/D* increases.

5. Based on the obtained results, the contour chart has been produced for stability number *N*, which can be used to relate it to the factor of safety (*FoS*) for any *C/D*.
6. The obtained upper and lower bounds results are within a few percentages from each other and compared favourably with those published and those obtained by the finite difference method.
7. Design charts, tables, and equations were produced using dimensionless ratios. It was discovered that one particularly useful practical application of the design charts, tables, and equations is the ability to determine a safe operating range for the pressure that can be applied to the tunnel excavation face by a tunnel boring machine during construction. Examples have been given to illustrate the practicality of the charts.

14.3 Key conclusions in Chapter 5

The following main conclusions were drawn based on the two-dimensional analysis of a single circular tunnel in cohesive undrained soil.

1. The relationship between the factor of safety (*FoS*) and the stability number (*N*), for any given depth ratio (*C/D*), was represented by a pair of identical hyperbolic curves. One curve relating to failure due to the collapse mechanism and the other relating to failure due to the blowout mechanism.
2. For each depth ratio (*C/D*), a unique critical stability number (N_c) was obtained by multiplying the "designed" stability number and the corresponding *FoS*, where N_c is a function of the depth ratio and increases nonlinearly as *C/D* increases.
3. For all scenarios analysed, it was found that the optimum factor of safety occurs at a stability number of zero, where the internal tunnel pressure equal to the overburden stress.
4. In the 2D analysis of circular tunnel in a cohesive soil, the study showed that the failure of the tunnel face propagates to the ground surface, and failure extent ratio increases linearly as *C/D* increases.
5. Based on the obtained *LB* results, the contour chart has been produced for stability number *N*, which can be used to relate it to the factor of safety (*FoS*) for any *C/D*.

6. The obtained upper and lower bounds results are within a few percentages from each other and compared favourably with the finite difference results and the available solutions reported in the literature.

7. It was noted that the stability of 2D circular tunnel is more critical than the stability of a 2D tunnel heading, and this is due to the difference in the geometry of the problems.

8. Design charts, tables, and equations were produced using dimensionless ratios. It was discovered that one particularly useful practical application of the design charts, tables, and equations is the ability to determine a safe operating range for the pressure that can be applied to the tunnel excavation face by a tunnel boring machine during construction. Examples have been given to illustrate the practicality of the charts.

14.4 Key conclusions in Chapter 6

The following main conclusions were drawn based on the three-dimensional analysis of a single circular tunnel heading in cohesive undrained soil.

1. The relationship between the factor of safety (*FoS*) and the stability number (*N*), for any given depth ratio (*C/D*), was represented by a pair of identical hyperbolic curves. One curve relating to failure due to the collapse mechanism and the other relating to failure due to the blowout mechanism.
2. Any combination of *N* and *FoS* on these curves yield a unique critical stability number (N_c) value, which is a function of the depth ratio and increases nonlinearly as *C/D* increases.

3. For all scenarios analysed, it was found that the optimum factor of safety occurs at a stability number of zero, where the internal tunnel pressure equal to the overburden stress.

4. The obtained upper and lower bounds results are within a few percentages from each other and compared favourably with the available solutions reported in the literature.

5. Based on the obtained results, the contour chart has been produced for stability number *N*, which can be used to relate it to the factor of safety (*FoS*) for any *C/D*

and to determine the safe operating pressure range that can be applied to the tunnel face by a tunnel boring machine during construction.

6. The study showed that a significant drop in the stability of the tunnel occurred as the unlined length ratio of the tunnel heading (*P/D*) increased from 0 to 3.

7. A comparison of the 3D *FELA* solutions with those published from experimental and kinematic analysis approaches showed a good agreement among the results, indicating that the used technical tool was capable of accurately analysing 3D circular tunnel heading stability related to the failure mechanism in collapse and blowout.

8. In general, the 3D results are approximately 70% - 80% greater than the 2D ones. The variations are mostly attributed to the differences in the geometry of problems.

9. The study of the failure mechanism indicated a 3D transformation from general failure to local failure occurs once *C/D* is greater than about 2, where it observed that the collapse failure did not propagate through to the ground surface. This finding is useful for the analytical upper bound, which requires a priori assumption in relation to the general form of the failure surface.

14.5 Key conclusions in Chapter 7

The following main conclusions were drawn based on the two-dimensional analysis of twin circular tunnels in cohesive undrained soil.

1. The relationship between the factor of safety (*FoS*) and the stability number (*N*), for any given depth ratio (*C/D*), was represented by a pair of identical hyperbolic curves. One curve relating to failure due to the collapse mechanism and the other relating to failure due to the blowout mechanism.
2. For all scenarios analysed, it was found that the optimum factor of safety occurs at a stability number of zero, where the internal tunnel pressure equal to the overburden stress.
3. It was found that the critical stability number (N_c) is a function of *C*/*D* and *S*/*D*, it increases nonlinearly as *S*/*D* increases. The gradient of the curves decreases as values of *S*/*D* increase and approach to zero when there is no interaction between the tunnels (each tunnel behaves as a single isolated tunnel). The minimum spacing

ratios required to avoid twin tunnel interaction determined for uses in practical designs.

4. The obtained upper and lower bounds results are within a few percentages from each other and compared favourably with the finite difference results and the available solutions in the literature.
5. In comparison with the existing published results, the *UB* and *LB* solutions of this study have been significantly improved owing to the use of adaptive mesh.
6. Design charts, tables, and equations were produced using dimensionless ratios. Examples have been given to illustrate the practicality of the charts.

14.6 Key conclusions in Chapter 8

The following main conclusions were drawn based on the three-dimensional analysis of twin circular tunnels heading in cohesive undrained soil.

1. The relationship between the factor of safety (*FoS*) and the stability number (*N*), for any given depth ratio (*C/D*), was represented by a pair of identical hyperbolic curves. One curve relating to failure due to the collapse mechanism and the other relating to failure due to the blowout mechanism.
2. For all cases analysed, it was found that the optimum factor of safety occurs at a stability number of zero, where the internal tunnel pressure equal to the overburden stress.
3. The critical stability number (N_c) is a function of the depth ratio (*C/D*) and the spacing ratio (*S/D*). N_c increases with the increasing of *C/D*. For each *C/D*, F_c increases nonlinearly as *S/D* increases until it reaches a constant value, which indicates that the twin tunnels stability is unaffected by the tunnel spacing.
4. The obtained upper and lower bounds results are within a few percentages from each other and compared favourably with the available solutions reported in the literature.
5. Based on the observation of the failure mechanism and the N_c results for each increase in the spacing ratio *S*/*D*, an equation was derived to calculate the critical spacing $(S/D)_{min}$ required for a single tunnel response (i.e. without overlapping effects).

6. The study showed that for close twin tunnels, the resulting surface failure area resembles an elliptical shape due to the twin tunnel effects. On the other hand, when there is a large value of *S/D* between the twin tunnels, it is not surprising to see a single tunnel response with a near-circular failure surface.

7. The comparison of the 3D results with some existing 2D solutions shows that the 3D results are significantly greater than the 2D results; the variations are mostly attributed to the differences in the two types of problems. The twin tunnels are assumed to be unlined and infinitely long in the plane strain 2D analysis, while the 3D analysis of twin tunnel is for the close face heading scenario.

14.7 Key conclusions in Chapter 9

The following main conclusions were drawn based on the two-dimensional analysis of tunnel heading in cohesive-frictional drained soil.

1. Unlike the traditional bearing capacity factors (N_c, N_s and N_γ), the tunnel stability factors (F_c, F_s and F_γ) are functions of the soil friction angle ϕ and the depth ratio (*C/D*).

2. The cohesion stability factor (F_c) increases as the depth ratio (*C/D*) increases, but it decreases as the soil friction angle ϕ increases. The F_c curves for various *C/D* merge into a single line at approximately $\phi = 30^\circ$.

3. The surcharge stability factor (F_s) decreases nonlinearly as the soil friction angle ϕ increases. F_s has a maximum value of one at $\phi = 0^\circ$ and a minimum value of zero at approximately $\phi = 35^\circ$ for all depth ratios (*C/D*). In general, the effect of surcharge load (σ_s) diminishes as the soil friction angle increases due to the development of soil arching.

4. The unit weight stability factor (F_γ) increases as the depth ratio (*C/D*) increases. F_γ has a maximum value of (*C/D* + 0.5) at $\phi = 0^\circ$ and decreases dramatically as the soil friction angle ϕ increases due to the development of soil arching. The F_γ curves merge into a single line at approximately $\phi = 25^\circ$.

5. The obtained results are compared and validated by using the finite-difference analysis as well as other available published results in the literature. A number of

examples are illustrated on how to use the factors to estimate tunnel heading pressures.

6. The tunnel stability factors of this study showed a good agreement with the published results despite that available solutions are for high friction angle ($\phi \geq 0^{\circ}$) and shallow depth ratios ($C/D \leq 3$). Also, the critical pressures calculated by using the stability factor of this study showed a good agreement with those produced by using the finite difference method.

14.8 Key conclusions in Chapter 10

The following main conclusions were drawn based on the two-dimensional analysis of a single circular tunnel in cohesive-frictional drained soil.

1. The tunnel stability factors (F_c, F_s and F_γ) are functions of the soil friction angle ϕ and the depth ratio (C/D).
2. The cohesion stability factor (F_c) increases as the depth ratio (C/D) increases, but it decreases as the soil friction angle ϕ increases. The F_c curves merge into a single line at approximately $\phi = 35^{\circ}$, and F_c reaches a minimum value of 1.19 at $\phi = 40^{\circ}$.
3. The surcharge stability factor (F_s) decreases nonlinearly as the soil friction angle ϕ increases. F_s has a maximum value of one at $\phi = 0^{\circ}$ (i.e. undrained clay) and a minimum value of zero at approximately $\phi = 40^{\circ}$. In general, the effect of surcharge load (σ_s) diminishes as the soil friction angle increases due to the development of soil arching.
4. The unit weight stability factor (F_γ) has a maximum value of ($C/D + 0.5$) at $\phi = 0^{\circ}$ (i.e. undrained clay) and decreases dramatically as the soil friction angle ϕ increases due to the development of soil arching. The deeper the tunnel is, the larger the F_γ (unit weight effect) is. Most C/D curves merge into one line at approximately $\phi \geq 25^{\circ}$. For $C/D \leq 2$, the curves merge at $\phi \geq 30^{\circ}$.
5. A comparison of the 2D *FELA* solutions with those published from similar technique showed a good agreement among the results,
6. The comparisons of the stability factors (F_c, F_s and F_γ) between this study and the 2D tunnel heading showed the same trend: i.e. the stability factors decrease with the increasing of the internal friction angle. However, circular tunnel stability factors produce higher internal tunnel pressure than tunnel heading stability

factors, which indicates that the stability of the circular tunnel is more critical than the stability of the tunnel heading.

14.9 Key conclusions in Chapter 11

The following main conclusions were drawn based on the three-dimensional analysis of a single circular tunnel heading in cohesive-frictional drained soil.

1. Unlike the traditional bearing capacity factors (N_c, N_s and N_γ), the tunnel stability factors (F_c, F_s and F_γ) are functions of both the soil friction angle ϕ and the depth ratio (C/D). The equation for estimating the tunnel face support pressures is $\sigma_t = -cF_c + \sigma_s F_s + \gamma D F_\gamma$

2. The cohesion stability factor (F_c) increases as the depth ratio (C/D) increases, but it decreases as the soil friction angle ϕ increases. The F_c curves for various C/D merge into a single line at approximately $\phi = 21^\circ$.

3. The surcharge stability factor (F_s) decreases nonlinearly as the soil friction angle ϕ increases. For all depth ratios (C/D), F_s has a maximum value of one at $\phi = 0^\circ$ and a minimum value of zero when $\phi > 20^\circ$. In general, the effect of surcharge load (σ_s) diminishes as the soil friction angle increases due to the development of soil arching.

4. The soil weight stability factor (F_γ) increases as the depth ratio (C/D) increases. F_γ has a maximum value of (C/D + 0.5) at $\phi = 0^\circ$ and decreases dramatically as the soil friction angle ϕ increases due to the development of soil arching. The F_γ curves merge into a single line at approximately $\phi = 17^\circ$.

5. For all stability factors (F_c, F_s and F_γ) presented in this study, there are good agreements between the upper and the lower bounds results, and the limits of each stability factor are within a few percentages from each other.

6. A comparison of the 3D *FELA* solutions with those published from experimental, kinematic and numerical approaches showed a good agreement in the trend of the curves of stability factors (F_c, F_s and F_γ), despite that the available results are for high friction angle ($\phi \geq 0^\circ$) and shallow depth ratios ($C/D \leq 3$).

7. Comprehensive tables, figures and equations were produced for the stability factors (F_c, F_s and F_γ). Examples were illustrated on how to use these factors to estimate the limit support pressure at collapse.

14.10 Key conclusions in Chapter 12

The following main conclusions were drawn based on the two-dimensional analysis of twin circular tunnels in cohesive-frictional drained soil.

1. A series of parametric studies for a wide range of angles of internal friction (ϕ = 0˚- 40˚), various depth ratios (*C/D*) and spacing ratios (*S/D*) were conducted to calculate the bounds of the stability factors (F_c, F_s and F_γ). An example was illustrated on how to use the factors to estimate limit support pressures. The following conclusions are drawn:

2. For undrained conditions, the stability factor F_c is a function of the depth ratio (*C/D*) and the spacing ratio (*S*/*D*) while the stability factor F_γ is a function of the depth ratio (*C/D*) only. Also, note that the stability factor F_s is independent of (*C/D*) and (*S*/*D*) in undrained condition.

3. It has been observed that the minimum spacing ratio ($(S/D)_{min}$) required to eliminate the interference effect of the twin tunnels increases with the increasing of the depth ratio (*C*/*D*). An equation has been derived for the determination of $(S/D)_{\min}$ for the undrained condition, which is considered as the worst scenario of the whole study.

4. The equation for estimating the tunnel critical support pressures is
   $\sigma_t = -cF_c + \sigma_s F_s + \gamma D F_\gamma$.

5. For drained conditions, these stability factors depend on the soil friction angle (ϕ), the depth ratio (*C/D*) and the spacing ratio (*S*/*D*). Due to the soil arching effects, the factors decrease with the increasing of ϕ. However, for large values of ϕ such as 40 degrees in this study, the stability factors are independent of the depth ratio (*C/D*) and the spacing ratio (*S*/*D*).

6. A comparison of the 2D *FELA* results with those published from 2D numerical and of twin tunnels in undrained clayey soil showed a very good agreement. However, the rigid block mechanism produced results that are approximately 30% - 40%

greater than the current upper and lower bounds. An example was provided to demonstrate the usefulness of the design charts.

14.11 Key conclusions in Chapter 13

The following main conclusions were drawn based on the three-dimensional analysis of twin circular tunnels heading in cohesive-frictional drained soil.

1. A series of parametric studies for a wide range of internal soil friction (ϕ = 0˚-40˚), depth ratios (*C*/*D*) and spacing ratios (*S*/*D*) were conducted to calculate the tunnel stability factors (F_c, F_s and F_γ). An example was illustrated on how to use the factors to estimate limit support pressures.
2. For the undrained condition (ϕ = 0˚), the stability factor F_c is a function of the spacing ratio (*S/D*) and the depth ratio (*C/D*), while the stability factors F_s and F_γ are independent of (*S/D*) and have constant values of F_s = 1 and F_γ = (*C* + 0.5). An equation has been derived for the determination of $(S/D)_{min}$, which is considered as the worst scenario of the whole study.
3. The equation for estimating the tunnel critical support pressures is:

   $$\sigma_t = -c F_c + \sigma_s F_s + \gamma D F_\gamma .$$

4. For drained conditions, the stability factors decrease with the increasing of ϕ. For $\phi \geq 20^\circ$, owing to the developing of soil arching, the stability factors are independent of the depth ratio (*C/D*) and the spacing ratio (*S/D*).
5. A comparison of the 3D *FELA* results with those published from 3D *FELA* of twin tunnels in undrained clayey soil showed a good agreement. However, significant variance between the 3D and 2D results. In general, the 3D stability results are approximately 2.5-3.0 fold higher than those in the 2D analysis. The variations are mostly attributed to the 2D analysis, which is cannot possibly capture the effect of arching in the soil. A practical example was provided to demonstrate the usefulness of the design charts.
6. The study showed that the 3D *FELA* is robust and computationally efficient. It is useful as both upper and lower bounds are calculated, providing great confidence to the end-users in using the tunnel stability factors. The proposed tunnel stability

factor approach to estimate tunnel face pressures, similar to the bearing capacity problem, is convenient and effective for practical engineers.

14.12 Recommendation for future work

When it comes to research, simplifications are always necessary for geotechnical engineering to develop models with confidence. This is mainly due to the uncertainty and complexity of the behaviour of soil and this is especially true with tunnel modelling. Not only is there the geometry, material properties and the complexity of simulating the tunnel construction, but also the possibility of many other complications such as surface surcharges (buildings, roads), sub-surface structures (pipelines, piles, other tunnels), and complex geology (layers).

With the recent advancements of numerical modelling, the accuracy of construction-related simulation has improved greatly. However, parametric studies are still important in the study to appreciate the response to changing variables. Using a wide range of practical parameters, it does provide insight into the likely behaviour. It also allows the development of some useful and simple design tools for preliminary work.

Following the research outcome in this study, some important areas have been identified for future investigation. The following recommendations for future work are presented.

1. Using the proposed Broms and Bennermarks' original stability number approach, it is recommended to extend the investigation into the undrained stability of other geotechnical stability problems such as trapdoor, a sinkhole with circular and square openings, square tunnel, rectangular tunnel, launch wall, earth pressure problems, and undrained stability of braced excavation.
2. Using the proposed stability factor approach, future work may include the investigation many other drained stability problems such as trapdoor, a sinkhole with circular and square openings, square tunnel, rectangular tunnel, launch wall, earth pressure problems, and undrained stability of braced excavation.
3. It is recommended to expand the current investigations to large-diameter tunnels (D > 10 m), where the earth pressure distribution is highly nonlinear.

4. It is recommended to expand the current investigation of tunnel stability to nonhomogeneous soil such as multi-layered formations and the increasing shear strength of the soil with depth.
5. It is recommended to expand the current study to the probabilistic analysis with special consideration to spatial variability of soil.

REFERENCES

Abbo, AJ, Wilson, DW, Sloan, SW & Lyamin, AV 2013, 'Undrained stability of wide rectangular tunnels', *Computers and Geotechnics*, vol. 53, pp. 46-59.

Anagnostou, G & Kovári, K 1996, 'Face stability conditions with earth-pressure-balanced shields', *Tunnelling and Underground Space Technology*, vol. 11, no. 2, pp. 165-73.

Anderheggen, E & Knöpfel, H 1972, 'Finite element limit analysis using linear programming', *International Journal of Solids and Structures*, vol. 8, no. 12, pp. 1413-31.

Arai, K & Tagyo, K 1985, 'Limit analysis of geotechnical problems by applying lower-bound theorem', *Soils and Foundations*, vol. 25, no. 4, pp. 37-48.

Assadi, A & Sloan, SW 1991, 'Undrained stability of shallow square tunnel', *Journal of geotechnical engineering*, vol. 117, no. 8, pp. 1152-73.

Atkinson, JH & Cairncross, AM 1973, 'Collapse of a shallow tunnel in a Mohr-Coulomb material', in *Proceedings of the Symposium on the Role of Plasticity in Soil Mechanics*, Cambridge, UK, pp. 202-6.

Atkinson, JH & Potts, DM 1977, 'Stability of a shallow circular tunnel in cohesionless soil', *Geotechnique*, vol. 27, no. 2, pp. 203-15.

Atkinson, JH & Mair, RJ 1981, 'Soil mechanics aspects of soft ground tunnelling', *Ground Engineering*, vol. 14, no. 5, pp. 20-8.

Augarde, CE, Lyamin, AV & Sloan, SW 2003, 'Stability of an undrained plane strain heading revisited', *Computers and Geotechnics*, vol. 30, no. 5, pp. 419-30.

Basudhar, P, Valsangkar, A & Madhav, M 1979, 'Optimal lower bound of passive earth pressure using finite elements and non-linear programming', *International Journal for Numerical and Analytical Methods in Geomechanics*, vol. 3, no. 4, pp. 367-79.

Belytschko, T & Hodge, PG 1970, 'Plane stress limit analysis by finite elements', *Journal of the Engineering Mechanics Division*, vol. 96, no. 6, pp. 931-44.

Biron, A & Charleux, G 1972, 'Limit analysis of axisymmetric pressure vessel intersections of arbitrary shape', *International Journal of Mechanical Sciences*, vol. 14, no. 1, pp. 25-41.

Bishop, A 1955, 'The use of the slip circle in the stability analysis of slopes', *Geotechnique*, vol. 93, pp. 7-17.

Bjerrum, L & Eide, O 1956, 'Stability of strutted excavations in clay', *Geotechnique*, vol. 6, no. 1, pp. 32-47.

Bottero, A, Negre, R, Pastor, J & Turgeman, S 1980, 'Finite element method and limit analysis theory for soil mechanics problems', *Computer Methods in Applied Mechanics and Engineering*, vol. 22, no. 1, pp. 131-49.

Broms, BB & Bennermark, H 1967, 'Stability of clay at vertical openings', *Journal of the Soil Mechanic and Foundations Division, Proceedings of the American Society of Civil Engineers*, vol. 93, pp. 71- 94.

Capsoni, A & Corradi, L 1997, 'A finite element formulation of the rigid–plastic limit analysis problem', *International Journal for Numerical Methods in Engineering*, vol. 40, no. 11, pp. 2063-86.

Chakeri, H, Hasanpour, R, Hindistan, MA & Ünver, B 2011, 'Analysis of interaction between tunnels in soft ground by 3D numerical modeling', *Bulletin of Engineering Geology and the Environment*, vol. 70, no. 3, pp. 439-48.

Chambon, P & Corte, J-F 1994, 'Shallow tunnels in cohesionless soil: stability of tunnel face', *Journal of geotechnical engineering*, vol. 120, no. 7, pp. 1148-65.

Chehade, FH & Shahrour, I 2008, 'Numerical analysis of the interaction between twin-tunnels: Influence of the relative position and construction procedure', *Tunnelling and Underground Space Technology*, vol. 23, no. 2, pp. 210-4.

Chen, RP, Li, J, Kong, LG & Tang, LJ 2013, 'Experimental study on face instability of shield tunnel in sand', *Tunnelling and Underground Space Technology*, vol. 33, pp. 12-21.

Ciria, HS 2004, 'Computation of upper and lower bounds in limit analysis using second-order cone programming and mesh adaptivity', Massachusetts Institute of Technology.

Davis, EH, Gunn, MJ, Mair, RJ & Seneviratine, HN 1980, 'The stability of shallow tunnels and underground openings in cohesive material', *Geotechnique*, vol. 30, no. 4, pp. 397-416.

FLAC 2D 2003, *Fast Lagrangian Analysis of Continua, Itasca Consulting Group*, Minneapolis, Minnesota, USA.

Fletcher, R & Reeves, CM 1964, 'Function minimization by conjugate gradients', *The computer journal*, vol. 7, no. 2, pp. 149-54.

Fortin, M & Glowinski, R 1983, *Augmented Lagrangian methods: applications to the numerical solution of boundary-value problems*, Elsevier.

Ghaboussi, J & Ranken, RE 1977, 'Interaction between two parallel tunnels', *International Journal for Numerical and Analytical Methods in Geomechanics*, vol. 1, no. 1, pp. 75-103.

Griffiths, D & Lane, P 1999, 'Slope stability analysis by finite elements', *Geotechnique*, vol. 49, no. 3, pp. 387-403.

Guglielmetti, V, Grasso, P, Mahtab, A & Xu, S 2008, *Mechanized tunnelling in urban areas: design methodology and construction control*, CRC Press.

Hodge, PG & Belytschko, T 1968, 'Numerical methods for the limit analysis of plates'.

Horn, N 1961, 'Horizontal earth pressure on the vertical surfaces of the tunnel tubes', in *Proceedings of the National Conference of the Hungarian Civil Engineering Industry*, Budapest, pp. 7–16 (in German).

Huang, M, Wang, H, Yu, J & Tang, Z 2019, 'Undrained stability analysis of a plane strain circular tunnel using streamline velocity fields', *International Journal of Geomechanics*, vol. 19, no. 5, p. 06019006.

Huh, H & Yang, WH 1991, 'A general algorithm for limit solutions of plane stress problems', *Int. J. Solids Struct*. 28, No. 6, 727–738.

Jiang, G-L 1994, 'Regularized method in limit analysis', *Journal of engineering mechanics*, vol. 120, no. 6, pp. 1179-97.

Jiang, GL 1995, 'Non-linear finite element formulation of kinematic limit analysis', *International Journal for Numerical Methods in Engineering*, vol. 38, no. 16, pp. 2775-807.

Kavlie, D & Moe, J 1971, 'Automated design of frame structures', *Journal of the Structural Division*, vol. 97, no. 1, pp. 33-62.

Keawsawasvong, S & Ukritchon, B 2017, 'Undrained stability of an active planar trapdoor in non-homogeneous clays with a linear increase of strength with depth', *Computers and Geotechnics*, vol. 81, pp. 284-93.

Kim, SH, Burd, HJ & Milligan, GWE 1998, 'Model testing of closely spaced tunnels in clay', *Geotechnique*, vol. 48, no. 3, pp. 375-88.

Kimura, T & Mair, R 1981, 'Centrifugal testing of model tunnels in soft clay', in *Proceedings of the 10th International Conference on Soil Mechanics and Foundation Engineering*, Stockholm, pp. 319-22.

Kirsch, A 2010, 'Experimental investigation of the face stability of shallow tunnels in sand', *Acta Geotechnica*, vol. 5, no. 1, pp. 43-62.

Klar, A, Osman, AS & Bolton, M 2007, '2D and 3D upper bound solutions for tunnel excavation using 'elastic'flow fields', *International Journal for Numerical and Analytical Methods in Geomechanics*, vol. 31, no. 12, pp. 1367-74.

Krabbenhoft, K & Damkilde, L 2003, 'A general non-linear optimization algorithm for lower bound limit analysis', *International Journal for Numerical Methods in Engineering*, vol. 56, no. 2, pp. 165-84.

Krabbenhoft, K & Lyamin, AV 2015, 'Strength reduction finite-element limit analysis', *Géotechnique Letters*, vol. 5, no. 4, pp. 250-3.

Krabbenhøft, K, Lyamin, AV & Sloan, SW 2007, 'Formulation and solution of some plasticity problems as conic programs', *International Journal of Solids and Structures*, vol. 44, no. 5, pp. 1533-49.

Krabbenhøft, K, Lyamin, AV & Sloan, SW 2008, 'Three-dimensional Mohr–Coulomb limit analysis using semidefinite programming', *Communications in Numerical Methods in Engineering*, vol. 24, no. 11, pp. 1107-19.

Krabbenhøft, K, Lyamin, AV, Hjiaj, M & Sloan, SW 2005, 'A new discontinuous upper bound limit analysis formulation', *International Journal for Numerical Methods in Engineering*, vol. 63, no. 7, pp. 1069-88.

Leca, E & Dormieux, L 1990, 'Upper and lower bound solutions for the face stability of shallow circular tunnels in frictional material', *Geotechnique*, vol. 40, no. 4, pp. 581-606.

Lee, CJ, Wu, BR, Chen, HT & Chiang, KH 2006, 'Tunnel stability and arching effects during tunneling in soft clayey soil', *Tunnelling and Underground Space Technology*, vol. 21, no. 2, pp. 119-32.

Liu, Y, Cen, Z & Xu, B 1995, 'A numerical method for plastic limit analysis of 3-D structures', *International Journal of Solids and Structures*, vol. 32, no. 12, pp. 1645-58.

Lyamin, A 1999, 'Three-dimensional lower bound limit analysis using nonlinear programming. PhD thesis', Department of Civil, Surveying and Environmental Engineering, University of Newcastle.

Lyamin, AV & Sloan, SW 2000, 'Stability of a plane strain circular tunnel in a cohesive-frictional soil', in *Developments in theoretical geomechanics : proceedings of the Booker Memorial Symposium*, Sydney, N.S.W., Australia, pp. 139-54.

Lyamin, AV & Sloan, SW 2002a, 'Upper bound limit analysis using linear finite elements and non-linear programming', *International Journal for Numerical and Analytical Methods in Geomechanics*, vol. 26, no. 2, pp. 181-216.

Lyamin, AV & Sloan, SW 2002b, 'Lower bound limit analysis using non-linear programming', *International Journal for Numerical Methods in Engineering*, vol. 55, no. 5, pp. 573-611.

Lyamin, AV, Jack, DL & Sloan, SW 2001, 'Collapse analysis of square tunnels in cohesive–frictional soils', in *Computational Mechanics–New Frontiers for the New Millennium*, Elsevier, pp. 405-14.

Lyamin, AV, Sloan, SW, Krabbenhøft, K & Hjiaj, M 2005, 'Lower bound limit analysis with adaptive remeshing', *International Journal for Numerical Methods in Engineering*, vol. 63, no. 14, pp. 1961-74.

Lysmer, J 1970, 'Limit analysis of plane problems in soil mechanics', *Journal of Soil Mechanics & Foundations Division, ASCE*, vol. 96, no. SM 4, pp. 1311-34.

Maier, G, Zavelani-Rossi, A & Benedetti, D 1972, 'A finite element approach to optimal design of plastic structures in plane stress', *International Journal for Numerical Methods in Engineering*, vol. 4, no. 4, pp. 455-73.

Mair, RJ 1979, 'Centrifuge modelling of tunnel construction in soft clay', *Ph. D Thesis, University of Cambridge*.

Makrodimopoulos, A & Martin, C 2006, 'Lower bound limit analysis of cohesive-frictional materials using second-order cone programming', *International Journal for Numerical Methods in Engineering*, vol. 66, no. 4, pp. 604-34.

Matsui, T & San, K-C 1992, 'Finite element slope stability analysis by shear strength reduction technique', *Soils and Foundations*, vol. 32, no. 1, pp. 59-70.

Michalowski, RL 2002, 'Stability charts for uniform slopes', *Journal of Geotechnical and Geoenvironmental Engineering*, vol. 128, no. 4, pp. 351-5.

Mirhabibi, A & Soroush, A 2012, 'Effects of surface buildings on twin tunnelling-induced ground settlements', *Tunnelling and Underground Space Technology*, vol. 29, pp. 40-51.

Mollon, G, Dias, D & Soubra, A-H 2009, 'Probabilistic analysis and design of circular tunnels against face stability', *International Journal of Geomechanics*, vol. 9, no. 6, pp. 237-49.

Mollon, G, Dias, D & Soubra, A-H 2010, 'Face stability analysis of circular tunnels driven by a pressurized shield', *Journal of Geotechnical and Geoenvironmental Engineering*, vol. 136, no. 1, pp. 215-29.

Mollon, G, Dias, D & Soubra, AH 2011, 'Rotational failure mechanisms for the face stability analysis of tunnels driven by a pressurized shield', *International Journal for Numerical and Analytical Methods in Geomechanics*, vol. 35, no. 12, pp. 1363-88.

Mollon, G, Dias, D & Soubra, AH 2013, 'Continuous velocity fields for collapse and blowout of a pressurized tunnel face in purely cohesive soil', *International Journal for Numerical and Analytical Methods in Geomechanics*, vol. 37, no. 13, pp. 2061-83.

Mühlhaus, HB 1985, 'Lower bound solutions for circular tunnels in two and three dimensions', *Rock Mechanics and Rock Engineering*, vol. 18, no. 1, pp. 37-52.

Narasimhan, T & Witherspoon, P 1976, 'An integrated finite difference method for analyzing fluid flow in porous media', *Water Resources Research*, vol. 12, no. 1, pp. 57-64.

Naylor, D 1982, 'Finite elements and slope stability', in *Numerical methods in geomechanics*, Springer, pp. 229-44.

Ng, CW, Lee, KM & Tang, DK 2004, 'Three-dimensional numerical investigations of new Austrian tunnelling method (NATM) twin tunnel interactions', *Canadian Geotechnical Journal*, vol. 41, no. 3, pp. 523-39.

Nguyen, HS, Trapletti, M & Ransart, D 1978, 'Quasi-lower bounds and upper bounds for the buckling pressure of shells of revolution by the finite element method and by nonlinear programming', *International Journal of Non-Linear Mechanics*, vol. 13, no. 2, pp. 79-102.

OptumCE 2017, *OptumG2. Copenhagen, Denmark: Optum Computational Engineering. See https://optumce.com/*.

OptumCE 2018, *OptumG3. Copenhagen, Denmark: Optum Computational Engineering. See https://optumce.com/*.

Osman, AS 2010, 'Stability of unlined twin tunnels in undrained clay', *Tunnelling and Underground Space Technology*, vol. 25, no. 3, pp. 290-6.

Osman, AS, Mair, RJ & Bolton, MD 2006, 'On the kinematics of 2D tunnel collapse in undrained clay', *Géotechnique.*, vol. 56, no. 9, pp. 585-95.

Pastor, J 1978, 'Analyse limit determination numerique de solutions statistique completes, Application au talus vertical', *J. de Mechanique Appliquee*, vol. 2, pp. 167-96.

Pastor, J & Turgeman, S 1976, 'Mise en oeuvre numérique des méthodes de l'analyse limite pour les matériaux de von Mises et de Coulomb standards en déformation plane', *Mechanics Research Communications*, vol. 3, no. 6, pp. 469-74.

Pastor, J & Turgeman, S 1982, 'Limit analysis in axisymmetrical problems: Numerical determination of complete statical solutions', *International Journal of Mechanical Sciences*, vol. 24, no. 2, pp. 95-117.

Pelizza, S 1996, 'Interview with ITA President', *Tunn. Undergr. Sp. Tech*, vol. 11, no. 2, pp. 135-9.

Qarmout, M, König, D, Gussmann, P, Thewes, M & Schanz, T 2019, 'Tunnel face stability analysis using Kinematical Element Method', *Tunnelling and Underground Space Technology*, vol. 85, pp. 354-67.

Sahoo, JP & Kumar, J 2013, 'Stability of long unsupported twin circular tunnels in soils', *Tunnelling and Underground Space Technology*, vol. 38, pp. 326-35.

Schofield, AN 1980, 'Cambridge geotechnical centrifuge operations', *Geotechnique*, vol. 30, no. 3, pp. 227-68.

Shiau, J & Kemp, R 2013, 'Developing a numerical model for the stability design of tunnel heading', in *Proceedings of Third International Conference on Geotechnique, Construction Materials, and Environment,*, Nagoya- Japan.

Shiau, J & Al-Asadi, F 2018, 'Revisiting Broms and Bennermarks' original stability number for tunnel headings', *Géotechnique Letters*, vol. 8, no. 4, pp. 310-315.

Shiau, J & Hassan, MM 2019, 'Undrained Stability of Active and Passive Trapdoors', Geotechnical Research, pp. 1-9.

Shiau, J & Sams, M 2019, 'Relating volume loss and greenfield settlement', *Tunnelling and Underground Space Technology*, vol. 83, pp. 145-52.

Shiau, J & Al-Asadi, F 2020a, 'Three-Dimensional Heading Stability of Twin Circular Tunnels', Geotechnical and Geological Engineering, pp. 1-16.

Shiau, J & Al-Asadi, F 2020b, 'Two-dimensional tunnel heading stability factors Fc, Fs and Fγ', Tunnelling and Underground Space Technology, vol. 97, p. 103293.

Shiau, J & Al-Asadi, F 2020c, 'Determination of critical tunnel heading pressures using stability factors', Computers and Geotechnics, vol. 119, p. 103345.

Shiau, J & Al-Asadi, F 2020d, 'Three-Dimensional Analysis of Circular Tunnel Headings using Broms and Bennermarks' Original Stability Number' International Journal of Geomechanics. https://doi.org/10.1061/(ASCE)GM.1943-5622.0001734

Shiau, J & Al-Asadi, F 2020e, "Stability Analysis of Twin Circular Tunnels Using Shear Strength Reduction Method", *Géotechnique Letters*, vol. 10, no. 2, pp. 1-9.

Shiau, J & Al-Asadi, F 2020f, 'Twin tunnels stability factors F_c, F_s and F_γ' *Geotechnical and Geological Engineering* (Under review; submitted on 25 February 2020).

Shiau, J, Lamb, B & Sams, M 2016, 'The use of sinkhole models in advanced geotechnical engineering teaching', International Journal of Geomate, vol. 10, no. 2, pp. 1718-24.

Shiau, J, Sams, M & Lamb, B 2016, 'Introducing advanced topics in geotechnical engineering teaching–Tunnel modelling', *International Journal of Geomate*, vol. 10, no. 1, pp. 1698-705.

Shiau, J, Lamb, B, Sams, M & Lobwein, J 2017, 'Stability charts for unsupported circular tunnels in cohesive soils', *International Journal*, vol. 13, no. 39, pp. 95-102.

Shiau, J, Sams, M, Al-Asadi, F & Mirza Hassan, M 2018, 'Stability charts for unsupported plane strain tunnel headings in homogeneous undrained clay', *International Journal of Geomate*, vol. 14, no. 41, pp. 19-26.

Shiau, JS, Lyamin, AV & Sloan, SW 2003, 'Bearing capacity of a sand layer on clay by finite element limit analysis', *Canadian Geotechnical Journal*, vol. 40, no. 5, pp. 900-15.

Shiau, JS, Augarde, CE, Lyamin, AV & Sloan, SW 2008, 'Finite element limit analysis of passive earth resistance in cohesionless soils', *Soils and Foundations*, vol. 48, no. 6, pp. 843-50.

Shiau, JS, Merifield, RS, Lyamin, AV & Sloan, SW 2011, 'Undrained stability of footings on slopes', *International Journal of Geomechanics*, vol. 11, no. 5, pp. 381-90.

Shiau, JS, Sams, MS, Zhang, J & Kemp, RJ 2014, 'Settlement analyses of underground circular tunneling in soft clay', in *In Geotechnical Aspects of Underground Construction in Soft Ground*, Taylor & Francis (CRC Press)/Balkema, Seoul, pp. 347-52.

Sloan, SW 1988a, 'A steepest edge active set algorithm for solving sparse linear programming problems', *International Journal for Numerical Methods in Engineering*, vol. 26, no. 12, pp. 2671-85.

Sloan, SW 1988b, 'Lower bound limit analysis using finite elements and linear programming', *International Journal for Numerical and Analytical Methods in Geomechanics*, vol. 12, no. 1, pp. 61-77.

Sloan, SW 1989, 'Upper bound limit analysis using finite elements and linear programming', *International Journal for Numerical and Analytical Methods in Geomechanics*, vol. 13, no. 3, pp. 263-82.

Sloan, SW 2013, 'Geotechnical stability analysis', *Geotechnique*, vol. 63, no. 7, pp. 531-72.

Sloan, SW & Assadi, A 1991, 'Undrained stability of a square tunnel in a soil whose strength increases linearly with depth', *Computers and Geotechnics*, vol. 12, no. 4, pp. 321-46.

Sloan, SW & Assadi, A 1992, 'Stability of shallow tunnels in soft ground', in *proceedings of the Wroth Memorial Symposiumon on Predictive Soil Mechanics, Oxford, UK 27-29 July 1992. Edited by G.T. Houlsby and A.N. Schofield*, Thomas Telford Ltd., London, pp. 644-63.

Sloan, SW & Assadi, A 1994, 'Undrained stability of a plane strain heading', *Canadian Geotechnical Journal*, vol. 31, no. 3, pp. 443-50.

Sloan, SW & Kleeman, PW 1995, 'Upper bound limit analysis using discontinuous velocity fields', *Computer Methods in Applied Mechanics and Engineering*, vol. 127, no. 1-4, pp. 293-314.

Soubra, A-H 2000, 'Three-dimensional face stability analysis of shallow circular tunnels', in *Isrm International Symposium*, International Society for Rock Mechanics.

Soubra, A-H 2002, 'Kinematical approach to the face stability analysis of shallow circular tunnels', in *Proceedings of the Eight International Symposium on Plasticity*, Canada, British Columbia, pp. 443–5.

Subrin, D & Wong, H 2002, 'Tunnel face stability in frictional material: a new 3D failure mechanism', *Comptes Rendus Mecanique*, vol. 330, no. 7, pp. 513-9.

Takano, D, Otani, J, Nagatani, H & Mukunoki, T 2006, 'Application of x-ray CT on boundary value problems in geotechnical engineering: research on tunnel face failure', in *GeoCongress 2006: Geotechnical Engineering in the Information Technology Age*, pp. 1-6.

Thakur, P 2014, 'Coal seam degasification', in *Coal Bed Methane*, Elsevier, pp. 155-75.

Ugai, K & Leshchinsky, D 1995, 'Three-dimensional limit equilibrium and finite element analyses: a comparison of results', *Soils and Foundations*, vol. 35, no. 4, pp. 1-7.

Ukritchon, B & Keawsawasvong, S 2017, 'Design equations for undrained stability of opening in underground walls', *Tunnelling and Underground Space Technology*, vol. 70, pp. 214-20.

Ukritchon, B, Whittle, AJ & Sloan, SW 2003, 'Undrained stability of braced excavations in clay', *Journal of Geotechnical and Geoenvironmental Engineering*, vol. 129, no. 8, pp. 738-55.

Ukritchon, B, Yingchaloenkitkhajorn, K & Keawsawasvong, S 2017, 'Three-dimensional undrained tunnel face stability in clay with a linearly increasing shear strength with depth', *Computers and Geotechnics*, vol. 88, pp. 146-51.

Ukritchon, B, Keawsawasvong, S & Yingchaloenkitkhajorn, K 2017, 'Undrained face stability of tunnels in Bangkok subsoils', *International Journal of Geotechnical Engineering*, vol. 11, no. 3, pp. 262-77.

Vermeer, PA, Ruse, N & Marcher, T 2002, 'Tunnel heading stability in drained ground', *Felsbau*, vol. 20, no. 6, pp. 8-18.

Wang, T, Lv, Q, Zhou, Y, Li, Y, Jiang, C & Yang, F 2011, 'Analysis on deformation and failure of surface borehole and casing due to coal extraction', in *The Second*

International FLAC/DEM Symposium on Numerical Modeling, 14–16 February 2011, Melborne, Victoria, Australia.

Wilson, DW, Abbo, AJ, Sloan, SW & Lyamin, AV 2011, 'Undrained stability of a circular tunnel where the shear strength increases linearly with depth', *Canadian Geotechnical Journal*, vol. 48, no. 9, pp. 1328-42.

Wilson, DW, Abbo, AJ, Sloan, SW & Lyamin, AV 2013, 'Undrained stability of a square tunnel where the shear strength increases linearly with depth', *Computers and Geotechnics*, vol. 49, pp. 314-25.

Wilson, DW, Abbo, AJ, Sloan, SW & Lyamin, AV 2014, 'Undrained Stability of Dual Circular Tunnels', *International Journal of Geomechanics*, vol. 14, no. 1, pp. 69-79.

Wilson, DW, Abbo, AJ, Sloan, SW & Lyamin, AV 2015, 'Undrained stability of dual square tunnels', *Acta Geotechnica*, vol. 10, no. 5, pp. 665-82.

Wu, BR & Lee, CJ 2003, 'Ground movements and collapse mechanisms induced by tunneling in clayey soil', *International Journal of Physical Modelling in Geotechnics*, vol. 3, no. 4, pp. 15-29.

Xie, J, Gunn, MJ & Rahim, A 2004, 'Collapse analysis for two parallel circular tunnels with different diameters in soil', in *Numerical Models in Geomechanics*, CRC Press, Ottawa, Canada, pp. 421-6.

Yamamoto, K, Lyamin, AV, Wilson, DW, Sloan, SW & Abbo, AJ 2013, 'Stability of dual circular tunnels in cohesive-frictional soil subjected to surcharge loading', *Computers and Geotechnics*, vol. 50, pp. 41-54.

Yamamoto, K, Lyamin, AV, Wilson, DW, Sloan, SW & Abbo, AJ 2014, 'Stability of dual square tunnels in cohesive-frictional soil subjected to surcharge loading', *Canadian Geotechnical Journal*, vol. 51, no. 8, pp. 829-43.

Yang, F & Yang, JS 2010, 'Stability of shallow tunnel using rigid blocks and finite-element upper bound solutions', *International Journal of Geomechanics*, vol. 10, no. 6, pp. 242-7.

Yang, F, Zhang, J, Yang, J, Zhao, L & Zheng, X 2015, 'Stability analysis of unlined elliptical tunnel using finite element upper-bound method with rigid translatory moving elements', *Tunnelling and Underground Space Technology*, vol. 50, pp. 13-22.

Zeinkiewicz, O, Humpheson, C & Lewis, R 1975, 'Associated and non-associated visco-plasticity in soils mechanics', *Journal of Geotechnique*, vol. 25, no. 5, pp. 671-89.

Zhang, C, Han, K & Zhang, D 2015, 'Face stability analysis of shallow circular tunnels in cohesive–frictional soils', *Tunnelling and Underground Space Technology*, vol. 50, pp. 345-57.

Zhang, F, Gao, YF, Wu, YX & Zhang, N 2018, 'Upper-bound solutions for face stability of circular tunnels in undrained clays', *Geotechnique*, vol. 68, no. 1, pp. 76-85.

Zheng, Y-R, Zhao, S-Y, Kong, W-X & Deng, C-J 2005, 'Geotechnical engineering limit analysis using finite element method', *Yantu Lixue(Rock Soil Mech.)*, vol. 26, no. 1, pp. 163-8.

Zouain, N, Herskovits, J, Borges, LA & Feijóo, RA 1993, 'An iterative algorithm for limit analysis with nonlinear yield functions', *International Journal of Solids and Structures*, vol. 30, no. 10, pp. 1397-417.